Generation, Propagation and Dissipation of Second Mode Internal Solitary Waves

---

A thesis
submitted in partial fulfillment
of the requirements for the Degree
of
Doctor of Philosophy in Civil Engineering
at the
University of Canterbury
by
Nathan Philip Schmidt

University of Canterbury
Christchurch, New Zealand
1998

ABSTRACT

The behaviour of large amplitude second mode internal solitary waves has been investigated. Waves were generated in the laboratory by a variety of methods and were observed using dye and particle visualisation techniques. Observations of wave generation, propagation and dissipation were used to develop new theories about the behaviour of such waves.

Waves were generated by exchange flow, forced inflow and gravity collapse. The generation sequence was found to be similar for all three methods, with the gravity collapse technique allowing the most rapid and repeatable generation of second mode waves.

External propagation characteristics (wave celerity and geometry) were investigated using waves of dimensionless amplitude up to $a/h = 11.6$. It was found that wave geometry was described well by existing theory over the entire range of amplitudes, but the existing wave celerity relationships were only accurate up to $a/h \cong 3$. A new analytical approach produced a relationship which is applicable to all large amplitude waves.

Internal propagation characteristics (internal circulation, entrainment and mass transport) were investigated using both particle visualisation and laser induced fluorescence techniques. It was found that internal circulation differs from the pattern suggested by existing numerical models. The interior of the wave is made up of an assemblage of vortices, symmetrical about the wave centreline, with a net flow rearwards along the centreline. These vortices are seen to play an important role in the entrainment of fluid into the wave. Entrainment appears to be caused by a non-symmetric Holmboe instability at the wave boundary. The entrainment into and expulsion of fluid from the wave results in the flushing of fluid from the wave. Measurements indicate that the rate of flushing is linearly proportional to distance and Richardson number during the primary flushing phase (from 100% to 10% tracer concentration). During the secondary flushing phase (from 10% to 1% tracer

concentration) the flushing rate is lower but also linearly proportional to distance and Richardson number.

Wave dissipation experiments indicate that wave amplitude decay rate is constant for any wave but varies with densimetric factor. Waves with larger densimetric factors decay at a slower rate. An expression for wave energy was formulated and the wave energy decay rate was examined. It was found that the radiation of first mode waves does not provide a significant contribution to wave decay. Wall shear was quantified and found to vary with flume width. In this study it was responsible for approximately 9% of the dissipation rate. The remaining dissipation is due to fluid drag (interfacial shear, pressure drag and mixing) and was quantified by a drag coefficient. The drag coefficient varies with the inverse of the cube root of densimetric factor.

ACKNOWLEDGMENTS

I would like to offer sincerest thanks to my advisor, Dr. Robert Spigel, for his support, guidance and understanding over the course of this work. I would also like to offer thanks to and acknowledge the input of Professor Emeritus Ian Wood, who was always willing to provide comments and support, Professor David Wilkinson, who set the groundwork for the study, and Dr. Bruce Hunt, who also provided a significant contribution to the study. Substantial thanks are also due to Ian Sheppard and Alan Poynter for their efforts and advice in the fluid mechanics laboratory.

I would like to thank the New Zealand Vice-Chancellor's Committee, the New Zealand Ministry of Foreign Affairs and Trade, and the Association of Universities and Colleges of Canada for selecting me for and funding the Commonwealth Scholarship which supported me over the course of this work.

On a more personal note, I would like to thank my fellow postgraduate students, for the friendship and support that I have received over the years. In particular, I would like to thank Dr. Wayne Munro and Dr. David Papps for their friendship and their help in settling into living in a new country and attending a new university. Last, but certainly not least, I would like to thank Alastair Chambers and Nigel Dixon for their friendship and company throughout our rides and for keeping me out of trouble but close enough to it that life stayed interesting.

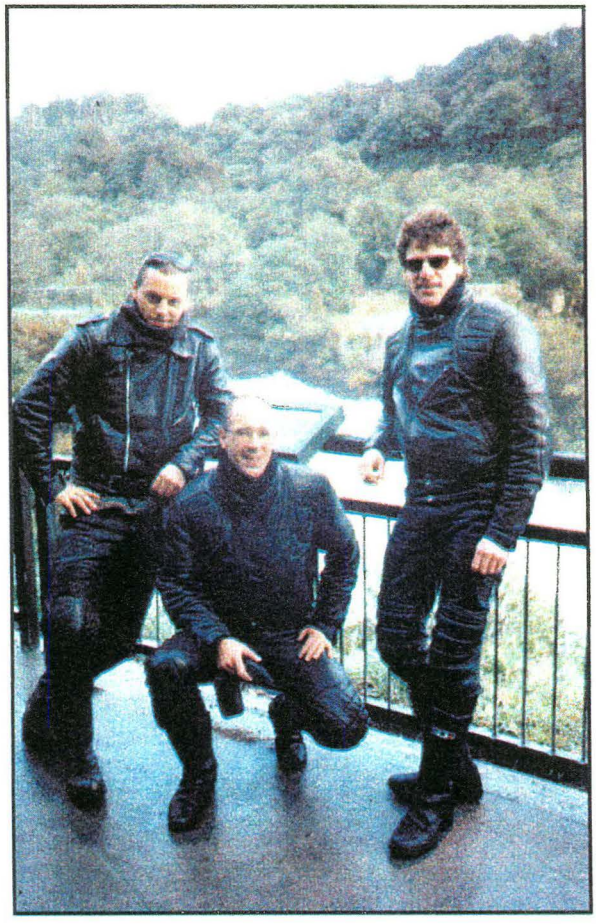

wish I was ocean size
they cannot move you
no one tries

i've seen the ocean
break on the shore
come together with no harm done

- Perry Farrell, *Ocean Size*

The whole design of the river seems disconcerted. First it runs smoothly, as if meaning to go down the descent as things were ordered; then it angles about and faces the shores; nor are there places wanting where it looks backward, as if unwilling to leave the wilderness, to mingle with the salt. Ay, lady, the fine cobweb-looking cloth you wear at your throat is coarse, and like a fish-net, to little spots I can show you, where the river fabricates all sorts of images, as if, having broke loose from order, it would try its hand at everything. And yet what does it amount to? After that water has been suffered to have its will for a time, like a headstrong man, it is gathered together by the Hand that made it, and a few rods below you may see it all flowing on steadily towards the sea, as was fore-ordained from the first foundation of the 'arth!

- James Fenimore Cooper, *The Last of the Mohicans*

well I go to the river
to soothe my mind
to ponder over
the crazy days in my life
just sit and watch the river flow

- Natalie Merchant, *Where I Go*

TABLE OF CONTENTS

LIST OF FIGURES

LIST OF TABLES

NOMENCLATURE

Symbols representing specific parameters are noted here. The parameter dimensions are included in parentheses (F = Force, M = mass, L = length, T = time, Θ = temperature)

Chapter 1

h Half-thickness of the pycnocline (L)
H Depth of homogeneous fluid layer (L)
λ Wavelength (L)
ρ_1 Density of upper fluid layer (M/L^3)
ρ_3 Density of lower fluid layer (M/L^3)

Chapter 2

a Wave amplitude (L)
$\bar{a}$ Average of upper and lower wave amplitudes (L)
A Dimensionless wave amplitude in Davis & Acrivos analysis (-)
c Wave celerity (L/T)
c_0 Celerity of an infinitesimal first mode solitary wave (L/T)
F Density function (M/L^3)
g Acceleration due to gravity (L/T^2)
G Function of upstream velocity distribution in Long's equation (T^{-1})
h Half-thickness of the pycnocline (L)
H Depth of homogeneous fluid layer (L)
J Richardson number (-)
k Wave number (L^{-1})
L Function in Long's equation analysis (ML/T)
p Pressure (F/L^2)
Re_h Interfacial Reynolds number (-)
Re_w Wall Reynolds number (-)
t Time (T)
u Fluid velocity in x-direction (L/T)
u_{max} Maximum fluid velocity within wave (L/T)
v Fluid velocity in y-direction (L/T)
w Width of flume (L)
x Lengthwise position ordinate, positive in direction of wave movement (L)
x^* Dimensionless x in Tung, Chan & Kubota analysis (-)
y Vertical position ordinate, positive upwards (L)
y^* Dimensionless y in Tung, Chan & Kubota analysis (-)
β Dispersion term coefficient (L^2)
δ Finite depth factor in wave celerity equation (-)
ε Perturbation factor (-)
ϕ Quantity in Benjamin analysis (-)

ϕ Streamline perturbation in Davis & Acrivos analysis (-)
ϕ^* Streamline perturbation in Tung, Chan & Kubota analysis (-)
γ Dispersion term coefficient (L)
Λ Dimensionless wave celerity (-)
η Undisturbed streamline height in Benjamin analysis (L)
κ Factor in Benjamin analysis (-)
λ Wavelength (L)
$\overline{\lambda}$ Average of upper and lower wavelengths (L)
ν Kinematic viscosity (L^2/T)
ρ Fluid density (M/L^3)
ρ_1 Density of upper fluid layer (M/L^3)
ρ_3 Density of lower fluid layer (M/L^3)
$\overline{\rho}$ Average density of upper and lower fluid layers (M/L^3)
$\Delta\rho$ Difference between upper and lower fluid layer densities (M/L^3)
σ Densimetric factor, $\approx 2\omega$ (-)
ω Densimetric factor (-)
ψ Stream function (L^2/T)
ψ^* Dimensionless stream function in Tung, Chan & Kubota analysis (-)
ξ Amplitude of first mode internal solitary wave (L)
ζ Perturbation value in Benjamin analysis (L)

Chapter 3

A Amplitude of sinusoidal curve in weir (L)
C Fluid conductivity (mS/cm)
M Mass fraction of salt in solution (-)
P Conductivity probe reading (-)
P_{atm} Atmospheric pressure (F/L^2)
T_{air} Period of oscillation of air in calibration (T^{-1})
T_{sample} Period of oscillation of fluid sample (T^{-1})
T_{water} Period of oscillation of water in calibration (T^{-1})
λ Wavelength of sinusoidal curve in weir (L)
ρ Density of fluid (M/L^3)
ρ_1 Density of upper layer of flume side (M/L^3)
ρ_2 Density of intrusion or collapsing region (M/L^3)
ρ_3 Density of lower layer of flume side (M/L^3)
ρ_{air} Density of air in calibration (M/L^3)
ρ_f Density of fresh water at given temperature (M/L^3)
ρ_{sample} Density of fluid sample (M/L^3)
ρ_{water} Density of water in calibration (M/L^3)
θ Water temperature (Θ)
θ_{air} Air temperature (Θ)

Chapter 4

c_0 Celerity of an infinitesimal first mode solitary wave (L/T)
g Acceleration due to gravity (L/T^2)
h Half-thickness of the pycnocline (L)
PE Potential energy (J)
t Interface thickening time (T)
y Vertical position ordinate, positive upwards (L)
κ Molecular diffusivity (L^2/T)
θ Water temperature (Θ)
ρ Fluid density (M/L^3)
ρ_1 Density of upper layer of flume side (M/L^3)
ρ_3 Density of lower layer of flume side (M/L^3)
$\overline{\rho}$ Average density of upper and lower fluid layers (M/L^3)
ω Densimetric factor (-)

Chapter 5

g Acceleration due to gravity (L/T^2)
h Half-thickness of the pycnocline (L)
H Depth of homogeneous fluid layer (L)
J Richardson number (-)
P Pressure (F/L^2)
t Time (T)
u Fluid velocity in x-direction (L/T)
x Lengthwise position ordinate, positive in direction of wave movement (L)
y Vertical position ordinate, positive upwards (L)
ρ Fluid density (M/L^3)
ρ_1 Density of upper layer of flume side (M/L^3)
ρ_2 Density of intrusion or collapsing region (M/L^3)
ρ_3 Density of lower layer of flume side (M/L^3)
ω Densimetric factor (-)

Chapter 6

a Wave amplitude (L)
a Length of semi-minor axis of ellipsoid wave approximation (L)
$\overline{a}$ Average of upper and lower wave amplitudes (L)
b Semi-major axis of ellipse (L)
c Wave celerity (L/T)
c_0 Celerity of an infinitesimal first mode solitary wave (L/T)
f Undisturbed complex flow potential (L^2/T)
$\overline{f}$ Conjugate of undisturbed complex flow potential (L^2/T)
g Acceleration due to gravity (L/T^2)
g' Densimetric acceleration due to gravity (L/T^2)

h Half-thickness of the pycnocline (L)
H Depth of homogeneous fluid layer (L)
$\hat{n}$ Unit vector normal to surface (-)
P Fluid pressure (F/L^2)
r_0 Radius of transformed circle (L)
t Time (T)
t Complex representation of circle cartesian coordinates (L)
U Fluid velocity (L/T)
U_∞ Uniform fluid velocity at great distance (L/T)
v Fluid velocity in y-direction (L/T)
w Complex flow potential (L^2/T)
x Lengthwise position ordinate, positive in direction of wave movement (L)
y Vertical position ordinate, positive upwards (L)
z Complex representation of ellipse cartesian coordinates (L)
ϕ Streamline perturbation in Tung, Chan & Kubota analysis (-)
Γ Control surface
η Vertical position ordinate in circle transformation (L)
λ Wavelength (L)
$\overline{\lambda}$ Average of upper and lower wavelengths (L)
θ Polar coordinate angle (-)
ρ_1 Density of upper layer of flume side (M/L^3)
ρ_2 Density of interior of wave region (M/L^3)
ρ_3 Density of lower layer of flume side (M/L^3)
ω Densimetric factor (-)
ψ Stream function divided by wave celerity (L)
ζ Lengthwise position ordinate in circle transformation (L)

Chapter 7

a Wave amplitude (L)
c Wave celerity (L/T)
c_0 Celerity of an infinitesimal first mode solitary wave (L/T)
g Acceleration due to gravity (L/T^2)
h Half-thickness of the pycnocline (L)
h_V Half-thickness of the shear profile (L)
J Richardson number (-)
Pr Prandtl number (-)
Re Reynolds number (-)
t Time (T)
u Fluid velocity in x-direction (L/T)
V Half velocity difference between layers (L/T)
x Lengthwise position ordinate, positive in direction of wave movement (L)
y Vertical position ordinate, positive upwards (L)
κ Thermal diffusivity (L^2/T)
ν Kinematic viscosity (L^2/T)

ρ Fluid density (M/L^3)
ω Densimetric factor (-)
ψ Stream function divided by wave celerity (L)

Chapter 8

a Wave amplitude (L)
A Cross-sectional area of wave interior (L^2)
b Width of strip in laminar drag analysis (L)
c Wave celerity (L/T)
c_g Group celerity of first mode solitary waves (L/T)
c_0 Celerity of an infinitesimal first mode solitary wave (L/T)
C_D Drag coefficient (-)
E Wave energy (ML^2/T^2)
F Force applied to wave (F)
g Acceleration due to gravity (L/T^2)
h Half-thickness of the pycnocline (L)
h_* Half-thickness of the pycnocline after wave passage (L)
k Added mass coefficient (-)
KE Kinetic energy of wave (ML^2/T^2)
l Height of water column (L)
L Length of strip in laminar drag analysis (L)
m Mass (M)
$\hat{n}$ Unit vector normal to surface (-)
PE Potential energy of wave (ML^2/T^2)
Re_h Interfacial Reynolds number (-)
Re_L Strip length Reynolds number (-)
Re_w Wall Reynolds number (-)
Re_λ Wavelength Reynolds number (-)
s Thickness of expulsion layer (L)
t Time (T)
V Wave celerity (L/T)
$\underline{V}$ Volume of body (L^3)
w Width of flume (L)
x Lengthwise position ordinate, positive in direction of wave movement (L)
ε Energy per unit area of first mode solitary wave (M/T^2)
λ Wavelength (L)
ν Kinematic viscosity (L^2/T)
ρ Fluid density (M/L^3)
ρ_1 Density of upper fluid layer (M/L^3)
ρ_2 Density of wave interior (M/L^3)
ρ_3 Density of lower fluid layer (M/L^3)
$\overline{\rho}$ Average density of upper and lower fluid layers (M/L^3)
$\Delta\rho$ Difference between upper and lower fluid layer densities (M/L^3)
ω Densimetric factor (-)
ξ Amplitude of first mode internal solitary wave (L)

1.0 Introduction

The following brief introduction to second mode internal solitary waves is meant to provide the reader with some perspective on how these waves relate to other more familiar wave phenomena. Motivation for the present study and the structure of the thesis are also described.

1.1 Background

In nature there exist many examples of wave motion as a mechanism for energy transfer. Electromagnetic energy in the form of radio signals or light, as well as mechanical energy in the form of earthquake tremors, sound or oceanic disturbances, all propagate as waves.

It is a specific case of the latter that this thesis will examine. Wind, planetary attraction and natural or artificial motions at fluid boundaries may all cause disturbances in the surface of a body of water. Surface water waves propagate due to the restoring forces of surface tension and gravity on the fluid, and where the latter predominates the resulting waves are referred to as gravity waves.

Several types of surface gravity waves have been observed and described mathematically, and some selected examples are shown on Figure 1.1. The ratio of water depth to wavelength determines whether these are shallow-water (long) waves or deep-water waves. In the former, wave celerity scales on the water depth, while in the latter the relevant length scale is the wavelength. The waves typically seen on the surface of the ocean can be described as a superposition of linear, periodic, deep-water waves of different amplitudes and wavelengths. Such "composite" waves are subject to dispersion, as component waves of larger wavelength travel faster than those with smaller wavelengths. When these waves approach regions of shallow water, non-linearity and steepening of the wave can result in breaking and the dissipation of energy through turbulence.

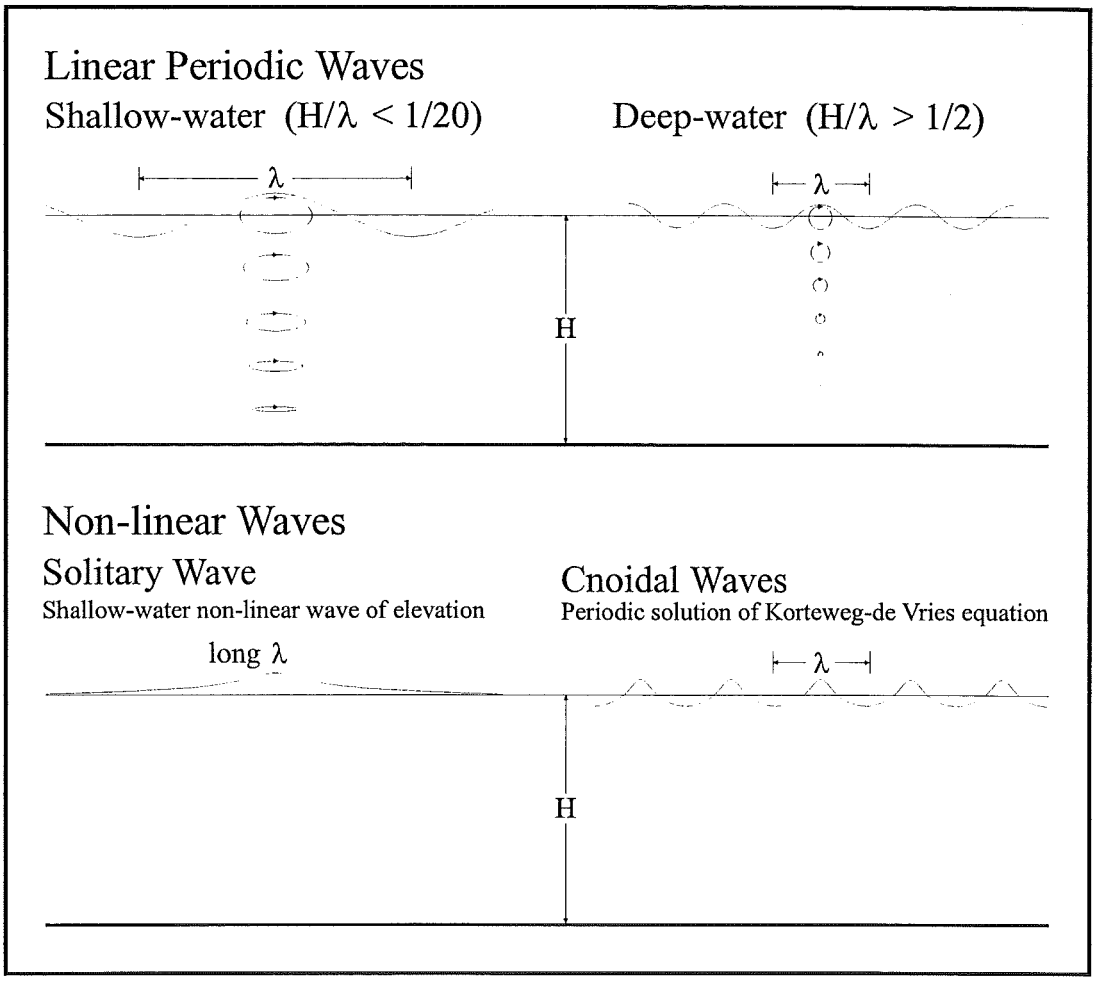

Figure 1.1 - Different types of surface gravity waves

A special type of surface wave known as a solitary wave was first reported by John Scott Russell, a Scottish civil engineer, in 1844. This is a long, shallow-water wave which propagates as a single, symmetrical hump entirely above the undisturbed free surface of the water. The remarkable ability of these waves to travel for long distances without change in form or celerity is one of their more notable characteristics. Subsequent work by Boussinesq (1871) and Rayleigh (1876) produced descriptions of the profile and celerity of the solitary wave, and the later mathematical analysis by Korteweg & de Vries (1895) yielded an equation revealing the balance between dispersion and nonlinearity which allows the solitary wave to propagate with constant form. The Korteweg-de Vries, or KdV, equation has since been used in the description of solitary waves occurring not just in the ocean and atmosphere, but also in such diverse fields as astronomy, biochemistry and solid state, high energy and plasma physics. The term soliton, denoting

particle-like behaviour, was coined by Zabusky & Kruskal (1965) after their numerical simulations showed that colliding solitary waves passed through each other with no change in form but a slight negative phase shift.

Gravity waves are readily visible on the surface of a body of water, but they may also exist below the surface, propagating along interfaces or surfaces of constant density in density-stratified fluids. Sharp density stratifications due to temperature or salinity gradients, known as pycnoclines, occur frequently in natural bodies of water. These support the propagation of internal gravity waves, with the restoring force of gravity being modified by a densimetric factor related to the difference in densities of the fluids on either side of the pycnocline. The surface wave is in fact an extreme case of the internal wave in which the difference in density between water and air causes the densimetric factor to be approximated as unity.

As surface solitary waves, being shallow-water waves, have a celerity which scales on the fluid depth, they cannot exist in fluids of infinite depth. It was once thought that this was also true for internal solitary waves, but this was refuted by Benjamin (1967) and Davis & Acrivos (1967). Their work showed that the scaling of wave celerity on the thickness of the pycnocline rather than the total fluid depth allowed for the existence of solitary waves in infinitely deep fluids. First mode waves were shown to exist as either waves of elevation or depression, in contrast to surface waves which do not exist in the latter form. Second mode internal solitary waves resemble a superposition of the two. They are a unique type of internal gravity wave in that at large amplitudes fluid is trapped within the wave, allowing the wave to transport not just energy, but also mass, over large distances. The different types of first and second mode internal solitary waves are shown in Figure 1.2, while a streakline image of a large amplitude second mode wave is shown in Figure 1.3.

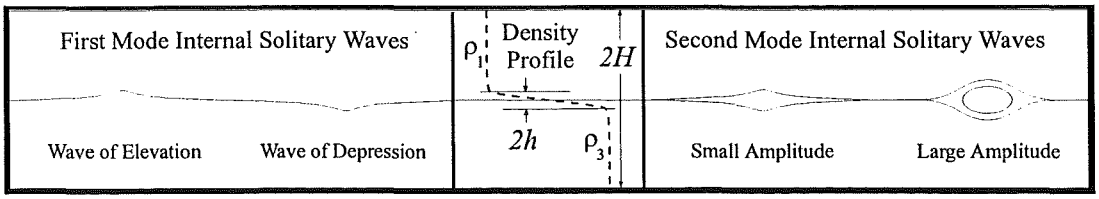

Figure 1.2 - Deformation of central streamline by internal solitary waves

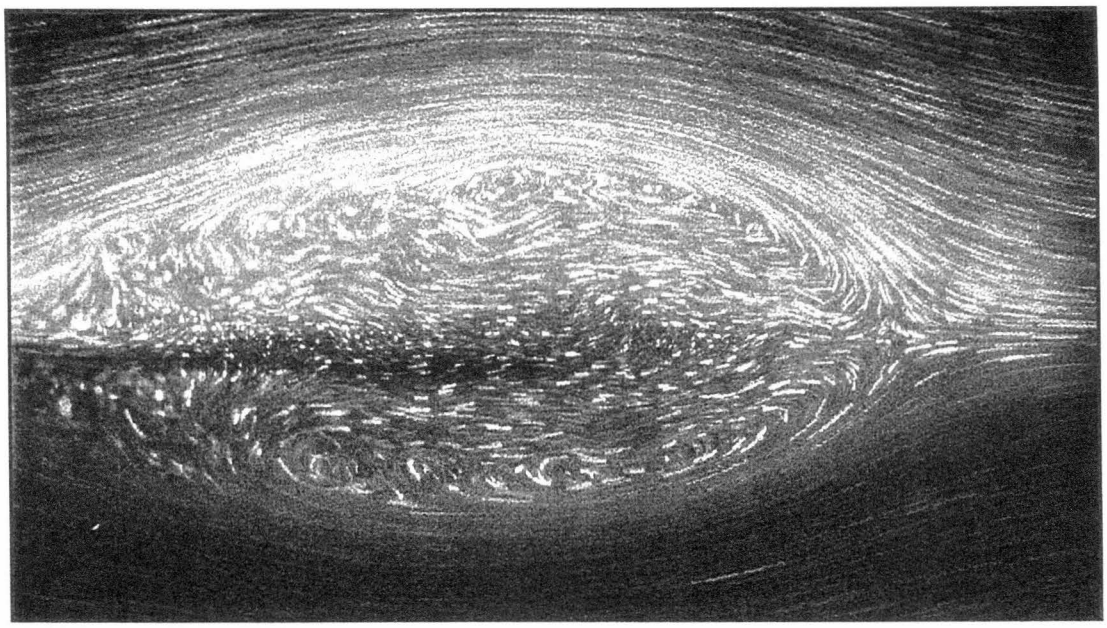

Figure 1.3 - Streakline image of a large amplitude second mode wave

1.2 Focus of Present Study

The primary goal of the present study was to use advanced flow visualisation and measurement techniques to perform a detailed examination of the generation, propagation and eventual decay of the second mode wave. Particular attention was to be paid to very large amplitude waves, allowing both a close examination of the internal structure of such waves and the investigation of their propagation characteristics. Time constraints prevented the completion of a numerical model, based on the laminar Navier-Stokes equations, which would have complemented the experimental and analytical components. It is hoped that the observations, measurements and analysis presented here will shed more light on the nature of these waves, and eventually be used in the calibration of an advanced numerical model.

The second chapter of this study contains a review of the literature on second mode waves. A detailed background description of internal solitary waves is followed by a summary and discussion of theoretical and experimental treatments. Specific needs for research and recommended experimental techniques are then presented.

Chapter three details the experimental techniques used in this research. The physical setup of the experimental apparatus, as well as flow visualisation and fluid

density measurement techniques, are described. The preparation of fluids and tracers for use in the experiments is outlined, details of the various methods by which second mode waves were generated in the laboratory are given, and particulars of the experimental procedure are described.

The thickness of the pycnocline in a sharply stratified ambient fluid is a very important parameter to be considered in the analysis of internal solitary waves. The fourth chapter of this study addresses the characteristics of the density interface: its shape, the definition and measurement of its thickness, and its evolution over time.

Chapter five contains the first experimental observations of second mode waves. Qualitative descriptions of the generation of waves by exchange flows, forced inflows and gravity-driven collapses illustrate the ubiquity of these waves and show how a range of natural disturbances may result in their generation.

The sixth chapter discusses observations of the second mode wave related to external propagation characteristics. The measurement of wave celerity, amplitude and wavelength are discussed. Existing empirical relationships describing the shape of the wave are examined and shown to agree well with the extended body of data with minor modifications. The analysis of the factors governing wave celerity first considers previous analyses and the existing body of experimental data. New experimental data which significantly extends the range of amplitudes is then presented. It is apparent from this data that existing theoretical wave celerity relationships are not valid for larger amplitudes. A novel analytical solution which provides a good fit to the data is then presented.

Chapter seven examines the internal structure of second mode waves. Particle visualisation techniques have produced detailed observations of the circulation within the wave both during and after the formation of a fully developed wave. The circulation pattern is shown to differ significantly from that predicted by inviscid numerical models. Dye visualisation is used to reveal the mechanism by which external fluid is entrained into the wave, and this is seen to be different from that suggested by previous studies. Lastly, a non-intrusive dye visualisation technique is

used to quantify the mass transport capability of large amplitude second mode waves.

The eighth chapter examines the dissipation characteristics of large amplitude waves. Though these waves have the ability to persist for long distances, their eventual decay is inevitable. The theory related to the mechanisms causing this loss of amplitude are examined, and new data is analysed using an analysis technique based on wave energy, allowing an examination of the relative contributions of each mechanism.

Chapter nine contains the conclusion to this study. Results and significant advances are discussed, and future research requirements are presented.

The appendices which follow contain detailed descriptions of data which were not included in the body of the thesis. Information on computer software written for this study, including that written for the numerical model, is also presented.

2.0 Literature Review

Only a limited number of studies on second mode internal solitary waves have been published since the first paper appeared in 1967. In this chapter, these studies will be described briefly. Then more detailed discussion will be given on the theories presented in the papers, the experimental techniques that were used, and the resulting observations and analyses of wave behaviour. Finally, opportunities for building on this earlier research will be addressed.

2.1 Introduction

Many of the studies reviewed here have included both theoretical and experimental work on second mode waves. In this introduction analytical and experimental components will be described separately, in order to keep a clearer focus on the sequence of developments in each area.

2.1.1 Analytical Studies

Four detailed theoretical studies of second mode waves were found in the literature. These all contained analytical treatments of the wave motion and presented equations relating wave amplitude and celerity. Two studies also presented numerical models which predicted the form of the wave.

The first analytical treatment of the second mode wave was that of Benjamin (1967). This was a strictly theoretical study which considered waves travelling in a variety of stratifications, both adjacent to and remote from boundaries, in fluids of great depth. The case of a wave propagating on a hyperbolic tangent density profile was considered, and a general equation predicting the celerity of any mode of wave propagation on this interface was presented.

The work of Davis & Acrivos (1967) considered only second mode waves travelling in deep water on an interface with a hyperbolic tangent profile. An equation predicting wave celerity as a function of amplitude was presented, though this appeared to deviate from the experimental data at higher amplitudes due to weak non-linear assumptions made in the analysis. A numerical study based on the same

theory predicted the existence of a 'closed streamline' region within the wave for larger amplitudes.

Kao & Pao (1979) performed a new analysis which was similar to that of Benjamin (1967), but applicable to situations where the total fluid depth was finite. This resulted in an equation relating the increment of wave celerity above that of an infinitesimal first mode solitary wave, c_0, to the ratio of maximum fluid velocity to c_0. The experimental results showed a good agreement with theoretical relationship, even for large amplitude waves.

The study of Tung, Chan & Kubota (1982) extended the analysis of Davis & Acrivos (1967) to the fully nonlinear case. The resulting relationship between wave celerity and amplitude showed good agreement with the data of the earlier study, even for larger amplitude waves. A numerical model based on the same equations examined the effect on the wave of finite depths of fluid, and also produced 'closed streamlines' for larger amplitude waves.

2.1.2 Experimental Studies

The first experiments on second mode waves were performed by Davis & Acrivos (1967) in conjunction with their analytical study. The aim of these experiments was to examine the relationship between fluid density, wave amplitude and celerity.

Hurdis & Pao (1975) generated second mode waves while studying the flow upstream of a flat plate which was towed through the interfacial region of a two-layer system. Measurements of wave amplitude and celerity were compared to the theory of Benjamin (1967) and Davis & Acrivos (1967). A subsequent study by Kao & Pao (1979) examined the wave behaviour, with specific attention paid to their internal velocity structure and bulk celerity, as well as longevity and decay over a series of collisions and end-wall reflections. Experimental observations of wave structure were compared with the analytical results presented in the same study.

Research by Maxworthy (1980) was undertaken to examine trains of nonlinear waves which were generated by the gravity-driven collapse of a mixed region of

fluid. Three methods were used to generate waves, but only the first of these produced two-dimensional waves. The three-dimensional waves generated by the latter two resembled gravity currents, so they will not be discussed here.

The work of Hachmeister & Rigby (1980) examined the generation of internal solitary waves, of both first and second mode, by the towing of an obstacle on the surface of the fluid. It was intended to model the interaction between the keel of a moving pack ice pressure ridge with the density stratification typically seen in the ocean during an arctic summer. Much of the study concentrated on drag effects resulting from the interaction, but observations of the behaviour of second mode waves were also recorded.

The work of Stamp & Griffiths (1992) and the subsequent study of Stamp & Jacka (1995) both described results of a single group of experiments, with the latter paper providing more detailed analysis and discussions of background and results. Three sets of experiments were performed. The goal of the first was to measure the profile, celerity and decay of a single second mode internal solitary wave. The second set examined the reflection of such waves from a vertical wall, while in the third the collision of two waves was investigated.

2.2 Theoretical Considerations

The discussion of the theory of second mode waves will first examine background theory on internal solitary waves before concentrating on more detailed descriptions of the theoretical treatments, both analytical and numerical, introduced in Section 2.1.1. This helps to put those treatments into an overall framework, giving a better perspective on their relationship to one another.

2.2.1 Background on Internal Solitary Waves

The existence of internal solitary waves was first discussed by Keulegan (1953) and Long (1956). These studies considered two-layer systems of finite depth in which the solitary wave propagated on the interface between the two layers and existed either as a wave of elevation (in the case of the upper layer being thicker than the

lower) or of depression (in the opposite case). The form of the wave, as well as the relationship between wave celerity and amplitude, was described.

Stamp & Jacka (1995) classified internal solitary waves as either 'shallow-water', 'deep-water' or 'finite-depth' waves, using dimensionless combinations of fluid depth, $2H$, stratification depth, $2h$, and wavelength, λ, to define which group a wave belonged to. Their classification and terminology is illustrated in Figure 2.1 and adopted below.

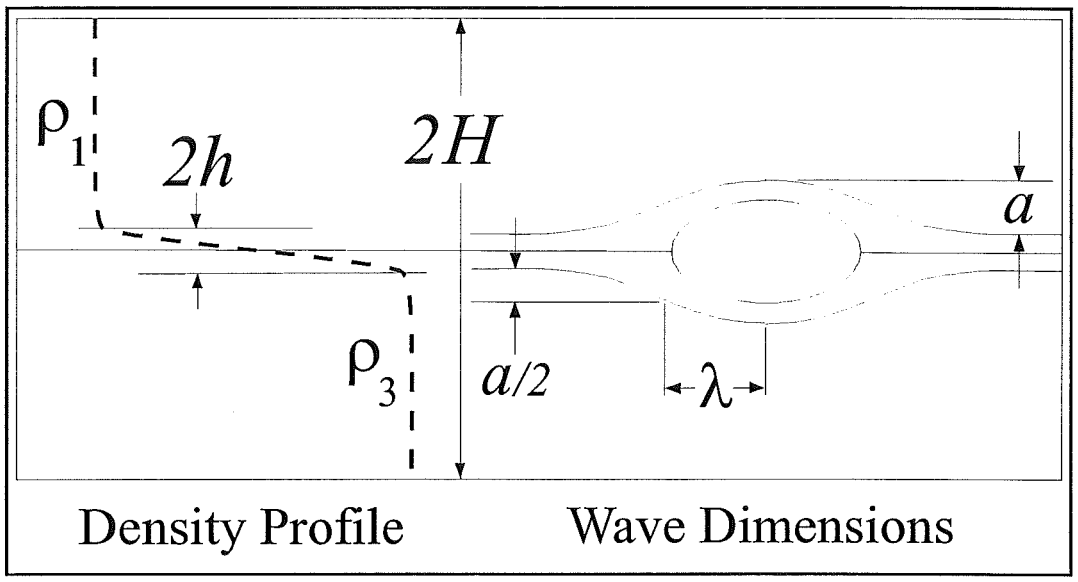

Figure 2.1 – Definition of wave and density profile dimensions

Shallow-water waves, propagating in continuously stratified fluids ($h/H = O(1)$) and with long wavelengths ($\lambda/H >> 1$), were first examined by Benney (1966) and Benjamin (1966). These waves were of a small, but finite, amplitude, a, and it was shown that the appropriate scaling for a balance between dispersion and non-linearity was:

$$\left(\frac{\lambda}{H}\right)^2 = O\left(\frac{a}{H}\right)^{-1} \tag{2.1}$$

The existence of deep-water waves ($\lambda/H \rightarrow 0$) was first addressed by Benjamin (1967) and Davis & Acrivos (1967). Solitary wave theory was previously thought to preclude the existence of such waves in fluids of infinite depth, but here it was shown that the appropriate length scale was the thickness of the pycnocline, and the

waves could still be described as long, since $\lambda/h >> 1$. The appropriate scaling for an internal wave which propagates without change in form was shown to be:

$$\frac{\lambda}{h} = O\left(\frac{a}{h}\right)^{-1} \tag{2.2}$$

The behaviour of waves in water of finite depth, where $h/H << 1$ and $\lambda/h >> 1$, was addressed by Joseph (1977) and Kubota, Ko & Dobbs (1978). These studies bridged the gap between deep- and shallow-water waves, showing that the phase speed of a wave of finite depth was dependent on the wave number ($k = 2\pi/\lambda$) and infinitesimal interfacial wave speed ($c_0 = \sqrt{g\omega h/2}$ where $\omega = (\rho_3 - \rho_1)/(\rho_3+\rho_1)$) as:

$$c = c_0\left[1 - \frac{1}{2}kh\left(\coth(kH) + \frac{1}{kH}\right)\right] \tag{2.3}$$

This equation reduces to that describing the shallow-water wave phase speed, $c = c_0(1 - \beta k^2)$, in the limit $kH << 1$, and the deep-water equation, $c = c_0(1 - \gamma|k|)$ in the limit $kH \rightarrow \infty$ (here β and γ are positive coefficients of the dispersion terms discussed in Kubota, Ko & Dobbs (1978)). Since the dispersive term varies with k^2 for shallow-water waves and with $|k|$ for deep-water waves, it would appear that for waves of similar dimensionless wavelengths, kh and kH, permanence of form would require a higher degree of nonlinearity from deep-water than for shallow-water waves, with that for finite depth waves falling somewhere in the middle.

2.2.2 Theoretical Treatments

The three studies which will be addressed here began with a similar governing equation and followed similar procedures to derive relationships which describe the form and behaviour of second mode waves. The derivation of the governing equation, known as Long's equation, is detailed in several references (Long, 1953; Benney & Ko, 1978; Tung, Chan & Kubota, 1982), and is outlined here for completeness. The two-dimensional Navier-Stokes equations, (Equations 2.4 and

2.5), and the continuity equation, (Equation 2.6) provide a starting point for the derivation.

$$\frac{\partial u}{\partial t} + u\frac{\partial u}{\partial x} + v\frac{\partial u}{\partial y} = -\frac{1}{\rho}\frac{\partial p}{\partial x} + \nu\left(\frac{\partial^2 u}{\partial x^2} + \frac{\partial^2 u}{\partial y^2}\right) \tag{2.4}$$

$$\frac{\partial v}{\partial t} + u\frac{\partial v}{\partial x} + v\frac{\partial v}{\partial y} = -\frac{1}{\rho}\frac{\partial p}{\partial y} - g + \nu\left(\frac{\partial^2 v}{\partial x^2} + \frac{\partial^2 v}{\partial y^2}\right) \tag{2.5}$$

$$\frac{\partial}{\partial x}(\rho u) + \frac{\partial}{\partial y}(\rho v) = -\frac{\partial \rho}{\partial t} \tag{2.6}$$

Assuming a steady state system ($\partial/\partial t = 0$, i.e. the equations are written from the point of view of an observer moving with the wave), an inviscid fluid ($\nu = 0$) and incompressibility ($\partial u/\partial x + \partial v/\partial y = 0$), and introducing a stream function ($u = \partial\psi/\partial y$ and $-v = \partial\psi/\partial x$), allows these equations to be reduced to:

$$\rho\left(\frac{\partial \psi}{\partial y}\frac{\partial^2 \psi}{\partial y \partial x} - \frac{\partial \psi}{\partial x}\frac{\partial^2 \psi}{\partial y^2}\right) = -\frac{\partial p}{\partial x} \tag{2.7}$$

$$\rho\left(-\frac{\partial \psi}{\partial y}\frac{\partial^2 \psi}{\partial x^2} + \frac{\partial \psi}{\partial x}\frac{\partial^2 \psi}{\partial x \partial y}\right) = -\frac{\partial p}{\partial y} - \rho g \tag{2.8}$$

$$\frac{\partial \psi}{\partial y}\frac{\partial \rho}{\partial x} - \frac{\partial \psi}{\partial x}\frac{\partial \rho}{\partial y} = 0 \tag{2.9}$$

Note that the assumption of steady-state implies that the wave cannot change shape as it propagates. It can neither steepen due to nonlinearity nor separate into components due to dispersion. Hence any wavelike solutions found to these equations will of necessity be those for waves "of permanent form". Now, the derivative of Equation 2.7 with respect to y and that of Equation 2.8 with respect to x are taken and the two resulting equations are subtracted to eliminate the pressure term. In addition, it is noted that Equation 2.9 implies that $\rho = F(\psi)$, so the following relationship results:

$$\frac{\partial}{\partial y}\left[F\left(\frac{\partial\psi}{\partial y}\frac{\partial^2\psi}{\partial y\partial x} - \frac{\partial\psi}{\partial x}\frac{\partial^2\psi}{\partial y^2}\right)\right] + \frac{\partial}{\partial x}\left[F\left(\frac{\partial\psi}{\partial y}\frac{\partial^2\psi}{\partial x^2} - \frac{\partial\psi}{\partial x}\frac{\partial^2\psi}{\partial x\partial y}\right) - Fg\right] = 0 \quad (2.10)$$

This relationship may be more simply expressed as:

$$\frac{\partial\psi}{\partial y}\frac{\partial L}{\partial x} - \frac{\partial\psi}{\partial x}\frac{\partial L}{\partial y} = 0 \quad (2.11)$$

$$\text{where } L = F\Delta\psi + \frac{1}{2}F'|\nabla\psi|^2 + gyF' \quad (2.12)$$

If it is taken that L is functionally related to ψ, then this equation may be expressed as:

$$\nabla^2\psi + \frac{F'(\psi)}{F(\psi)}\left[gy + \frac{1}{2}|\nabla\psi|^2\right] = G(\psi) \quad (2.13)$$

Equation 2.13 is known as Long's equation, where F and G are functions of the upstream density and velocity distributions, respectively. For the case of a uniform upstream velocity field ($\psi \rightarrow cy$), G is defined by the following equation:

$$G(\psi) = \frac{F'(\psi)}{F(\psi)}\left[\frac{1}{2}c^2 - g\frac{\psi}{c}\right] \quad (2.14)$$

Combining Equations 2.13 and 2.14 produces:

$$\nabla^2\psi + \frac{F'(\psi)}{F(\psi)}\left[g\left(y + \frac{\psi}{c}\right) + \frac{1}{2}\left(|\nabla\psi|^2 - c^2\right)\right] = 0 \quad (2.15)$$

This equation, or variations of it, was used in the analyses of Benjamin (1967), Davis & Acrivos (1967), Tung, Chan & Kubota (1982) and Kao & Pao (1978). The specific governing equations, assumptions and results of the individual studies will now be discussed.

2.2.2.1 Benjamin (1967)

This study examined the motion of a second mode wave in a fluid of great depth. Long's equation (Equation 2.15) was transformed by the technique outlined in

Benjamin (1966), whereby $\partial\psi/\partial x = -c(\partial y/\partial x)/(\partial y/\partial \eta)$ and $\partial\psi/\partial\eta = c/(\partial y/\partial\eta)$. The transformation resulted in the following governing equation:

$$\rho\left(\frac{\frac{d^2y}{dx^2}}{\frac{dy}{d\eta}} - \frac{2\frac{dy}{dx}\frac{d^2y}{dxd\eta}}{\frac{dy}{d\eta}^2}\right) - \frac{1}{2}\frac{d}{d\eta}\left(\frac{\rho}{\frac{dy}{d\eta}^2}\right)\left(1 + \frac{dy}{dx}^2\right) = \frac{d\rho}{d\eta}\left(\frac{g}{c^2}(y - \eta) - \frac{1}{2}\right) \quad (2.16)$$

In Equation 2.16, x represents the horizontal distance, y the streamline height, η the undisturbed streamline height (i.e. that at great distance from the wave), and c the wave celerity which is to be solved for. The fluid was assumed to be incompressible and non-diffusive, and its density, ρ, taken to be a function of η. This equation was to be solved, subject to the boundary conditions $y = 0$ for $\eta = 0$ and $(y - \eta) \rightarrow 0$ for $\eta \rightarrow \infty$. First, the streamline height, y, was expressed as a perturbation from the far field value by substituting the following equation into Equation 2.16:

$$y = \eta + \varepsilon\zeta(x,\eta) \quad (2.17)$$

Note that both y and η extend to ∞ for a fluid of "great depth". When the resulting equation was linearised in ε, the following equation was produced:

$$\rho\frac{d^2\zeta}{dx^2} + \frac{d}{d\eta}\left(\rho\frac{d\zeta}{d\eta}\right) - \frac{d\rho}{d\eta}\kappa\zeta = 0 \quad (2.18)$$

In Equation (2.18), $\kappa = g/c^2$. Setting $\zeta(x,\eta)$ to $\phi(\eta)e^{ikx}$ for real values of k produced:

$$\frac{d}{d\eta}\left(\rho\frac{d\phi}{d\eta}\right) - \left(\rho k^2 + \kappa\frac{d\rho}{d\eta}\right)\phi_0 = 0 \quad (2.19)$$

Recognising that both ϕ and κ might be expanded in power series ($\phi(\eta) = \phi_0(\eta) + |k|\,\phi_1(\eta) + k^2\phi_2(\eta) + \ldots$, $\kappa = \kappa_0 + |k|\,\kappa_1 + k^2\,\kappa_2 + \ldots$) and that the wave celerity was largest for $k = 0$, Equation (2.19) was then approximated as:

$$\frac{d}{d\eta}\left(\rho\frac{d\phi_0}{d\eta}\right) - \kappa_0\frac{d\rho}{d\eta}\phi_0 = 0$$
$$\text{where} \quad \phi_0 = 0 \text{ at } \eta = 0 \qquad (2.20)$$
$$\frac{d\phi_0}{d\eta} = 0 \text{ at } \eta = h$$
$$\text{and} \quad \kappa_0 = g/c_0^2$$

Applying the Boussinesq approximation (setting $\rho = \rho(0)$) to this produced:

$$\frac{d^2\phi_0}{d\eta^2} + \frac{g}{c_0^2\,\rho(0)}\frac{d\rho}{d\eta}\phi_0 = 0 \qquad (2.21)$$

The density profile of the fluid was assumed to resemble the hyperbolic tangent function and was expressed as:

$$\rho(\eta) = \overline{\rho}\left(1 - \omega\tanh\left(\eta/h\right)\right) \qquad (2.22)$$

In the preceding equation, h represented the half-thickness of the pycnocline and ω the dimensionless densimetric factor (equal to the density difference between the upper and lower layers divided by their sum). Equation 2.22 was then substituted into Equation 2.21 to show that:

$$\frac{d^2\phi_0}{d\eta^2} + \left(\frac{g\omega\mathrm{sech}^2\left(y/h\right)}{h\,c_0^2}\right)\phi_0 = 0 \qquad (2.23)$$

Equation 2.23 was then solved to produce the following expression for wave celerity, where a was equal to the wave amplitude:

$$c^2 = \frac{g\omega h}{2}\left(1 + \frac{3}{5}\frac{a}{h}\right) \qquad (2.24)$$

The recognition that the coefficient of the term in parenthesis in Equation 2.24 was the square of the infinitesimal long wave speed on the interface, c_0, allowed this equation to be rewritten as:

$$\left(\frac{c}{c_0}\right)^2 = 1 + \frac{3}{5}\frac{a}{h} \qquad (2.25)$$

In the concluding remarks of this study, it was noted that the results presented represented only a first approximation to the solution and were likely to be unreliable for the case of waves with amplitudes approaching $a/h = 1$. It was recognised that the occurrence of stagnation points and recirculating regions in the flow for larger amplitudes invalidated the transformation of Long's equation which produced the governing equation of this analysis. The author further recommended that the "direct numerical solution of the unsimplified governing equations... [was] likely to be more rewarding" in dealing with large amplitude waves.

2.2.2.2 Davis & Acrivos (1967)

This analysis also used Long's equation as the starting point for the analysis. In the particular form of this equation which follows, ψ is the dimensionless stream function, $2h$ the interface thickness, $-c$ the wave celerity and y the vertical distance from the centre of the interface:

$$\nabla^2\psi + \frac{d\ln\rho}{d\psi}\frac{gh}{c^2}(y - \psi) = \frac{1}{2}\frac{d\ln\rho}{d\psi}\left(1 - \psi_x^2 - \psi_y^2\right) \qquad (2.26)$$

It was then assumed that for a weakly stratified fluid, the right hand side of Equation 2.26 may be neglected, resulting in the following:

$$\nabla^2\phi + \Lambda F(\phi + y)\phi = 0 \qquad (2.27)$$

In Equation 2.27, $\phi = \psi - y$, and $\phi \rightarrow 0$ as $x^2 + y^2 = \infty$. The quantity $d\ln\rho/d\psi$ has been expressed as $(d\ln\rho/d\psi)_{max}\, F(\psi)$ with $F \geq 0$, and $\Lambda = -(2gh/c^2)\,(d\ln\rho/d\psi)_{max}$. This equation was solved analytically by two methods, by either dividing the fluid into three layers or into an inner and outer region. Key steps in this solution were the stretching of x-coordinates by the factor ε (with $\varepsilon << 1$), following the shallow-water assumption that x-derivatives of the stream function are $O(\varepsilon)$ smaller than y-derivatives, as well as the assumption that $\phi << 1$. The principal variables in Equation 2.27 were expanded in ε and terms of $O(\varepsilon^3)$ were neglected. The two methods produced similar results, and the following wave celerity equation resulted:

$$\Lambda = 2.0 - 1.2A \tag{2.28}$$

In the preceding equation, A represented an amplitude parameter which was approximately equal to a/h and Λ was defined as $(gh/c^2)\ln(\rho_3/\rho_1)/2$. Recognising that the quantity $\ln(\rho_3/\rho_1)/2$ was approximately equal to the densimetric factor ω revealed that $\Lambda = 2(c_0/c)^2$. Equation 2.28 provided a good fit to the experimental data for small amplitude ($a/h < 1$) waves, but for larger amplitudes the linearised theory deviated from the observed data.

Davis & Acrivos (1967) also used Equation 2.27 to numerically model the second mode wave for a variety of amplitudes. This model produced streamlines which seemed to resemble experimentally observed waves, and also predicted the existence of a closed streamline region within the wave for sufficiently large amplitudes ($a/h > 1.2$; the present study will concentrate on these waves, with observed amplitudes up to $a/h \approx 12$). Though such large amplitude waves were observed, it was noted that the model could not be accepted as valid for these waves due to the neglect of viscosity, which would be responsible for the diffusion of vorticity. This would eventually result in a constant value of vorticity in the core of the wave, and meant that the value of vorticity would need to be determined based on a knowledge of flow along the boundary of the entire closed streamline region rather than from the governing equations. Despite this, the authors felt that the numerical model still represented a "significant extension of the approximate analytic solutions."

2.2.2.3 Tung, Chan & Kubota (1982)

This study considered the motion of second mode waves in bodies of fluid with finite depths, representing a significant advance on previous studies. They used the variation of Long's equation shown below as the starting point for their analysis.

$$\left(\frac{\partial^2}{\partial x^{*2}}+\frac{\partial^2}{\partial y^{*2}}\right)\psi^* - \Lambda\frac{F'(\psi^*)}{1-\sigma F(\psi^*)}(y^* - \psi^*) = \frac{1}{2}\frac{\sigma F'(\psi^*)}{1-\sigma F(\psi^*)}\left(\psi^{*2}_{x^*} + \psi^{*2}_{y^*} - 1\right) \tag{2.29}$$

In the preceding equation, the asterisk denoted a quantity which was rendered dimensionless ($y^* = y/h$, $x^* = x/h$, $\psi^* = \psi/ch$). The relative density change across

the pycnocline was σ (roughly equal to 2ω) and the quantity $\Lambda = \sigma gh/c^2$. The density profile of the fluid was described by:

$$\rho = \rho_0(0)\left(1 - \sigma F(\psi^*)\right) \tag{2.30}$$

Dropping the asterisk notation and expressing Equation 2.29 in terms of the perturbation stream function ϕ^*, where $\psi^* = y^* + \phi^*$, resulted in the following equation:

$$\nabla^2\phi + \Lambda\frac{F'(y+\phi)}{1 - \sigma F(y+\phi)}\phi = \frac{1}{2}\frac{F'(y+\phi)}{1 - \sigma F(y+\phi)}\left(\phi_x^2 + \phi_y^2 + 2\phi_y\right) \tag{2.31}$$

The Boussinesq approximation ($\sigma << 1$) was then applied to Equation 2.31, removing the right hand side of the equation (and its non-linear contribution) and simplifying it to the following equation with the noted boundary conditions:

$$\begin{aligned} &\nabla^2\phi + \Lambda F'(y+\phi)\phi = 0 \\ &\phi \to 0 \text{ as } x \to \pm\infty \\ &\phi = 0 \text{ at } y = H_1,\ -H_2 \end{aligned} \tag{2.32}$$

This equation was then solved numerically, yielding information about the relationships between wavelength and amplitude, wave celerity and amplitude, and the effect of varying the total depth of fluid. It was shown that a dimensionless depth of $h/H = 40$ approximated the deep water case. The existence of closed streamline regions, as seen in the numerical study of Davis & Acrivos (1967) was also predicted by this study. Moreover, it was observed that increased wave amplitudes corresponded to decreasing wavelengths, with a $\lambda \propto (a/h)^{-1/2}$ relationship, up to a limit point of approximately $a/h = 1.2$. After this point, which coincided with the formation of recirculating regions within the wave, wavelengths were observed to increase with increasing amplitude.

2.2.2.4 Kao & Pao (1979)

This study was the first to consider second mode waves in water of finite depth. Its authors followed the procedure of Benney (1966) to formulate an equation which

was identical to Equation 2.23 as derived by Benjamin (1967). This equation was solved to show that:

$$\frac{\Delta c}{c_0} = 0.35 \frac{u_{\max}}{c_0} \tag{2.33}$$

In this equation, u_{max} represented the maximum velocity within the wave, c_0 the celerity of an infinitesimal solitary wave travelling on the interface, and $\Delta c = c - c_0$, where c was the celerity of a first mode wave. The quantity c_0 was calculated with the following equation:

$$c_0 = \left[\frac{g\omega h}{2 + 3\delta}\right]^{1/2} \tag{2.34}$$

The parameter δ in the preceding equation modified this equation for application to fluids of finite depth, whereas previous equations for calculating the celerity of an infinitesimal internal solitary wave were applicable to fluids of great depth only. The value of this parameter was calculated using the following equation:

$$\delta = \left[\ln\left(\cosh\frac{H}{h}\right)\right]^{-1} \tag{2.35}$$

Equation 2.33 will not be compared to the results of the other three studies due to dissimilarities in format and the fact that the present study deals only with deep water waves.

The relationships between dimensionless wave amplitude and celerity as predicted by the studies of Benjamin (1967), Davis & Acrivos (1967) and Tung, Chan & Kubota (1982) are plotted in Figure 2.2. It can be seen from this figure that the three techniques which derive from Long's equation produce a range of solutions, perhaps comparable for small amplitude ($a/h < 1$) waves, but sharply divergent for larger ones. It must again be noted that none of these studies claimed to be applicable to large amplitude waves due to the assumptions present in their derivations. The accuracy of these solutions will be addressed in Section 2.5.3 where experimental results are discussed.

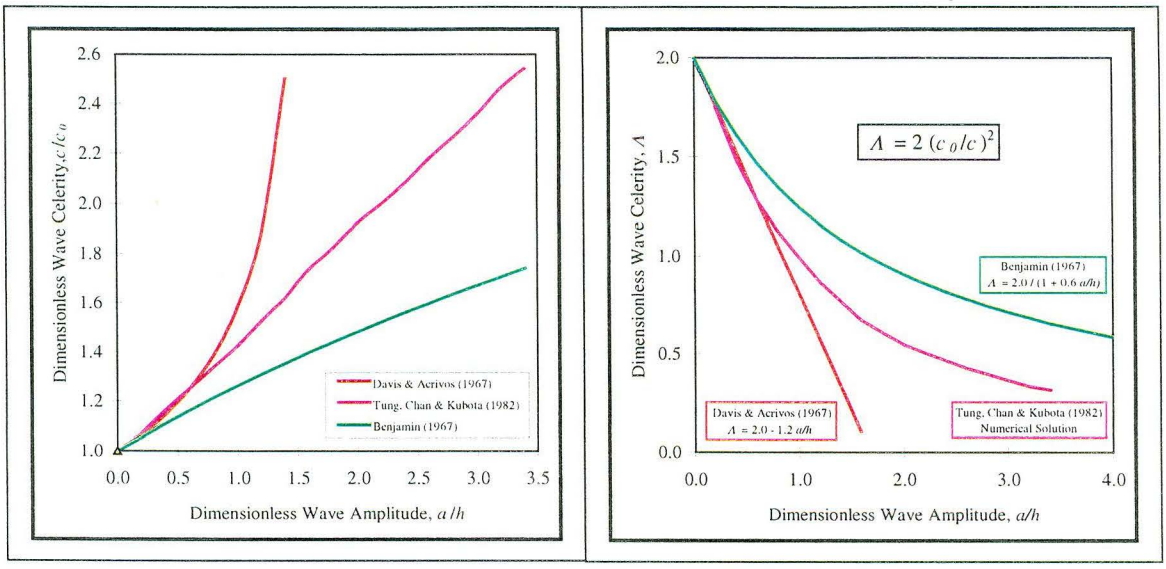

Figure 2.2 - Deep-water wave propagation celerity relationships

The numerical solutions of Davis & Acrivos (1967) and Tung, Chan & Kubota (1982) produced similar plots of streamlines for large amplitude waves. These were typified by the existence of a stagnation point at the nose of the wave and an interior recirculating region which consisted of two elongated, counter-rotating vortices on opposite sides of the wave centreline. The rotation of these vortices was such that flow was forwards along the centreline of the wave and backwards on its outer boundaries. The form of the wave as predicted by these numerical studies is illustrated in Figure 2.3.

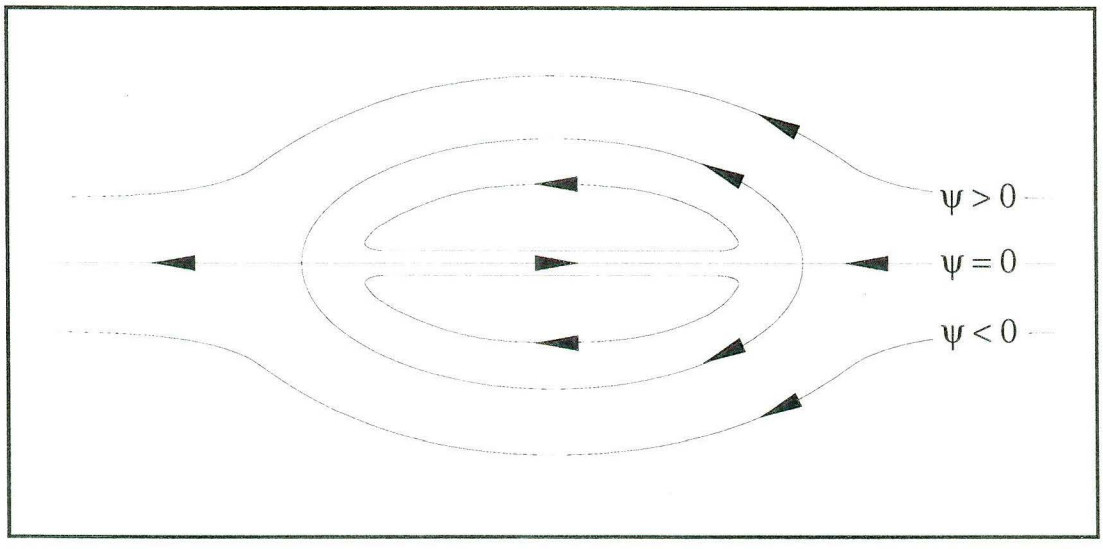

Figure 2.3 - Streamline pattern as modelled by Tung, Chan & Kubota (1982)

Experimental observations of the internal structure of the wave will be discussed in Section 2.5.4.

2.3 Experimental Techniques

The six experimental studies which are discussed here made use of a range of equipment and generation methods as well as visualisation and measurement techniques. The physical parameters of the experiments also varied over the range of experiments. Details of methods and wave parameters are summarised and discussed in this section.

2.3.1 Experimental Setup

In the laboratory, second mode waves have typically been generated in long rectangular flumes, where the depth of the flow exceeded its width. The flume volume has varied from 81 to 7300 litres. All flumes had transparent sides to allow a clear view of the flow.

The constant cross-section in these flumes ensured that geometric dispersion did not contribute to wave dissipation. One study (Maxworthy, 1980) conducted additional experiments on waves which spread radially, experiencing this sort of dispersion, but this issue will not be addressed in this thesis.

The experiments of Hachmeister & Rigby (1980) were the only ones done with unequal depths of fresh and saline water. In that study, the total depth was held constant while the thickness of the upper layer was varied.

In all of the experiments, the initial density stratification was set up by adding salt water to the flume before introducing a fresh water layer by means of floating diffusers. In some cases, the resulting interface was left to thicken, while in others a younger, sharper interface was used. All studies assumed that the interface adopted a hyperbolic tangent profile as discussed by Benjamin (1967). The range of interfacial thicknesses will be discussed in Section 2.3.2.

Each study used a different method to generate second mode waves. These methods are summarised in Table 2.1, and a more detailed discussion of generation observations will follow in Section 2.4.2.

Table 2.1 - Summary of flume and generation details

Study	Flume Size (mm) Filling Method	Generation Method
Davis & Acrivos (1967)	2500 x 400 x 100 Fresh on saline	Fluid at interfacial level drawn in by plunger and rapidly re-injected.
Hurdis & Pao (1975)	10000 x 600 x 360 Fresh on saline	Flat, 25.4 mm high plate towed along interface.
Kao & Pao (1979)	8000 x 600 x 350 Fresh on saline	Fluid mixed by oscillatory rotation of four bladed paddle constructed of nylon line on wire frame.
Maxworthy (1980)	8200 x 300 x 200 Fresh on saline	Fluid behind barrier mixed to form intermediate density fluid. Collapse upon barrier release.
Hachmeister & Rigby (1980)	14600 x 1000 x 500 Fresh on saline	Smooth floating keel towed on surface of fluid.
Stamp & Griffiths (1992) Stamp & Jacka (1995)	1800 x 300 x 150 Fresh on saline	Flat, 70 mm high paddle impulsively pushed through 250 mm distance to meet tank baffles

2.3.2 Flow Visualisation and Measurement

These studies made use of a variety of techniques to visually enhance and record the observed wave motion. Observations of fluid movement provided information about wave amplitudes and celerities, while other means were used to measure density profiles. The various methods used for flow visualisation and measurement are summarised in Table 2.2.

A range of dyes were used to track fluid movement. Immiscible fluids would settle at a level at which they were neutrally buoyant, and by blending mixtures of two or more of these fluids to a range of densities, it was possible to produce a set of parallel dye lines in the undisturbed stratification. The wave was then easily tracked by observing distortions in these lines. Miscible dyes contained in the wave or the interfacial region facilitated observations of fluid movement into and out of the wave. Vertical streaks of dye were created by dropping crystals into the flume.

More detailed observations of the flow structure were made possible by seeding the flow with neutrally buoyant particles. These were illuminated by slit lighting and time lapse photography produced streakline images of the flow.

Table 2.2 - Summary of visualisation and measurement techniques

Study	Visualisation Techniques	Measurement Techniques
Davis & Acrivos (1967)	Neutrally buoyant immiscible droplets of a mixture of carbon tetrachloride, toluene and red oil dye.	Still photographs taken during run. Sample densities measured with hydrometer.
Hurdis & Pao (1975)	Neutrally buoyant immiscible droplets of a mixture of carbon tetrachloride, mineral oil and red dye. Nigrosine crystals dropped in flume to create vertical dye streaks.	Still photographs taken at time intervals during run. Conductivity probe for density profiles.
Kao & Pao (1979)	Miscible dye introduced to interfacial region. Seeding of flow with neutrally buoyant Pliolite particles illuminated by two slit light boxes.	Still photographs taken at long and short exposures. Fluid velocity on centreline measured at two points with hot film anemometers.
Maxworthy (1980)	Neutrally buoyant immiscible droplets of a mixture of carbon tetrachloride, mineral oil and red dye. Miscible dye in interfacial region.	Still photographs taken at time intervals during run. Conductivity probe for density profiles as well as measurement of wave passage.
Hachmeister & Rigby (1980)	Horizontal dye lines in interfacial region.	Still photographic slides and 16 mm colour movie film taken during run. Conductivity probe for density profiles.
Stamp & Griffiths (1992) Stamp & Jacka (1995)	Neutrally buoyant immiscible droplets of a mixture of heptane, 1-bromopentane and sudan-3 dye. Horizontal miscible dye lines in interfacial region.	Video recorded during run. Conductivity probe and thermistor for density profiles. Samples checked with density meter.

Photographs, film and video recorded during the run aided in the measurement of flow velocities, flow paths and wave amplitudes. It should be noted that all of the studies discussed here made use of static cameras, with none following the wave as it moved. This makes the observation of the finer velocity structures much more difficult, as the magnitude of the internal flows relative to the wave celerity is often quite small.

Velocities were also obtained from hot-film anemometers placed on the centreline of the stratification in one study (Kao & Pao, 1979). These provided an accurate measurement of the wave's internal velocity structure along the centreline as well as furnishing time-displacement data. With the decay of the wave to unobservable amplitudes, this method also provided a measure of the infinitesimal solitary wave speed.

Most runs used a conductivity probe to provide a measure of the density profiles before and during the experiment. In some cases, a hydrometer or an Anton-Paar density meter (Section 3.3.1) was used to either measure or check the densities of fluid samples.

2.3.3 Wave Parameters

Wide ranges of densimetric factors, interfacial half-thicknesses and dimensionless depths were covered in the studies considered here. As well, a range of dimensionless wave amplitudes was observed. The relevant parameters for each experimental study are summarised in Table 2.3, where it should be noted that some values have been estimated from measurements of other parameters.

The densimetric factors used in the experiments ranged from $\omega = 0.0077$ to 0.0917, which correspond to lower layer mass fractions of 2.3% to 26% sodium chloride at 20°C. For comparison purposes, seawater has a densimetric factor of approximately 0.0125.

Table 2.3 - Summary of wave parameters

Study	Densimetric Factors Interfacial Half Thicknesses	Largest Dimensionless Amplitude Dimensionless Depth Range
Davis & Acrivos (1967)	$\omega = 0.0253, 0.0453, 0.0775$ $h = 5$ mm	$a/h = 2.0$ $H/h = 40$
Hurdis & Pao (1975)	$\omega = 0.0077, 0.0141, 0.0142$ $h = 4.1 - 34.5$ mm	$a/h = 3.7$ $H/h = 9 - 73$
Kao & Pao (1979)	$\omega = 0.0100$ $h = 11.4 - 29.2$ mm	$a/h = 4.8$ $H/h = 7 - 17$
Maxworthy (1980)	$\omega = 0.0244$ $h = 15$ mm	$a/h = 2$ $H/h = 10$
Hachmeister & Rigby (1980)	$\omega = 0.0113, 0.0123, 0.0125$ $h = 11 - 26$ mm	$a/h = 2.7$ $H/h = 20 - 45$
Stamp & Griffiths (1992) Stamp & Jacka (1995)	$\omega = 0.0253, 0.0485, 0.0707, 0.0917$ $h = 2.25 - 2.75$ mm	$a/h = 3.1$ $H/h = 51 - 62$

Interfacial half-thicknesses, h, ranged from 2.25 to 34.5 mm, with the corresponding dimensionless layer depths ranging from $H/h = 73$ to 7. It appears that smaller flumes make it easier to establish thinner interfaces, which makes sense if mixing during filling due to both diffusion and turbulence are considered. It should be

noted that deep water assumptions are not valid for *H/h* smaller than 40 (Tung, Chan & Kubota, 1982), which was the case in some of these experiments.

2.4 Wave Generation

Maxworthy (1980) stated that second mode waves were ubiquitous, in that "if a given physical system is capable of supporting solitary wave motions then such motions will invariably arise from quite general excitations." Davis & Acrivos (1967) had previously noted that virtually any disturbance of the density interface resulted in the formation of such a wave. Further support is provided by an examination of the range of techniques by which such waves have been generated in the laboratory. Virtually any action which causes mixing across the density interface seems to result in their formation.

In this section, the natural mechanisms and experimental methods by which second mode waves are generated will be discussed.

2.4.1 Natural Mechanisms

The ubiquity of internal solitary waves is reinforced by observations of their existence in a variety of situations. They have been recognised in density stratifications in both gases and liquids.

In the atmosphere, these waves have been seen to be generated by sea breeze and cold fronts. The 'morning glory' cloud phenomenon observed in the nocturnal inversion in northern Australia has been attributed to them (Christie, 1992). It has also been speculated they feature prominently in the Jovian atmosphere (Maxworthy, Redekopp & Weidman, 1978). Maxworthy (1980) suggested that such waves might also be generated by thunderstorm downdrafts, katabatic winds and spreading natural gas spills.

Second mode waves have also been observed to exist in lakes, fiords and oceans. Several studies (Ostrovsky & Stepanyants, 1989; Farmer & Smith, 1978) described the generation of waves by flow over submarine topography. Waves are thought to be produced by the passage of arctic pack ice pressure ridges under typical summer

stratifications (Hachmeister & Rigby, 1980). Maxworthy (1980) demonstrated how the impingement of a thermal on a sharp density stratification can result in the formation of second mode waves.

2.4.2 Experimental Techniques

Six different wave generation methods have been used in the experimental studies discussed here. At first they may appear quite different, but in fact they have much in common. All of the methods involve mixing interfacial fluid, which increases its potential energy. Some methods also directly impart kinetic energy to the mixed fluid, but even if this is not the case, the gravity driven collapse of the mixed region soon converts its potential energy to kinetic energy, initiating wave motion.

Davis & Acrivos (1967) generated waves by means of a plunger apparatus. This was used to draw in fluid through a slit at the level of the interface at the tank's end. It was then impulsively ejected back into the interfacial region, creating a chaotic disturbance which transformed itself into a second mode wave within a short distance.

The study of Hurdis & Pao (1975) was intended to examine the behaviour of a region upstream of a moving, flat, vertical plate. Second mode waves were observed to be generated as a consequence of this motion. The movement of the plate seemed to cause a thickening of the interface upstream of the plate which then collapsed to form a wave.

A followup study by Kao & Pao (1979) made use of a different method of generating waves. A four-bladed paddle was constructed of nylon fishing line tied around a wire frame. This was vigorously moved back and forth through a 260° rotation over several seconds to create a mixed region, which then collapsed and quickly formed two similar waves which travelled in opposite directions.

Maxworthy (1980) generated waves by inserting a barrier near one end of the flume, after which fluid behind the barrier was mechanically mixed. The subsequent removal of the barrier caused the collapse of the mixed region and the rapid formation of trains of solitary waves. The number of waves in each train was

observed to be a function of the length and height of the mixed region, and they were ordered by amplitude.

The study of Hachmeister & Rigby (1980) was intended to simulate the generation of second mode waves by pressure ridges in the arctic ice pack. Waves were generated by towing a floating keel on the surface of the flume. Second mode waves followed in the wake behind the keel, with increases in keel velocity matched by increases in wave amplitude and celerity. A critical wave celerity was computed based on layer densities and the thickness of the pycnocline, and this was used to establish whether towing speeds were sub- or supercritical. It was found that subcritical towing speeds resulted in the formation of trains of second mode waves, while supercritical speeds formed single second mode waves. Increases in the towing speed much above supercritical resulted in the generation of only first mode waves.

The studies of Stamp & Griffiths (1992) and Stamp & Jacka (1995) appear to be based on one set of experimental data. The generation method involved a 70 mm high paddle, aligned perpendicular to the density interface, which was moved 250 mm from the end of the tank until it rested between two polystyrene baffles. It then served as a perpendicular end wall for the tank. It was observed that interfacial fluid displaced by the paddle collapsed along the interface, with billowing instabilities removing some fluid from the intrusion before it transformed into a single, large amplitude wave. This was generally accomplished in a very short distance. This method seemed to produce a fairly consistent wave amplitude, with the authors noting their inability to generate waves above a dimensionless amplitude of 3.1.

It is evident that there are many possible methods that might be used for producing second mode waves in the laboratory. In choosing a method for further experiments, it would be advantageous to select one which lends itself to easy setup, measurement and repeatability. The ability to produce a wide range of wave amplitudes would also be advantageous. This indicates that a method similar to that of Maxworthy (1980) would likely be the best option to pursue in further experimentation.

2.5 Wave Propagation

Aspects of wave propagation which have been examined include behaviour as true solitary waves as well as details of external and internal flows. Examinations of the external flow generally focus on the dependence of wave celerity on other parameters, while internal flows deal with the entrainment of fluid into and expulsion of fluid out of the wave, as well as the associated issues of mass transport by the wave. A review of general observations of the second mode wave will precede the discussion of these issues.

2.5.1 General Observations

General observations about second mode solitary waves include details of their shape (including two-dimensionality, variations of aspect ratio and form with amplitude, and asymmetries about the centreline) as well as the movement of fluid in their lee.

The theoretical treatments of Benjamin (1967) and Davis & Acrivos (1967) both made assumptions of two-dimensionality for second mode waves, and these assumptions were reinforced by the experimental study of the latter. The flow was described as "extremely two-dimensional with no noticeable velocity parallel to the wave front and without significant interaction with the walls of the wave tank." These observations were in agreement with those of Stamp & Jacka (1995) which stated "the waves were aligned straight across the channel, the sidewall boundary layers were too thin to observe and there were no noticeable motions along the wave-front." The only experimental observations contrary to these were made by Maxworthy (1980), who noted that where a wave front was long relative to its thickness, the fluid within the wave might adopt a cellular structure. The observed expulsion of fluid from the wave in streaks instead of in a flat sheet was taken as evidence of this.

The distinction between waves of large and small amplitude was addressed in Davis & Acrivos (1967), where the distinction was made based on the propagation characteristics of the wave. Large amplitude waves were identified by 'closed

streamline' regions in which fluid was carried along at the same celerity as the wave (in the numerical model this occurred above $a/h \approx 1.2$), while small amplitude waves propagated faster than any individual fluid component. This criterion was also adopted by Stamp & Jacka (1995).

Second mode waves were described as symmetrical about the centre of the density gradient by both Davis & Acrivos (1967) and Kao & Pao (1979). More detailed observations by Stamp & Jacka (1995) revealed slight asymmetries in the form of the wave. The upper amplitude of the wave was consistently measured as being larger than the lower amplitude, and the upper and lower portions of the wave were frequently out of phase, though wavelengths were generally similar. This was explained as being caused by the difference between the free surface and closed boundary conditions above and below.

With regards to wave profile, Stamp & Griffiths (1992) noted a constant wave aspect ratio (wavelength divided by amplitude) of 2.2. Stamp & Jacka (1995), though, observed that for small amplitude waves, increases in amplitude were accompanied by decreases in wavelength, while for large amplitude waves, amplitude and wavelength increased together. A linear relationship between dimensionless wavelength and amplitude, which is shown in the following equation, was presented.

$$\frac{\overline{\lambda}}{h} = 0.95 + 2.10\,\frac{\overline{a}}{h} \quad \text{for } 1.0 \leq \frac{\overline{a}}{h} \leq 3.1 \tag{2.36}$$

Here $\overline{a}$ and $\overline{\lambda}$ represented the average of the upper and lower amplitudes and wavelengths, respectively. Note that this equation is applicable to a more restricted range than Equation 2.37, as for small amplitude waves it was difficult to measure the amplitudes and wavelengths.

A further observation of second mode waves was that waves were frequently generated in their lee. Davis & Acrivos (1967) reported the shedding of semiperiodic waves from behind the wave, while the existence of a following train of internal waves was observed by Kao & Pao (1979). The presence of a first mode

wave immediately behind the second mode wave was observed by Hachmeister & Rigby (1980), and this observation was supported by the work of Stamp & Jacka (1995). The latter study noted that this wave production may be a mechanism for the transfer of energy from the second mode wave, and also that the existence of the first mode wave was predicted in the work of Akylas & Grimshaw (1992).

2.5.2 Soliton Behaviour

Whether or not the wave under consideration is actually a solitary wave was a topic touched on by several studies. Its longevity and constant form was certainly taken as an indication of its status as a solitary wave (Davis & Acrivos, 1967). As more rigorous proof, Kao & Pao (1979) measured the internal velocity structure of the wave and found it to agree with the sech^2 waveform corresponding to a Korteweg-de Vries type wave, as well as noting that the wave's performance during collisions and reflections was typical of solitary waves. Maxworthy (1980) noted that though these waves sometimes occurred in trains of several waves, and also decayed with time, they were accurately described as solitary because of the balance between frequency dispersion and nonlinear steepening. Several studies reported negative phase shifts during wave reflections, which was noted in Stamp & Jacka (1995) as being typical of solitary waves on a free surface.

Most of the studies considered here have examined the collision of second mode internal solitary waves with each other as well as their reflection from vertical walls. The first experimental observations of Davis & Acrivos (1967) included a brief note that reflection of waves from the end walls of the tank resulted in a minimal energy loss, and that waves could collide and pass through each other without a further loss of shape. Kao & Pao (1979) made similar observations, noting that during collisions of two waves of equal size, the amplitude appeared to double, pointing to a superposition of the two waves. A negative phase shift of the wave during collisions or reflections was also reported, though no correlation of the length of the shift with wave amplitude was possible. It was also observed that when two waves collided, though momentum was transferred, the actual fluid of which the waves

were composed was not. When two waves of equal size collided, it was as if they had each reflected from a vertical wall at the point of collision.

Maxworthy (1980) also reported a negative phase shift at reflections which was noted as being characteristic of solitary waves. Stamp & Griffiths (1992) reported a difference in the behaviour of large and small amplitude waves during reflections. The latter experienced no energy loss and their behaviour was not dependent on amplitude. In contrast, large amplitude waves were always smaller after reflection, with larger ones breaking away from the boundary and ejecting some trapped fluid. Smaller large amplitude waves reflected from the boundary without breaking, but ejected all of the fluid trapped within and were transformed into small amplitude waves. Both large and small amplitude waves experienced a doubling of amplitude when deformed during the reflection. Collisions were described as being similar to reflections in terms of fluid flow reversal and wave breaking, with fluid only passing the collision point when necessary to satisfy conservation of momentum during the collision of waves of unequal size. Stamp & Jacka (1995) reported a slight negative phase shift during reflections.

2.5.3 External Flow

The wave's external flow characteristics are defined by its form, size and speed. The shape of the wave has been discussed previously, so this section will concentrate on the relationship between wave amplitude and celerity.

Davis & Acrivos (1967) compared their experimental results to the relationship defined by Equation 2.28, which was derived in their paper. They found good agreement for smaller amplitude waves, though for dimensionless amplitudes above approximately one, it appeared that non-linear effects caused the data to diverge from the theory. Hurdis & Pao (1975) compared their data as well as those of Davis & Acrivos (1967) to the latter's theory as well as that of Benjamin (1967; Equation 2.25), which was found to provide a better fit to the data for larger amplitude waves. Kao & Pao (1979) compared the result of their theoretical analysis (Equation 2.33) to their experimental data and also found a good agreement. Stamp & Griffiths

(1992) fitted the following expression to their own experimental data as well as that of Davis & Acrivos (1967):

$$\frac{c}{c_o} = 1 + 0.4930\,\frac{a}{h} \quad \text{for } 0.08 \le \frac{a}{h} \le 2.85 \tag{2.37}$$

Equation 2.37 shows that the wave celerity, c, when nondimensionalised by the speed of a long, linear wave, c_o (defined in Equation 2.34), is linearly related to the dimensionless amplitude. This was taken to show that wave celerity was proportional to the square root of the densimetric factor, ω, and that the linear relationship applied over the entire range of large and small amplitude waves. These results were said to be in agreement with the numerical solution of Tung, Chan & Kubota (1982). The later paper of Stamp & Jacka (1995) modified Equation 2.37 by changing the coefficient of dimensionless amplitude to 0.49, and extending the lower and upper bounds of the range of applicability to 0.1 and 3.1, respectively, as well as considering the average of upper and lower amplitudes and wavelengths.

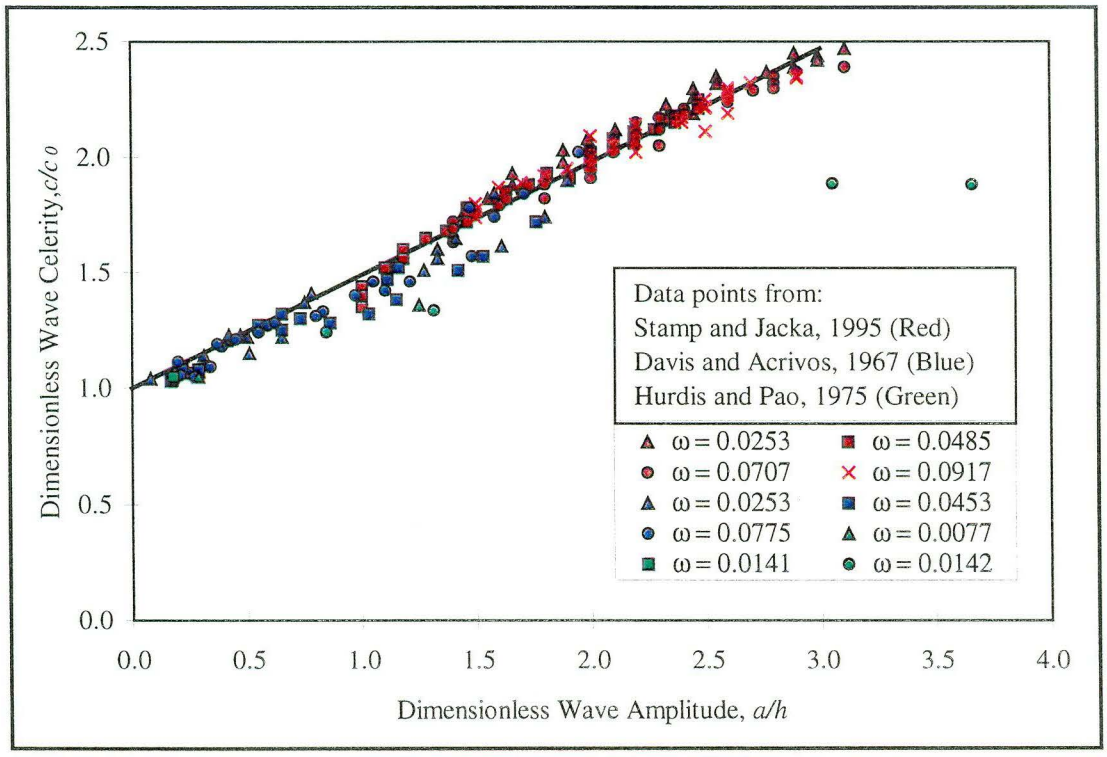

Figure 2.4 - Relationship between dimensionless wave amplitude and celerity

The experimental data of Davis & Acrivos (1967), Hurdis & Pao (1975) and Stamp & Jacka (1995), with a line corresponding to Equation 2.37, are shown in Figure 2.4. There is good agreement with all of the data, except that of the larger amplitude waves of Hurdis & Pao (1975). This indicates that the primary avenue for further research here would be to obtain measurements for larger amplitude waves, to investigate whether the theoretical relationships already presented are valid if the upper range is extended. The deviation of the noted data points representing large amplitude waves may hint at a deviation of the theory at such amplitudes. The experimental data of Davis & Acrivos (1967), Hurdis & Pao (1975) and Stamp & Jacka (1995) are presented in detail in Appendices 1, 2 and 3.

2.5.4 Internal Flow

The entrainment, transport and expulsion of fluid by the wave are all important components of the internal flow of the second mode wave. The wave's potential for mass transport was recognised well before observations of expulsion and later entrainment were published.

Mass transport by large amplitude waves was predicted by the theories of Benjamin (1967) and Davis & Acrivos (1967) and was first observed by the latter. The fluid in the interior of the wave was noted as travelling at the same velocity as the wave itself, as opposed to fluid in smaller amplitude solitary waves in which fluid velocities were less than the wave celerity itself. The later studies of Kao & Pao (1979), Hachmeister & Rigby (1980) and Maxworthy (1980) all noted the transport of bodies of fluid inside of second mode waves. Davis & Acrivos (1967) recognised that "naturally occurring internal waves may play a significant role in transport processes within oceans and estuaries, either directly by convection or indirectly by the generation of turbulence." However, neither their study, nor any other, attempts to quantify the mass transport capacity of the second mode wave.

Maxworthy (1980) reported the first observations of the expulsion of fluid from second mode waves. He noted that dye from the original collapsing region was carried along inside the wave, concentrated in two elliptical regions centred about the axis of symmetry of the wave. Thin tendrils of dye extended from these dyed

regions to the original collapsing region, and this was taken as an indication that dye was constantly being ejected from the wave. No mention was made of any uptake of fluid into the wave, and the supposition that the dye ejection must result in a gradual loss of wave amplitude indicates that the possibility of fluid uptake was not considered. Stamp & Griffiths (1992) noted laminar ejection of fluid from the recirculating region along the centreline of the density interface, as well as turbulent ejection of fluid from the lee of the wave above and below the centreline. The former was held responsible for a thickening of the density interface behind the wave. The later paper by Stamp & Jacka (1995) observed that the recirculating region consisted of two counterrotating cells, as described by the numerical models of Davis & Acrivos (1967) and Tung, Chan & Kubota (1982), located above and below the centreline of the density interface, though no clear boundary separated the cells.

Stamp & Griffiths (1992) were the first to report an uptake of interfacial fluid from ahead of the wave into the closed streamline region. Interfacial fluid was reported as being slowly mixed in at a constant rate along the entire length of the boundary streamlines by turbulent diffusion. Stamp & Jacka (1995) noted that it would be more accurate to describe the closed streamline as an 'intermittency surface', but they retained traditional nomenclature to avoid confusion.

These observations of wave entrainment and expulsion as well as mass transport were quite qualitative, leaving considerable scope for further research into the wave's capacity for mass transport. The existence of an "intermittency surface" also begs the question of whether previous observations of waves' internal circulation are complete. The use of particles rather than dye, in conjunction with a moving camera to track the wave, would seem to allow one to make more detailed observations of the internal structure of the wave.

2.6 Wave Dissipation

Davis & Acrivos (1967) observed second mode waves to be long-lived, exhibiting "the same remarkable property of persistence that is familiarly observed in practical examples of the classical solitary wave." Experimental observations, though, have

inevitably included mention of their eventual decay. No quantitative description of the rate of wave dissipation has been made until recently, however, and no conclusive evidence as to the reason for this decay has been put forward.

2.6.1 Experimental Observations

Davis & Acrivos (1967) first recognised the difference in attenuation behaviour between large and small amplitude waves. Large amplitude waves with "closed streamline" regions were noted as decaying rapidly, until they became small waves which were more long-lived and decayed slowly. A gradual attenuation was also reported by Kao & Pao (1979). Maxworthy (1980) noted that the measured decrease in wave celerity with time was indicative of a reduction in amplitude as mixed fluid was ejected from the closed streamline region inside the wave. Stamp & Griffiths (1992) reported a rapid decay of large amplitude waves into smaller amplitude ones in which the rate of decay was slowed. The latter study provided the first quantitative description of wave decay, noting a linear relationship between amplitude and displacement. Data from Stamp & Griffiths' (1992) study are shown in Figure 2.5.

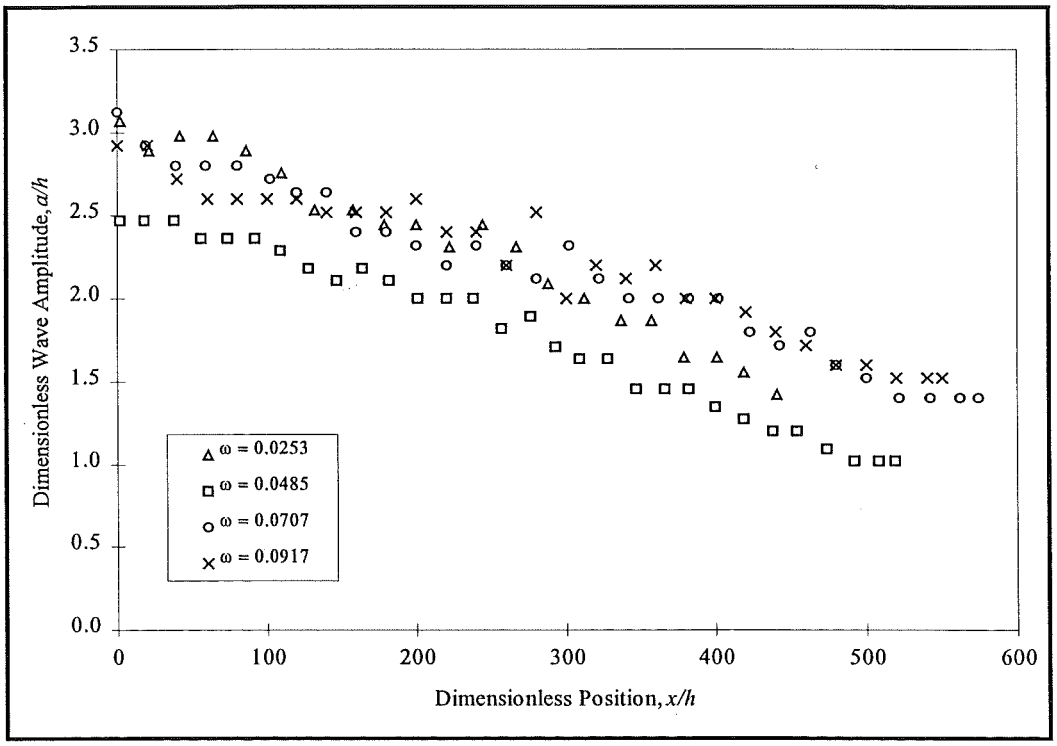

Figure 2.5 - Decay of second mode waves

2.6.2 Analysis

Speculation as to the cause of the decay of these waves has been made in several studies. Davis & Acrivos (1967) attributed wave decay to viscous dissipation and the generation of semiperiodic waves in the lee of the wave, while Kao & Pao (1979) noted only "viscosity" as the cause. Viscous wall effects or wave breaking were presented as possible causes by Stamp & Griffiths (1992). This study recognised that the rate of decay was lower for waves with higher densimetric factors, and that this latter factor was related to the Reynolds number of the flow.

Stamp & Jacka (1995) further discussed the linear nature of second mode wave decay, noting that both free surface (Lighthill, 1978) and interfacial (Koop & Butler, 1981) waves typically exhibit higher rates of decay for larger amplitude waves. It was stated that the difference was primarily due to differences in the decay mechanisms, and it was further recognised that due to the limited range of wave amplitudes examined, it was not possible to definitively state that the linear decay behaviour was valid for larger amplitudes.

In an attempt to define the relative importance of potential decay mechanisms, Stamp & Jacka (1995) performed further analysis of various related parameters. Viscous stresses at the sidewall or interface, turbulent mixing converting kinetic into potential energy through the thickening of the density interface, and wave radiation as first mode waves generated in the lee of the wave, were considered.

Stamp & Jacka (1995) assumed that if viscous stresses were responsible for the dissipation of the wave, some relationship should be evident between the rate of decay and a Reynolds number which was representative of the flow. The rate of decay was observed to be independent of wave amplitude (and therefore celerity), so the relevant velocity scale was taken to be the speed of a long, infinitesimal wave on the density interface. The kinematic viscosity of fluid of a density equal to the average density of the upper and lower layers was used as the viscosity scale. Two relevant length scales were chosen for examination, these being the width of the channel (for sidewall dissipation) and the interfacial half-thickness (for interfacial dissipation). The two Reynolds numbers are shown in Equations 2.38 and 2.39.

$$Re_h = \frac{c_0 h}{\nu} \propto \frac{\left(g\,\omega\,h^3\right)^{1/2}}{\nu\left(\bar{\rho}\right)} \tag{2.38}$$

$$Re_w = \frac{c_0 w}{\nu} \propto \frac{\left(g\,\omega\,h\right)^{1/2} w}{\nu\left(\bar{\rho}\right)} \tag{2.39}$$

Figure 2.6 shows the variation of wave decay rate with the sidewall and interface Reynolds numbers as well as the densimetric factor. Values on the x-axis have been normalised by dividing by the highest value and series have been offset for clarity. These results were taken by Stamp & Jacka (1995) to indicate that rates of decay increased with decreases in channel width, interfacial thickness and densimetric factors.

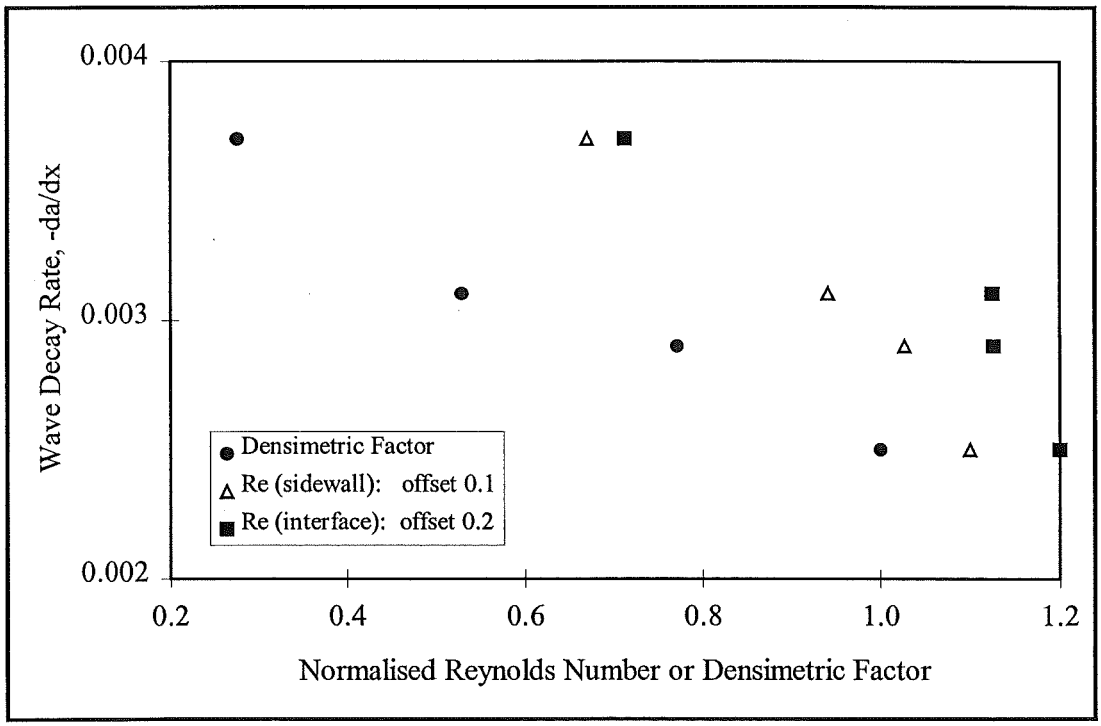

Figure 2.6 - Decay rate dependence on Reynolds number and densimetric factor

A Richardson number was assumed to provide an index of the amount of energy drained from the wave by mixing of fluid due to shear instabilities. The relevant density scales were taken as those of the upper and lower layers, with the length scale chosen as the interfacial half-thickness. The velocity scale was once again

chosen as the infinitesimal long wave celerity, giving the following expression for Richardson number:

$$J \propto \frac{g\,\Delta\rho\,h}{\overline{\rho}\,c_0^2} = \frac{g\,\Delta\rho\,h}{\overline{\rho}\left(g\,\omega\,h\right)} = \text{constant} \tag{2.40}$$

It was apparent from the preceding equation that the calculated Richardson number was constant for all waves, indicating a similar shear instability behaviour across the entire range of wave parameters. This was taken to mean that turbulent mixing could not explain the variation in the rate of wave attenuation with density difference.

A rough estimate of energy losses due to wave radiation was made by substituting empirical equations for wave celerity and aspect ratio into a relationship describing the temporal rate of energy loss as a function of the energy of the first mode waves being generated in the wake of the second mode wave. The resulting relationship, in which ξ is the amplitude of the first mode wave, follows:

$$\frac{da}{dx} \propto \frac{h\xi^2}{a^3} \tag{2.41}$$

The preceding equation shows that the rate of decay would vary proportionally to the square of first mode wave amplitude and would be inversely proportional to the cube of the second mode wave amplitude. The fact that the experimentally measured rates of decay did not vary with wave amplitude was taken as an indication that wave radiation was not a primary cause of wave decay.

Stamp & Jacka (1995) observed that wave attenuation appeared to be a result of wave radiation, turbulent mixing and viscous stresses. The Reynolds number dependence of the decay rate pointed to the latter as the primary mechanism, but the limited range of data and the admittedly crude scaling estimates left considerable scope for further investigation.

2.7 Strategy for Present Study

The preceding examination of existing studies on second mode waves shows that there remains considerable scope for study on this topic. In this section, possible avenues of further research, as well as variations in experimental techniques, are discussed.

2.7.1 Research Goals

Any complete examination of second mode waves must alternately focus on the generation, propagation and eventual dissipation of the wave. The propagation component must be considered to include external characteristics such as the relationship between wave amplitude and celerity as well as an examination of the internal structure of the wave.

Previous studies do not make detailed observations of the development of a second mode wave, and generally include only brief notes on the transition from a mixed region to a fully fledged wave. Regardless of the generation method, the use of improved visualisation and image acquisition techniques should allow a more complete description of wave development.

A good agreement has been observed between experimental observations and theoretical relationships for wave celerity, but the existing body of experimental data does not include waves of very large amplitudes. If very large amplitude waves can be generated, this will allow an examination of the applicability of existing equations to such waves. Alternate theoretical derivations for very large amplitude waves may also be entertained.

Observations of the internal velocity structure of the wave have been primarily qualitative. This leaves open the possibility for the application of quantitative visualisation techniques to an examination of this motion. No study to date has followed the flow with imaging devices, providing the moving frame of reference which has been adopted in theoretical derivations. This method would no doubt enhance observations of fine scale motions within the wave.

A recent study has made progress towards isolating the mechanisms by which these waves decay, but results were inconclusive. A larger body of data would no doubt assist in the study of this aspect of wave motion.

Existing numerical studies have made use of governing equations which assumed an inviscid, steady state flow. The development of a numerical model, based on the complete, two-dimensional Navier-Stokes equations could provide information on all of the preceding aspects of wave behaviour, from generation though to decay.

2.7.2 Experimental Techniques

A range of wave generation techniques have been used by previous studies. In the interests of repeatability and quantification of parameters, it would be advantageous to select a technique in which an excess of potential, rather than kinetic, energy results in wave generation. This points towards a generation method similar to that of Maxworthy (1980), though variations on this procedure should be considered.

Conventional dyes are available for flow visualisation, as are fluorescent dyes which may be used in conjunction with a laser illumination system to provide quantitative measurements of fluid dispersion. The flow may also be seeded with neutrally buoyant particles to track flow patterns. Photographic and digital video cameras are available to record the flow. As previously mentioned, the ability to follow a wave to provide a moving frame of reference could prove to be a great advantage, so a system which allows this should be adopted if possible.

The visualisation techniques mentioned here should place this study at a considerable advantage over previous ones, allowing detailed, quantitative observations of wave motion.

A conductivity probe, as used in several studies, as well as an oscillatory density meter, are available to measure fluid densities and density profiles.

3.0 Experimental Equipment and Methods

All experiments involved in this project were performed between September 1993 and November 1996 in the Civil Engineering Fluid Mechanics Laboratory at the University of Canterbury. The experimental apparatus was situated in a dark room where laser, video and computer equipment were used to record and analyse the experiments. Both dyes and particles were used to visualise flows, and fluid densities were measured by two methods. Fluids were premixed in tanks on a platform above the dark room and introduced to the tank by gravity feed. A variety of release mechanisms were used over the course of the experiments.

3.1 Tank Setup

Preliminary experiments were performed in a 5300 mm long perspex flume which measured 250 mm wide by 400 mm deep. The flume was divided into two sections, with a 1500 mm length at one end used to hold intermediate density fluid. This left 3800 mm for development and propagation of the solitary wave. This flume is pictured in Figure 3.1.

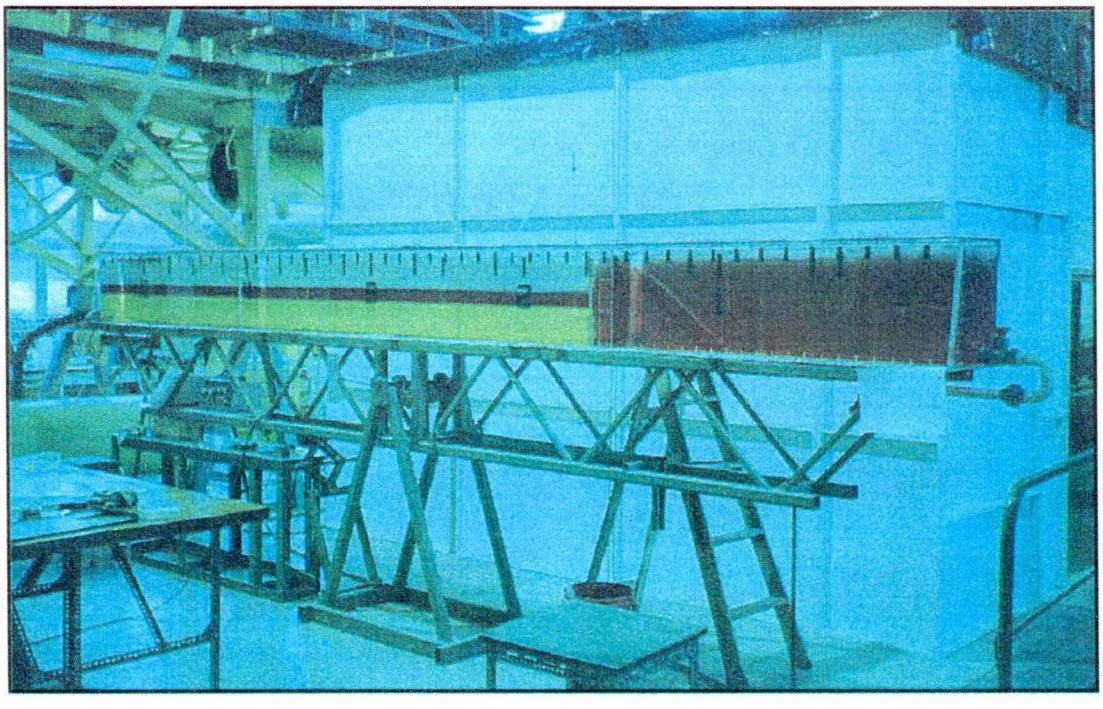

Figure 3.1 - Flume used for preliminary experiments (dark room in which main experiments were carried out is visible in background)

For the main body of experiments, it was necessary to operate in a darkened room with the visualisation equipment which is described in Section 3.2. The darkened tank room was of light braced plywood construction, with a ceiling made of chain link panels covered with opaque polyethylene sheets. It contained a laser illumination setup, computer and video equipment, and a motorised camera trolley. This equipment, in conjunction with a larger water tank, was used on several other research projects over the course of these experiments. To minimise new setups and to smooth transitions between projects, a removable flume insert was designed for this tank. The tank measured 6000 mm long by 1500 mm wide and was 1080 mm deep. Filling and draining was accomplished through four, 100 mm diameter pipes which were connected to the tank floor and which were fitted with individual valve controls and connected to the same water main. A flume was constructed in this tank by placing a 600 mm high vertical sheet of 6 mm perspex into the tank, 250 mm from its front wall. The perspex sheet was supported at the bottom by a strip of perspex, secured to the tank floor by silicone sealant, and was propped up by buttresses every 1250 mm. Since this setup was not strong enough to counter the hydrostatic forces when the flume was filled, it was necessary to fill the entire tank during experiments, with forces from fluid outside the flume balancing that from those inside. The tank and flume insert are shown in Figure 3.2.

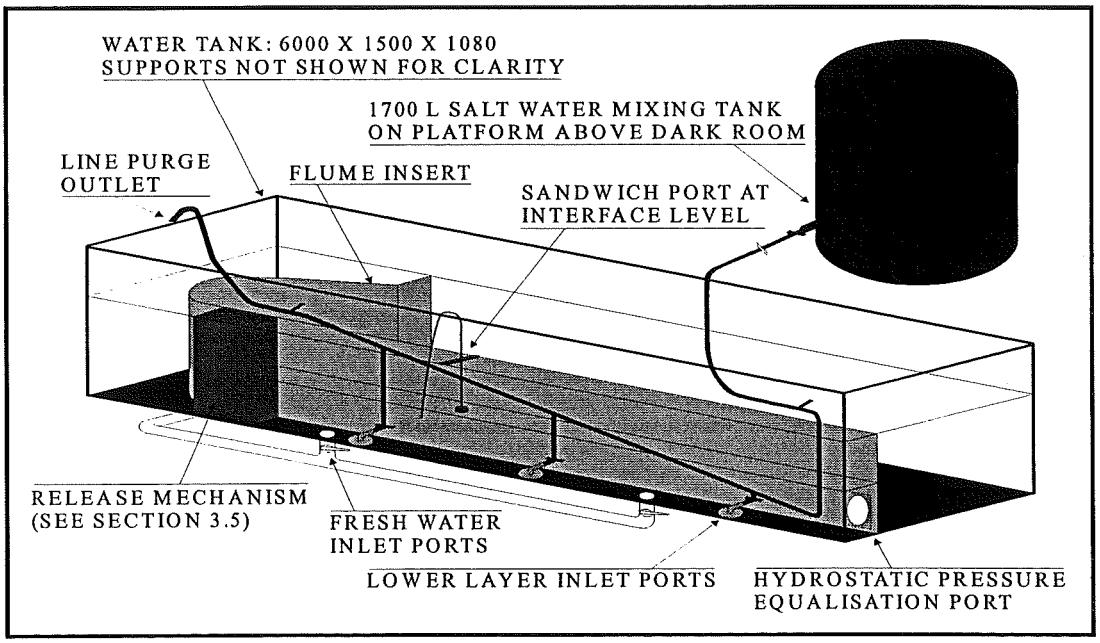

Figure 3.2 - Flume located in large tank

Loading of fluid into the tank was accomplished by first filling the tank with fresh water to a depth greater than the height of the flume. A port in the flume wall was left open to equalise hydrostatic pressures on either side, but after filling, it was blocked. The lower layer of salt water was then established by introducing fluid through three inlet ports consisting of 25 mm diameter pipes flowing into a 6 mm deep gap between the tank floor and a 150 mm diameter perspex disc. These ports were connected to a common hose attached to a mixing tank located on a platform above the dark room.

In some experiments, sandwich inlet/outlet ports were used to place fluid on or extract fluid from the interfacial region. Ports with diameters of 50 and 100 mm were used for such purposes as drawing off fluid to sharpen the interface, introducing dye to the interfacial region, and loading fluid to the collapsing region when a collapse release mechanism was used.

Several release mechanisms, which will be discussed at length in Section 3.5, were used during these experiments. These were located in the flume and secured by silicone sealant.

3.2 Flow Visualisation

Fluorescent dye as well as neutrally buoyant particles were used to visualise the flows in these experiments. Preparation of these tracers will be discussed in Section 3.4. Flows were illuminated by a sheet of laser light and recorded on film and video. The errors associated with the measurement of experimental parameters by these methods are discussed in Appendix 12.

A motorised trolley system was used to track the wave, providing a moving frame of reference which transformed an unsteady flow into a steady one. An AuCodrive SEDH58-8 variable frequency controller, manufactured by AuCom Electronic Motor Control Systems, was used to control two trolleys. One of these ran on rails mounted atop the tank, and this was used in the last batch of experiments to mount a mirror used to aim the laser light sheet as described in Section 3.2.1. The other moved on rails on an elevated bench in front of the tank, where it held the cameras

described in Sections 3.2.2-4. Both trolleys were powered by 250 watt electric motors, and the controller allowed them to be operated in synchronisation. The trolley configuration is illustrated in Figure 3.3.

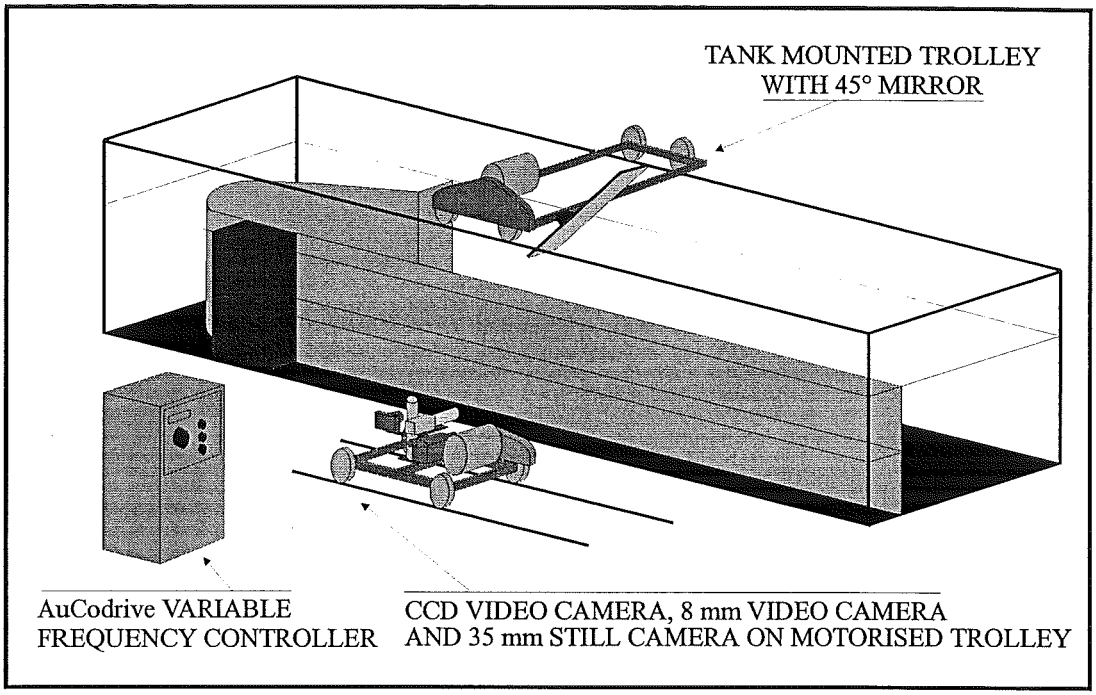

Figure 3.3 - Motorised trolley configuration

3.2.1 Illumination

Flows were illuminated using a system involving a laser complemented with several types of mirrors. At the heart of the setup was a Coherent Innova 70A Ar-I laser which generated 2.4 W in single line mode (514.5 nm) or 6.0 W in multiline mode (458 - 529 nm). The former was used in conjunction with fluorescent dye, while the higher beam intensity was used for particle visualisation experiments, where the wavelength of light was not important.

It was necessary to transform the laser beam into a sheet before it was useful for flow visualisation experiments. A Lincoln Laser Company M-660-010-LVWOB octagonal rotating mirror was initially used to change the 1.5 mm thick beam into a sheet. As the mirror spun, the reflected beam scanned through an arc. This produced a light sheet in which the intensity dropped rapidly with distance from the mirror, as the individual beams composing the sheet diverged. At distances of

greater than approximately 1.5 m from the rotating mirror, light intensities became too low to be useful. This problem was solved by the acquisition of a 750 mm scanning beam box, manufactured by Optical Flow Systems, which used the same rotating mirror in conjunction with a parabolic mirror to produce a light sheet composed of parallel rather than divergent beams.

Initially, this sheet was projected into the tank from one end, but problems with loss of light intensity arose due to refraction by the density interface and absorption of light by the salt water layer. This was remedied by raising the scanning beam box above the tank, mounting a mirror on the tank trolley at an angle of 45°, and using it to deflect the light sheet downwards. The three mirror configurations used over the course of the experiments are shown on Figure 3.4.

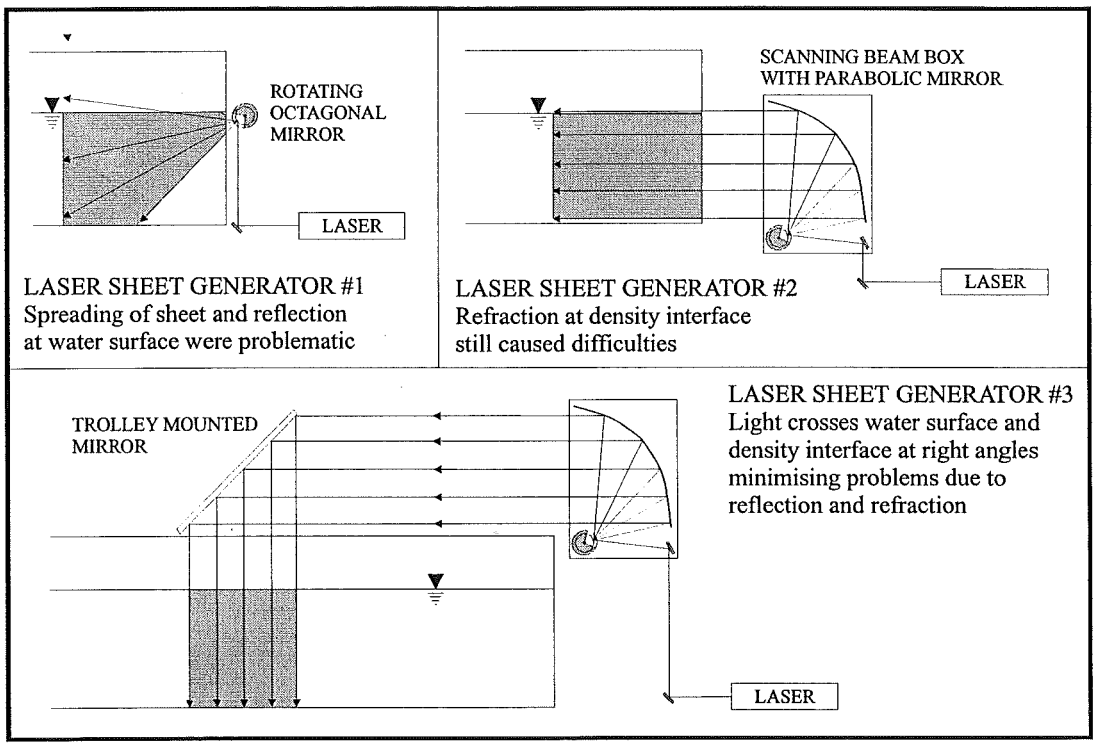

Figure 3.4 - Mirror configurations used with laser to generate light sheet

3.2.2 Digital Video

Experiments were recorded using a Pulnix TM 765 CCD video camera with image intensifier, connected to both a video recorder and a computer equipped with a frame grabber. This camera had a resolution of 1024 x 1024 pixels. The video

recorder was a Panasonic NV-FS200EC Super-VHS model which allowed for a maximum 400 lines of resolution, an improvement on the 240 that a regular VHS recorder would allow. The frame grabber was a Data Translation DT-2867, installed in a 486 personal computer, which allowed the acquisition of images of dimension 512 x 768 pixels. These digital images were saved in Tagged Interchange File Format (TIFF) files for later analysis and insertion into this document. The frame grabber allowed the acquisition of both single and time-averaged images, with the latter producing a pattern of streaklines. The device connections are schematised in Figure 3.5.

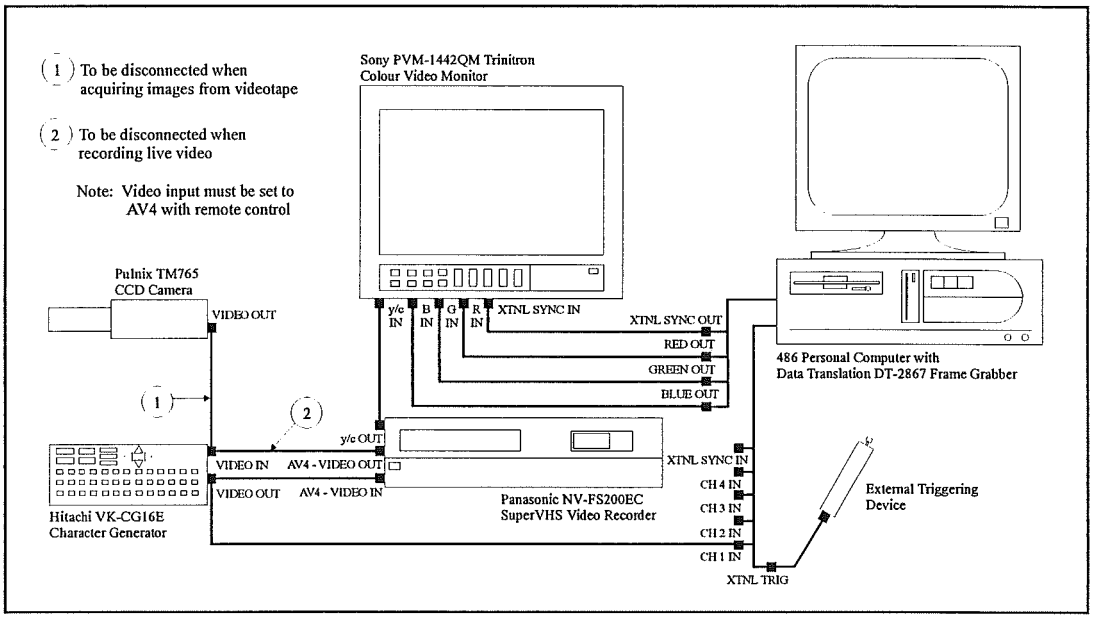

Figure 3.5 - Schematic diagram of video/frame grabber setup

Cosmicar television lenses, in both 50 and 75 mm sizes, were used to control both focus and aperture. When using laser induced fluorescence for flow visualisation, a yellow sharp cut-off glass filter was placed in front of the CCD camera. This filter, a Melles Griot model OG 530, prevented passage of light of wavelength shorter than 530 nm, blocking the green (514.5 nm) laser light. Thus, in the absence of extraneous light, the camera only recorded the yellow (560 nm) light of the fluorescing dye.

3.2.3 8 mm Video

A Sony 8 mm Handicam was also used to record images of the wave. Whereas the CCD camera was intended to provide a detailed view of a small area, the 8 mm camera was fitted with a wide angle lens to record motion behind the wave as well as more of the area above and below it. These recordings were later dubbed to a VHS tape for storage.

3.2.4 Still Photography

Still photographs were taken during some experiments. An Olympus OM-2 35 mm camera, fitted with motor drive, electronic timer and 150 mm zoom lens, was mounted on the trolley with the two video cameras. The timer was set to expose the film at one or two second intervals over the course of the experiment. When using particles for flow visualisation, a one-half second time lapse was generally used to create a streakline effect, while with fluorescent dye shorter exposures were required.

Though some colour print film was used, the camera was typically loaded with Ilford 400 ASA black and white print film. Prints or contact sheets were developed for inspection, but digital images were used for analysis and insertion in this document. A Kodak Professional RFS 2035 Plus film scanner was used with Adobe Photoshop 3.0 running on a Macintosh 7100/80 Power PC to produce TIFF files for these purposes.

3.3 Fluid Density Measurement

The measurement of fluid densities in these experiments was crucial, in that the calculated values of two important quantities, the densimetric factor, ω, and the interfacial half-thickness, h, were dependent on measured density values.

To calculate the former quantity required knowledge of only the representative density of the upper and lower layers of fluid. Approximate values of these densities were known from the preparation of the fluid, which is discussed in

Section 3.4.1, but evaporation losses, temperature changes and errors during mixing all had the potential to cause the actual density to vary from that desired. During the latter batches of experiments fluid samples were taken and later analysed with a density meter through a procedure outlined in Section 3.3.1, to determine the actual fluid densities.

To determine the interfacial half-thickness, it was necessary to determine the density profile of the fluid column. This was accomplished by using a linear potentiometer and conductivity probe, connected to a computer via an analog-digital interface, to record the relationship between depth and fluid conductivity. The latter was then converted to a density via a technique described in Section 3.3.2.

Error estimates for the two density measurement techniques are discussed in Appendix 12.

3.3.1 Anton-Paar Density Meter

Fluid samples were obtained by drawing off fluid after the experiment had been set up. A length of small diameter (4 mm) plastic tubing was used to siphon enough fluid to fill a 35 mm film canister. The container was then sealed, labelled with the date, region sampled (collapse or lower layer) and fluid temperature, and stored for analysis at a later date.

The density measurement equipment consisted of an Anton-Paar DMA 60 density meter connected to a DMA 602HP external measuring cell. To control the temperature of the test cell, a Grant Instruments LTD6-P constant temperature bath was used to heat or cool the circulating water to a tolerance of 0.1°C.

The Anton-Paar density meter operated by vibrating a tube filled by a sample of fluid and measuring its frequency of oscillation. The period of oscillation of the sample tube was displayed on the meter, and when compared to the calibration values obtained from samples of two other fluids of known density, yielded the density of the fluid sample.

Air and distilled water were used as calibration fluids. The density of air was determined from the following equation (Anton-Paar, 1975):

$$\rho_{air} = \frac{1.2930}{1 + 0.00367\,\theta_{air}} \frac{P_{atm}}{1013.25} \tag{3.1}$$

In the equation above, ρ_{air} represents the density of the air sample in kg/m^3, θ_{air} the temperature of the sample in °C, and P_{atm} the atmospheric pressure in millibars. The air temperature was measured with a digital thermometer in the test cell, while the atmospheric pressure was measured with a mercury barometer.

The density of distilled water was calculated with the equation below (Bigg, 1967):

$$\rho_{water} = 999.842594 + 6.793952 \times 10^{-2}\,\theta - 9.095290 \times 10^{-3}\,\theta^2 + 1.001685 \times 10^{-4}\,\theta^3 - 1.120083 \times 10^{-6}\,\theta^4 + 6.536332 \times 10^{-9}\,\theta^5 \tag{3.2}$$

In the equation above, ρ_{water} represents the density of the water sample in kg/m^3 and θ the temperature of the sample in °C. This equation is only valid over the range 0-40°C. The water temperature was once again measured with a digital thermometer in the test cell.

When processing the fluid samples, it was necessary to perform calibration measurements at every temperature at which a fluid sample was taken. Thus, for a given sample, three measurements were required, these being period counts for the air and distilled water calibration fluids as well as for the fluid sample. Once these values were determined, one of the following equations (Anton-Paar, 1975) was used to calculate the density of the sample:

$$\rho_{sample} = \rho_{water} + \left(\frac{\rho_{water} - \rho_{air}}{T^2_{water} - T^2_{air}}\right)\left(T^2_{sample} - T^2_{water}\right) \tag{3.3a}$$

$$\rho_{sample} = \rho_{air} + \left(\frac{\rho_{water} - \rho_{air}}{T^2_{water} - T^2_{air}}\right)\left(T^2_{sample} - T^2_{air}\right) \tag{3.3b}$$

In the equations above, ρ represents the density of the sample or air or water calibration fluids, in kg/m^3, while T represents the period of oscillation of the fluid.

Samples were injected into the measuring cell with a disposable plastic syringe and after allowing the fluid to stabilise at the required temperature, the period of oscillation was recorded. The fluid was then drawn out of the measuring cell with the syringe before blowing air through the cell to expel any remaining fluid. Acetone was then injected to displace any fluid adhering to the walls of the test cell. It was then drawn off and blown out with air to evaporate the remainder and leave a clean, dry cell for the next measurement. The Anton-Paar density meter has a stated accuracy of $\pm 1.5 \times 10^{-6}$ g/cm^3.

3.3.2 PME Conductivity Probes

The use of sodium chloride to modify the density of fresh water allowed the density of a sample of fluid to be calculated as a function of its measured temperature and electrical conductivity. Four-electrode conductivity probes constructed by Precision Measurement Engineering (PME) (Head, 1983) were used to measure the latter. This technique provided a fast response with a fine spatial resolution, while resulting in a minimal disturbance to the existing density stratification. Their fragility presented a problem, though, in that any disturbance of the platinum electrodes rendered the probe susceptible to drift, flattened its response curve (making it difficult to measure higher conductivities) and necessitated the repetition of calibration measurements. For this reason, it was necessary to perform calibrations on a regular basis during the course of experiments, as damage to the probe tip was not always obvious to the naked eye.

The PME conductivity probes were used in conjunction with a probe controller and a traverse mechanism connected to a linear potentiometer. The latter was an Amphenol Model 205 with a maximum resistance of 5 kΩ and a tolerance of ±3%. Both the potentiometer and probe controller were connected to an analog to digital card in a 286 personal computer. A data acquisition program sampled potentiometer and probe measurements at 200 Hz, and after each 30 measurements the values were averaged and recorded in a data file. These values ranged from 0 to 4095, with the full scale value corresponding to a reading of 10.0 V, the voltage at which the external power supply was set. The entire profiling mechanism was

located on the tank mounted trolley, to allow it to be moved the length of the flume for multiple measurements. The setup is illustrated in Figure 3.6.

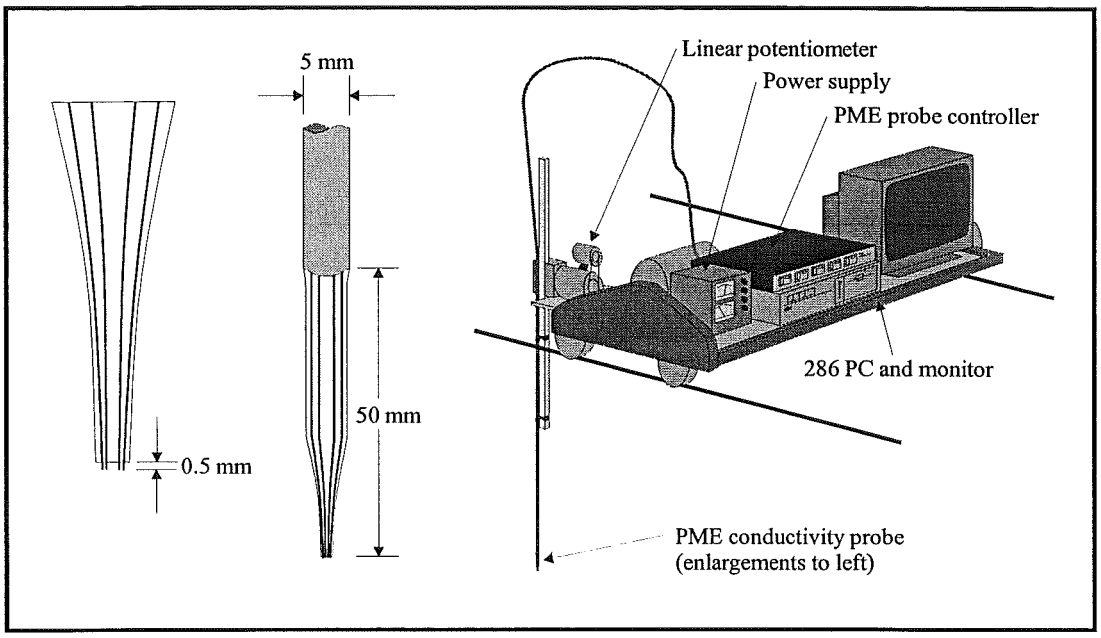

Figure 3.6 - Density profiling mechanism with probe tip enlargements

To convert the potentiometer readings in the data file into depths required a set of calibration readings. A sample calibration curve is shown on Figure 3.7. From this it is apparent that the potentiometer provided a linear response. The resulting linear regression equation was then used to convert readings into probe depths.

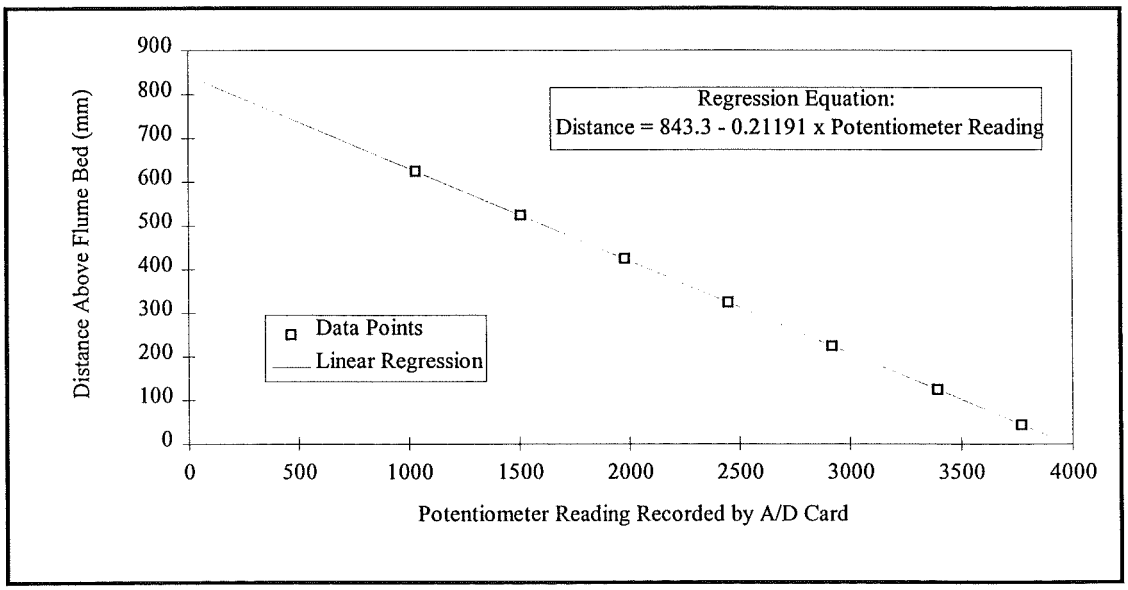

Figure 3.7 - Sample linear potentiometer calibration curve

Conversion of conductivity probe readings into actual conductivities required that the probe and controller be calibrated to define that relationship. This was done by first testing a solution of the maximum salt concentration likely to be encountered over the course of experiments. The gain setting on the controller was then adjusted so that the probe reading was close to, but less than, the maximum reading of 4095. A series of solutions of lesser, known concentrations were then tested, providing a set of readings which were then compared to theoretical conductivities as detailed in the CRC Handbook of Chemistry and Physics (Weast, 1984). These data defined a probe response curve, an example of which is shown in Figure 3.8. Note that these curves tended towards linear for probes in pristine condition, but disturbance of the probe electrodes result in a flattening of the curve for higher conductivities. All of these measurements were performed with the solution temperature held at 20.0±0.1°C with the constant temperature bath mentioned in Section 3.3.1.

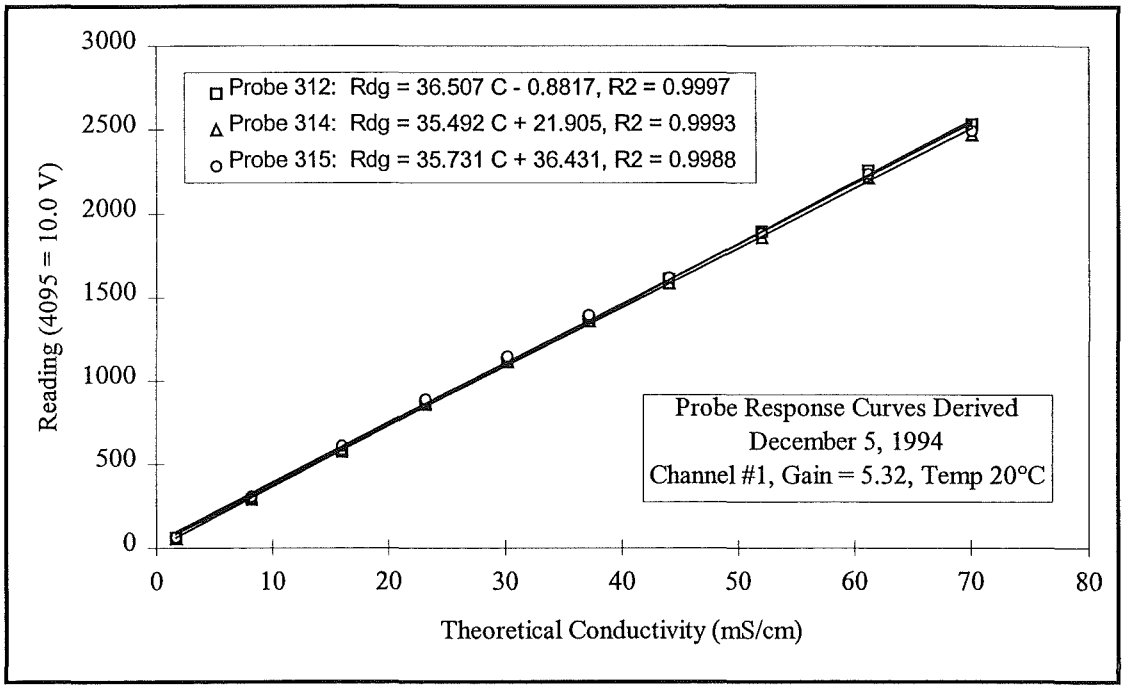

Figure 3.8 - Sample probe response curves for new probes

Converting conductivities to densities required the derivation of an equation which expressed solution density as a function of conductivity and temperature. To derive such an equation, first a probe response curve was constructed. Then, the densities of NaCl solutions were measured over a range of concentrations and temperatures. This established the variation of density with concentration and temperature. Then

probe readings for the same range of concentrations and temperatures were recorded. Using the probe response curve, conductivities for these measurements were calculated. Then an equation for solution density as a function of conductivity and temperature was derived. The resulting equation was valid even when the probe or gain setting were changed, though this necessitated the derivation of a new probe response curve. This required only a limited number of probe measurements at a single temperature.

The density of the NaCl solutions was measured over a range of temperatures and concentrations with an Anton-Paar density meter as detailed in Section 3.3.1. Reagent grade solutions were measured at 5°C increments from 5 to 25°C. The result of these measurements is displayed in Figure 3.9. The family of lines is represented by the following equation:

$$\rho = \rho_f + (7.545 - 0.0194\,\theta)\,M \tag{3.4}$$

Here ρ, θ and M represent the density (kg/m^3), temperature (°C) and NaCl mass fraction (%), respectively, and ρ_f the fresh water density at that temperature.

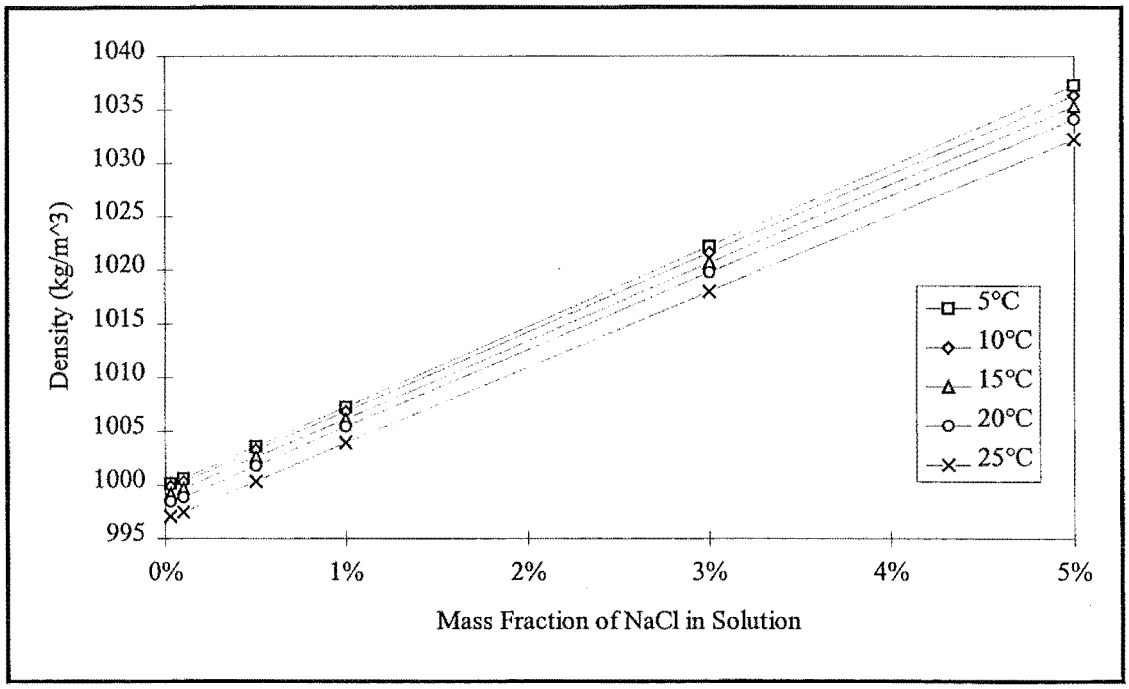

Figure 3.9 - Variation of salt water density with temperature and mass fraction

The conductivity probes available in the laboratory at the time of these tests had different response curves, indicating a previous disturbance of their electrodes. The probe in best condition was chosen for the testing. Measurements were made of the entire range of NaCl solutions at 20°C, and a probe response curve, presented in Figure 3.10, was prepared. Note that the nonlinearity of the response curve is symptomatic of electrode disturbance. The response curve for this probe was fit by the following fifth order polynomials, where C and P represent the conductivity (in mS/cm) and the probe reading (4095 = 10.0 V), respectively:

$$P = 1.6850 \times 10^{-6} C^5 - 1.3736 \times 10^{-4} C^4 - 4.2382 \times 10^{-3} C^3 + 1.9904 \times 10^{-1} C^2 + 41.5 C + 5 \quad (3.5a)$$

$$C = -6.3257 \times 10^{-15} P^5 + 3.8968 \times 10^{-11} P^4 - 7.1731 \times 10^{-8} P^3 + 5.1055 \times 10^{-5} P^2 + 1.1042 \times 10^{-2} P + 0.23 \quad (3.5b)$$

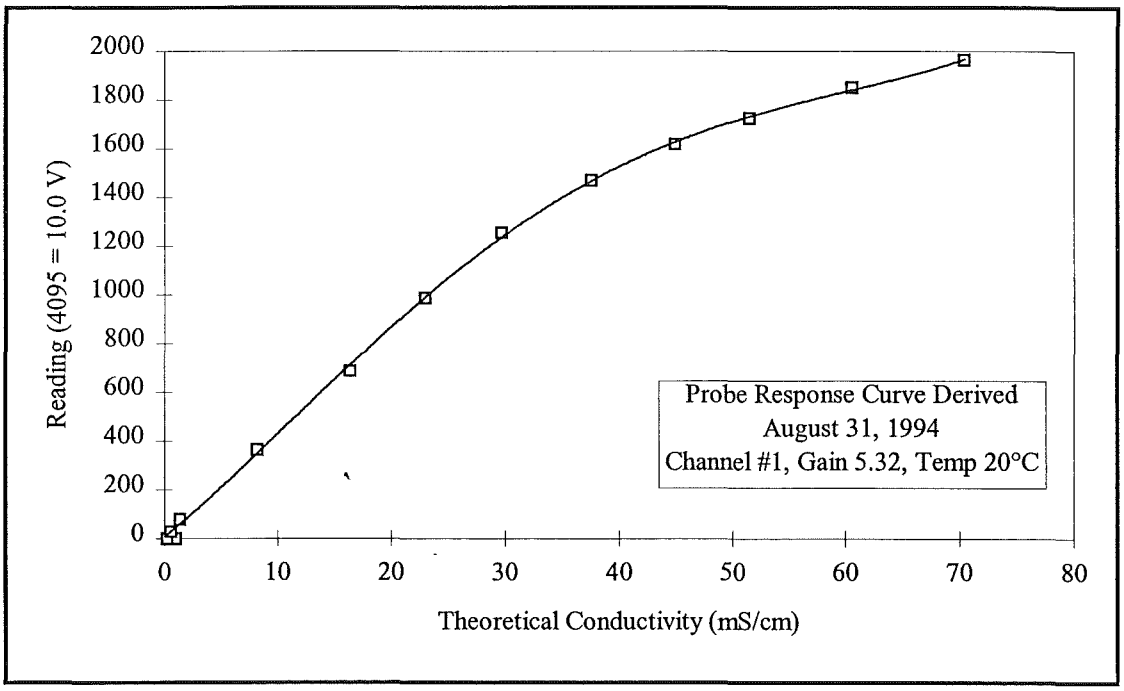

Figure 3.10 - Response curve for probe #7

This curve was then used to determine conductivities for the range of NaCl solutions at 5, 10, 15 and 25°C, and the relationship between conductivity, density and temperature was examined. The relevant data are plotted in Figure 3.11.

Also shown is a family of curves that are described by the following equation, which was fit by trial and error. This equation may be used with any conductivity for which a probe response curve is known:

$$\rho = (5.000 - 0.060\theta) \times 10^{-5} C^3 + (4.000 - 0.350\theta + 0.005\theta^2) \times 10^{-3} C^2 + (6.883 - 0.124\theta) \times 10^{-1} C + (1000.93 - 0.150\theta) \quad (3.6)$$

Here, ρ is the density of the NaCl solution at a temperature, θ (in °C), and a conductivity, C (in mS/cm). This equation is only valid over the range of 5 to 25°C and for densities up to approximately 1035 kg/m^3.

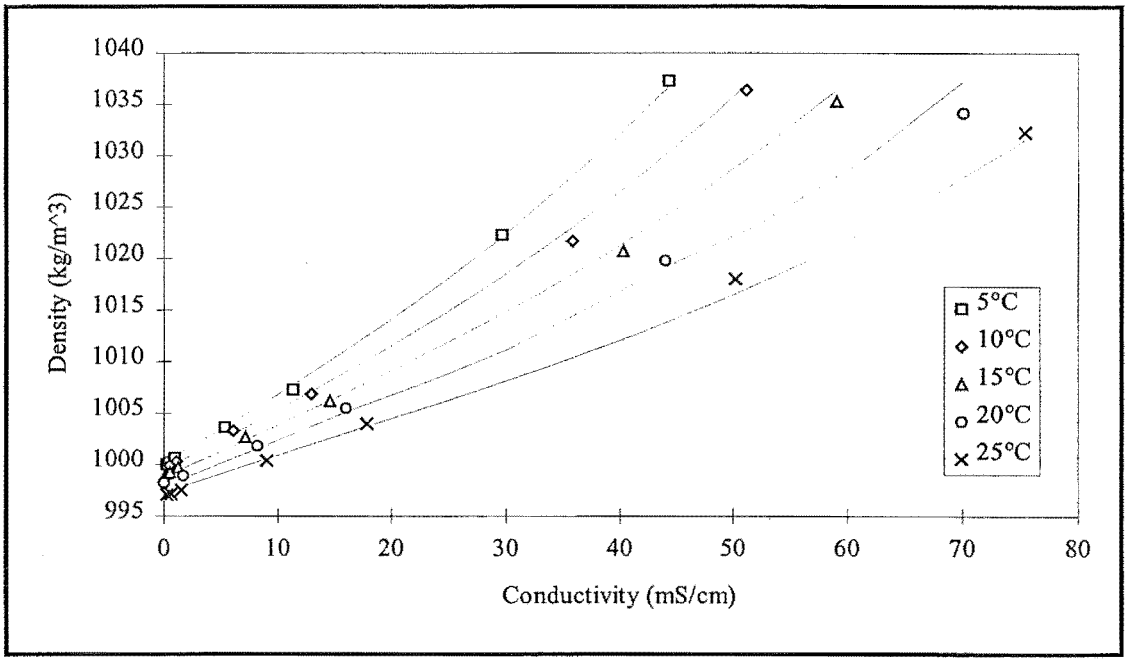

Figure 3.11 - Variation of salt water density with conductivity and temperature

Note that the conductivity probe was primarily used to determine the shape of the density profile, not the densimetric factor, so that a high degree of accuracy in Equation 3.6 is not necessarily required as the representative layer densities are determined by other methods. This method should not be used for the measurement of NaCl solution densities where utmost accuracy is desired.

3.4 Fluid Preparation

In experiments involving density stratifications, the density of fresh water was modified by the addition of salt. This ensured that different layers of fluid remained

miscible and interfaces could be thickened by mechanical mixing or molecular diffusion. In addition, fluorescent dye or neutrally buoyant particles were added to the fluid to aid in flow visualisation.

3.4.1 Salt Water Solutions

Fluids with densities greater than that of fresh water were made by mixing sodium chloride with water from the Christchurch municipal water supply. This water is pumped directly from gravel aquifers underlying the city and is not treated. The sodium chloride was Pacific pure dried vacuum standard salt refined by Dominion Salt Limited.

Quantities of salt to be added to water were determined from CRC Handbook of Chemistry and Physics (Weast, 1984). To produce the desired density of solution, the specified concentrations of water and salt were used to determine the respective masses to be mixed. For example, a 5.0% by weight solution of NaCl corresponded to a density of 1034.0 kg/m^3 at 20°C. To produce 1000 L of this solution, the table was consulted and specified values of 51.7 g/L salt and 982.3 g/L water were obtained. Thus, a mass of 51.7 kg of salt was added to 982.3 kg of water to produce the required solution. The mass of salt was determined using an electronic scale, while since the water quantity was measured using a Kent 1.5 inch flow through meter, a further conversion was required to obtain a value for water volume. In the example case, 984.1 L of fresh water, with a density of 998.2 kg/m^3 at 20°C, was used.

Mixing was performed in a 1700 L plastic water tank with a mixer consisting of three stainless steel vanes attached to a shaft driven by a 370 watt electric motor. Generally, batches in excess of 1000 L were mixed and this provided enough fluid for several experimental runs. The fluid was mixed for a further ten minutes immediately before use to ensure that any density stratifications that may have occurred due to thermal effects would be mixed away.

3.4.2 Fluorescent Dye Tracers

In some experiments, Rhodamine 6G fluorescent dye, manufactured by Lambda Physik, was used as a tracer. When excited by light at one wavelength, this dye emitted light at another wavelength. Rhodamine 6G had an absorption peak at 530 nm, though the 514.5 nm green light of the laser caused sufficient excitation, and an emission peak at 560 nm which appeared yellow. The intensity of emission was linearly proportional to light absorption and dye concentration, which made this dye useful for non-intrusive measurements of dilution.

The Rhodamine 6G came in a solid, granular form which was combined with distilled water to produce a solution with a concentration of 50 mg/L. This solution was pipetted into salt water solutions at a proportion of one part in one thousand to produce a final concentration of 50 μg/L. At this concentration the dye had a negligible effect on the salt water solution density. Calibrations involved in experiments using dye tracer are discussed in Section 3.6.

No Material Safety Data Sheet (MSDS) was available for this substance, but it has been noted as having mutagenic properties, so care was taken when handling it, especially in its more concentrated forms.

3.4.3 Particle Tracers

In experiments where particles were used for flow visualisation, a small quantity of neutrally buoyant particles was added to the fluid to reflect light and act as a flow tracer. The particles used were made of Goodyear Pliolite VTAC resin. This is a substance commonly used in tyre and carpet manufacture and was available at a modest price, though some preparation was required before it was suitable for use in experiments.

Pliolite has a specific gravity of 1.03, which means it is close to neutrally buoyant. In fact, for a 100 μm particle in fresh water at 20°C, Stokes' law indicated a fall velocity of 0.16 mm/s. In denser fluid, this was reduced to the point where the particle became slightly buoyant. The MSDS for Pliolite indicated that it was a

white granular material, essentially odourless, and insoluble with a softening point of 47-53°C. It was noted as being non-hazardous, but the presence of residual monomers could cause eye, skin or lung irritation and thus it should be treated as hazardous. Safety glasses, protective gloves and respiratory protection were recommended when handling it.

To make the granular particles suitable for use in experiments, it was necessary to control their size and somehow make them freely mix with water. A sieve analysis on a raw sample, shown in Figure 3.12, shows that three quarters of the mass of Pliolite was greater than 250 μm in size, and only 3% fell in the range of 100-150 μm which was most convenient for flow seeding. To produce a large quantity of particles of consistent size, quantities of Pliolite were first ground to reduce the size of the larger particles. Both a household coffee grinder and blender were used for these purposes, with the latter preferred for its larger capacity. It was important to ensure that the grinder was not run long enough to heat up the resin to its softening point, as this risked a stall of the grinder followed by hardening of the resin. This event required a laborious disassembly and cleaning of the grinder with methyl ethyl ketone. When the particles were thoroughly ground, they were run through a series of sieves of gradually decreasing size, each trapping particles of a specific gradation. It was found to be advantageous to perform wet sieves, first mixing the particles into a slurry, as this reduced the amount of dust clinging to larger particles and produced a cleaner end product. As Pliolite is non-soluble and also non-wetting, this required the addition of a surfactant to reduce the surface tension and allow it to mix well with water. A photographic wetting agent manufactured by Ilford was used for this purpose. This was mixed with water at one part to one hundred before the addition of particles, and then the resulting slurry was mixed by shaking in a closed container.

Once a sufficient quantity of particles was produced by sieving, they were mixed into a more dilute suspension for introduction to the experimental fluid. Approximately 10 g of particles were combined with a litre of water, and if necessary, a few millilitres of wetting agent were added. This mixture was then introduced to the flume by pouring it in at the surface, ensuring that it mixed well

with the upper 10 cm or so of fresh water. As these particles sank, more particles were added, but in general no more than 30 g of particles were added to the tank for any run. At these concentrations, the particles had a negligible effect on fluid density.

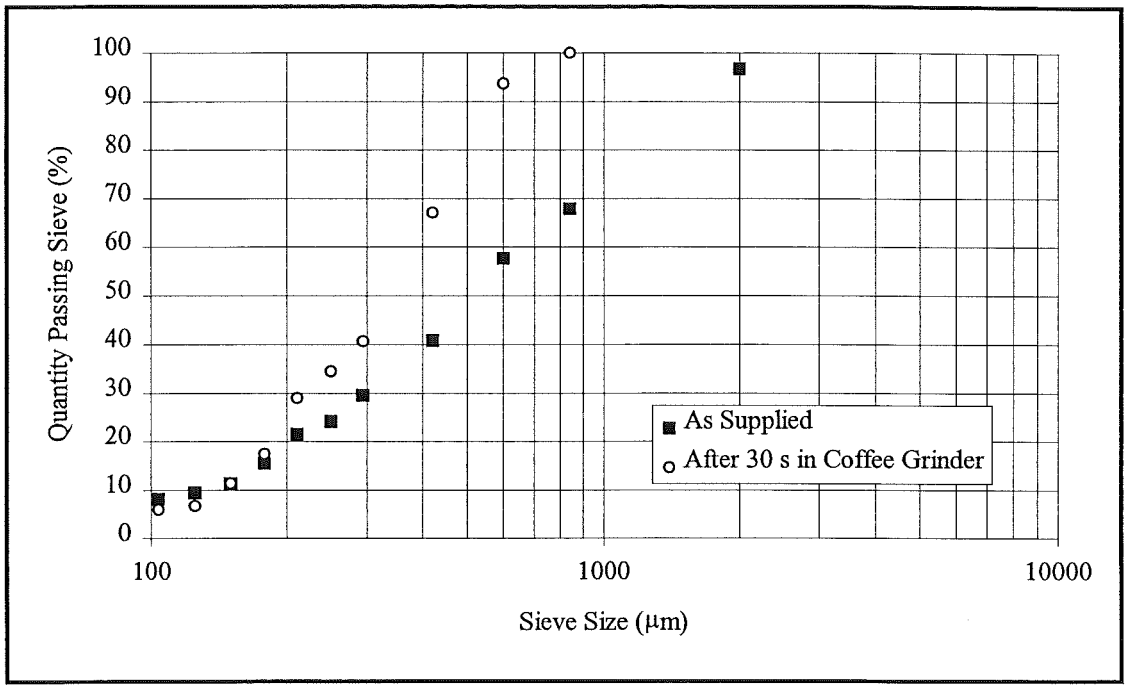

Figure 3.12 - Sieve analysis of raw Pliolite resin

3.5 Wave Generation Techniques

It is possible to generate second mode internal solitary waves by a variety of techniques, and some of the methods used by other researchers are discussed in Chapter 2. The current study made use of three different ways of producing these waves. Initial experiments involved generation with a three layer exchange flow. Later ones saw intermediate density fluid forced into the interfacial region at a steady rate, with both long and short flow durations. In the most recent sets of experiments, waves were produced by the collapse of a thickened body of intermediate density fluid lying on the interface.

3.5.1 Exchange Flow

It was felt that a three layer exchange flow would provide a steady, easily quantifiable and reproducible method of generating these waves. The technique involved releasing a gate which separated two regions of fluid, one density-stratified and one well-mixed. The well mixed fluid would then intrude along the interface of the stratified region, while the upper and lower layers returned fluid through the gate into the well-mixed reservoir. It was hoped that a large volume of intrusive fluid would produce a steady flow which could be quantified by its discharge and density.

Preliminary experiments used a gate apparatus that resembled two sharp-crested weirs located opposite one another on the flume top and bottom. Flow through the adjustable gap was observed to be stable, with smooth interfaces between the intrusion and both upper and lower layers of fluid. Inside the well-mixed region, though, the shear flow became unstable, producing turbulent billows as upper layer fluid moved towards the surface and lower layer fluid fell to the floor of the flume.

For subsequent experiments, an attempt was made to reduce turbulent mixing in the gate region by replacing the sharp-crested weirs with broader ones. With a vertical face on the stratified side, these adopted a sinusoidal shape before matching a 2:1 slope on the other side. As with the previous setup, the two gate components were easily repositioned to adjust the gap between them. The two gate configurations are pictured in Figure 3.13.

The exchange flow method was relatively reliable for producing waves, though stronger flows would often persist as intrusive gravity currents for the length of the flume. In these cases, the head of the initial intrusion would never fully separate from the following current. Observations of flow at the gate also revealed that the flow was less steady than anticipated, with the initial movement as the gate was released being only the first of a series of such surges. The flow through the gate was especially sensitive to the elevation of the water surface on either side. Since the flow was intended to be driven by hydrostatic pressures resulting from density differences of magnitude much less than those which would result from differences

in water surface elevation, it was important to ensure that the water surface on either side of the gate was balanced. Of course, this was easily accomplished by maintaining a layer of water above the flume insert in the tank, but that had the drawback of allowing fluid to flow over the partitions, disrupting the exchange flow through the gate. It was decided to set up the experiment so that the water surface in the tank was established just above the partition, ensuring that flows would not be driven by differences in water surface elevation, while minimising flow over the partition. Flows remained unsteady, though, and repeatability posed a problem, so other options for wave generation were examined.

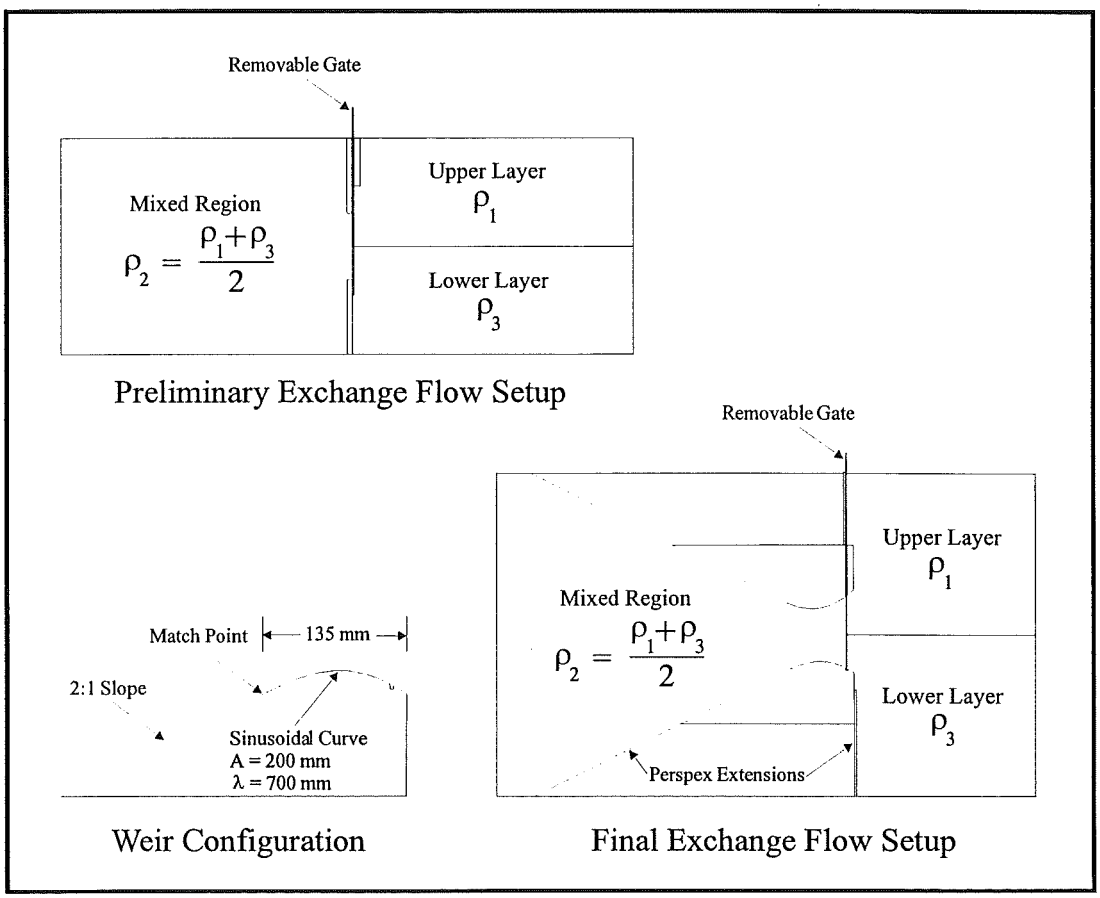

Figure 3.13 - Gate configurations used in exchange flow generation

3.5.2 Steady Inflow

To ensure a steady inflow of intermediate density fluid into the interfacial region, an apparatus was constructed to introduce a metered flow, driven by gravity from another mixing tank. The flow rate was measured with a Rotameter Metric 14S

float-in-tube meter and remained constant over the course of the experimental run. The steady inflow device is pictured on Figure 3.14. The subsequent series of experiments displayed a more steady flow, but was less reliable in generating second mode waves. In most instances, the flow would persist as an intrusive gravity current for the duration of the experiment. In an attempt to produce waves sooner, experiments were performed introducing a steady inflow for a shorter duration before halting it. This method proved somewhat more successful, though often waves did not fully form by the time the intrusion reached the end of the tank. Options for more reliable methods were considered once again.

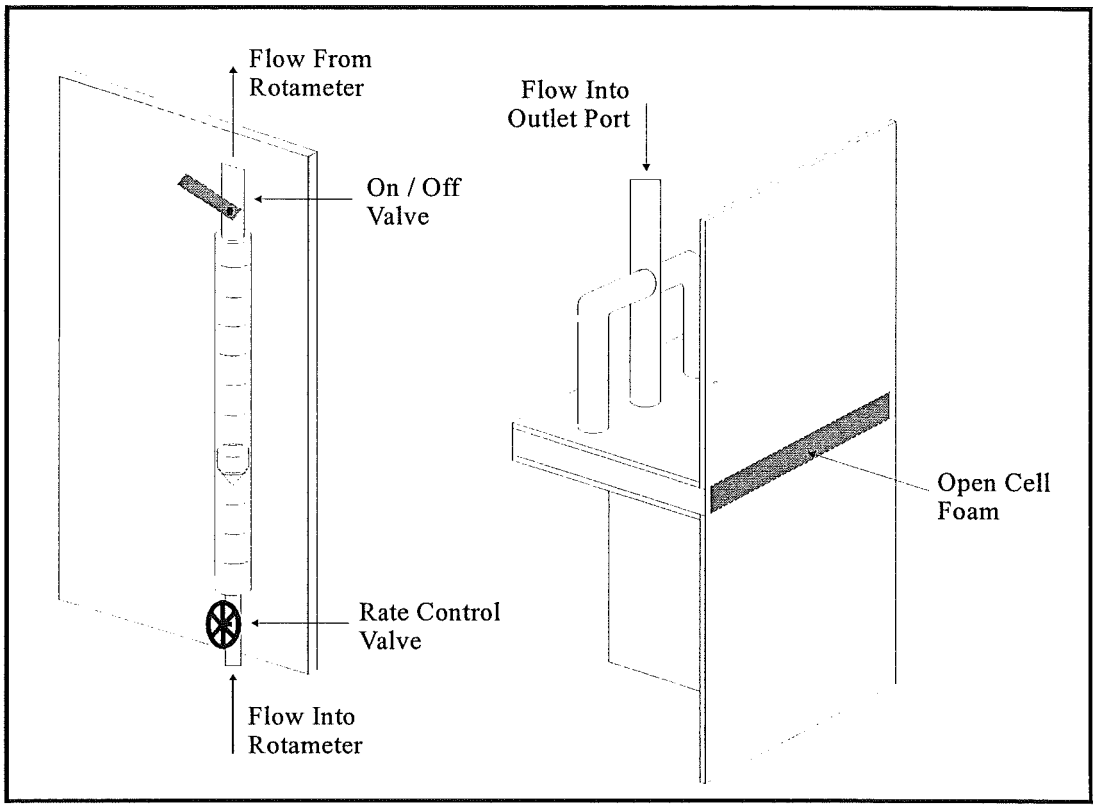

Figure 3.14 - Steady inflow apparatus and measurement device

3.5.3 Collapse

Generation of a second mode wave by the collapse of a thickened interfacial region proved to be both effective and repeatable. A thin partition was inserted near one end of the flume and intermediate density fluid was slowly introduced at the level of the density interface with a sandwich port as described in Section 3.1. This was

continued until the desired depth of intermediate density fluid, never more than one quarter of the total fluid depth, was reached.

The wave was generated by the smooth and rapid removal of the partition, allowing hydrostatic forces to collapse the body of intermediate density fluid. Figure 3.15 shows the setup for this method.

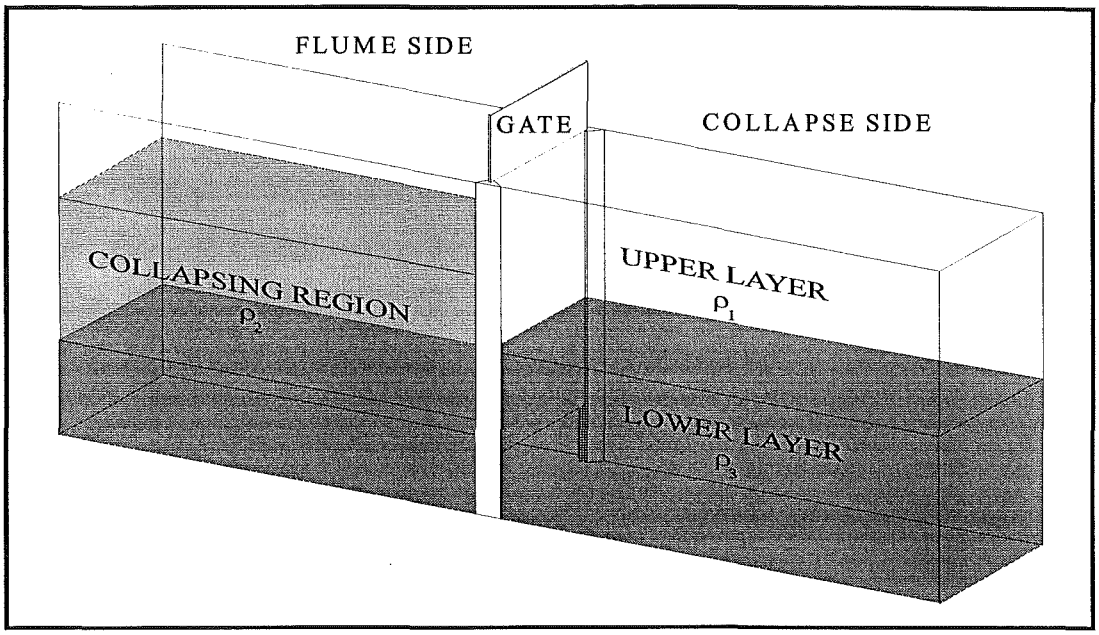

Figure 3.15 - Collapse release mechanism

3.6 Experimental Procedures

The steps involved in preparing for, performing and cleaning up after the experiment are discussed in this section. These procedures include the filling of the tank, alignment and operation of the laser and mirrors involved in the creation of the light sheet, setup of cameras and performing of calibrations associated with the video record of the experiments, loading of salt water solutions and tracer materials, measurement of fluid densities, carrying out the experiment itself and then shutting down equipment afterwards.

3.6.1 Tank Filling

Preparation for an experiment typically commenced a minimum of four hours before the generation of the solitary wave. At this point the tank was filled with

fresh water by closing the main drain, opening the four tank fresh water inlet ports and opening the inlet valve until the water level was above the flume barrier. This allowed the water time to sit so that the air could come out of solution, forming bubbles on the tank walls. Bubble formation and growth was most rapid when the tank was initially filled, but slowed with time, so ideally the filled tank was left to sit overnight. Before performing a dye calibration or loading salt water into the flume, bubbles were removed from the glass wall and flume partition with a heavy, long-handled brush. This prevented them from being mistaken for stationary particles or reducing the quality of a dye image. When the tank was filled, all inlet ports were closed. This was necessary to prevent salt water from passing from the flume through the inlet pipe network into the main tank when it was filled. Hydrostatic pressure equalisation ports were closed at this time for the same reason.

3.6.2 Laser Alignment and Operation

Proper alignment of the laser was important, and this was generally attended to before commencing a set of experiments. The flume had a 25 mm wide strip painted in flat black centred along its bottom, and the scanning beam box or rotating mirror was placed in the vertical plane defined by this strip. The laser was aligned so as to hit the centre of the 45° mirror below the scanning beam box, and this mirror as well as the one immediately inside the box were adjusted so that the beam fell on the centre of the rotating mirror and reflected to the centre of the parabolic strip mirror. This configuration was illustrated previously on Figure 3.4. Further minor adjustments to the two adjustable mirrors were required to ensure that the resulting sheet fell on the centreline of the flume and its component rays were level with the top of the flume. Small adjustments of the strip mirror were occasionally required to straighten the line of the laser sheet. This was accomplished with small lateral movements of the mirror strip beneath its support strap. In the final laser sheet configuration, the large 45° mirror was then adjusted on the trolley so that it was above the centreline of the flume and sent the sheet directly downwards. This was checked at a variety of positions along the length of the flume, as it was important that the sheet hit the black strip to minimise measurement errors caused by reflected light.

The laser was started up a minimum of an hour before the experimental run, to allow it to attain its maximum output. Powering up of the laser was accomplished by first ensuring a minimum cooling water flow rate of 8.5 L/min, though the recommended flow rate of 12-15 L/min was generally easily obtained. Lower flow rates were taken as a sign that the filter in the cooling system was in need of replacement. Power was then switched on, first at the 440 V mains supply and then at the transformer box. The key switch at the main control box was then switched on, causing the adjacent red light to flash if sufficient cooling water was flowing. An inadequate flow rate would cause this light to remain lit. After ensuring that the laser shutter was closed and setting the mode control to "CUR" (current regulation), power was switched on at the remote control box and the power knob was rotated fully clockwise to its maximum setting. Pressing the start button then initiated laser operation. The green "laser" light was continuously lit, while the red "water" light flashed twice to once again indicate an adequate flow of cooling water. After approximately 30 seconds, the laser tube ionised and a beam would be emitted from the shutter when opened. The laser was operated in current regulated mode except when performing experiments or calibrations, when it was switched to light regulated mode ("LO") at the remote control box. A laser light power of 2.4 W was used when in single line mode for laser induced fluorescence experiments, while a power of approximately 6.0 W was available when in multiline mode for particle visualisation experiments. If these values were not attainable at full power after warming up the laser, it was likely necessary to realign the laser's internal mirror. The reader is referred to the laser manual for more information about this procedure. The laser reached maximum power in two hours, with 98% of this value attained after 30 minutes of operation (Papps, 1995).

Before opening the laser shutter, it was necessary to ensure that the rotating mirror, whether operated alone or with the scanning beam box, was in operation. Neglecting this could result in heat damage to the octagonal mirror or to the parabolic mirror in the box, as the laser's energy would be concentrated in one spot rather than being distributed throughout the sheet. The rotating mirror was set in motion simply by turning it on at its control box. After a few seconds the motor reached full speed and was ready for operation. At this point the shutter could be

opened. It was necessary to have the shutter open during calibrations and experiments, and it was also advantageous to keep it open during salt water filling, as the light sheet made the location of the interface easier to ascertain.

Laser shutdown was accomplished by reversing the steps for powering up. The shutter was closed and then power switches were shut off at the remote control box, main control box, transformer and mains supply, in that order. The cooling water was allowed to flow for a further few minutes to ensure that any residual heat was properly dissipated from the laser. After the shutter was closed, the rotating mirror could be powered down. While doing this, it was important to ensure that the mains power supply was not interrupted until both the "motor" and "logic" lights on the control box were extinguished. The latter of these remained lit for some time after the power switch was turned off.

3.6.3 Camera Operation

The Pulnix CCD camera required some setup before use. It was raised or lowered on the trolley so that its field of view was centred on the density interface, and was aligned perpendicular to the front of the tank by rotating it about a vertical axis until the reflection of the camera lens was in the centre of the resulting video image. The mounting for the camera was previously shown on Figure 3.3. The focus was also set at this point by observing the image on the video display. The video image was routed through the frame grabber, which had its offset and reference values set to -75 mV and 1024 mV, before being viewed. When using particles as a tracer, the camera gain setting was not critical, and the image intensity was adjusted by changing the camera aperture setting. Dye experiments required more attention to these settings. During the dye calibration, the aperture f-stop was usually set to 4.0, and then the gain was adjusted so that the dye image produced peak pixel values of less than, but close to, the maximum possible value of 255. The camera focus, aperture and gain settings were then secured with tape. Any change in these necessitated a recalibration. The camera was powered up at least an hour, but no more than two, before the wave was generated, as tests (Papps, 1995) indicated that its response was stable to within 2% over this interval. The Hitachi character

generator was used to set up a title page detailing the date, layer densities and visualisation method of the experiment at hand, and this was superimposed on a dark image and recorded for ten seconds on the Super-VHS tape. The character generator was then set to display a small digital timer in the lower right of the image in anticipation of the start of the experiment.

The 8 mm camera was aligned and focussed, and a short bit of tape was run to record the date on screen. The camera was then switched to display the time before it was switched off until the start of the experiment.

The 35 mm still camera was loaded with film, aligned and focussed before the run. The zoom lens was set to 100 mm, with an aperture setting of f 4.0, and the exposure time was set. The remote control unit was set to take a full set of exposures (either 24 or 36, depending on the film used) at the prescribed interval, so that one press of the start button would initiate the sequence.

3.6.4 Calibrations

When the cameras were set up, images were taken of a rigid plastic sheet upon which a 10 mm grid had been drawn. This was intended to aid in subsequent physical measurements. This was not done in every experiment, but rather only when camera settings or lenses were changed.

Prior to performing dye experiments, a dye calibration was performed. Collapsing region fluid which had been mixed previously was siphoned into a transparent perspex test cell of dimension 1000 x 700 x 100 mm. After the CCD camera and laser had been warmed up, and the laser power set to 2.4 W, the test cell was positioned in the flume and the camera set up as discussed in the last section. With all light except for that of the laser extinguished, 30 seconds of Super-VHS video were recorded for later analysis. This procedure was performed at intervals of approximately 300 mm along the length of the flume. Before recording the calibration image, the Hitachi character generator was used to title the subsequent footage. After recording all of the calibration footage, the calibration cell was removed from the flume and, if it had not been contaminated with fresh water

during removal, the dyed salt water was returned to its mixing tank. Video footage for providing zero images, obtained where the laser sheet was at the prescribed power but no dye was present, was then acquired in a similar fashion.

3.6.5 Fluid Loading

After all calibrations were performed, the release gate was installed if necessary and the lower salt water layer was established. The salt water in the mixing tank was first mixed for at least ten minutes to ensure that it was of homogeneous density. Any fluid in the supply piping was purged by first opening the upper and lower supply valves and then the line purge outlet valve. After sufficient fluid was drained, the latter valve was closed. The valves at the three lower layer inlet ports were then opened. The flow rate was controlled at the lower supply valve, and was kept low to prevent turbulent mixing at the inlet port until the interface was well above the port level. Filling continued until the interface was raised to mid-height in the flume. Locations of the valves and ports described here were previously illustrated in Figure 3.2.

When using an exchange flow generation technique, intermediate density fluid was loaded into its reservoir in a similar fashion to that of the lower layer, though no purging of the lines was allowed for. Fluid was filled until it spilled over the vertical reservoir barrier, ensuring that the effect of any dilution due to mixing during filling was minimised. When generating waves by a collapse, a small sandwich port was inserted at the level of the interface and intermediate density fluid was slowly siphoned in through 4 mm diameter plastic tubing. Filling was continued until the collapsing region was of the desired depth, at which point a small quantity of fluid was siphoned back out for the purpose of density measurement, as described in Section 3.6.6, and the port was carefully removed to minimise any disturbance of the interface.

Where a sharp interface was desired, filling continued until the interface was a minimum of 30 mm above the mid-height of the flume. Two or three sandwich ports with 4 mm diameter plastic tubing were placed at mid-height on equal

intervals along the flume and used to siphon off approximately equal depths of first salt and then fresh water. This minimised the effects of any mixing which might have occurred in the interfacial region during filling. The ports were then carefully removed to avoid any additional mixing.

In some experiments, dye was added to portions of the interfacial region by placing sandwich ports at mid-height in the flume and siphoning in intermediate density fluid which contained dye at the usual concentration. This was done at a very slow rate which was accomplished by siphoning from containers held less than one metre above the water surface, through 4 mm diameter plastic tubes which were clamped partially shut to restrict the flow rate. Again, after dye placement ports were removed with the utmost care to prevent any mixing.

Where particles were used for visualisation, the dilute suspension discussed in Section 3.4.3 was initially added to the fresh water before the introduction of salt water into the flume, and added to the salt water solutions in the mixing tanks. It soon proved advantageous, though, to introduce these particles after the salt water layer had been established in the flume. The dilute suspension was poured into the fresh water layer along the length of the flume and the initial turbulence, internal circulation and their settling velocity soon resulted in a reasonably uniform dispersion of the particles. Two or three applications of particles, commencing 40 minutes or so before the generation of the wave, was necessary to compensate for the fall rate of the particles, though due to the limited field of view of the CCD camera, it was only necessary to have particles in the middle third of the depth.

3.6.6 Density Measurements

Immediately before the generation of the wave, density profiles were taken using the PME conductivity probe as detailed in Section 3.3.2. In the early stages of the experimental program, only one profile was taken in the flume region, but in later experiments four profiles were taken at regular intervals along the length of the flume region as well as one profile in the collapsing region. This latter measurement provided a more accurate value for the depth of the collapsing fluid

than a visual observation. After the completion of the experiment, a single additional profile was taken near the midway point of the flume. These profiles were saved as individual text files with different names for later analysis by the method of Section 3.3.2.

A sample of intermediate density fluid was taken during filling as discussed in Section 3.6.5, while a sample of lower layer fluid was obtained shortly after the experiment by siphoning from the middle of the lower layer. These samples were stored in labelled 35 mm film containers for later analysis by the procedure outlined in Section 3.3.1.

Temperatures of the fluid in the upper and lower layers as well as the intermediate density fluid reservoir were measured with a mercury thermometer and recorded on the film canisters as well as in the experimental log book. These temperatures were required for both methods of density analysis.

3.6.7 Experimental Run

When density measurements had been performed, and the trolley controller was switched on at the mains box outside of the tank room, the door to the tank room was shut and locked to prevent it being opened during the experiment. The Super-VHS video recorder was set to record the signal from the CCD camera and the timer on the Hitachi character generator was set to zero and started. The 8 mm video camera was also turned on and set to record. The trolleys were set to their start position so that the CCD camera field of view just included the starting point of the wave, whether that be at the exchange gate, inlet port or collapse gate. All light within the tank room, with the exception of the laser and the dimmed video screen, was then extinguished.

The experiment was begun by either a smooth, rapid release of the gate or the opening of the Rotameter valve, depending on the generation technique. The trolley was then started at the controller and its speed was adjusted to match that of the wave by means of a rotary dial. Minor trolley speed adjustments were made over the course of the run, with a clear view of the video screen allowing the wave to be

tracked in a smooth fashion. If the 35 mm camera was being used, the photograph sequence was started immediately after the first trolley speed adjustment by pressing the start button on the remote control, which was mounted with the camera on the trolley.

The wave was tracked by performing fine, manual adjustments to the trolley speed until the wave reached the end of the flume and reflected. The trolley was then stopped, though frequently the videos were left to run for a few minutes before being switched off.

3.6.8 Post-run Procedures

After the completion of the experiment all cameras and recording devices were switched off. The laser and rotating mirror were then shut down by the procedure outlined in Section 3.6.2, the post-run density measurements outlined in Section 3.6.6 were performed, and the trolley control unit was switched off. The main tank was then drained, after first ensuring that any pressure equalisation ports in the flume dividers were open, by opening all four fresh water inlet ports as well as the main drain.

4.0 The Pycnocline

The interface between two layers of unequal density has been described in the literature by a variety of terms. Where density differences are the result of a temperature gradient, it is correctly called a thermocline, whereas if the density differences are the result of a salinity gradient it is called a halocline. A more general term which denotes a density gradient without further reference to its nature is pycnocline, the first use of which is attributed to Hutchinson (1957). This word derives from the Greek words for "thick" or "dense" (*πυκνος*) and "to incline" (*κλινειν*) (*Oxford English Dictionary*). The shape and thickness of the pycnocline are important parameters in the consideration of internal waves due to their influence on wave propagation characteristics.

4.1 Interface Shape

In discussing the case of wave motion along a density interface remote from any boundary, Benjamin (1967) assumed a density profile with a hyperbolic tangent shape. Theoretically, the error function might be a more appropriate choice for describing the density profile, as it is the solution to the diffusion equation, but the hyperbolic tangent profile provides an excellent approximation and greater ease of use. This profile is described by Equation 4.1, in which the fluid density is a function of the distance, y, from the centreline of the interface, the interfacial half-thickness, h, the average density, $\bar{\rho}$, and a densimetric factor, ω. The latter two parameters are functions of the upper, ρ_1, and lower, ρ_3, layer densities only, as seen in Equations 4.2-3.

$$\rho(y) = \bar{\rho}\left(1 - \omega \tanh\frac{y}{h}\right) \tag{4.1}$$

$$\bar{\rho} = \frac{\rho_1 + \rho_3}{2} \tag{4.2}$$

$$\omega = \frac{\rho_3 - \rho_1}{\rho_3 + \rho_1} \tag{4.3}$$

A typical measured profile is shown in Figure 4.1, where good agreement with the fitted theoretical profile is observed. The deviation from the theoretical curve seen at the upper edge of the pycnocline was sometimes observed and should not affect the subsequent measurement of the interfacial half-thickness, h, or the use of that value in other equations. The measurement of the interfacial half-thickness will be discussed further in Section 4.2. It appears that a sharp interface allowed to thicken by molecular diffusion can be approximated by the hyperbolic tangent profile, and given enough time, interfaces of other shapes will also thicken to a tanh profile (Kao and Pao, 1979). Davis and Acrivos (1967) made use of a slightly different form of equation, still based on the hyperbolic tangent, but all subsequent experimental studies have used the particular profile described by Equation 4.1.

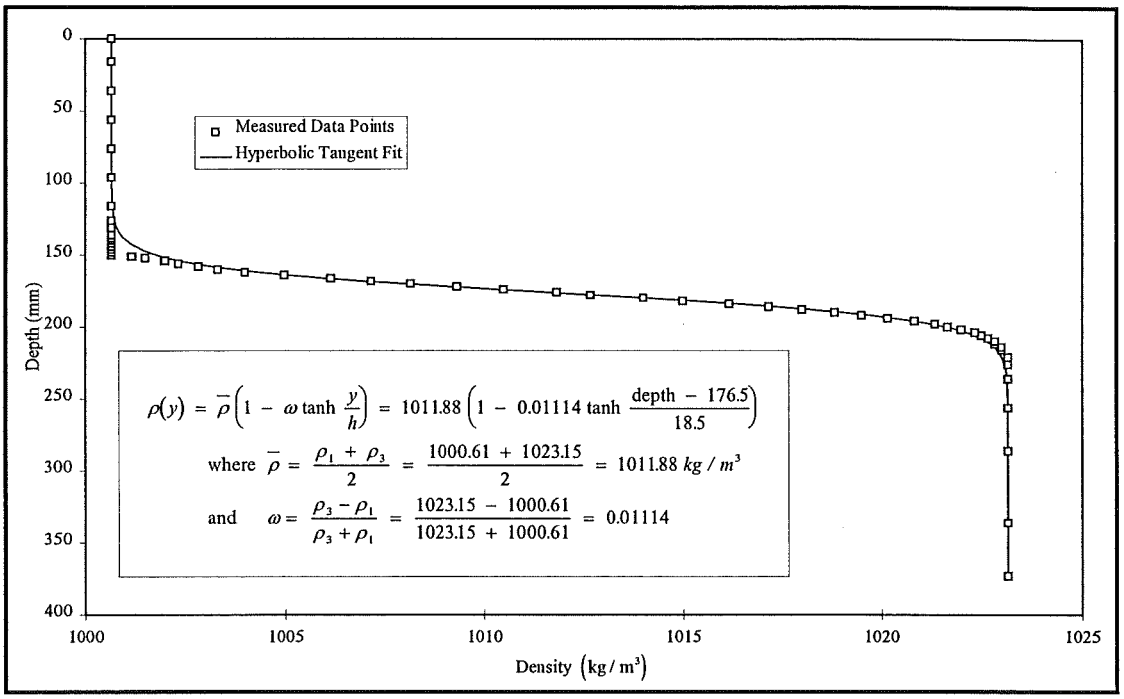

Figure 4.1 - Sample density profile showing hyperbolic tangent shape

The celerity of waves (including solitary waves) travelling along a pycnocline depends on the shape of the density profile. Benjamin (1967) and others calculated the speed of an infinitesimal long wave travelling along a pycnocline with the profile given by Equation 4.1 as:

$$c_0 = \left(\frac{g\,\omega\,h}{2}\right)^{1/2} \tag{4.4}$$

Here the wave celerity is based only on gravitational acceleration, densimetric factor, interfacial half-thickness and the assumption of a hyperbolic tangent profile in an infinitely deep fluid.

4.2 Interface Thickness

The thickness of the pycnocline is a length scale used to nondimensionalise depth in the density profile equation as well as amplitude in wave celerity equations; therefore in any experimental work its definition and measurement are of utmost importance. An understanding of the temporal variation of this thickness is also important in experimentation as the interfacial thickening in small scale, thin interface models can be a good deal more rapid than in larger scale models or prototypes.

4.2.1 Determination of Thickness

The definition of the thickness of a density interface might be considered an arbitrary judgment at best, since there is no real boundary between the interfacial region and the upper or lower layers. Instead, the density gradient decreases with distance from the centre of the pycnocline, hereafter called the centreline, with the density eventually becoming indistinguishable from the representative layer density. This raises the questions of how the pycnocline thickness is defined and measured.

An obvious option for defining the interfacial thickness is to use the distance from the centreline to that at which the density reaches some fraction of the representative layer density, in much the same fashion as the thickness of a boundary layer is defined. Equation 4.1 provides a means to calculate this fraction. By setting the distance from the centreline, $\pm y$, equal to the interfacial half-thickness, h, it is possible to calculate the densities at the upper and lower bounds of the pycnocline.

As the value of $tanh(1) = 0.762$, it is readily apparent that this approach defines the bounds of the density interface as the distance from the centreline at which the density is equal to the average layer density less 76% of the difference between the average and representative layer densities.

Defining the thickness based on only two data points requires a good deal of confidence in those measurements. In practice, data points from the entire central portion of the density profile were examined. This part of the hyperbolic tangent curve is remarkably linear, so a linear regression was fitted and used to estimate the depth at the upper and lower densities. It was found that examining the central 46% of the profile, as $tanh(0.5) = 0.462$, provided a more accurate and direct estimate of the half-thickness of the pycnocline, as shown in the following example. Figure 4.2 shows two identical hyperbolic tangent profiles, corresponding to an average density of 1010 kg/m^3, a densimetric factor, ω, of 0.0099 and an interfacial half-thickness, h, of 20 mm. The calculations of half-thicknesses based on the linear regressions of the central 46% and 76% of the profiles are shown in Equations 4.5-6. From these it is apparent that this approach provides a reasonably accurate, repeatable and robust method of determining the interfacial half-thickness.

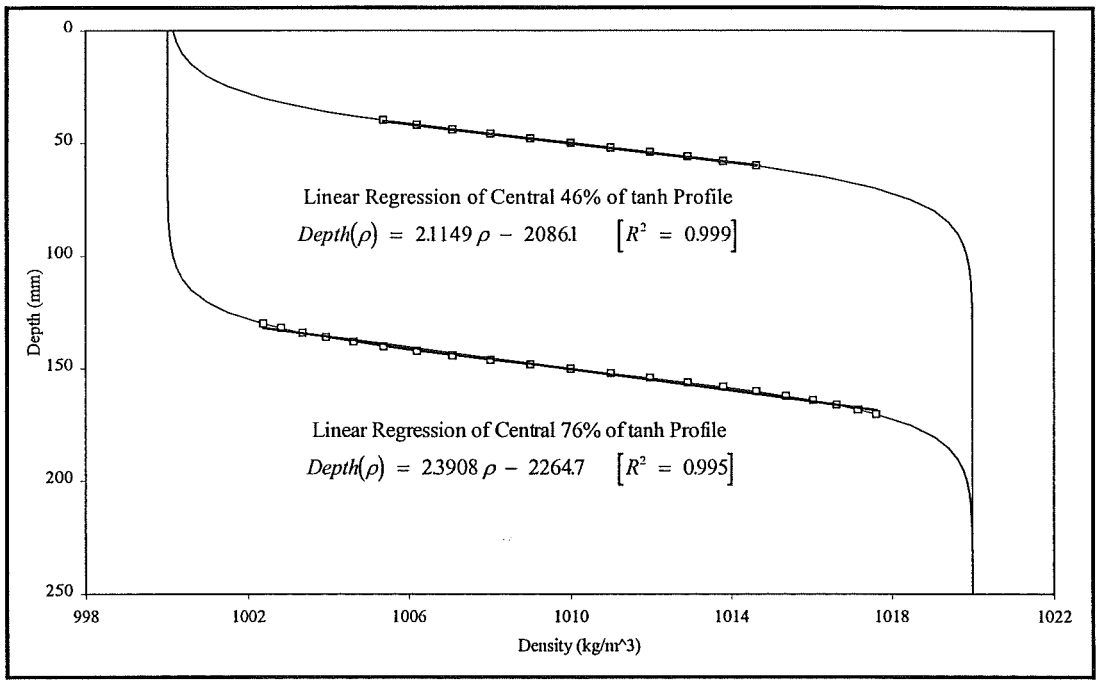

Figure 4.2 - Fit of linear regression to central portion of tanh profile

$$\rho\left(\frac{y}{h} = \pm 0.5\right) = 1010\left(1 - 0.0099\ tanh(\pm 0.5)\right) = 1005.38,\ 1014.62\ kg/m^3$$
$$Depth(1014.62) = 59.72\ mm \qquad Depth(1005.38) = 40.18\ mm \qquad (4.5)$$
$$Pycnocline\ Half-thickness = 59.72 - 40.18 = 19.54\ mm$$
[*Regression value is 2.3% less than* tanh *profile value*]

$$\rho\left(\frac{y}{h} = \pm 1\right) = 1010\left(1 - 0.0099\ tanh(\pm 1)\right) = 1002.38,\ 1017.62\ kg/m^3$$
$$Depth(1017.62) = 168.23\ mm \qquad Depth(1002.38) = 131.79\ mm \tag{4.6}$$
$$Pycnocline\ Half-thickness = (168.23 - 131.79)/2 = 18.22\ mm$$
$$[\ Regression\ value\ is\ 8.9\%\ less\ than\ tanh\ profile\ value\ ]$$

During experiments, density profiles were measured using the techniques outlined in Section 3.3.2. The height and conductivity readings were saved in a text file which was loaded into an Excel spreadsheet for further analysis. Using the appropriate calibration equations, the readings were converted into actual values of height and density, and the resulting profiles were plotted.

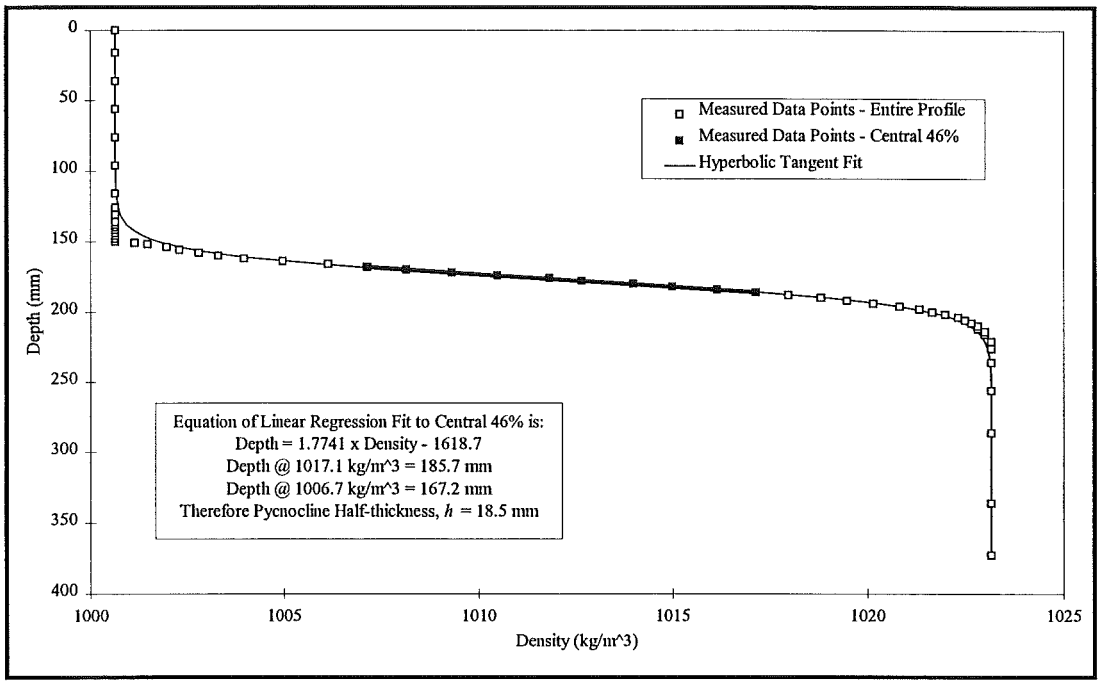

Figure 4.3 - Sample density profile and half-thickness calculation

A linear regression was fitted to the data points from the middle portion of the profile, and the resulting equation was used to determine the respective heights at the upper and lower boundaries of the pycnocline. The difference of these two then provided a value for the thickness. For experiments where more than one density profile was measured, the thicknesses were compared for consistency and then averaged. A sample profile is shown in Figure 4.3.

4.2.2 Interface Thickening

A density interface may be thickened by both turbulent mixing and molecular diffusion. When a stratified body of fluid is mixed, the centre of gravity of the fluid is raised, resulting in an increase in potential energy. This increase in potential energy comes from energy which was transferred to the body of fluid as it was being mixed. A sample calculation of the increase in potential energy for the case of a sharply stratified fluid which has been fully mixed is shown on Figure 4.4.

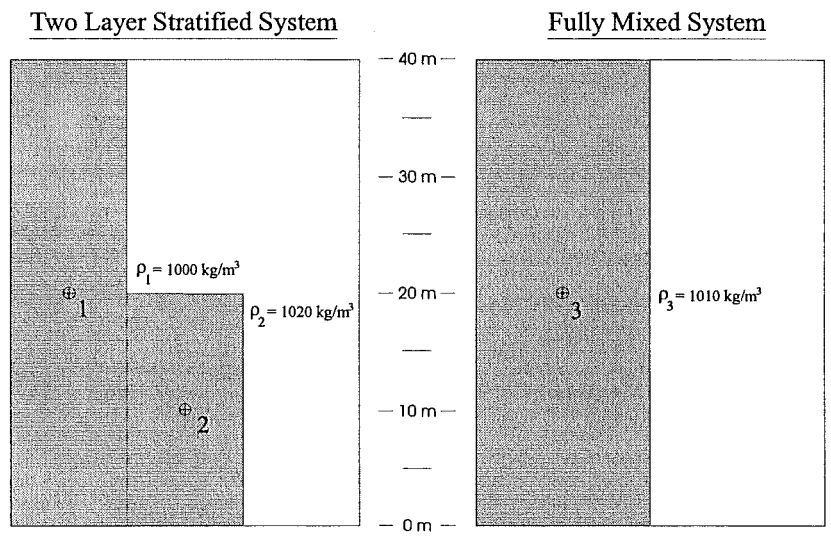

Potential Energy per Unit Surface Area = density x depth x gravity x height of centre of mass

$$PE_{1+2} = 1000 \times 40 \times 9.81 \times 20 + 20 \times 20 \times 9.81 \times 10 = 7.89 \times 10^6 \text{ J/m}^2$$

$$PE_3 = 1010 \times 40 \times 9.81 \times 20 = 7.93 \times 10^6 \text{ J/m}^2$$

$$3.9 \times 10^4 \text{ J/m}^2 = \Delta PE$$

Figure 4.4 - Example of potential energy increase by mixing

In a similar fashion, the interfacial region of a two-layer system may be thickened by turbulent mixing, be it by mechanical means or due to turbulence generated by shear instabilities during the passage of a wave. This results in an increase in the potential energy of the system, and in the case of thickening resulting from wave action it is obvious that the increase in potential energy must be accompanied by a corresponding decrease in wave energy.

Molecular diffusion occurs on a longer time scale than turbulent mixing, but the end result is still a thickening of the interface. The interfacial thickness may be

computed as a function of molecular diffusivity, κ, and the time since the interface had zero thickness, t, using Equation 4.7 (Fischer, 1979).

$$2h = \sqrt{4 \pi \kappa t} \tag{4.7}$$

Strictly speaking, the molecular diffusivity is a function of both temperature and salinity, but within the range of salinities encountered in these experiments, Equation 4.8 is suitable for its calculation (Tabor and Weinberger, 1981). This relationship is noted as being valid over the range of temperatures $\theta = 20$ - 90 °C and provides a value in m^2/s.

$$\kappa = 1.39 \left(1 + 0.029 \left(\theta - 20\right)\right) x\, 10^{-9} \tag{4.8}$$

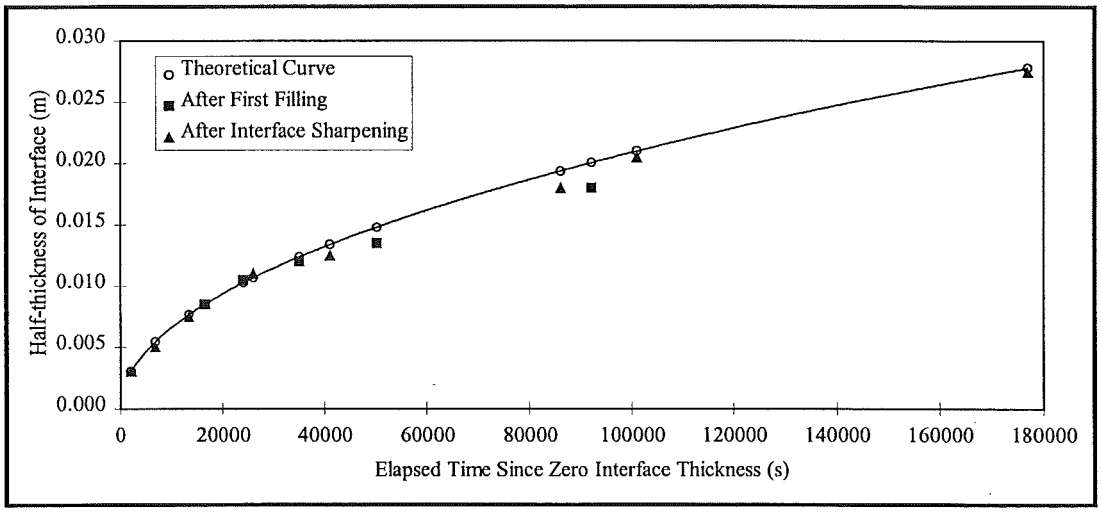

Figure 4.5 - Thickening of a saline density interface by molecular diffusion

A series of experiments were performed to test the applicability of Equations 4.7-8 and to gain some appreciation for the time scales involved in the thickening of a halocline by molecular diffusion. The data from these experiments, shown in Figure 4.5, showed a good agreement with the theoretical relationships. The interface thickening experiments are described in detail in Appendix 5.

Theoretical thickening times for the first ten millimetres of thickening are contained in Table 4.1, where it may be seen that thickening is initially quite rapid, but slows with time as the interface thickens. This explains why there is a lower bound of pycnocline thickness that might be achieved in experimental work, even when the

interface is sharpened by drawing off fluid, as the interface continues to thicken during both filling and drawing off. It also shows that when multiple measurements of interface thickness are made, whether for comparison purposes or to measure thickening after the passage of a wave, it is important that the measurements be done over as short a time as possible, especially for situations involving thin interfaces.

Table 4.1 - Thickening of a Saline Density Interface by Molecular Diffusion

Interfacial Half-thickness h (mm)	Time to Thickness @ 20°C $t_i - t_0$ (s)	Incremental Time $t_i - t_{i-1}$ (s)
1	229	229
2	916	687
3	2061	1145
4	3664	1603
5	5725	2061
6	8244	2519
7	11221	2977
8	14656	3435
9	18549	3893
10	22900	4351

4.3 Conclusions

Consideration of the shape and thickness of the density interface, or pycnocline, is important as both influence the celerity of an internal wave travelling on the interface. Knowledge of the thickness is also important as it is an important length scale in the analysis of internal solitary waves.

The density profile is described by a hyperbolic tangent function which depends on the upper and lower layer densities as well as the pycnocline thickness. In practice, the latter quantity is estimated by fitting a linear function to the central portion of the profile.

The pycnocline may be thickened by turbulent mixing or by molecular diffusion. Turbulent mixing may be caused mechanically or by shear instabilities resulting from wave passage, while molecular diffusion is a function of temperature and salinity and progresses with time. Thickening by diffusion is initially quite rapid, but gradually slows, as the interface thickness is proportional to the square root of time. For this reason it is important to recognise the temporal thickness variation for thin interfaces.

5.0 Results - Wave Generation

The methods of wave generation used in this study were previously discussed in Chapter 3, where it was noted that the three techniques were all capable of producing second mode waves, but varied in their effectiveness. The exchange flow method generally created solitary waves, but repeatability was difficult and slow wave development hindered observations. The forced inflow method commonly resulted in only an intrusive gravity current which never transformed itself into a solitary wave, though changing this to an unsteady inflow proved slightly more effective. The gravity collapse method proved most repeatable and robust, almost always producing waves within a short distance of the gate. In this chapter wave development after the initiation of flow will be described.

5.1 Exchange Flows

The exchange flow through the gate described in Section 3.5.1 was driven by hydrostatic pressure differences resulting from dissimilar density profiles on either side of the gate. As previously discussed, when generating solitary waves by this method it was essential that the intrusion as well as the return flows in the exchange flowed through the gate so that the flow was symmetric. It was also essential to balance the water levels on either side of the gate to ensure that the hydrostatic pressure differences driving the flow resulted only from density differences rather than from water surface elevation differences. The density differences in these experiments were so small that even a small imbalance in water levels would result in greatly different intrusion characteristics, making repeatability of experiments difficult. For instance, a typical experimental setup with a 600 mm total depth of fluid and a density factor of $\omega = 0.01$, an imbalance of 3 mm to the reservoir side would double the peak hydrostatic driving pressure from 30 to 60 Pa. Balancing of the water levels was achieved by keeping the water level above the flume partition, but this solution was in direct conflict with the goal of ensuring all flow went through the gate, as a flow path above the partition prevented a pure exchange flow. In the end, a compromise was adopted in which the thickness of the layer of water atop the flume partition was kept as thin as possible. This proved reasonably

effective, though the method was later abandoned for other reasons. The various flow patterns and hydrostatic pressure profiles are shown on Figure 5.1, though it must be noted that the hydrostatic pressure profiles are not to scale. In this figure, as in the experiments, the intrusion density, ρ_2, is midway between the upper, ρ_1, and lower, ρ_3, layer densities. The upper and lower layer depths, H, are equal, and the intrusion layer depth is equal to $2H$.

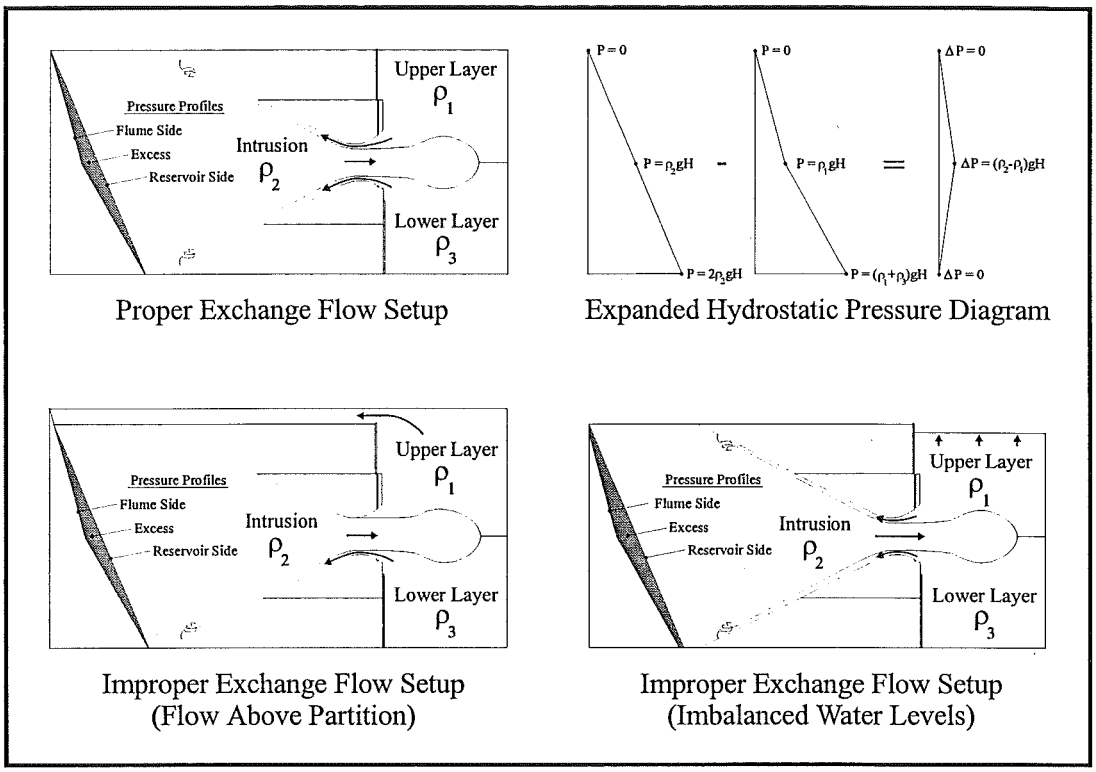

Figure 5.1 - Exchange flow method flow patterns and pressure profiles

A well-behaved exchange flow typically displayed a thick intrusion which was balanced by two thinner return currents along the upper and lower boundaries in the gate apparatus. To satisfy continuity, the thinner flows were necessarily more rapid than the thicker one, and this was borne out by observations. No shear instabilities were evident until the thin flows had travelled most of the way down the weir, so mixed fluid was not taken into the intrusion.

It was anticipated that the large volume of the reservoir (greater than the volume of the entire flume side) would allow a steady inflow for the length of each experiment. This proved to be false, as observations of the flow showed it to be unsteady and characterised by surges, which in extreme cases resulted in

momentary reversals of the exchange flow. It is felt that these occurred due to an imbalance in water levels after the initial surge, and were unavoidable with that generation technique, which led to the search for a more steady, repeatable technique.

Regardless of the drawbacks of the exchange flow method, it was relatively successful in meeting its goal of wave generation. The intrusive gravity current immediately formed a head which was thicker than the following current, as described by Holyer and Huppert (1980) and Britter and Simpson (1981). A typical intrusive gravity current is both diagrammed and pictured in Figure 5.2.

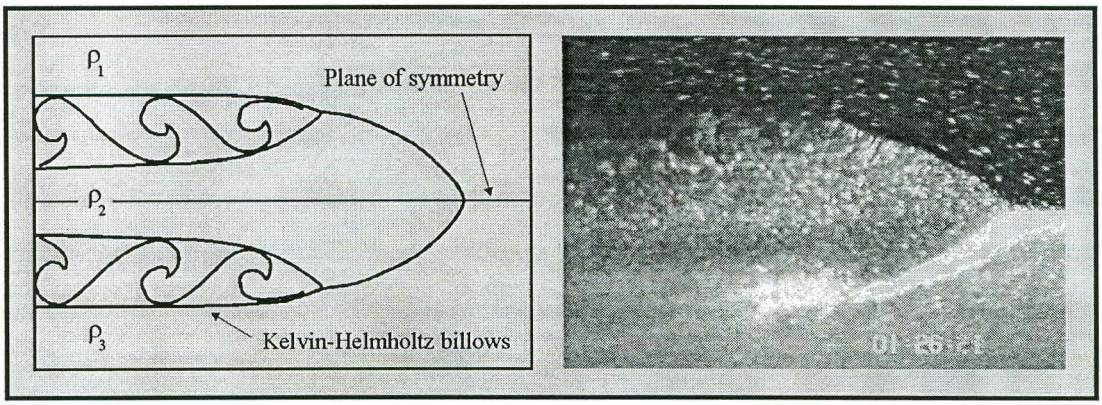

Figure 5.2 - Diagram and video image of intrusive gravity current

With a steady, intermediate density intrusion into a sharply stratified fluid, the interfacial fluid on the flume side splits about the head of the intrusion according to its density. Simpson (1987) noted that whereas a boundary gravity current would exhibit two instabilities of the density gradient region, a Kelvin-Helmholtz shear instability and a Tollmein-Schlichting instability due to bed friction and overrunning of fluid, the intrusive gravity current is only subject to the former, as shown on Figure 5.2. The head of an intrusive gravity current is thus smoother and more regular than that of a boundary current, with the flow being sheet-like and essentially two dimensional. The Kelvin-Helmholtz instability occurs where the local Richardson number, *J*, drops below 0.25 (Thorpe, 1968), and is seen in the lee of the intrusion. It is an important mechanism in the dissipation of excess energy as the intrusion progresses. The Richardson number, which may be calculated using Equation 5.1, is a dimensionless number which represents a balance between

gravity forces, as quantified by the numerator of the equation, and inertial forces, as quantified by the denominator (Yih, 1980).

$$J = -\frac{g\dfrac{d\rho}{dy}}{\rho\left(\dfrac{du}{dy}\right)^2} \tag{5.1}$$

The unsteadiness of the intrusion appeared to be crucial in the transformation of the head of the intrusion into a second mode wave. Surging, as well as the tendency for fluid entering the flume to eventually contribute more to thickening of the intrusion than its longitudinal advance, contributed to the slowing of the intrusion. Its head, in the meantime, maintained its amplitude and celerity and travelled ahead of the following current, which then developed a new head with a smaller amplitude corresponding to its reduced celerity. An image of a lead wave with a following intrusive gravity current is shown on Figure 5.3. In this experiment the interfacial region was dyed yellow, while the intrusive fluid was red.

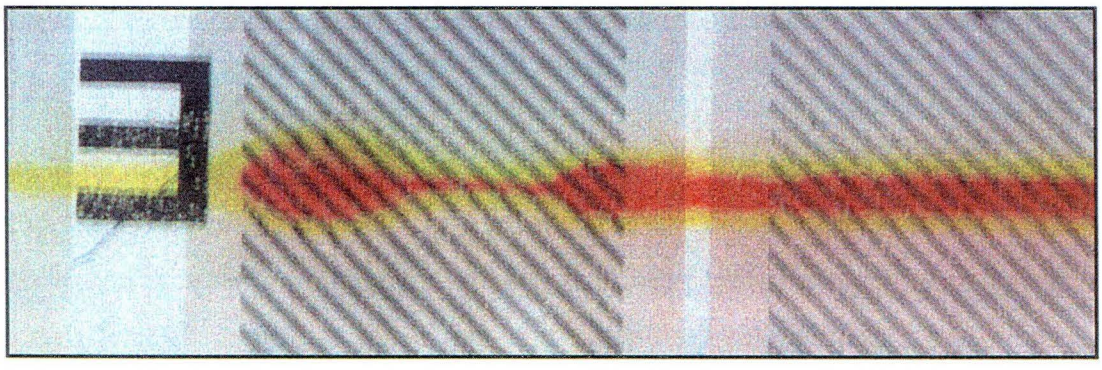

Figure 5.3 - Fully formed solitary wave with following gravity current

Some strong intrusive currents travelled a significant distance before they formed solitary waves. A sequence of images (from run 50121PE050) showing the transition from intrusive gravity current to second mode internal solitary wave is shown in Figure 5.4.

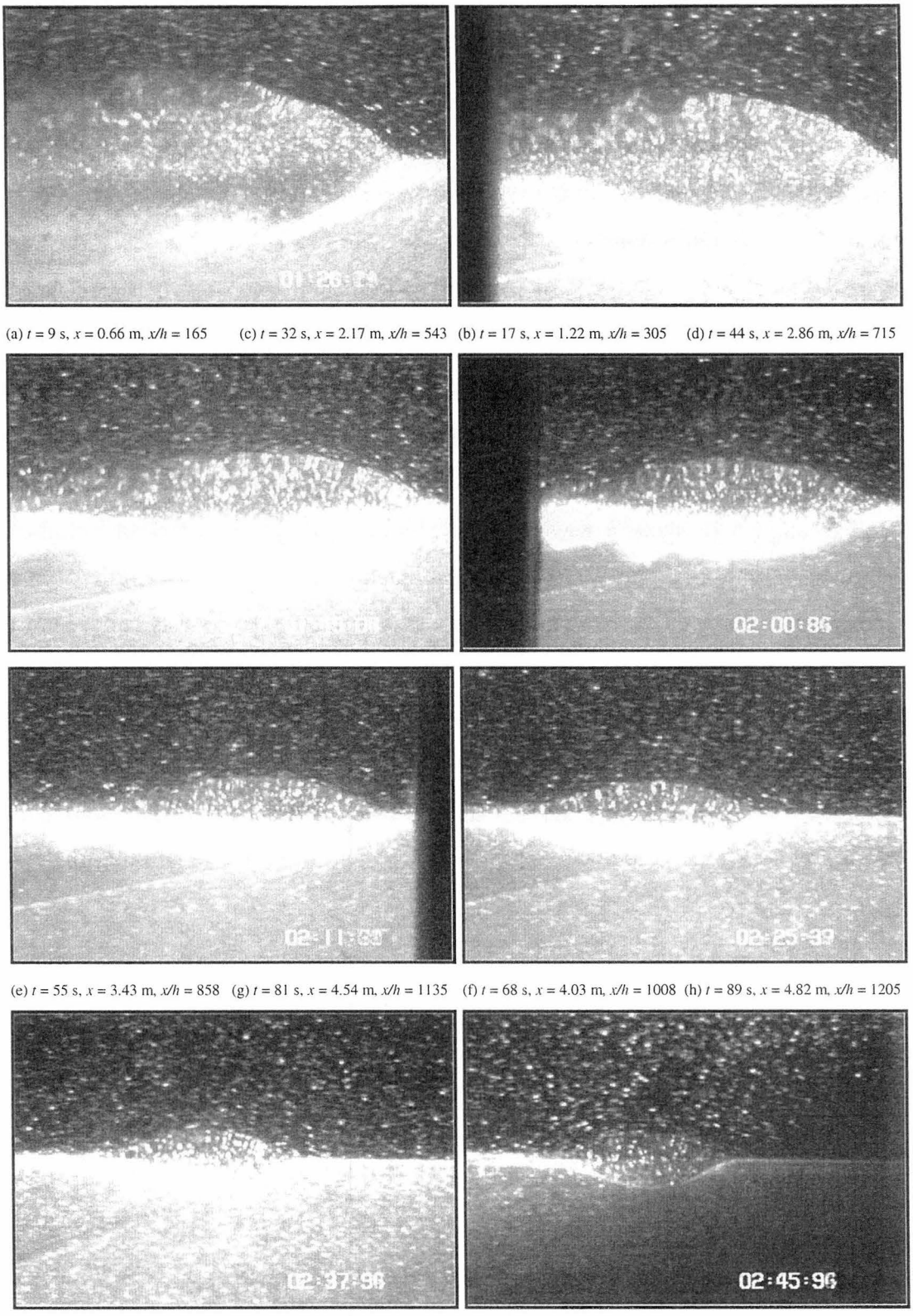

(a) t = 9 s, x = 0.66 m, x/h = 165 (c) t = 32 s, x = 2.17 m, x/h = 543 (b) t = 17 s, x = 1.22 m, x/h = 305 (d) t = 44 s, x = 2.86 m, x/h = 715

(e) t = 55 s, x = 3.43 m, x/h = 858 (g) t = 81 s, x = 4.54 m, x/h = 1135 (f) t = 68 s, x = 4.03 m, x/h = 1008 (h) t = 89 s, x = 4.82 m, x/h = 1205

Figure 5.4 - Sequence of images showing wave development from intrusion

Figure 5.4a shows a typical intrusive gravity current, which at this point had an amplitude (measured from interface to peak) of 43 mm and a celerity of 71 mm/s. As the intrusion slowed, the location of the Kelvin-Helmholtz instability moved

towards the lee of the head, as seen on Figure 5.4b where the height of the intrusion had dropped to 38 mm and the celerity to 67 mm/s. Figure 5.4c shows a radical change in the form of the head, which now exhibits most of the characteristics of a second mode wave. The intrusive current had slowed, dropping behind the head and no longer providing fluid to replace that lost during mixing caused by the instability, and the instability had moved even further to the lee of the wave and become much less vigorous. The transition from intrusion head to second mode wave is assumed to be complete in Figures 5.4d and 5.4e. These images show that the wave had become independent of the following current, though shear instabilities were still apparent, particularly on its lower portion. Over this time the wave amplitude fell from 26 to 22 mm and its celerity from 55 to 49 mm/s. Figures 5.4f through 5.4h show a wave which exhibited no sign of a Kelvin-Helmholtz shear instability, though the amplitude continued to fall, in this case from 19 to 15 mm. This is typical of a large-amplitude wave, which this wave was representative of by virtue of its trapped inner region and its amplitude, which even at the end of the tank was four times the interfacial half-thickness. The interface in this example had a half-thickness of $h = 4.0$ mm and a density factor of $\omega = 0.0176$. Particles were used to aid in visualisation and sharp density interfaces were also visible due to refraction of the laser sheet and the effect of salt in the lower layer on the laser light.

5.2 Forced Inflows

The forced inflow method was adopted in an attempt to produce steady inflows and experiments which were repeatable. Unfortunately, it was soon apparent that the first goal was counterproductive, as steadier flows resulted in intrusive currents which took longer to develop into solitary waves than the gradually weakening flows of the preceding method. Thickening of the interface still resulted in a slowing of the intrusion with distance, so for weaker inflows, wave development proceeded in a similar fashion to that described in the previous section. It should be noted that it was during these experiments that the circulation reversal discussed in Section 7.1 was observed.

During the latter portion of the forced inflow experiments, an unsteadiness was imparted to the inflow by stopping the inflow after only a short duration. This proved slightly more effective at wave generation, but the transition to a solitary wave still required a good deal of time, often leaving only a small length of tank to examine the fully developed wave. This made certain aspects of the wave motion, in particular mass transport and wave decay, difficult to observe, and led to the search for an alternate method for wave generation.

5.3 Gravity Collapse

The gravity collapse method adopted was similar to that used by Maxworthy (1980), though the collapsing fluid was premixed and loaded into the collapse reservoir rather than mixed in place. Thus the initial hydrostatic imbalance was easily controlled by varying the depth of the collapsing fluid and experiments were readily repeatable. This was important when trying to produce a wave with similar characteristics over a series of runs making use of different visualisation techniques. The gravity collapse technique also had the advantage of producing solitary waves within a very short distance from the gate.

A sequence of images from a typical experiment (run 61030PC030) using the collapse wave generation technique is shown in Figure 5.5. Figure 5.5a shows an intrusive current similar to those produced by other generation methods. The head of the intrusion has an amplitude (from interface to peak) of 43 mm and has a strong following current. Figure 5.5b shows that a necking of the following current has occurred, and by Figure 5.5c it is apparent that the head of the current has completely separated from the rest of the collapsing fluid. At this point the wave had an amplitude of 42 mm and a celerity of 58 mm/s. Figures 5.5d through 5.5h show the progress of the wave as it traversed the remaining 3.5 m of the tank, its amplitude decreasing to 35 mm and its celerity to 52 mm/s. It should be noted that the significant difference between this example and that shown in Figure 5.4 is the rapid development of the wave, providing more of an opportunity to study it.

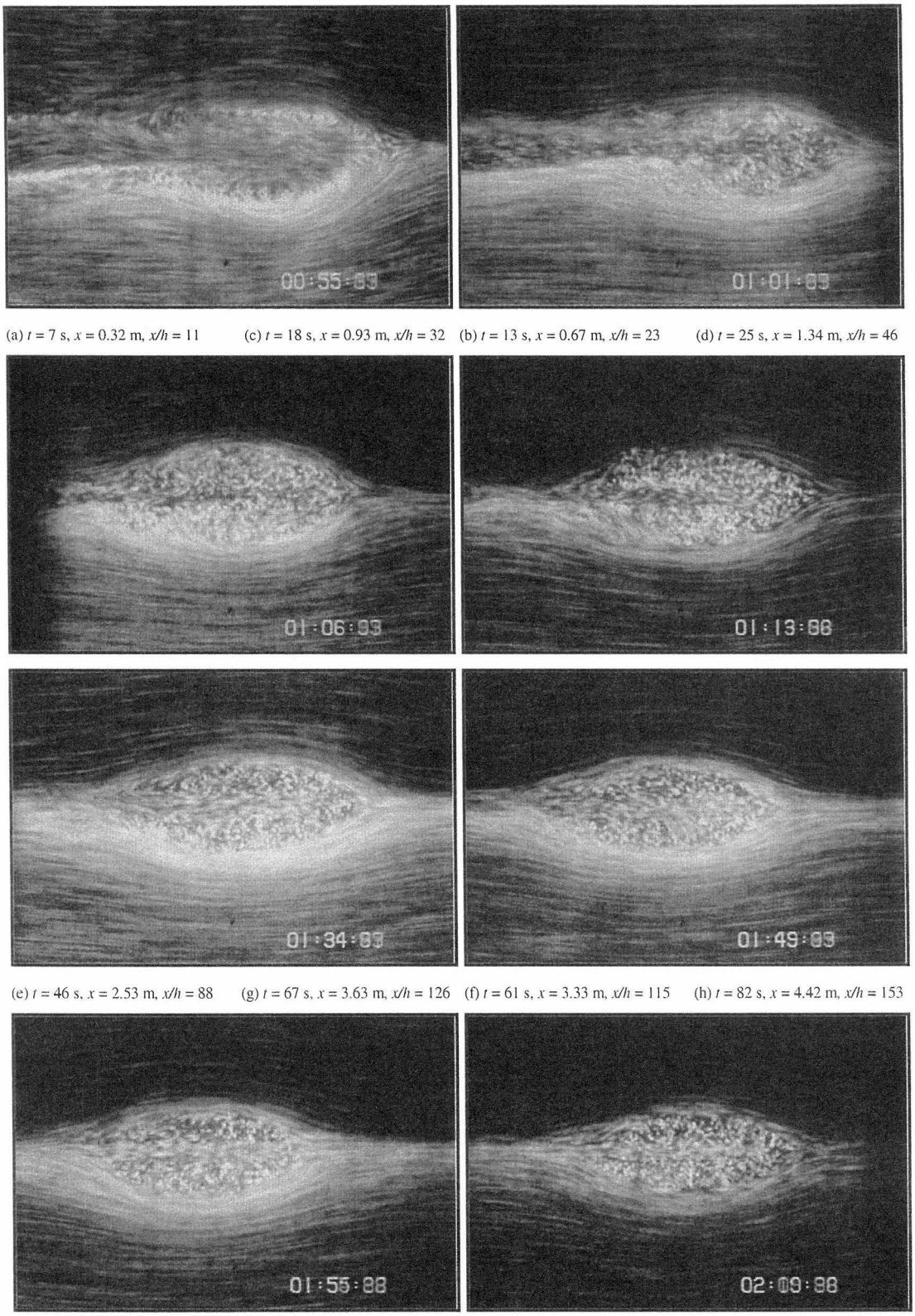

(a) t = 7 s, x = 0.32 m, x/h = 11 (c) t = 18 s, x = 0.93 m, x/h = 32 (b) t = 13 s, x = 0.67 m, x/h = 23 (d) t = 25 s, x = 1.34 m, x/h = 46

(e) t = 46 s, x = 2.53 m, x/h = 88 (g) t = 67 s, x = 3.63 m, x/h = 126 (f) t = 61 s, x = 3.33 m, x/h = 115 (h) t = 82 s, x = 4.42 m, x/h = 153

Figure 5.5 - Sequence of images showing wave development from collapse

The collapsing region in this example had a length of 410 mm and a depth of 100 mm, while the interface had a half-thickness of h = 28.9 mm and a density factor of ω = 0.0106. The reader is directed to Figure 7.2 to view images of wave

development from a collapse which provide more detailed observations of the internal circulation of the wave.

5.4 Conclusions

The present study made use of three generation methods, using an exchange flow, a forced inflow and finally a gravity driven collapse to produce second mode internal solitary waves. The first method presented repeatability problems, while both the first and the second often produced waves only after an intrusive gravity current traversed a significant length of the flume. The gravity driven collapse was most effective in the rapid, repeatable generation of second mode waves.

The mechanism for wave generation was similar for all three methods, with an intrusive gravity current forming a head which had an amplitude greater than that of the following current. The wave was formed when the head separated from the following current. In the cases of the exchange flow and forced inflow, this separation occurred as the inflow began to contribute more to thickening of the interfacial region than the longitudinal progress of the intrusion. In the former case, unsteadiness of the inflow also contributed to the separation. In the case of a gravity collapse or a short duration inflow, the finite quantity of fluid available for the intrusion resulted in a more rapid wave formation.

In all cases, the remaining intrusion behind the leading wave would form another head. Because of its reduced celerity, its amplitude was somewhat less than that of the initial intrusion, but a wave was often still able to form. In this way trains of solitary waves, ordered by amplitude as described by Maxworthy (1980), were able to form.

6.0 Results - Wave Propagation: External Flow

The shape of a second mode internal solitary wave and its propagation celerity are the two components essential to the description of its external flow. These have both been addressed in the literature, but the present study examined waves of larger amplitude than have been observed in the past, providing an opportunity to extend the range of applicability of equations describing the external flow. In this chapter, the methods used to measure wave celerity, wavelength and amplitude will be described. The data from the experiments will then be presented and compared to previous experimental and theoretical results. In addition, a novel theoretical solution for predicting wave celerity will be presented and examined.

6.1 Measurement of Relevant Parameters

Wave celerities, wavelengths and amplitudes were determined from the video record by using a frame grabber to capture still images from which times, positions and dimensions could be measured.

6.1.1 Celerity Measurement

Wave celerities, and their variation with time, were calculated by using elapsed times and displacements from video records of the experiments. A character generator was used to place a time stamp on the video image, and by using the single frame advance capability of the video recorder it was possible to ascertain the time to within one twenty-fifth of a second. Initially, the time of the arrival of the wave at up to twenty positions along the tank was recorded, but soon it was found to be quicker and just as accurate to use the seven tank supports as markers.

The time-position data were then placed in a Microsoft Excel spreadsheet and a quadratic regression equation was fitted to them. The use of a quadratic equation was arbitrary and based on observations that an excellent fit was provided over the entire range of experiments. It can also be demonstrated that this choice is consistent with subsequent experimental observations and derived relationships. In

Section 6.3.3, it is shown that wave celerity is proportional to the square root of wave amplitude, or:

$$c^2 \propto a \tag{6.1}$$

In Section 8.1, it is shown that the rate of decay with displacement is constant, or:

$$\frac{da}{dx} = \text{constant} \tag{6.2}$$

The wave celerity expression (Equation 6.1) may be differentiated and combined with that for wave decay (Equation 6.2) to show that:

$$2\,c\frac{dc}{dx} \propto \frac{da}{dx} = \text{constant} \tag{6.3}$$

Recognising that celerity is the time derivative of displacement means that:

$$2\,\frac{dx}{dt}\frac{dc}{dx} \propto \frac{dc}{dt} = \text{constant} \tag{6.4}$$

This means that second mode waves undergo constant acceleration, which is consistent with the choice of a quadratic curve fit to the time-displacement data.

Once an equation was ascertained, it was differentiated with respect to time to determine the wave celerity as a function of time, and its second derivative was calculated to determine the wave acceleration. It is apparent from this that the celerity was observed to be linearly related to time, and the acceleration constant. When fitting the regression equation, the curve was not forced through the origin, as typically there was a lag between the gate release and development of motion as potential energy was converted to kinetic energy. Typical time-position data, with the corresponding position, celerity and acceleration equations, are shown in Figure 6.1.

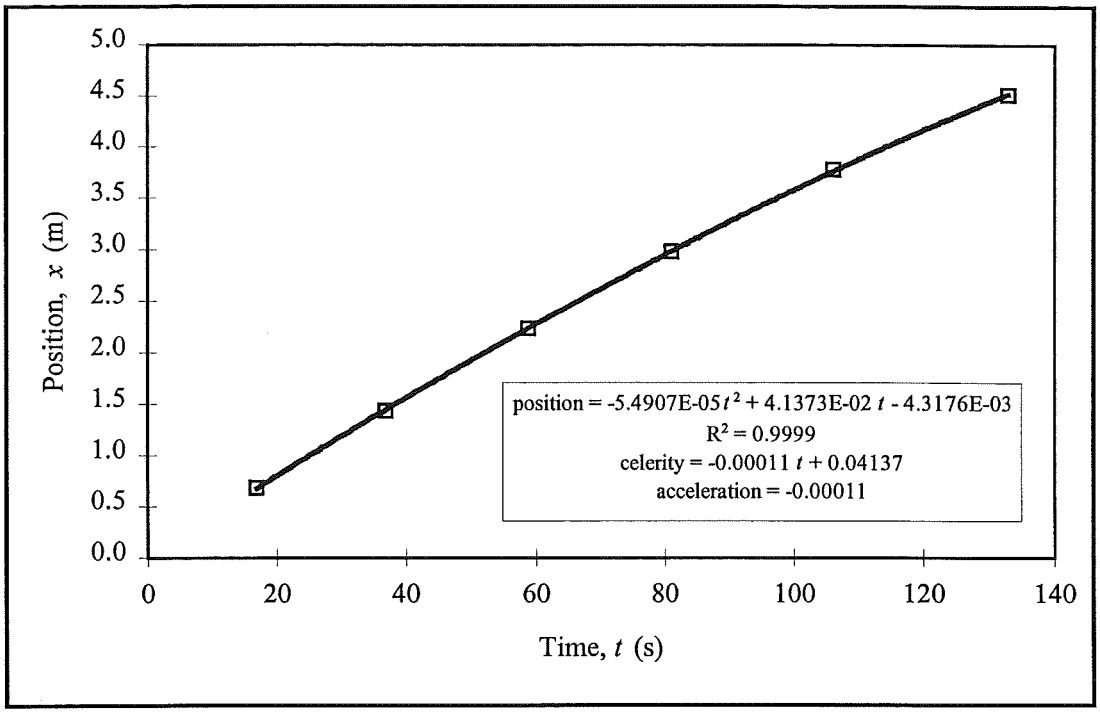

Figure 6.1 - Derivation of celerity and acceleration from time-position data

6.1.2 Amplitude Measurement

Previous studies have typically defined the amplitude of a wave in terms of the displacement of a streamline from its position before the passage of the wave. The amplitude parameter of Davis and Acrivos (1967) used the maximum displacement of any streamline modified by a density factor, while those of Hurdis and Pao (1975) and Stamp and Jacka (1995) defined amplitude as the maximum displacement of the streamlines at $\pm h$. Dye droplets placed at $\pm h$ aided in the measurement of the displacement in the latter study.

This study centred on large amplitude waves, the amplitude being defined as half of the thickness of the interior region of the wave. This was identified by using the Data Translation frame grabber to acquire time-averaged images from the video record. On these images, averaging the image intensity over approximately one-half second caused the external flow to appear as streaklines while the interior region remained essentially unchanged. This clearly revealed the boundary of the interior region and allowed measurement of the wave amplitude. A typical time-averaged streakline image is shown in Figure 6.2. Measurements were aided by the

superposition of a calibration grid image on the streakline image. The calibration grid was used to correct for distortion of the image by the video camera lens and consisted of a video image of a grid which was shot during experimentation. Both vertical and horizontal lines adopted a slight convexity towards the centre of the image, resulting in slightly different linear scales depending on where the image was measured.

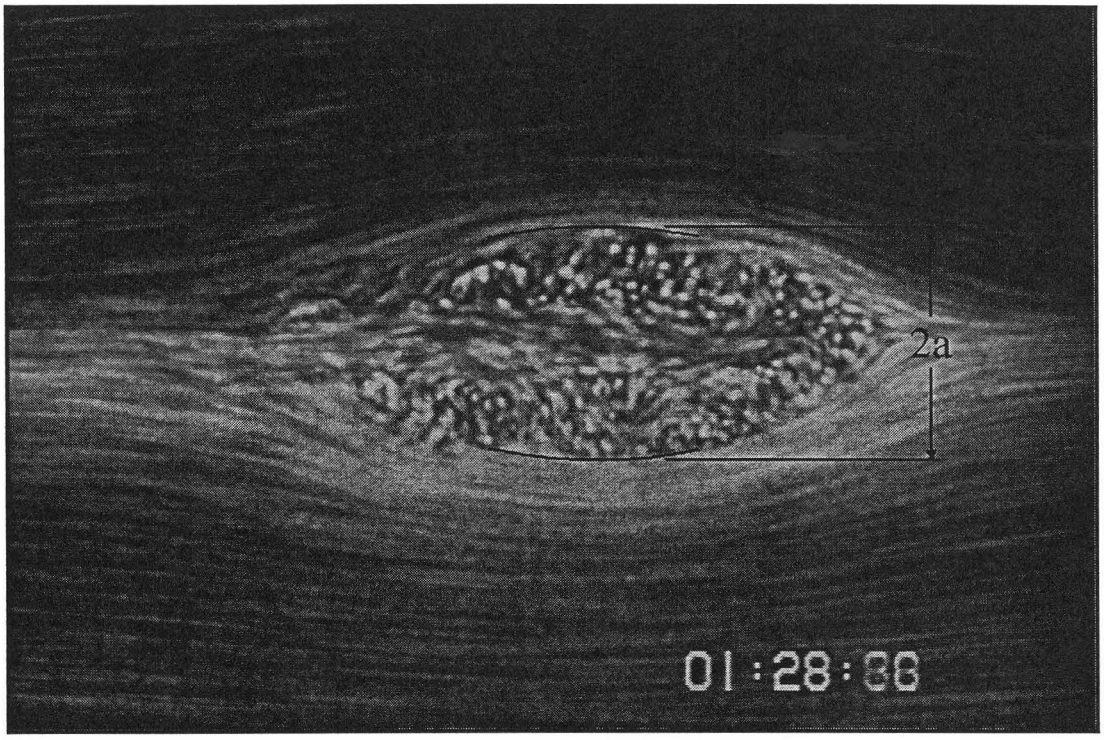

Figure 6.2 - Sample wave amplitude measurement. The pictured wave had a celerity of 57 mm/s and the image was averaged over 15 frames or 0.6 s.

The definition of amplitude adopted here is similar to that of Stamp and Jacka (1995), with the difference being equal to the difference between the interfacial half-thickness at some distance from the wave and its narrowed value as the wave passes. Where large amplitude waves are concerned, this difference is small and thus the two amplitudes should be similar. The two wave definitions are illustrated in Figure 6.3.

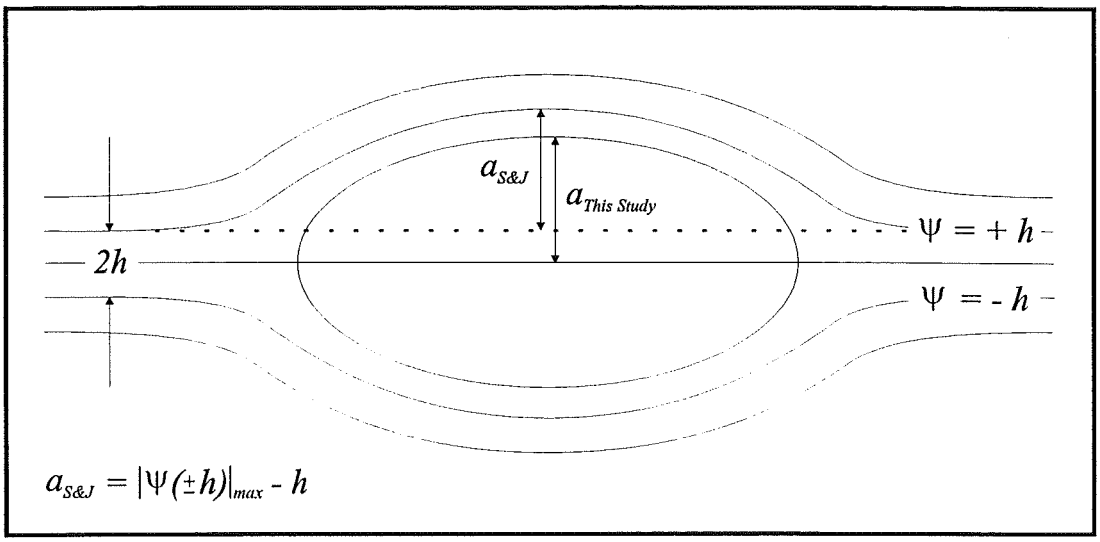

Figure 6.3 - Definition of wave amplitude. Notation follows Stamp & Jacka (1995), who scaled the stream function by wave celerity, c.

6.1.3 Wavelength Measurement

The measurement of the wavelength of a second mode wave presents some difficulty, as it is difficult to define exactly the limits of such a long wave. Previous studies (Tung, Chan & Kubota, 1982; Stamp & Jacka, 1995) have typically defined the wavelength based on the distance between the two points at which the wave amplitude is one-half of its maximum.

As this study centred on large amplitude waves, and the boundary of the interfacial region was not visually identifiable, an alternate method was used to define the wavelength. Framegrabbed streakline images were used to identify the interior region of the wave, as in the amplitude measurement procedure, and an ellipse was fitted to the boundary of this region. Just as the length of the semi-minor axis of this ellipse provided the amplitude measurement, the length of the semi-major axis yielded a measure of the wavelength. A sample wavelength measurement is shown on Figure 6.4, performed on the same image as that presented in Figure 6.2.

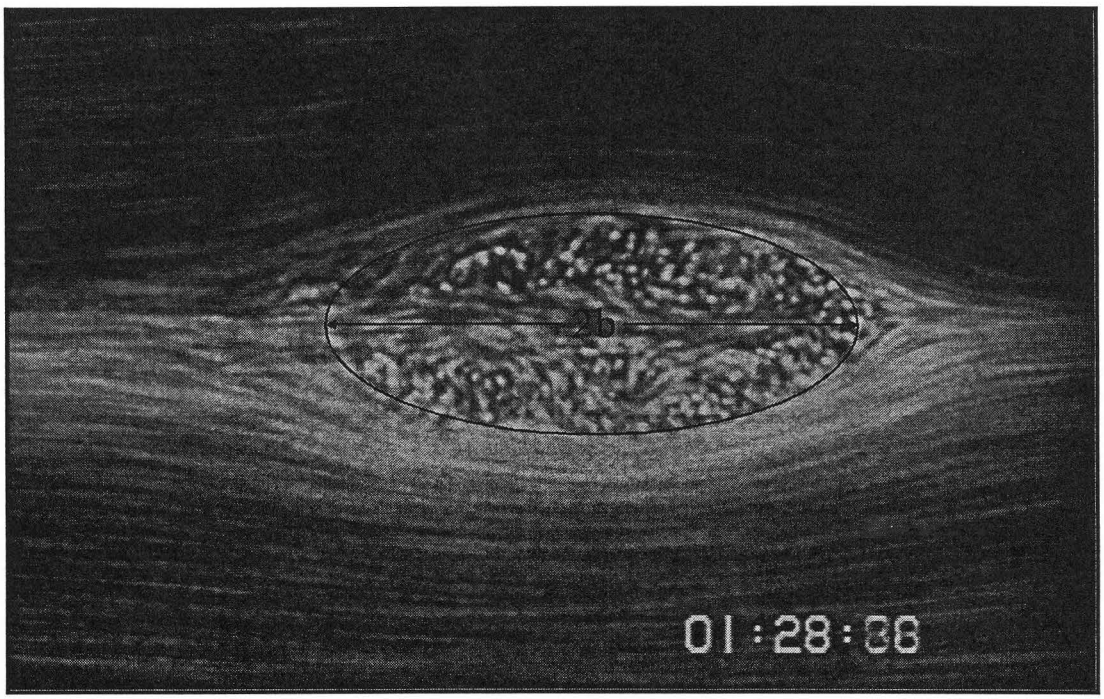

Figure 6.4 - Sample wavelength measurement

To compare the results of this study to previous studies it was necessary to convert the length of the semi-major axis of the ellipse into a measure which corresponded to the wavelength measurement of Stamp & Jacka (1995). The quantities involved in that study as well as the present one are shown on Figure 6.5.

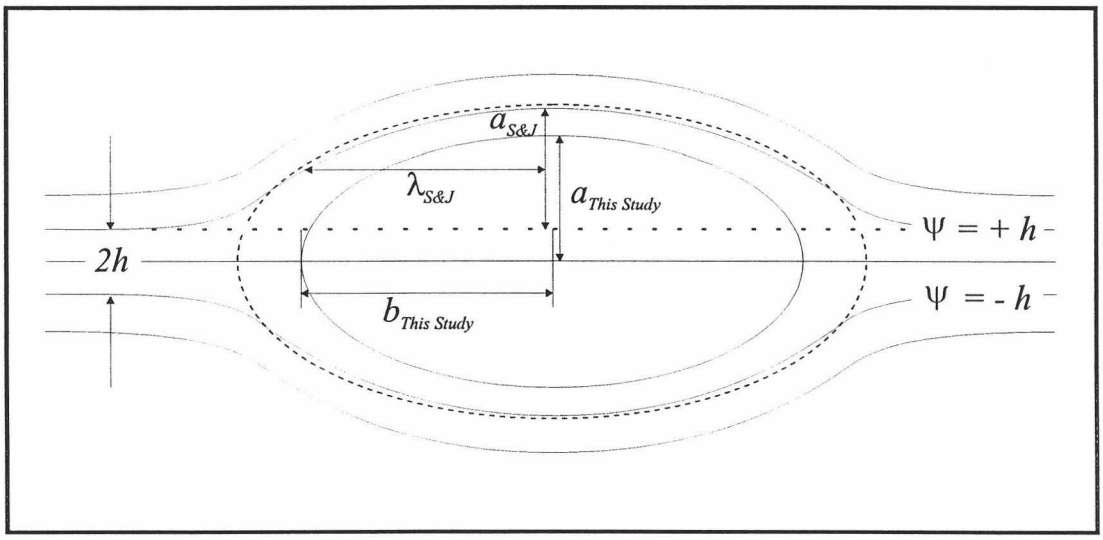

Figure 6.5 - Definition of wavelength

To convert the semi-major axis measurement of the present study to a value approximately equal to the wavelength measurement of Stamp & Jacka (1995), the ellipse measured in this study was first scaled up so that its semi-minor axis

extended to $\pm h$ at the point of maximum amplitude. An analysis of the experimental data yielded an average aspect ratio (b/a) of 2.1, so the length of the semi-major axis was increased by $2.1h$. The resulting ellipse is shown in dashed lines on Figure 6.5. The geometric formula describing this larger ellipse is then:

$$\frac{x^2}{(b + 2.1h)^2} + \frac{y^2}{(a + h)^2} = 1 \tag{6.5}$$

Equation 6.5 may then be rearranged with $x = \lambda$ and $y = 0.5a + h$ to calculate a wavelength which is consistent with that measured by Stamp & Jacka (1995):

$$\lambda = \sqrt{(b + 2.1h)^2 \left[1 - \frac{(0.5a + h)^2}{(a + h)^2}\right]} \tag{6.6}$$

All parameters on the RHS of Equation 6.6 are those measured in the fashion described in this study. Presentations of relevant data will make use of the wavelength calculated in this fashion.

6.2 Analysis of Wave Shape

The question of the variation of wave shape with amplitude has been addressed by several analytical and experimental studies. In this section these observations will be discussed and examined in light of new data which extend the range of experimental data.

6.2.1 Review of Previous Work

The distinction between waves of large and small amplitude was addressed in Davis & Acrivos (1967). Large amplitude waves were identified by 'closed streamline' regions in which fluid was carried along at the same celerity as the wave, while small amplitude waves propagated faster than any individual fluid component. In numerical simulations, the bifurcation of the central streamline around the closed region was observed to occur at amplitudes greater than $a/h = 1.2$. These observations were confirmed by Tung, Chan & Kubota (1982) and Stamp & Jacka

(1995), and both studies noted that approximate analytic solutions based on weakly non-linear theory were not valid in this large amplitude region. Examples of the two types of waves are shown in Figure 6.6.

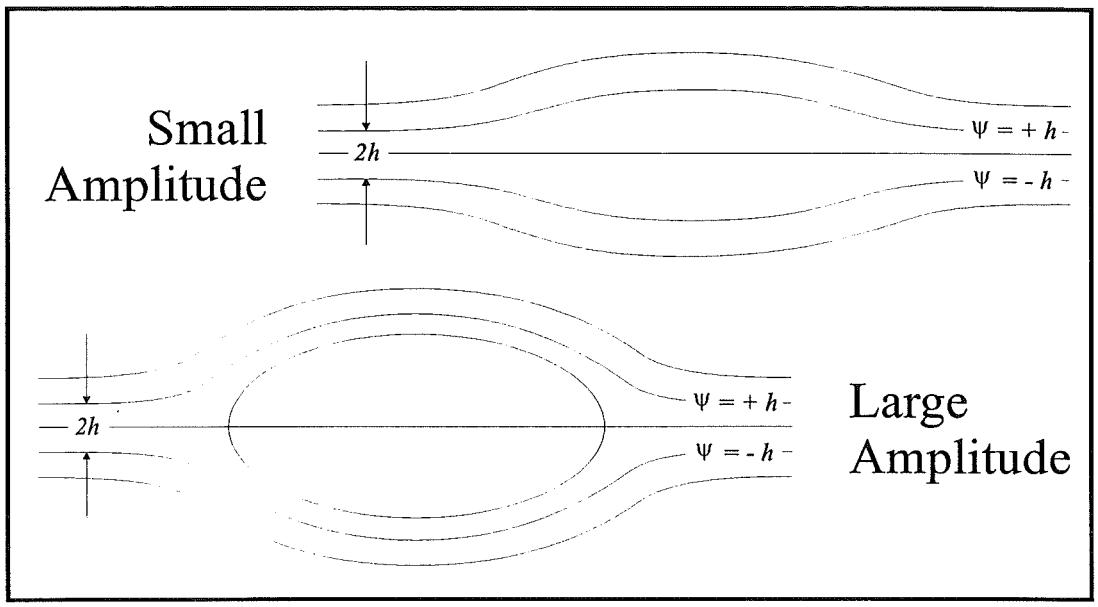

Figure 6.6 - Streamlines of small and large amplitude second mode waves

Second mode waves were described as symmetrical about the centre of the density gradient by both Davis & Acrivos (1967) and Kao & Pao (1979). More detailed observations by Stamp & Jacka (1995) revealed slight asymmetries in the form of the wave. The upper amplitude of the wave was consistently measured as being larger than the lower amplitude, and the upper and lower portions of the wave were frequently slightly out of phase (either ahead or behind), though wavelengths were generally similar. This was explained as being caused by the difference between the free surface and closed boundary conditions above and below. In this study, upper and lower amplitudes and wavelengths have not been measured, but the measurement procedure as shown in Figures 6.2 and 6.4 ensures that an average value is used in calculations.

With regard to wave profile, Benjamin's (1967) theory predicted an inverse relationship between wavelength and amplitude, as expressed in the following equation:

$$\frac{\lambda}{h} = \frac{385}{144}\left(\frac{a}{h}\right)^{-1} \qquad (6.7)$$

The numerical model of Tung, Chan & Kubota (1982) predicted that for very small amplitude waves, the wavelength would decrease as the amplitude increased with the approximate scaling being $\lambda = (a/h)^{-1/2}$. As the amplitude approached the thickness of the pycnocline, the wavelength would cease to contract, and for yet larger amplitudes, the wavelength would begin to increase. The enlargement of the wavelength for these large amplitude waves was taken to be a consequence of the appearance of the recirculating region within the wave and its enlargement with increase in wave amplitude.

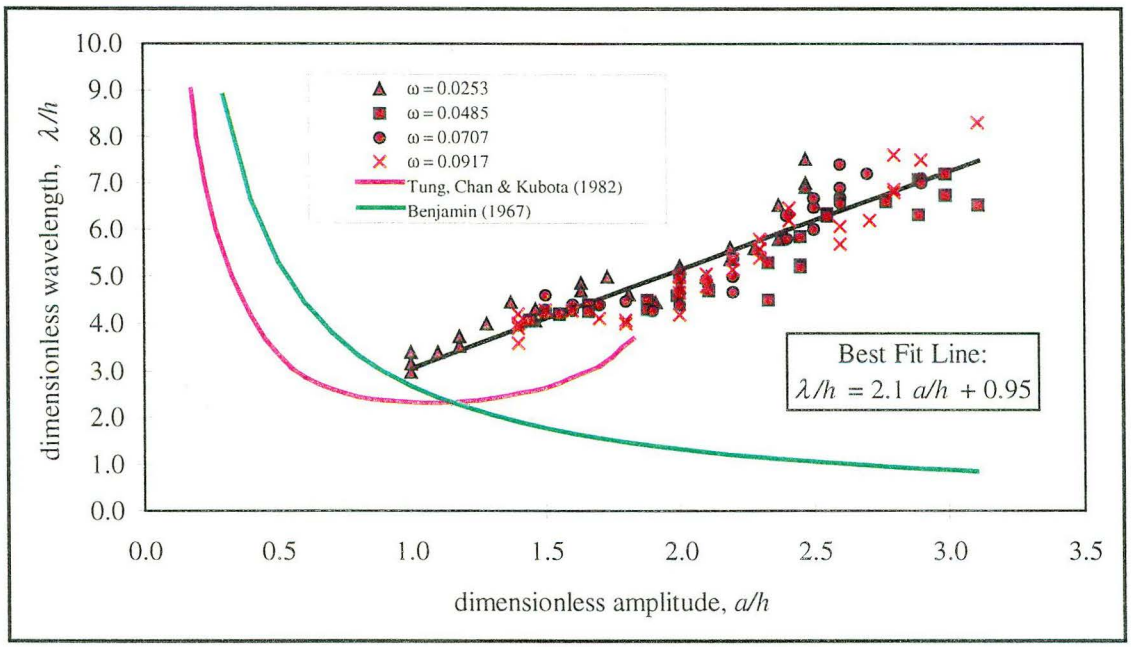

Figure 6.7 - Relationship between dimensionless wavelength and amplitude

For large amplitude waves, Stamp & Griffiths (1992) noted a constant wave aspect ratio (λ/a) of 2.2. Stamp & Jacka (1995) later modified this and presented a linear relationship between wavelength and amplitude, which is shown in the following equation, where $\bar{a}$ and $\bar{\lambda}$ represent the average of the upper and lower amplitudes and wavelengths, respectively.

$$\frac{\bar{\lambda}}{h} = 0.95 + 2.10\,\frac{\bar{a}}{h} \quad \text{for } 1.0 \le \frac{\bar{a}}{h} \le 3.1 \qquad (6.8)$$

The theoretical relationships of Benjamin (1967) and Tung, Chan & Kubota (1982), as well as the data of Stamp & Jacka (1995) are shown on Figure 6.7.

6.2.2 Present Study

The present experiments provided wave data for a range up to an amplitude of a/h = 11.6, extending the body of data from Stamp & Jacka (1995), which examined a maximum value of 3.1. The present study considered experiments involving deep water waves with densimetric factors ranging from ω = 0.0028 - 0.0176.

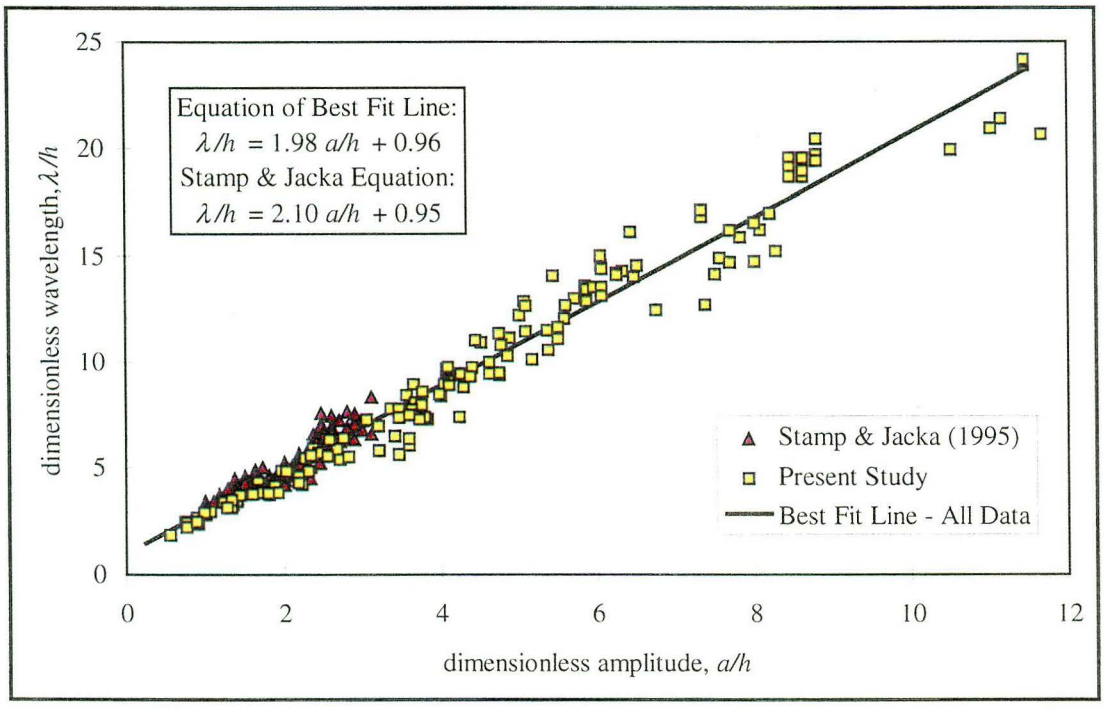

Figure 6.8 - New wavelength-amplitude data

From Figure 6.8, it is obvious that the form of Equation 6.8 matches the entire body of experimental data. This confirms the conclusion of Stamp & Jacka (1995) that all second mode waves of $a/h > 1$ are similar in shape and differ only by a scaling factor. The new data significantly extends the range of Equation 6.8 and introduces a slight modification to the values of the constant and amplitude coefficient, producing the following equation:

$$\frac{\overline{\lambda}}{h} = 0.96 + 1.98\,\frac{\overline{a}}{h} \quad \text{for } 0.5 \le \frac{\overline{a}}{h} \le 11.6 \tag{6.9}$$

The experimental results for individual runs are displayed in a more detailed form in Appendix 6, where results from previous studies are also found. These figures also display error bars based on the error analysis presented in Appendix 12.

6.3 Analysis of Factors Governing Wave Celerity

Several previous studies have presented theoretical relationships governing the propagation celerity of a second mode wave. These have typically expressed the wave celerity, rendered dimensionless by the infinitesimal first mode wave celerity, as a function of the dimensionless wave amplitude. These relationships and the accompanying experimental data were previously discussed in Sections 2.2.2 and 2.5.3 and will be reviewed briefly here. New experimental data which extends the range of amplitudes will then be presented in conjunction with a novel theoretical treatment which is applicable to these larger amplitude waves.

6.3.1 Review of Previous Work

The experimental data of Davis & Acrivos (1967), Hurdis & Pao (1975) and Stamp & Jacka (1995) show reasonably good agreement with the relationship between celerity and amplitude presented in the latter study. This relation, as well as rearrangements of those presented by Benjamin (1967) and Davis & Acrivos (1967) are shown in Equations 6.10-12. The latter equation, with an amplitude coefficient of 0.453, matches the deep-water numerical solution of Tung, Chan & Kubota (1982). In all of these equations, the dimensionless wave celerity (dimensional wave celerity, c, divided by infinitesimal first mode wave speed, c_0, the latter of which is defined in Equation 2.34) is expressed as a function of the dimensionless wave amplitude (dimensional wave amplitude, a, divided by the interfacial half-thickness, h).

$$\frac{c}{c_0} = \sqrt{1 + \frac{3}{5}\frac{a}{h}} \quad \text{Benjamin, 1967 } \textit{(Equation 2.2.5)} \qquad (6.10)$$

$$\frac{c}{c_0} = \sqrt{\frac{1}{1 - 0.6\frac{a}{h}}} \quad \text{Davis \& Acrivos, 1967 } \textit{(Equation 2.2.8)} \qquad (6.11)$$

$$\frac{c}{c_o} = 1 + 0.49\,\frac{a}{h} \quad \text{Stamp \& Jacka (1995) } \textit{(Equation 2.3.7)} \qquad (6.12)$$

The noted theoretical relationships and experimental data are displayed on Figure 6.9.

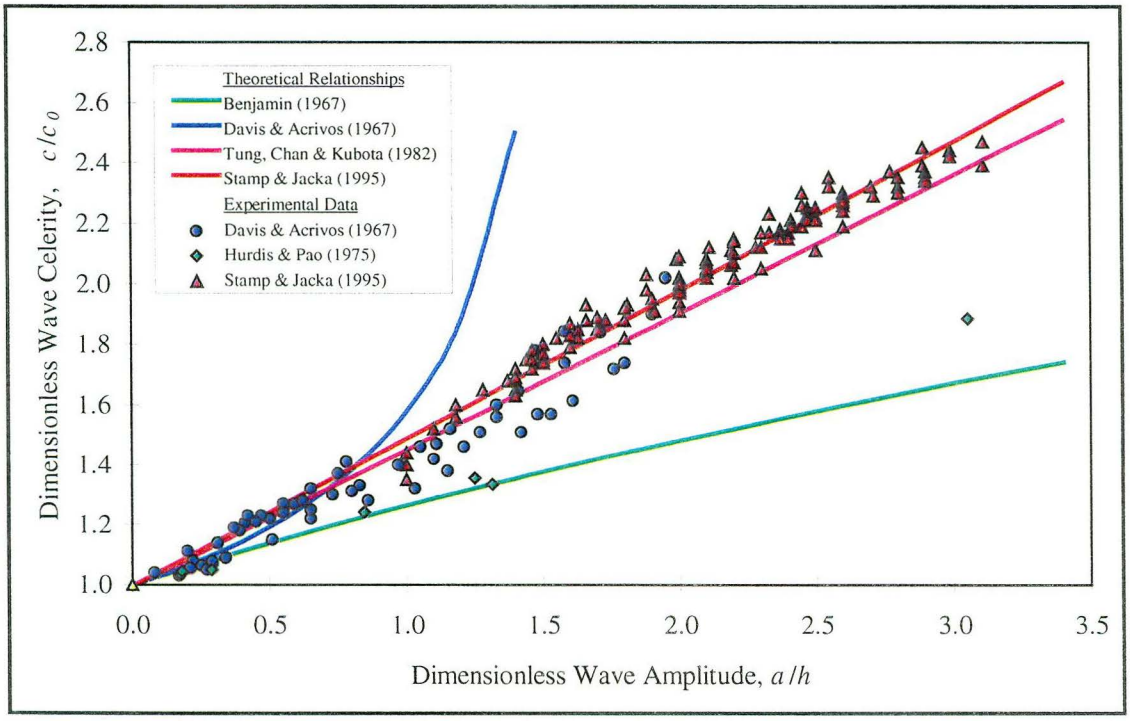

Figure 6.9 - Theoretical and experimental amplitude-celerity relationships

It is apparent from Figure 6.9 that these relations show a good agreement with the data and each other for small ($a/h < 0.5$) amplitude waves, while only the latter provides a good fit for larger (up to $a/h = 3.1$) waves. The question of whether larger waves are similarly accommodated will be addressed in the next section.

6.3.2 Present Study

One of the goals of this study was to generate and examine larger amplitude waves than have previously been observed. Second mode waves of amplitudes up to a/h = 11.6 were successfully created during the present experimental investigation. This

makes possible an examination of the validity of applying the theoretical relationships presented here over a larger range of amplitudes.

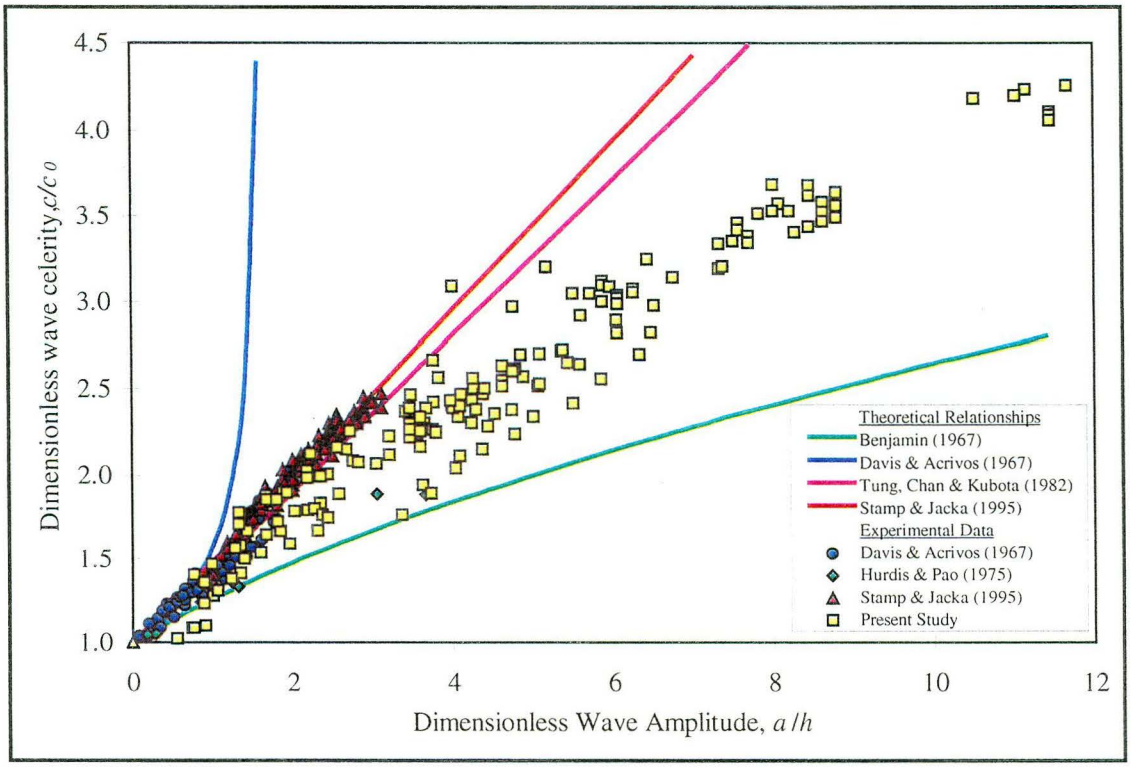

Figure 6.10 - New data applied to existing data and theoretical relationships

Data from the present study, along with data and theoretical curves from previous investigations, are shown on Figure 6.10. From this figure, it is again apparent that the relationships described by Tung, Chan & Kubota (1982) and Stamp & Jacka (1995) fit the data well for amplitudes below $a/h = 3$. However, above this limit, the linear relationship between wave celerity and amplitude appears to deviate significantly from the experimental data. This casts doubt on the validity of the application of Equation 6.12 to waves of large amplitude. A different theoretical approach to describe the celerity of waves in this range is presented in the next section.

The data presented here come from experimental runs with densimetric factors ranging from $\omega = 0.0028$ - 0.0176. A more detailed description of the present experimental data is contained in Appendix 6, with data from previous studies contained in Appendices 1-3. These figures also display error bars based on the error analysis presented in Appendix 12.

6.3.3 Analytical Solution

Previous methods of calculating the propagation celerity of the second mode internal solitary wave have been based on analytical derivations as discussed in Chapter 2. Weakly nonlinear solutions (Benjamin, 1967; Davis & Acrivos, 1967) involve the assumption of small amplitudes and long wavelengths. The fully nonlinear numerical solution of Tung, Chan & Kubota (1982) is also noted as being limited to amplitudes which are "not too large" (i.e. $|\phi|_{max}$ not >> 1) and wavelengths which are "not too short". Thus it is recognised that none of these solutions are necessarily applicable to second mode waves of large amplitude.

In this section a solution which is applicable to large amplitude waves will be developed. The large amplitude second mode wave is approximated by a stationary ellipse in a two-dimensional flow. The solution is based on two methods of calculating the flow velocity at a point on the surface of the ellipse. The first involves applying the Bernoulli equation along the ellipse's boundary, while the second makes use of a potential flow solution. Equating the two makes it possible to solve for the magnitude of a uniform flow far upstream of the stationary ellipse, which is equivalent to the velocity of the ellipse in a still fluid. Both solutions involve assumptions of two-dimensional, irrotational, inviscid and incompressible flow, with sharp density interfaces.

6.3.3.1 Bernoulli Equation Solution

In order to solve for the fluid velocity at any point on the surface, the problem is set up as shown on Figure 6.11, in which there is a moving frame of reference such that the wave appears as a static body and a uniform flow field exists at great distance. The body of the wave is also assumed to adopt an ellipsoid shape which closely approximates the shape of experimentally observed waves, and the thickness of the density interface is assumed to be small, which will presumably limit the applicability of the result of this derivation to large amplitude waves.

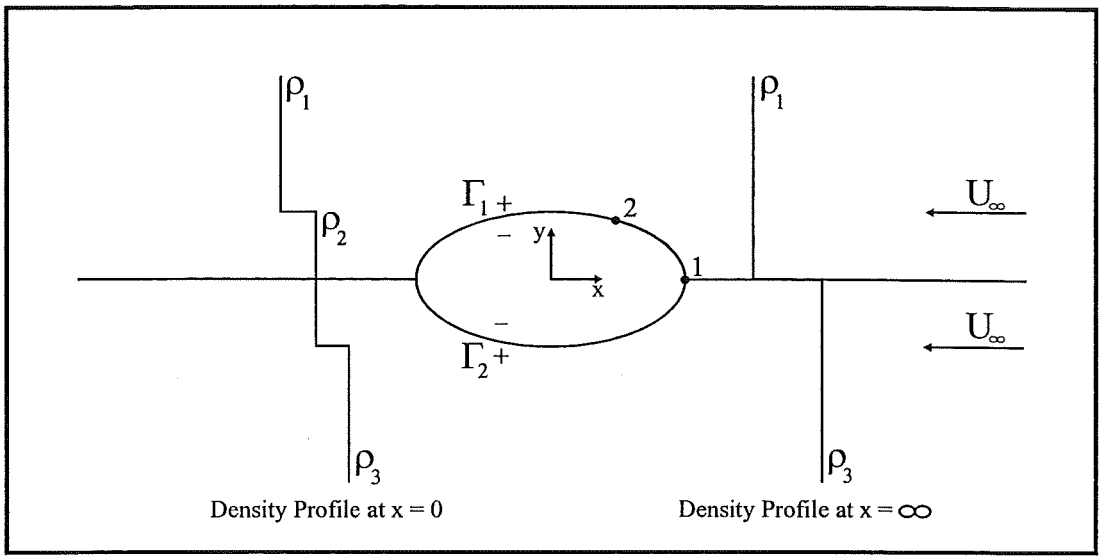

Figure 6.11 - Analytical solution density profiles, boundaries and velocities

If point 1 is assumed to be a stagnation point which lies on the elevation datum, and the Bernoulli equation is applied from point 1 to point 2, the following equation results:

$$P_1 = P_2 + \rho_1 g y_2 + \frac{1}{2}\rho_1 U_2^2 \tag{6.13}$$

An examination of the interior of the body shows, if pressure is assumed hydrostatic within the body, that:

$$P_1 = P_2 + \rho_2 g y_2 \tag{6.14}$$

Subtracting Equation 6.14 from Equation 6.13 yields the following:

$$0 = (\rho_1 - \rho_2) g y_2 + \frac{1}{2}\rho_1 U_2^2 \tag{6.15}$$

Equation 6.15 may then be rearranged to show that:

$$U_2 = \sqrt{2g' y_2} \quad \text{with} \quad g' = \frac{\rho_2 - \rho_1}{\rho_1} g \tag{6.16}$$

Since U_2/U_∞ is a unique number, the boundary condition expressed in Equation 6.16 and knowledge of the magnitude of y_2 fixes U_∞. The equation for flow velocity at the upper shoulder of the ellipse, where $(x,y) = (0,a)$ is then:

$$U_{(0,a)} = \sqrt{2g\left(\frac{\rho_2 - \rho_1}{\rho_1}\right)a} \tag{6.17}$$

Equation 6.17 will later be combined with another expression for $U_{(0,a)}$ to produce an expression for wave celerity.

On the bottom half of the ellipsoid, the boundary condition becomes:

$$U_2 = \sqrt{2g'|y_2|} \quad \text{with} \quad g' = \frac{\rho_3 - \rho_2}{\rho_3} g \quad \text{and} \quad y_2 < 0 \tag{6.18}$$

Thus the specification of the layer and wave densities should be sufficient to determine both the body geometry and U_∞. To summarise:

$$\text{On } \Gamma_1, \ \overline{U_+} \cdot \hat{n} = 0 \quad \text{and} \quad U_+ = \sqrt{2g\left(\frac{\rho_2 - \rho_1}{\rho_1}\right)y} \tag{6.19}$$

$$\text{On } \Gamma_2, \ \overline{U_+} \cdot \hat{n} = 0 \quad \text{and} \quad U_+ = \sqrt{2g\left(\frac{\rho_2 - \rho_3}{\rho_3}\right)(-y)} \tag{6.20}$$

Equations 6.19-20 indicate that flow is tangential to the ellipse at every point and the magnitude of its velocity varies with elevation and density difference. All velocities are assumed to be zero within the ellipse. The symmetry of the boundary conditions about the y-axis suggests that the flow will be symmetric about the y-axis. If the upper and lower density differences are equal, the boundary conditions are also symmetric about the x-axis and the flow will be symmetric about the x-axis.

6.3.3.2 Potential Flow Solution

The second solution for fluid velocity involves a potential flow solution. Since the flow resembles that about an ellipse, the exterior flow pattern is approximated as shown on Figure 6.12.

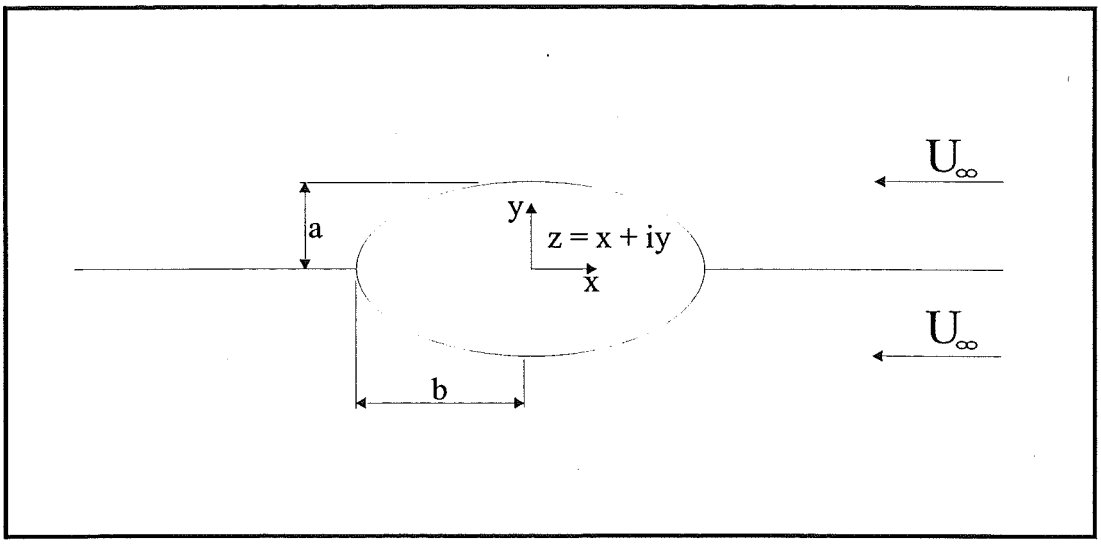

Figure 6.12 - Ellipsoid wave showing dimensional nomenclature

The flow about the ellipsoid of Figure 6.12 approximates that seen in experiments, but the hydrodynamic solution for the flow is more readily reached by first transforming the ellipse into a circle. The transformation is shown in Figure 6.13.

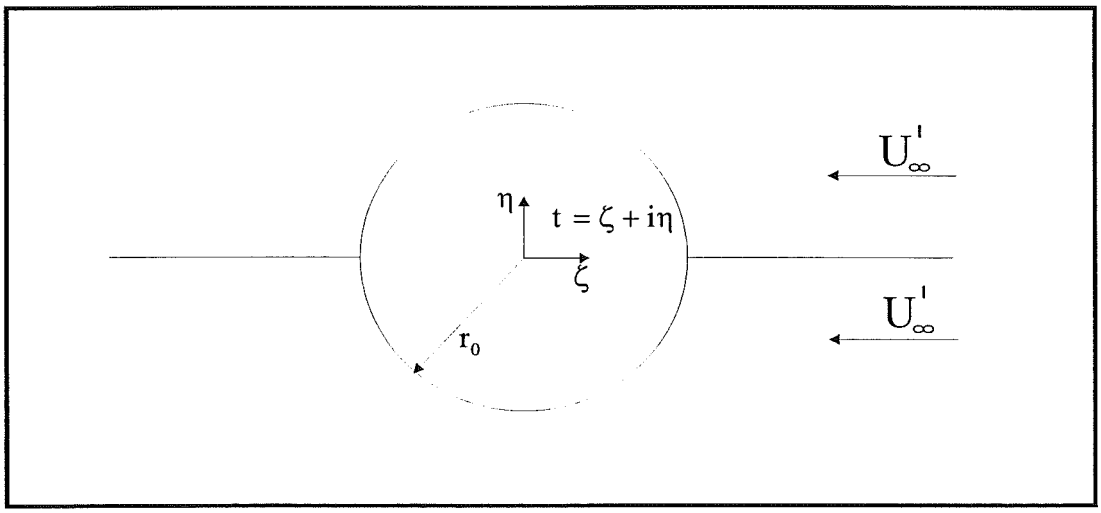

Figure 6.13 - Circular transformation of flow about an ellipse

The ellipse shown on Figure 6.12 has a semi-major axis length of b and a semi-minor axis length of a. The Cartesian coordinates (x,y) may be expressed in complex form as:

$$z = x + iy \tag{6.21}$$

In order to solve for the wave celerity, it is convenient to transform the ellipse into a circle by mapping coordinates from the z-plane to those of the t-plane shown in Figure 6.13, where:

$$t = \varsigma + i\eta \tag{6.22}$$

The transformation from the z-plane to the t-plane is performed with Equation 6.19:

$$z = t + \frac{1}{t} \tag{6.23}$$

The boundary of a circle of radius r_0 in the t-plane may also be expressed in polar coordinates as:

$$t = r_0 e^{i\theta} \tag{6.24}$$

Substituting Equation 6.24 into Equation 6.23 produces:

$$z = r_0 e^{i\theta} + \frac{1}{r_0 e^{i\theta}} = r_0 e^{i\theta} + \frac{1}{r_0} e^{-i\theta} \tag{6.25}$$

If it is recognised that $e^{i\theta} = \cos\theta + i\sin\theta$ and $e^{-i\theta} = \cos\theta - i\sin\theta$, these identities may be substituted into Equation 6.25 to yield:

$$z = r_0(\cos\theta + i\sin\theta) + \frac{1}{r_0}(\cos\theta - i\sin\theta) \tag{6.26}$$

Equation 6.26 may be separated into its real and imaginary parts as:

$$z = \left(r_0 + \frac{1}{r_0}\right)\cos\theta + i\left(r_0 - \frac{1}{r_0}\right)\sin\theta \tag{6.27}$$

Looking back to Equation 6.21, it is apparent from this that:

$$x = \left(r_0 + \frac{1}{r_0}\right)\cos\theta \tag{6.28}$$

$$y = \left(r_0 - \frac{1}{r_0}\right) \sin\theta \tag{6.29}$$

Separating the sines and cosines out of Equations 6.28 and 6.29 and substituting them into the trigonometric identity $\cos^2\theta + \sin^2\theta = 1$ yields:

$$\frac{x^2}{\left(r_0 + \frac{1}{r_0}\right)^2} + \frac{y^2}{\left(r_0 - \frac{1}{r_0}\right)^2} = 1 \tag{6.30}$$

Equation 6.30 may be recognised as an equation describing the ellipse of Figure 6.12 if:

$$a = r_0 - \frac{1}{r_0} \tag{6.31}$$

$$b = r_0 + \frac{1}{r_0} \tag{6.32}$$

Dividing Equation 6.31 by Equation 6.32 yields:

$$\frac{a}{b} = \frac{r_0 - \frac{1}{r_0}}{r_0 + \frac{1}{r_0}} = \frac{r_0^2 - 1}{r_0^2 + 1} \tag{6.33}$$

Equation 6.33 may then be rearranged to show that:

$$r_0 = \sqrt{\frac{1 + a/b}{1 - a/b}} \tag{6.34}$$

The velocity field at great distance from the ellipse of Figure 6.12 (uniform with a velocity of $-U_\infty$) may then be examined to determine the corresponding velocity field at great distance from the transformed circle of Figure 6.13. The complex potential far upstream of the ellipse may be expressed as:

$$w(z) = \phi(x,y) + i\psi(x,y) = -U_\infty z \tag{6.35}$$

Examining Equation 6.23, it is apparent that as $|t| \rightarrow \infty$, $z \rightarrow t$ and:

$$\frac{dw}{dt} = \frac{dw}{dz}\frac{dz}{dt} \rightarrow -U_\infty \tag{6.36}$$

With the transformation of the ellipse to a circle and the accompanying transformation of the velocity field at great distance, use may be made of the Milne-Thompson circle theorem (Milne-Thompson, 1968) to solve for the velocity field about the circle. The circle theorem states that if $w(t) = f(t)$ is the complex potential for 2-dimensional flow with no circle present, then the complex potential for flow about a circle of radius r_0 placed in the flow is given by:

$$w(t) = f(t) + \overline{f}\left(\frac{r_0^2}{t}\right) \tag{6.37}$$

Here $\overline{f}$ is the conjugate of the complex potential. Since in this case the imaginary part of the complex potential is zero, the complex conjugate is identical to the complex potential, and:

$$w(t) = -U_\infty t - U_\infty \frac{r_0^2}{t} \tag{6.38}$$

The complex potential in the t-plane must then be mapped back to the z-plane and differentiated to solve for fluid velocities:

$$\frac{dw}{dz} = \frac{dw}{dt}\frac{1}{dz/dt} = \left(-U_\infty + U_\infty \frac{r_0^2}{t^2}\right)\frac{1}{1 - 1/t^2} \tag{6.39}$$

Equation 6.24 may be substituted into Equation 6.39 to produce:

$$\frac{dw}{dz} = -U_\infty\left(1 - e^{-i2\theta}\right)\frac{1}{1 - \frac{1}{r_0^2}e^{-i2\theta}} \tag{6.40}$$

Into Equation 6.40 may be inserted the identity:

$$e^{-i2\theta} = \cos 2\theta - i\sin 2\theta \tag{6.41}$$

This yields the following equation:

$$\frac{dw}{dz} = u + iv = -U_\infty \left(1 - (\cos 2\theta - i\sin 2\theta)\right) \frac{1}{1 - \frac{1}{r_0^2}(\cos 2\theta - i\sin 2\theta)} \tag{6.42}$$

The following substitutions are then made to Equation 6.42 and it is separated into its real and imaginary parts by the following method:

$$\begin{aligned} Let \quad & A = (1 - \cos 2\theta); & B &= \sin 2\theta; \\ & C = 1 - \frac{1}{r_0^2}\cos 2\theta; & D &= \frac{1}{r_0^2}\sin 2\theta \end{aligned} \tag{6.43}$$

$$u + iv = \left[-U_\infty A - iU_\infty B\right] \frac{1}{C + iD} \tag{6.44}$$

$$u + iv = \left[-U_\infty A - iU_\infty B\right] \frac{C - iD}{C^2 + D^2} \tag{6.45}$$

$$u + iv = \frac{-U_\infty}{C^2 + D^2}(AC + BD) + \frac{iU_\infty}{C^2 + D^2}(-BC + AD) \tag{6.46}$$

The magnitude of the fluid velocity may then be calculated:

$$|U| = \left(u^2 + v^2\right)^{1/2} = \frac{U_\infty}{C^2 + D^2}\left((AC + BD)^2 + (-BC + AD)^2\right)^{1/2} \tag{6.47}$$

So, the fluid velocity at any point on the surface of the ellipse may be expressed as a function of the upstream uniform velocity:

$$U = \gamma U_\infty \quad \text{where} \quad \gamma = \frac{\left((AC + BD)^2 + (-BC + AD)^2\right)^{1/2}}{C^2 + D^2} \tag{6.48}$$

This expression will later be combined with Equation 6.18 to produce an expression for second mode wave celerity.

As a partial check on the validity of this solution, it can be shown that Equation 6.48 yields the proper solution for the limiting cases where $a \rightarrow 0 \left(u \rightarrow U_\infty\right)$ and $a \rightarrow b \left(u \rightarrow 2U_\infty\right)$.

6.3.3.3 *Wave Celerity Solution*

At this point, the RHS of Equation 6.17 may be equated to the RHS Equation 6.48 to produce:

$$\sqrt{2g\frac{\rho_2-\rho_1}{\rho_1}\varepsilon a} = \gamma U_\infty \tag{6.49}$$

On the LHS of Equation 6.49, the factor ε is equal to sinθ and has been added to convert the circular transformation back to physical coordinates. Rearranging Equation 6.49, recognising that the density factor on the LHS of the equation is approximately equal to the densimetric factor, ω, and the uniform velocity at great distance, U_∞, is equal to the wave celerity, c, yields the following expression for wave celerity:

$$c=\frac{1}{\gamma}\sqrt{2g\omega\varepsilon a} \tag{6.50}$$

Introducing the interfacial half-thickness, h, to this equation yields:

$$c=\frac{1}{\gamma}\sqrt{\frac{g\omega h}{2}}\sqrt{\frac{4\varepsilon a}{h}} \tag{6.51}$$

The first radical in this expression can be recognised as being equal to the infinitesimal solitary wave celerity, c_0, so that Equation 6.51 may be rearranged to show:

$$\frac{c}{c_0}=\frac{2\sqrt{\varepsilon}}{\gamma}\sqrt{\frac{a}{h}} \tag{6.52}$$

The value of the wave amplitude coefficient on the RHS of Equation 6.52 varies depending on the point on the surface of the ellipse at which it is calculated. Figure 6.14 displays the variation of this coefficient with position. Discounting values calculated near the nose of the ellipse (where the hydrostatic pressure assumption is least acceptable), a mean value of 1.33 for the coefficient is calculated.

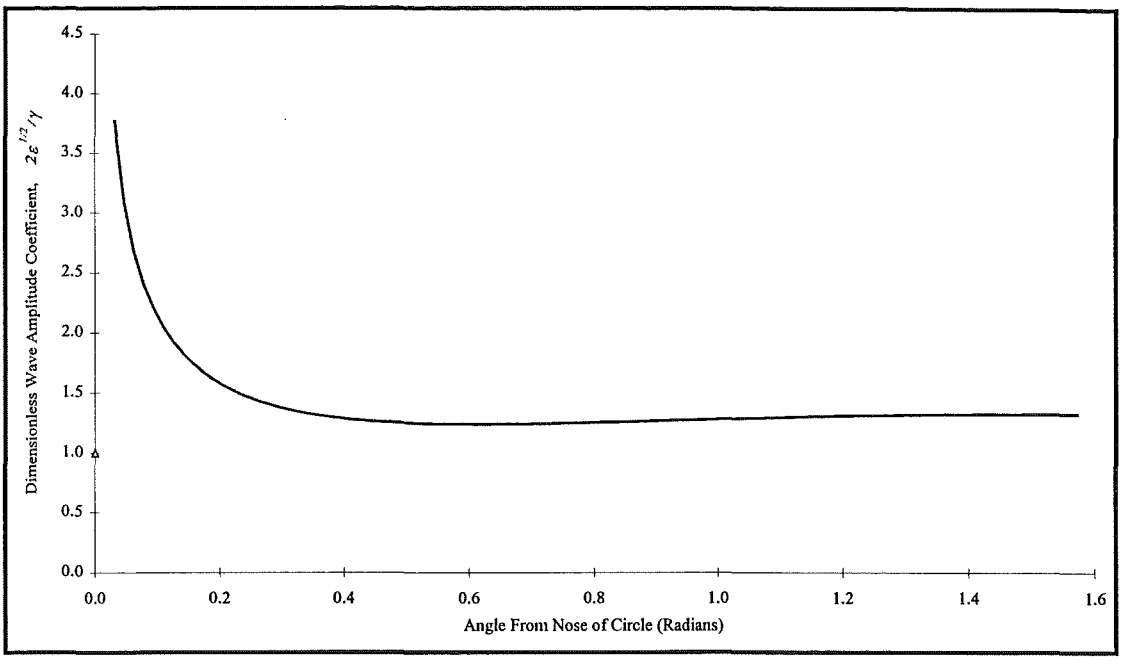

Figure 6.14 – Calculation of dimensionless wave amplitude coefficient

This allows Equation 6.52 to be restated as:

$$\frac{c}{c_0} = \frac{4}{3}\sqrt{\frac{a}{h}} \tag{6.53}$$

The curve plotted by this equation is shown on Figure 6.15, where it may be compared to the experimental data and theoretical equations previously presented on Figure 6.10.

The theoretical relationship resulting from the preceding analysis appears to provide a good fit to the experimental data for large amplitude waves. It also appears to provide a good agreement with both the experimental data and the relation of Stamp & Jacka (1995) over the lower range of amplitudes, down to a value of approximately $a/h = 1$. This is despite the assumption of a small ($a >> h$) density interface in the analysis. It is recommended that Equation 6.53 not be applied to waves of amplitude below $a/h = 1$, but above this, and particularly above $a/h = 3$, this relationship appears to provide the most reliable estimate of wave celerity. The fact that most data points fall on or below the theoretical curve may indicate that the wave celerity is slightly overestimated by the theoretical relationship of Equation 6.53.

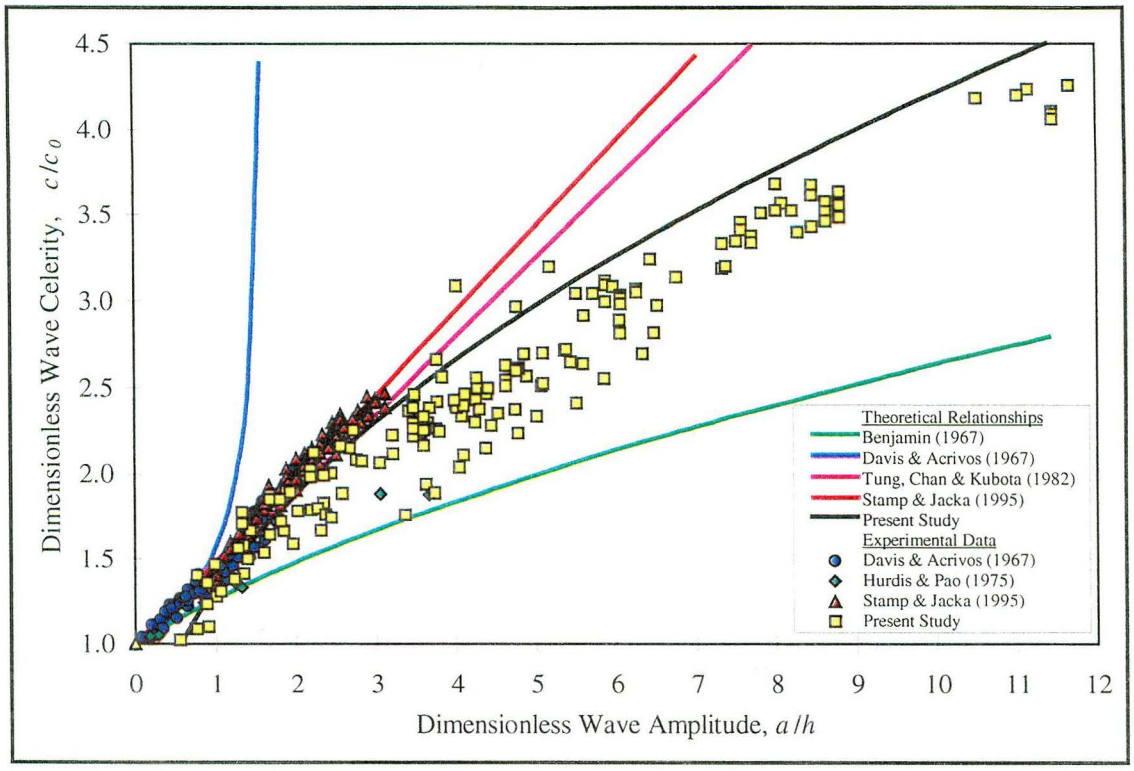

Figure 6.15 - New theory with previous data and theoretical relationships

In examining possible sources of error which may have contributed to the scatter of the experimental data, it is difficult to identify any single cause. The values of a, c, h and ω influence the position of data points, and the measurement of these parameters was quite straightforward. The presence of grossly incorrect density values is unlikely due to the checks made during mixing and measurement procedures, and it has been noted that neither the presence of dye or particles significantly altered the fluid density. Also, the theoretical curve of Figure 6.15 is relatively insensitive to all but very gross errors in the values of h and ω. Though all waves examined were classed as deep-water ($H/h > 40$) by the criterion of Tung, Chan & Kubota (1995), the large amplitude waves (a/h up to 11.6) examined may have been influenced by the finite depth of the fluid. In fact, values of H/a fall as low as 7 in some instances, and this may account for the tendency of data points to fall below the theoretical curve (i.e. travel slower than predicted).

6.4 Conclusions

The external flow of the second mode wave is described by its shape and celerity. Previous studies have confirmed the existence of two types of second mode wave. In small amplitude waves, the wave travels faster than any individual fluid particle, with the flow resembling the superposition of a wave of elevation and a wave of depression. Large amplitude waves, which exist for amplitudes above $a/h = 1.2$, contain what has been described as a 'closed streamline' region in which fluid is carried along with the wave at its propagation celerity.

Weakly nonlinear models of the wave predict that small amplitude waves will experience decreases in wavelength as they increase in amplitude. However, numerical models, as well as experimental observations, show that when waves become large, the wavelength necessarily increases to allow the expansion of the interior region of the wave. The experiments of Stamp & Jacka (1995) confirm a linear relationship between amplitude and wavelength for large amplitude waves. With minor changes to this equation, the range of applicability of this linear relationship has been extended from $a/h = 3.1$ to 11.6.

Previous analytic and numerical models have expressed wave celerity (c/c_0) as a function of amplitude (a/h). The initial, weakly nonlinear analyses of Benjamin (1967) and Davis & Acrivos (1967) fit the experimental data well for small amplitude waves, but rapidly diverge for larger amplitudes. The more recent models of Tung, Chan & Kubota (1982) and Stamp & Jacka (1995) match the data well for amplitudes up to $a/h = 3.1$. The present study examined waves of amplitudes up to $a/h = 11.6$, and thus provided the opportunity to examine the validity of these latter models for larger amplitude waves. These theories did not match the new experimental data well for amplitudes above $a/h = 3$.

A new solution for wave celerity, based on energy methods and the assumption of two-dimensional, irrotational, inviscid and incompressible flow, with a sharp density interface, produced a solution which also expressed wave celerity as a function of amplitude. This solution was expected to provide a valid solution for very large amplitude waves, and did in fact fit the experimental data well in this

region. Happily, it also matched the experimental data for amplitudes down to $a/h = 1$.

7.0 Results - Wave Propagation: Internal Flow

Numerical models of the second mode internal wave (Davis and Acrivos, 1967) (Tung, Chan and Kubota, 1982) have described a mass of fluid with closed streamlines, yet experimental studies (Maxworthy, 1980) (Stamp and Jacka, 1995) have noted both an uptake of external fluid to and an expulsion of internal fluid from the wave. This points to the significant cross-streamline movement of fluid and some sort of circulation pattern within the wave. Thus, in examining the internal motion of the wave, there are several issues which must be addressed. The first is the pattern of circulation within the wave and the comparison of experimental observations to established theoretical solutions. The second is the question of entrainment of external fluid into the wave and the mechanism by which it is achieved, and the third, an examination of the capacity of the wave for mass transport.

7.1 Internal Circulation

Numerical models of second mode waves have in past studies been compared with experimental observations, with a favourable agreement noted in most cases. However, detailed measurements of the wave during its development, from a collapse and beyond, point to a more complex structure than has been previously described.

7.1.1 Background

Both Davis and Acrivos (1967) and Tung, Chan and Kubota (1982) developed numerical models of the second mode wave and presented plots of streamlines with a moving frame of reference. This streamline pattern is shown on Figure 7.1. This figure shows a mass of fluid surrounded by closed streamlines, within which there are two counter-rotating cells located above and below the line of symmetry. Flow along the line of symmetry within the closed streamline region is directed forwards, towards a stagnation point at the nose of the wave. Observations of the external flow about the wave would seem to support this description of its internal structure.

It would appear to make sense that the rearward shear exerted on the wave by the external flow would result in a rearward flow in the outer portions of the wave, and that continuity would require that flow along the middle of the wave proceed forwards towards the stagnation point at its nose.

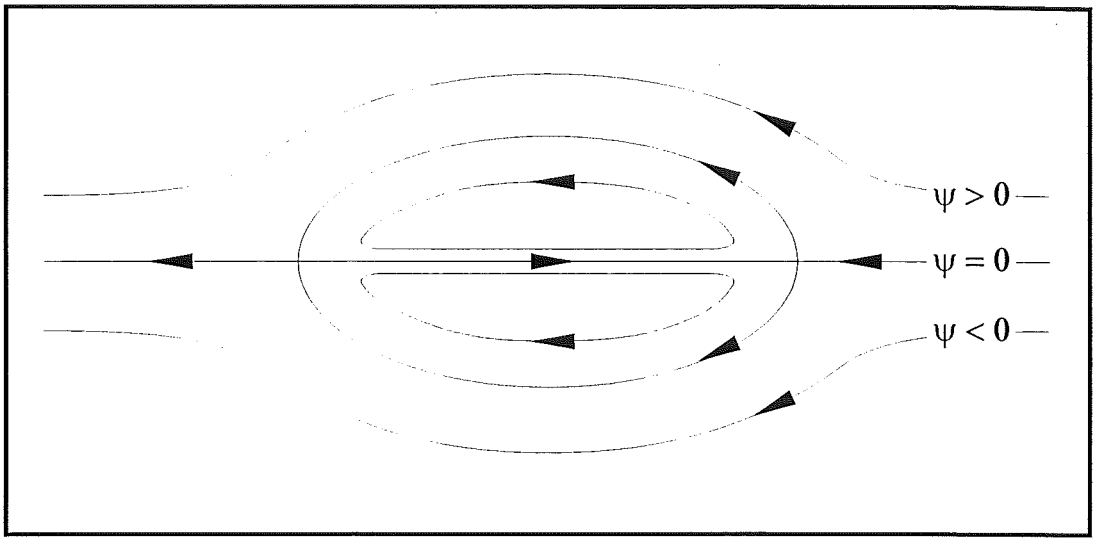

Figure 7.1 - Theoretical streamlines presented by Tung, Chan & Kubota (1982)

The observations of Maxworthy (1980) and Stamp and Jacka (1995) provided the first clues that this description of the internal structure of the wave is not wholly accurate. Waves in the former study were generated by the collapse of a mixed region of fluid into which dye had been introduced, and it was observed that as the wave travelled this dye moved into two elliptically shaped regions placed symmetrically about its centreline. Furthermore, thin sheets of dye were seen to be continuously ejected from the rear of the wave, pointing to flow across the streamlines in this region. Maxworthy attributed the gradual loss of wave amplitude to this loss of fluid, and no mention was made of any entrainment of fluid into the wave. Stamp and Jacka generated waves by the impulsive movement of a paddle in the interfacial region, and used both miscible and immiscible dyes to visualise the flow. Along the open streamlines of Figure 7.1, observations described the "flow [as] laminar and the fluid stratified" but within closed streamlines "the flow was turbulent and the fluid well-mixed". Upper and lower recirculating cells, as described by the numerical solutions, were also recognised, though it was noted that there was no defined boundary between the cells and fluid was continuously

entrained into and ejected from this area. It was noted that the entrainment appeared to be distributed evenly along the boundary of these cells, and that turbulent mixing was indicated by the rapid spread of dye throughout the region. Stamp and Jacka note that this boundary would thus be more accurately represented as an "intermittency surface" (Townsend, 1976). It was also observed that turbulent shear instabilities in the lee of the wave occasionally resulted in the entrainment of fluid in that region, with entrained dye droplets being carried for a short time before being ejected from the wave.

7.1.2 Observations of Wave Development

Detailed observations made during the course of this study have shed more light on circulation within the wave. In presenting these observations, it might be helpful to first examine the changing characteristics of this internal circulation as an intrusion develops into a fully-fledged second mode internal wave. Figure 7.2 shows four streakline images which show the wave at various points in its development. This wave, from run 61030PC030, was formed by the collapse of a 100 mm thick, 410 mm long body of intermediate density fluid into a 600 mm deep stratified ambient fluid with an interfacial half-thickness, h, of 28.9 mm, and a densimetric factor, ω, of 0.0106.

Figure 7.2a shows the head of an intrusion 8 seconds and 0.36 m (x/h = 12) after the release of the gate allowed the collapse of the intermediate density fluid. At this point the flow resembles a starting jet, with strong forward motion of intrusive fluid along the centreline and two counter-rotating vortices located above and below the centreline of the intrusion. The direction of vortex rotation at this point agrees with that shown in Figure 7.1. A stagnation point is clearly visible at the nose of the intrusion, and there is evidence of Kelvin-Helmholtz shear instability in the upper portion of the lee of its head. At this point the intrusion has a velocity of 59 mm/s and an amplitude (from centreline to maximum head height) of 43 mm.

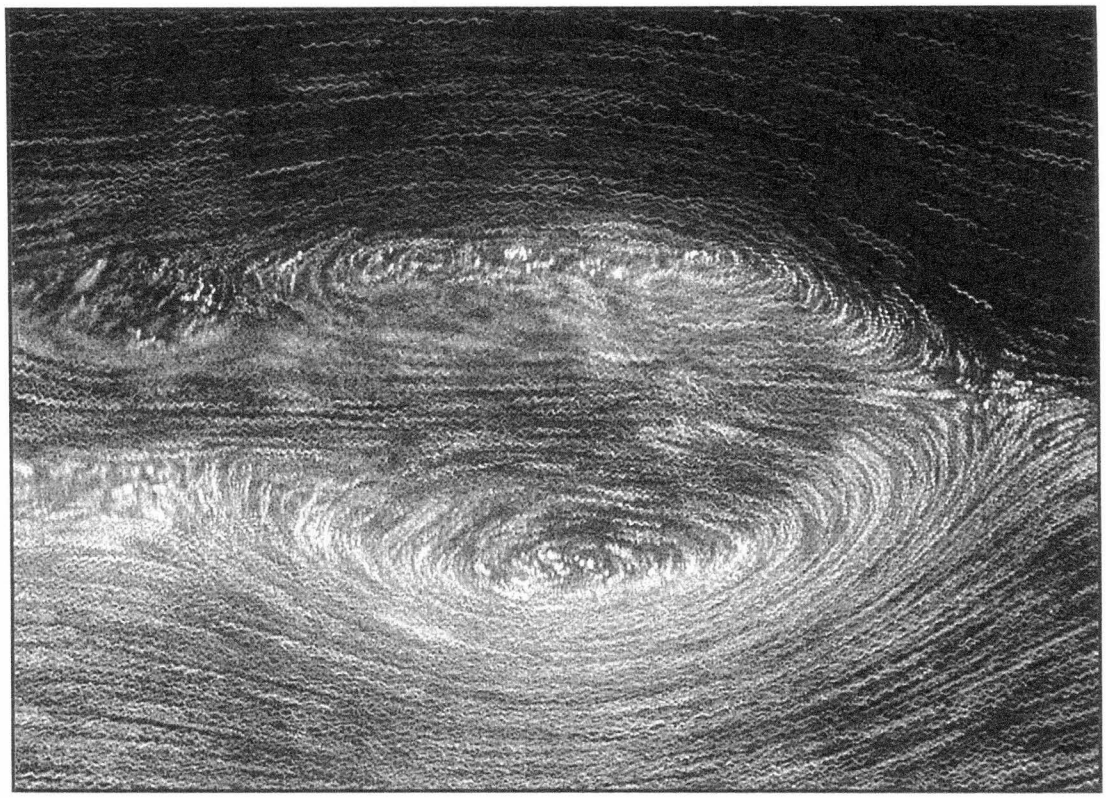

Figure 7.2a - Streakline image of developing wave t = 8 s, x = 0.36 m, x/h = 12

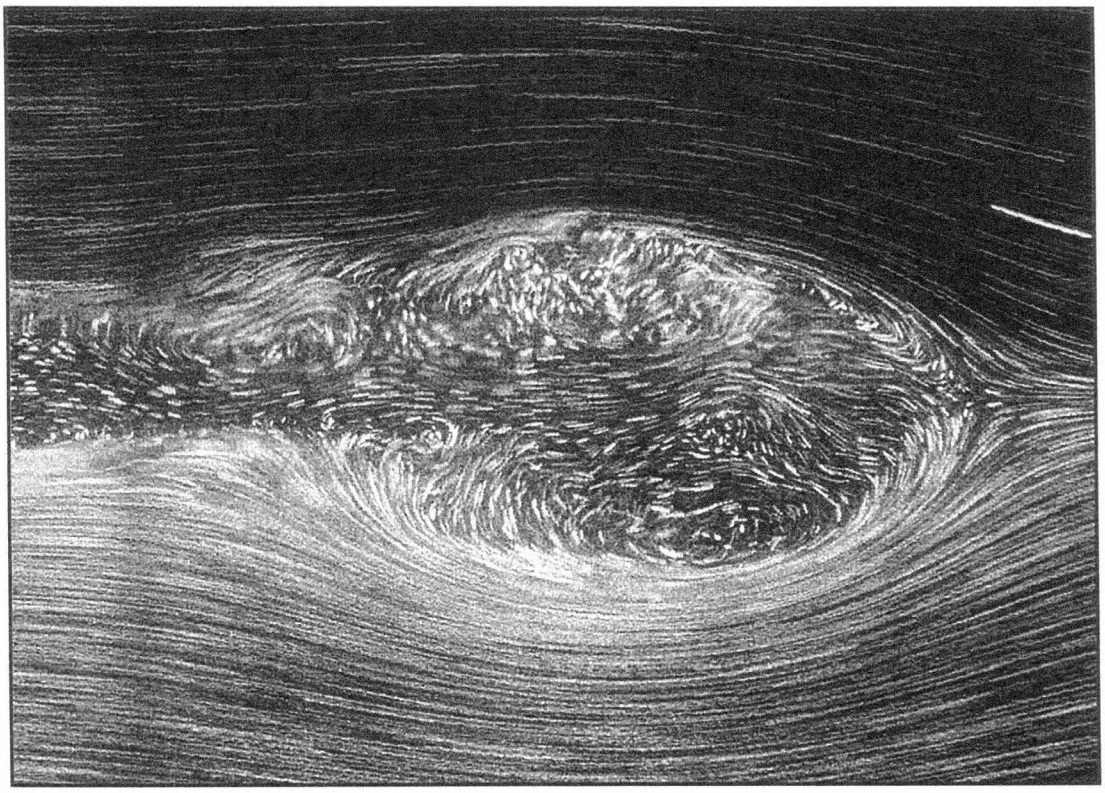

Figure 7.2b - Streakline image of developing wave t = 10 s, x = 0.47 m, x/h = 16

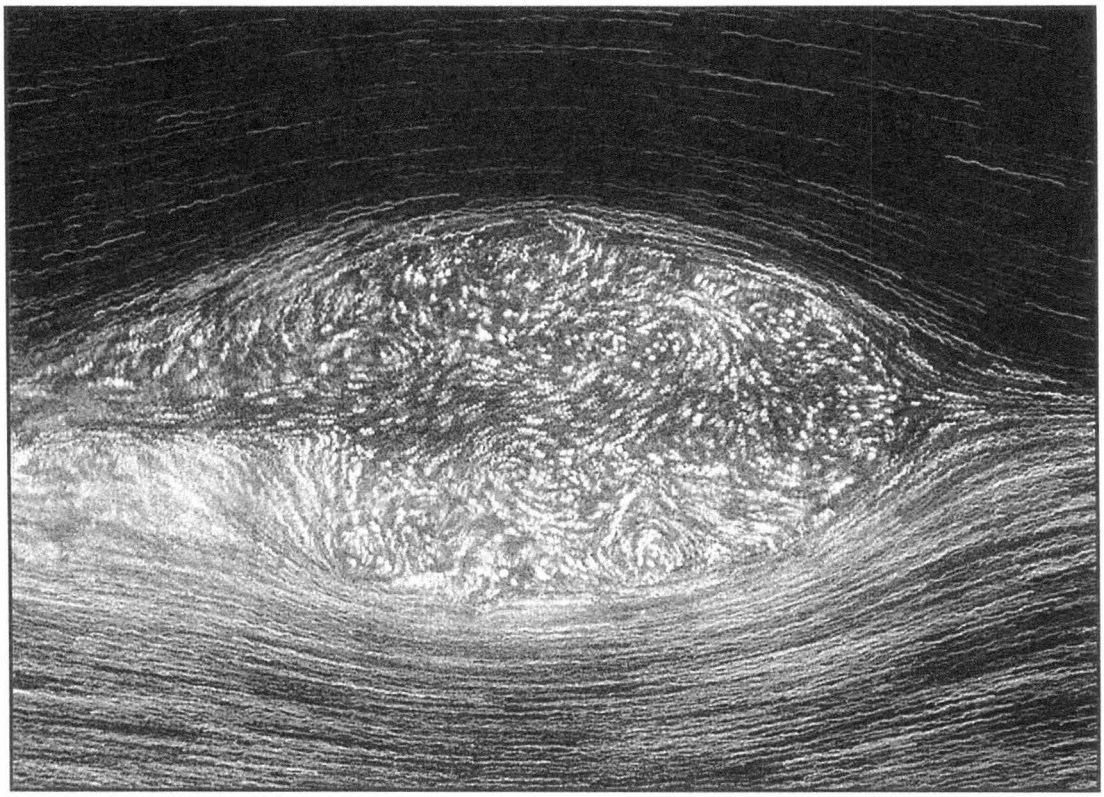

Figure 7.2c - Streakline image of developing wave t = 20 s, x = 1.05 m, x/h = 36

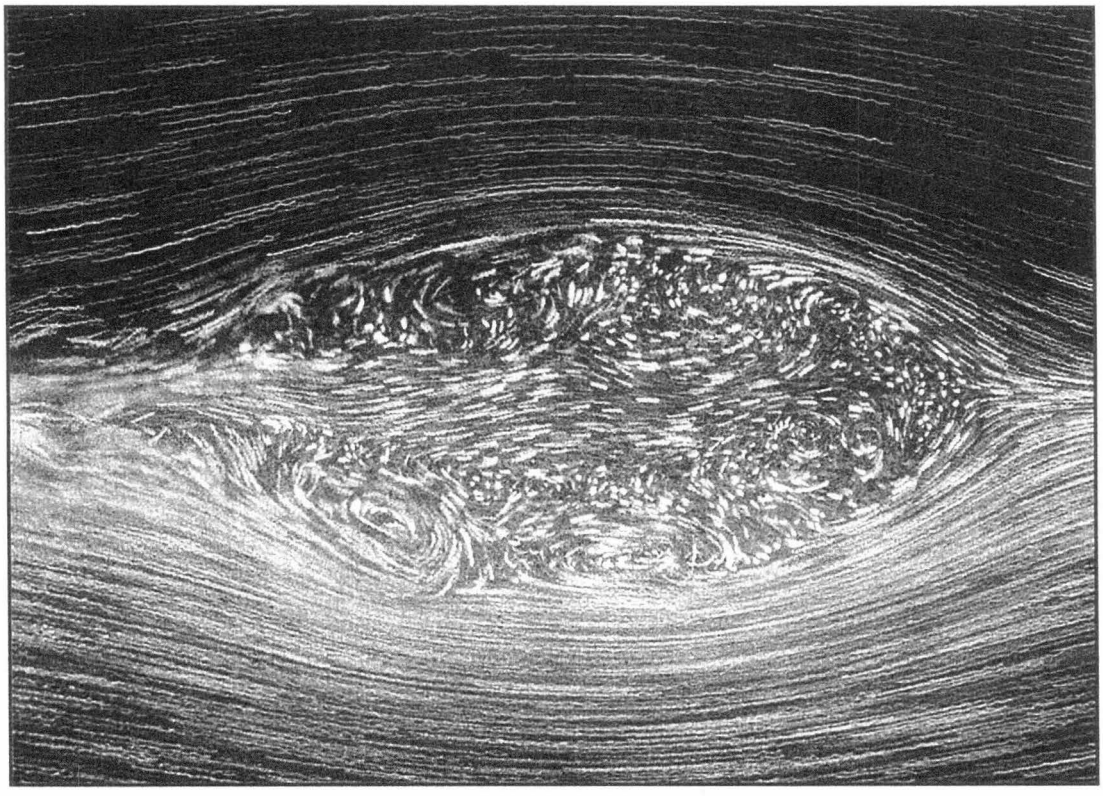

Figure 7.2d - Streakline image of developing wave t = 34 s, x = 1.84 m, x/h = 64

Two seconds and 0.11 m later ($x/h = 16$), Figure 7.2b shows significant pinching off of the intrusion head. Flow forwards along the centreline of the wave has diminished and the strength of the upper and lower vortices has dropped considerably. These observations point to a reduction in the velocity of the intrusion behind its head, though the head has maintained its amplitude and velocity. The stagnation point at the nose of the intrusion is still visible, and it appears that the vortex in the lee of the wave has increased somewhat in strength.

Figure 7.2c shows what may now be called a wave, as it is fully pinched off from the following current, after it has travelled for a further 10 seconds and 0.58 metres ($x/h = 36$). The stagnation point at the nose remains visible, and the smearing of the streaklines in the lee of the wave points to turbulent mixing in that region. No strong flows are apparent within the wave, though it appears that several weak vortices may be forming within. At this point the wave has virtually maintained its original amplitude and velocity, with these values dropping slightly to 42 mm and 58 mm/s, respectively.

The fully developed wave, which had travelled a further 14 seconds and 0.79 metres, for a total of 34 seconds and 1.84 metres ($x/h = 64$), is shown on Figure 7.2d. The wave at this point had maintained its previous amplitude and velocity, and now exhibited a regular internal velocity structure. Several small vortices are visible on either side of the centreline of the wave, with the outer ones appearing to be driven by the external shear flow, and the inner ones by the outer ones. These vortices transport fluid forward in the wave, not at the level of the centreline as predicted by the numerical model, but closer to the wave boundary. This forward flow is then balanced by a rearward flow along the centreline, from which fluid is ejected from the wave. Evidence of turbulent mixing in the form of smeared streaklines is still apparent in the lee of the wave.

7.1.1 Observations of Developed Wave

The preceding observations point to significant differences between the circulation described by the numerical models of Davis and Acrivos (1967) and Tung, Chan

and Kubota (1982) and the actual physical behaviour of the wave. Instead of one vortex following the closed streamline pattern as shown on Figure 7.1, it appears that several smaller vortices exist in this region. Vortices near the boundary of the wave are driven by the external flow, and these in turn drive vortices closer to the centreline of the wave. The result is a net forward flow within the wave in the region midway between the wave boundary and its centreline, with a relatively strong rearward flow (in this case equal to slightly less than 25% of the wave celerity) along the centreline of the wave. This circulation is illustrated once again in Figure 7.3, which shows a streakline image of another fully developed wave. This wave, from run 61031PC050, was generated in a similar fashion to that of Figure 7.2, but the ambient had an interfacial half-thickness, h, of 20.0 mm and a densimetric factor, ω, of 0.0172. This resulted in a faster wave, which exhibited an amplitude of 39 mm and a velocity of 74 mm/s at the time the image was acquired.

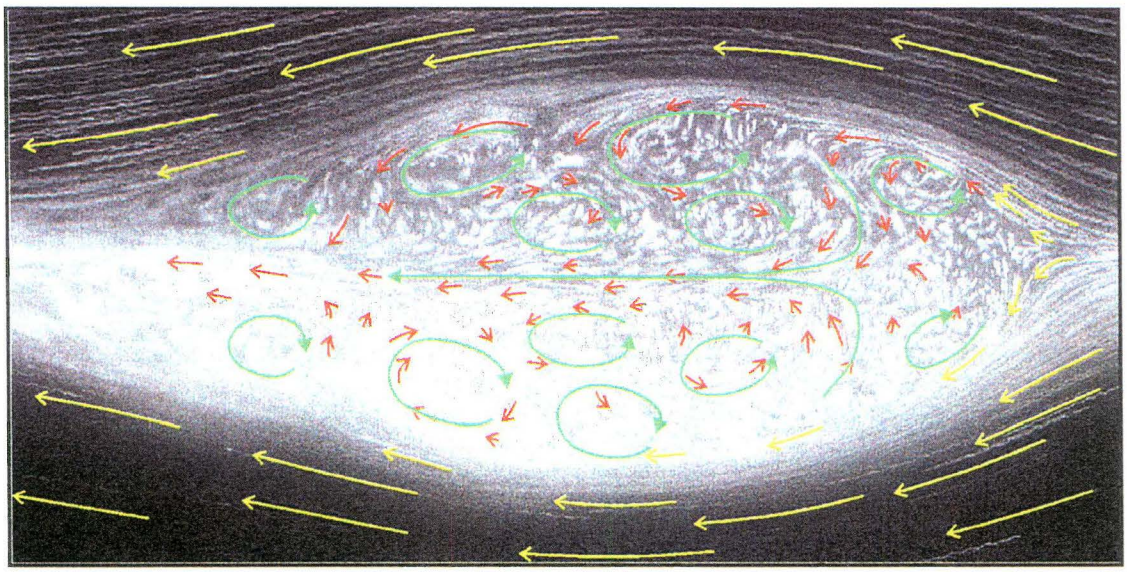

Figure 7.3 - Streakline image of fully developed wave

On Figure 7.3, selected streaklines from the external flow are highlighted in yellow, while selected internal flow streaklines are shown in red. These should provide some description of both the magnitude and direction of flow. Green flow lines have been added to clarify the location of vortices and to highlight the rearward flow in the wave. Highlighted streaklines were placed by examining the enlarged graphic image in conjunction with recorded video footage of the flow.

It should be noted that the wake of the wave is the only place where turbulent mixing is observed. This is in conflict with the conclusion of Stamp & Jacka (1995) that "the rapid spread of dye through the [upper and lower recirculating] cells was indicative of turbulent mixing." Similar circulation patterns are observed in the vortex street present in the wake of a cylinder. In a description of the vortex street, Tritton (1988) notes that the counter-rotating vortices produced are not turbulent, as the term turbulence "implies the existence of highly irregular rapid velocity fluctuations." Additionally, Tennekes & Lumley (1972) state that "turbulence is rotational and three-dimensional... the random vorticity fluctuations that characterise turbulence could not maintain themselves if the velocity fluctuations were two-dimensional."

The circulation within the wave was observed to be predominantly two-dimensional, with particles staying within the light sheet for many wavelengths. In a flow with a significant three-dimensional component, particles would be expected to move in and out of the light sheet. These observations are in accord with previous studies which described the flow as "extremely two-dimensional with no noticeable velocity parallel to the wavefront" (Davis & Acrivos, 1967) and noted that "waves were aligned straight across the channel... and there were no noticeable motions along the wavefront" (Stamp & Jacka, 1980). With the experimental techniques of this study, it was not possible to investigate the observation of Maxworthy that long wavefronts adopted a cellular structure. It is possible that such a structure could form due to secondary flows caused by the flume walls, in a similar fashion to those which exist in open channel flows. Investigation of this phenomenon will be left to future studies.

7.1.2 Conclusions

It is readily apparent from Figures 7.2d and 7.3 that the internal velocity structure of a large amplitude second mode wave is more complex than that described by existing numerical models. It has been shown that the assemblage of vortices inside the wave appear to be driven by the external flow and quite clearly produce a net flow out of the wave on its centreline. However, in the wave shown in Figure 7.2, it

was shown that as it propagated, only a small loss in amplitude was observed, despite the ejection of fluid from the wave. Therefore, it seems that fluid must be somehow taken into the wave to offset this outflow. This issue will be examined further in the next section.

7.2 Fluid Entrainment

The incorporation of external fluid into second mode waves is something which has been recognised only recently. The small waves which have been studied in the past have made it difficult to make detailed observations of this motion, but the visualisation techniques used here have shed further light on the mechanism by which fluid is taken up into the wave.

7.2.1 Background

The first observations of entrainment into the second mode wave were in Stamp and Jacka (1995), where it was noted that the internal structure of the wave was similar to that detailed in Figure 7.1, and that external fluid was entrained into the two counter-rotating cells evenly along their outer boundaries, and that once inside was mixed in a turbulent fashion before being expelled from the wave. For this reason it was noted that the closed streamlines of Figure 7.1 would be more properly termed an "intermittency surface", though the closed streamline nomenclature was maintained due to historical precedent and to avoid confusion.

Observations of the internal structure of the wave in Section 7.1 indicate that the circulation described by Figure 7.1 is not an accurate representation of this structure, and this in turn raises the question of whether the entrainment observations of Stamp and Jacka (1995) are entirely accurate.

7.2.2 Observations of Entrainment

The images of Figure 7.4 help clarify the path by which fluid is entrained into a second mode wave. These images show a wave approaching three separate bodies

of neutrally buoyant, miscible dyed fluid which had been placed in the interfacial region during the setup of the experiment.

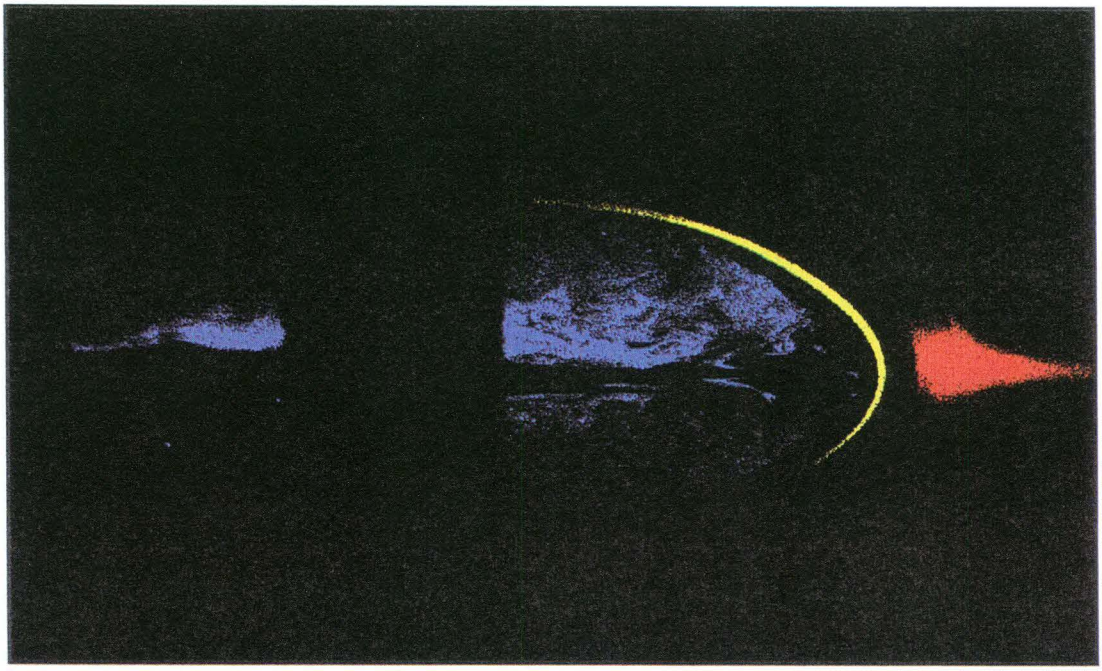

Figure 7.4a - Colour enhanced image of wave at t = 40 s, x = 2.37 m, x/h = 95

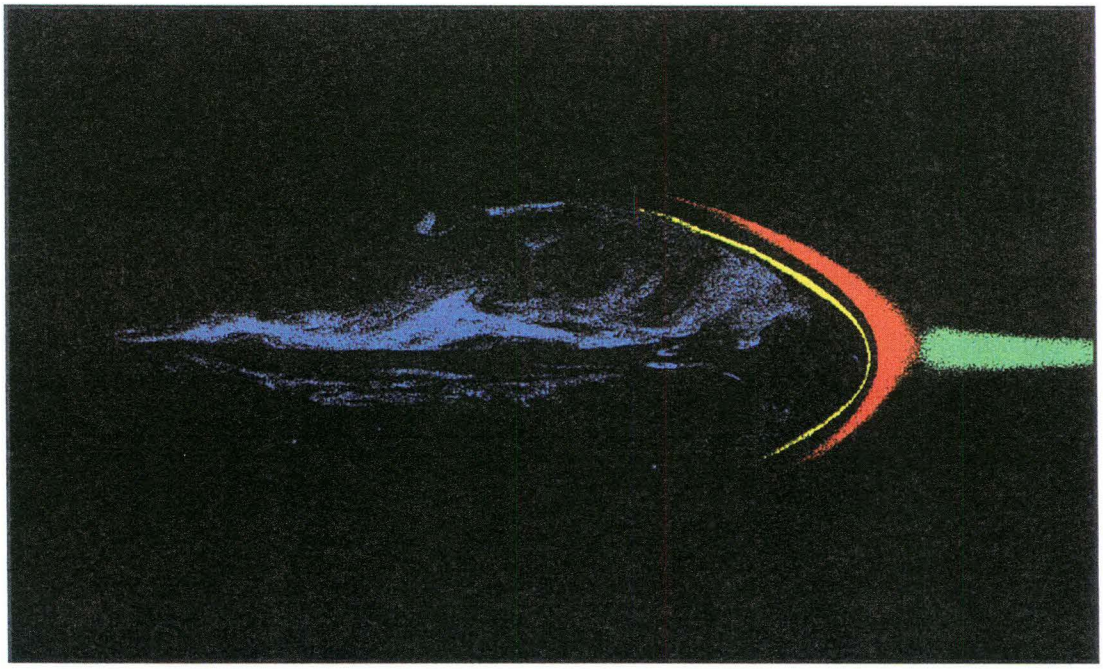

Figure 7.4b - Colour enhanced image of wave at t = 42 s, x = 2.49 m, x/h = 100

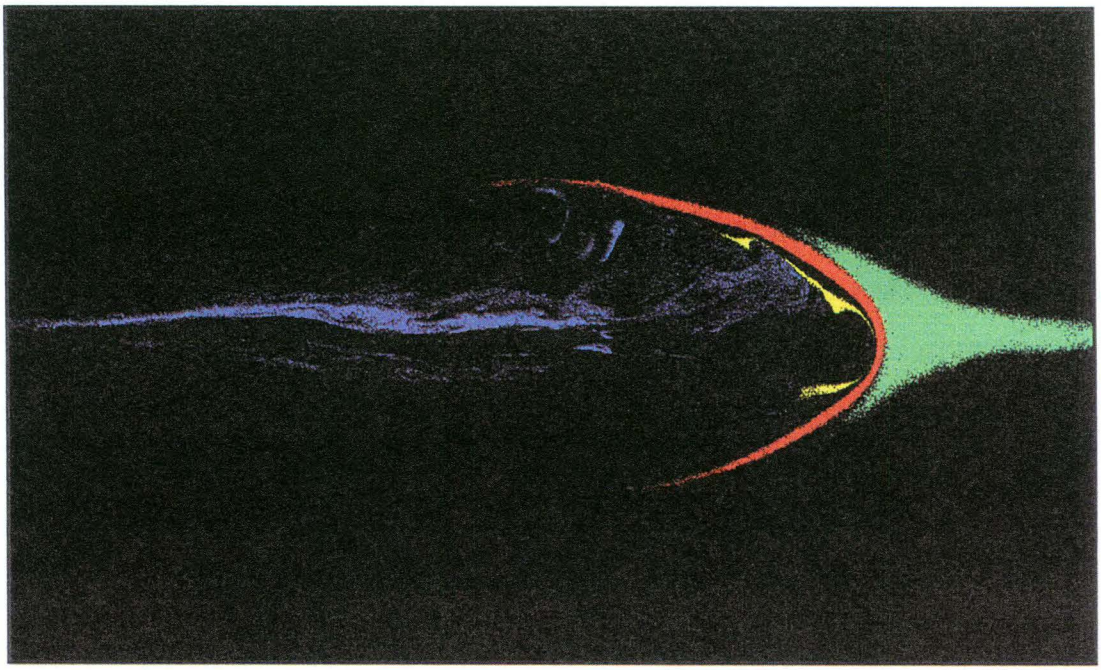

Figure 7.4c - Colour enhanced image of wave at t = 44 s, x = 2.61 m, x/h = 105

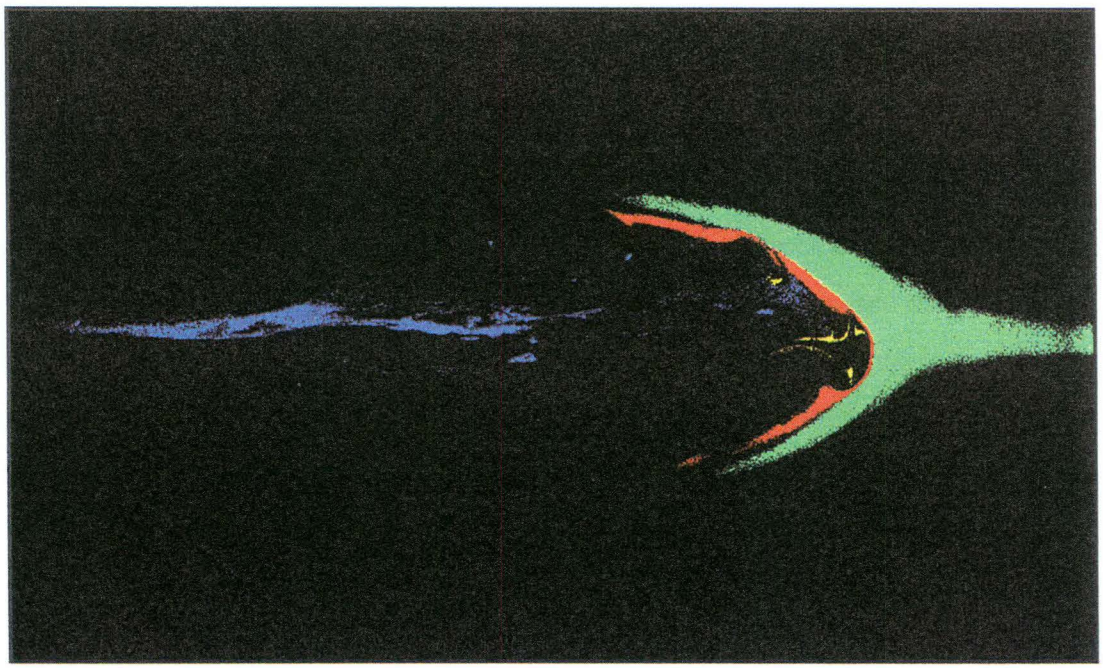

Figure 7.4d - Colour enhanced image of wave at t = 46 s, x = 2.73 m, x/h = 105

These images were scanned from black and white photographic negatives, filtered for intensity threshold and contrast, and manually colour-enhanced to highlight the separate dyed regions. Areas of low intensity, corresponding to low dye concentrations, are without colour, so the reader may note that conservation of mass may appear to be violated, as the concentration of a mixture of dyed and undyed fluid may not have fluoresced at a sufficiently high intensity to exceed the filter threshold. The wave in these images, from run 61025DC030, was generated by the collapse of a 150 mm thick region of intermediate density fluid into a 600 mm deep ambient with an interfacial half-thickness, h, of 24.9 mm and a densimetric factor, ω, of 0.0110. Dye remaining in the wave since its generation is coloured purple, with two small regions of interfacial dye coloured yellow and red and a larger one coloured green. These will be referred to as red, yellow, purple and green dye, though it must be recognised that in the experiment all the dye was Rhodamine 6G and therefore simply appeared yellow when fluorescing.

Figure 7.4a shows the wave emerging from behind one of the tank supports after travelling for 40 seconds and 2.37 metres (x/h = 95) from release. Two dilute lobes of original dyed fluid are evident within the wave, with little or no dye present on the outer boundaries of the wave or along its centreline. The region of yellow dye was the first to be encountered, and it has been stretched along the outer boundary of the wave. Thickening of the red dyed area is apparently due to the influence of the approaching wave.

In Figure 7.4b, two seconds and 0.12 metres (x/h = 100) further on, more stretching of the yellow region is evident, and its thickness appears to be less regular than in the previous image. The first sign of what resembles a cusping of this line of fluid is apparent. The red-dyed region has begun to stretch about the body of the wave in the same fashion as the yellow had done, and first notice is made of the third, larger body of dye. The concentration of purple dye in the wave has dropped considerably, with most of the drop occurring along the outer middle portion of the wave.

After a further two seconds and 0.12 metres (x/h = 105), a radical change in the distribution of the yellow dye is seen. In Figure 7.4c, the dyed region appears to thicken and be drawn into the wave at some locations, while at others it is stretched thinner and stays on the outer perimeter of the wave. The red dye is showing the first signs of this distortion, while the green has begun to thicken and envelop the nose of the wave. The concentration of original purple dye has now dropped even further.

Figure 7.4d (x/h = 110) shows that the purple dye concentration has dropped further still as internal fluid is flushed from the wave. Yellow dye has entered the wave at discrete intervals, not evenly along the surface of the wave, and the red dye has followed in a similar fashion. It should be noted that dye has not appeared to enter at the nose of the wave where a stagnation point has previously been identified, but at this point the line of dye has thinned and entered the wave at points above and below the nose. The large region of green dye has enveloped the front portion of the wave and the irregularity of its interior region indicates that it too was being entrained into the wave.

The image sequence of Figure 7.5 shows the same wave as Figure 7.4, with different image processing. Lower brightness threshold and contrast values have been applied, and no colour enhancements have been introduced, though the dyed region highlighted in green on Figure 7.4 has been artificially removed to focus attention on the behaviour of the two smaller dye masses. These images were acquired from videotape and are spaced at roughly 1/4 second intervals.

The entrainment of fluid into the wave is further illustrated in Figure 7.6. This figure is identical to Figure 7.3, but regions of inflow to the wave are highlighted with blue arrows. It appears that fluid is entrained at the lee side of the exterior vortices within the wave. The entrainment appears to be strongest near the front of the wave, as evidenced by both the dye images of Figure 7.4-5 and the streakline image of Figure 7.6. The former figure also indicates entrainment immediately adjacent to the nose, both above and below. This entrainment may in fact be occurring in the wave shown in Figure 7.6, but due to the strength and resolution of the streaklines it is not possible to make a positive judgment on this.

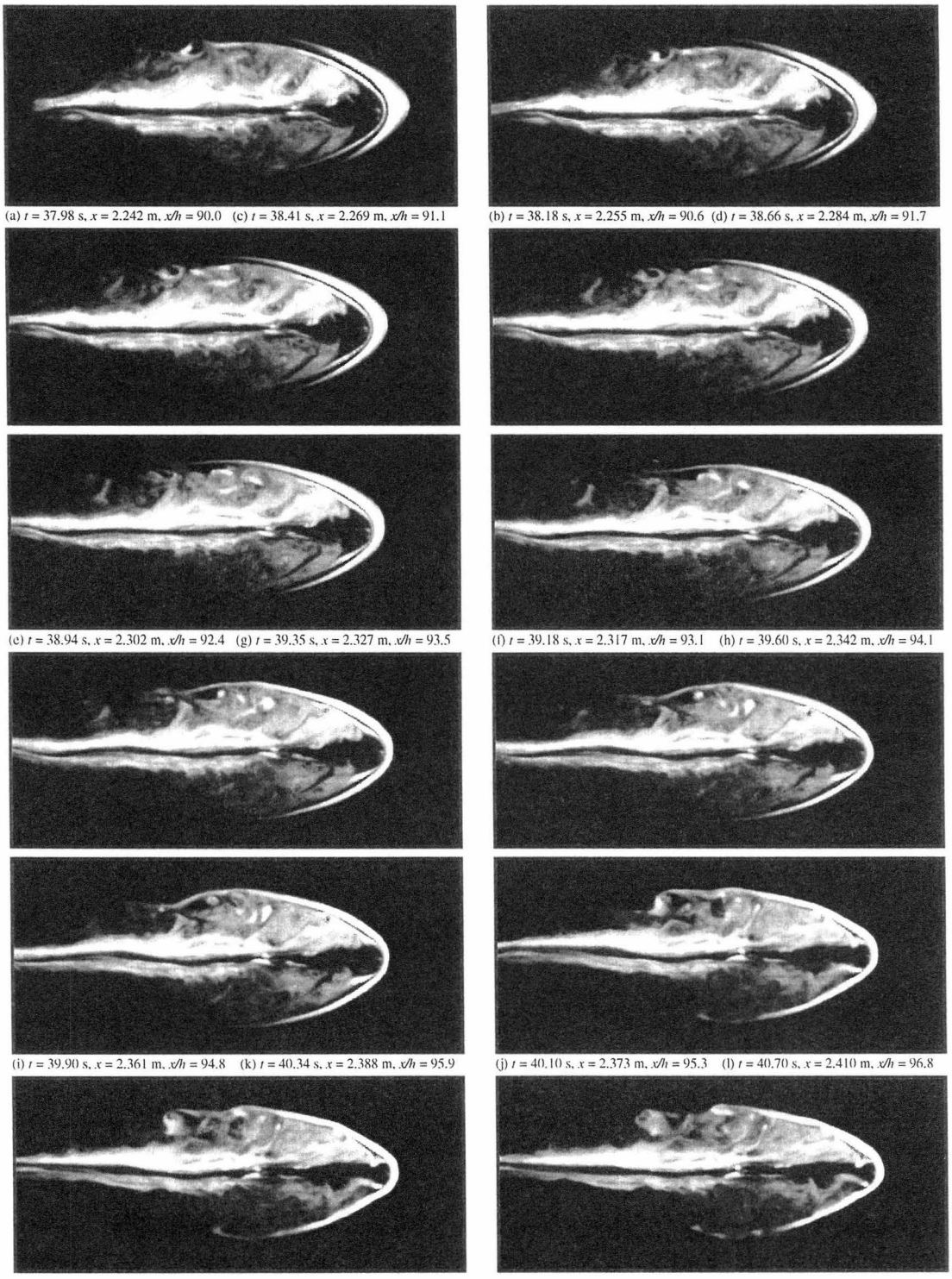

(a) t = 37.98 s, x = 2.242 m, x/h = 90.0 (c) t = 38.41 s, x = 2.269 m, x/h = 91.1

(b) t = 38.18 s, x = 2.255 m, x/h = 90.6 (d) t = 38.66 s, x = 2.284 m, x/h = 91.7

(e) t = 38.94 s, x = 2.302 m, x/h = 92.4 (g) t = 39.35 s, x = 2.327 m, x/h = 93.5

(f) t = 39.18 s, x = 2.317 m, x/h = 93.1 (h) t = 39.60 s, x = 2.342 m, x/h = 94.1

(i) t = 39.90 s, x = 2.361 m, x/h = 94.8 (k) t = 40.34 s, x = 2.388 m, x/h = 95.9

(j) t = 40.10 s, x = 2.373 m, x/h = 95.3 (l) t = 40.70 s, x = 2.410 m, x/h = 96.8

Figure 7.5 - Dye visualisation of fluid entrainment into wave

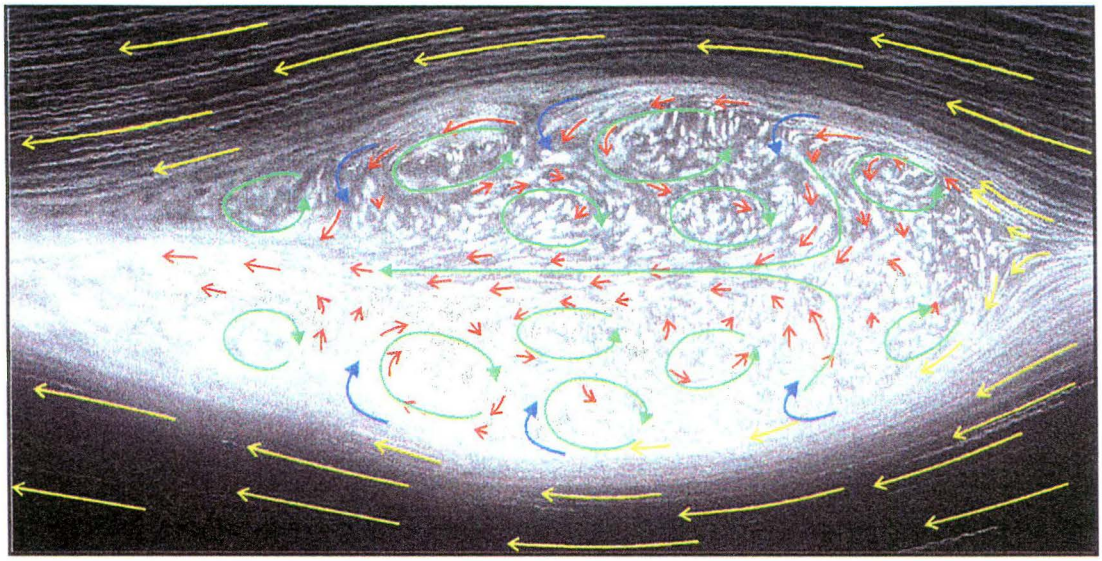

Figure 7.6 - Streakline image of wave showing circulation and entrainment zones

A shear instability, thought to be a form of Holmboe instability, also known as a Holmboe wave, may be responsible for the entrainment of fluid into the wave. This instability was first reported by Holmboe (1962). Early studies (Browand & Winant, 1973; Smyth, Klaassen & Peltier, 1988) described the Holmboe instability as existing in a parallel shear flow within which is embedded a thin, stable, symmetrically positioned density stratification. It appears as a superposition of two disturbances, one above and one below the centre of the shear layer, which propagate in opposite directions. Whereas the Kelvin-Helmholtz shear instability is found to occur only for Richardson numbers of $J < 0.25$ (as defined in Equation 7.1), the Holmboe instability may exist for any positive value of J.

$$J = -\frac{g\dfrac{d\rho}{dy}}{\rho\left(\dfrac{du}{dy}\right)^2} \tag{7.1}$$

Later studies (Smyth & Peltier, 1989; Smyth & Peltier, 1991) focused on the transition between the two types of shear instability and showed that a structural relationship exists between Holmboe and Kelvin-Helmholtz instabilities at the transition. The latter study identified the dominant instability over a range of Richardson and Reynolds numbers (Re = $h_v V/\nu$, where h_v is the half-thickness of the velocity profile, V half the velocity difference between the two layers and ν the

kinematic viscosity), the range depending on a Prandtl number (Pr = ν/κ, where κ is the thermal diffusivity) and ratio h_v/h.

The instability regime diagram of Smyth & Peltier (1991) is shown in Figure 7.7. This diagram is applicable to fluids with a Prandtl number of 9 and an h_v/h value of 3. The former value is close to that of thermally stratified water, with salt-stratified water (as used in this study) characterised by values of Pr of order 10^3. Flows in the experimental work of the present study would typically have Reynolds numbers on the order of 10^3. Three dimensional Holmboe instabilities, which develop a secondary instability oblique to the direction of primary flow, were unlikely to be generated in the present study, with the presence of 2-D instabilities possible at all interfaces which were not subject to Kelvin-Helmholtz instability.

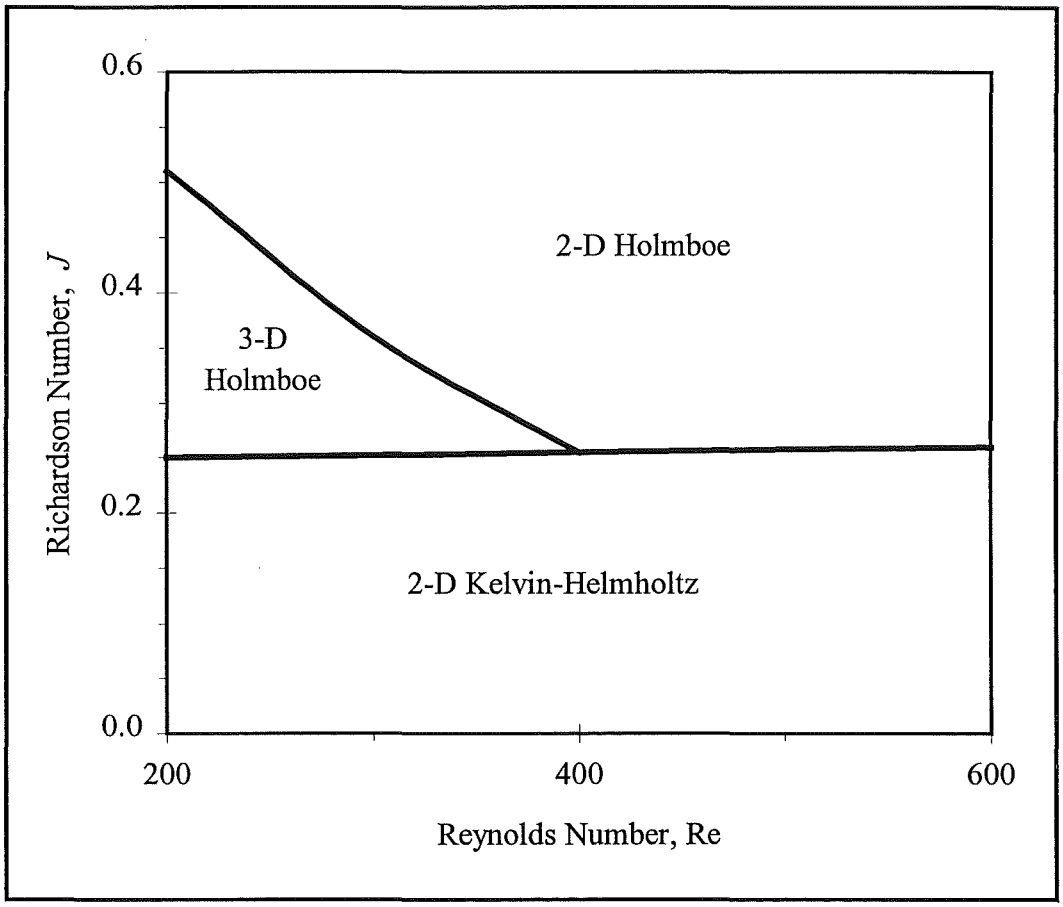

Figure 7.7 - Instability regimes for shear flow, Pr = 9, $h_v/h = 3$

The flow pattern in the vicinity of the wave boundary in Figure 7.6 appears to be anything but symmetric about the boundary, and as will be shown later in Figure

7.8b, neither is the density gradient centred on the shear flow. The issue of a non-symmetric instability is addressed in Lawrence, Browand & Redekopp (1991), where it is shown that if the density gradient is eccentric from the centre of the shear flow, one of the two symmetric instabilities decreases in strength until at a shift of $h_V/2$ it disappears. A subsequent paper (Haigh & Lawrence, 1996) produced a numerical model of these non-symmetric Holmboe waves, with high eccentricity instabilities closely resembling those seen inside large amplitude second mode solitary waves.

Plots of two similar waves using streakline and dye visualisation to highlight shear instabilities are shown in Figure 7.8. The image of Figure 7.8a is in fact the non-enhanced image of Figure 7.4d. Both of the waves in Figure 7.8 were generated by the collapse of a 150 mm thick intermediate density region into a 600 mm deep ambient with a densimetric factor, ω, of 0.0110. That of Figure 7.8a (run 61025DC030) had an interfacial half-thickness, h, of 24.9 mm, while Figure 7.8b (run 61028PC030) was 40.6 mm. Both images were taken 46 seconds after the release of the gate to generate the wave, with the former having travelled 2.73 metres (x/h = 110) and the latter 2.91 m (x/h = 72). The wave in Figure 7.8a had an amplitude of 52 mm (a/h = 2.1) and a celerity of 65 mm/s, while that of Figure 7.8b had an amplitude of 55 mm (a/h = 1.4) and a celerity of 66 mm/s. The behaviour of these waves was therefore quite similar and they are thought suitable for comparison.

In Figure 7.8b, density and velocity profiles have been drawn at three sections, labelled A, B and C, in the vicinity of the wave. Section A was chosen in an apparently stable region upstream of the wave, with section B at a location where the Holmboe instability only was observed. Section C was chosen in the lee of the wave in a region of turbulent mixing. Lines of constant density were drawn at the level of intermediate density, as well as the outer extremities of the interface, with the aid of streaklines. For the purposes of computing a density gradient, it was assumed that there was a linear density distribution between these lines. It is evident from the figure that the density gradient increases up to the midpoint of the wave, and decreases thereafter. Profiles of velocity in the x-direction were

constructed by dividing the length of streaklines by the 0.5 second exposure time. The profile appears to be relatively uniform in front of the wave, with some slowing occurring along the centreline. Inside the wave it becomes much more complex due to the internal circulation, with large gradients near the wave boundaries and both positive and negative velocities inside the wave due to the internal vortex structure.

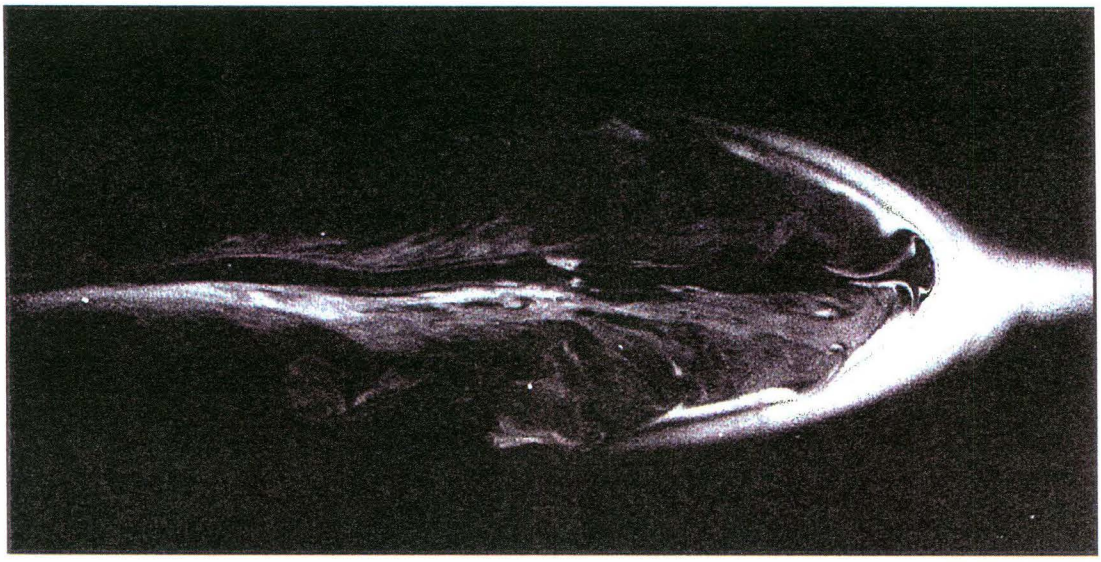

Figure 7.8a - Wave showing Holmboe instability with dye visualisation

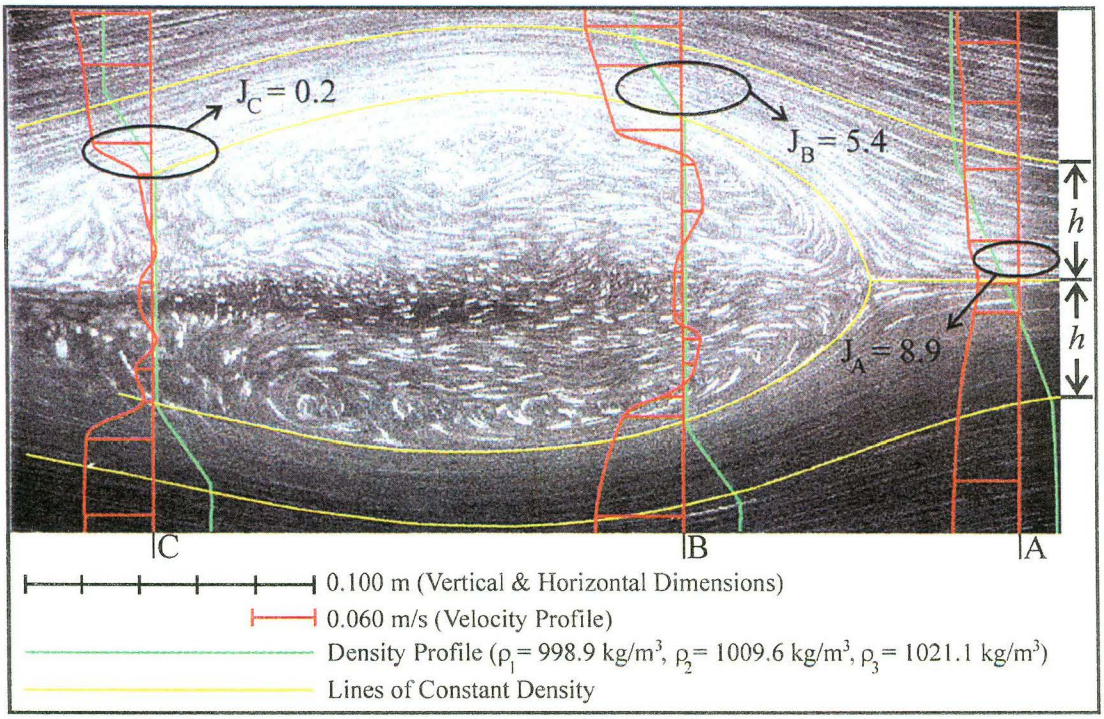

Figure 7.8b - Streakline wave image showing density and velocity profiles

Richardson numbers, as computed with Equation 7.1, were calculated in the density gradient regions of the three labelled sections. At section A, where the wave has begun to influence the fluid immediately ahead of it, a density gradient of -259 kg/m^4 and a small velocity gradient of 0.53 s^{-1} combine to yield a value of $J = 8.9$. This is much greater than the stable level of 0.25. Part way along the wave at section B, a density gradient of -476 kg/m^4 and a larger velocity gradient of 0.93 s^{-1} combine to yield a value of $J = 5.4$, which is still stable. In the lee of the wave, at section C, a decrease in the density gradient to -412 kg/m^4 and a further increase in the velocity gradient to 4.56 s^{-1} result in a dramatic drop in the value of J to 0.2. This is slightly less than the critical value, and is indicative of the more vigorous nature of the instability in this region. The limit errors for the calculated Richardson numbers are calculated in Appendix 12 to be approximately ±10%.

It should be noted that some entrainment of fluid was also observed in the lee of the wave, where turbulent mixing in the wake resulted in fluid being brought into the wave. This turbulent entrainment was also noted by Stamp & Jacka (1995). Fluid brought into the wave in this fashion did not advance forward in the wave and was soon expelled.

7.2.3 Conclusions

It is apparent from the observations presented here that there is in fact a significant movement of fluid across the density interface between the body of the wave and the external fluid. The wave is of a density midway between that of the upper and lower layers, and as it propagates, it splits the interfacial region in half. This results in a density gradient across the boundary layer which exists on the wave's surface. The local Richardson number in this region is seldom small enough to allow mixing by a Kelvin-Helmholtz instability; rather mixing across the interface is accomplished by a Holmboe instability. This occurs when interfacial fluid stretches along the boundary of the wave and internal vortices entrain it in what resembles a cusping action.

7.3 Mass Transport

Earlier studies of second mode waves noted their capacity for mass transport but no attempts have been made to quantify this capability. The visualisation techniques used in this study have allowed the measurement of the rates of flushing of passive tracer from second mode waves. The analysis of data from a range of experiments has resulted in the formulation of a dimensionless equation describing the mass transport capacity of second mode waves.

7.3.1 Background

Typical descriptions of mass transport by second mode waves in previous studies have included: "the motion [had] the appearance of a 'lump' of fluid moving through the region of varying density" (Davis & Acrivos, 1967), "the mixed region fluid was partly entrained in these waves, which propagated unchanged for very long distances" (Kao & Pao, 1979) and "as the wave propagates it carries this mixed fluid along with it at the appropriate wave speed" (Maxworthy, 1980). With the recognition that the expulsion of fluid from within a second mode wave was balanced by the entrainment of interfacial fluid from ahead of the wave (Stamp & Griffiths, 1992) came a realisation that the wave's ability to transport mass was limited. Stamp & Griffiths (1992) stated that "at large amplitude they carry mass over large distances. The fluid being transported is, however, continually exchanged through addition from ahead of the wave and ejection at the rear, so that passive tracer is transported only a finite difference." In the present study, a Laser Induced Fluorescence (LIF) technique was used to measure the spatial and temporal distribution of dye within the wave. This enabled detailed qualitative and quantitative descriptions of the mass transport capacity of the wave.

7.3.2 Experimental Observations

Selected colour enhanced images from an experiment (Run 61010DC050) are shown in Figure 7.9, which illustrates the flushing behaviour of a typical wave.

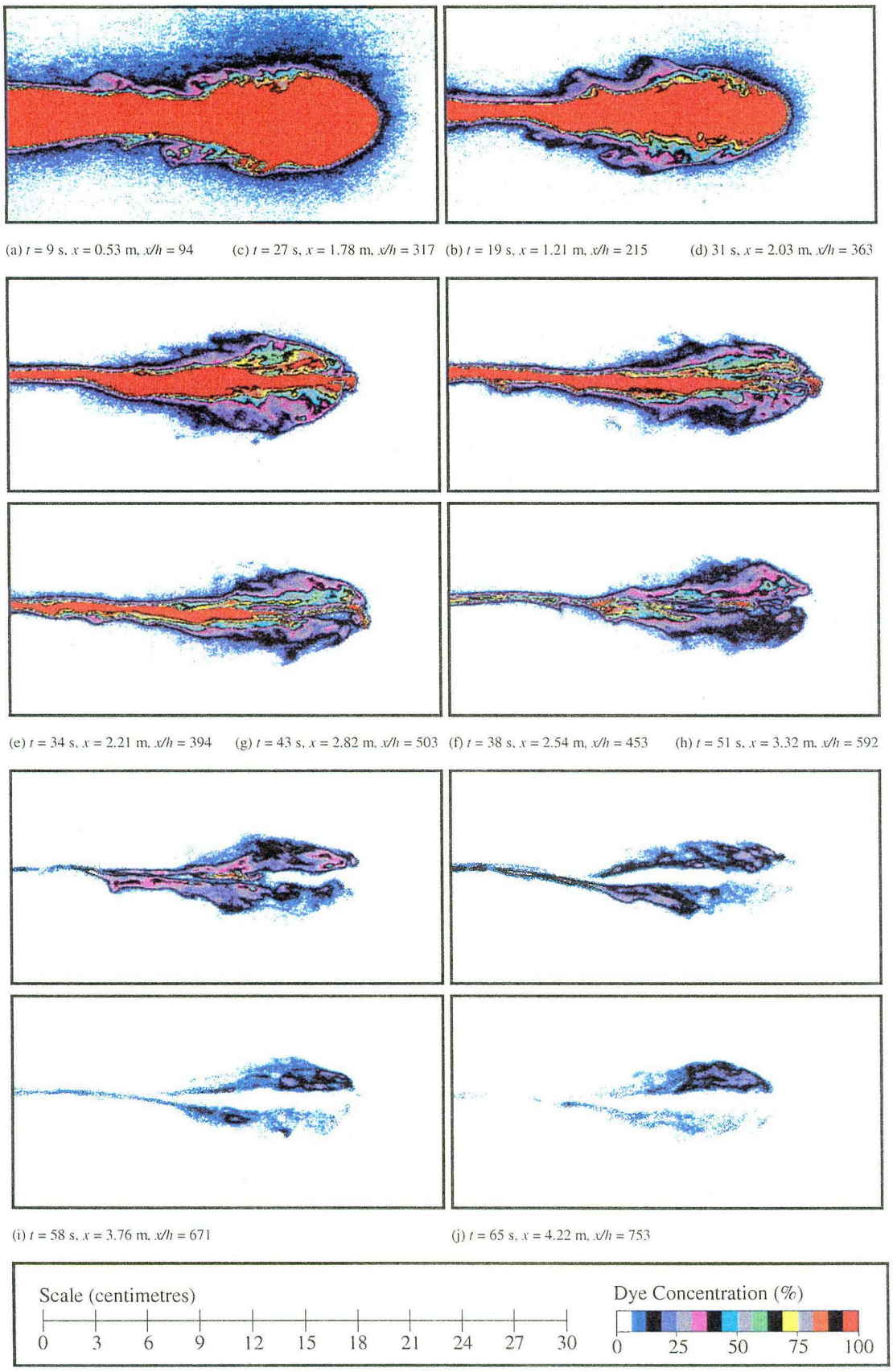

Figure 7.9 - Time lapse images showing flushing of fluid from wave

In Figure 7.9a it is apparent that little fluid has been entrained into the wave, with mixing only due to shear instabilities in the lee. Figures 7.9b through 7.9e show the entrainment of interfacial fluid along the outer boundary of the wave (as described in Section 7.2), with a clear progression of mixed entrained fluid observed from the boundaries of the wave, towards its front and then back out along its centreline. Starting with Figure 7.9f, the progression of undyed entrained fluid along the centreline of the wave, separating the remaining dyed fluid into two lobes, is apparent. These lobes retained residual concentrations of dye which appear to be flushed as new interfacial fluid is entrained.

These observations agree with the previously described circulation patterns within the wave, though it is now apparent that dye is retained longer within the vortices above and below the centreline of the wave than in the rearward flowing region along the centreline. Dye appears to be gradually flushed from the vortices as the wave progresses. The wave in this figure was generated by the collapse of a 100 mm thick body of intermediate density fluid into a 600 mm deep ambient with an interfacial half-thickness, h, of 5.6 mm and a densimetric factor, ω, of 0.0173. A slight decay of the wave was observed over the run, from an initial amplitude and velocity of 65 mm and 70 mm/s to final values of 55 mm and 61 mm/s, respectively.

7.3.3 Flushing Analysis

The LIF procedure involved the preparation of a fluorescent dye tracer as described in Section 3.4.2, after which calibrations were performed and recorded on videotape as described in Section 3.6.4. To produce an image in which dye concentrations were presented as a percentage of that in the intermediate density collapsing fluid, the following steps were taken. A calibration image of full-strength dyed fluid (i.e. that of the intermediate density fluid prior to collapse) was acquired from videotape, as was a zero image taken in the absence of dye but in the presence of laser and background light. An image of the wave, hereafter called the run image, was also acquired from the videotaped record of the experimental run. In these 768 x 512 pixel digital images, each pixel had a value, proportional to light intensity, between

0 and 255. The zero image was subtracted from both the calibration and run images, and then the resulting adjusted run image was divided by the adjusted calibration image to yield concentrations expressed as a fraction of that of the full strength dyed fluid. In the resulting concentration image, a value of 255 corresponded to full strength dye with values decreasing linearly to 0 in the absence of dye. The image analysis performed here was done with the aid of a computer program which is described in Appendix 7.

Measurements of the concentration of dye in the wave were made by analysing the concentration images with the same computer program. An ellipse the size of the fully developed wave was superimposed on each image in the set of data from each experiment. The sum of the values of all pixels within this ellipse was then calculated, and this, divided by the number of pixels, provided a value for average pixel intensity within the wave. Dividing this value by the maximum value of 255 thus yielded the fraction of dye remaining from the initial generation of the wave, and the examination of a sequence of images from an experimental run allowed the measurement of the loss of dye from the wave with time.

Flushing data from a typical experiment (Run 61008DC050) are shown in Figure 7.10. This figure illustrates the behaviour of a typical wave as well as some of the problems that were associated with processing of the experimental data. The wave typically displays three distinct types of behaviour from its generation until all dye is flushed. As the wave develops, little or no loss of dye is seen. During development, dye may actually be entering the wave as the following current pushes it along, and little dye is lost before the internal structure develops a rearward current along the centreline of the wave. Once this current develops, strong flushing occurs as external fluid is entrained into the wave and collapsing region fluid is expelled. The wave seems to discharge dye at a constant rate until dye concentrations fall to below 10% of the initial maximum concentration. This seems to coincide with the first expulsion of undyed fluid from the wave, as is seen in Figure 7.9h. After this point, any remaining, diluted dye is carried only in the vortex lobes above and below the centreline of the wave, and the discharge of dye from the wave slows dramatically.

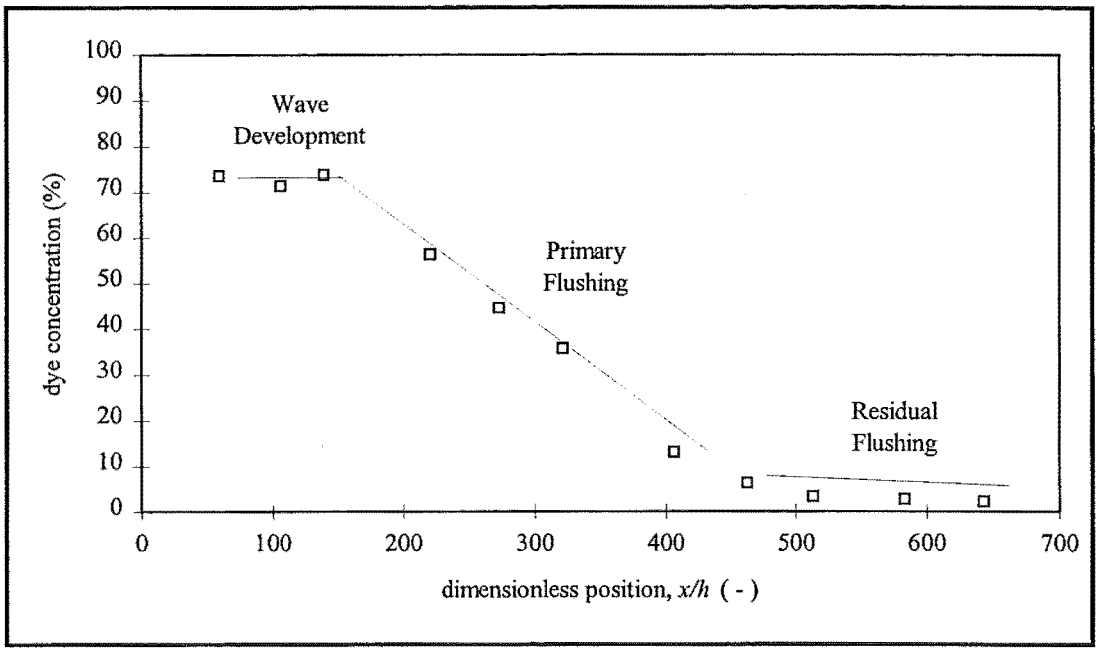

Figure 7.10 - Flushing of dye from a typical wave (Run 61008DC050)

The wave generation technique used in these experiments resulted in waves which entered the primary flushing phase at a range of distances with a range of initial concentrations. The distance range was a consequence of the varying development lengths, whereas the initial concentration was frequently well below 100% due to mixing during the initial gate release. The linearity of the flushing curve in its primary flushing phase was utilised to introduce a consistent starting point for the wave. A linear regression fitted to the central portion of this curve for each run was used to calculate the value of x/h at a concentration of 100%. The offset required to adjust this value to zero was then calculated and applied to the raw x/h values. Data from the wave development phase were also dropped from the analysis at this point.

Unfortunately, the resulting data did not display any similitude between runs, but it was recognised that the various flushing curves were ordered according to their Richardson number. As the Richardson number varies along the length of the wave, a bulk value was computed with Equation 7.2. This dimensionless parameter is based on the assumptions that the density and velocity profiles are linear and both vary over the interfacial half-thickness, h. This bulk value itself tended to increase with wave decay, so a value equal to the average value over the experimental run, was taken as being representative.

$$J = \frac{g\,\dfrac{d\rho}{dy}}{\rho\left(\dfrac{du}{dy}\right)^2} = \frac{g\,\dfrac{(\rho_2 - \rho_1)}{h}}{\rho\left(\dfrac{c}{h}\right)^2} = \frac{g\,\omega h}{c^2} = \frac{2\,c_0^2}{c^2} \qquad (7.2)$$

It would seem to make sense that the bulk Richardson number of the wave, which is indicative of the stability of the interface between the wave and the external fluid, would influence the rate of fluid transport across that interface. Common sense would say that a less stable interface (with a lower Richardson number) would result in a higher rate of transport and a more rapid flushing of the wave. The experimental evidence, though, runs contrary to this supposition, with lower Richardson numbers corresponding to lower flushing rates, and the relationship between the two appearing to be linear.

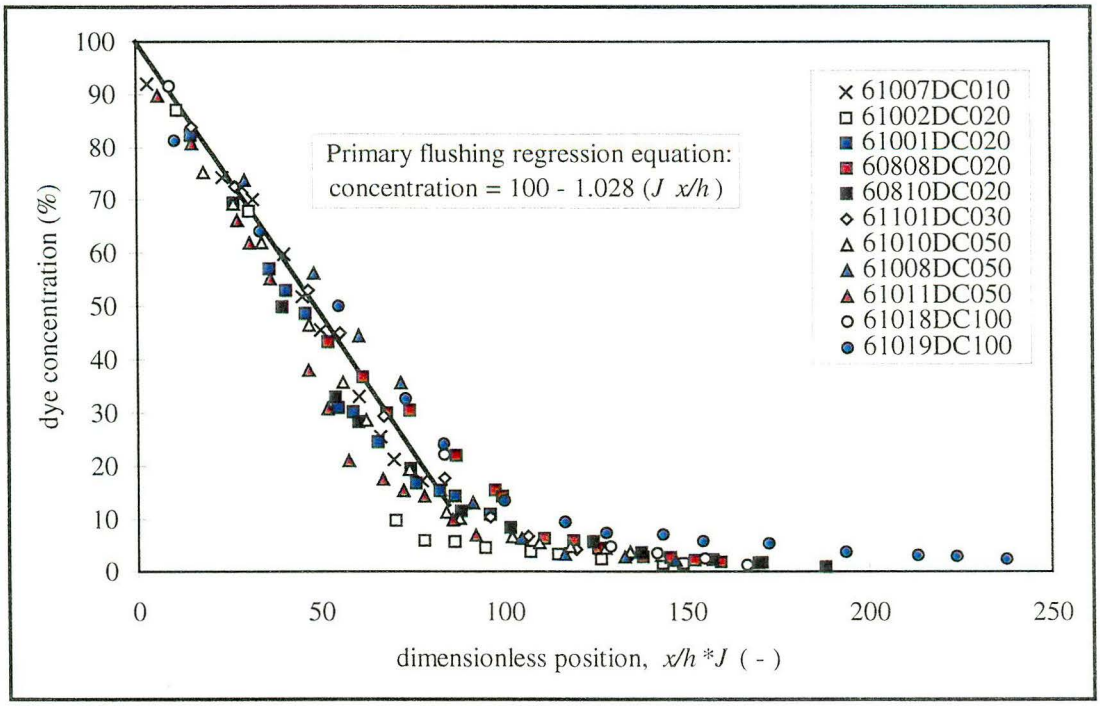

Figure 7.11 - Flushing of dye from second mode waves

The effect of factoring the representative Richardson number by the dimensionless distance is shown in Figure 7.11, where a high degree of similitude over the range of experimental runs is displayed. Error bars for these data, based on the error analysis in Appendix 12, are shown in Appendix 8. The relationship between Richardson number and flushing rate is seems to be counterintuitive, but a similar

relationship was seen in a study of the mixing of dense river inflows into lakes (Leong, 1988). In this study it was found that the dilution of such an inflow varied inversely with its densimetric Froude number, which is the inverse of a Richardson number. It is thought that this may be due to the Richardson number dependence of the vortex structure adjacent to the mixing interface. It may be that higher interface stability allows more coherent vortex structures to develop, which in turn are more efficient at entraining fluid than any small-scale, disorganised motion that might occur at lower stabilities. It should also be noted that factoring the dimensionless displacement by the Richardson number effectively removes the interfacial half-thickness, h, from the dimensionless quantity.

The linear regression shown in Figure 7.9 was fitted to data from the primary flushing phase of the experiment (spanning dye concentrations from 100 to 10%). This equation indicates that a wave containing a given mass of fully mixed tracer will be flushed of 90% of that tracer within a dimensionless distance of approximately 90. With Richardson numbers in this study ranging from J = 0.18 - 0.88, this equates to an x/h value of between 100 and 500.

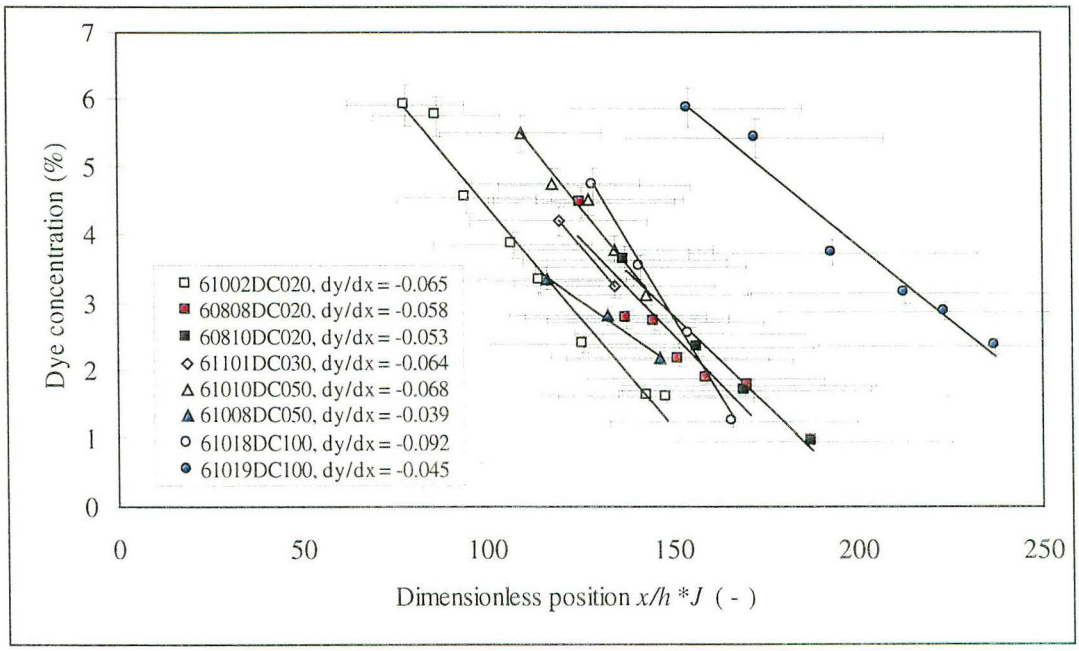

Figure 7.12 - Residual dye flushing from second mode waves

Wave behaviour during the residual flushing phase also appears to vary linearly with dimensionless distance. Figure 7.12 shows this variation for the experiments

where measured dye concentrations fell below 6%. Whereas during primary flushing, the wave exhibited a flushing rate of approximately 1% per unit dimensionless distance, in this phase the flushing rate falls to approximately 0.06%.

Concentration images, associated data and more information on the dye flushing analysis procedures are contained in Appendix 8.

7.3.4 Conclusions

The analysis of the experimental data presented here shows a dimensional similarity over the range of experimental runs. Here the distance parameter is rendered dimensionless by dividing by the interfacial half-thickness as well as multiplying by the bulk Richardson number.

There appear to be two phases in the flushing of a wave which is initially full of a passive tracer. The first phase, here called 'primary flushing', occurs until the dye concentration decreases to approximately 10% of its capacity. The end of this phase coincides with the first expulsion from the wave of undyed, recently entrained fluid. At this point, diluted dye is retained in two lobes located above and below the centreline of the wave. These lobes contain the assemblage of vortices described in Section 7.1, and the gradual expulsion of dye from these regions is here termed 'residual flushing'. Flushing of dye in both phases occurs at a constant rate, though the residual flushing rate is approximately one-sixteenth of the primary flushing rate of 1% per unit dimensionless distance. Between the two phases, from approximately 10% to 6% of capacity, is a transition region, but below the latter concentration the waves seem to experience only residual flushing.

No measurements were taken for dye concentrations below 1% of wave capacity, so it is not possible to define the point at which all original tracer is flushed from the wave. It is possible that a third flushing phase, in which dye lingers in the vortex regions of the wave, exists.

7.4 Conclusions

Observations and measurements made here have shed new light on the internal structure and entrainment characteristics of large amplitude second mode waves. This study has considered circulation within the wave, entrainment into the wave, and transport of mass by the wave. These phenomena are all interrelated, as observations show that fluid is entrained into the wave, circulated and then expelled, indicating a limited capacity for mass transport.

Circulation patterns within the wave appear to be more complex than the closed streamline, counterrotating vortex structure predicted by previous numerical solutions. It appears that an assemblage of vortices exists on either side of the centreline of the wave. Vortices adjacent to the wave boundary are driven by the external flow, while those away from the boundary are driven by the former, and thus rotate in the opposite direction. The latter vortices drive a rearward flow along the centreline of the wave. This flow carries fluid which is expelled from the lee of the wave.

The boundary-proximate vortices within the wave play a vital role in the entrainment of external fluid into the wave. Interfacial fluid which is split apart by the propagating wave and stretched along the wave boundary is brought into the wave in cusp-like structures where these vortices rotate inwards. This motion appears to be typical of Holmboe instability, which can occur along density interfaces for any Richardson number greater than zero.

The entrainment and expulsion of fluid into and out of the wave indicates that fluid is not carried along indefinitely by the wave and that the wave has a limited capacity for mass transport. Experiments performed here show that a wave containing a fully mixed tracer will lose that tracer at a constant rate until approximately 10% of tracer remains. During this 'primary flushing' phase, tracer is lost from the wave at a rate of approximately 1% of initial mass per unit dimensionless distance. After a short transition region, the wave enters its 'residual flushing' phase, in which it loses tracer at a much slower rate. This rate, again constant, is approximately one-sixteenth of the primary flushing rate. The residual

flushing phase continues until only approximately 1% of the initial tracer remains in the wave. No measurements were taken below this concentration, so it is not possible to determine the flushing rate below this point. Possibly fluid lingering within the vortex regions of the wave would be flushed nonlinearly with time.

8.0 Results - Wave Decay

Though the persistence of second mode waves is perhaps one of their most striking features, most experimental studies have made note of their eventual decay. It is only very recently (Stamp & Jacka, 1995) that any quantitative description of the wave dissipation rate has been made, and even this study failed to ascertain the specific decay mechanism.

This chapter will first present the experimental data from this study, augmented by that of Stamp & Jacka (1995). This entire body of data will then be subjected to the analysis procedure of Stamp & Jacka (1995) which examined the amplitude decay rate of the waves. The wave amplitude decay rate will then be related to the energy decay rate, and the relationship of the latter to retarding forces will then allow a detailed examination of the mechanisms responsible for wave decay.

8.1 Experimental Observations

Wave amplitudes for a series of experimental runs exhibiting significant decay were measured as detailed in Chapter 6. Dimensionless amplitudes, a/h, were plotted against the dimensionless distance travelled by the wave, x/h. The data from the present study are shown in Figure 8.1a-b, while those from the study of Stamp & Jacka (1995) are contained in Figure 8.1c. The data have been split into three plots for clarity, with those of Stamp & Jacka (1995) shown at a different scale. Error bars, based on the error analysis presented in Appendix 12, are provided for the current data.

As in the study of Stamp & Jacka (1995), it was found that wave amplitude decayed linearly with distance, though the decay rate, da/dx, varied between experimental runs. As in Stamp & Jacka (1995), it was observed that the rate of decay depended on the densimetric factor, ω, with waves with smaller values of ω decaying more rapidly. Stamp & Jacka (1995) examined waves with values of ω = 0.0253 to 0.0917, while the present study covers a range from ω = 0.0053 to 0.0176. The results of the present study agree with those of Stamp & Jacka (1995) which were previously shown in Figure 2.5, and their data plus those from the present study are

presented in Figure 8.2, where it is seen that all data collapse onto a single curve. Stamp & Jacka (1995) concluded that viscous stresses were the primary mechanism for decay.

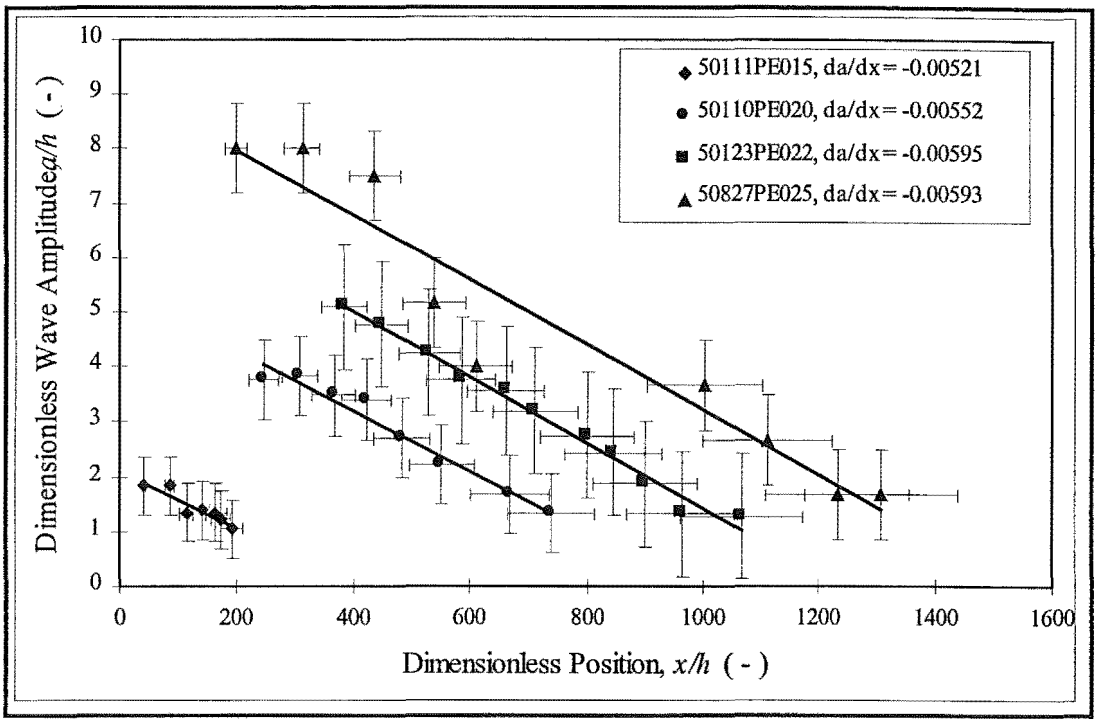

Figure 8.1a - Wave amplitude decay curves from present study

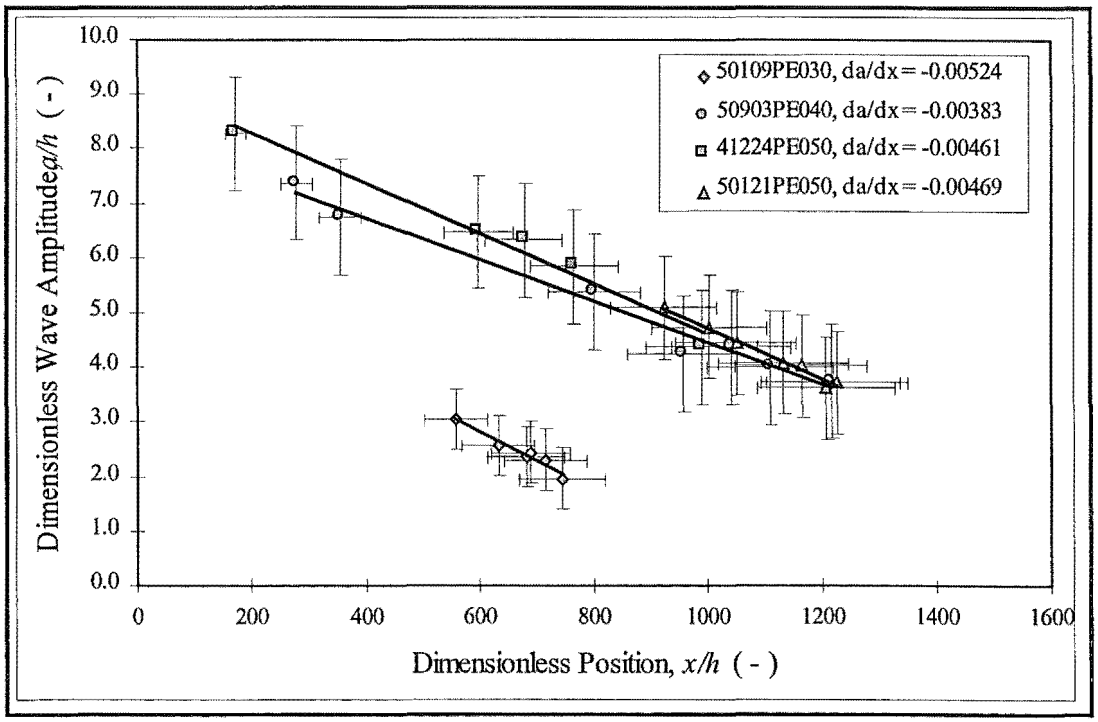

Figure 8.1b - Wave amplitude decay curves from present study

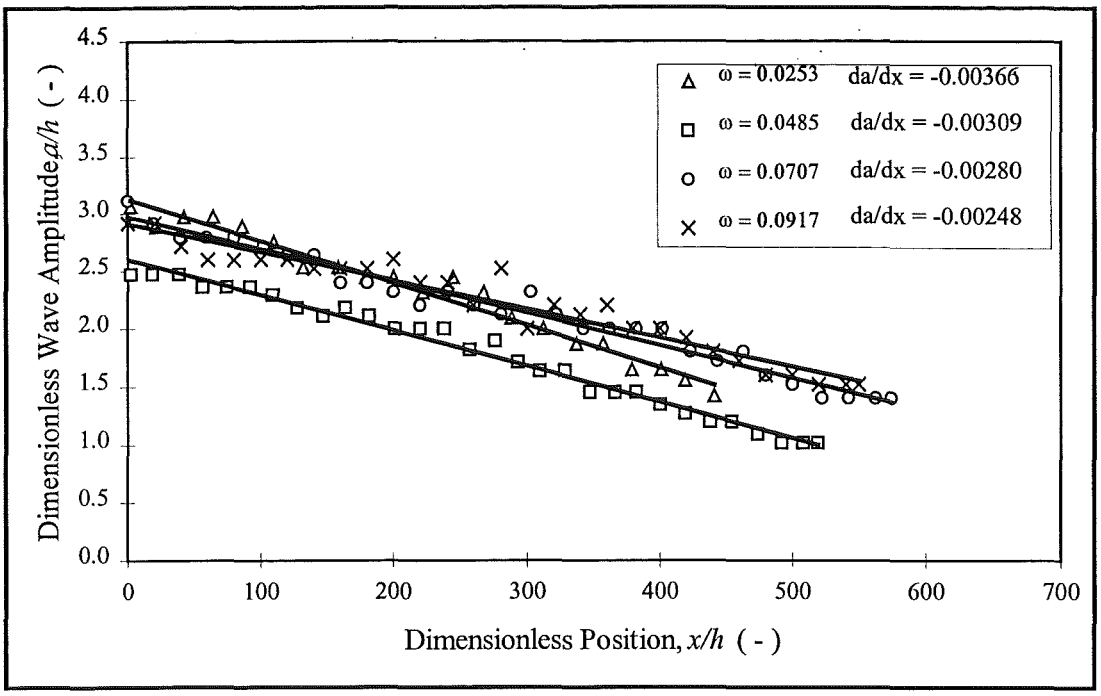

Figure 8.1c - Wave amplitude decay curves from Stamp & Jacka (1995)

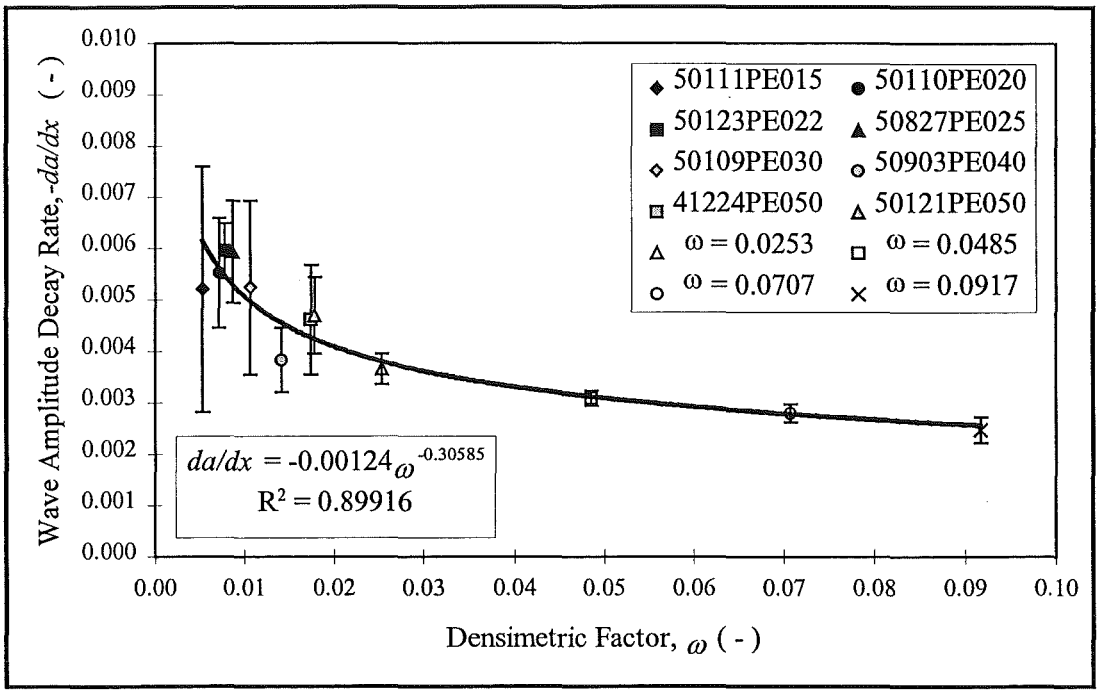

Figure 8.1d - Wave amplitude decay rate vs. densimetric factor

The curve fitted to the data of Figure 8.2 shows that wave amplitude decay rate, *da/dx*, varies approximately with the inverse 1/3 power of densimetric factor, ω. Error bars were calculated for each data point after the fashion of Stamp & Jacka (1995), with the larger error bars attached to data points from the present study due

to the smaller numbers of data points contributing to the respective amplitude decay curves.

8.2 Review of Previous Analyses

Stamp & Jacka (1995) identified four potential mechanisms for wave decay and examined their relative importance. The possibilities included wave radiation, turbulent mixing, and viscous stresses at both the flume sides (wall shear) and the density interface (interfacial shear). These decay mechanisms are schematised in Figure 8.3. The analysis of Stamp & Jacka (1995) will be discussed and applied to the data of the present study in the following sections.

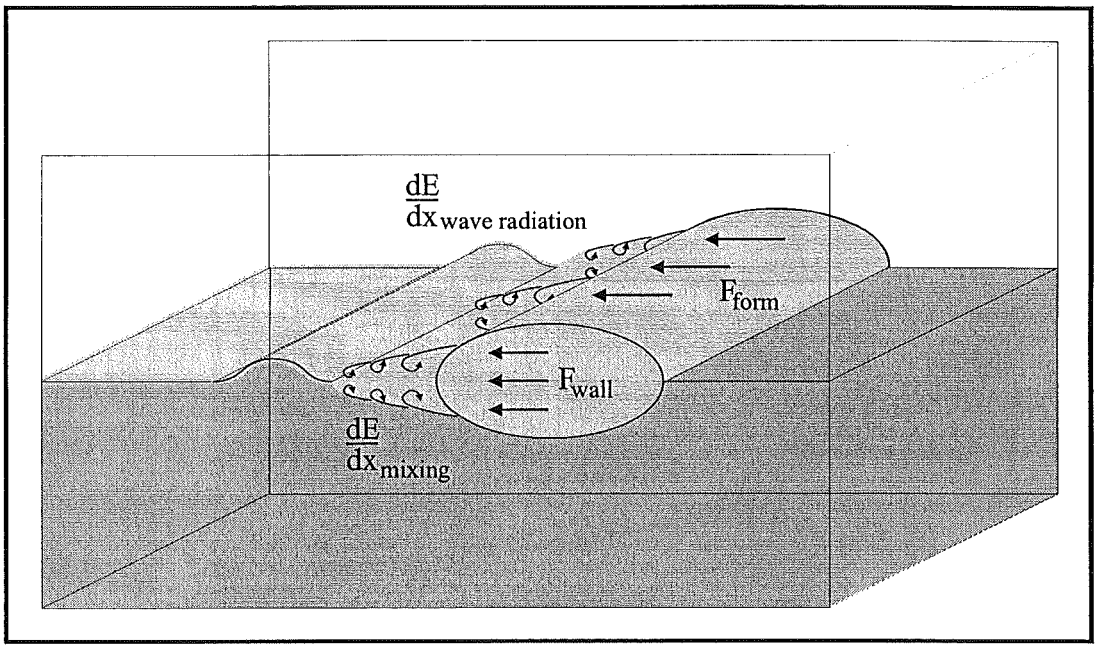

Figure 8.3 - Potential wave decay mechanisms

8.2.1 Wave Radiation

The existence of a first mode wave in the lee of a second mode wave was predicted by Akylas & Grimshaw (1992). Experimental observations of their presence have been made by Hachmeister & Rigby (1980) and Stamp & Jacka (1995), with both studies noting the following first mode waves to be of much smaller amplitude than the second mode wave. Akylas & Grimshaw (1992) suggested these first mode waves as a possible attenuation mechanism for the leading second mode wave, but

did not quantify this effect. Stamp & Jacka (1995) formulated an estimate based on the energy of a second mode wave and the energy radiation in a first mode lee wave train.

The estimate of Stamp & Jacka (1995) was based on an equation describing the energy of a second mode wave:

$$E \propto w\lambda(\rho ac^2 + g\Delta\rho a^2) \tag{8.1}$$

In Equation 8.1 w represents the width of the channel and $\Delta\rho$ the density difference between fluid above and below the interface. Empirical relationships for the wavelength and celerity (Equations 2.36 and 2.37, respectively) were substituted into Equation 8.1. In the limit of $a/h >> 1$, this reduced to:

$$E \propto \frac{wg\bar{\rho}\omega}{h}a^4 \tag{8.2}$$

Equation 8.2 was then differentiated to show that:

$$\frac{dE}{dt} \propto \frac{wg\bar{\rho}\omega}{h}a^3\frac{da}{dt} = \frac{wg\bar{\rho}\omega}{h}ca^3\frac{da}{dx} \tag{8.3}$$

It was then recognised that the first mode lee wave train would radiate energy at the following rate, where c_g is the group velocity, ε the energy per unit area and ξ the amplitude, all of the following waves:

$$\frac{dE}{dt} \propto w\left(c - c_g\right)\varepsilon = w\left(c - \frac{c}{2}\right)\frac{g\Delta\rho\xi^2}{2} \tag{8.4}$$

By equating Equations 8.3 and 8.4, it was shown that:

$$\frac{da}{dx} \propto \frac{h\xi^2}{a^3} \tag{8.5}$$

Stamp & Jacka (1995) noted that the amplitude, ξ, of the attached waves appeared to be constant, and this indicated that according to Equation 8.5, the second mode wave attenuation rate should depend on the amplitude, a, of the second mode wave.

As this did not appear to be the case, wave radiation was discounted as a significant mechanism for wave attenuation.

The role of wave radiation in the decay of second mode waves will be discussed further in Section 8.4.1.

8.2.2 Turbulent Mixing

Turbulent mixing, in which kinetic energy is converted to potential energy as the wave causes mixing of different density fluids and a corresponding thickening of the density interface, is another potential mechanism for wave decay. Mixing has been observed to occur in the lee of second mode waves where shear instabilities occur. Stamp & Jacka (1995) also suggested that mixing occurred inside the wave as fluid was entrained and mixed in a turbulent fashion. Doubt is cast on this by the observations presented in Chapter 7. It appears that the fluid entrained into the wave is of intermediate density, as only fluid from the thin layer adjacent to the core of the wave is brought in. Once in the vortex region within the wave, significant mixing does not occur. In particular, fluid entrained above the wave centreline remains above the centreline until it is expelled from the wave.

Stamp & Jacka (1995) assumed that a Richardson number would be representative of the amount of energy being taken from the wave by mixing of fluid due to shear instabilities. The relevant density scales were taken as those of the upper, ρ_1, and lower, ρ_3, layers, with interfacial half-thickness, h, again chosen as the length scale. The relevant velocity scale was once again identified as the infinitesimal long wave celerity, c_0. This produced the following Richardson number:

$$J \propto \frac{g\,\Delta\rho\,h}{\overline{\rho}\,c_0^2} = \frac{g\,\Delta\rho\,h}{\overline{\rho}\left(g\,\omega\,h\right)} = \text{constant} \qquad (8.6)$$

It is apparent from Equation 8.6 that the calculated Richardson number is constant for all waves, indicating a similar shear instability behaviour across the range of waves. This was taken to mean that turbulent mixing could not explain the variation in the rate of wave attenuation with density difference.

The role of turbulent mixing in the decay of second mode waves will be discussed further in Section 8.4.2.

8.2.3 Wall Shear

Stamp & Jacka (1995) reasoned that the rate of wave decay, if dependent on viscous stresses, would depend on a representative Reynolds number. The observation that the wave decay rate, *da/dx*, was independent of amplitude suggested that the Reynolds number should also be independent of amplitude. In the examination of decay due to wall shear, the relevant velocity scale was then taken to be the speed of a long infinitesimal wave, c_0, while the length scale chosen was the flume width, w. Taking the representative viscosity to be that of the intermediate density fluid, $\nu(\bar{\rho})$, produced the following Reynolds number:

$$Re_w = \frac{c_0 w}{\nu} \propto \frac{(g\,\omega\,h)^{1/2} w}{\nu(\bar{\rho})} \tag{8.7}$$

The data of Stamp & Jacka (1995), shown in Figure 2.5, indicated that the attenuation rate decreased with increasing Re_w, and this was taken to indicate that the attenuation rate would decrease with an increase in either densimetric difference ω, interfacial thickness h, or flume width w. Figure 8.4 contains the data of Stamp & Jacka (1995) as well as that from the present study.

From Figure 8.4 it is apparent that there is no consistent relationship between Re_w and *da/dx*. The results of Stamp & Jacka (1995) do show a reasonably linear relationship, but it must be noted that their experiments were performed with a very narrow range of interfacial half-thicknesses h, and that flume width, w, was not varied, so the observed relationship appears to be a consequence of the densimetric factor dependence seen in Figure 8.2.

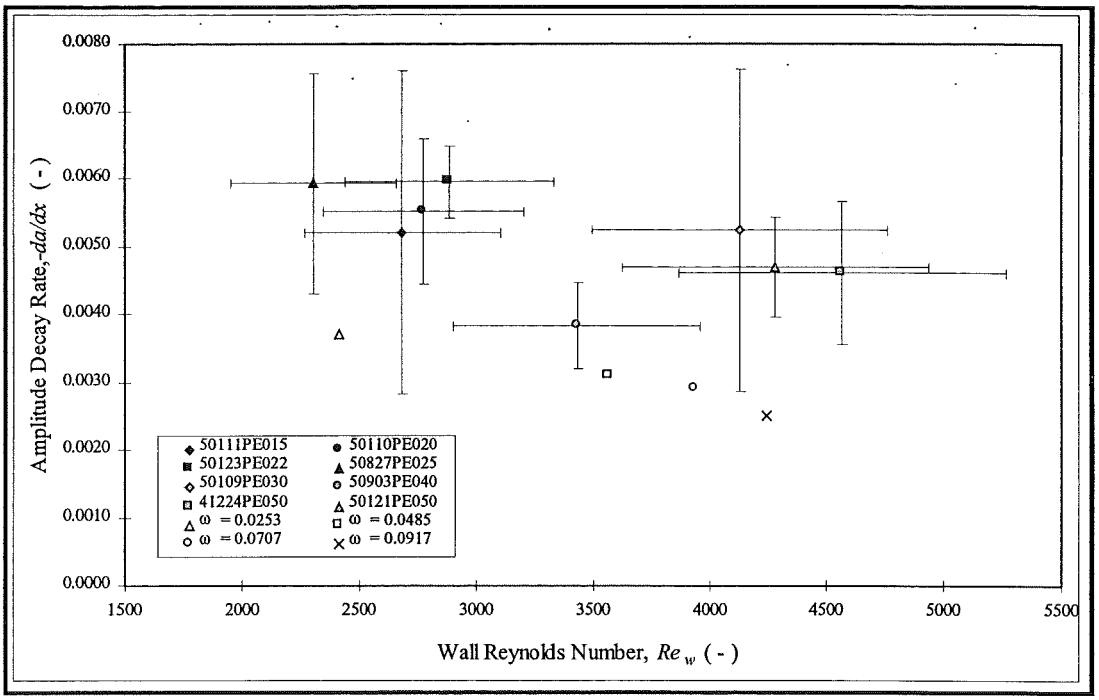

Figure 8.4 - Wave amplitude decay rate vs. wall Reynolds number. Symbols labelled with values of ω represent data from Stamp & Jacka (1995).

The role of wall shear in the decay of second mode waves will be discussed further in Section 8.4.3.

8.2.4 Interfacial Shear

Wave decay due to viscous stresses at the interface was treated by Stamp & Jacka (1995) in a similar fashion to that due to wall shear stress. In this case the representative Reynolds number was again based on the speed of a long infinitesimal wave, c_0, while the length scale chosen was the interfacial half-thickness, h. This produced the following Reynolds number:

$$Re_h = \frac{c_0 h}{\nu} \propto \frac{\left(g\,\omega h^3\right)^{1/2}}{\nu\left(\bar{\rho}\right)} \tag{8.8}$$

The data of Stamp & Jacka (1995), shown earlier in Figure 2.5, indicated that the attenuation rate decreased with increasing Re_h, and this was taken to indicate that the attenuation rate would decrease with an increase in either densimetric

difference, ω, or interfacial thickness, *h*. Figure 8.5 contains the data of Stamp & Jacka (1995) combined with that from the present study.

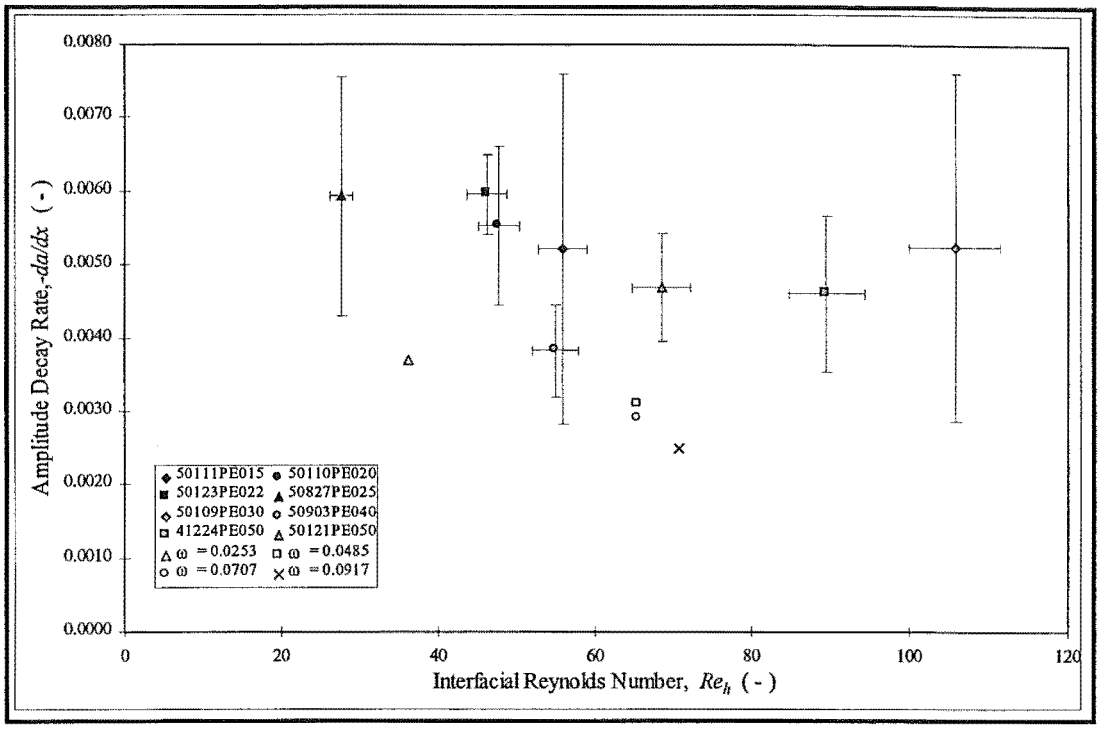

Figure 8.5 - Wave amplitude decay rate vs. interfacial Reynolds number. Symbols labelled with values of ω represent data from Stamp & Jacka (1995).

From Figure 8.5 it is apparent that there is no consistent relationship between Re_h and *da/dx*. The results of Stamp & Jacka (1995) do show a reasonably linear relationship, but it must be noted that their experiments were performed with a very narrow range of interfacial half-thicknesses, *h*, so the observed relationship appears to be a consequence of the densimetric factor dependence seen in Figure 8.2.

The role of interfacial shear in the decay of second mode waves will be discussed further in Section 8.4.4.

8.3 Energy Considerations

The analysis of Stamp & Jacka (1995) was based on the comparison of wave amplitude decay rates to scaling estimates representing various decay mechanisms. In the present study, energy decay rates will be compared with retarding forces to estimate the contribution of the various decay mechanisms to wave decay. Energy

decay rates will first be calculated by a variety of methods and compared to ensure the accuracy of calculated values. The energy of the wave will be computed based on an equation which considers both kinetic and potential energy. The differentiation of curves fit to the resulting data-sets will provide one estimate of energy decay rates, while the differentiation of the energy equation will provide another. A conservation of momentum analysis will provide a third, entirely independent, estimate of the energy decay rates to be compared to retarding forces in Section 8.4.

8.3.1 Derivation of Energy Equation

Stamp & Jacka (1995) presented the following relation to describe the energy of a large amplitude second-mode wave:

$$E \propto w\lambda(\rho ac^2 + g\Delta\rho a^2) \tag{8.9}$$

In Equation 8.9, the first term within brackets describes the bulk kinetic energy of the wave, while potential energy and any remaining kinetic energy contributions are represented by the latter. The computation of actual wave energy requires the determination of coefficients to modify the expression in Equation 8.9 to a proper equation. The derivation of these coefficients follows.

8.3.1.1 Kinetic Energy

The kinetic energy within the wave is estimated by assuming it to be an ellipse of constant density, ρ_2, and uniform velocity in the *x*-direction, *c*. The semi-major and semi-minor axes of the ellipse are taken to be λ and *a*, respectively. Note that the relationship between λ and *b*, the semi-major axis of an ellipse superimposed on the flow, was discussed in Section 6.1.3, and the two values tend to be quite similar. The internal kinetic energy is then equal to:

$$KE_{int} = \frac{1}{2}mv^2 = \frac{1}{2}\rho_2 \pi a\lambda w c^2 \tag{8.10}$$

Kinetic energy also exists due to the passage of the wave, as fluid is moved around it. It is difficult to formulate a scaling estimate of this energy, therefore the strategy that is adopted here was to approximate a stream function for flow around the wave, calculate velocities from this, and numerically integrate over the external portion of the control volume to determine the ratio of external energy to internal energy for a deep-water wave. The analysis was done by approximating the wave using a 2:1 Rankine oval and calculating the increase in flow energy outside the oval above that of an undisturbed flow. Details of the procedure are contained in Appendix 9. The result of the analysis indicated that over a wide range of wave amplitudes and celerities, the external wave energy was calculated as approximately 53% of the internal wave energy, implying a total kinetic wave energy of:

$$KE_{total} = \frac{1}{2}(1.53)\rho_2 \pi a \lambda w c^2 \tag{8.11}$$

8.3.1.2 Potential Energy

The potential energy of a second mode wave may be approximated by calculating the difference between the potential energies of a control volume with and without the wave present. In Figure 8.6 the top half of two such control volumes are shown. The wave is approximated by an ellipse with a semi-major axis of λ and a semi-minor axis of a, and density interfaces are assumed to be sharp (i.e. representing the large-amplitude limit of $a/h >> 1$). The lower edge of each control volume corresponds to an elevation datum of zero, and the height of each control volume was arbitrarily set to $4a$ (any value greater than a would be suitable).

The potential energy of the control volume without the wave, labelled (1) in Figure 8.6, is easily shown to be:

$$PE_1 = mgh = (\rho_1 \cdot 4a \cdot 2\lambda \cdot w)(g)(2a) = 16\rho_1 g w \lambda a^2 \tag{8.12}$$

where h is the elevation of the centre of gravity of the system above the datum. The potential energy within the wave, labelled (2) in Figure 8.6, is calculated to be:

$$PE_2 = \left(\rho_2 \cdot \frac{\pi a \lambda}{2} \cdot w\right)(g)\left(\frac{4a}{3\pi}\right) = \frac{2}{3}\rho_2 g w \lambda a^2 \qquad (8.13)$$

It follows that the potential energy outside the wave, labelled (3) in Figure 8.6, is:

$$PE_3 = \frac{46}{3}\rho_1 g w \lambda a^2 \qquad (8.14)$$

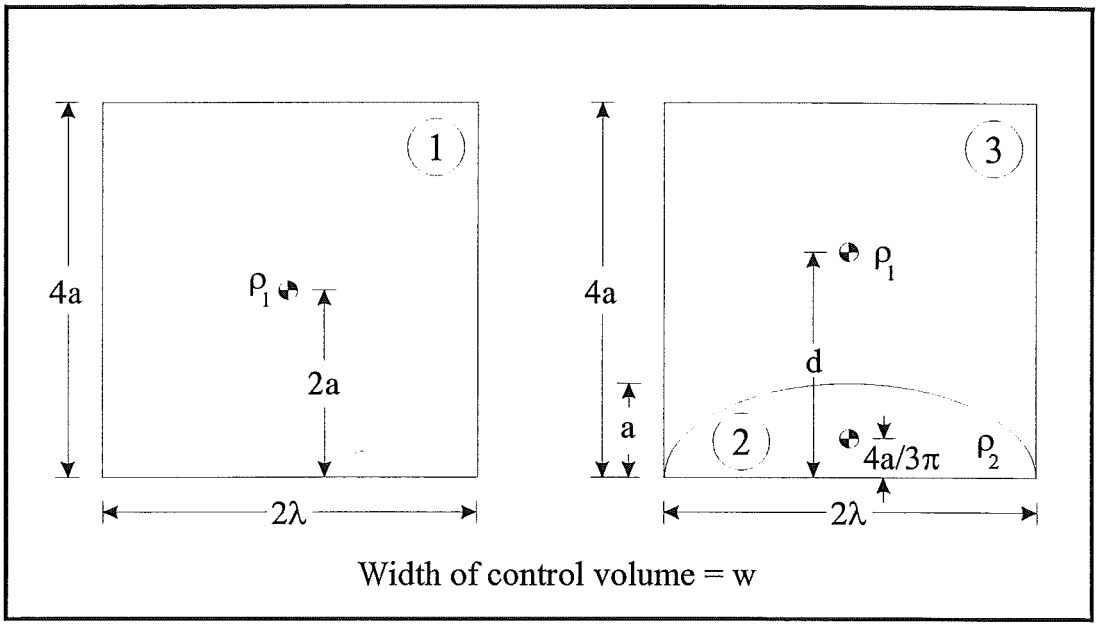

Figure 8.6 - Derivation of wave potential energy

The excess potential energy due to the presence of the wave is then:

$$PE = PE_3 + PE_2 - PE_1 = \frac{2}{3}(\rho_2 - \rho_1) g w \lambda a^2 = \frac{1}{3}\Delta\rho g w \lambda a^2 \qquad (8.15)$$

Here $\Delta\rho = \rho_3 - \rho_1$ and it is assumed that ρ_2 lies midway between ρ_1 and ρ_3. Recognising that the preceding derivation was done for only the upper half of the wave leads to the following expression for the full potential energy of the wave:

$$PE = \frac{2}{3}\Delta\rho g w \lambda a^2 \qquad (8.16)$$

8.3.1.3 Total Energy

The total energy of a second mode wave may then be expressed by combining Equations 8.11 and 8.16:

$$E = w\lambda\left(0.765\,\pi\rho_2\,a\,c^2 + \frac{2}{3}\Delta\rho\,g\,a^2\right) \tag{8.17}$$

At this point it may be recognised that $\rho_2 = \Delta\rho/2\omega$, and that for large amplitude deep water waves, the wave celerity expression from Chapter 6 (Equation 6.53) may be rearranged to show that:

$$c = \frac{4}{3}c_0\sqrt{\frac{a}{h}} \quad \text{where} \quad c_0 = \sqrt{\frac{g\omega h}{2}}; \quad \text{thus} \quad c^2 = \frac{8}{9}g\omega a \tag{8.18}$$

Substitution of Equation 8.18 into Equation 8.17 yields the following equation, which may be compared to the proportional relationship in Equation 8.1:

$$E = 1.735\,w\,g\,\Delta\rho\,\lambda\,a^2 \tag{8.19}$$

Figures 8.7a-b show the total wave energy (calculated with Equation 8.19) decay curves from the present study, while those from Stamp & Jacka (1995) (also calculated with Equation 8.19, using raw data contained in Appendix 3) are shown in Figure 8.7c. The data have been separated into three figures for clarity, due to the large range in wave energies observed. All of the data sets appear to be fitted well by the quadratic polynomial regression curves which are included on the plots. The equations of these curves will be differentiated with respect to x to provide the first estimate of wave energy decay rate, dE/dx, for comparison in Section 8.3.4. Error bars have been calculated for the current data based on the error analysis presented in Appendix 12.

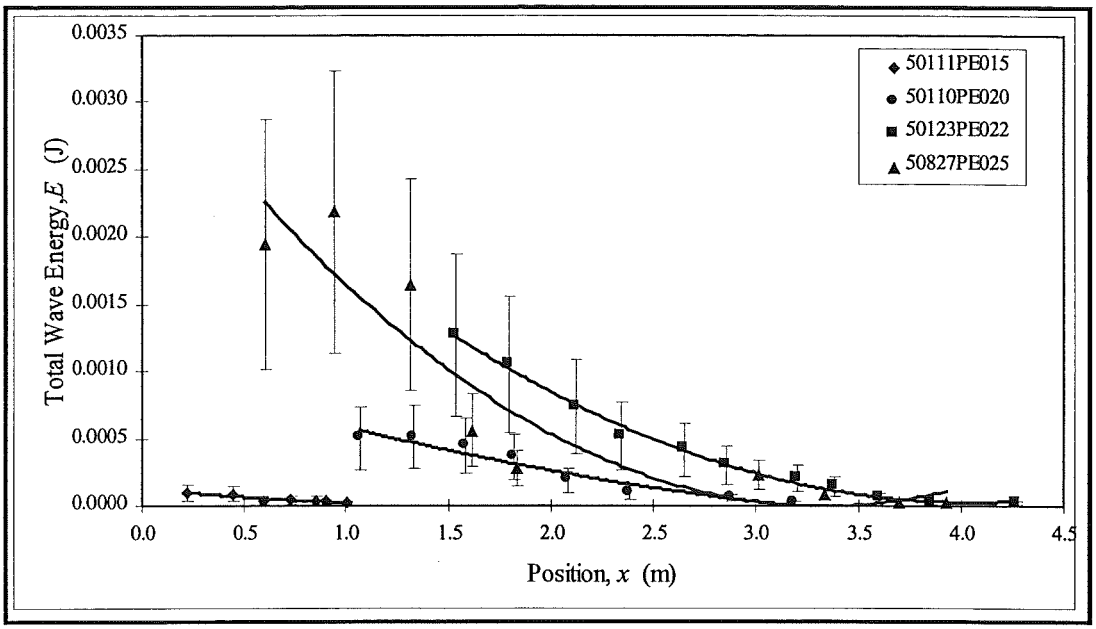

Figure 8.7a - Total wave energy decay curves from present study

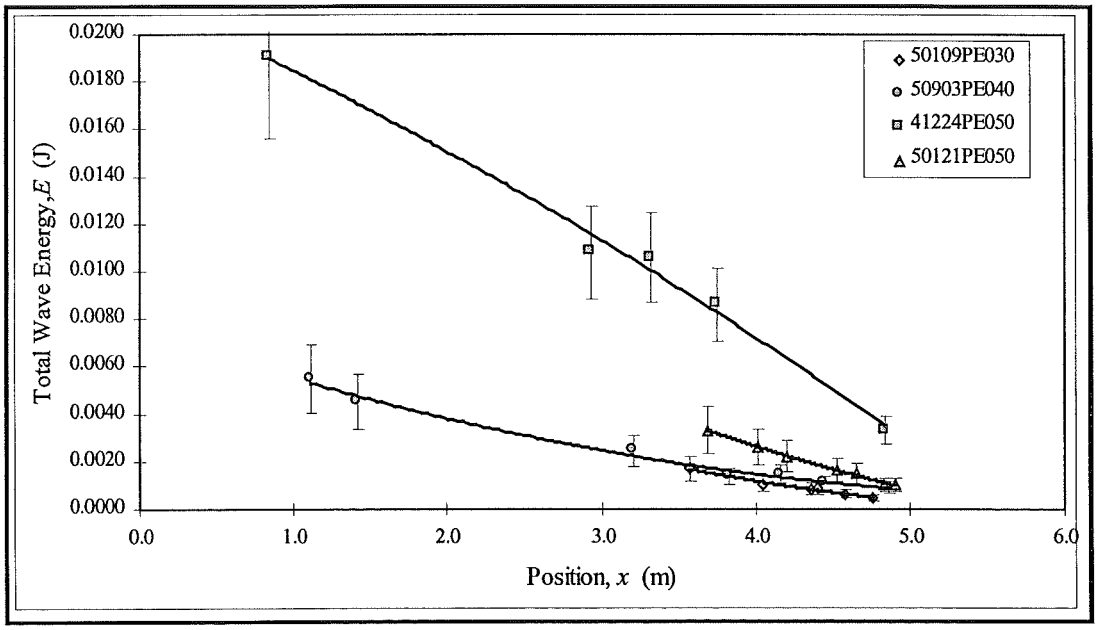

Figure 8.7b - Total wave energy decay curves from present study

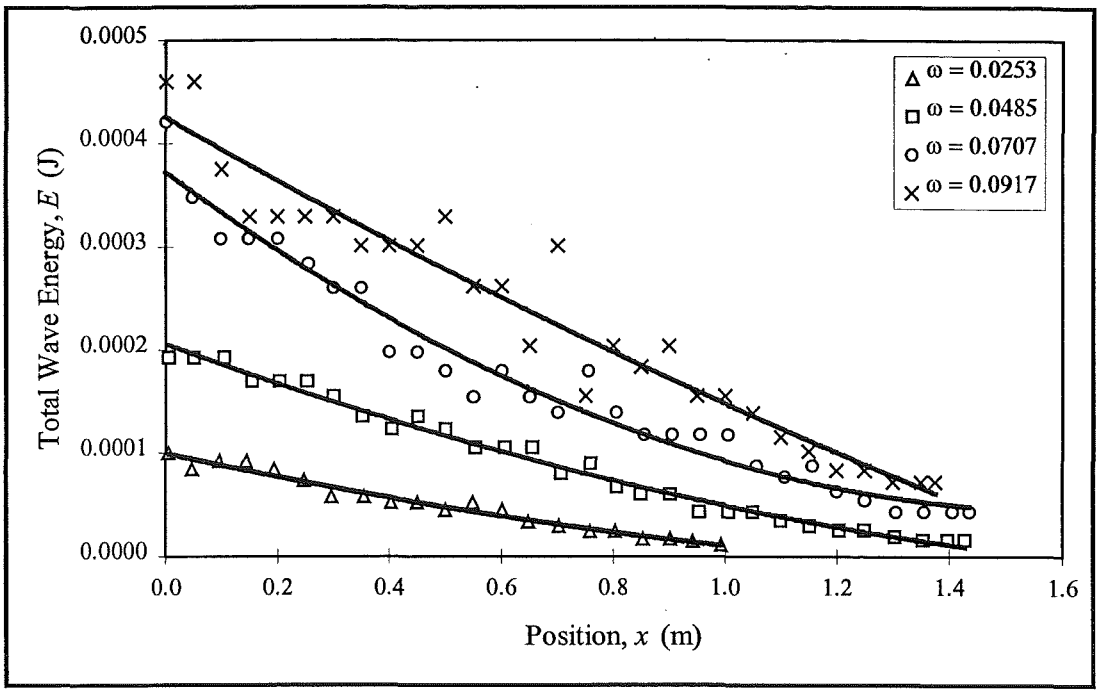

Figure 8.7c - Total wave energy decay curves from Stamp & Jacka (1995)

8.3.2 Differentiation of Energy Equation

The equation for total wave energy (Equation 8.19) may also be differentiated with respect to x to provide another estimate of the wave energy decay rate, dE/dx. It is first necessary to replace the wavelength, λ, with the empirical relationship from Equation 6.9, which yields:

$$E = 1.735\, w\, g\, \Delta\rho\, \left(0.96h + 1.98a\right) a^2 \tag{8.20}$$

Differentiating Equation 8.20 with respect to x produces:

$$\frac{dE}{dx} = 1.735\, w\, g\, \Delta\rho\, h^2 \left(1.92\left(\frac{a}{h}\right) + 5.94\left(\frac{a}{h}\right)^2\right) \frac{da}{dx} \tag{8.21}$$

This equation should provide a more direct estimate of wave energy decay rate, and is likely to provide a greater degree of accuracy than the method of the previous section, especially in the case of the curve fits of Figure 8.7a which in some cases exhibit a "ski jump" at their lower end. These second estimates of dE/dx will be computed for comparison in Section 8.3.4.

8.3.3 Momentum Analysis

In this section, the conservation of momentum equation will be applied to the control volume defined by the large amplitude wave in an attempt to relate the amplitude decay rate and the energy decay rate. The analysis considers a control volume (illustrated in Figure 8.8) which surrounds the interior portion of a large amplitude wave. It accounts for a non-inertial (accelerating) reference frame, a deformable control volume and a net flux out of the wave.

The flow is assumed to be two dimensional, resulting in the following formulation for conservation of momentum per unit width in the x-direction (White, 1986):

$$\frac{F_x}{w} - \iint_{c.a.} \rho \frac{dV_f}{dt} dA = \frac{d}{dt} \iint_{c.a.} V_x \rho \, dA + \int_{c.l.} V_f \rho \left(V_{rx} \cdot n\right) ds \qquad (8.22)$$

net force on wave — noninertial reference frame — deformable control volume — flux term

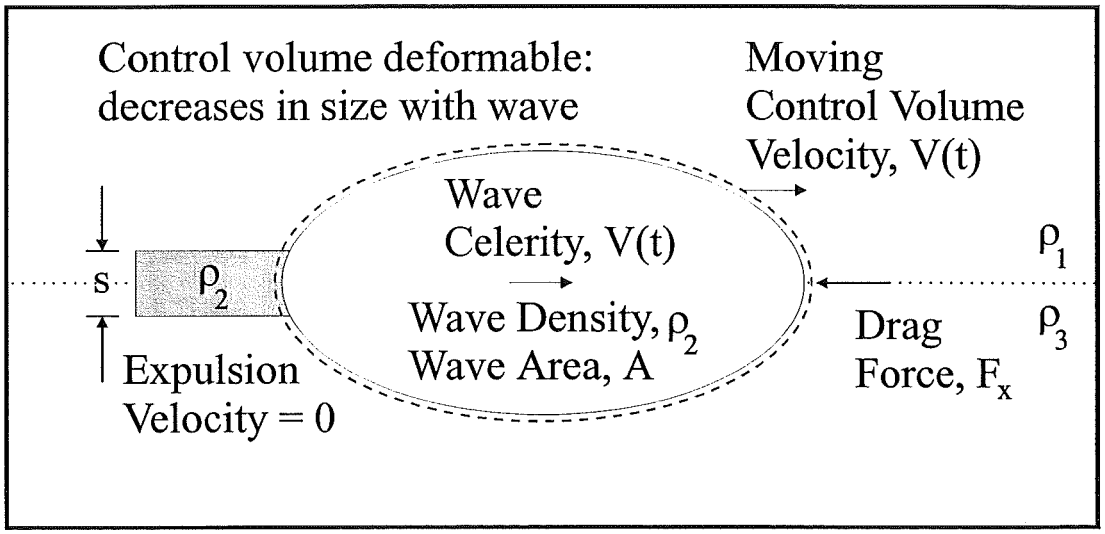

Figure 8.8 - Diagram for momentum analysis; all velocities are shown relative to stationary axes

In Equation 8.22, F_X represents the net horizontal force acting on the wave. This is primarily a drag force, acting in opposition to the wave motion, though there is a small contribution from hydrostatic pressure acting in the direction of wave motion due to the mixed region behind the wave. The drag force includes both form and

friction drag. The velocity terms in Equation 8.22 are related to experimentally measured wave celerities in the following way:

$$\begin{aligned} V_f &= \text{reference frame velocity} = \text{wave celerity} = c \\ V_x &= \text{control volume velocity } w.\text{r.t. reference frame} = 0 \\ V_{rx} &= \text{relative flux velocity} = \text{wave celerity} = c \\ \frac{dV_f}{dt} &= \text{reference frame acceleration} = \frac{dx}{dt}\frac{dV_f}{dx} = c\frac{dc}{dx} \end{aligned} \tag{8.23}$$

This allows Equation 8.22 to be expressed as:

$$\underbrace{\frac{F_x}{w}}_{\text{net force on wave}} = \underbrace{\iint_{c.a.} \rho\, c \frac{dc}{dx}\, dA}_{\text{noninertial reference frame}} + \underbrace{\int_{\text{c.l.}} c\rho\,(c \cdot n)\, ds}_{\text{flux term}} \tag{8.24}$$

In Equation 8.24, the double integrals are taken over the area of the wave (or volume, in three dimensions) while the single integral is taken over the control surface. The terms accounting for the noninertial reference frame and fluid flux will now be examined in turn to relate them to the wave amplitude decay rate and other measureable parameters. Note that the deformable control volume term drops out due to the fact that the control volume velocity with respect to the moving frame of reference is zero, as stated in Equation 8.23.

In the work that follows, empirical relations for aspect ratio (Equation 6.5) and wave celerity (Equation 6.48) will be used, with the former being substituted into an equation describing the area of an ellipse:

$$\begin{aligned} A &= \text{wave area} = \pi a\lambda = \pi\left(0.96ha + 1.98a^2\right) \\ dA &= \pi\left(0.96h + 3.96a\right) da \end{aligned} \tag{8.25}$$

$$c = \frac{4}{3}c_0\sqrt{\frac{a}{h}} \quad \text{where} \quad c_0 = \sqrt{\frac{g\omega h}{2}} \quad \text{for deep water waves} \tag{8.26}$$

8.3.3.1 *Noninertial Reference Frame*

The momentum equation term for noninertial reference frame accounts for the fact that the control volume (or in this two-dimensional formulation, control area) is not inertial (i.e. it is not at rest or moving at a constant velocity):

$$\iint_{c.a.} \rho c \frac{dc}{dx} dA \tag{8.27}$$

If it is assumed that the fluid density is constant within the control area, and the expression for dA from Equation 8.25 is substituted in, this may be expressed as:

$$\pi \rho \int_0^a c \frac{dc}{dx} \left(0.96h\, da + 3.96a\, da\right) \tag{8.28}$$

Inserting the expression for wave celerity from Equation 8.26 allows this to be rearranged to yield:

$$\pi \rho \int_0^a \frac{4}{3} c_0 \sqrt{\frac{a}{h}} \frac{d}{dx} \left(\frac{4}{3} c_0 \sqrt{\frac{a}{h}}\right) \left(0.96h\, da + 3.96a\, da\right) \tag{8.29}$$

This may then be rearranged to show that:

$$\frac{16}{9} \pi \frac{\rho c_0^2}{h} \int_0^a a^{1/2} \frac{da^{1/2}}{dx} \left(0.96h\, da + 3.96a\, da\right) \tag{8.30}$$

Recognising that $da^n/dx = na^{n-1}da/dx$ and assuming that da/dx is a constant produces:

$$\frac{8}{9} \pi \frac{\rho c_0^2}{h} \frac{da}{dx} \int_0^a \left(0.96h\, da + 3.96a\, da\right) \tag{8.31}$$

Performing the integration, inserting the expression for c_0 from Equation 8.26, recognising that $\rho = \Delta\rho/2\omega$, and rearranging yields:

$$\frac{2}{9} \pi g \Delta\rho h^2 \left(0.96\left(\frac{a}{h}\right) + 1.98\left(\frac{a}{h}\right)^2\right) \frac{da}{dx} \tag{8.32}$$

Equation 8.32 may then be substituted into the conservation of momentum equation (Equation 8.27).

8.3.3.2 Fluid Flux

The flux term of the conservation of momentum equation takes into account the loss of fluid from the control volume across the control surface (or in this two-dimensional formulation, control line):

$$\int_{c.l.} c\rho(c \cdot n)ds \tag{8.33}$$

It is important to note that this analysis considers the net flux across the control surface by neglecting any entrainment by the wave (as discussed in Chapter 7) and assuming that any reduction in the area of the wave is accounted for by a single outflow in the lee of the wave, as illustrated in Figure 8.9.

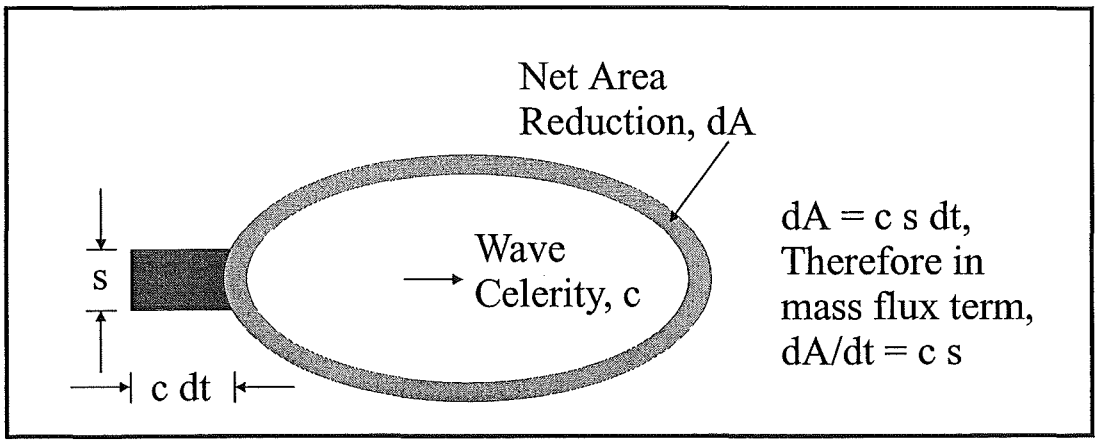

Figure 8.9 - Calculation of magnitude of s in flux term

If it is assumed that fluid density and velocity are constant over the control line, and that fluid is expelled in the negative x-direction, Equation 8.33 may be rewritten as:

$$\rho c^2 \int_{c.l.} ds = \rho c^2 s \tag{8.34}$$

In analysing this term it is necessary to make an assumption concerning the depth over which fluid is expelled from the control volume. If it is assumed that fluid

exiting the control volume loses all momentum, then it is apparent (see Figure 8.9) that:

$$\frac{dA}{dt} = c \cdot s \quad \text{or} \quad s = \frac{1}{c}\frac{dA}{dt} = \frac{dA}{dx} \tag{8.35}$$

Equation 8.35 may then be rewritten as:

$$\rho c^2 \frac{dA}{dx} = \pi \rho c^2 \left(0.96h + 3.96a\right) \frac{da}{dx} \tag{8.36}$$

With the substitution of the wave celerity expressions from Equation 8.26, recognising that $\rho = \Delta\rho/2\omega$, this yields:

$$\frac{4}{9}\pi\, g\Delta\rho h^2 \left(0.96\left(\frac{a}{h}\right) + 3.96\left(\frac{a}{h}\right)^2\right) \frac{da}{dx} \tag{8.37}$$

Equation 8.37 may then be substituted into the conservation of momentum equation (Equation 8.27).

8.3.3.3 Combining Terms

When the component expressions for noninertial reference frame (Equation 8.32) and fluid flux (Equation 8.37) are examined, it is readily apparent that both terms have a similar form. When they are substituted into the equation for conservation of momentum (Equation 8.27), the following expression results:

$$\frac{dE}{dx} = F_x = \frac{2}{9}\pi\, w g\Delta\rho h^2 \left(2.88\left(\frac{a}{h}\right) + 9.90\left(\frac{a}{h}\right)^2\right) \frac{da}{dx} \tag{8.38}$$

Before Equation 8.38 is put to use, it must be modified to account for fluid outside of the control volume which is displaced due to the movement of fluid within the control volume. Vallentine (1959) noted that for the case of flow about a solid cylinder (analogous to the present case) it is necessary "to consider what is known as the virtual mass of a solid moving through a fluid. The total kinetic energy of the solid, and of the fluid set in motion by it, can be regarded as the kinetic energy of a

solid of the same dimensions, but of increased mass, the increase being known as the 'virtual mass'." In applications of Newton's second law, the virtual mass is equal to the sum of the actual mass and an added mass. The added mass is equal to ρkV, where ρ is the density of the surrounding fluid, V the volume of the body and k a quantity known as the added mass coefficient. The added mass coefficient varies with the body shape, orientation and surroundings, and for the case of a 2:1 elliptical cylinder in deep water, $k = 0.500$ (Robertson, 1965). In the present case, the Boussinesq approximation sets the internal and external densities equal, and the coefficient of Equation 8.38 may be increased by 50% to produce:

$$\frac{dE}{dx} = F_x = \frac{3}{9}\pi\, w\, g\Delta\rho\, h^2 \left(2.88\left(\frac{a}{h}\right) + 9.90\left(\frac{a}{h}\right)^2\right) \frac{da}{dx} \qquad (8.39)$$

The value of $k = 0.500$ for the added mass coefficient is consistent with the earlier finding (Section 8.3.1) that the excess kinetic energy of fluid set in motion by the passage of the wave is approximately 50% of the kinetic energy of the fluid within the wave.

These third, completely independent estimates of *dE/dx* will be computed for comparison in Section 8.3.4. It should be noted that for a very large amplitude wave (i.e. $a/h >> 1$), the contribution of the noninertial reference frame term amounts to approximately 1/5 of the total value of *dE/dx*, with the flux term contributing approximately 4/5.

8.3.4 Comparison of Energy Decay Expressions

The analyses of the energy (Section 8.3.2) and momentum (Section 8.3.3) equations yielded two independent equations relating the wave amplitude, amplitude decay rate and energy decay rate. The results (Equations 8.21 and 8.39) are strikingly similar in form and with some rearrangement of coefficients may be compared directly:

$$\text{(was 8.21)} \quad \frac{dE}{dx} = w\, g\, \Delta\rho\, h^2 \left(2.71\left(\frac{a}{h}\right) + 10.67\left(\frac{a}{h}\right)^2\right) \frac{da}{dx} \qquad (8.40)$$

$$\text{(was 8.39)} \qquad \frac{dE}{dx} = w g \Delta\rho \, h^2 \left(3.02 \left(\frac{a}{h} \right) + 10.37 \left(\frac{a}{h} \right)^2 \right) \frac{da}{dx} \qquad (8.41)$$

It is apparent that the second term within the brackets in both equations will dominate for any values of *a/h* above unity (in fact, these equations should not be used below this value due to the assumptions involved in the derivations). Over the entire range of large-amplitude waves, it appears that Equation 8.41 (momentum analysis) will produce energy decay rates less than 3% different from those from Equation 8.40 (energy analysis).

The experimental energy decay rates, *dE/dx*, resulting from the curve fits to Equation 8.19 will now be compared to those calculated with Equation 8.40. This should indicate whether the derivation (including the substitution of relations) was done properly and provides meaningful results. Figure 8.10 shows a comparison of these values.

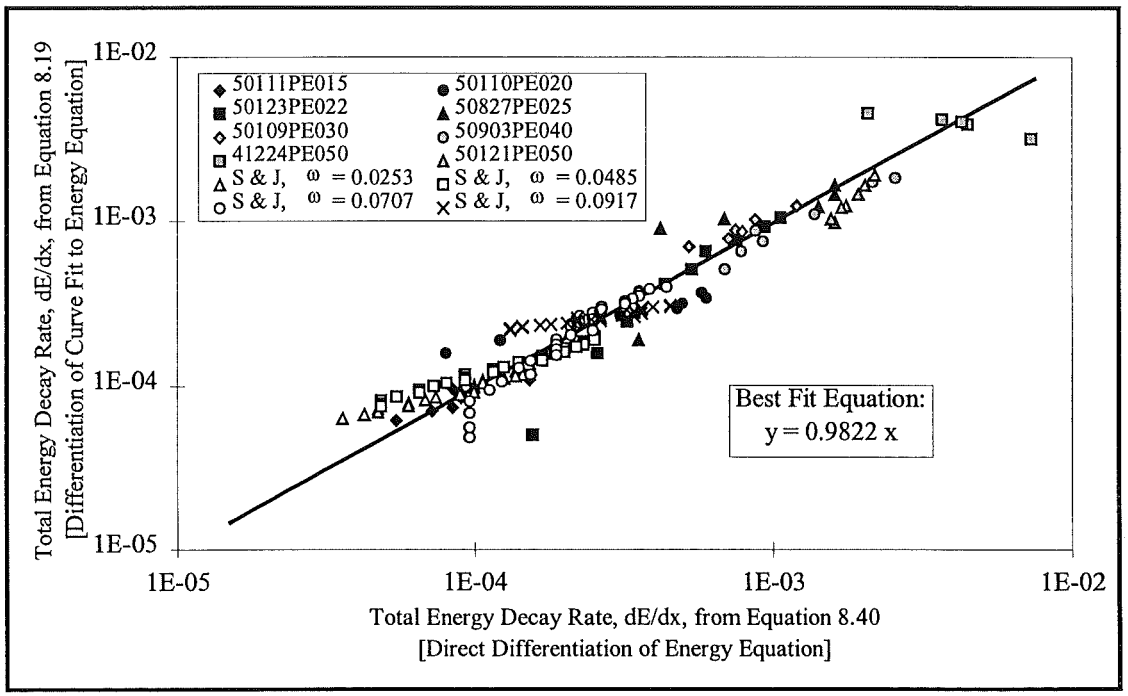

Figure 8.10 - Comparison of energy decay rates from Equations 8.19 and 8.40

Figure 8.10, in which the experimental energy decay rates span two orders of magnitude, confirms the accuracy of the derivation which produced Equation 8.40. The comparision of the two methods of calculating *dE/dx* shows a 0.98:1 slope with

a correlation coefficient of $r^2 = 0.943$. It should be noted that the first and last data points from Run 41224PE050 were discarded in computing these values, as they were thought to exert an undue influence on the regression. With these two values included, the slope changes to 0.83:1 and the correlation coefficient to $r^2 = 0.764$.

The work done in this section provides estimates of wave energy and energy decay rates which may be used in confidence when comparing the retarding forces which are responsible for the wave decay. These forces will be examined in Section 8.4.

8.4 Energy Analysis

In this chapter, the experimentally measured wave energy decay rates, derived by the methods outlined in Section 8.3, will be compared to estimates of decay rates from possible decay mechanisms. Energy losses from wave radiation and turbulent mixing will be examined first. Then losses due to wall shear will be quantified. Then other drag forces (both form drag and interfacial shear) will be examined to see if the energy decay rate might be described by using a drag coefficient.

8.4.1 Wave Radiation

The method of Stamp & Jacka (1995) will be followed in the analysis of this decay mechanism, though the new energy relationships which have been developed here will be used. When Equation 8.20 is taken in the limit of $a/h \gg 1$, this produces the following equation which may be compared to Equation 8.2:

$$E \propto wg\Delta\rho a^3 \tag{8.42}$$

Equation 8.42 may be differentiated with respect to time, t, to show that:

$$\frac{dE}{dt} \propto w\, g\Delta\rho\, a^2 \frac{da}{dt} = w\, g\Delta\rho\, c\, a^2 \frac{da}{dx} \tag{8.43}$$

Equation 8.43 may be equated to Equation 8.4, which describes the temporal energy decay rate as a function of the first mode wave characteristics, to yield:

$$\frac{da}{dx} \propto \frac{\xi^2}{a^2} \tag{8.44}$$

Comparing Equation 8.44 to Equation 8.5 shows similarities between the equations, with the RHS of the latter equal to the RHS of the former divided by the dimensionless second mode wave amplitude, a/h. A scaling estimate for the spatial energy decay rate, *dE/dx* can be obtained by substituting Equation 8.44 into Equation 8.21. When this is taken in the limit $a/h >> 1$, the following results:

$$\frac{dE}{dx} \propto wg\Delta\rho\,\xi^2 \tag{8.45}$$

Equation 8.45 indicates that, if the first mode wave amplitude is constant (as indicated by Stamp & Jacka (1995), the energy attenuation rate should also remain constant over the course of an experimental run. This was not the case, as it is obvious from Equation 8.21 that if *da/dx* is a constant, *dE/dx* must vary with a^2. The implication is that wave radiation cannot be responsible for a significant portion of second mode wave decay.

8.4.2 Turbulent Mixing

Stamp & Jacka (1995) concluded that mixing due to shear instability could not explain the variation in amplitude decay rate, *da/dx*, with densimetric factor, ω, (Figure 8.2) as all waves exhibited a constant Richardson number. This number was taken as being representative of the susceptibility of the wave to shear instability, and was calculated using the infintesimal long wave celerity, c_0, as the velocity scale. This conclusion is in conflict with observations made during the course of this study, where large, fast waves were seen to exhibit more shear instability than smaller, slower ones. A more representative Richardson number would make use of the local wave celerity as shown in the following equation:

$$J \propto \frac{g\,\Delta\rho\,h}{\rho c^2} = \frac{2\,g\,\omega\,h}{c^2} = \frac{4\,c_0^2}{c^2} \tag{8.46}$$

The RHS of Equation 8.46 is seen to be equal to the square of the inverse of the propagation celerity equation of Equation 6.48, and thus the local Richardson number may be expressed in terms of the dimensionless amplitude as:

$$J \propto \frac{9}{4}\frac{h}{a} \tag{8.47}$$

This indicates that the Richardson number, J, varies with the inverse of the dimensionless wave amplitude. It does not, however, account for the variation in amplitude decay rate with densimetric factor.

The question of whether turbulent mixing represents a significant component of wave decay might be examined by comparing the wave energy decay rate, dE/dx, to the potential energy increase in the water column caused by interfacial thickening due to wave passage. No measurements of interfacial thickening were made in this study, but Stamp & Jacka (1995) provide data which may be subjected to such an analysis. To determine the increase in potential energy in the water column (equal to the loss in kinetic energy from the wave due to mixing) due to the passage of a wave, it is necessary to know the depths and densities of the two layers of fluid and the half-thickness of the interface, h, before and after the passage of the wave.

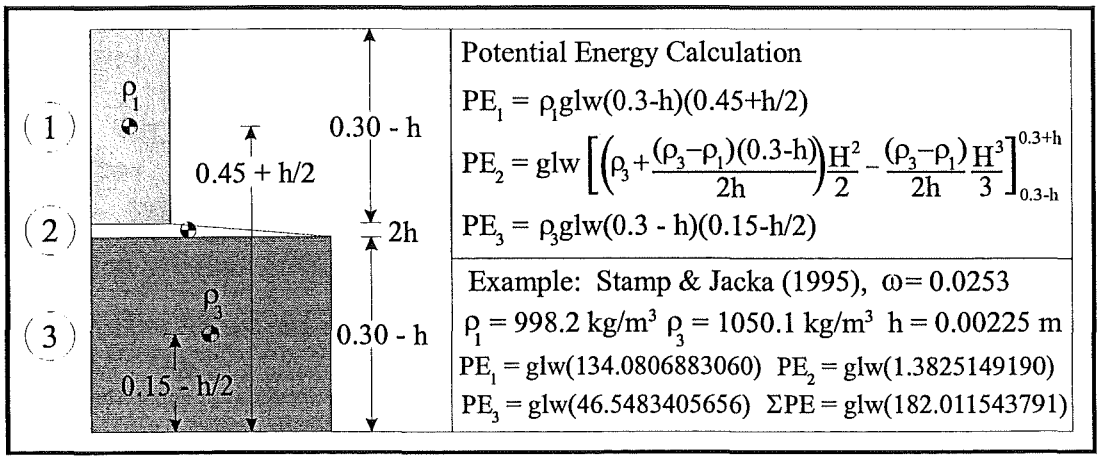

Figure 8.11 - Sample potential energy calculation

The potential energy of the water column may then be calculated by the procedure shown in Figure 8.11, in which it is assumed that the upper and lower fluid densities are constant and there is a linear variation of density in the interfacial region. In the

potential energy calculations of Figure 8.11; l and w represent the height and width, respectively, of the water column.

Values of relevant parameters and the resulting potential energies from the experiments of Stamp & Jacka (1995) are given in Table 8.1. Here ρ_1 and ρ_3 are the densities of the upper and lower layers, respectively, while h and h_* represent the interfacial half-thicknesses before and after the passage of the wave, respectively.

Table 8.1 - Potential energy calculations from raw data of Stamp & Jacka (1995)

ω	0.0253	0.0485	0.0707	0.0917
ρ_1 (kg/m^3)	998.2	998.2	998.2	998.2
ρ_3 (kg/m^3)	1050.1	1109.9	1150.0	1199.7
h (m)	0.00225	0.00275	0.00250	0.00250
h_* (m)	0.00300	0.00325	0.00290	0.00300
$\Sigma PE/gwl$ (kg/m)	182.0115438	184.7026408	186.5071581	188.7437099
$\Sigma PE*/gwl$ (kg/m)	182.0115779	184.7026966	186.5072128	188.7438023
$\Delta PE/gwl$ (kg/m)	3.41×10^{-5}	5.58×10^{-5}	5.46×10^{-5}	9.24×10^{-5}

In estimating the portion of wave energy decay rate, dE/dx_{mixing}, attributable to turbulent mixing, several problems now present themselves. Three questions arise about the value of post-passage interfacial half-thicknesses, h_*, presented by Stamp & Jacka (1995).

Firstly, if larger waves cause more turbulent mixing, the rate of energy extracted from the wave should vary with wave amplitude, resulting in a variation in the value of h_* along the length of the flume. Of course, hydrostatic forces would in time produce an equilibrium value, but by this time the action of other thickening mechanisms would make it impossible to determine the proper value. To determine an accurate value for dE/dx_{mixing}, it is necessary for the density profile reading to be taken after the wave has passed and its wake has collapsed to an equilibrium state, but before any interfacial thickening occurs due to the advance of the gravity intrusion following the wave. To determine the ratio of dE/dx_{mixing} to dE/dx it is necessary to know the wave amplitude at the mixing point. Stamp & Jacka (1995)

provide no information on the temporal or spatial location of the post-passage density profile.

Secondly, not all of the interfacial thickening occurs due to turbulent mixing. Some portion of it must be attributed to the net expulsion of fluid from the wave. This may be easily calculated as the thickening of the interface due to expulsion, Δh_{exp}, must be equal to the rate of change of area of the interior section of the wave, dA/dx, and from Equation 8.25 it may be shown that:

$$dA = \pi(0.96h + 3.96a)\, da \tag{8.48}$$

Estimated values for interfacial thickening due to fluid expulsion, resulting from the application of Equation 8.48 to the data of Stamp & Jacka (1995) are found in Table 8.2.

Thirdly, with very thin interfaces, molecular diffusion can be responsible for significant increases in interfacial thickness. Recalling the discussion of interfacial thickening in Section 4.2, Equation 4.7 may be used to show that for an interface with a half-thickness, h, of 0.00250 m, it takes only 5 minutes to increase in thickness to 0.00275 m and 10.5 minutes to reach 0.00300 m. With interfacial half-thicknesses on the scale of those observed by Stamp & Jacka (1995), relatively small lapses in time between the measurement of the pre- and post-passage density profiles could result in significant thickening due to molecular diffusion.

Table 8.2 contains estimates of the rate of extraction of energy from the wave due to turbulent mixing, based on the data of Stamp & Jacka (1995). It is assumed that density profiles were taken so as to minimise the effects of molecular diffusion, and that measurements were taken of the wave at its maximum amplitude. The values of $\Delta PE/gwl$ from Table 8.1 have been multiplied by gw to produce a value which might be compared directly with the wave energy decay rate, dE/dx. The estimate for dE/dx_{mixing} is equal to the total $\Delta PE/l$ less that attributable to expulsion of fluid from the wave.

Table 8.2 - Wave energy decay due to turbulent mixing

ω	0.0253	0.0485	0.0707	0.0917
dE/dx (J/m)	15.3×10^{-5}	25.1×10^{-5}	43.7×10^{-5}	45.1×10^{-5}
$\Delta PE/l$ (J/m)	5.0×10^{-5}	8.2×10^{-5}	8.0×10^{-5}	13.6×10^{-5}
Δh_{exp} (m)	0.000175	0.000145	0.000150	0.000125
$\Delta PE/l_{exp}$ (J/m)	1.0×10^{-5}	2.2×10^{-5}	2.9×10^{-5}	3.2×10^{-5}
dE/dx_{mixing} (J/m)	4.0×10^{-5}	6.0×10^{-5}	5.1×10^{-5}	10.4×10^{-5}
dE/dx_{mixing} / dE/dx	0.26	0.24	0.12	0.23

From the ratio of dE/dx_{mixing} to dE/dx shown in Table 8.2, it appears that turbulent mixing may be responsible for a significant portion of wave decay. However, the assumptions involved in the calculation of these values mean that without further experimentation, no definite judgment as to the proportion of total wave decay due to turbulent mixing may be made.

8.4.3 Wall Shear

In an attempt to more closely examine wave decay due to viscous shear forces at the flume walls, the Blasius solution (White, 1986) for shear on a flat plate in a laminar boundary layer will be adapted to the situation present in this study.

In this derivation, the contact area of the wave on the flume wall is assumed to be elliptical in shape, with the semi-major axis equal to the wavelength, λ, and the semi-minor axis equal to the wave amplitude, a. The wave is assumed to be symmetrical about its centreline, and the upper half is approximated by an arbitrary number (in this case, 5) of horizontal strips. The free stream velocity is assumed to be equal to the wave celerity. The drag force contribution of each strip is then computed with the following equation:

$$F_{drag} = C_D \frac{1}{2} \rho \, c^2 \, b \, L \tag{8.49}$$

In Equation 8.49, ρ represents the density of the fluid within the wave, c the wave celerity, b the width of a component strip and L its length. C_D is a drag coefficient which is a function of a Reynolds number based on the wave celerity, fluid viscosity and the length of the strip. The derivation for the drag force applied by one wall of the flume is shown in Figure 8.12.

This derivation implies that the total drag force due to both walls of the flume is approximately:

$$F_{wall} = \frac{3.31\rho\, c^2 a\lambda}{\mathrm{Re}_\lambda^{1/2}} \quad \text{where} \quad \mathrm{Re}_\lambda^{1/2} = \frac{c\lambda}{\nu} \tag{8.50}$$

Drag forces computed with Equation 8.50 may then be compared to the total energy decay rate computed with Equation 8.40 to determine the component of the total energy decay rate that is attributable to viscous forces at the walls of the flume. The experimental data used to examine this relationship are shown in Figure 8.13.

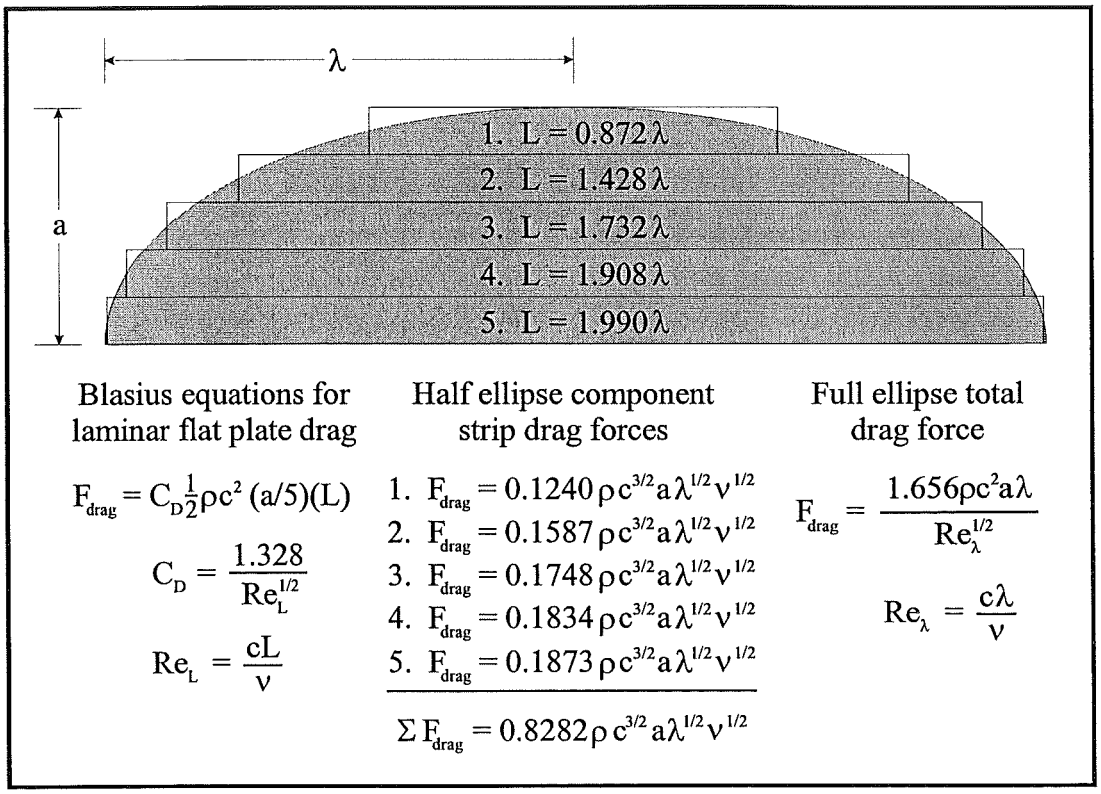

Figure 8.12 - Derivation of laminar drag on a flat ellipse

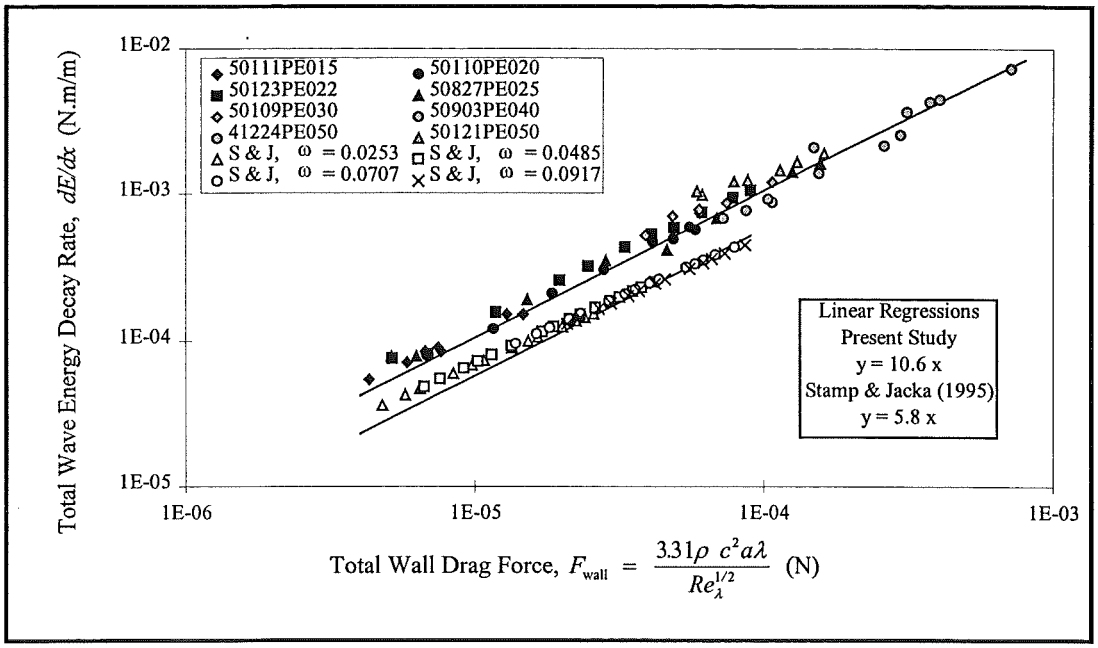

Figure 8.13 - Wave energy decay rate from Equation 8.40 vs. wall drag force

Several things are made apparent by Figure 8.13. It is obvious that there is a linear relationship between wave energy decay rate, *dE/dx*, and wall drag force. This would indicate that as a given wave decays, wall shear accounts for a constant proportion of the decay. It is also obvious that there is a difference between the wall shear proportions of the present study and of Stamp & Jacka (1995). In the present study, wall shear accounts for slightly more than 9% of the total wave energy decay, while in that of Stamp & Jacka (1995) it accounts for approximately 17% of the decay. This difference is due to the difference in flume widths between the two studies. If the remainder of the decay in the Stamp & Jacka (1995) study is scaled up by a factor equal to the ratio of flume widths between the two studies (5/3 = 0.25 m/0.15 m), the wall shear is predicted to represent 11% of the wave decay, which is consistent with the value of the present study. At any rate, it is apparent that for any reasonably wide channel, the effect of wall shear would be minor compared to that of other decay mechanisms which act along the entire wavefront.

8.4.4 Fluid Drag

In this section, the interfacial drag decay mechanism will be examined by assuming the wave to be a two-dimensional body, and then calculating its drag force (denoted

as fluid drag to distinguish it from wall drag) based on frontal area, $2aw$, celerity, c, and fluid density, ρ:

$$F_{\text{fluid}} = \frac{1}{2} w \rho C_D c^2 (2a) \tag{8.51}$$

This expression for drag force is similar to that of Equation 8.49, with a drag coefficient, C_D, which is estimated for a 2:1 ellipsoid to be on the order of 0.6 (laminar flow) or 0.2 (turbulent flow) for Reynolds numbers ($\text{Re} = 2ac/\nu$) above 10^4 (White, 1986). It must be noted that the drag described by Equation 8.51 includes two components: shear drag along the surface of the wave (the interfacial drag of Section 8.2.4) as well as pressure drag in the lee of the wave where the flow has separated.

If it is assumed that all wave decay not attributable to wall shear is due to fluid drag (including interfacial shear, pressure drag and mixing effects) then the following equation describes the magnitude of the fluid drag:

$$F_{\text{fliud}} = \frac{dE}{dx} - F_{\text{wall}} \tag{8.52}$$

where, due to the inconclusive results of Section 8.4.2, it is convenient to include the effects of turbulent mixing in the calculation of any drag coefficient applied to the decay of these waves. Without making any judgment as to the value of C_D for the time being, it is possible to test the relationship of Equation 8.52 by plotting its RHS against the quantity $w\rho c^2 a$. The experimental data describing this relationship are shown in Figure 8.14.

The arrangement of the data in the logarithmic plot of Figure 8.14, in which the data all follow a trend with a 1:1 slope, indicates that there is a linear relationship between form drag and the portion of the energy decay rate which is not attributable to wall shear. This means that a drag coefficient, C_D, of the sort present in Equation 8.51 may be used to describe the energy decay rate attributable to fluid drag, dE/dx_{fluid}. This drag coefficient appears to be relatively constant over the range of Reynolds numbers observed within an experimental run, since all the points within

a single run tend to lie on a single line. However, because the lines for different runs (with different values of ω) are offset from one another, it appears that C_D varies over the range of densimetric factors, ω.

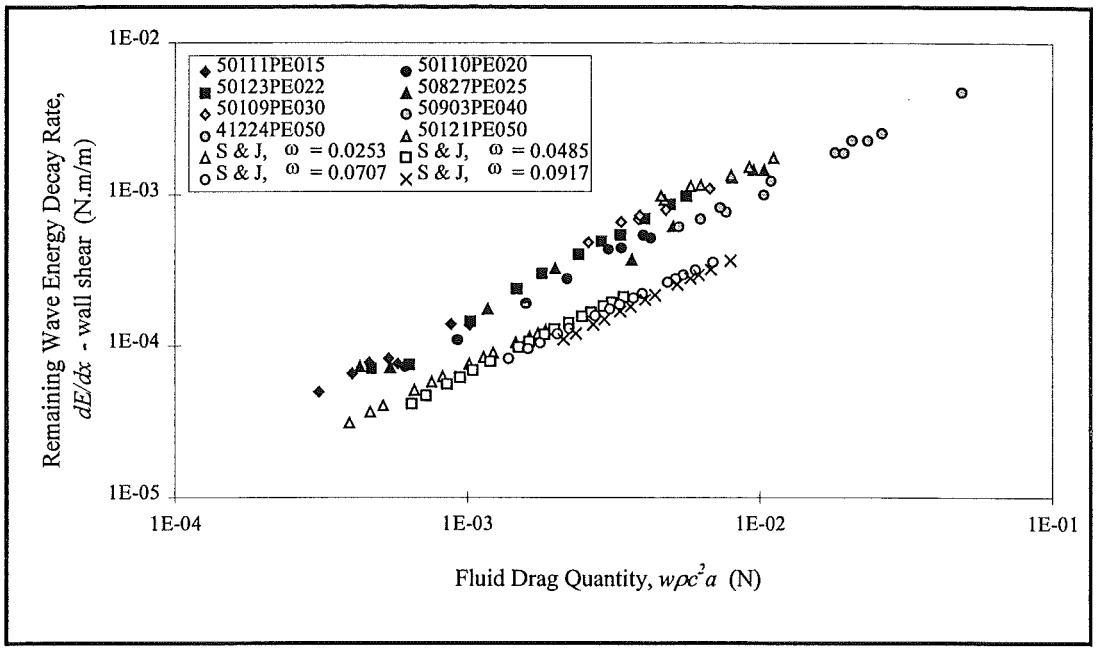

Figure 8.14 - Energy decay not attributable to wall shear vs. fluid drag quantity

The ordering of dE/dx_{fluid} according to densimetric factor, apparent in Figure 8.14, will now be investigated. First, to produce an expression for C_D, Equations 8.40, 8.50 and 8.51 are substituted into Equation 8.52:

$$\frac{1}{2} w\rho C_D c^2 (2a) = gw\Delta\rho h^2 \left(2.71\frac{a}{h} + 10.67\left(\frac{a}{h}\right)^2 \right) \frac{da}{dx} - \frac{3.31\rho c^2 a\lambda}{Re_\lambda^{1/2}} \quad (8.53)$$

Equation 8.53 may then be rearranged to solve for C_D:

$$C_D = \frac{g\Delta\rho h^2}{\rho c^2 a} \left(2.71\frac{a}{h} + 10.67\left(\frac{a}{h}\right)^2 \right) \frac{da}{dx} - \frac{3.31\lambda}{w Re_\lambda^{1/2}} \quad (8.54)$$

Recalling once again that $\Delta\rho/\rho = 2\omega$ and substituting the expression for wave celerity from Equation 8.18 allows Equation 8.54 to be expressed as:

$$C_D = \frac{9}{4}\left(\frac{h}{a}\right)^2 \left(2.71\frac{a}{h} + 10.67\left(\frac{a}{h}\right)^2 \right) \frac{da}{dx} - \frac{3.31\lambda}{w Re_\lambda^{1/2}} \quad (8.55)$$

The values of drag coefficient calculated with Equation 8.55 appear to vary only slightly with Reynolds number ($Re_{2a} = 2ac/\nu$) over the range observed during each experimental run, so the mean was chosen as a representative value. Data from the present study as well as that of Stamp & Jacka (1995) are shown in Table 8.3, where it can be seen that C_D decreases with increasing ω.

When the values of C_D and ω from Table 8.3 are plotted against each other as in Figure 8.15, it is apparent that the relationship between the two resembles that between da/dx and ω shown in Figure 8.2. This is not unexpected, as equating Equation 8.40 and 8.51 and applying the limit of $a/h >> 1$ shows that the drag coefficient and wave amplitude decay rate are proportional to one another (specifically, $C_D = -24\ da/dx$).

Table 8.3 - Calculated Reynolds numbers and drag coefficients

Run	ω	Re_{2a} Range	C_D Range	C_D Mean
50111PE015	0.0053	370 - 160	0.128 - 0.141	0.134
50110PE020	0.0071	960 - 220	0.128 - 0.147	0.133
50123PE022	0.0078	1270 - 190	0.134 - 0.160	0.144
50827PE025	0.0087	1630 - 150	0.132 - 0.152	0.139
50109PE030	0.0106	1330 - 660	0.120 - 0.127	0.124
50903PE040	0.0141	2600 - 930	0.081 - 0.085	0.083
50121PE050	0.0176	1770 - 970	0.104 - 0.108	0.100
41224PE050	0.0176	5050 - 1680	0.099 - 0.103	0.106
Stamp & Jacka	0.0253	600 - 200	0.081 - 0.091	0.085
Stamp & Jacka	0.0485	700 - 200	0.070 - 0.082	0.074
Stamp & Jacka	0.0707	1000 - 300	0.061 - 0.069	0.065
Stamp & Jacka	0.0917	1000 - 400	0.058 - 0.064	0.060

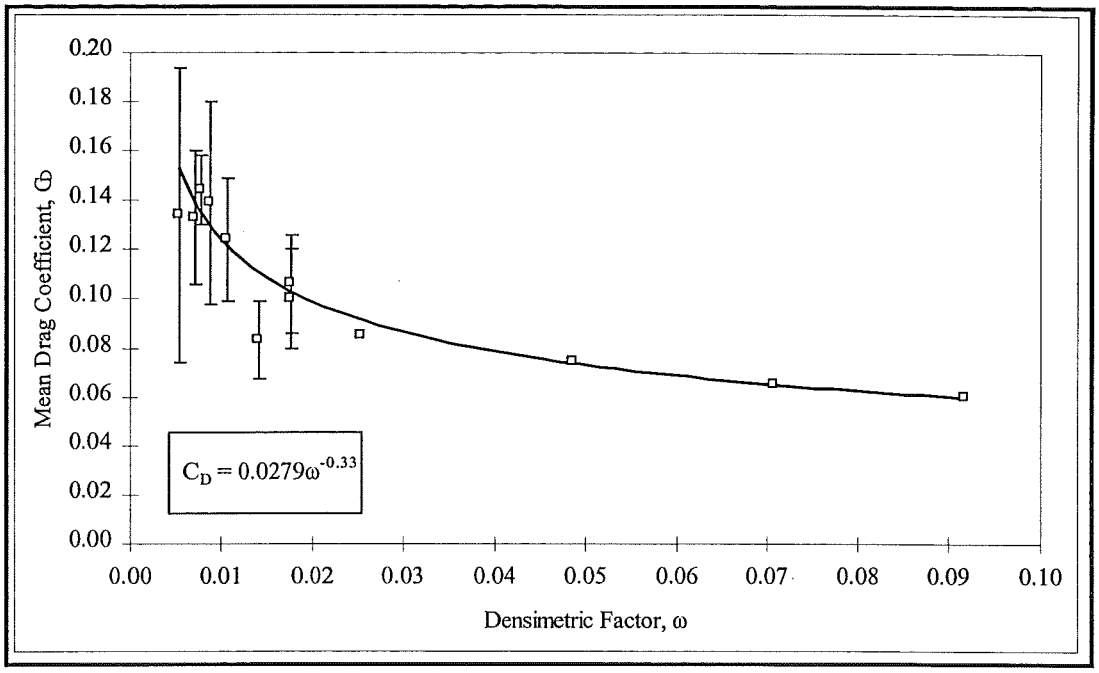

Figure 8.15 - Variation of drag coefficient with densimetric factor

Applying the curve fit shown on Figure 8.15 to Equation 8.51 means that the latter equation may be expressed as:

$$F_{fluid} = C_D w \rho c^2 a, \quad where\ C_D = \frac{0.0248}{\omega^{1/3}} \tag{8.56}$$

As a further check on the analysis, the drag forces computed in Equations 8.50 and 8.56 may be compared with the measured wave energy decay rate, *dE/dx*. This comparison is shown on Figure 8.16, where it can be seen that there is a good agreement over the entire range of wave energies observed during this study.

The question of why the wave amplitude decay rate varies with densimetric factor still remains to be answered. The wall drag component of energy decay appears to be independent of the densimetric factor, indicating that the densimetric factor must influence fluid drag only. The question is thus narrowed to an examination of the components of fluid drag: interfacial shear, pressure drag and turbulent mixing. The processes at work at the wave interface (entrainment; lack of a no-slip condition; separation at wake) make it difficult to estimate values of interfacial shear and pressure drag, and the complexity of performing accurate measurements of mixing have been discussed in Section 8.4.2. It is possible that the densimetric

factor would have some influence on any or all of the growth of the boundary layer at the wave interface, the point of flow separation (influencing the size of the wake) and turbulent mixing in the wake, but any definitive judgments on this will be left for future studies.

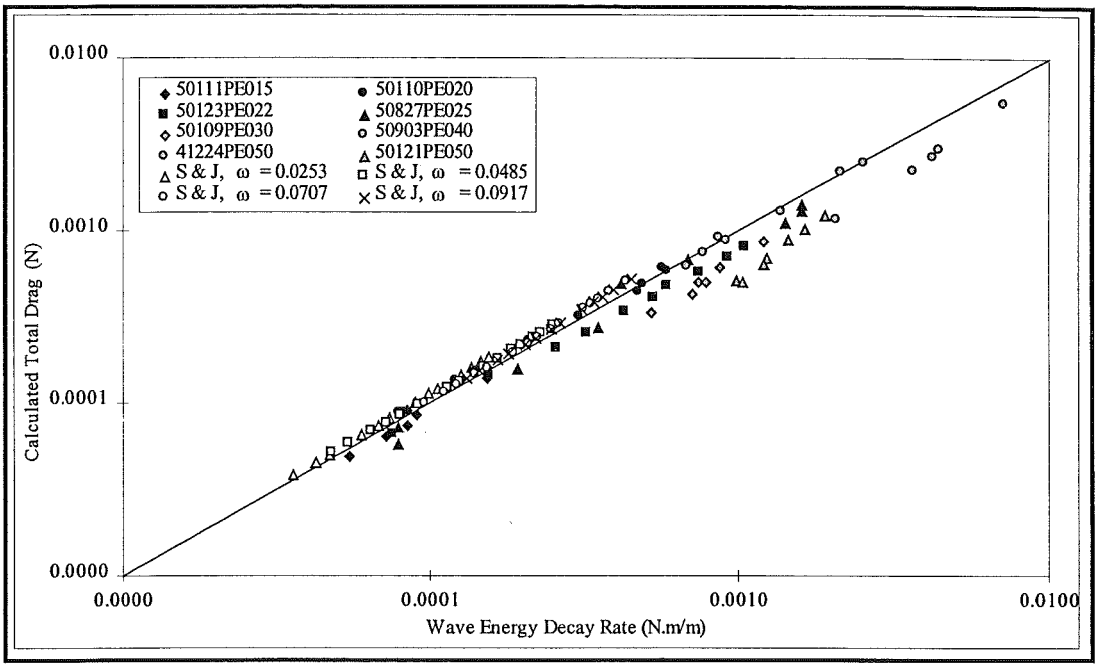

Figure 8.16 - Variation of calculated total drag with wave energy decay rate

8.5 Conclusion

The study of wave dissipation in this chapter examined eight experimental runs from the present study and also used data from Stamp & Jacka (1995). Each run exhibited a constant wave amplitude decay rate, *da/dx*, though this varied with densimetric factor, ω, over the range of experiments.

The new data was analysed using the methods of Stamp & Jacka (1995), where wave amplitude decay rate was compared to various dimensionless quantities. Four possible dissipation mechanisms (wave radiation, turbulent mixing, wall shear and interfacial shear) were examined. It was not possible to make any conclusions based on these analysis methods.

A new approach to the wave dissipation problem, based on an examination of wave energy, rather than amplitude, decay was adopted. The energy decay rate, *dE/dx*,

was estimated by three methods. The first two involved first deriving an equation for wave energy by considering the contributions of internal and external kinetic energy as well as potential energy. The differentiation of a quadratic equation fit to experimental data provided one estimate of dE/dx, while the differentiation of the equation itself provided another. The two methods were found to produce similar results. The third method involved estimating the retarding force on the wave (equal to dE/dx) with a momentum balance which accounted for an accelerating, deformable control volume with a net outward fluid flow. This method also showed good agreement with the previous two.

The four possible decay mechanisms were then examined. Scaling estimates indicated that wave radiation is not responsible for a significant portion of wave decay. An analysis of turbulent mixing produced inconclusive results, with a decision to combine mixing effects with the fluid drag resulting from interfacial shear and pressure drag. The magnitude of drag force at the wall was estimated using a technique based on the Blasius solution for shear on a flat plate in a laminar boundary layer. It was found that wall shear accounted for a portion of total energy loss which varied with flume width only. When this was subtracted from the total energy loss, the remainder was assumed to be due to fluid drag only. This was described by a standard drag force equation ($F_{fluid} = C_D\, w\, \rho\, c^2 a$) in which the drag coefficient varies only with densimetric factor.

The variation of drag coefficient with densimetric factor remains unexplained, but it is possible that the densimetric factor influences the interfacial shear by affecting the growth of the boundary layer on the wave, as well as affecting pressure drag and turbulent mixing by influencing the point of flow separation and the size of the wave's wake.

9.0 Conclusion

This thesis began with an introduction to the topic at hand in Chapter 1, followed by a detailed review of previous analytical and experimental studies in Chapter 2. A description of the experimental methods employed in the present study was put forward in Chapter 3. The presentation of experimental results began with a discussion of the pycnocline in Chapter 4, followed by a discussion of wave generation in Chapter 5. External wave propagation characteristics were addressed in Chapter 6, with aspects of internal circulation covered in Chapter 7. The investigation of wave dissipation was presented in Chapter 8.

9.1 Background

The goal of the present study was to use advanced flow visualisation and measurement techniques to perform a detailed examination of the generation, propagation and dissipation of second mode internal solitary waves. It was hoped that the observations, measurements and analysis presented in this study would shed more light on the nature of these waves and could then be used in the calibration of a numerical model. Some work was done on a numerical model (detailed in Appendix 11) but time and resource constraints prevented the model's completion. Particular attention has been paid in this study to large amplitude waves, which have been observed to transport fluid over significant distances.

Chapter 2 reviewed the current state of theory on second mode waves. Initial analytical studies (Benjamin, 1967; Davis & Acrivos, 1967) involved assumptions which limited the applicability of theoretical propagation relationships to waves of small amplitude. Later numerical and experimental studies (Tung, Chan & Kubota, 1982; Stamp & Jacka, 1995) presented relationships applicable to moderately large ($a/h = 3$) waves, but it was not known whether these could be extended to larger amplitude waves. A conflict between theoretically predicted wave circulation patterns (Davis & Acrivos, 1967; Tung, Chan & Kubota, 1982) and observations of entrainment and expulsion (Stamp & Jacka, 1995) was also identified.

The experimental methods of previous studies were also examined to provide a basis for developing new techniques. Previous experimental observations of all aspects of wave motion were then summarised and commented upon. Finally, specific research goals and techniques for the present study were identified.

The experimental techniques used in the present study were detailed in Chapter 3. Experiments were performed in a glass-walled tank into which a flume insert was placed. Waves were generated by exchange flow, direct inflow and gravity collapse techniques, with salt added to water used to produce density differences. The use of salt water solutions allowed conductivity probes to be used to indirectly measure fluid densities. Layer densities were also checked by using an Anton-Paar density meter. A laser sheet was used to illuminate the flow and visualisation was enhanced with either fluorescent dye or neutrally buoyant particle tracers. All flows were recorded with 8 mm and digital video cameras, while a 35 mm still camera was used in some instances. The use of trolley-mounted cameras allowed waves to be viewed from a moving frame of reference which enhanced the observation of weak circulation within the wave. Specific procedures involved in the experiments were also outlined in Chapter 3.

9.2 Experimental Results

Preliminary experiments described in Chapter 4 confirmed previously established spatial and temporal characteristics of the density interface. The pycnocline was found to adopt a hyperbolic tangent profile, and a linear equation was fitted to the central portion of the profile to provide a measure of the interfacial thickness. Interfacial thickening due to molecular diffusion was also examined.

Chapter 5 addressed the generation of second mode waves by three methods: exchange flow, forced inflow and gravity collapse. The latter was found to be the most effective method for the rapid, repeatable generation of second mode waves. The mechanism for wave generation was found to be similar for all methods. An intrusive gravity current forms a head of thickness greater than the following current. When the following current slows due to thickening of the intrusive layer,

unsteady surging or a deficit of intrusive fluid, the momentum of the head allows it to pinch off and form a second mode wave. The slower, following current then forms another, smaller head which may itself form another second mode wave. Sequences of images showing the development of waves from an exchange flow and from a gravity collapse were presented, and revealed the fundamental change in internal circulation that accompanies the transformation of intrusion head to second mode wave.

In chapter 6, the external propagation characteristics (i.e. the geometry and celerity) of large amplitude second mode waves were examined. The range of applicability of the linear relationship between wavelength and amplitude presented by Stamp and Jacka (1995) was extended from a/h = 3.1 to 11.6. The new body of large amplitude wave data showed that the wave celerity relationship of Stamp & Jacka (1995) was not valid for waves of amplitude much above a/h = 3. A new relationship based on the Bernoulli equation and assumptions of 2-D, irrotational, inviscid flow with sharp density interfaces was developed and showed good agreement with experimental data over the entire range of large amplitude waves.

The internal propagation characteristics of the wave were examined in Chapter 7. Circulation within the wave was found to differ dramatically from that predicted by the numerical models of Davis & Acrivos (1967) and Tung, Chan & Kubota (1982). The internal circulation pattern was shown to resemble an assemblage of vortices, symmetric about the wave centreline, with outer vortices driven by the external flow, inner vortices driven by the outer ones, and these in turn driving a rearward flow along the wave's centreline. Holmboe instabilities were found to have a major role in the entrainment of external fluid into the wave, with fluid being brought in via cusp-like structures where the density interface at the wave boundary is distorted by the outer vortices inside the wave. This is in contrast to the observations of Stamp & Jacka (1995), who stated that fluid was brought in at a constant rate at all points along the wave boundary.

The mass transport capacity of the wave was examined by using Laser Induced Fluorescence techniques to measure the flushing of dye tracer from the wave. It was found that dye is flushed from the wave at a constant rate during the primary

flushing phase, in which the dye concentration within the wave drops from 100% to 10%. The primary flushing phase ends when flushing of undyed, recently entrained fluid begins. Residual flushing then occurs at a lesser, but also constant, rate, down to a dye concentration of approximately 1%. No measurements were performed below this concentration. It was found that larger Richardson numbers (i.e. stronger interfaces) resulted in faster entrainment and higher rates of flushing.

In Chapter 8, second mode wave dissipation was studied. Here wave energy decay was examined, in contrast to the study of Stamp & Jacka (1995) which looked at wave amplitude decay. The spatial wave energy decay rate was compared directly with forces due to form and wall drag. It was found that wave decay is primarily attributable to drag due to interfacial shear, wake pressure deficit and possibly mixing. This combination was represented by a drag coefficient which varies with densimetric factor, ω. Wall drag was quantified and found to vary with flume width, contributing to less than 10% of energy decay in the present study. Wave radiation losses were shown to be negligible.

9.3 Future Work

The present study has answered some important questions on the behaviour of second mode internal solitary waves, from generation to dissipation. It has also raised some new issues which are worthy of further examination.

The role of asymmetric Holmboe instabilities in the entrainment of fluid into the wave has been identified, but some questions remain to be resolved. In particular, the relationship between Richardson number and entrainment rate discussed in Section 7.3.3 should be examined in light of the behaviour of the Holmboe instability. Whether the value of densimetric factor or interfacial thickness affect the existence or strength of the instability should also be investigated.

The relative contributions of interfacial shear, pressure drag and mixing to the dissipation of wave energy are also worthy of examination. The examination of interfacial shear is complicated by the absence of a no-slip condition at the wave

boundary, while both pressure drag and mixing are likely to be influenced by the character of the wave wake.

The development of a numerical model would allow a further examination of the wave over its entire lifetime, without the complications of physical constraints, such as flume length and width, or difficulties associated with measurement of flow characteristics. Experimental data from the present study should prove invaluable in the calibration of such a model.

References

Akylas, T.R. and R.H.J. Grimshaw, 1992. "Solitary Internal Waves with Oscillatory Tails," Journal of Fluid Mechanics, vol. 242, pp 279-298.

Anton-Paar, 1975. "DMA Density Meter Operating Instructions," Anton-Paar KG, Graz, Austria.

Benjamin, T.B., 1966. "Internal Waves of Finite Amplitude and Permanent Form," Journal of Fluid Mechanics, vol 25, pp 241-270.

Benjamin, T.B., 1967. "Internal Waves of Permanent Form in Fluids of Great Depth," Journal of Fluid Mechanics, vol 29, pp 559-592.

Benney, D.J., 1966. "Long Non-linear Waves in Fluid Flows," Journal of Mathematics and Physics, vol 45, pp 52-63.

Benney, D.J. and D.R.S. Ko, 1978. "The Propagation of Long Large Amplitude Internal Waves," Studies in Applied Mathematics, vol 59, pp 187-199.

Bigg, P.H., 1967. "Density of Water in SI Units Over the Range 0-40°C," British Journal of Applied Physics, vol 18, pp 521-524.

Boussinesq, J., 1871. "Theorie de l'Intumescence Liquide Appelee Onde Solitaire ou de Translation se Propageant dans un Canal Rectangulaire," Institut de France, Academie des Sciences, Comptes Rendus, June 19, 1871, p. 755.

Britter, R.E. and J.E. Simpson, 1981. "A Note on the Structure of the Head of an Intrusive Gravity Current," Journal of Fluid Mechanics, vol 112, pp 459-466.

Browand, F.K, and C.D. Winant, 1973. "Laboratory Observations of Shear Instability in a Stratified Fluid," Boundary-Layer Meteorology, vol 5, pp 67-77.

Christie, D.R., 1992. "The Morning Glory of the Gulf of Carpentaria: A Paradigm for Non-linear Waves in the Lower Atmosphere," Australian Meteorology Magazine, vol 41, pp 21-60.

Davis, R.E. and A. Acrivos, 1967. "Solitary Internal Waves in Deep Water," Journal of Fluid Mechanics, vol 29, pp 593-607.

Davis, R.W. and E.F. Moore, 1982. "A Numerical Study of Vortex Shedding from Rectangles," Journal of Fluid Mechanics, vol 116, pp 475-506.

Farmer, D.M. and J.D. Smith, 1978. "Nonlinear Internal Waves in a Fjord," In: Hydrodynamics of Estuaries and Fjords, Proceedings of the Ninth International Liege Colloquium on Ocean Hydrodynamics, J.C.J. Nihoul, ed., Elsevier, Amsterdam, pp 465-493.

Fischer, H.B., E.J. List, J. Imberger, N.H. Brooks and R.Y.C. Koh, 1979. Mixing in Inland and Coastal Waters, Academic Press, New York, 483 p.

Fletcher, C.A.J., 1988. "Computational Techniques for Fluid Dynamics, Volume II - Specific Techniques for Different Flow Categories," Springer Series in Computational Physics, Springer-Verlag, 484 p.

Hachmeister, L.E. and F.A. Rigby, 1980. "Laboratory Studies of Stratified Flow Interaction with Topography," Second International Symposium on Stratified Flow, Trondheim, Norway, 24-27 June, pp 623-635.

Haigh, S.P. and G.A. Lawrence, 1996. "The Evolution of Symmetric and Non-symmetric Holmboe Waves," Paper submitted to the Journal of Fluid Mechanics, 27 p.

Harlow, F.H. and J.E. Welch, 1965. "Numerical Calculation of Time-Dependent Viscous Incompressible Flow of Fluid with Free Surface," The Physics of Fluids, vol 8, no 12, pp 2182-2189.

Head, M.J., 1983. "The Use of Miniature Four-Electrode Conductivity Probes for High Resolution Measurement of Turbulent Density or Temperature Variations in Salt-Stratified Water Flows," Doctor of Philosophy Thesis, The University of California, San Diego, 211 p.

Holmboe, J., 1962. "On the Behavior of Symmetric Waves in Stratified Shear Flows," Geofysiske Publikationer, vol 24, pp 67-113.

Holyer, J.Y. and H.E. Huppert, 1980. "Gravity Currents Entering a Two-Layer Fluid," Journal of Fluid Mechanics, vol 100, pp 739-768.

Hurdis, D.A. and H.-P. Pao, 1975. "Experimental Observation of Internal Solitary Waves in a Stratified Fluid," Physics of Fluids, vol 18, pp 385-386.

Hutchinson, G.E., 1957. A Treatise on Limnology (Volume I), John Wiley & Sons, New York, 1015 p. (reference on p. 282)

Joseph, R.I., 1977. "Solitary Waves in a Finite Depth Fluid," Journal of Physics A: Mathematical and General, vol 10, pp L225-L227.

Kao, T.W. and H-P. Pao, 1979. "Wake Collapse in the Thermocline and Internal Solitary Waves," Journal of Fluid Mechanics, vol 97, pp 115-127.

Keulegan, G.H., 1953. "Characteristics of Internal Solitary Waves," Journal of Research of the National Bureau of Standards, vol 51, pp 133-140.

Koop, C.G. and G. Butler, 1981. "An Investigation of Internal Solitary Waves in a Two-Fluid System," Journal of Fluid Mechanics, vol 112, pp 225-251.

Korteweg, D.J. and G. de Vries, 1895. "On the Change of Form of Long Waves Advancing in a Rectangular Canal, and on a New Type of Long Stationary Waves," Philosophical Magazine, Volume 39, pp 422-443.

Kubota, T., D.R.S. Ko and L.D. Dobbs, 1978. "Propagation of Weakly Nonlinear Waves in a Stratified Fluid of Finite Depth," AIAA Journal of Hydronautics, vol 12, pp 157-165.

Lawrence, G.A, F.K. Browand and L.G. Redekopp, 1991. "The Stability of a Sheared Density Interface," Physics of Fluids A, vol 3, no 10, pp 2360-2370.

Leong, D.C.K., 1988. "Mixing of Dense River Inflows to Lakes," Master of Engineering Research Project, The University of Canterbury, 81 p.

Lighthill, M.J., 1978. Waves in Fluids, Cambridge University Press, Cambridge, 504 p.

Long, R.R., 1953. "Some Aspects of the Flow of Stratified Fluids - I. A Theoretical Investigation," Tellus, vol 5, pp 42-58.

Long, R.R., 1956. "Solitary Waves in One- and Two-Fluid Systems," Tellus, vol 8, pp 460-471.

Maxworthy, T., Redekopp, L.G. and P.D. Weidman, 1978. "On the Production and Interaction of Planetary Solitary Waves: Applications to the Jovian Atmosphere," Icarus, vol 33, pp 388-409.

Maxworthy, T., 1980. "On the Formation of Nonlinear Internal Waves from the Gravitational Collapse of Mixed Regions in Two and Three Dimensions," Journal of Fluid Mechanics, vol 96, pp 47-64.

Milne-Thompson, L.M., 1968. Theoretical Hydrodynamics, 5th Edition, MacMillan and Company, London, 743 p.

Ostrovsky, L.A. and Y.A. Stepanyants, 1989. "Do Internal Solitons Exist in the Ocean?" Reviews of Geophysics, vol 27, pp 293-310.

Papps, D.A., 1995. "Merging Buoyant Jets in Stationary and Flowing Ambients," Ph.D. Thesis, The University of Canterbury, 298 p.

Rayleigh, Lord, 1876. "On waves," London, Dublin and Edinburgh, Philosophical Magazine, Series 5, Volume 1.

Robertson, J.M., 1965. Hydrodynamics in Theory and Application, Prentice-Hall, Englewood Cliffs, New Jersey, 652 p.

Rouse, H., ed., 1949. "Engineering Hydraulics," Proceedings of the Fourth Hydraulics Conference, Iowa Institute of Hydraulic Research, 1039 p.

Scott Russell, J., 1844. "Report on Waves," British Association Reports.

Simpson, J.E., 1987. Gravity Currents: in the Environment and the Laboratory, Ellis-Horwood Limited, Chichester, 244 p.

Smyth, W.D., G.P. Klaassen and W.R. Peltier, 1988. "Finite Amplitude Holmboe Waves," Geophysical and Astrophysical Fluid Dynamics, vol 43, pp 181-222.

Smyth, W.D. and W.R. Peltier, 1989. "The Transition between Kelvin-Helmholtz and Holmboe Instability: An Investigation of the Overreflection Hypothesis," Journal of the Atmospheric Sciences, vol 46, no 24, pp 3698-3720.

Smyth, W.D. and W.R. Peltier, 1991. "Instability and Transition in Finite-Amplitude Kelvin-Helmholtz and Holmboe Waves," Journal of Fluid Mechanics, vol 228, pp 387-415.

Stamp, A. and R.W. Griffiths, 1992. "Large Amplitude Mode 2 Deep-Water Internal Solitary Waves," 11th Australasian Fluid Mechanics Conference, University of Tasmania, Hobart, 14-18 December 1992, pp 315-317.

Stamp, A.P. and M. Jacka, 1995. "Deep-Water Internal Solitary Waves," Journal of Fluid Mechanics, vol 305, pp 347-371.

Tabor, H. and Z. Weinberger, 1981. "Nonconvecting Solar Ponds," In: Solar Energy Handbook, J.F. Kreider and F. Kreith, eds., McGraw-Hill, New York, pp 10.1-10.29.

Tennekes, H. and J.L. Lumley, 1972. A First Course in Turbulence, The M.I.T. Press, Cambridge, Massachussetts, 300 p.

Thorpe, S.A., 1968. "A Method of Producing a Shear Flow in a Stratified Fluid," Journal of Fluid Mechanics, vol 32, part 4, pp 693-704.

Townsend, A.A., 1976. The Structure of Turbulent Shear Flow, 2nd Edition, Cambridge University Press.

Tritton, D.J., 1988. Physical Fluid Dynamics, 2nd Edition, Oxford University Press, Oxford, 519 p.

Tung, K.K., T.F. Chan and T. Kubota, 1982. "Large Amplitude Internal Waves of Permanent Form," Studies in Applied Mathematics, vol 66, pp 1-44.

Vallentine, H.R., 1959. Applied Hydrodynamics, Plenum Press, New York, 296 p.

Weast, R.C., ed., 1984. CRC Handbook of Chemistry and Physics, CRC Press, Boca Raton.

White, F.M, 1986. Fluid Mechanics, 2nd Edition, McGraw-Hill, New York, 732 p.

Yih, C.S., 1980. Stratified Flows, Academic Press, New York, 418 p.

Zabusky, N.J, and M.D. Kruskal, 1965. "Interaction of solitons in a collisonless plasma and the recurrence of initial states," Physical Review Letters, Vol 15, pp 240-243.

Appendix 1 - Experimental Data from Davis & Acrivos (1967)

Davis & Acrivos (1967) provided experimental data relating dimensionless wave amplitude, a, and celerity, Λ. The dimensionless amplitude is approximately equal to the dimensionless amplitude, a/h, used in this study and the dimensionless wave celerity, $\frac{1}{2}\,(gh/c^2)\,ln(\rho_3/\rho_1)$, has been shown in Section 2.2.2 to be equal to the quantity $2(c_0/c)^2$. Data from the three experimental runs have been scaled from Figure 6 (page 606) of their paper. The scaled values are presented in Figure A1.1, which corresponds to Figure 6 of Davis & Acrivos (1967). These values have been converted to quantities used in this study, with all values shown in Tables A1.1-3. Note that in all cases, $\rho_1 = 1.000$ g/cm^3

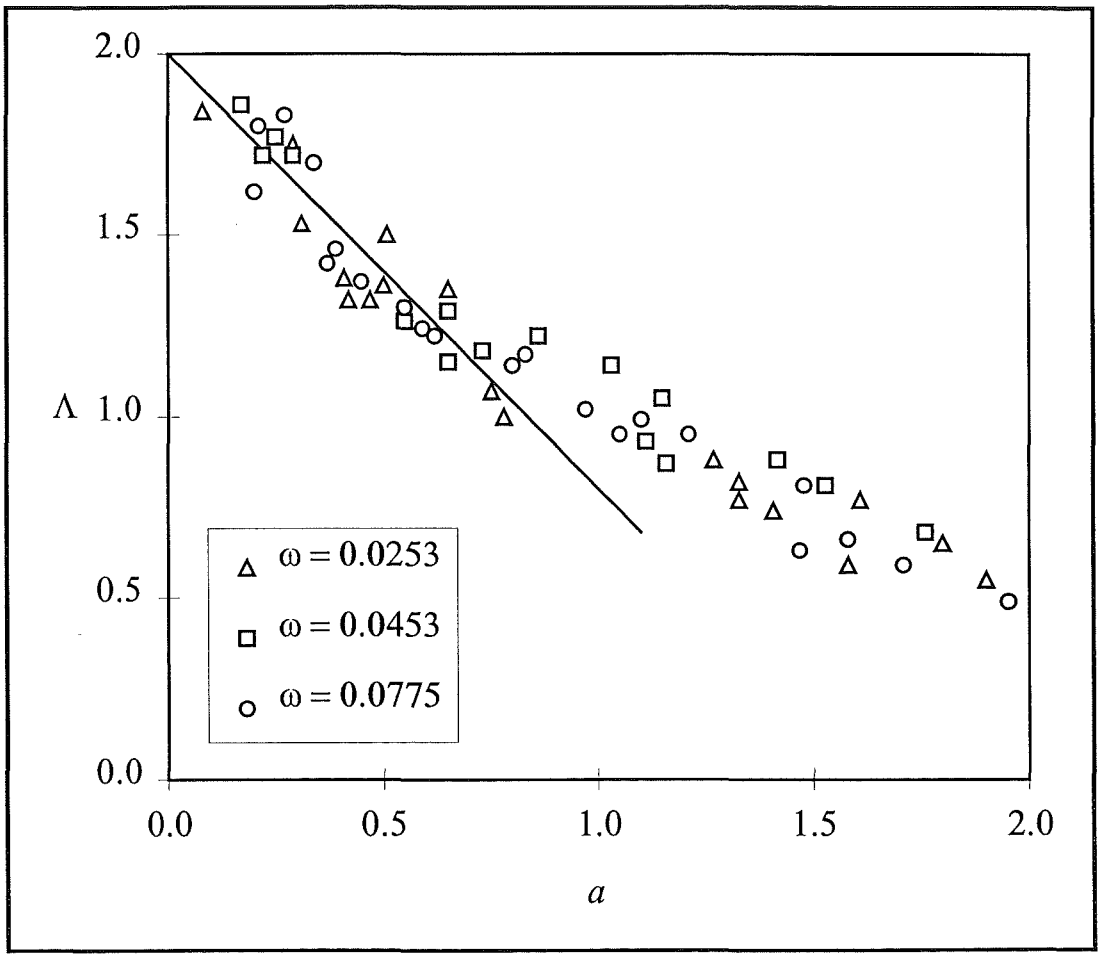

Figure A1.1 - Dimensionless celerity vs. amplitude (Davis & Acrivos, 1967)

Table A1.1 - Data from Davis & Acrivos (1967), $\rho_3 = 1.052$ g/cm^3 ($\omega = 0.0253$)

$a \cong a/h$	$\Lambda \cong 2(c_0/c)^2$	c/c_0	$a \cong a/h$	$\Lambda \cong 2(c_0/c)^2$	c/c_0
0.08	1.84	1.04	0.78	1.00	1.41
0.29	1.75	1.07	1.27	0.88	1.51
0.31	1.53	1.14	1.33	0.82	1.60
0.51	1.50	1.15	1.33	0.77	1.56
0.41	1.38	1.21	1.61	0.77	1.61
0.50	1.36	1.22	1.41	0.74	1.65
0.65	1.35	1.22	1.80	0.65	1.74
0.42	1.32	1.23	1.58	0.59	1.84
0.47	1.32	1.23	1.90	0.55	1.90
0.75	1.07	1.37			

Table A1.2 - Data from Davis & Acrivos (1967), $\rho_3 = 1.095$ g/cm^3 ($\omega = 0.0454$)

$a \cong a/h$	$\Lambda \cong 2(c_0/c)^2$	c/c_0	$a \cong a/h$	$\Lambda \cong 2(c_0/c)^2$	c/c_0
0.17	1.86	1.03	1.03	1.14	1.32
0.25	1.77	1.06	1.15	1.05	1.38
0.22	1.72	1.08	0.73	1.18	1.30
0.29	1.72	1.08	1.11	0.93	1.47
0.65	1.29	1.32	1.42	0.88	1.51
0.55	1.26	1.27	1.16	0.87	1.52
0.86	1.22	1.28	1.53	0.81	1.57
0.65	1.15	1.25	1.76	0.68	1.72

Table A1.3 - Data from Davis & Acrivos (1967), $\rho_3 = 1.168$ g/cm^3 ($\omega = 0.0775$)

$a \cong a/h$	$\Lambda \cong 2(c_0/c)^2$	c/c_0	$a \cong a/h$	$\Lambda \cong 2(c_0/c)^2$	c/c_0
0.27	1.83	1.05	0.80	1.14	1.31
0.21	1.80	1.06	0.97	1.02	1.40
0.34	1.70	1.09	1.10	0.99	1.42
0.20	1.62	1.11	1.05	0.95	1.46
0.39	1.46	1.18	1.21	0.95	1.46
0.37	1.42	1.19	1.48	0.81	1.57
0.45	1.37	1.21	1.58	0.66	1.74
0.55	1.30	1.24	1.47	0.63	1.78
0.59	1.24	1.27	1.71	0.59	1.84
0.62	1.22	1.28	1.95	0.49	2.02
0.83	1.17	1.33			

Appendix 2 - Experimental Data from Hurdis & Pao (1975)

Hurdis & Pao (1975) provided experimental data relating dimensionless wave amplitude, a/h, and celerity, Λ. The dimensionless wave celerity as first presented by Davis & Acrivos (1967), $\frac{1}{2}(gh/c^2)\ ln(\rho_3/\rho_1)$, has been shown in Section 2.2.2 to be equal to the quantity $2(c_0/c)^2$. Data from the eight experimental runs have been taken from Table 1 (page 386) of their paper. The scaled values are presented in Figure A2.1, which corresponds to Figure 1 of Hurdis & Pao (1975). These values have been converted to quantities used in this study, with all values shown in Table A2.1.

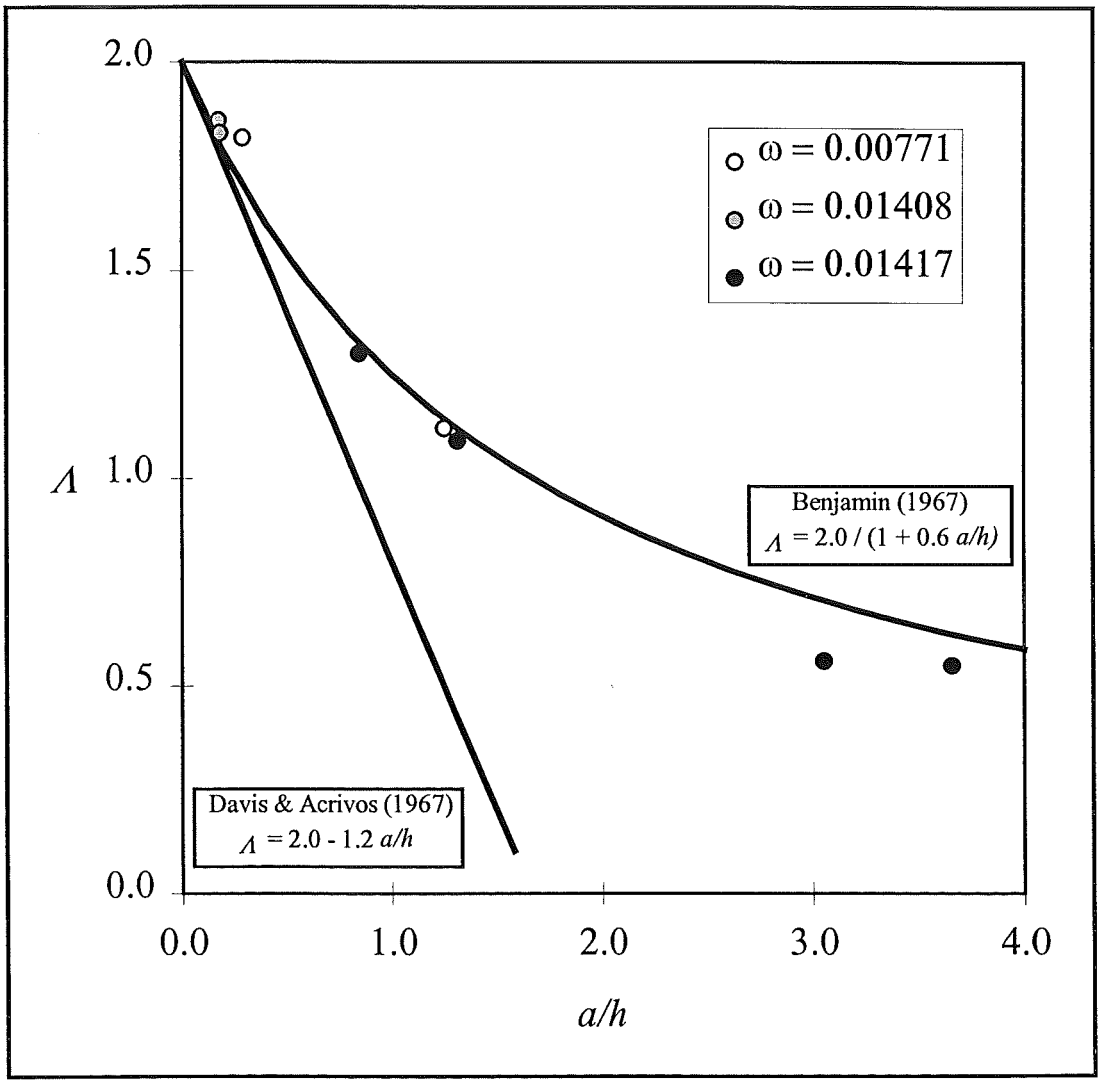

Figure A2.1 - Dimensionless celerity vs. amplitude (Hurdis & Pao, 1975)

Table A2.1 - Data from Hurdis & Pao (1975)

ω	h^{-1} (m^{-1})	c_0 (m/s)	a (m)	Λ	c (m/s)	h (m)	a/h	c/c_0
0.00771	50	0.0275	0.025	1.087	0.0373	0.0200	1.250	1.356
0.00771	48	0.0281	0.006	1.815	0.0295	0.0208	0.288	1.050
0.01417	244	0.0169	0.015	0.565	0.0318	0.0041	3.660	1.882
0.01417	109	0.0252	0.028	0.563	0.0475	0.0092	3.052	1.885
0.01417	73	0.0308	0.018	1.123	0.0411	0.0137	1.314	1.334
0.01417	65	0.0327	0.013	1.297	0.0406	0.0154	0.845	1.242
0.01408	30	0.0480	0.006	1.829	0.0502	0.0333	0.180	1.046
0.01408	29	0.0488	0.006	1.868	0.0505	0.0345	0.174	1.035

Appendix 3 - Experimental Data from Stamp & Jacka (1995)

Stamp & Jacka (1995) provided experimental data relating dimensionless wave amplitude, a/h, and celerity, c/c_0, as used in the present study. Dimensionless wavelengths, λ/h, and distances, x/h, have also been presented. Amplitude-celerity data from the four experimental runs have been scaled from Figure 8 (page 361) of their paper, while amplitude-wavelength data have been scaled from Figure 7 (page 360) and amplitude-distance data have been scaled from Figure 9a (page 362). The dimensionless amplitude-celerity, amplitude-wavelength and amplitude-distance relationships are presented in Figures A3.1-3, respectively. All scaled values are shown in Tables A3.1-4. Note that in all cases, $\rho_1 = 0.9982$ g/cm^3.

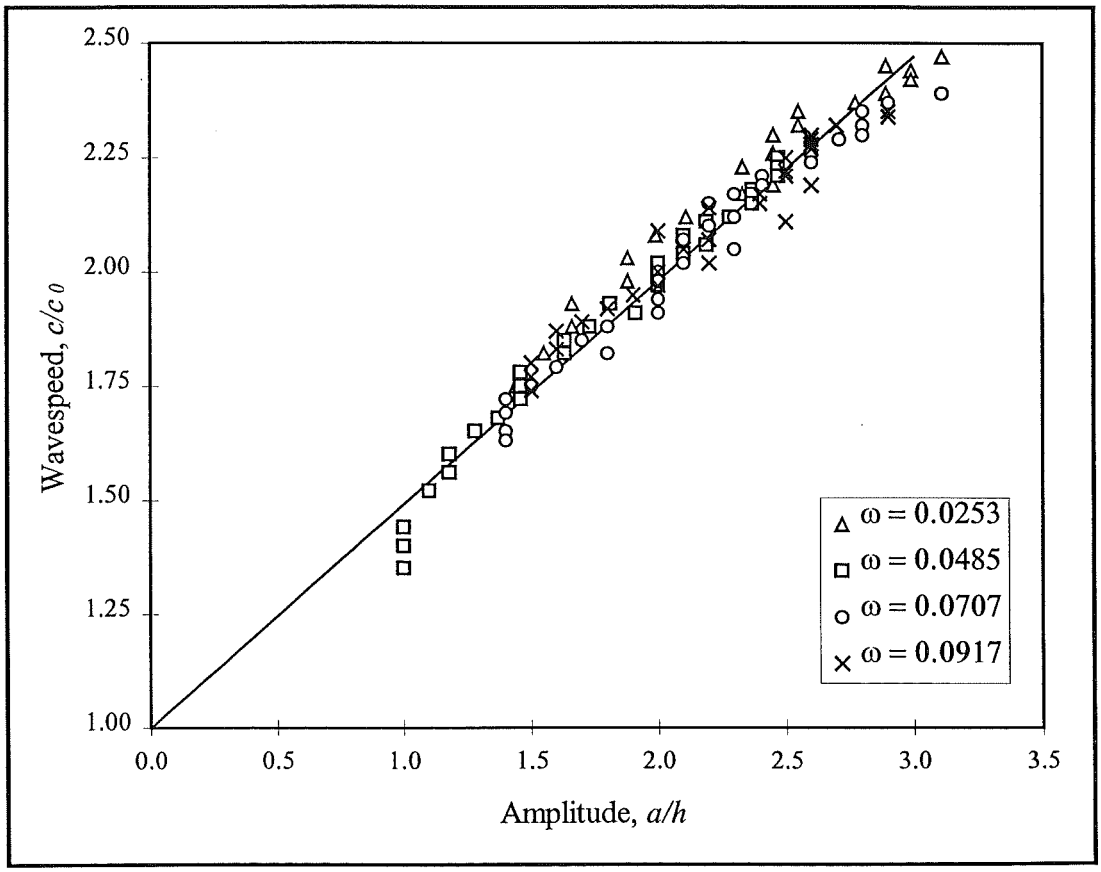

Figure A3.1 - Dimensionless celerity vs. amplitude (Stamp & Jacka, 1995)

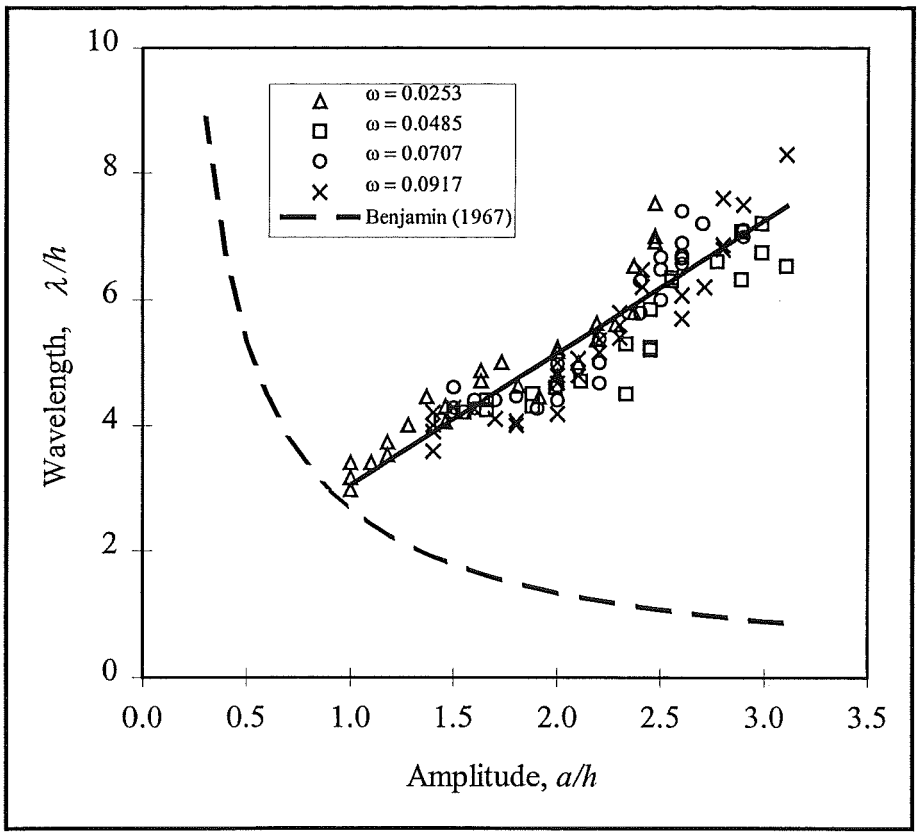

Figure A3.2 - Dimensionless wavelength vs. amplitude (Stamp & Jacka, 1995)

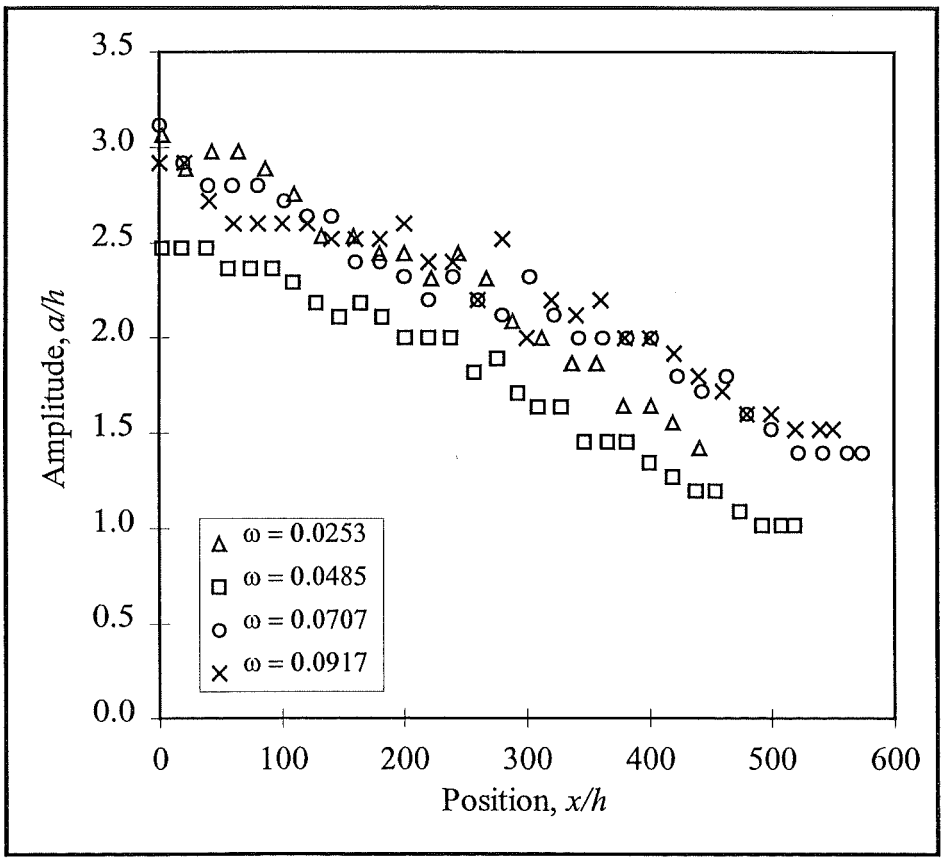

Figure A3.3 - Dimensionless distance vs. amplitude (Stamp & Jacka, 1995)

Table A3.1 - Data from Stamp & Jacka (1995), $\rho_3 = 1.050$ g/cm^3 ($\omega = 0.0253$)

x/h	a/h	λ/h	c/c_0	x/h	a/h	λ/h	c/c_0
2	3.11	6.53	2.47	244	2.45	5.20	2.19
21	2.45	7.07	2.45	267	2.33	4.50	2.17
42	2.99	7.20	2.44	288	2.11	4.70	2.12
64	2.99	6.75	2.42	312	1.99	4.60	2.08
86	2.89	6.32	2.39	337	1.88	4.50	2.03
110	2.77	6.60	2.37	357	1.88	4.30	1.98
132	2.55	6.35	2.35	379	1.66	4.40	1.93
158	2.55	6.30	2.32	401	1.66	4.25	1.88
179	2.45	5.85	2.30	419	1.55	4.20	1.82
200	2.45	5.25	2.26	441	1.44	4.07	1.75
222	2.33	5.30	2.23				

Table A3.2 - Data from Stamp & Jacka (1995), $\rho_3 = 1.110$ g/cm^3 ($\omega = 0.0485$)

x/h	a/h	λ/h	c/c_0	x/h	a/h	λ/h	c/c_0
2	2.47	7.52	2.25	276	1.91	4.45	1.91
18	2.47	7.00	2.23	293	1.73	5.00	1.88
38	2.47	6.92	2.21	309	1.63	4.87	1.85
56	2.37	6.53	2.18	328	1.63	4.70	1.82
74	2.37	5.80	2.17	347	1.46	4.30	1.78
92	2.37	5.80	2.15	366	1.46	4.30	1.75
109	2.28	5.60	2.12	382	1.46	4.05	1.68
128	2.19	5.62	2.11	400	1.37	4.45	1.65
147	2.10	5.00	2.08	419	1.28	4.00	1.60
164	2.19	5.37	2.06	438	1.18	3.72	1.56
182	2.10	5.00	2.04	454	1.18	3.52	1.72
201	2.00	5.23	2.02	474	1.10	3.40	1.52
220	2.00	5.17	1.99	492	1.00	3.40	1.44
238	2.00	4.80	1.97	508	1.00	3.16	1.40
257	1.81	4.62	1.93	519	1.00	2.97	1.35

Table A3.3 - Data from Stamp & Jacka (1995), $\rho_3 = 1.150$ g/cm^3 ($\omega = 0.0707$)

x/h	a/h	λ/h	c/c_0	x/h	a/h	λ/h	c/c_0
0	3.11	8.30	2.39	302	2.30	5.40	2.05
19	2.90	7.50	2.37	322	2.10	4.80	2.02
39	2.80	7.60	2.35	342	2.00	5.00	2.00
59	2.80	6.87	2.32	362	2.00	4.80	1.98
80	2.80	6.80	2.30	382	2.00	4.67	1.94
102	2.71	6.20	2.29	402	2.00	4.18	1.91
120	2.60	6.07	2.26	423	1.80	4.06	1.88
140	2.60	5.70	2.24	443	1.70	4.10	1.85
160	2.41	6.47	2.21	463	1.80	4.00	1.82
180	2.41	6.20	2.19	480	1.60	4.26	1.79
200	2.30	5.80	2.17	500	1.50	4.28	1.75
220	2.20	5.37	2.15	522	1.40	4.20	1.72
240	2.30	5.60	2.12	542	1.40	4.00	1.69
260	2.20	5.16	2.10	562	1.40	3.90	1.65
280	2.10	5.06	2.07	574	1.40	3.58	1.63

Table A3.4 - Data from Stamp & Jacka (1995), $\rho_3 = 1.200$ g/cm^3 ($\omega = 0.0917$)

x/h	*a/h*	*λ/h*	*c/c0*	*x/h*	*a/h*	*λ/h*	*c/c0*
0	2.90	7.10	2.35	300	2.00	4.98	2.09
20	2.90	7.00	2.34	320	2.20	5.00	2.07
40	2.70	7.20	2.32	340	2.10	4.92	2.05
60	2.60	7.40	2.30	360	2.20	4.67	2.02
80	2.60	6.90	2.29	380	2.00	4.63	2.00
100	2.60	6.70	2.28	400	2.00	4.40	1.97
120	2.60	6.65	2.27	420	1.90	4.27	1.95
140	2.50	6.67	2.25	440	1.80	4.46	1.92
160	2.50	6.48	2.22	460	1.70	4.40	1.89
180	2.50	6.00	2.21	480	1.60	4.40	1.87
200	2.60	6.57	2.19	500	1.60	4.27	1.83
220	2.40	5.80	2.17	520	1.50	4.60	1.80
240	2.40	6.30	2.15	540	1.50	4.28	1.77
260	2.20	5.38	2.14	550	1.50	4.20	1.74
280	2.50	6.00	2.11				

Appendix 4 - Details of Equipment Manufacturers and Suppliers

Amphenol Controls Division
(Model 205 Linear Potentiometer)
Janesville, Wisconsin, United States

Anton-Paar KG
(DMA 60 Density Meter with DMA 602HP Measuring Cell)
Karntnerstrasse 322
A-8054 Graz, Austria

AuCom Electronic Motor Control Systems
(SEDH58-8 Variable Frequency Controller)
123 Wrights Road
Addington, Christchurch, New Zealand
tel (03) 338-8280

Coherent, Inc.
(Innova 70-A Ar-I Laser)
Laser Products Division
3210 Porter Drive
P.O. Box 10321
Palo Alto, California, United States 94303

Cosmicar Lens Division
(50 and 75 mm TV Camera Lenses)
Asahi Precision Co., Ltd.
1-1-21, Shirako, Wako-Shi, Saitama-Ken
351-01, Japan
tel (0484) 66-8801 fax (0484) 66-8909

Data Translation, Inc.
(DT-2867 Frame Grabber and Global Lab Analysis Software)
100 Locke Drive
Marlboro, Massachussetts, United States 01752-1192
tel (508) 481-3700 fax (508) 481-8620

Grant Instruments (Cambridge) Limited
(LTD6-P Constant Temperature Bath)
Barrington, Cambridge, England CB2 5QZ

Hitachi Zosen Corporation
(VK-CG16E Video Character Generator)
3-28 Nishikujo 5-chome,
Osaka 554, Japan

Ilford Photo Corporation
(HP5 Plus B&W Print Film, Photographic Wetting Agent)
West 70 Century Road
Paramus, New Jersey, United States 07653

Lambda Physik
(Rhodamine 6G Dye)
289 Great Road
Acton, Massachussetts, United States 01720
tel (508) 263-1100 fax (508) 263-4296

Lincoln Laser Company
(M-660-010-LVWOB Rotating Octagonal Mirror)
234 E. Mohave
Phoenix, Arizona, United States 85004
tel (602) 257-0407 fax (602) 257-0728

Matsushita Electric Industrial Co. Ltd.
(Panasonic NV-FS200EC Super-VHS Video Recorder)
Central P.O. Box 288
Osaka 530-91, Japan

Melles Griot Limited
(OG 530 Yellow, Sharp-Cutoff Glass Filter)
1770 Kettering Street
Irvine, California, United States 92714
tel (714) 261-5600 fax (714) 261-7589

Olympus Optical Co. Ltd.
(OM-2 35 mm Camera with Motor Drive)
2-3 Kuboyama-cho, Hachioji-shi
Tokyo 192, Japan

Optical Flow Systems Limited
(750 mm Scanning Beam Box)
Edinburgh Technology Transfer Centre
The King's Buildings
Mayfield Road
Edinburgh, United Kingdom EH9 3JL

Precision Measurement Engineering Ltd.
(PME Conductivity Probes)
699 N. Vulcan #88
Encinitas, California, United States 92024
tel (619) 942-5860

Pulnix America Incorporated
(TM 765 CCD Video Camera)
770 Lucerne Drive
Sunnyvale, California, United States 94086
tel (408) 733-1560 fax (408) 747-0880

Sony
(8 mm Handicam Video Camera/Recorder)
(14'' Trinitron Color Video Monitor Model PVM-1442QM)
Pacific Regional Office
Sony International (Singapore) Ltd.
Asia Components Marketing Company
10 Hoe Chiang Road
#21-00 Keppel Towers
Singapore 0208
tel (65) 329-1550 fax (65) 329-1590

Appendix 5 - Density Interface Thickening Experiments

These experiments were done early (December 1993) in the experimental program to establish the proper method of measuring the thickness of a halocline, to gain an appreciation for its variation with time, and to test the effectiveness of drawing off fluid to sharpen the interface. The method outlined in Section 3.3.2 was not used for determining densities, as that technique had not yet been developed. Rather, a PME conductivity probe was used in conjunction with a digital multimeter, and densities were determined from a calibration equation relating voltage reading to density. All experiments and calibration measurements were performed at ambient temperature (approximately 20 °C).

The flume used for the preliminary experiments (Section 3.1) was initially filled to a depth of 175 mm with fresh water before adding a further 200 mm depth of salt water to bring the depth up to 375 mm. Density profiles were measured at intervals for approximately 22 hours, at which point the central 65 mm of fluid was drawn off to sharpen the interface. Density profiles were again measured for a further 48 hours. The resulting profiles were analysed to provide values of interfacial half-thickness and these were plotted against time to compare with the theoretical curve defined by Equation 4.7. Since the first measurement after filling and sharpening did not occur at zero pycnocline thickness, it was necessary to calculate an effective time for the first measurements by rearranging Equation 4.7 to solve for the time. Subsequent measurements had their times offset by this value to provide a value of effective time. The interfacial thickness data are shown on Figure 4.5 and are also tabulated on the following page. The raw data, calculated values and density profiles also follow.

Table A5.1 - Interfacial Thickness Data

Elapsed Time (s)	Measured Half-Thickness (m)	Effective Time (s)	Initial Offset (s)	Calculated Half-Thickness (m)
4400	0.0071	11544	7144	0.0071
12000	0.0099	19144		0.0091
23000	0.0122	30144		0.0115
38000	0.0136	45144		0.0140
80000	0.0184	87144		0.0195
0	0.0034	2647	2647	0.0034
4700	0.0057	7347		0.0057
11400	0.0073	14047		0.0078
24000	0.0115	26647		0.0108
39000	0.0130	41647		0.0135
84000	0.0177	86647		0.0195
99000	0.0209	101647		0.0211
175000	0.0268	177647		0.0279

Saline Filling Commenced @ 10:24 TUESDAY
Readings From 11:30 - 11:45 TUESDAY

Pycnocline Half-Thickness		7.1	mm		
	Upper Depth	173.7	mm	Upper Density	1006.7
	Lower Depth	180.8	mm	Lower Density	1017.1
Unadjusted Time		4400	s		
Adjusted Time		11500	s		
	rhobar	1011.79	kg/m^3		
	omega	0.01123	-		
	centreline	176.5	mm		

Reading	Depth	Voltage	Adjusted	Density	Tanh
263	373	1.380	2.08	1023.15	1023.2
290	346	1.400	2.11	1023.49	1023.2
330	306	1.410	2.13	1023.65	1023.2
340	296	1.410	2.13	1023.65	1023.2
350	286	1.410	2.13	1023.65	1023.2
360	276	1.410	2.13	1023.65	1023.1
370	266	1.410	2.13	1023.65	1023.1
375	261	1.410	2.13	1023.65	1023.1
380	256	1.410	2.13	1023.65	1023.1
385	251	1.410	2.13	1023.65	1023.1
390	246	1.410	2.13	1023.65	1023.1
395	241	1.410	2.13	1023.65	1023.1
400	236	1.410	2.13	1023.65	1023.1
405	231	1.410	2.13	1023.65	1023.1
410	226	1.410	2.13	1023.65	1023.1
415	221	1.410	2.13	1023.65	1023.1
420	216	1.410	2.13	1023.65	1023.1
425	211	1.410	2.13	1023.65	1023.1
430	206	1.410	2.13	1023.65	1023.1
435	201	1.410	2.13	1023.65	1023.1
440	196	1.400	2.11	1023.49	1023.1
441	195	1.340	2.02	1022.49	1023
442	194	1.340	2.02	1022.49	1023
443	193	1.300	1.96	1021.83	1022.9
444	192	1.280	1.93	1021.50	1022.9
445	191	1.270	1.91	1021.33	1022.8
446	190	1.260	1.90	1021.16	1022.6
447	189	1.240	1.87	1020.83	1022.5
448	188	1.220	1.84	1020.50	1022.3
449	187	1.180	1.78	1019.84	1022
450	186	1.150	1.73	1019.34	1021.7
451	185	1.140	1.72	1019.17	1021.2
452	184	1.120	1.69	1018.84	1020.7
453	183	1.090	1.64	1018.35	1020
454	182	1.070	1.61	1018.01	1019.2
455	181	1.030	1.55	1017.35	1018.1
456	180	0.940	1.42	1015.86	1017
457	179	0.840	1.27	1014.20	1015.6
458	178	0.750	1.13	1012.71	1014.1
459	177	0.720	1.09	1012.21	1012.6
460	176	0.660	0.99	1011.21	1011
462	174	0.350	0.53	1006.70	1008
464	172	0.220	0.33	1003.92	1005.4
466	170	0.100	0.15	1001.93	1003.6
468	168	0.020	0.03	1000.60	1002.3
470	166	0.010	0.02	1000.43	1001.6
475	161	0.010	0.02	1000.43	1000.7
480	156	0.010	0.02	1000.43	1000.5
485	151	0.010	0.02	1000.43	1000.4
490	146	0.010	0.02	1000.43	1000.4
495	141	0.010	0.02	1000.43	1000.4
500	136	0.010	0.02	1000.43	1000.4
520	116	0.010	0.02	1000.43	1000.4
620	16	0.010	0.02	1000.43	1000.4
636	0	0.010	0.02	1000.43	1000.4

Saline Filling Commenced @ 10:24 TUESDAY
Readings From 13:35 - 13:50 TUESDAY

Pycnocline Thickness		9.9	mm		
	Upper Depth	173.0	mm	Upper Density	1006.7
	Lower Depth	182.9	mm	Lower Density	1017.1
Unadjusted Time		12000	s		
Adjusted Time		19100	s		
	rhobar	1011.81	kg/m^3		
	omega	0.01121	-		
	centreline	176.5	mm		

Reading	Depth	Voltage	Adjusted	Density	Tanh
263	373	1.390	2.08	1023.16	1023.2
280	356	1.390	2.08	1023.16	1023.2
300	336	1.390	2.08	1023.16	1023.2
340	296	1.390	2.08	1023.16	1023.2
380	256	1.380	2.07	1022.99	1023.2
400	236	1.380	2.07	1022.99	1023.2
420	216	1.370	2.05	1022.83	1023.1
425	211	1.370	2.05	1022.83	1023.1
430	206	1.360	2.04	1022.66	1023.1
432	204	1.360	2.04	1022.66	1023.1
434	202	1.360	2.04	1022.66	1023
436	200	1.350	2.02	1022.50	1023
437	199	1.350	2.02	1022.50	1022.9
438	198	1.350	2.02	1022.50	1022.9
439	197	1.340	2.01	1022.33	1022.8
440	196	1.340	2.01	1022.33	1022.7
441	195	1.330	1.99	1022.17	1022.6
442	194	1.320	1.98	1022.01	1022.5
443	193	1.310	1.96	1021.84	1022.4
444	192	1.290	1.93	1021.51	1022.2
445	191	1.280	1.92	1021.35	1022
446	190	1.260	1.89	1021.02	1021.8
447	189	1.230	1.84	1020.53	1021.5
448	188	1.210	1.81	1020.20	1021.1
449	187	1.180	1.77	1019.70	1020.7
450	186	1.150	1.72	1019.21	1020.3
451	185	1.120	1.68	1018.72	1019.7
452	184	1.070	1.60	1017.90	1019.1
453	183	1.020	1.53	1017.07	1018.4
454	182	0.960	1.44	1016.09	1017.5
455	181	0.900	1.35	1015.10	1016.6
456	180	0.850	1.27	1014.28	1015.7
457	179	0.780	1.17	1013.13	1014.6
458	178	0.710	1.06	1011.98	1013.5
459	177	0.650	0.97	1010.99	1012.4
460	176	0.590	0.88	1010.00	1011.2
461	175	0.520	0.78	1008.85	1010.1
462	174	0.440	0.66	1007.54	1009
463	173	0.390	0.58	1006.71	1008
464	172	0.330	0.49	1005.73	1007
465	171	0.290	0.43	1005.07	1006.1
466	170	0.230	0.34	1004.08	1005.3
467	169	0.190	0.28	1003.42	1004.5
468	168	0.150	0.22	1002.77	1003.9
469	167	0.110	0.16	1002.11	1003.4
470	166	0.080	0.12	1001.62	1002.9
472	164	0.040	0.06	1000.96	1002.1
474	162	0.010	0.01	1000.46	1001.6
480	156	0.010	0.01	1000.46	1000.8
490	146	0.010	0.01	1000.46	1000.5
500	136	0.010	0.01	1000.46	1000.5
520	116	0.010	0.01	1000.46	1000.5
550	86	0.010	0.01	1000.46	1000.5
600	36	0.010	0.01	1000.46	1000.5
636	0	0.010	0.01	1000.46	1000.5

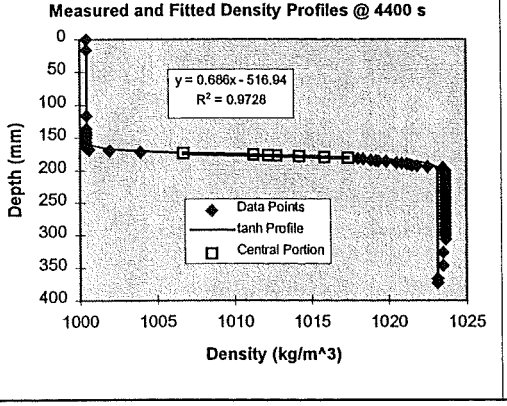

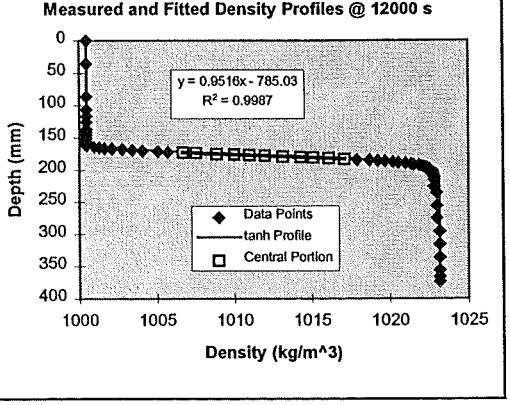

Saline Filling Commenced @ 10:24 TUESDAY
Readings From 16:40 - 16:52 TUESDAY

Pycnocline Thickness	12.2	mm			
Upper Depth	171.7	mm	Upper Density	1006.7	
Lower Depth	183.9	mm	Lower Density	1017.1	
Unadjusted Time	23000	s			
Adjusted Time	30100	s			
rhobar	1011.81	kg/m^3			
omega	0.01121	-			
centreline	176.5	mm			

Reading	Depth	Voltage	Adjusted	Density	Tanh
263	373	1.350	2.08	1023.16	1023.2
280	356	1.350	2.08	1023.16	1023.2
300	336	1.350	2.08	1023.16	1023.2
320	316	1.350	2.08	1023.16	1023.2
340	296	1.350	2.08	1023.16	1023.2
360	276	1.350	2.08	1023.16	1023.2
380	256	1.350	2.08	1023.16	1023.2
390	246	1.350	2.08	1023.16	1023.2
400	236	1.350	2.08	1023.16	1023.2
410	226	1.350	2.08	1023.16	1023.2
420	216	1.350	2.08	1023.16	1023.1
426	210	1.340	2.06	1022.99	1023.1
428	208	1.340	2.06	1022.99	1023
430	206	1.340	2.06	1022.99	1023
432	204	1.340	2.06	1022.99	1022.9
434	202	1.330	2.05	1022.82	1022.8
436	200	1.330	2.05	1022.82	1022.7
438	198	1.320	2.03	1022.65	1022.5
440	196	1.310	2.02	1022.48	1022.3
442	194	1.290	1.99	1022.14	1021.9
444	192	1.250	1.93	1021.46	1021.5
446	190	1.210	1.86	1020.79	1020.9
448	188	1.140	1.76	1019.60	1020.2
450	186	1.080	1.66	1018.59	1019.2
452	184	0.990	1.53	1017.06	1018
454	182	0.890	1.37	1015.37	1016.6
456	180	0.810	1.25	1014.01	1015
458	178	0.700	1.08	1012.15	1013.2
460	176	0.600	0.92	1010.46	1011.3
462	174	0.490	0.75	1008.60	1009.5
464	172	0.390	0.60	1006.90	1007.8
466	170	0.300	0.46	1005.38	1006.3
468	168	0.220	0.34	1004.02	1005
470	166	0.160	0.25	1003.01	1003.9
472	164	0.100	0.15	1001.99	1003.1
474	162	0.050	0.08	1001.15	1002.4
476	160	0.020	0.03	1000.64	1001.9
478	158	0.010	0.02	1000.47	1001.5
480	156	0.010	0.02	1000.47	1001.2
485	151	0.010	0.02	1000.47	1000.8
490	146	0.010	0.02	1000.47	1000.6
500	136	0.010	0.02	1000.47	1000.5
520	116	0.010	0.02	1000.47	1000.5
550	86	0.010	0.02	1000.47	1000.5
600	36	0.010	0.02	1000.47	1000.5
620	16	0.010	0.02	1000.47	1000.5
636	0	0.010	0.02	1000.47	1000.5

Saline Filling Commenced @ 10:24 TUESDAY
Readings From 20:55 - 21:03 TUESDAY

Pycnocline Thickness	13.6	mm			
Upper Depth	170.6	mm	Upper Density	1006.7	
Lower Depth	184.2	mm	Lower Density	1017.1	
Unadjusted Time	38000	s			
Adjusted Time	45100	s			
rhobar	1011.98	kg/m^3			
omega	0.01138	-			
centreline	176.5	mm			

Reading	Depth	Voltage	Adjusted	Density	Tanh
263	373	1.370	2.11	1023.50	1023.5
280	356	1.360	2.10	1023.33	1023.5
300	336	1.370	2.11	1023.50	1023.5
320	316	1.370	2.11	1023.50	1023.5
340	296	1.360	2.10	1023.33	1023.5
360	276	1.360	2.10	1023.33	1023.5
380	256	1.360	2.10	1023.33	1023.5
390	246	1.360	2.10	1023.33	1023.5
400	236	1.360	2.10	1023.33	1023.5
410	226	1.360	2.10	1023.33	1023.5
420	216	1.360	2.10	1023.33	1023.4
426	210	1.360	2.10	1023.33	1023.3
428	208	1.360	2.10	1023.33	1023.3
430	206	1.350	2.08	1023.16	1023.2
432	204	1.350	2.08	1023.16	1023.1
434	202	1.340	2.06	1022.99	1023
436	200	1.330	2.05	1022.82	1022.8
438	198	1.320	2.03	1022.65	1022.6
440	196	1.290	1.99	1022.14	1022.3
442	194	1.260	1.94	1021.63	1021.9
444	192	1.220	1.88	1020.96	1021.4
446	190	1.180	1.82	1020.28	1020.7
448	188	1.110	1.71	1019.09	1019.9
450	186	1.050	1.62	1018.08	1018.9
452	184	0.980	1.51	1016.89	1017.8
454	182	0.900	1.39	1015.54	1016.4
456	180	0.810	1.25	1014.01	1014.9
458	178	0.720	1.11	1012.49	1013.2
460	176	0.620	0.96	1010.80	1011.6
462	174	0.530	0.82	1009.27	1009.9
464	172	0.440	0.68	1007.75	1008.3
466	170	0.360	0.55	1006.40	1006.9
468	168	0.280	0.43	1005.04	1005.6
470	166	0.220	0.34	1004.02	1004.5
472	164	0.160	0.25	1003.01	1003.6
474	162	0.120	0.18	1002.33	1002.9
476	160	0.080	0.12	1001.65	1002.3
478	158	0.050	0.08	1001.15	1001.9
480	156	0.030	0.05	1000.81	1001.5
484	152	0.010	0.02	1000.47	1001.1
486	150	0.010	0.02	1000.47	1000.9
490	146	0.010	0.02	1000.47	1000.7
495	141	0.010	0.02	1000.47	1000.6
500	136	0.010	0.02	1000.47	1000.5
510	126	0.010	0.02	1000.47	1000.5
520	116	0.010	0.02	1000.47	1000.5
530	106	0.010	0.02	1000.47	1000.5
540	96	0.010	0.02	1000.47	1000.5
560	76	0.010	0.02	1000.47	1000.5
580	56	0.010	0.02	1000.47	1000.5
600	36	0.010	0.02	1000.47	1000.5
620	16	0.010	0.02	1000.47	1000.5
636	0	0.010	0.02	1000.47	1000.5

Measured and Fitted Density Profiles @ 23000 s

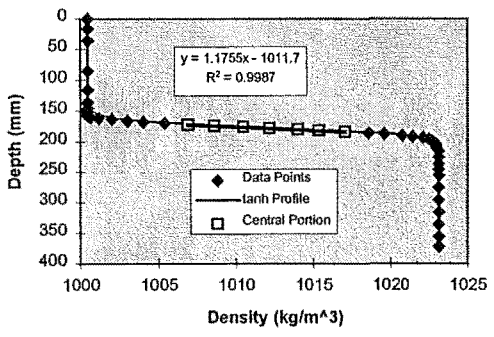

Measured and Fitted Density Profiles @ 38000 s

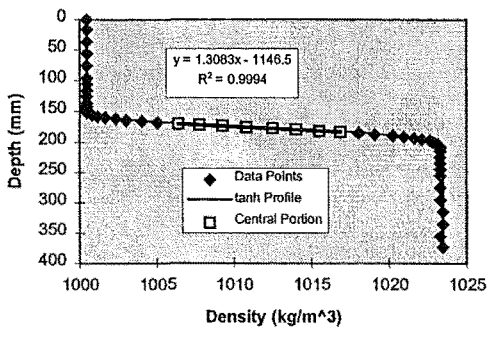

Saline Filling Commenced @ 10:24 TUESDAY
Readings From 08:30 - 08:41 WEDNESDAY

Pycnocline Thickness	18.4	mm			
Upper Depth	167.3	mm	Upper Density	1006.7	
Lower Depth	185.8	mm	Lower Density	1017.1	
Unadjusted Time	80000	s			
Adjusted Time	87100	s			
rhobar	1011.90	kg/m^3			
omega	0.01113	-			
centreline	176.5	mm			

Reading	Depth	Voltage	Adjusted	Density	Tanh
263	373	1.370	2.08	1023.16	1023.2
300	336	1.370	2.08	1023.16	1023.2
350	286	1.370	2.08	1023.16	1023.2
380	256	1.370	2.08	1023.16	1023.2
400	236	1.370	2.08	1023.16	1023.1
410	226	1.370	2.08	1023.16	1023.1
415	221	1.370	2.08	1023.16	1023
420	216	1.360	2.06	1022.99	1022.9
422	214	1.360	2.06	1022.99	1022.8
424	212	1.350	2.05	1022.82	1022.7
426	210	1.350	2.05	1022.82	1022.6
428	208	1.340	2.03	1022.66	1022.4
430	206	1.330	2.02	1022.49	1022.3
432	204	1.320	2.00	1022.32	1022.1
434	202	1.300	1.97	1021.99	1021.8
436	200	1.280	1.94	1021.66	1021.5
438	198	1.260	1.91	1021.32	1021.2
440	196	1.230	1.87	1020.82	1020.7
442	194	1.190	1.81	1020.15	1020.2
444	192	1.150	1.75	1019.49	1019.6
446	190	1.110	1.69	1018.82	1018.9
448	188	1.060	1.61	1017.99	1018.1
450	186	1.010	1.53	1017.15	1017.2
452	184	0.950	1.44	1016.15	1016.2
454	182	0.880	1.34	1014.98	1015.2
456	180	0.820	1.24	1013.98	1014
458	178	0.740	1.12	1012.65	1012.8
460	176	0.690	1.05	1011.81	1011.6
462	174	0.610	0.93	1010.48	1010.4
464	172	0.540	0.82	1009.31	1009.2
466	170	0.470	0.71	1008.14	1008.1
468	168	0.410	0.62	1007.14	1007
470	166	0.350	0.53	1006.14	1006.1
472	164	0.280	0.43	1004.97	1005.2
474	162	0.220	0.33	1003.97	1004.5
476	160	0.180	0.27	1003.30	1003.9
478	158	0.150	0.23	1002.80	1003.3
480	156	0.120	0.18	1002.30	1002.8
482	154	0.100	0.15	1001.97	1002.4
484	152	0.070	0.11	1001.47	1002.1
485	151	0.050	0.08	1001.13	1002
486	150	0.020	0.03	1000.63	1001.8
488	148	0.020	0.03	1000.63	1001.6
490	146	0.020	0.03	1000.63	1001.4
492	144	0.020	0.03	1000.63	1001.3
494	142	0.020	0.03	1000.63	1001.2
496	140	0.020	0.03	1000.63	1001.1
500	136	0.020	0.03	1000.63	1000.9
520	116	0.020	0.03	1000.63	1000.7
540	96	0.020	0.03	1000.63	1000.6
560	76	0.020	0.03	1000.63	1000.6
580	56	0.020	0.03	1000.63	1000.6
600	36	0.020	0.03	1000.63	1000.6
620	16	0.020	0.03	1000.63	1000.6
636	0	0.020	0.03	1000.63	1000.6

Drawing Off Of Interface Completed @ 10:28 WEDNESDAY
Readings From 10:28 - 10:37 WEDNESDAY

Pycnocline Thickness	3.4	mm			
Upper Depth	141.2	mm	Upper Density	1006.7	
Lower Depth	144.6	mm	Lower Density	1017.1	
Unadjusted Time	0	s			
Adjusted Time	2600	s			
rhobar	1011.90	kg/m^3			
omega	0.01113	-			
centreline	143.0	mm			

Reading	Depth	Voltage	Adjusted	Density	Tanh
263	305	1.340	2.08	1023.16	1023.2
300	268	1.340	2.08	1023.16	1023.2
320	248	1.340	2.08	1023.16	1023.2
340	228	1.340	2.08	1023.16	1023.2
360	208	1.340	2.08	1023.16	1023.2
380	188	1.340	2.08	1023.16	1023.2
390	178	1.340	2.08	1023.16	1023.2
400	168	1.340	2.08	1023.16	1023.2
405	163	1.340	2.08	1023.16	1023.2
408	160	1.340	2.08	1023.16	1023.2
410	158	1.330	2.06	1022.99	1023.2
412	156	1.330	2.06	1022.99	1023.1
414	154	1.330	2.06	1022.99	1023.1
416	152	1.320	2.05	1022.82	1023
418	150	1.310	2.03	1022.65	1022.8
419	149	1.300	2.02	1022.47	1022.5
420	148	1.270	1.97	1021.96	1022
421	147	1.230	1.91	1021.28	1021.2
422	146	1.160	1.80	1020.09	1019.8
423	145	1.060	1.65	1018.38	1017.8
424	144	0.890	1.38	1015.48	1015.1
425	143	0.680	1.06	1011.90	1011.9
426	142	0.530	0.82	1009.34	1008.7
427	141	0.350	0.54	1006.27	1006
428	140	0.200	0.31	1003.71	1004
429	139	0.070	0.11	1001.49	1002.6
430	138	0.020	0.03	1000.64	1001.8
431	137	0.020	0.03	1000.64	1001.3
432	136	0.020	0.03	1000.64	1001
434	134	0.020	0.03	1000.64	1000.8
435	133	0.020	0.03	1000.64	1000.7
440	128	0.020	0.03	1000.64	1000.6
450	118	0.020	0.03	1000.64	1000.6
460	108	0.020	0.03	1000.64	1000.6
480	88	0.020	0.03	1000.64	1000.6
500	68	0.020	0.03	1000.64	1000.6
530	38	0.020	0.03	1000.64	1000.6
550	18	0.020	0.03	1000.64	1000.6
568	0	0.020	0.03	1000.64	1000.6

Measured and Fitted Density Profiles @ 80000 s

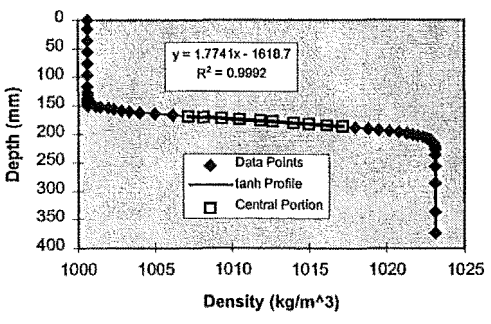

Measured and Fitted Density Profiles @ 0 s

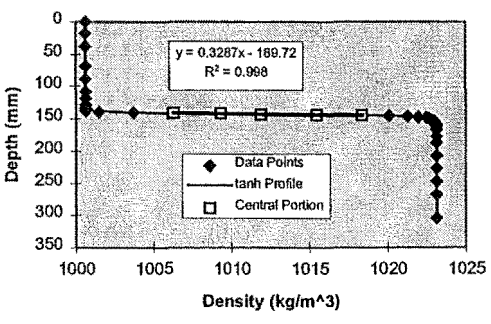

Drawing Off Of Interface Completed @ 10:28 WEDNESDAY
Readings From 10:28 - 10:37 WEDNESDAY

Pycnocline Thickness	5.7	mm			
Upper Depth	138.4	mm	Upper Density	1006.7	
Lower Depth	144.1	mm	Lower Density	1017.1	
Unadjusted Time	4700	s			
Adjusted Time	7300	s			
rhobar	1011.86	kg/m^3			
omega	0.01117	-			
centreline	143.0	mm			

Reading	Depth	Voltage	Adjusted	Density	Tanh
263	305	1.790	2.08	1023.16	1023.2
400	168	1.790	2.08	1023.16	1023.2
405	163	1.790	2.08	1023.16	1023.1
410	158	1.790	2.08	1023.16	1023
412	156	1.780	2.07	1023.03	1022.9
414	154	1.780	2.07	1023.03	1022.7
415	153	1.770	2.06	1022.90	1022.5
416	152	1.760	2.05	1022.77	1022.2
417	151	1.740	2.02	1022.52	1021.9
418	150	1.720	2.00	1022.26	1021.4
419	149	1.690	1.96	1021.88	1020.7
420	148	1.640	1.91	1021.24	1019.8
421	147	1.580	1.84	1020.48	1018.7
422	146	1.520	1.77	1019.71	1017.3
423	145	1.420	1.65	1018.43	1015.7
424	144	1.310	1.52	1017.03	1013.8
425	143	1.180	1.37	1015.37	1011.9
426	142	0.990	1.15	1012.94	1009.9
427	141	0.850	0.99	1011.15	1008
428	140	0.720	0.84	1009.49	1006.4
429	139	0.600	0.70	1007.96	1005
430	138	0.460	0.53	1006.17	1003.9
431	137	0.270	0.31	1003.75	1003
432	136	0.130	0.15	1001.96	1002.3
433	135	0.040	0.05	1000.81	1001.8
434	134	0.040	0.05	1000.81	1001.5
440	128	0.040	0.05	1000.81	1000.7
460	108	0.040	0.05	1000.81	1000.6
480	88	0.040	0.05	1000.81	1000.6
500	68	0.040	0.05	1000.81	1000.6
520	48	0.040	0.05	1000.81	1000.6
540	28	0.010	0.01	1000.43	1000.6
568	0	0.020	0.02	1000.56	1000.6

Drawing Off Of Interface Completed @ 10:28 WEDNESDAY
Readings From 13:38 - 13:47 WEDNESDAY

Pycnocline Thickness	7.3	mm			
Upper Depth	137.9	mm	Upper Density	1006.7	
Lower Depth	145.1	mm	Lower Density	1017.1	
Unadjusted Time	11400	s			
Adjusted Time	14000	s			
rhobar	1011.87	kg/m^3			
omega	0.01116	-			
centreline	143.0	mm			

Reading	Depth	Voltage	Adjusted	Density	Tanh
263	305	1.630	2.08	1023.16	1023.2
280	288	1.640	2.09	1023.30	1023.2
300	268	1.640	2.09	1023.30	1023.2
320	248	1.650	2.11	1023.44	1023.2
340	228	1.650	2.11	1023.44	1023.2
360	208	1.650	2.11	1023.44	1023.2
380	188	1.620	2.07	1023.02	1023.2
390	178	1.620	2.07	1023.02	1023.2
400	168	1.610	2.05	1022.88	1023.1
405	163	1.610	2.05	1022.88	1023.1
410	158	1.600	2.04	1022.74	1022.8
412	156	1.590	2.03	1022.60	1022.5
414	154	1.570	2.00	1022.32	1022.1
416	152	1.540	1.97	1021.90	1021.4
417	151	1.510	1.93	1021.47	1020.9
418	150	1.480	1.89	1021.05	1020.3
419	149	1.430	1.82	1020.35	1019.5
420	148	1.380	1.76	1019.65	1018.6
421	147	1.330	1.70	1018.95	1017.5
422	146	1.260	1.61	1017.97	1016.3
423	145	1.180	1.51	1016.85	1014.9
424	144	1.080	1.38	1015.44	1013.4
425	143	0.980	1.25	1014.04	1011.9
426	142	0.880	1.12	1012.64	1010.3
427	141	0.780	1.00	1011.24	1008.8
428	140	0.670	0.85	1009.70	1007.5
429	139	0.570	0.73	1008.29	1006.2
430	138	0.470	0.60	1006.89	1005.1
431	137	0.390	0.50	1005.77	1004.2
432	136	0.310	0.40	1004.65	1003.5
433	135	0.250	0.32	1003.81	1002.8
434	134	0.180	0.23	1002.82	1002.3
435	133	0.130	0.17	1002.12	1001.9
436	132	0.090	0.11	1001.56	1001.6
437	131	0.050	0.06	1001.00	1001.4
438	130	0.030	0.04	1000.72	1001.2
439	129	0.020	0.03	1000.58	1001.1
440	128	0.020	0.03	1000.58	1000.9
442	126	0.020	0.03	1000.58	1000.8
444	124	0.020	0.03	1000.58	1000.7
446	122	0.020	0.03	1000.58	1000.7
450	118	0.020	0.03	1000.58	1000.6
460	108	0.020	0.03	1000.58	1000.6
480	88	0.020	0.03	1000.58	1000.6
500	68	0.020	0.03	1000.58	1000.6
540	28	0.020	0.03	1000.58	1000.6
568	0	0.020	0.03	1000.58	1000.6

Measured and Fitted Density Profiles @ 4700 s

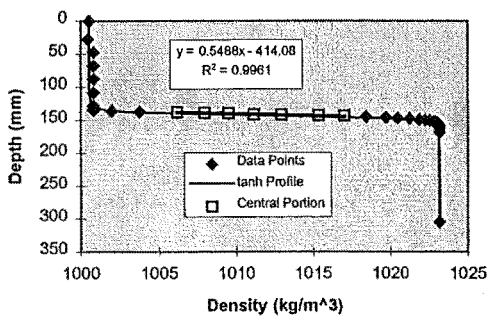

Measured and Fitted Density Profiles @ 11400 s

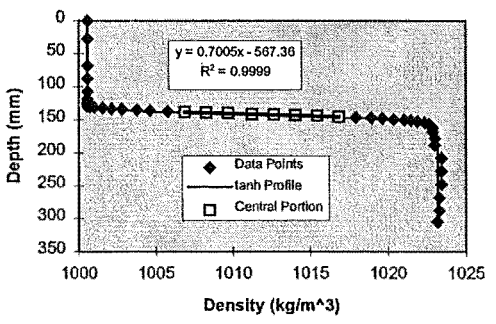

Drawing Off Of Interface Completed @ 10:28 WEDNESDAY
Readings From 17:05 - 17:18 WEDNESDAY

Pycnocline Thickness	11.5	mm			
Upper Depth	136.1	mm	Upper Density	1006.7	
Lower Depth	147.6	mm	Lower Density	1017.1	
Unadjusted Time	24000	s			
Adjusted Time	26600	s			
rhobar	1011.87	kg/m^3			
omega	0.01115	-			
centreline	143.0	mm			

Reading	Depth	Voltage	Adjusted	Density	Tanh
263	305	1.590	2.08	1023.16	1023.2
300	268	1.580	2.07	1023.01	1023.2
320	248	1.580	2.07	1023.01	1023.2
340	228	1.580	2.07	1023.01	1023.2
360	208	1.580	2.07	1023.01	1023.2
380	188	1.570	2.05	1022.87	1023.1
390	178	1.560	2.04	1022.73	1023.1
400	168	1.540	2.01	1022.44	1022.9
405	163	1.530	2.00	1022.29	1022.5
410	158	1.510	1.98	1022.01	1021.6
412	156	1.480	1.94	1021.58	1021
414	154	1.430	1.87	1020.86	1020.3
416	152	1.380	1.81	1020.14	1019.3
418	150	1.280	1.67	1018.70	1018
420	148	1.190	1.56	1017.41	1016.5
422	146	1.080	1.41	1015.83	1014.8
424	144	0.950	1.24	1013.96	1012.9
426	142	0.810	1.06	1011.94	1010.9
428	140	0.680	0.89	1010.08	1009
430	138	0.550	0.72	1008.21	1007.2
432	136	0.460	0.60	1006.91	1005.7
434	134	0.310	0.41	1004.76	1004.5
436	132	0.220	0.29	1003.46	1003.5
438	130	0.160	0.21	1002.60	1002.7
440	128	0.110	0.14	1001.88	1002.1
442	126	0.070	0.09	1001.31	1001.7
444	124	0.060	0.08	1001.16	1001.4
446	122	0.060	0.08	1001.16	1001.2
450	118	0.030	0.04	1000.73	1000.9
460	108	0.020	0.03	1000.59	1000.6
480	88	0.020	0.03	1000.59	1000.6
500	68	0.020	0.03	1000.59	1000.6
550	18	0.020	0.03	1000.59	1000.6
568	0	0.020	0.03	1000.59	1000.6

Drawing Off Of Interface Completed @ 10:28 WEDNESDAY
Readings From 21:22 - 21:28 WEDNESDAY

Pycnocline Thickness	13.0	mm			
Upper Depth	134.9	mm	Upper Density	1006.7	
Lower Depth	147.9	mm	Lower Density	1017.1	
Unadjusted Time	39000	s			
Adjusted Time	41600	s			
rhobar	1011.86	kg/m^3			
omega	0.01117	-			
centreline	143.0	mm			

Reading	Depth	Voltage	Adjusted	Density	Tanh
263	305	1.790	2.08	1023.16	1023.2
300	268	1.790	2.08	1023.16	1023.2
320	248	1.780	2.07	1023.03	1023.2
340	228	1.780	2.07	1023.03	1023.2
360	208	1.780	2.07	1023.03	1023.2
380	188	1.780	2.07	1023.03	1023.1
390	178	1.780	2.07	1023.03	1023.1
395	173	1.770	2.06	1022.90	1022.9
400	168	1.770	2.06	1022.90	1022.7
402	166	1.760	2.05	1022.77	1022.5
404	164	1.750	2.03	1022.65	1022.3
406	162	1.730	2.01	1022.39	1022
408	160	1.710	1.99	1022.14	1021.6
410	158	1.670	1.94	1021.62	1021.1
412	156	1.630	1.89	1021.11	1020.5
414	154	1.570	1.82	1020.35	1019.7
416	152	1.500	1.74	1019.45	1018.6
418	150	1.420	1.65	1018.43	1017.4
420	148	1.320	1.53	1017.16	1016
422	146	1.200	1.39	1015.62	1014.4
424	144	1.070	1.24	1013.96	1012.7
426	142	0.960	1.12	1012.56	1011
428	140	0.830	0.96	1010.90	1009.3
430	138	0.690	0.80	1009.11	1007.7
432	136	0.570	0.66	1007.58	1006.3
434	134	0.450	0.52	1006.05	1005.1
436	132	0.350	0.41	1004.77	1004.1
438	130	0.270	0.31	1003.75	1003.2
440	128	0.200	0.23	1002.85	1002.6
442	126	0.140	0.16	1002.09	1002.1
444	124	0.100	0.12	1001.58	1001.7
446	122	0.050	0.06	1000.94	1001.4
447	121	0.030	0.03	1000.68	1001.3
448	120	0.020	0.02	1000.56	1001.2
450	118	0.020	0.02	1000.56	1001
455	113	0.020	0.02	1000.56	1000.8
460	108	0.020	0.02	1000.56	1000.7
480	88	0.020	0.02	1000.56	1000.6
500	68	0.020	0.02	1000.56	1000.6
520	48	0.020	0.02	1000.56	1000.6
540	28	0.020	0.02	1000.56	1000.6
568	0	0.020	0.02	1000.56	1000.6

Measured and Fitted Density Profiles @ 24000 s

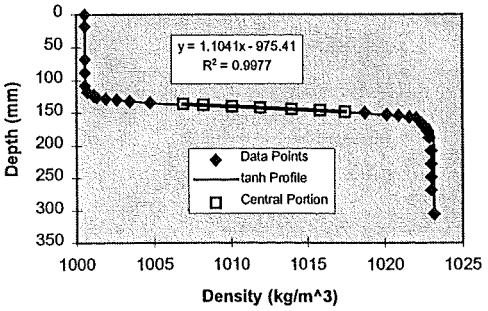

Measured and Fitted Density Profiles @ 39000 s

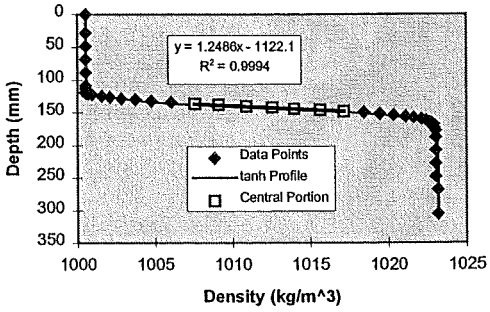

Drawing Off Of Interface Completed @ 10:26 WEDNESDAY
Readings From 09:50 - 09:58 THURSDAY

Pycnocline Thickness	17.7	mm			
Upper Depth	134.4	mm	Upper Density	1006.7	
Lower Depth	152.1	mm	Lower Density	1017.1	
Unadjusted Time	84000	s			
Adjusted Time	86600	s			
rhobar	1011.90	kg/m^3			
omega	0.01112	-			
centreline	143.0	mm			

Reading	Depth	Voltage	Adjusted	Density	Tanh
253	305	1.970	2.08	1023.16	1023.2
280	278	1.970	2.08	1023.16	1023.2
300	258	1.970	2.08	1023.16	1023.2
330	228	1.970	2.08	1023.16	1023.2
340	218	1.970	2.08	1023.16	1023.2
350	208	1.970	2.08	1023.16	1023.1
360	198	1.970	2.08	1023.16	1023.1
370	188	1.960	2.07	1023.04	1023
375	183	1.950	2.06	1022.93	1022.9
380	178	1.940	2.05	1022.81	1022.7
382	176	1.930	2.04	1022.69	1022.6
384	174	1.920	2.03	1022.58	1022.5
386	172	1.900	2.01	1022.34	1022.3
388	170	1.880	1.98	1022.11	1022.1
390	168	1.860	1.96	1021.88	1021.9
392	166	1.830	1.93	1021.53	1021.6
394	164	1.800	1.90	1021.18	1021.2
396	162	1.760	1.86	1020.72	1020.8
398	160	1.710	1.81	1020.14	1020.3
400	158	1.650	1.74	1019.44	1019.7
402	156	1.580	1.67	1018.63	1018.9
404	154	1.520	1.60	1017.94	1018.1
406	152	1.430	1.51	1016.89	1017.2
408	150	1.350	1.43	1015.96	1016.1
410	148	1.250	1.32	1014.80	1015
412	146	1.150	1.21	1013.64	1013.8
414	144	1.040	1.10	1012.37	1012.5
416	142	0.950	1.00	1011.32	1011.3
418	140	0.830	0.88	1009.93	1010
420	138	0.730	0.77	1008.77	1008.8
422	136	0.640	0.68	1007.73	1007.7
424	134	0.540	0.57	1006.57	1006.6
426	132	0.450	0.48	1005.52	1005.7
428	130	0.370	0.39	1004.59	1004.9
430	128	0.310	0.33	1003.90	1004.2
432	126	0.260	0.27	1003.32	1003.5
434	124	0.220	0.23	1002.85	1003
436	122	0.180	0.19	1002.39	1002.6
438	120	0.120	0.13	1001.69	1002.2
439	119	0.080	0.08	1001.23	1002.1
440	118	0.050	0.05	1000.88	1001.9
441	117	0.030	0.03	1000.65	1001.8
445	113	0.030	0.03	1000.65	1001.4
450	108	0.030	0.03	1000.65	1001.1
460	98	0.030	0.03	1000.65	1000.8
480	78	0.030	0.03	1000.65	1000.7
500	58	0.030	0.03	1000.65	1000.6
520	38	0.030	0.03	1000.65	1000.6
540	18	0.030	0.03	1000.65	1000.6
558	0	0.030	0.03	1000.65	1000.6

Drawing Off Of Interface Completed @ 10:28 WEDNESDAY
Readings From 13:53 - 14:02 THURSDAY

Pycnocline Thickness	20.9	mm			
Upper Depth	133.6	mm	Upper Density	1006.7	
Lower Depth	154.5	mm	Lower Density	1017.1	
Unadjusted Time	99000	s			
Adjusted Time	101600	s			
rhobar	1011.89	kg/m^3			
omega	0.01113	-			
centreline	143.0	mm			

Reading	Depth	Voltage	Adjusted	Density	Tanh
253	305	2.080	2.08	1023.16	1023.2
300	258	2.080	2.08	1023.16	1023.2
320	238	2.070	2.07	1023.05	1023.2
340	218	2.060	2.06	1022.94	1023.1
360	198	2.040	2.04	1022.72	1023
370	188	2.020	2.02	1022.50	1022.9
375	183	2.000	2.00	1022.28	1022.7
380	178	1.980	1.98	1022.06	1022.4
385	173	1.940	1.94	1021.62	1022
390	168	1.870	1.87	1020.85	1021.3
392	166	1.840	1.84	1020.52	1020.9
394	164	1.800	1.80	1020.08	1020.5
396	162	1.740	1.74	1019.42	1020
398	160	1.690	1.69	1018.87	1019.5
400	158	1.630	1.63	1018.21	1018.8
402	156	1.560	1.56	1017.44	1018.1
404	154	1.490	1.49	1016.67	1017.3
406	152	1.410	1.41	1015.79	1016.5
408	150	1.340	1.34	1015.03	1015.5
410	148	1.250	1.25	1014.04	1014.5
412	146	1.160	1.16	1013.05	1013.5
414	144	1.070	1.07	1012.06	1012.4
416	142	0.980	0.98	1011.07	1011.4
418	140	0.870	0.87	1009.86	1010.3
420	138	0.780	0.78	1008.87	1009.2
422	136	0.690	0.69	1007.88	1008.2
424	134	0.600	0.60	1006.89	1007.3
426	132	0.530	0.53	1006.12	1006.4
428	130	0.440	0.44	1005.14	1005.7
430	128	0.360	0.36	1004.26	1004.9
432	126	0.300	0.30	1003.60	1004.3
434	124	0.240	0.24	1002.94	1003.8
436	122	0.200	0.20	1002.50	1003.3
438	120	0.170	0.17	1002.17	1002.9
440	118	0.140	0.14	1001.84	1002.5
442	116	0.110	0.11	1001.51	1002.2
443	115	0.090	0.09	1001.29	1002.1
444	114	0.080	0.08	1001.18	1001.9
445	113	0.050	0.05	1000.85	1001.8
450	108	0.040	0.04	1000.74	1001.4
460	98	0.040	0.04	1000.74	1000.9
480	78	0.040	0.04	1000.74	1000.7
500	58	0.040	0.04	1000.74	1000.6
520	38	0.030	0.03	1000.63	1000.6
540	18	0.030	0.03	1000.63	1000.6
558	0	0.030	0.03	1000.63	1000.6

Measured and Fitted Density Profiles @ 84000 s

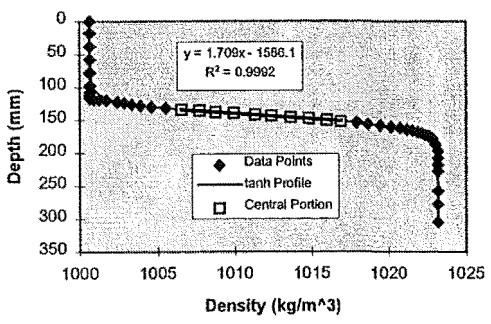

Measured and Fitted Density Profiles @ 99000 s

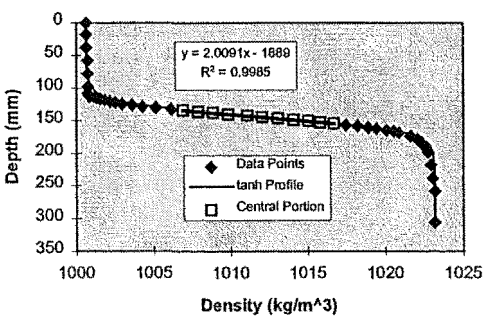

Drawing Off Of Interface Completed @ 10:28 WEDNESDAY
Readings From 11:11 - 11:22 FRIDAY

Pycnocline Thickness		26.8	mm		
Upper Depth		128.3	mm	Upper Density	1006.7
Lower Depth		155.1	mm	Lower Density	1017.1
Unadjusted Time		175000	s		
Adjusted Time		177600	s		
rhobar		1011.92	kg/m^3		
omega		0.01110	-		
centreline		143.0	mm		

Reading	Depth	Voltage	Adjusted	Density	Tanh
310	305	1.760	2.08	1023.16	1023.2
340	275	1.760	2.08	1023.16	1023.2
360	255	1.740	2.06	1022.90	1023.2
400	215	1.740	2.06	1022.90	1023.1
410	205	1.730	2.04	1022.77	1022.9
420	195	1.710	2.02	1022.51	1022.7
430	185	1.690	2.00	1022.25	1022.2
432	183	1.680	1.99	1022.12	1022.1
434	181	1.660	1.96	1021.86	1021.9
436	179	1.650	1.95	1021.73	1021.7
438	177	1.630	1.93	1021.47	1021.5
440	175	1.620	1.91	1021.34	1021.3
442	173	1.590	1.88	1020.95	1021
444	171	1.570	1.86	1020.69	1020.7
446	169	1.540	1.82	1020.30	1020.3
448	167	1.520	1.80	1020.04	1019.9
450	165	1.490	1.76	1019.65	1019.5
452	163	1.460	1.73	1019.26	1019
454	161	1.420	1.68	1018.74	1018.5
456	159	1.380	1.63	1018.22	1017.9
458	157	1.330	1.57	1017.57	1017.3
460	155	1.280	1.51	1016.92	1016.6
462	153	1.230	1.45	1016.27	1015.9
464	151	1.170	1.38	1015.49	1015.2
466	149	1.120	1.32	1014.85	1014.4
468	147	1.060	1.25	1014.07	1013.6
470	145	1.000	1.18	1013.29	1012.8
472	143	0.950	1.12	1012.64	1011.9
474	141	0.880	1.04	1011.73	1011.1
476	139	0.820	0.97	1010.95	1010.3
478	137	0.750	0.89	1010.04	1009.5
480	135	0.700	0.83	1009.39	1008.7
482	133	0.630	0.74	1008.48	1007.9
484	131	0.570	0.67	1007.70	1007.2
486	129	0.520	0.61	1007.05	1006.5
488	127	0.460	0.54	1006.27	1005.9
490	125	0.410	0.48	1005.62	1005.3
492	123	0.370	0.44	1005.11	1004.8
494	121	0.320	0.38	1004.46	1004.3
496	119	0.290	0.34	1004.07	1003.9
498	117	0.250	0.30	1003.55	1003.5
500	115	0.210	0.25	1003.03	1003.2
502	113	0.180	0.21	1002.64	1002.9
504	111	0.150	0.18	1002.25	1002.6
506	109	0.130	0.15	1001.99	1002.3
508	107	0.110	0.13	1001.73	1002.1
510	105	0.100	0.12	1001.60	1001.9
512	103	0.080	0.09	1001.34	1001.8
514	101	0.060	0.07	1001.08	1001.6
516	99	0.040	0.05	1000.82	1001.5
518	97	0.030	0.04	1000.69	1001.4
520	95	0.030	0.04	1000.69	1001.3
540	75	0.030	0.04	1000.69	1000.8
580	35	0.030	0.04	1000.69	1000.7
615	0	0.030	0.04	1000.69	1000.7

Measured and Fitted Density Profiles @ 175000 s

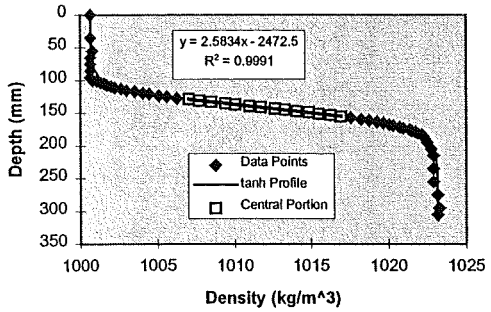

Appendix 6 - External Propagation Data from Present Study

Detailed data from the twenty-seven experimental runs which were used in Chapter 6 (Results: Propagation - External Flow) are presented in this appendix. The relevant data are given in Tables A6.1-27, which provide values for quantities corresponding to run parameters and wave measurements. These quantities include:

Run Parameters:

Run name
Densimetric factor, ω
Interfacial half-thickness, h
Dimensionless depth, H/h
Finite depth quantity, δ (calculated with Equation 2.35)
Infinitesimal first mode wave celerity, c_0 (calculated with Equation 2.34)
Coefficients of time-position equation $x = k_1 t^2 + k_2 t + k_3$

Measured Dimensional Wave Parameters:

Time stamp (time of gate release noted)
Time from gate release, t
Position, x (from time-position equation)
Wave amplitude, a
Ellipse semi-major axis, b
Wave celerity, c (from differentiation of time-position equation)

Calculated Dimensionless Wave Parameters:

Wave position, x/h
Wave amplitude, a/h
Wavelength, λ/h
Wave celerity, c/c_0

Run names are given in the format **YMMDDVGFFF**, where the first five digits give the date of the experimental run (**Y** is the last digit of the year, **MM** the month from 1-12 and **DD** the day from 1-31). **V** stands for the flow visualisation method, and is either "D" for fluorescent dye or "P" for neutrally buoyant particles. **G** stands for the wave generation method, with "E", "I", and "C" representing the

exchange flow, forced inflow and collapse methods, respectively. The last three characters, **FFF**, stand for the mass fraction of salt in the lower layer, multiplied by ten. As an example, the run name 51007PC050 would represent a run performed on 7 October 1995, using particle visualisation and a collapse generation technique, with a lower layer salt mass fraction of 5.0%.

Wave time-distance data are shown on Figures A6.1a-27a and density profiles are shown on Figures A6.1b-27b. On the density profiles, the data points represented by circles are the ones to which the central region linear regression was fit. Plots of dimensionless wave amplitude vs. celerity are provided on Figures A6.28a-c and dimensionless wave amplitude vs. wavelength on Figures A6.29a-c. Figures A6.28 and A6.29 are provided as a comparison to Figures 6.8, 6.10 and 6.14, where it is not possible to ascertain which data points ascribe to which experimental runs.

Table A6.1 - Experimental data from run 50117PE008

50117PE008		Infinitesimal Wave Speed Parameters					Distance Equation Coefficients		
		ω	h	H/h	δ	c_0	k_1	k_2	k_3
		0.0028	0.0072	42	0.024	0.0098	-2.15E-05	1.20E-02	8.37E-02
(start)	time	position	amplitude	semi-major	celerity	position	amplitude	wavelength	celerity
timeprint	t	x	a	b	c	x/h	a/h	λ/h	c/c_0
(1:46.39)	(s)	(m)	(m)	(m)	(m/s)				
2:18.65	32.26	0.45	0.0054	0.0135	0.011	62	0.743	2.449	1.087
2:15.74	29.35	0.42	0.0066	0.0112	0.011	58	0.910	2.364	1.099
2:33.53	47.14	0.60	0.0040	0.0080	0.010	84	0.556	1.831	1.021

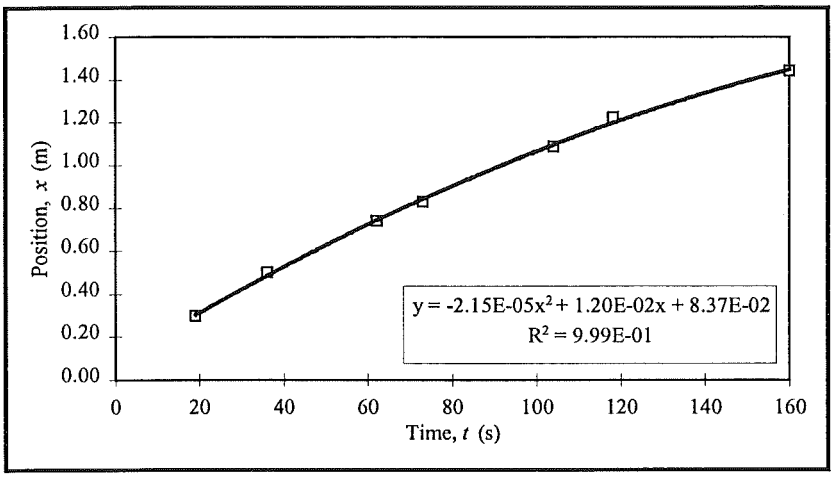

Figure A6.1a - Time-position data from run 50117PE008

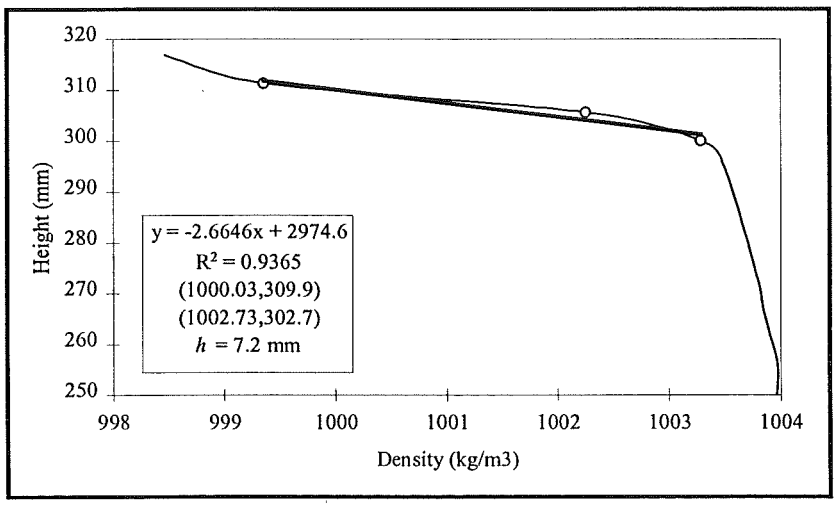

Figure A6.1b - Interfacial region density profile from run 50117PE008

Table A6.2 - Experimental data from run 41228PE010

41228PE010		Infinitesimal Wave Speed Parameters					Distance Equation Coefficients		
		ω	h	H/h	δ	c_0	k_1	k_2	k_3
		0.0035	0.0075	40	0.025	0.0111	-1.05E-05	1.57E-02	2.95E-01
(start)	time	position	amplitude	semi-major	celerity	position	amplitude	wavelength	celerity
timeprint	t	x	a	b	c	x/h	a/h	λ/h	c/c_0
(1:25.37)	(s)	(m)	(m)	(m)	(m/s)				
2:40.0	69.37	1.33	0.0076	0.0158	0.014	178	1.007	2.782	1.279
3:18.0	92.63	1.66	0.0067	0.0149	0.014	221	0.887	2.628	1.235
4:16.0	170.63	2.67	0.0058	0.0133	0.012	356	0.767	2.409	1.088

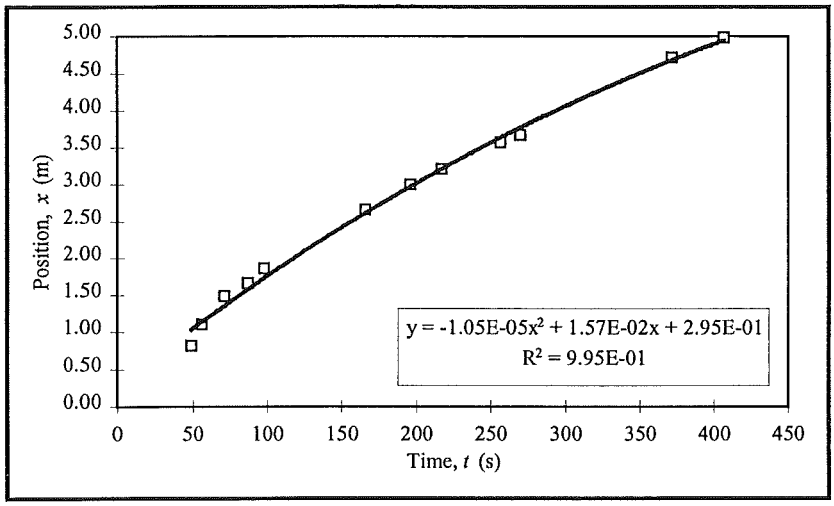

Figure A6.2a - Time-position data from run 41228PE010

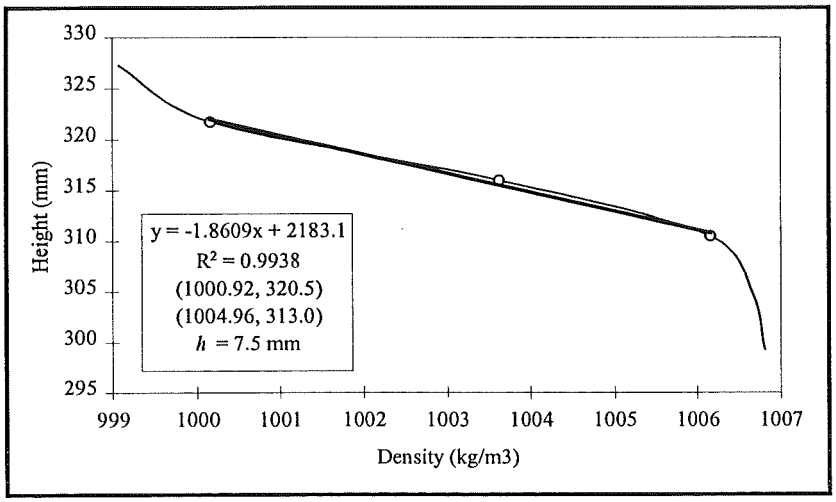

Figure A6.2b - Interfacial region density profile from run 41228PE010

Table A6.3 - Experimental data from run 50112PE010

50112PE010		Infinitesimal Wave Speed Parameters					Distance Equation Coefficients		
		ω	h	H/h	δ	c_0	k_1	k_2	k_3
		0.0035	0.0057	53	0.019	0.0098	2.07E-06	1.34E-02	1.53E-14
(start)	time	position	amplitude	semi-major	celerity	position	amplitude	wavelength	celerity
timeprint	t	x	a	b	c	x/h	a/h	λ/h	c/c_0
(0:34.30)	(s)	(m)	(m)	(m)	(m/s)				
1:50.05	75.75	1.03	0.0044	0.0084	0.014	180	0.763	2.215	1.406

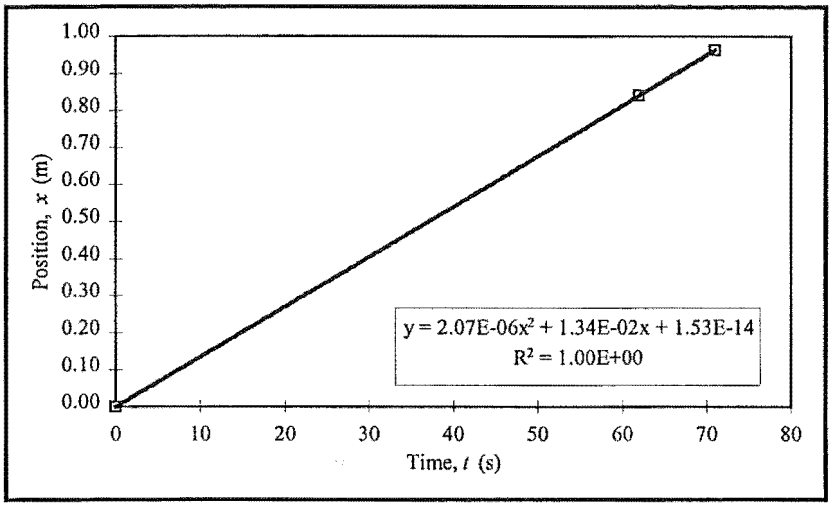

Figure A6.3a - Time-position data from run 50112PE010

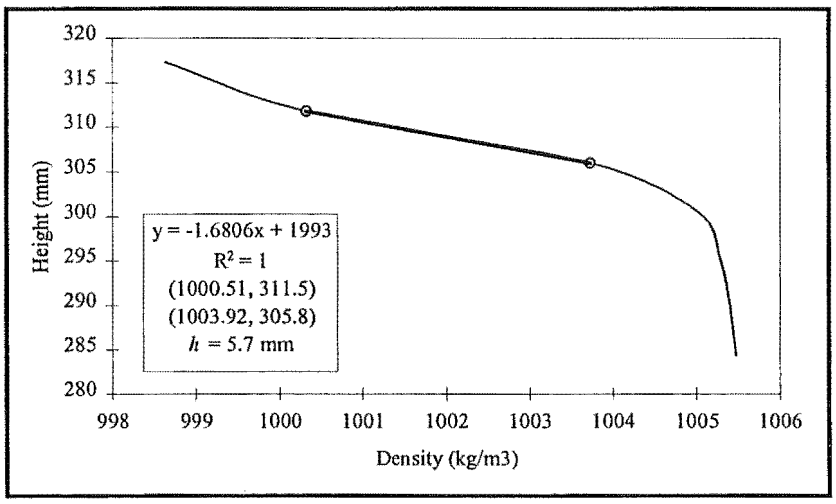

Figure A6.3b - Interfacial region density profile from run 50112PE010

Table A6.4 - Experimental data from run 50111PE015

50111PE015		Infinitesimal Wave Speed Parameters					Distance Equation Coefficients		
		ω	h	H/h	δ	c_0	k_1	k_2	k_3
		0.0053	0.0052	58	0.018	0.0115	-6.26E-05	2.16E-02	4.51E-02
(start)	time	position	amplitude	semi-major	celerity	position	amplitude	wavelength	celerity
timeprint	t	x	a	b	c	x/h	a/h	λ/h	c/c_0
(0:37.00)	(s)	(m)	(m)	(m)	(m/s)				
0:45.20	8.2	0.22	0.0114	0.0197	0.021	42	2.183	4.439	1.793
0:56.53	19.53	0.44	0.0096	0.0184	0.019	85	1.846	4.157	1.669
1:04.70	27.7	0.60	0.0070	0.0133	0.018	114	1.346	3.265	1.580
1:12.08	35.08	0.73	0.0073	0.0143	0.017	140	1.394	3.421	1.499
1:19.98	42.98	0.86	0.0070	0.0153	0.016	165	1.346	3.535	1.413
1:22.70	45.7	0.90	0.0064	0.0146	0.016	173	1.231	3.385	1.384
1:29.29	52.29	1.00	0.0055	0.0119	0.015	193	1.058	2.937	1.312

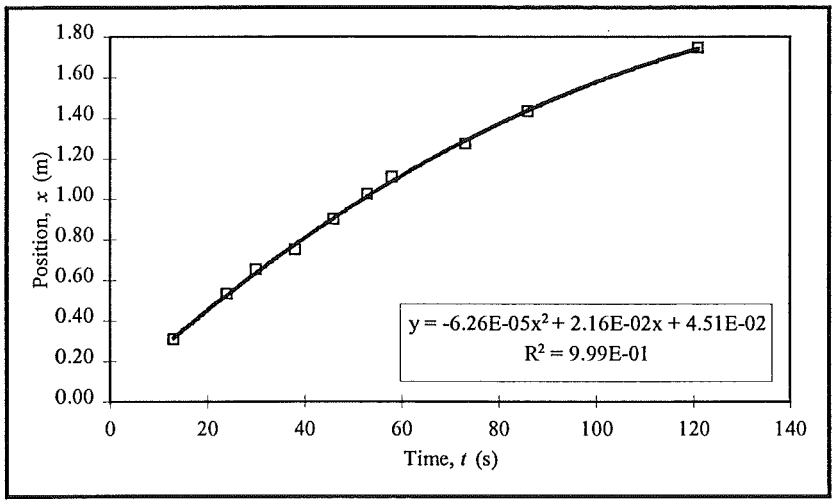

Figure A6.4a - Time-position data from run 50111PE015

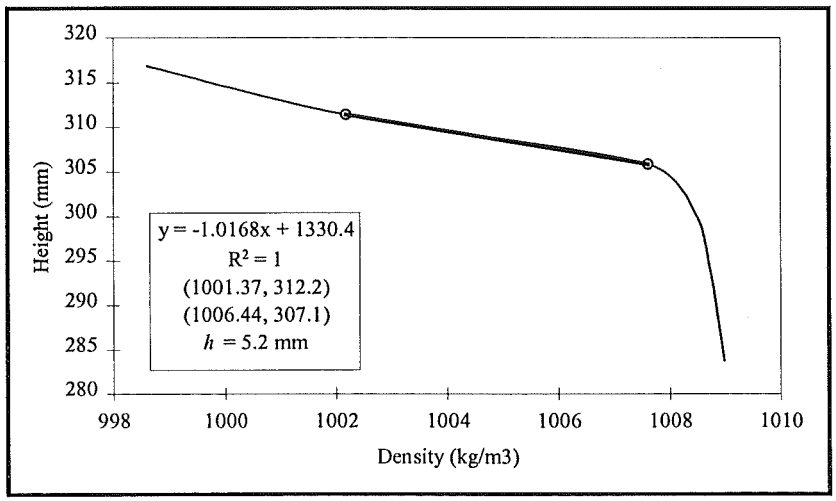

Figure A6.4b - Interfacial region density profile from run 50111PE015

Table A6.5 - Experimental data from run 41231PE017

41231PE017		Infinitesimal Wave Speed Parameters					Distance Equation Coefficients		
		ω	h	H/h	δ	c_0	k_1	k_2	k_3
		0.0060	0.0078	38	0.026	0.0149	-3.68E-05	3.28E-02	1.88E-02
(start) timeprint (1:34.00)	time t (s)	position x (m)	amplitude a (m)	semi-major b (m)	celerity c (m/s)	position x/h	amplitude a/h	wavelength λ/h	celerity c/c_0
2:49.50	75.5	2.29	0.0183	0.035	0.027	293	2.340	5.007	1.833
2:55.50	81.5	2.45	0.0177	0.0395	0.027	314	2.263	5.424	1.804
3:11.50	97.5	2.87	0.0141	0.0233	0.026	368	1.808	3.739	1.724
3:22.90	108.9	3.15	0.0112	0.0243	0.025	404	1.429	3.695	1.668
4:03.30	149.3	4.10	0.0077	0.0179	0.022	525	0.981	2.895	1.468
4:24.90	170.9	4.55	0.0069	0.0135	0.020	583	0.885	2.466	1.361

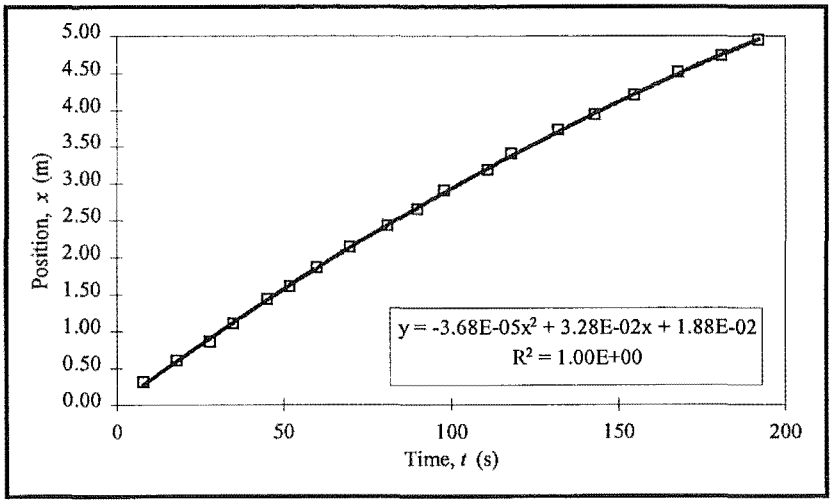

Figure A6.5a - Time-position data from run 41231PE017

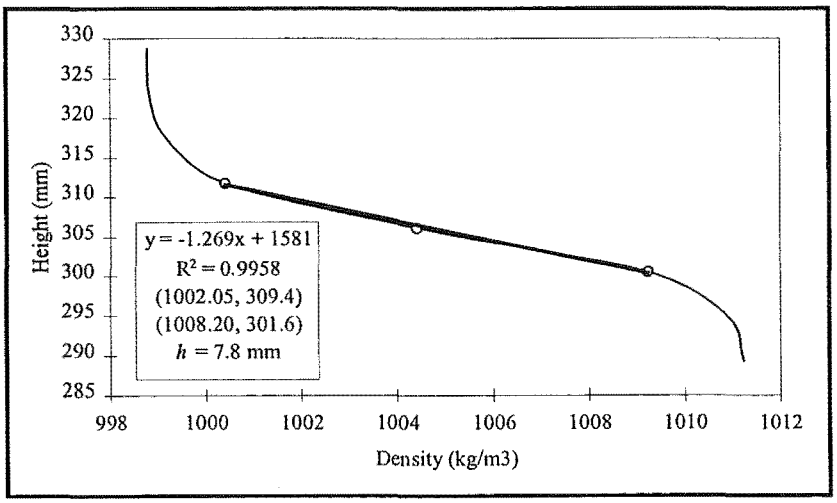

Figure A6.5b - Interfacial region density profile from run 41231PE017

Table A6.6 - Experimental data from run 50110PE020

50110PE020		Infinitesimal Wave Speed Parameters					Distance Equation Coefficients		
		ω	h	H/h	δ	c_0	k_1	k_2	k_3
		0.0071	0.0043	70	0.014	0.0121	-7.19E-05	3.65E-02	4.31E-02
(start)	time	position	amplitude	semi-major	celerity	position	amplitude	wavelength	celerity
timeprint	t	x	a	b	c	x/h	a/h	λ/h	c/c_0
(1:04.30)	(s)	(m)	(m)	(m)	(m/s)				
1:33.70	29.7	1.06	0.0162	0.0308	0.032	247	3.756	7.365	2.662
1:41.98	37.98	1.33	0.0165	0.0301	0.031	308	3.826	7.255	2.564
1:50.38	46.38	1.58	0.0150	0.0324	0.030	368	3.477	7.622	2.464
1:58.60	54.6	1.82	0.0147	0.0262	0.029	424	3.407	6.470	2.366
2:07.90	63.9	2.08	0.0117	0.0209	0.027	484	2.709	5.369	2.256
2:19.08	75.08	2.38	0.0096	0.0150	0.026	553	2.221	4.222	2.123
2:39.78	95.78	2.88	0.0072	0.0165	0.023	670	1.663	4.302	1.877
2:53.87	109.87	3.19	0.0057	0.0101	0.021	741	1.326	3.110	1.710

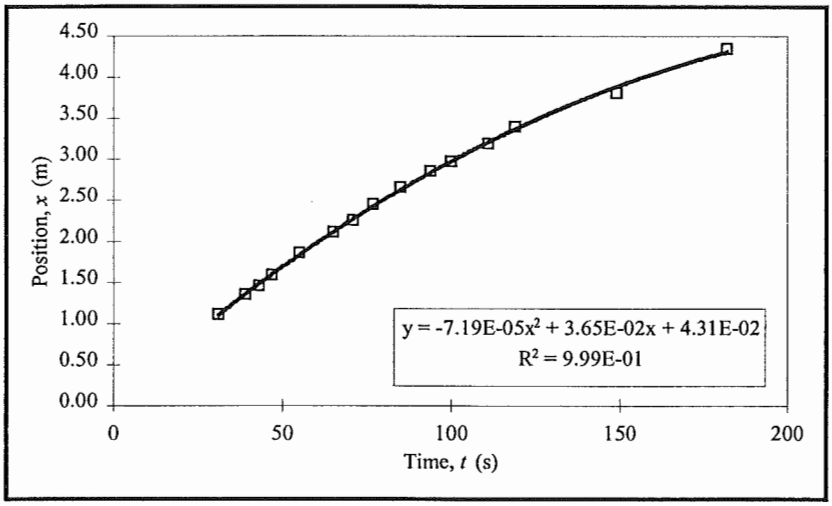

Figure A6.6a - Time-position data from run 50110PE020

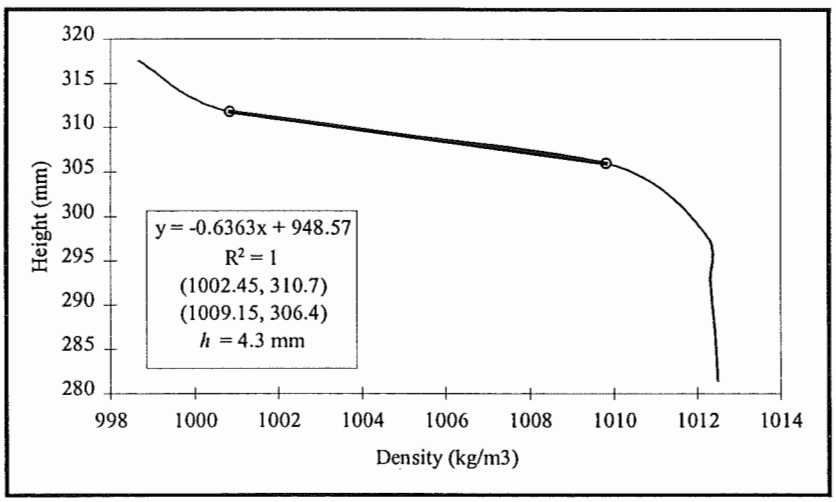

Figure A6.6b - Interfacial region density profile from run 50110PE020

Table A6.7 - Experimental data from run 50630PI020

50630PI020		Infinitesimal Wave Speed Parameters					Distance Equation Coefficients		
		ω	h	H/h	δ	c_0	k_1	k_2	k_3
		0.0070	0.0039	77	0.013	0.0115	-2.27E-05	5.27E-02	-9.07E-02
(start)	time	position	amplitude	semi-major	celerity	position	amplitude	wavelength	celerity
timeprint	t	x	a	b	c	x/h	a/h	λ/h	c/c_0
(0:52.54)	(s)	(m)	(m)	(m)	(m/s)				
2:18.20	85.66	4.26	0.0455	0.0875	0.049	1092	11.667	20.659	4.259
2:23.70	91.16	4.52	0.0435	0.0910	0.049	1160	11.154	21.388	4.238
2:32.70	100.16	4.96	0.0430	0.0890	0.048	1272	11.026	20.949	4.202
2:37.10	104.56	5.17	0.0410	0.0845	0.048	1326	10.513	19.951	4.185

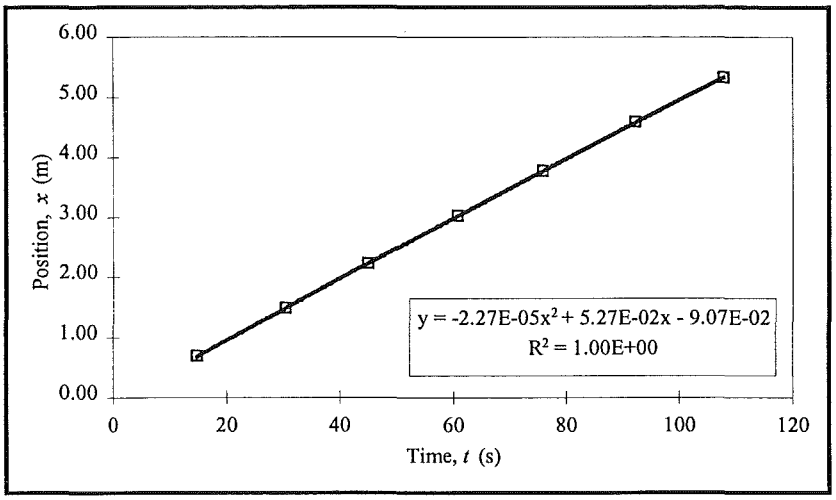

Figure A6.7a - Time-position data from run 50630PI020

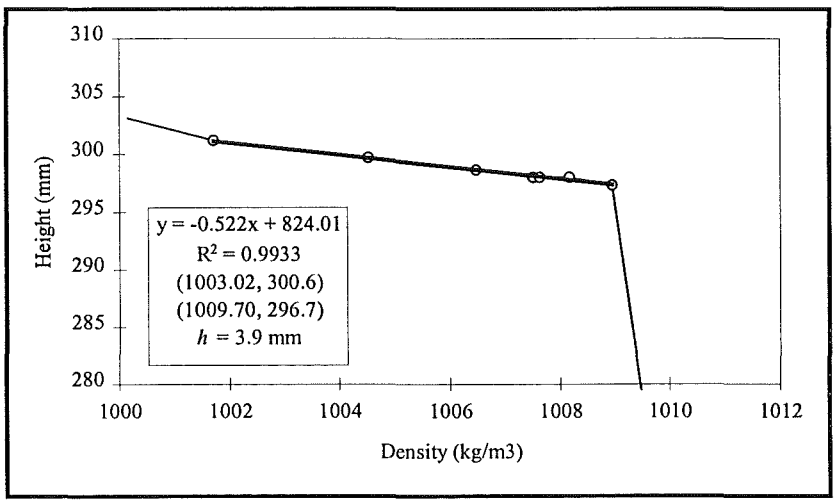

Figure A6.7b - Interfacial region density profile from run 50630PI020

Table A6.8 - Experimental data from run 50701PI020

50701PI020		Infinitesimal Wave Speed Parameters					Distance Equation Coefficients		
		ω	h	H/h	δ	c_0	k_1	k_2	k_3
		0.0070	0.0039	77	0.013	0.0115	-2.26E-05	4.43E-02	-1.63E-01
(start)	time	position	amplitude	semi-major	celerity	position	amplitude	wavelength	celerity
timeprint	t	x	a	b	c	x/h	a/h	λ/h	c/c_0
(1:27.63)	(s)	(m)	(m)	(m)	(m/s)				
2:42.20	74.57	3.01	0.0315	0.0680	0.041	773	8.077	16.250	3.572
2:52.30	84.67	3.43	0.0320	0.0715	0.040	878	8.205	17.007	3.532
2:56.80	89.17	3.61	0.0305	0.0665	0.040	925	7.821	15.909	3.514
3:11.00	103.37	4.17	0.0295	0.062	0.040	1070	7.564	14.930	3.458
3:21.30	113.67	4.58	0.0295	0.062	0.039	1175	7.564	14.930	3.417
3:30.20	122.57	4.93	0.0300	0.061	0.039	1263	7.692	14.728	3.382
3:39.80	132.17	5.30	0.0300	0.068	0.038	1358	7.692	16.218	3.344

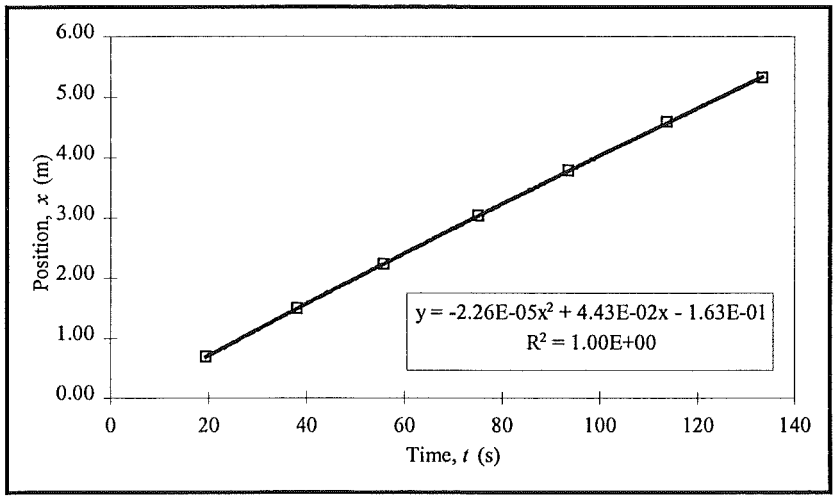

Figure A6.8a - Time-position data from run 50701PI020

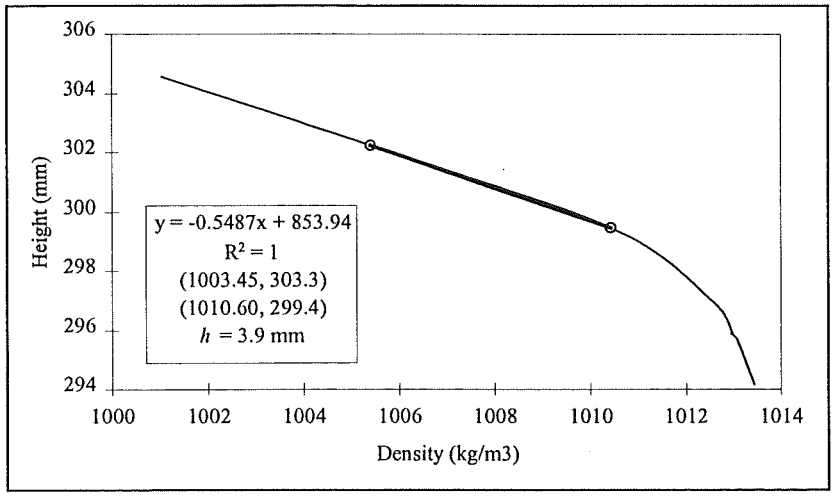

Figure A6.8b - Interfacial region density profile from run 50701PI020

Table A6.9 - Experimental data from run 50703PI020

50703PI020		Infinitesimal Wave Speed Parameters					Distance Equation Coefficients		
		ω	h	H/h	δ	c_0	k_1	k_2	k_3
		0.0070	0.0059	51	0.020	0.0140	-1.98E-05	3.76E-02	-1.51E-01
(start)	time	position	amplitude	semi-major	celerity	position	amplitude	wavelength	celerity
timeprint	t	x	a	b	c	x/h	a/h	λ/h	c/c_0
(1:04.59)	(s)	(m)	(m)	(m)	(m/s)				
2:31.70	87.11	2.97	0.0250	0.0565	0.034	504	4.237	9.380	2.435
2:42.10	97.51	3.33	0.0235	0.0500	0.034	564	3.983	8.457	2.406
2:54.70	110.11	3.75	0.0240	0.0550	0.033	635	4.068	9.149	2.370
3:06.00	121.41	4.12	0.0240	0.0590	0.033	699	4.068	9.692	2.338
3:19.90	135.31	4.57	0.0215	0.0540	0.032	775	3.644	8.937	2.299
3:30.00	145.41	4.90	0.0215	0.0540	0.032	830	3.644	8.937	2.270
3:41.00	156.41	5.25	0.0210	0.0500	0.031	889	3.559	8.382	2.239

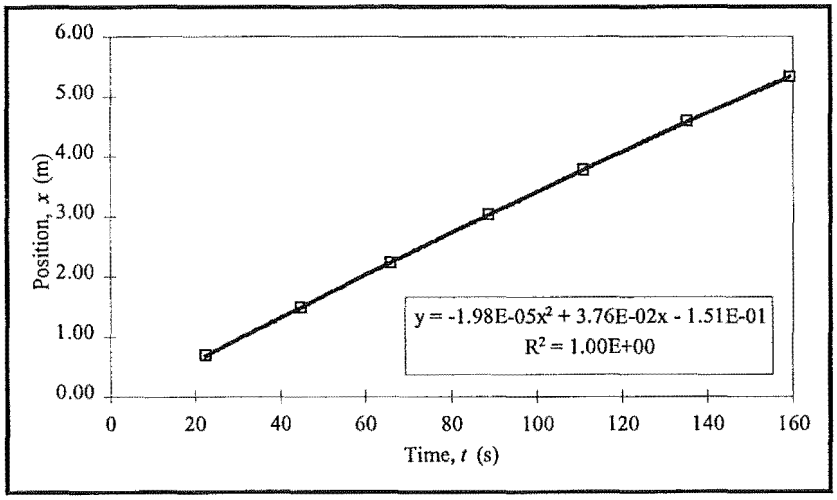

Figure A6.9a - Time-position data from run 50703PI020

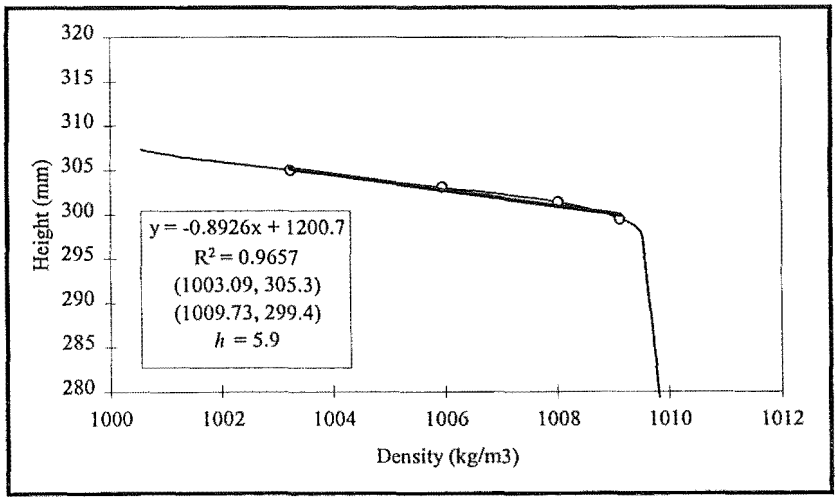

Figure A6.9b - Interfacial region density profile from run 50703PI020

Table A6.10 - Experimental data from run 50726PI020

50726PI020		Infinitesimal Wave Speed Parameters					Distance Equation Coefficients		
		ω	h	H/h	δ	c_0	k_1	k_2	k_3
		0.0071	0.0043	70	0.014	0.0121	-9.86E-05	5.50E-02	2.05E-01
(start)	time	position	amplitude	semi-major	celerity	position	amplitude	wavelength	celerity
timeprint	t	x	a	b	c	x/h	a/h	λ/h	c/c_0
(1:15.13)	(s)	(m)	(m)	(m)	(m/s)				
2:29.20	74.07	3.74	0.0315	0.0785	0.040	869	7.326	16.864	3.337
2:38.00	82.87	4.09	0.0315	0.0800	0.039	950	7.326	17.153	3.193
2:51.30	96.17	4.58	0.0280	0.0670	0.036	1066	6.512	14.570	2.977
3:01.00	105.87	4.92	0.0260	0.0675	0.034	1145	6.047	14.612	2.819
3:12.00	116.87	5.29	0.0240	0.0545	0.032	1229	5.581	12.078	2.639

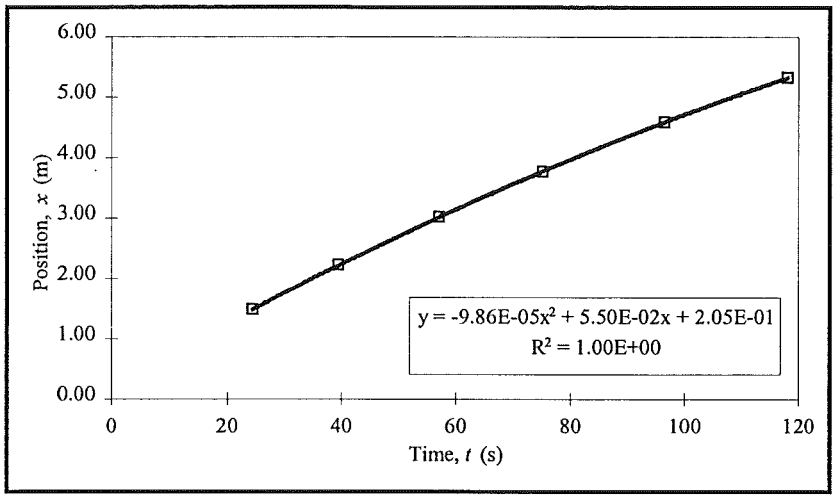

Figure A6.10a - Time-position data from run 50726PI020

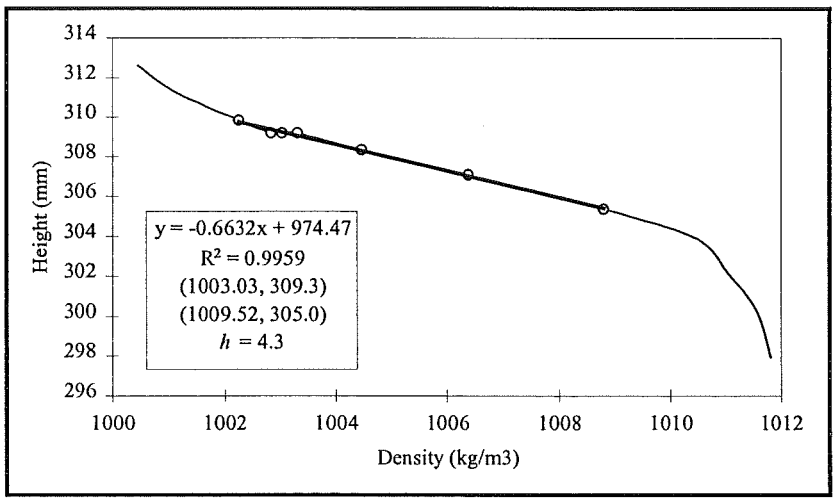

Figure A6.10b - Interfacial region density profile from run 50726PI020

Table A6.11 - Experimental data from run 50727PI020

50727PI020		Infinitesimal Wave Speed Parameters					Distance Equation Coefficients		
		ω	h	H/h	δ	c_0	k_1	k_2	k_3
		0.0071	0.0042	71	0.014	0.0120	-8.74E-05	5.10E-02	1.64E-01
(start)	time	position	amplitude	semi-major	celerity	position	amplitude	wavelength	celerity
timeprint	t	x	a	b	c	x/h	a/h	λ/h	c/c_0
(1:44.22)	(s)	(m)	(m)	(m)	(m/s)				
2:53.70	69.48	3.29	0.0270	0.0735	0.039	782	6.429	16.141	3.247
3:07.20	82.98	3.79	0.0240	0.0580	0.036	903	5.714	13.022	3.049
3:16.10	91.88	4.11	0.0235	0.0565	0.035	979	5.595	12.715	2.919
3:30.00	105.78	4.58	0.0225	0.0505	0.033	1091	5.357	11.519	2.716
3:40.00	115.78	4.90	0.0205	0.0490	0.031	1166	4.881	11.165	2.570
3:52.90	128.68	5.28	0.0180	0.037	0.029	1257	4.286	8.772	2.382

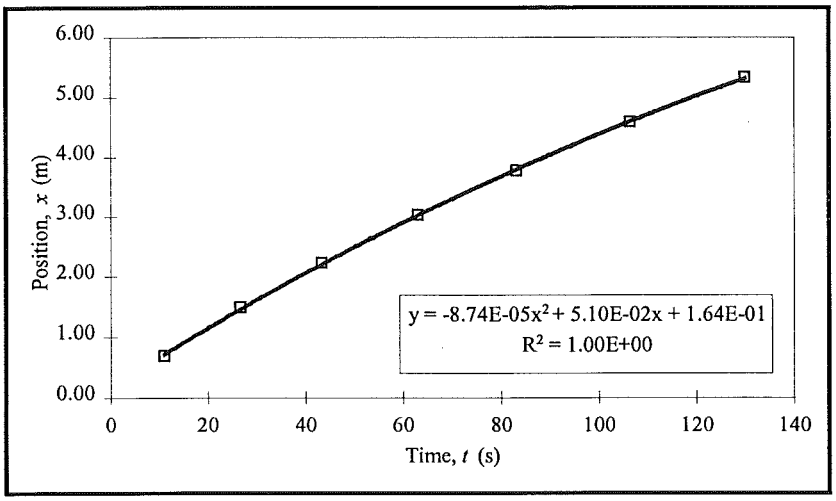

Figure A6.11a - Time-position data from run 50727PI020

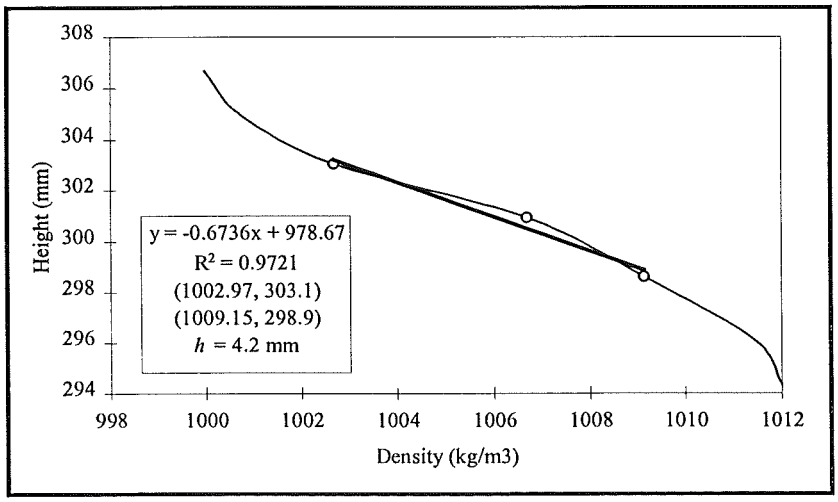

Figure A6.11b - Interfacial region density profile from run 50727PI020

Table A6.12 - Experimental data from run 50123PE022

50123PE022		Infinitesimal Wave Speed Parameters					Distance Equation Coefficients		
		ω	h	H/h	δ	c_0	k_1	k_2	k_3
		0.0078	0.0040	75	0.013	0.0122	-6.64E-05	3.87E-02	1.50E-02
(start)	time	position	amplitude	semi-major	celerity	position	amplitude	wavelength	celerity
timeprint	t	x	a	b	c	x/h	a/h	λ/h	c/c_0
(0:58.69)	(s)	(m)	(m)	(m)	(m/s)				
1:41.05	42.36	1.54	0.0204	0.0480	0.033	384	5.088	11.465	2.700
1:48.94	50.25	1.79	0.0191	0.0450	0.032	448	4.775	10.802	2.615
1:59.34	60.65	2.12	0.0171	0.0387	0.031	529	4.263	9.464	2.502
2:06.76	68.07	2.34	0.0151	0.0347	0.030	585	3.763	8.569	2.422
2:17.39	78.7	2.65	0.0143	0.0306	0.028	662	3.563	7.719	2.306
2:24.67	85.98	2.85	0.0128	0.0269	0.027	713	3.200	6.921	2.227
2:38.02	99.33	3.20	0.0110	0.0245	0.026	801	2.750	6.365	2.083
2:45.24	106.55	3.38	0.0098	0.0218	0.025	846	2.438	5.757	2.004
2:54.59	115.9	3.61	0.0075	0.0140	0.023	902	1.875	4.137	1.903
3:05.89	127.2	3.86	0.0053	0.0115	0.022	966	1.325	3.469	1.781
3:25.70	147.01	4.27	0.0051	0.0096	0.019	1067	1.275	3.124	1.566

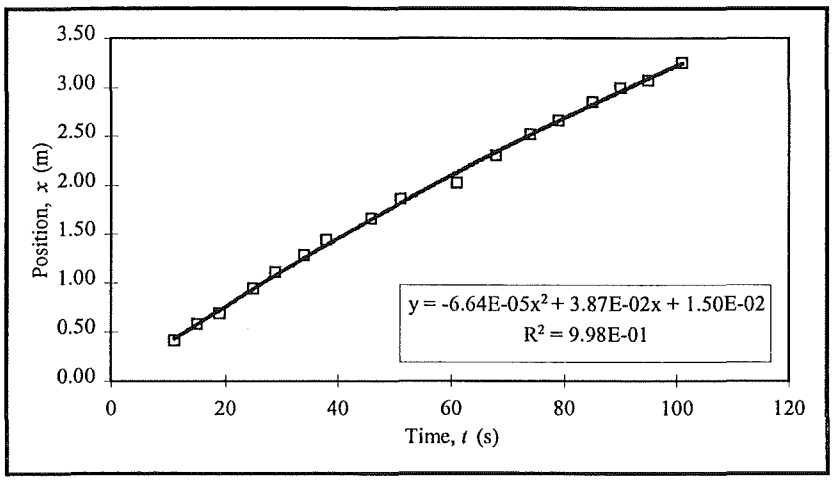

Figure A6.12a - Time-position data from run 50123PE022

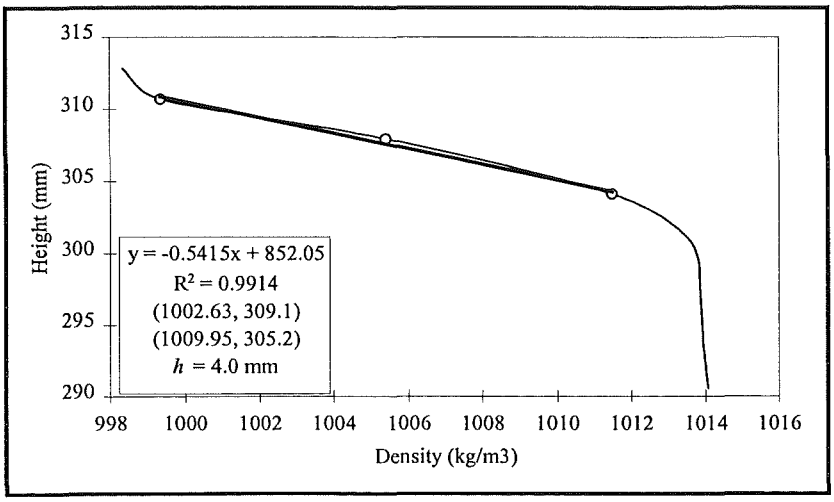

Figure A6.12b - Interfacial region density profile from run 50123PE023

Table A6.13 - Experimental data from run 50111PE025

50111PE025		Infinitesimal Wave Speed Parameters					Distance Equation Coefficients		
		ω	h	H/h	δ	c_0	k_1	k_2	k_3
		0.0088	0.0039	77	0.013	0.0128	-1.27E-04	5.68E-02	1.01E-01
(start) timeprint (2:23.40)	time t (s)	position x (m)	amplitude a (m)	semi-major b (m)	celerity c (m/s)	position x/h	amplitude a/h	wavelength λ/h	celerity c/c_0
3:40.58	77.18	3.73	0.0236	0.0632	0.037	956	6.038	15.027	2.895
3:52.97	89.57	4.17	0.0212	0.0592	0.034	1069	5.436	14.094	2.650
3:59.78	96.38	4.40	0.0198	0.0537	0.032	1127	5.064	12.889	2.515
4:08.65	105.25	4.67	0.0195	0.0506	0.030	1198	5.000	12.233	2.340
4:13.70	110.3	4.82	0.0186	0.0439	0.029	1236	4.769	10.816	2.240

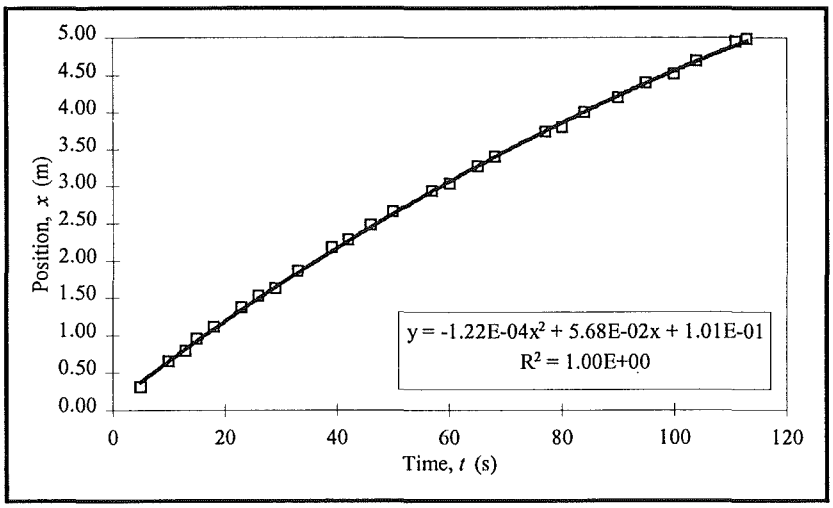

Figure A6.13a - Time-position data from run 50111PE025

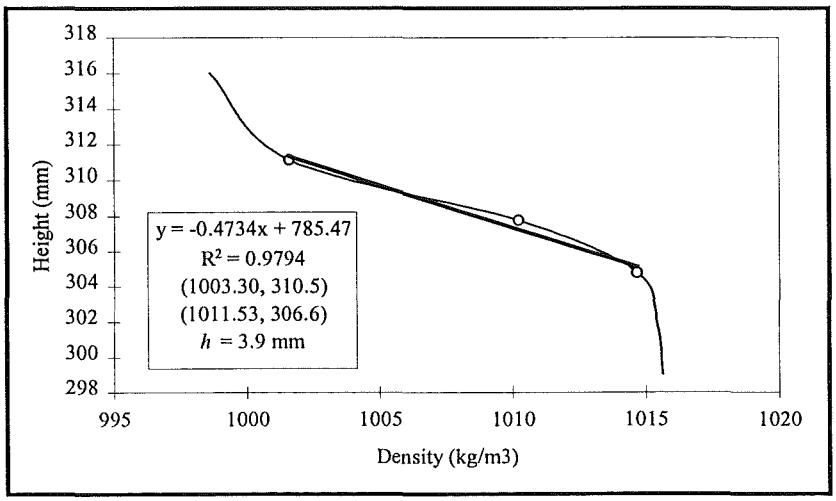

Figure A6.13b - Interfacial region density profile from run 50111PE025

Table A6.14 - Experimental data from run 50827PE025

50827PE025		Infinitesimal Wave Speed Parameters					Distance Equation Coefficients		
		ω	h	H/h	δ	c_0	k_1	k_2	k_3
		0.0087	0.0030	100	0.010	0.0112	-1.03E-04	4.42E-02	1.23E-02
(start)	time	position	amplitude	semi-major	celerity	position	amplitude	wavelength	celerity
timeprint	t	x	a	b	c	x/h	a/h	λ/h	c/c_0
(1:10.55)	(s)	(m)	(m)	(m)	(m/s)				
1:24.22	13.67	0.60	0.0240	0.0470	0.041	199	8.000	14.773	3.685
1:32.63	22.08	0.94	0.0240	0.0535	0.040	313	8.000	16.574	3.531
1:42.27	31.72	1.31	0.0225	0.0450	0.038	437	7.500	14.181	3.354
1:50.60	40.05	1.62	0.0155	0.0310	0.036	539	5.167	10.119	3.201
1:56.70	46.15	1.83	0.0120	0.0250	0.035	611	4.000	8.347	3.089
2:35.00	84.45	3.01	0.0110	0.0240	0.027	1003	3.667	8.025	2.387
2:47.90	97.35	3.34	0.0080	0.0165	0.024	1113	2.667	5.863	2.150
3:04.00	113.45	3.70	0.0050	0.0100	0.021	1234	1.667	3.946	1.855
3:15.50	124.95	3.93	0.0050	0.0095	0.018	1309	1.667	3.825	1.644

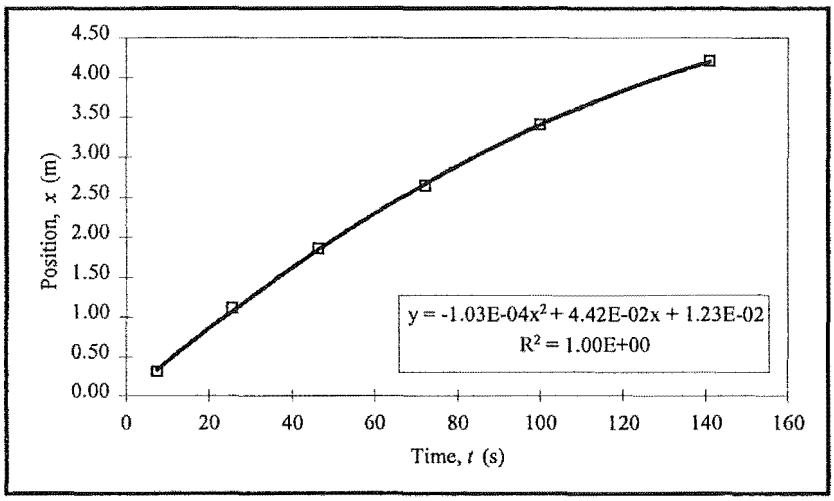

Figure A6.14a - Time-position data from run 50827PE025

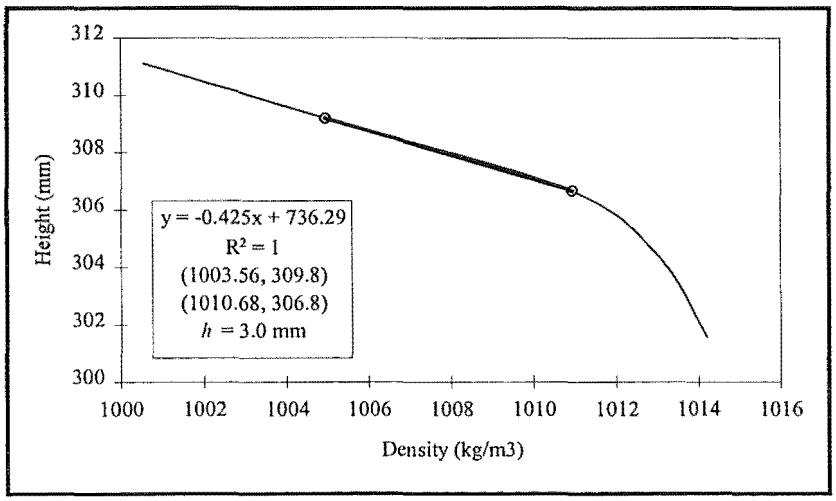

Figure A6.14b - Interfacial region density profile from run 50827PE025

Table A6.15 - Experimental data from run 50125PE028

50125PE028		Infinitesimal Wave Speed Parameters					Distance Equation Coefficients		
		ω	h	H/h	δ	c_0	k_1	k_2	k_3
		0.0099	0.0031	97	0.010	0.0122	-1.39E-04	5.90E-02	1.14E-01
(start)	time	position	amplitude	semi-major	celerity	position	amplitude	wavelength	celerity
timeprint	t	x	a	b	c	x/h	a/h	λ/h	c/c_0
00:48.69	(s)	(m)	(m)	(m)	(m/s)				
2:45.08	106.4	4.82	0.0171	0.0378	0.029	1554	5.500	11.675	2.417

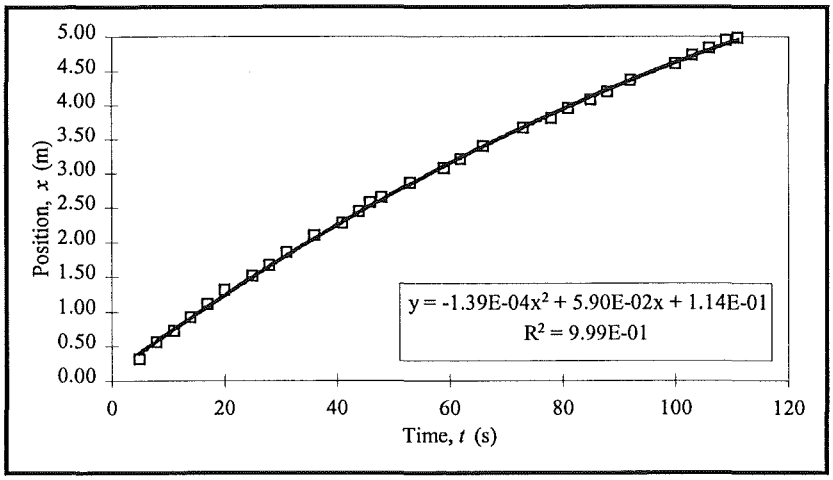

Figure A6.15a - Time-position data from run 50125PE028

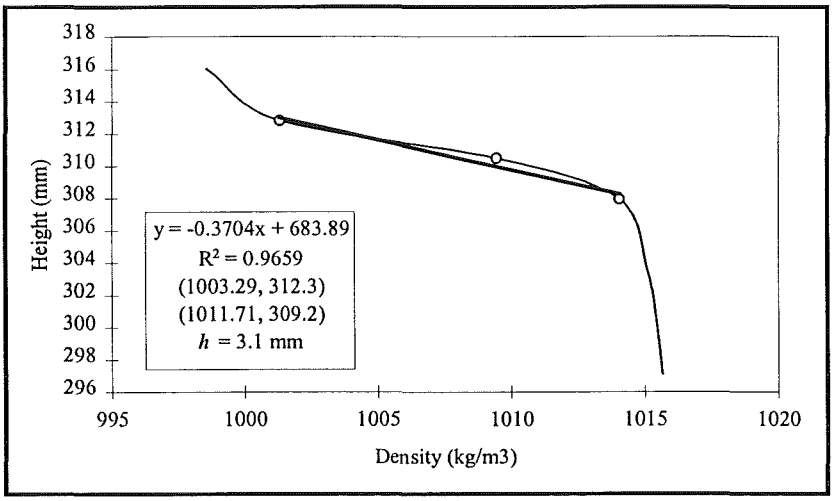

Figure A6.15b - Interfacial region density profile from run 50125PE028

Table A6.16 - Experimental data from run 50109PE030

50109PE030		Infinitesimal Wave Speed Parameters					Distance Equation Coefficients		
		ω	h	H/h	δ	c_0	k_1	k_2	k_3
		0.0106	0.0064	47	0.022	0.0180	-1.17E-04	5.49E-02	6.47E-02
(start)	time	position	amplitude	semi-major	celerity	position	amplitude	wavelength	celerity
timeprint	t	x	a	b	c	x/h	a/h	λ/h	c/c_0
(1:46.77)	(s)	(m)	(m)	(m)	(m/s)				
3:03.00	76.23	3.57	0.0195	0.0457	0.037	558	3.047	7.224	2.064
3:16.50	89.73	4.05	0.0165	0.0389	0.034	633	2.570	6.284	1.889
3:26.00	99.2	4.36	0.0152	0.0361	0.032	681	2.367	5.892	1.765
3:27.30	100.53	4.40	0.0156	0.0342	0.031	688	2.438	5.686	1.748
3:33.30	106.53	4.59	0.0148	0.0273	0.030	716	2.305	4.824	1.670
3:39.30	112.53	4.76	0.0126	0.0283	0.029	744	1.961	4.842	1.591

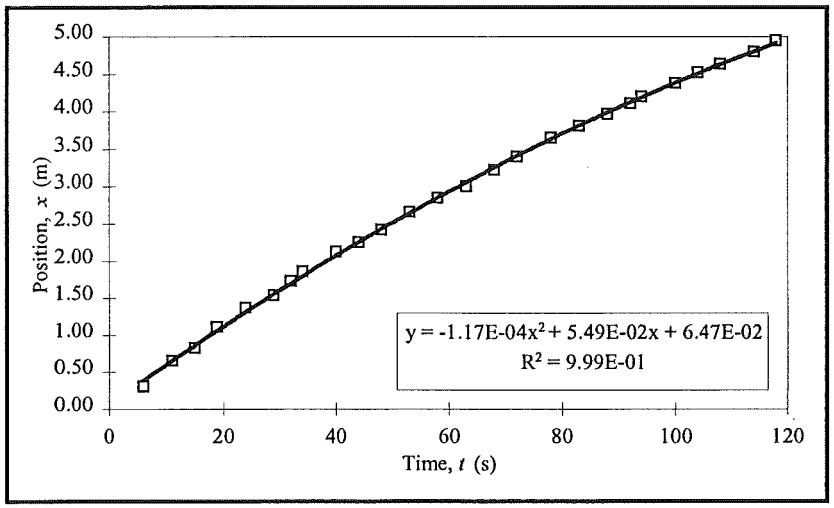

Figure A6.16a - Time-position data from run 50109PE030

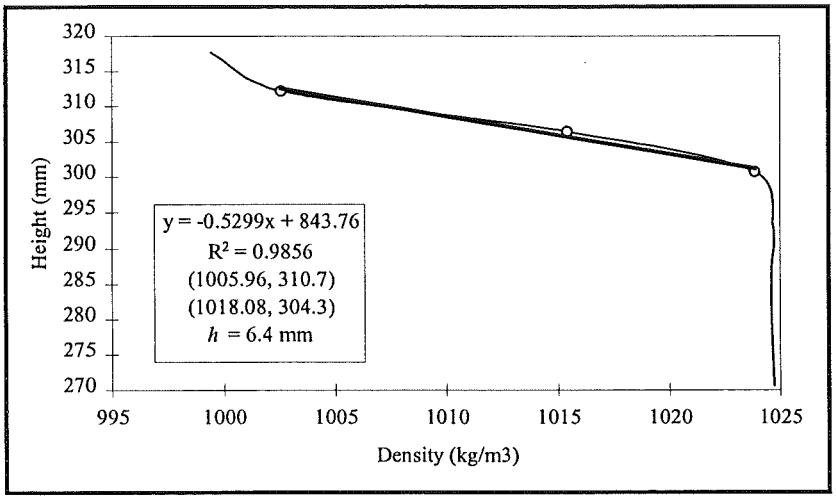

Figure A6.16b - Interfacial region density profile from run 50109PE030

Table A6.17 - Experimental data from run 50919PE030

50919PE030		Infinitesimal Wave Speed Parameters					Distance Equation Coefficients		
		ω	h	H/h	δ	c_0	k_1	k_2	k_3
		0.0105	0.0047	64	0.016	0.0154	-1.07E-04	5.19E-02	4.02E-02
(start)	time	position	amplitude	semi-major	celerity	position	amplitude	wavelength	celerity
timeprint	t	x	a	b	c	x/h	a/h	λ/h	c/c_0
(1:28.09)	(s)	(m)	(m)	(m)	(m/s)				
2:55.30	87.21	3.75	0.0120	0.0240	0.033	798	2.553	5.533	2.162
3:07.40	99.31	4.14	0.0110	0.0245	0.031	881	2.340	5.559	1.993
3:22.20	114.11	4.57	0.0095	0.0205	0.027	972	2.021	4.823	1.787
3:40.00	131.91	5.02	0.0075	0.0145	0.024	1069	1.596	3.740	1.539

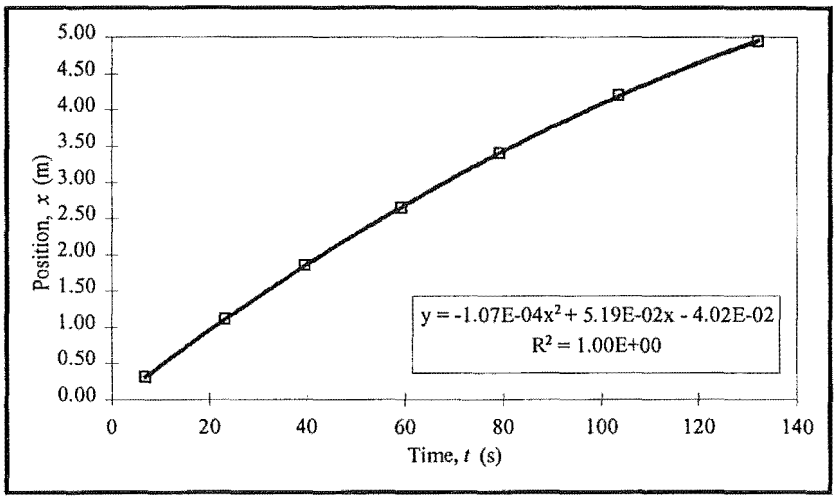

Figure A6.17a - Time-position data from run 50919PE030

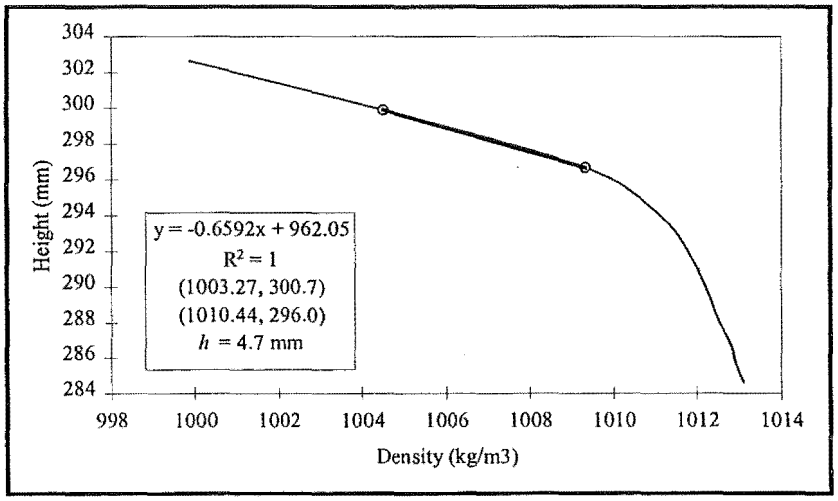

Figure A6.17b - Interfacial region density profile from run 50919PE030

Table A6.18 - Experimental data from run 50903PE040

50903PE040		Infinitesimal Wave Speed Parameters					Distance Equation Coefficients		
		ω	h	H/h	δ	c_0	k_1	k_2	k_3
		0.0141	0.0040	75	0.013	0.0165	-9.32E-05	5.63E-02	9.57E-02
(start) timeprint (1:33.51)	time t (s)	position x (m)	amplitude a (m)	semi-major b (m)	celerity c (m/s)	position x/h	amplitude a/h	wavelength λ/h	celerity c/c_0
1:52.21	18.70	1.12	0.0295	0.0530	0.053	279	7.375	12.720	3.207
1:58.01	24.50	1.42	0.0270	0.0520	0.052	355	6.750	12.464	3.142
2:06.13	32.62	1.83	0.0220	0.0460	0.050	458	5.500	11.108	3.050
2:13.01	39.50	2.17	0.0190	0.0380	0.049	544	4.750	9.392	2.972
2:35.00	61.49	3.21	0.0215	0.0435	0.045	801	5.375	10.584	2.723
2:49.20	75.69	3.82	0.0170	0.0385	0.042	956	4.250	9.422	2.562
2:57.40	83.89	4.16	0.0175	0.038	0.041	1041	4.375	9.340	2.469
3:04.40	90.89	4.44	0.0160	0.0345	0.039	1111	4.000	8.580	2.390
3:15.50	101.99	4.87	0.0150	0.0315	0.037	1217	3.750	7.940	2.264

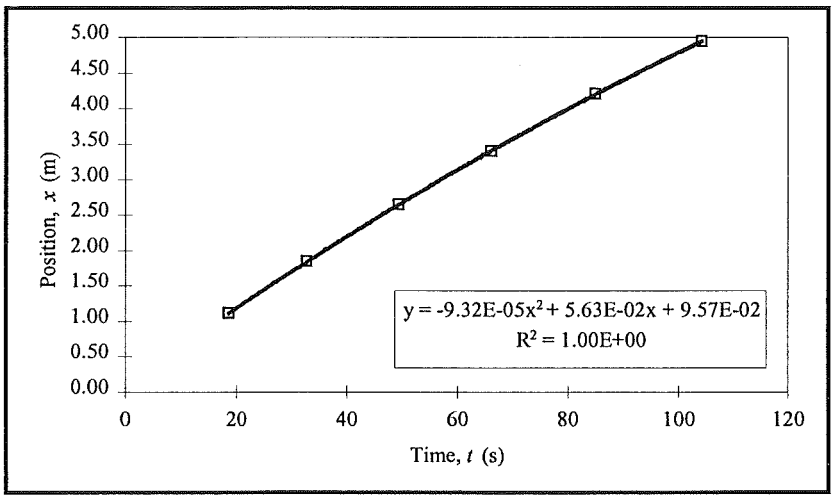

Figure A6.18a - Time-position data from run 50903PE040

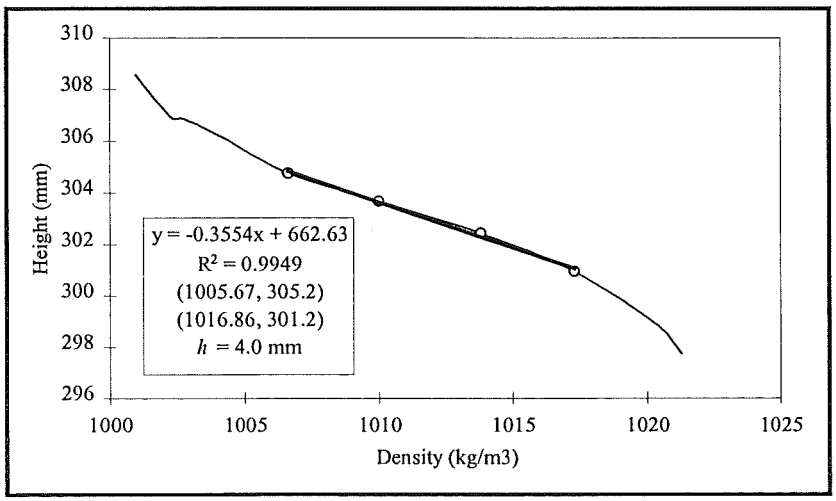

Figure A6.18b - Interfacial region density profile from run 50903PE040

Table A6.19 - Experimental data from run 50923PE040

50923PE040		Infinitesimal Wave Speed Parameters					Distance Equation Coefficients		
		ω	h	H/h	δ	c_0	k_1	k_2	k_3
		0.0141	0.0033	91	0.011	0.0150	-1.12E-04	5.73E-02	2.44E-02
(start)	time	position	amplitude	semi-major	celerity	position	amplitude	wavelength	celerity
timeprint	t	x	a	b	c	x/h	a/h	λ/h	c/c_0
(1:06.71)	(s)	(m)	(m)	(m)	(m/s)				
2:22.20	75.49	3.71	0.0160	0.0350	0.040	1125	4.848	10.301	2.696
2:35.00	88.29	4.21	0.0145	0.0330	0.038	1276	4.394	9.746	2.504
2:42.00	95.29	4.47	0.0135	0.0305	0.036	1354	4.091	9.089	2.400
2:52.00	105.29	4.82	0.0125	0.0235	0.034	1459	3.788	7.346	2.250

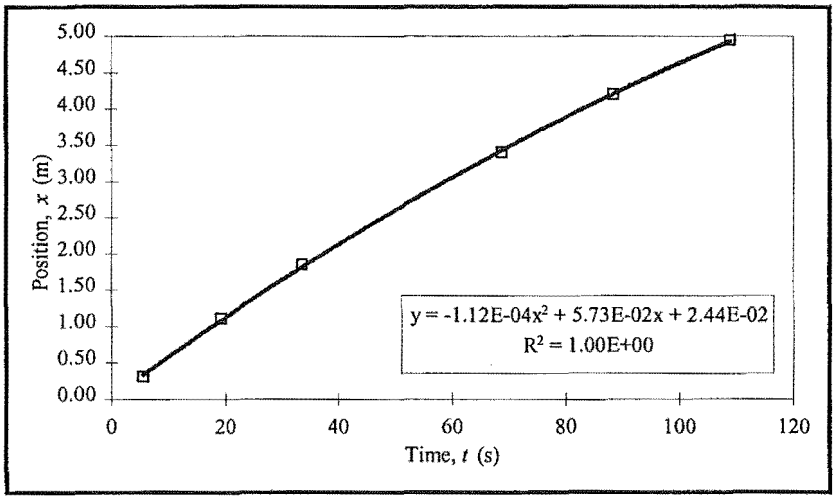

Figure A6.19a - Time-position data from run 50923PE040

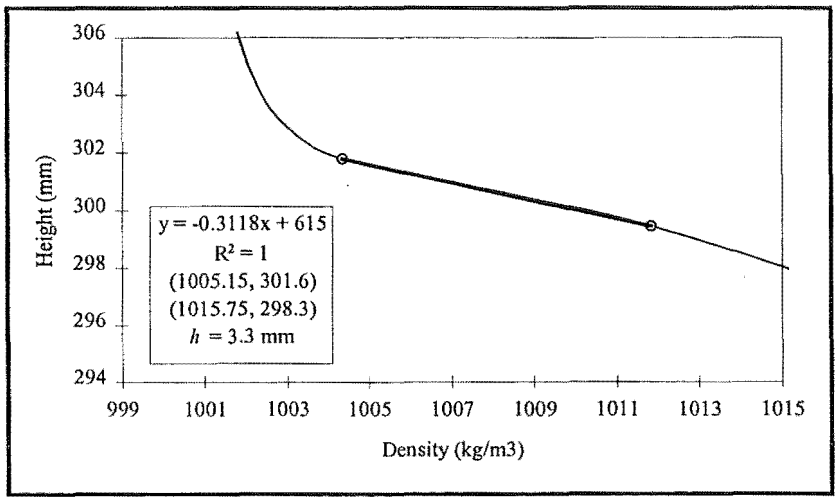

Figure A6.19b - Interfacial region density profile from run 50923PE040

Table A6.20 - Experimental data from run 41223PE050

41223PE050		Infinitesimal Wave Speed Parameters					Distance Equation Coefficients		
		ω	h	H/h	δ	c_0	k_1	k_2	k_3
		0.0176	0.0064	47	0.022	0.0231	-1.88E-04	7.29E-02	7.46E-02
(start)	time	position	amplitude	semi-major	celerity	position	amplitude	wavelength	celerity
timeprint	t	x	a	b	c	x/h	a/h	λ/h	c/c_0
(7:08.89)	(s)	(m)	(m)	(m)	(m/s)				
7:57.84	48.95	3.19	0.0289	0.0732	0.054	499	4.516	10.924	2.356
8:34.17	85.28	4.92	0.0215	0.0495	0.041	769	3.359	7.757	1.765

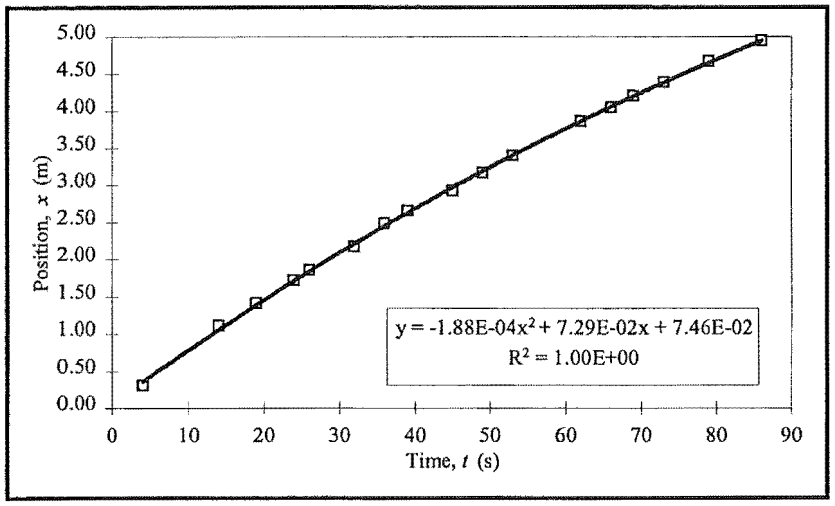

Figure A6.20a - Time-position data from run 41223PE050

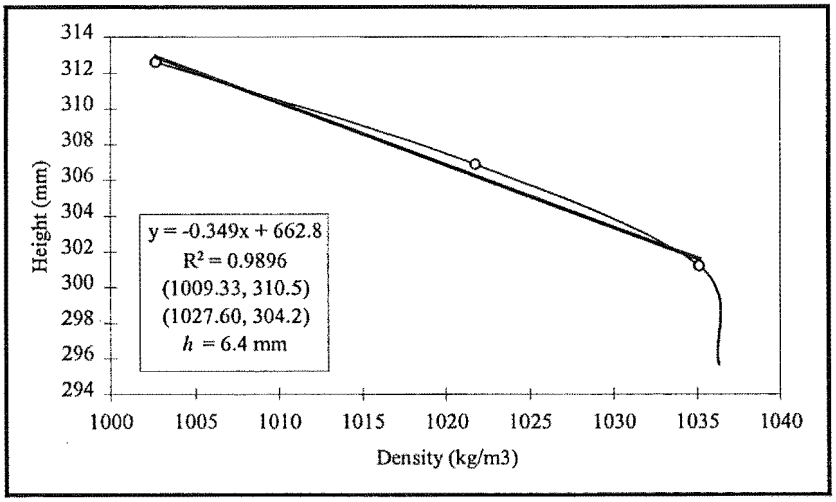

Figure A6.20b - Interfacial region density profile from run 41223PE050

Table A6.21 - Experimental data from run 41224PE050

41224PE050		Infinitesimal Wave Speed Parameters					Distance Equation Coefficients		
		ω	h	H/h	δ	c_0	k_1	k_2	k_3
		0.0176	0.0049	61	0.017	0.0203	-1.79E-04	7.33E-02	3.36E-03
(start) timeprint (0:51.81)	time t (s)	position x (m)	amplitude a (m)	semi-major b (m)	celerity c (m/s)	position x/h	amplitude a/h	wavelength λ/h	celerity c/c_0
1:03.52	11.71	0.84	0.0406	0.0796	0.069	171	8.276	15.265	3.404
1:36.70	44.89	2.93	0.0317	0.0732	0.057	599	6.469	14.036	2.819
1:43.62	51.81	3.32	0.0310	0.0751	0.055	678	6.327	14.331	2.697
1:51.63	59.82	3.75	0.0287	0.0711	0.052	765	5.847	13.613	2.556
2:14.70	82.89	4.85	0.0214	0.0464	0.044	990	4.367	9.314	2.149

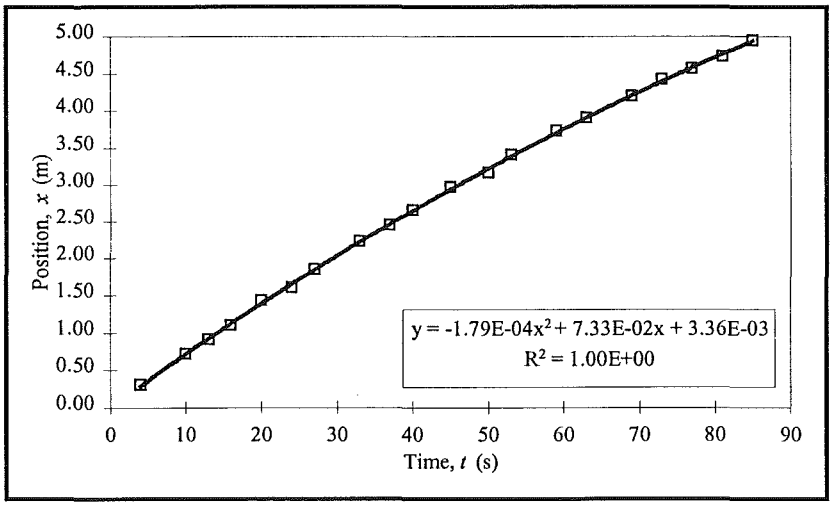

Figure A6.21a - Time-position data from run 41224PE050

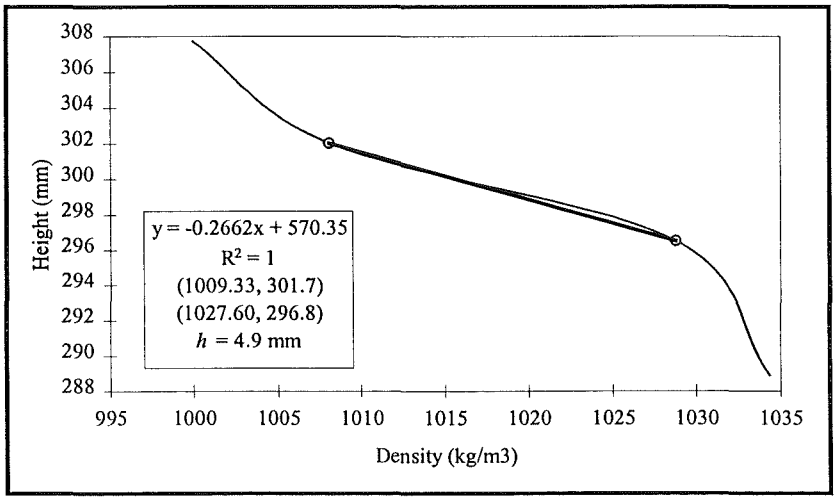

Figure A6.21b - Interfacial region density profile from run 41224PE050

Table A6.22 - Experimental data from run 50121PE050

50121PE050		Infinitesimal Wave Speed Parameters					Distance Equation Coefficients		
		ω	h	H/h	δ	c_0	k_1	k_2	k_3
		0.0176	0.0040	75	0.013	0.0184	-1.95E-04	7.03E-02	1.28E-01
(start)	time	position	amplitude	semi-major	celerity	position	amplitude	wavelength	celerity
timeprint	t	x	a	b	c	x/h	a/h	λ/h	c/c_0
(1:17.26)	(s)	(m)	(m)	(m)	(m/s)				
2:18.26	61	3.69	0.0204	0.0540	0.047	923	5.088	12.674	2.528
2:25.38	68.12	4.01	0.0190	0.0477	0.044	1003	4.738	11.353	2.377
2:29.79	72.53	4.20	0.0178	0.0464	0.042	1050	4.438	11.042	2.284
2:37.95	80.69	4.53	0.0164	0.0404	0.039	1133	4.088	9.766	2.111
2:41.31	84.05	4.66	0.0162	0.0363	0.038	1165	4.038	8.946	2.039
2:45.95	88.69	4.83	0.0145	0.0305	0.036	1207	3.625	7.710	1.941
2:48.27	91.01	4.91	0.0149	0.0281	0.035	1228	3.725	7.260	1.892

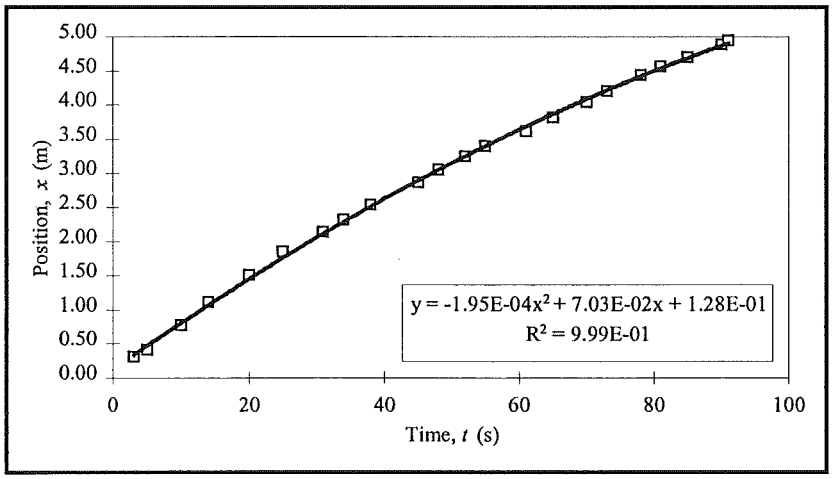

Figure A6.22a - Time-position data from run 50121PE050

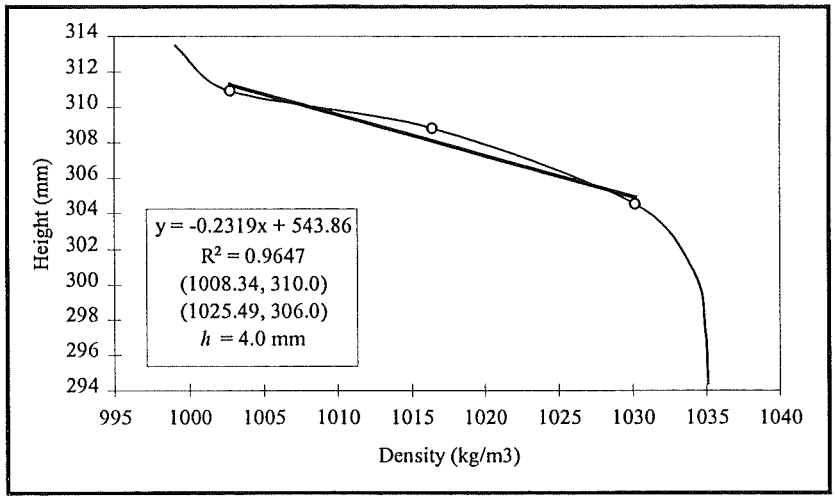

Figure A6.22b - Interfacial region density profile from run 50121PE050

Table A6.23 - Experimental data from run 50710PI050

50710PI050		Infinitesimal Wave Speed Parameters					Distance Equation Coefficients		
		ω	h	H/h	δ	c_0	k_1	k_2	k_3
		0.0176	0.0039	77	0.013	0.0182	-4.05E-05	4.48E-02	-2.60E-01
(start)	time	position	amplitude	semi-major	celerity	position	amplitude	wavelength	celerity
timeprint	t	x	a	b	c	x/h	a/h	λ/h	c/c_0
(1:32.03)	(s)	(m)	(m)	(m)	(m/s)				
2:08.20	36.17	1.31	0.0165	0.0275	0.042	335	4.231	7.351	2.304
2:19.00	46.97	1.75	0.0140	0.0215	0.041	450	3.590	6.039	2.256
2:27.00	54.97	2.08	0.0135	0.0195	0.040	533	3.462	5.615	2.220
2:39.10	67.07	2.56	0.0140	0.0230	0.039	657	3.590	6.344	2.167
2:49.80	77.77	2.98	0.0125	0.0205	0.039	764	3.205	5.778	2.119
2:59.30	87.27	3.34	0.0110	0.0195	0.038	857	2.821	5.509	2.076
3:10.70	98.67	3.77	0.0085	0.0155	0.037	966	2.179	4.578	2.026
3:20.10	108.07	4.11	0.0085	0.014	0.036	1053	2.179	4.288	1.984
3:39.80	127.77	4.80	0.0075	0.012	0.034	1232	1.923	3.838	1.896
3:49.00	136.97	5.12	0.0070	0.012	0.034	1312	1.795	3.801	1.855

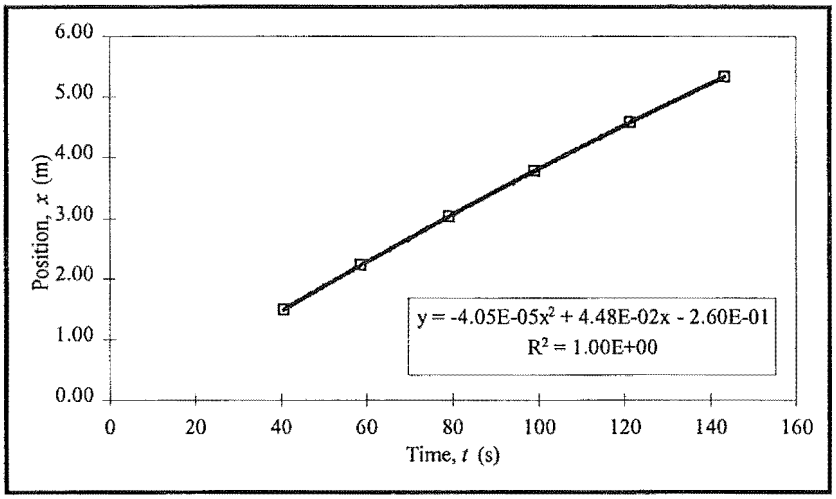

Figure A6.23a - Time-position data from run 50710PI050

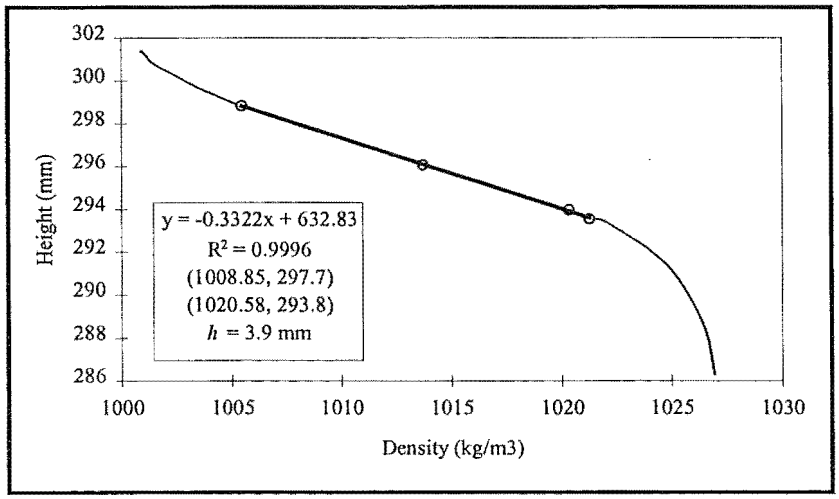

Figure A6.23b - Interfacial region density profile from run 50710PI050

Table A6.24 - Experimental data from run 50711PI050

50711PI050		Infinitesimal Wave Speed Parameters					Distance Equation Coefficients		
		ω	h	H/h	δ	c_0	k_1	k_2	k_3
		0.0175	0.0039	77	0.013	0.0181	-4.49E-05	5.11E-02	6.22E-04
(start) timeprint (1:08.50)	time t (s)	position x (m)	amplitude a (m)	semi-major b (m)	celerity c (m/s)	position x/h	amplitude a/h	wavelength λ/h	celerity c/c_0
1:46.70	38.20	1.89	0.0180	0.0385	0.048	484	4.615	9.674	2.631
1:52.70	44.20	2.17	0.0185	0.0375	0.047	557	4.744	9.484	2.601
2:03.30	54.80	2.67	0.0180	0.0375	0.046	684	4.615	9.467	2.549
2:10.10	61.60	2.98	0.0180	0.0400	0.046	764	4.615	9.985	2.515
2:19.40	70.90	3.40	0.0160	0.0350	0.045	871	4.103	8.876	2.469
2:26.90	78.40	3.73	0.0155	0.0330	0.044	957	3.974	8.445	2.432
2:35.80	87.30	4.12	0.0135	0.0300	0.043	1056	3.462	7.744	2.388
2:46.10	97.60	4.56	0.0140	0.0285	0.042	1169	3.590	7.462	2.336
2:54.30	105.80	4.90	0.0135	0.0280	0.042	1258	3.462	7.338	2.296
3:00.80	112.30	5.17	0.0135	0.0280	0.041	1326	3.462	7.338	2.264

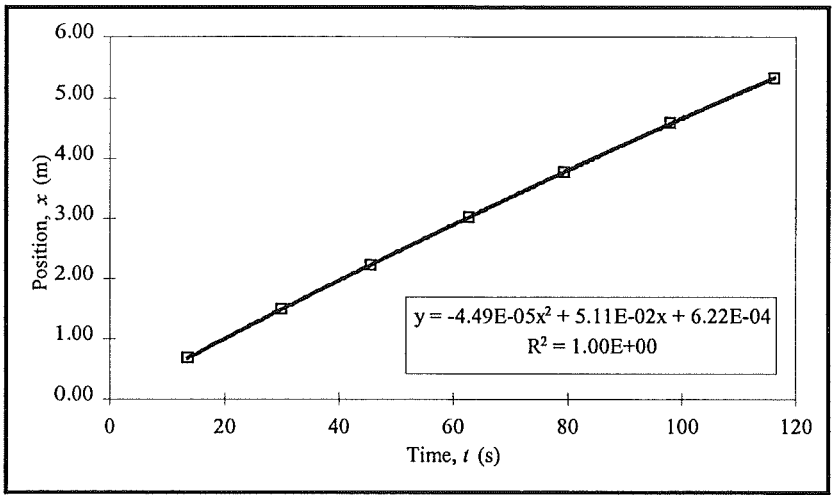

Figure A6.24a - Time-position data from run 50711PI050

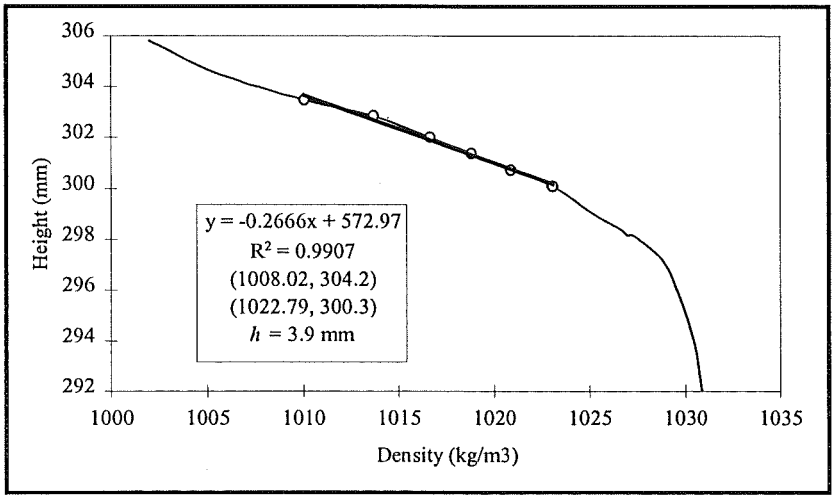

Figure A6.24b - Interfacial region density profile from run 50711PI050

Table A6.25 - Experimental data from run 50712PI050

50712PI050		Infinitesimal Wave Speed Parameters					Distance Equation Coefficients		
		ω	h	H/h	δ	c_0	k_1	k_2	k_3
		0.0175	0.0029	103	0.010	0.0157	-3.54E-05	6.05E-02	-1.63E-01
(start) timeprint (1:00.21)	time t (s)	position x (m)	amplitude a (m)	semi-major b (m)	celerity c (m/s)	position x/h	amplitude a/h	wavelength λ/h	celerity c/c_0
1:40.90	40.69	2.24	0.0245	0.0620	0.058	772	8.448	19.564	3.679
1:49.30	49.09	2.72	0.0255	0.0625	0.057	938	8.793	19.737	3.641
1:54.00	53.79	2.99	0.0245	0.0605	0.057	1031	8.448	19.133	3.619
2:02.00	61.79	3.44	0.0250	0.0590	0.056	1186	8.621	18.716	3.583
2:06.30	66.09	3.68	0.0255	0.0615	0.056	1269	8.793	19.449	3.564
2:15.10	74.89	4.17	0.0250	0.0620	0.055	1438	8.621	19.579	3.524
2:22.10	81.89	4.55	0.0255	0.0650	0.055	1570	8.793	20.456	3.492
2:26.90	86.69	4.82	0.0250	0.06	0.054	1661	8.621	19.003	3.471
2:34.20	93.99	5.21	0.0245	0.059	0.054	1797	8.448	18.702	3.438

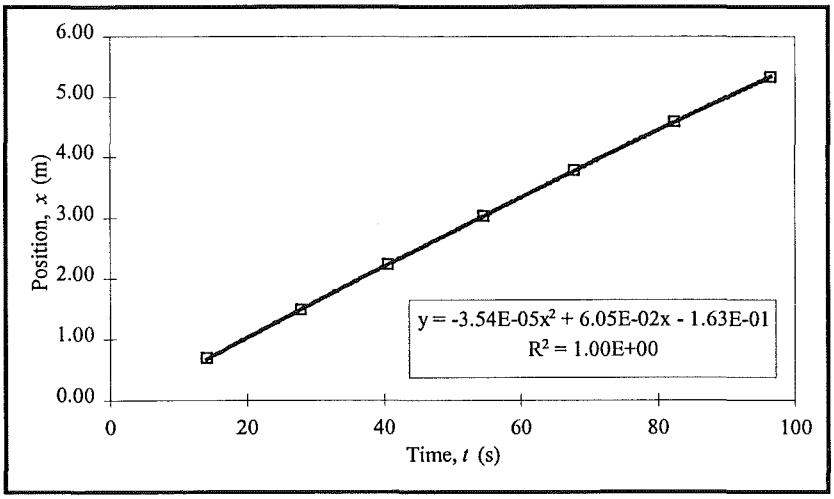

Figure A6.25a - Time-position data from run 50712PI050

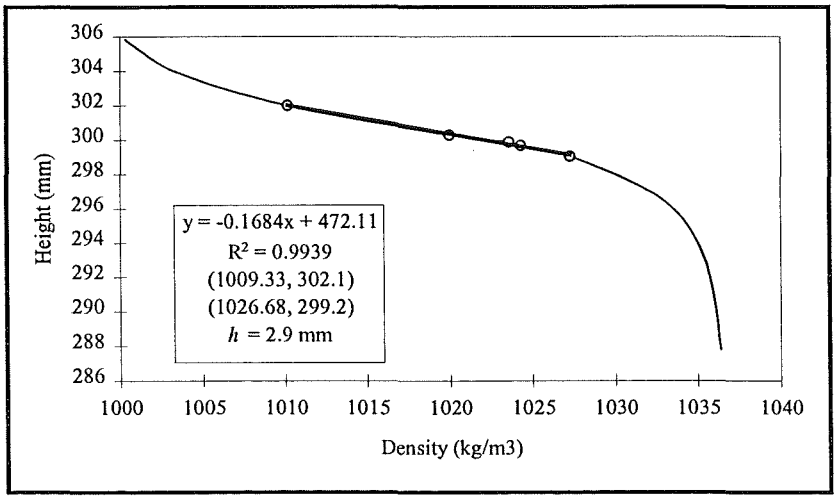

Figure A6.25b - Interfacial region density profile from run 50712PI050

Table A6.26 - Experimental data from run 50713PI050

50713PI050		Infinitesimal Wave Speed Parameters					Distance Equation Coefficients		
		ω	h	H/h	δ	c_0	k_1	k_2	k_3
		0.0175	0.0052	58	0.018	0.0209	-2.76E-05	6.70E-02	-1.81E-01
(start)	time	position	amplitude	semi-major	celerity	position	amplitude	wavelength	celerity
timeprint	t	x	a	b	c	x/h	a/h	λ/h	c/c_0
(1:13.20)	(s)	(m)	(m)	(m)	(m/s)				
1:48.20	35.00	2.13	0.0305	0.0745	0.065	410	5.865	13.465	3.120
1:57.30	44.10	2.72	0.0305	0.0745	0.065	523	5.865	13.465	3.096
2:00.50	47.30	2.93	0.0310	0.0750	0.064	563	5.962	13.555	3.088
2:05.70	52.50	3.26	0.0325	0.0790	0.064	627	6.250	14.221	3.074
2:12.80	59.60	3.71	0.0325	0.0785	0.064	714	6.250	14.141	3.055
2:19.70	66.50	4.15	0.0315	0.0805	0.063	799	6.058	14.435	3.037
2:26.00	72.80	4.55	0.0315	0.0750	0.063	875	6.058	13.566	3.020
2:33.30	80.10	5.01	0.0305	0.071	0.063	963	5.865	12.913	3.001
2:38.00	84.80	5.30	0.0315	0.0725	0.062	1020	6.058	13.172	2.988

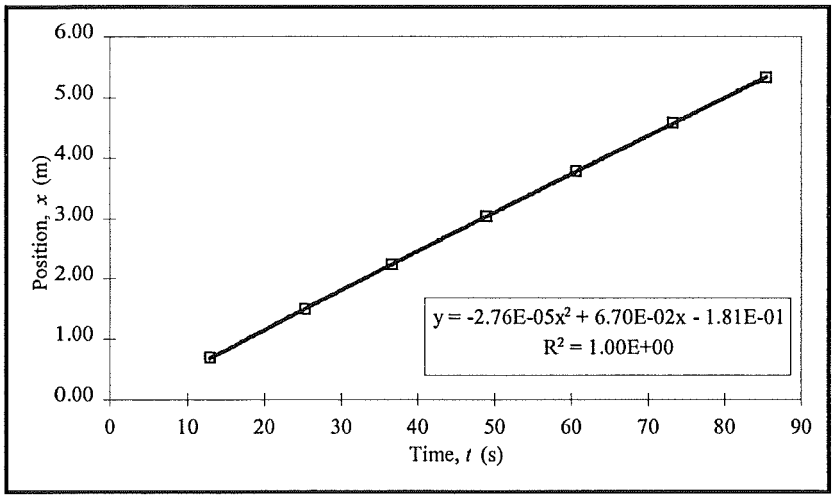

Figure A6.26a - Time-position data from run 50713PI050

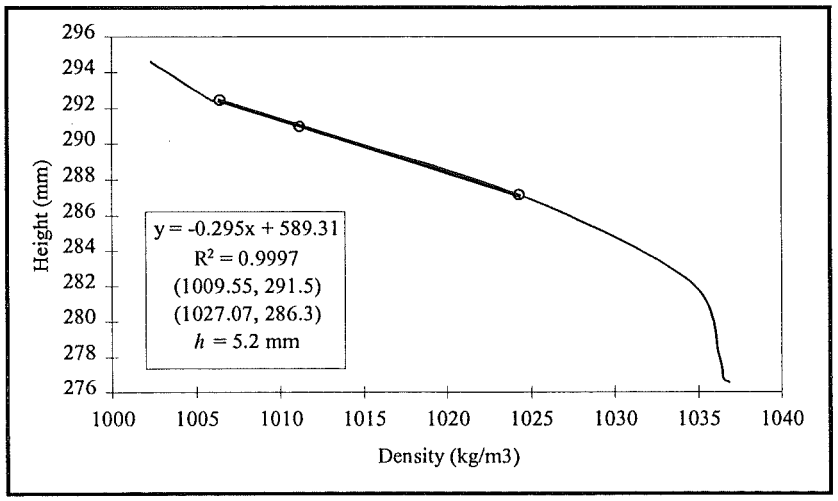

Figure A6.26b - Interfacial region density profile from run 50713PI050

Table A6.27 - Experimental data from run 50717PI050

50717PI050		Infinitesimal Wave Speed Parameters					Distance Equation Coefficients		
		ω	h	H/h	δ	c_0	k_1	k_2	k_3
		0.0176	0.0031	97	0.010	0.0162	-3.50E-05	7.14E-02	-1.14E-01
(start)	time	position	amplitude	semi-major	celerity	position	amplitude	wavelength	celerity
timeprint	t	x	a	b	c	x/h	a/h	λ/h	c/c_0
(0:42.07)	(s)	(m)	(m)	(m)	(m/s)				
1:49.70	67.63	4.55	0.0355	0.0815	0.067	1469	11.452	23.892	4.107
1:54.00	71.93	4.84	0.0355	0.0820	0.066	1562	11.452	24.028	4.088
2:00.20	78.13	5.25	0.0355	0.0825	0.066	1694	11.452	24.164	4.062

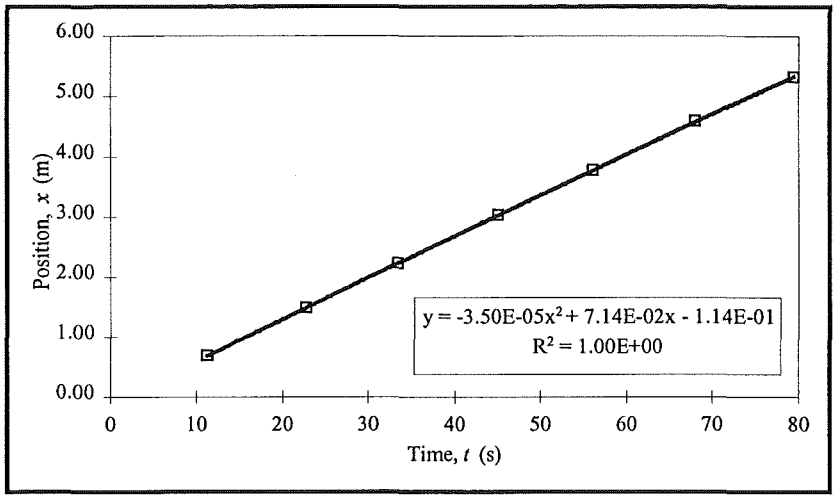

Figure A6.27a - Time-position data from run 50717PI050

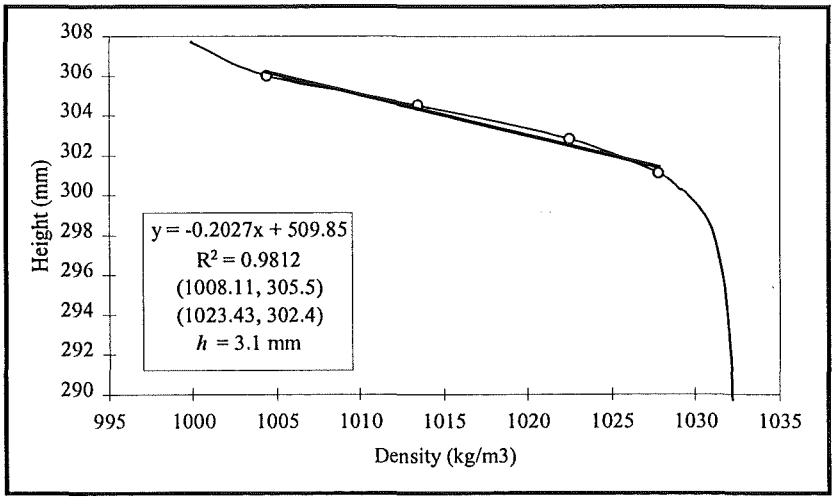

Figure A6.27b - Interfacial region density profile from run 50717PI050

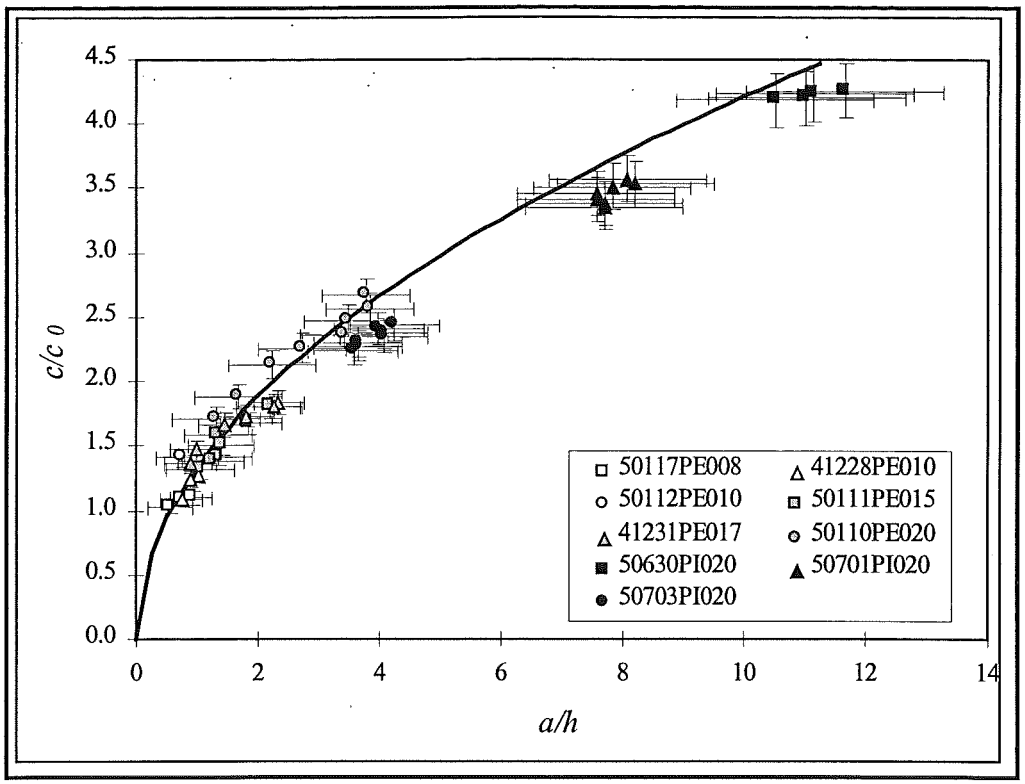

Figure A6.28a - Dimensionless wave celerity vs. amplitude

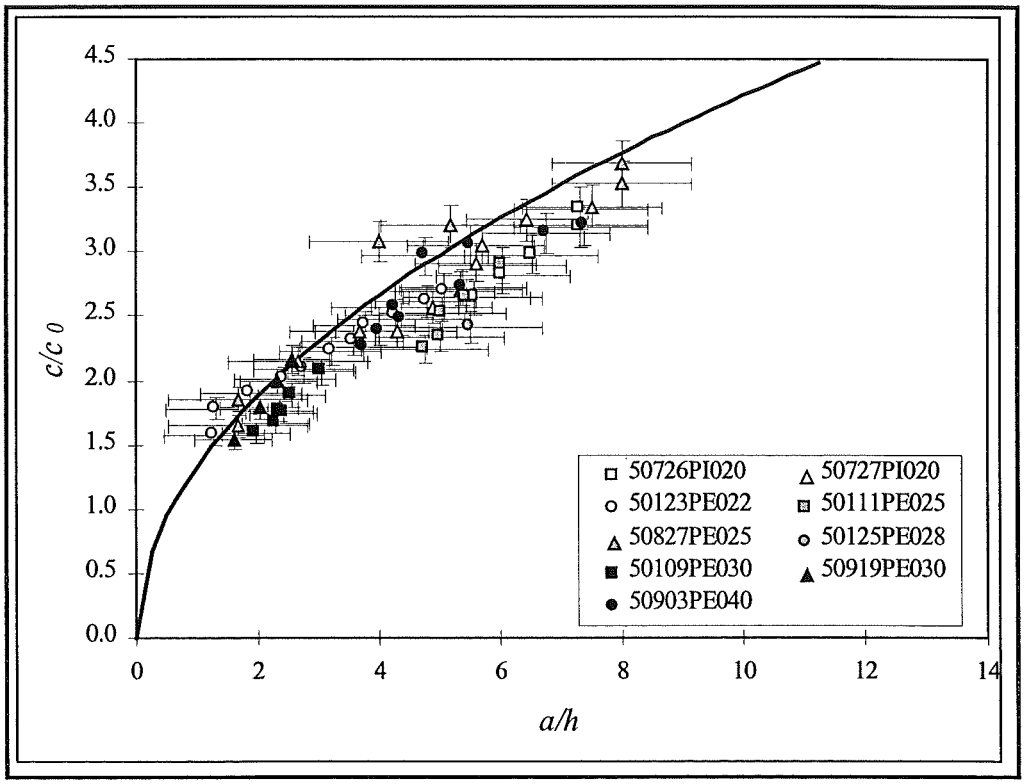

Figure A6.28b - Dimensionless wave celerity vs. amplitude

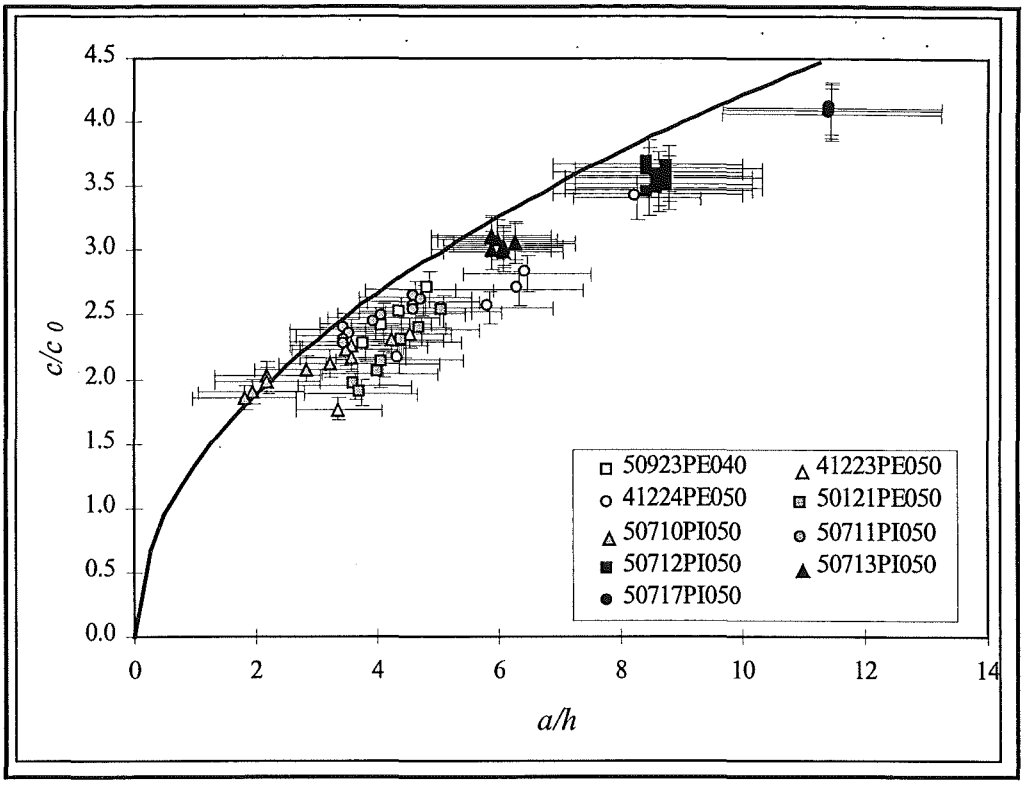

Figure A6.28c - Dimensionless wave celerity vs. amplitude

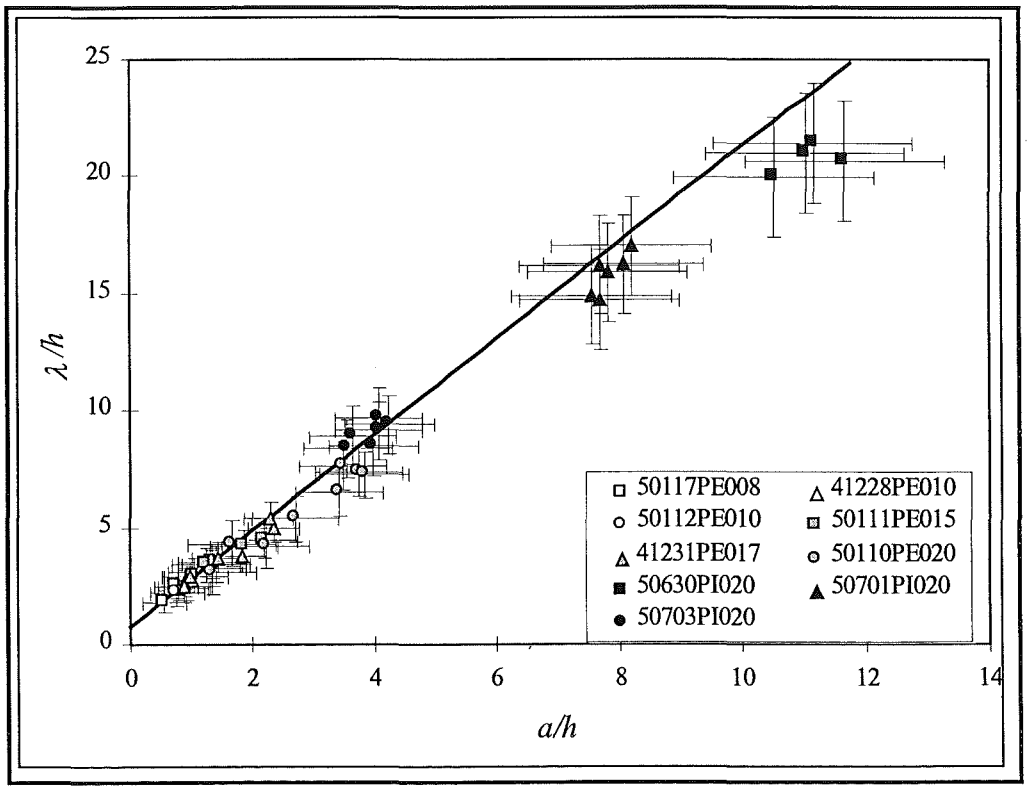

Figure A6.29a - Dimensionless wavelength vs. amplitude

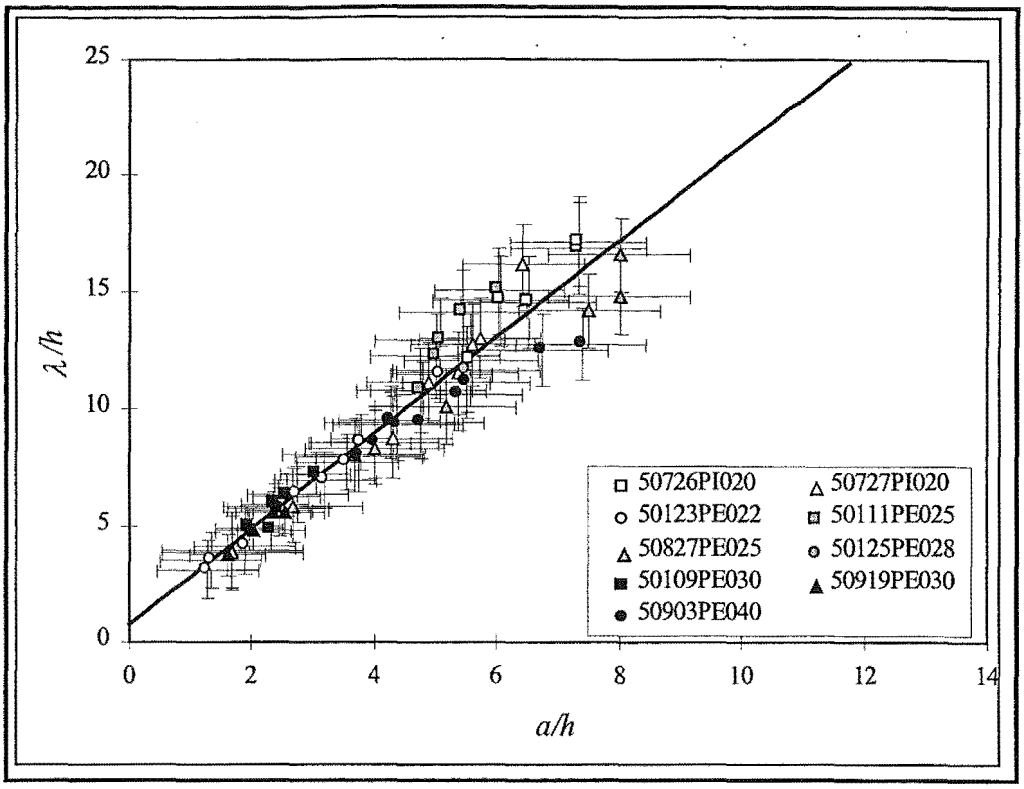

Figure A6.29b - Dimensionless wavelength vs. amplitude

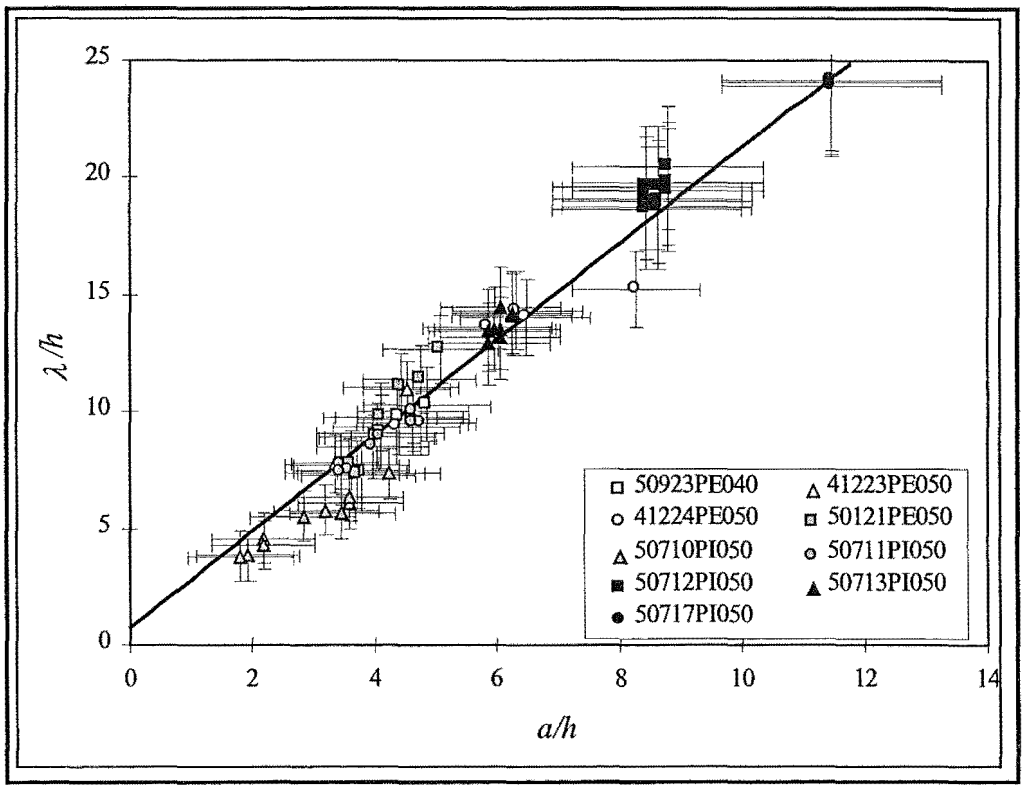

Figure A6.29c - Dimensionless wavelength vs. amplitude

Appendix 7 - Image Analysis Software

The analysis of dye images required the use of the following program to subtract and divide images, determine dye concentrations and apply colour mapping. The program is written in Fortran 77 and was run on a DEC Ultrix system.

```
      program tiffany
C
C  this program is an image analysis and manipulation program
C  that will handle tiff images up to 512 x 768.
C
C  written by:  Nathan Schmidt, University of Canterbury
C
C  Date:       August 1996 (Updated March 1997)
C
      implicit none
      integer*2 dcols,drows,bufno
      real*4 version,hash_pointer,hunk
      parameter (version=1.1)
      integer*2 j,k,jopt,cols,rows
      integer*2 buffer(768,512,3)
      integer*2 iopt,ix,iy,fgetc,length,lnblnk
      integer*2 status,system,kopt,rawfile(400000)
      integer*4 i,file_size
      byte      bite_o_file
      character*1 ans
      character*24 date_string
      character*256 fname,bufaname,bufbname,bufcname
      logical fexist
      integer*2 noffset
      integer*4 strip_offset(256),strip_byte_count(256)

      status = system('clear')
C
C  Page setup for initial situation
C
      bufaname = '<empty buffer>'
      bufbname = '<empty buffer>'
      bufcname = '<empty buffer>'
      ans = 'A'
      go to 151
C
C  find out what user wants to do
C
150   status = system('clear')
151   iopt = 1
C
C  Output program version and date
C
      write(*,'(/," ### program TIFFANY version ",
     +                          f5.2," ### "/)') version
      call fdate (date_string)
      write(*,'(//,1x,a)') date_string
C
C  Display current buffer status
C
      write(*,'(/," File in buffer A is: ",a24)') bufaname
      write(*,'(" File in buffer B is: ",a24)') bufbname
      write(*,'(" File in buffer C is: ",a24)') bufcname
C
C  Display program options
C
      write(*,'(//," Options are:",//,
     +   "   (1) load new image into buffer A or B",/,
     +   "   (2) subtract images (A - B = C) ",/,
     +   "   (3) blend images (weighted average of A and B = C)",/,
     +   "   (4) divide images (A / B = C) ",/,
     +   "   (5) output grayscale result from buffer C",/,
     +   "   (6) output colormapped result from buffer C",/,
     +   "   (7) move images in between buffers",/,
     +   "   (8) determine dye concentration in buffer C",/,
     +   "   (9) exit "/)')
      call help_read_i(iopt,iopt,'Enter choice',2,1,0,5,15)
C
      if ( iopt.lt.1 .or. iopt.gt.9 ) goto 150
C
C new image wanted ------------------------------------------------
C
      if ( iopt.eq.1 ) then

15    call help_read_c(ans,ans,'Input file to buffer A or B',
     +  2,1,0,6,15)
        if (ans.eq.'A' .or. ans.eq.'a') then
          bufno = 1
        else if (ans.eq.'B' .or. ans.eq.'b') then
          bufno = 2
        else
          go to 15
        end if
C
C  get file name and check file size
C
30    call get_name(fname,fexist,file_size)
      if ( .not. fexist ) then
        write(*,'(/," file does not exist - files in directory are:"
     +        ,/)')
        status = system('ls *.tif')
        goto 30
        end if
C
C  load entire raw file into vector RAWFILE
C
      length = lnblnk(fname)
      write(*,'(/," loading file ",a,/)')
     +  fname(1:length)
      hunk = real(512)*real(768)/70.0
      hash_pointer = 0.0
C
      open(unit=9,file=fname,status='OLD',form='UNFORMATTED')
C
      do i = 1,file_size
       status = fgetc(9,bite_o_file)
       rawfile(i) = bite_o_file
       if ( rawfile(i).lt.0 ) then
        rawfile(i) = rawfile(i) + 256
       end if
       if ( status.eq.-1 ) then
        if ( i.eq.file_size ) then
          goto 111                                    ! EOF as expected
        else
        write(*,'(//," ## EOF earlier than expected in",
     +                " read_image ## "/)')
        end if
       else if ( status.gt.0 ) then
        write(*,'(//," ## system error in read_image ##"/)')
       end if
C
C  show loading progress
C
       hash_pointer = hash_pointer + 1.0
       if ( hash_pointer.gt.hunk ) then
        write(*,'("#",$)')
         hash_pointer = 0.0
       end if
111   end do
C
       call tiff_header (fname,ix,iy,noffset,strip_offset,
     +                 strip_byte_count,rawfile)
C
      write(*,'(/," greyscale TIFF binary file detected with ",
     +                 i4," columns and ",i4," rows "/) ix,iy
      cols = ix
      rows = iy
      call read_tiff_image(fname,buffer,bufno,cols,rows,drows,dcols,
     +   noffset,strip_offset,strip_byte_count,rawfile)
      call pauser()
      if ( bufno.eq.1 ) then
      bufaname = fname
      ans = 'B'
      else if ( bufno.eq.2 ) then
        bufbname = fname
        ans = 'A'
       end if
C
C subtract images -------------------------------------------------
C
      else if ( iopt.eq.2 ) then
        call subtract(buffer)
        bufcname = 'unnamed file'
C
C divide images ---------------------------------------------------
C
```

```
      else if ( iopt.eq.4 ) then
        call divide(buffer)
        bufcname = 'unnamed file'
C
C blend images ------------------------------------------------------
C
      else if ( iopt.eq.3 ) then
        call blend(buffer)
        bufcname = 'unnamed file'
C
C get out of here ---------------------------------------------------
C
      else if ( iopt.eq.9 ) then
                stop
C
C output of grayscale result----------------------------------------------------
C
      else if ( iopt.eq.5 ) then
        call gray_output(buffer,bufcname)
C
C output of colormapped result--------------------------------------------------
C
      else if ( iopt.eq.6 ) then
        call rgb_output(buffer,bufcname)
C
C move images between buffers ---------------------------------------
C
      else if ( iopt.eq.7 ) then
        call swap(buffer,bufaname,bufbname,bufcname)
C
C determine dye mass ------------------------------------------------
C
      else if ( iopt.eq.8 ) then
        call dyemass(buffer)
      end if

      go to 150

      end
C
C-------------------------------------------------------------
C
      subroutine subtract(buffer)
C
C  subroutine to subtract the contents of buffer B from buffer A
C
      implicit none
      integer*2 buffer(768,512,3),i,j

      do i = 1,768
        do j = 1,512
          buffer(i,j,3) = buffer(i,j,1) - buffer(i,j,2)
          if (buffer(i,j,3).lt.0) then
            buffer(i,j,3) = 0
          end if
        end do
      end do

      return
      end
C
C-------------------------------------------------------------
C
      subroutine divide(buffer)
C
C  subroutine to divide the contents of buffer A by buffer B
C
      implicit none
      integer*2 buffer(768,512,3),i,j

      do i = 1,768
        do j = 1,512
          if (buffer(i,j,2).eq.0) then
            buffer(i,j,3) = 0
          else
          buffer(i,j,3) = int(real(buffer(i,j,1))/
     +                  real(buffer(i,j,2))*255)
          if (buffer(i,j,3).gt.255) then
            buffer(i,j,3) = 255
          end if
        end if
       end do
      end do

      return
      end
C
C-------------------------------------------------------------
C
      subroutine blend(buffer)
C
C  subroutine to provide a weighted average of buffer A and B
C
      implicit none
      integer*2 buffer(768,512,3)

      return
      end
C     .
C-------------------------------------------------------------
C
      subroutine get_name(fnamein,fexist,file_size)
C
C  get input filename, add extensions and open files
C
      implicit none
      integer*2 ierr,length,lnblnk,status,stat
      integer*4 file_size,statb(12)
      character*50 string
      character*256 fnamein,temp_name
      logical fexist
C
      call help_read_c(fnamein,fnamein,
     +   'Enter the input filename',1,1,0,19,15)
      length = lnblnk(fnamein) + 1
      temp_name = fnamein
      fnamein(length:length) = char(0)
      if ( length.le.1 ) then
      fexist = .false.
      else
        INQUIRE(file=fnamein,exist=fexist)
      end if
      if ( .not. fexist ) return
C
      status = stat(fnamein,statb)
      file_size  = statb(8)
      write(*,'(/," input file ",i8," bytes ")') file_size
C
      return
      end
C
C--------------------------------------------------------------------
C
      subroutine tiff_header (fname,ix,iy,noffset,strip_offset,
     +                        strip_byte_count,rawfile)
C
C  this subroutine will determine where the data starts
C  in a tiff file and how many pixels across and down, plus
C  locations of strips of data
C
      implicit none
      integer*1 int_out
      integer*2 ix,iy,status,fgetc,j,k
      integer*4 i,ifd,word,strip_offset(256),strip_byte_count(256)
      integer*4 bcoffset,offset,bps
      integer*2 no_bits,mode,rawfile(400000)
      integer*4 is,pointer
      character*256 fname
      byte bite_o_file
      integer*2 ctr,nifde,dtag,mmflag
      integer*2 noffset,nbcoffset

C     open(unit=9,file=fname,status='OLD',form='UNFORMATTED')
C
      mmflag = 0
      pointer = 1
      call get_word(word,mmflag,rawfile,pointer)
      if ( word.eq.704662861) then
        mmflag = 1
        write(*,'(/," big endian byte order detected ")')
      else
        write(*,'(/," little endian byte order detected ")')
      endif
C
C     determine offset of 0th IFD
C
      pointer = 5
      call get_word(word,mmflag,rawfile,pointer)
      ifd = word
      write(*,'(" loading image file directory at offset : ",
     +    i8)') ifd
      pointer = ifd+1
      ctr = rawfile(pointer)
      pointer = pointer + 1
      if ( ctr.lt.0 ) then
        ctr = ctr + 256
      end if
      if ( mmflag.eq.0 ) then
        nifde = ctr
      else
        nifde = ctr*256
      end if
      ctr = rawfile(pointer)
      pointer = pointer + 1
      if ( ctr.lt.0 ) then
        ctr = ctr + 256
      end if
      if ( mmflag.eq.0 ) then
        nifde = nifde + ctr*256
      else
        nifde = nifde + ctr
      end if
      write(*,'(" there are ",i2," entries present in the ",
     +        "image file directory: ")') nifde
```

```
C
C     examine directory entry tags for row, column, compression
C      and bits per sample information
C
      do j = 1, nifde
       ctr = rawfile(pointer)
       pointer = pointer + 1
       if ( ctr.lt.0 ) then
        ctr = ctr + 256
       end if
       if ( mmflag.eq.0 ) then
        dtag = ctr
       else
        dtag = ctr*256
       end if
       ctr = rawfile(pointer)
       pointer = pointer + 1
       if ( ctr.lt.0 ) then
        ctr = ctr + 256
       end if
       if ( mmflag.eq.0 ) then
        dtag = dtag + ctr*256
       else
        dtag = dtag + ctr
       end if
C
C       check directory tag for image width
C
       if ( dtag.eq.256 ) then
        do k = 1,6
         pointer = pointer + 1
         i = i + 1
        end do
        call get_word(word,mmflag,rawfile,pointer)
        pointer = pointer + 4
        ix = word
        i = i + 4
        write(*,'(" entry ",i2," image ",i4," pixels",
     +          " wide ")') j,ix
C
C       check directory tag for image length
C
       else if ( dtag.eq.257 ) then
        do k = 1,6
         pointer = pointer + 1
         i = i + 1
        end do
        call get_word(word,mmflag,rawfile,pointer)
        pointer = pointer + 4
        iy = word
        i = i + 4
        write(*,'(" entry ",i2," image ",i4," pixels ",
     +          "long ")') j,iy
C
C       check directory tag for bits per sample
C
       else if ( dtag.eq.258 ) then
        do k = 1,6
         pointer = pointer + 1
         i = i + 1
        end do
        call get_word(word,mmflag,rawfile,pointer)
        pointer = pointer + 4
        bps = word
        i = i + 4
        write(*,'(" entry ",i2," ",i5," bits per ",
     +          "sample ")') j,bps
        no_bits = 2**bps
        if ( no_bits.ne.256 ) then
         write(*,'(" ## expecting 255 grey levels ## ",/,
     +                          " ## ",i4," found ## ")')
        end if
C
C       check directory tag for compression info
C
        else if ( dtag.eq.259 ) then
        do k = 1,6
         pointer = pointer + 1
         i = i + 1
        end do
        call get_word(word,mmflag,rawfile,pointer)
        pointer = pointer + 4
        i = i + 4
        bps = word
        if ( bps.eq.1 ) then
         write(*,'(" entry ",i2," ## uncompressed ",
     +          "file found ## ")') j
        else if ( bps.eq.32773 ) then
         write(*,'(" entry ",i2," ## compressed file ",
     +          "found ## ")') j
        else
         write(*,'(" entry ",i2," ## unknown ",
     +          "compression found ## ")') j
        end if
C
C       check directory tag for strip offset
C
        else if ( dtag.eq.273 ) then
         do k = 1,2
          pointer = pointer + 1
          i = i + 1
         end do
         call get_word(word,mmflag,rawfile,pointer)
         pointer = pointer + 4
         i = i + 4
         noffset = word
         call get_word(word,mmflag,rawfile,pointer)
         pointer = pointer + 4
         i = i + 4
         offset = word
         if ( noffset.ne.1 ) then
          write(*,'(" entry ",i2," ",i3," strip offsets ",
     +          "stored at offset ",i8)') j,noffset,offset
         else
          write(*,'(" entry ",i2," single strip offset ",
     +          "value is ",i8)') j,offset
         end if
C
C       check directory tag for strip byte count offsets
C
        else if ( dtag.eq.279 ) then
         do k = 1,2
          pointer = pointer + 1
          i = i + 1
         end do
         call get_word(word,mmflag,rawfile,pointer)
         pointer = pointer + 4
         i = i + 4
         nbcoffset = word
         call get_word(word,mmflag,rawfile,pointer)
         pointer = pointer + 4
         i = i + 4
         bcoffset = word
         if ( nbcoffset.gt.1 ) then
          write(*,'(" entry ",i2," ",i3," strip byte ",
     +          "counts stored at offset "
     +          ,i8)') j,nbcoffset,bcoffset
         else
          write(*,'(" entry ",i2," single strip byte count ",
     +          "value is ",i8)') j,bcoffset
         end if
C
C       other tags don't have essential information
C
        else
         write(*,'(" entry ",i2," found tag ",i4)') j,dtag
         do k = 1, 10
          pointer = pointer + 1
          i = i + 1
         end do
        end if
       end do
C
C      find offset of next IFD
C
       call get_word(word,mmflag,rawfile,pointer)
       pointer = pointer + 4
       i = i + 4
       bps = word
C
C      If this is a single image, bps should equal zero
C
       if ( bps.eq.0 ) then
        write(*,'(" single image verified  ")')
       else
        write(*,'(/," ## multiple images in file ## ",
     +      /," ## loading first only ## ",/,
     +      " ## next ifd at offset ",i8," ## ")')
       end if
C
C     move to start of strip offsets, read and store
C
       if ( noffset.eq.1 ) then
        strip_offset(1) = offset
       else
        pointer = offset+1
        do j = 1,noffset
         call get_word(word,mmflag,rawfile,pointer)
         strip_offset(j) = word
         pointer = pointer+4
         i = i + 4
        end do
       end if
C
C     move to start of strip byte counts, read and store
C
       if ( nbcoffset.eq.1 ) then
        strip_byte_count(1) = bcoffset
       else
        do j = 1,nbcoffset
         pointer = bcoffset+1
         call get_word(word,mmflag,rawfile,pointer)
         pointer = pointer + 4
         strip_byte_count(j) = word
```

```
        end do
       end if

C       call pauser()
       return

             end
C
C-------------------------------------------------------------------
C
      subroutine read_tiff_image(fname,buffer,bufno,cols,rows,
     + drows,dcols,noffset,strip_offset,strip_byte_count,rawfile)
C
C  this subroutine will read in an uncompressed tiff image file
C  of name FNAME into an integer*2 array BUFFER
C
C  note that the file should already be closed
C
      implicit none
      integer*2 fgetc,lnblnk,length
      integer*2 drows,dcols,bufno
      byte bite_o_file
      integer*2 cols,rows,buffer(768,512,3),status
      integer*2 mode,rawfile(400000)
      real*4 hunk,hash_pointer,pointer
      character*256 fname
      integer*2 i,j,k
      integer*2 noffset
      integer*4 ii,jj,strip_offset(256),strip_byte_count(256)
C
C  note ii is pointer to _next_byte to be read
C
      k = 1
      j = 1                              ! Set row to 1
      i = 1                              ! Set col to 1

      length = lnblnk(fname)
      write(*,'(/," loading pixel array from ",a,/)')
     + fname(1:length)
      hunk = real(rows)*real(cols)/70.0
      hash_pointer = 0.0

      do k = 1,noffset
       pointer = strip_offset(k)
       do jj = pointer+1,pointer+strip_byte_count(k)

        buffer(i,j,bufno) = rawfile(jj)      ! load pixel
        ii = ii + 1                          ! increment byte count

        if ( buffer(i,j,bufno).lt.0 ) then
         buffer(i,j,bufno) = buffer(i,j,bufno) + 256
        end if
        if ( rawfile(jj).eq.-1 ) then
         if ( i.eq.cols .and. j.eq.rows ) then
          goto 111          ! EOF as expected
         else
          write(*,'(//," ## EOF earlier than expected ## ",/)')
          return
         end if
        end if

        i = i + 1
        if ( i.gt.cols ) then
         i = 1
         j = j + 1
        end if
C
C  show loading progress if only one strip
C
       if ( noffset.eq.1 ) then
        hash_pointer = hash_pointer + 1.0
        if ( hash_pointer.gt.hunk ) then
         write(*,'("#",$)')
         hash_pointer = 0.0
        end if
       end if
C
      end do
     end do
C
C  array has been loaded
C
111   continue
C
     if ( bufno.eq.1 ) then
      write(*,'(/," pixel array loaded into buffer A")')
     else if ( bufno.eq.2 ) then
      write(*,'(/," pixel array loaded into buffer B")')
     end if
C
     return
     end
C
C-------------------------------------------------------------------
C
     subroutine gray_output(buffer,fnameout)

C  This subroutine will create a TIFF file
C  Hash pointer routine lifted from David Luketina (UNSW)

     implicit     none
     byte         bite_o_file
     logical      fexist
     integer*1    int_in
     integer*2    fputc,status,ic,i,j,k,m,n
     integer*2    jj,kk,iu,iv,ii
     integer*2    buffer(768,512,3),outf
     integer*4    word,words(40)
     character*1  char_out
     character*3  string
     character*50  str
     character*256 fnameout
     real*4       hunk,hash_pointer,tt,dummy

C
C  Define output filename
C
13    call help_read_c(fnameout,fnameout,
     +   'Enter the output filename',1,1,0,19,15)
       call checkfile(fnameout,fexist)
       if (fexist) go to 13
       write(*,'(" opening file ",a,$)') fnameout(1:12)
       open(unit=9,file=fnameout,status='NEW',
     +      form='UNFORMATTED')
C
C  Put out TIFF format header
C
      write(*,'(" writing header ",$)')

      word = 2771273                    ! Write II42
      call write_word(word)
      word = 8                          ! Write IFD offset
      call write_word(word)
      bite_o_file = 13                  ! Write number of
      status = fputc(9,bite_o_file)             ! IFD entries
      bite_o_file = 0
      status = fputc(9,bite_o_file)
C
C  Write Image File Directory entries
C
      data words/262398,1,0,196864,1,0,196865,1,0,196866,1,8,
     + 196867,1,1,196870,1,1,262417,1,170,
     + 196885,1,1,196886,1,
     + 0,262423,1,0,327962,1,182,327963,1,182,196904,1,2,0/

      words(6) = 768
      words(9) = 512
      words(30) = 768*512

      do j = 1,40
       word = words(j)
       call write_word(word)
      end do
C
C  Write out data
C
      write(*,'(" writing pixel array ")')
      hunk = 768*512/70.0
      hash_pointer = 0.0

      do k = 1,512
       do j = 1,768
        int_in = buffer(j,k,3)
        call convert(int_in,char_out)
        status = fputc(9,char_out)
C
C  Show loading progress
C
        hash_pointer = hash_pointer + 1.0
        if ( hash_pointer.gt.hunk ) then
         write(*,'("#",$)')
         hash_pointer = 0.0
        end if
       end do
      end do

      close(9)
      write(*,'(/," finished writing output file ")')

      return
      end
C
C-------------------------------------------------------------------
C
      subroutine rgb_output(buffer,fnameout)

C  This subroutine will create an RGB TIFF file showing concentrations
C  represented by a user-defined colormap.
C  Hash pointer routine lifted from David Luketina (UNSW)

      implicit     none
      byte         bite_o_file
      logical      fexist
      integer*1    int_in
```

```
      integer*2    fputc,status,ic,i,j,k,l,m,n
      integer*2    jj,kk,iu,iv,ii,px,py
      integer*2    buffer(768,512,3),outf
      integer*2    colormap(16,3),colormap_red(16),colormap_grn(16)
      integer*2    colormap_blu(16)
      integer*2    incr,incrcm
      integer*4    word,words(40)
      character*1  char_out,ans
      character*3  string
      character*100  str
      character*256 fnameout
      real*4       hunk,hash_pointer,tl,dummy,rho1,rho3,delta,width
C
C  Define output filename
C
13    call help_read_c(fnameout,fnameout,
     +   'Enter the output filename',1,1,0,19,15)
      call checkfile(fnameout,fexist)
      if (fexist) go to 13
      write(*,'(" opening file ",a,$)') fnameout(1:12)
      open(unit=9,file=fnameout,status='NEW',
     +      form='UNFORMATTED')
C
C  Put out TIFF format header
C
      write(*,'(" writing header ",$)')

      word = 2771273                    ' ! Write II42
      call write_word(word)
      word = 8                          ! Write IFD offset
      call write_word(word)
      bite_o_file = 14                  ! Write number of
      status = fputc(9,bite_o_file)             ! IFD entries
      bite_o_file = 0
      status = fputc(9,bite_o_file)
C
C  Write Image File Directory entries
C  Note:  262398 = tag 254 (NewSubfile Type), 196864 = tag 256
C  (ImageWidth), 196865 = tag 257 (Image Length), 196866 = tag
C  258 (BitsPerSample), 196867 = tag 259 (Compression), 196870
C  = tag 262 (PhotometricInterpretation), 262417 = tag 273
C  (StripOffsetValue), 196885 = tag 277 (SamplesPerPixel), 196886
C  = tag 278 (RowsPerStrip), 262423 = tag 279
C  (StripByteCountValue), 327962 = tag 282 (Xresolution), 327963
C  = tag 283 (Yresolution), 196904 = tag 296 (ResolutionUnit)
C
C  Differences from grayscale are:  BitsPerSample becomes 8,8,8
C                          PhotometricInterpretation becomes 2
C                          SamplePerPixel becomes 3
C
      data words/262398,1,0,196864,1,0,196865,1,0,196866,1,8,
     + 196867,1,1,196870,1,2,262417,1,170,196885,1,3,
     + 196886,1,0,262423,1,0,327962,1,182,327963,1,
     + 182,196904,1,2,0/

      words(6) = 768
      words(9) = 512
      words(30) = 768*512

      do j = 1,40
        word = words(j)
        call write_word(word)
      end do
C
C  Initialise colormap
C
      data colormap_red/255,0,0,127,127,255,0,0,127,0,0,255,127,
     +          255,0,255/
      data colormap_grn/255,0,0,0,127,0,0,255,127,255,0,255,127,
     +          100,0,0/
      data colormap_blu/255,255,0,255,127,255,0,255,127,0,0,0,127,
     +          0,0,0/
      do i = 1,16
        colormap(i,1) = colormap_red(i)
        colormap(i,2) = colormap_grn(i)
        colormap(i,3) = colormap_blu(i)
      end do
C
C  Add colormapping legend to plot
C
      do j = 1,16          ! to 768
        do k = 450,490     ! to 512
          do l = 450,464
            buffer(l+15*j,k,3) = j*16-8
          end do
        end do
      end do
C
C  Box around colormapping legend
C
      do k = 449,491
        buffer(465,k,3) = 100
        buffer(705,k,3) = 100
      end do
      do j = 465,705
        buffer(j,449,3) = 100
        buffer(j,491,3) = 100
      end do
C
C  Add scale at top of image
C
31    ans = 'y'
      call help_read_c(ans,ans,'Add scale?',2,1,0,6,15)
      if (ans.eq.'Y' .or. ans.eq.'y') then

        do j = 1,701
          buffer(j,30,3) = 100
          buffer(j,31,3) = 100
        end do
        do j = 1,701,50
          do k = 20,30
            buffer(j,k,3) = 100
          end do
        end do
      end if
C
C  Put frame around plot
C
      do j = 1,768
        buffer(j,1,3) = 100
        buffer(j,512,3) = 100
      end do
      do k = 1,512
        buffer(1,k,3) = 100
        buffer(768,k,3) = 100
      end do
C
C  Write out data
C
22    write(*,'(" writing pixel array ")')
      hunk = 768*512*3/70.0
      hash_pointer = 0.0

      do k = 1,512
        do j = 1,768
          do i = 1,3
C
C         ASSIGN COLORMAPPING
C
          int_in = colormap(int(buffer(j,k,3)/16)+1,i)
C
          call convert(int_in,char_out)
          status = fputc(9,char_out)
C
C  Show loading progress
C
          hash_pointer = hash_pointer + 1.0
          if ( hash_pointer.gt.hunk ) then
            write(*,'("#",$)')
            hash_pointer = 0.0
          end if
        end do
      end do
      end do

      close(9)
      write(*,'(/," finished writing output file ")')

      return
      end
C
C-----------------------------------------------------------------
C
      subroutine pauser
      implicit none
      character*1 ans
C
      write(*,'(/," press return key to continue ")')
      read(*,'(a)') ans
      return
      end
C
C-----------------------------------------------------------------
C
      subroutine convert(int_in,int_out)
      implicit none
      integer*1 int_in,int_out
C
      int_out = int_in
      return
      end
C
C-----------------------------------------------------------------
C
      subroutine get_word(word,mmflag,rawfile,pointer)
C
C     subroutine gets four byte word from TIFF file
C     written by NPS when TIFF capability added in Feb 96
C
      implicit none
      integer*2 i,mmflag,rawfile(400000)
      integer*2 fgetc,status
      integer*4 word,ctr,pointer
      byte bite_o_file
```

```
      word = 0

      if ( mmflag.eq.0 ) then          ! little endian byte order
        do i = 0,3
          ctr = rawfile(pointer+i)
          if ( ctr.lt.0 ) then
            ctr = ctr + 256
          end if
          word = word + ctr*256**i
        end do
      else                             ! big endian byte order
        do i = 3,0,-1
          ctr = rawfile(pointer+i)
          if ( ctr.lt.0 ) then
            ctr = ctr + 256
          end if
          word = word + ctr*256**i
        end do
      end if

      return
      end
C
C-----------------------------------------------------------------------
C
      subroutine write_word(word)
C
C     subroutine writes four byte word to TIFF file
C     written by NPS when TIFF capability added in Feb 96
C     writes in little endian byte order
C
      implicit none
      integer*2 fputc,status2,i,j
      integer*4 ctr,word
      byte bite_o_file

      do i = 0,3
        ctr = word
        do j = 2,i,-1
          ctr = ctr-int(ctr/256**(j+1))*256**(j+1)
        end do
        bite_o_file = int(ctr/256**i)
        status2 = fputc(9,bite_o_file)
      end do

      return
      end
C
C-----------------------------------------------------------------------
C
      subroutine checkfile(fnameout,fexist)

C     This subroutine checks to see if any density or combined output
C     files exist from previous runs, and allows their removal or
C     quitting of the program (note: program will crash if they are
C     left alone).

      character*1   ans
      character*256 fnameout
      logical       fexist

      inquire(file=fnameout,exist=fexist)
      if (fexist) then
        write(*,'(/," Warning! File ",a12," already exists."
     +          )') fnameout
        ans = 'n'
10      call help_read_c(ans,ans,'Hit (y) to delete or (n) to leave',
     +    2,1,0,7,15)
        if (ans.eq.'y' .or. ans.eq.'Y') then
          status = system('rm ',fnameout)
        else if (ans.eq.'n' .or. ans.eq.'N') then
          go to 11
        else
          go to 10
        end if
      end if

11    return
      end
C
C-----------------------------------------------------------------------
C
      subroutine swap(buffer,bufaname,bufbname,bufcname)

      implicit none
      integer*2 swapcell
      integer*2 i,j,iopt
      integer*2 buffer(768,512,3)
      character*1 ans
      character*256 fname,bufaname,bufbname,bufcname,swapname

C     Display current buffer status

      write(*,'(/," File in buffer A is: ",a24)') bufaname
      write(*,'(" File in buffer B is: ",a24)') bufbname
      write(*,'(" File in buffer C is: ",a24)') bufcname
C
C     Display program options
C
150   iopt = 1
        write(*,'(//," Options are:",//,
     +            "  (1) swap contents of buffers A and B",/,
     +            "  (2) swap contents of buffers A and C ",/,
     +            "  (3) swap contents of buffers B and C",/,
     +            "  (4) return ")')
        call help_read_i(iopt,iopt,'Enter choice',2,1,0,5,15)
C
        if ( iopt.lt.1 .or. iopt.gt.4 ) goto 150
C
C     swap A and B ------------------------------------------------
C
        if ( iopt.eq.1 ) then
          do i = 1,768
            do j = 1,512
              swapcell = buffer(i,j,1)
              buffer(i,j,1) = buffer(i,j,2)
              buffer(i,j,2) = swapcell
            end do
          end do
          swapname = bufaname
          bufaname = bufbname
          bufbname = swapname
C
C     swap A and C ------------------------------------------------
C
        else if ( iopt.eq.2 ) then
          do i = 1,768
            do j = 1,512
              swapcell = buffer(i,j,1)
              buffer(i,j,1) = buffer(i,j,3)
              buffer(i,j,3) = swapcell
            end do
          end do
          swapname = bufaname
          bufaname = bufcname
          bufcname = swapname
C
C     swap B and C ------------------------------------------------
C
        else if ( iopt.eq.3 ) then
          do i = 1,768
            do j = 1,512
              swapcell = buffer(i,j,2)
              buffer(i,j,2) = buffer(i,j,3)
              buffer(i,j,3) = swapcell
            end do
          end do
          swapname = bufbname
          bufbname = bufcname
          bufcname = swapname
C
C     return ------------------------------------------------------
C
        else if ( iopt.eq.4 ) then
          return
        end if

        return
        end
C
C-----------------------------------------------------------------------
C
        subroutine dyemass(buffer)
C
C     get input filename, add extensions and open files
C
        implicit    none
        integer*2   xctr,xsa,yctr,ysa,buffer(768,512,4)
        integer*2   j,k,maskcount,x,y,dash
        integer*4   mass,area
        real*4      conc,pconc
        character*1 ans
C
        write(*,'(/,"Sum and concentration of dye mass in specified",
     +      " area will be calculated.",/)')
C
C     query for dimensions of area to be counted
C
1       write(*,'(/," enter dimensions of ellipse ",/)')

        call help_read_i(xctr,xctr,'enter x centre (pixels)',
     +    2,3,0,3,15)
        call help_read_i(yctr,yctr,'enter y centre (pixels)',
     +    2,3,0,3,16)
        call help_read_i(xsa,xsa,'enter semimajor axis (pixels)',
     +    2,3,0,3,17)
        call help_read_i(ysa,ysa,'enter semiminor axis (pixels)',
     +    2,3,0,3,18)
2       call help_read_c(ans,ans,'Hit (c) to continue or (r) to
     +    re-enter values',2,1,0,5,19)
        if (ans.eq.'c' .or. ans.eq.'C') then
          go to 3
        else if (ans.eq.'r' .or. ans.eq.'R') then
```

```
      go to 1
     else
      go to 2
3    end if

17   mass = 0
     area = 0
     maskcount = 0
     do j = (xctr-xsa),(xctr+xsa)
      x = abs(xctr-j)
      y = int((real(ysa*ysa)*(real(1)-real((x*x))/real((xsa*xsa))))
    + **0.5)
      do k = yctr-y,yctr+y
       if(j.lt.643.and.j.gt.473.and.k.lt.487.and.k.gt.457)then
        maskcount = maskcount + 1
       else
        mass = buffer(j,k,3) + mass
        area = area + 1
       end if
      end do
     end do
     write(*,'(/,i7" pixels of time stamp area masked.")')maskcount
     conc = real(mass)/real(area)
     pconc = conc*100/255

     write(*,'(/,"Total mass in area of ",i6," pixels is ",
    +     i9,".")')area,mass
     write(*,'(/,"This yields mean concentration of ",f5.1,
    +     " or ",f4.1," percent.")')conc,pconc

13   call help_read_c(ans,ans,
    + 'Do you wish to place outline on image? (y/n)',1,1,0,19,15)
     if (ans.eq.'Y'.or.ans.eq.'y') then

14   dash = 255
     do x = 0,xsa
       y = int((real(ysa*ysa)*(real(1)-real((x*x))/real((xsa*xsa))))
    + **0.5)
       buffer(xctr+x,yctr+y,3) = dash
       buffer(xctr+x,yctr-y,3) = dash
       buffer(xctr-x,yctr+y,3) = dash
       buffer(xctr-x,yctr-y,3) = dash
       if ( dash.eq.255 ) then
        dash = 0
       else
        dash = 255
       end if
     end do

     else if (ans.eq.'N'.or.ans.eq.'n') then
      go to 14
     else
      go to 13
     end if

15   return
     end
```

Appendix 8 - Dye Flushing Experiment Data and Analysis

Eleven dye flushing experiments were performed to observe and measure the mass transport capability of second mode waves. Images from these experiments are displayed on the following pages. These images were acquired from the videotaped record of the experiments and were processed by the procedure described in Section 7.3. A detailed description of the analysis procedure is found in the first section of this appendix, which includes Figures A8.1-4. After this follows details of relevant run and wave parameters in Tables A8.1-11, wave time-position data in Figures A8.5a-15a, and density profiles in Figure A8.5b-15b. Grayscale images corresponding to the measurements are included in Figures A8.5c-15c. The recorded run and wave parameters are as follows:

Run Parameters:

Run name
Densimetric factor, ω
Interfacial half-thickness, h
Dimensionless depth, H/h
Finite depth quantity, δ (calculated with Equation 2.35)
Infinitesimal first mode wave celerity, c_0 (calculated with Equation 2.34)
Coefficients of time-position equation $x = k_1t^2 + k_2t + k_3$

Measured Dimensional Wave Parameters:

Time stamp (time of gate release noted)
Time from gate release, t
Position, x (from time-position equation)
Wave celerity, c (from differentiation of time-position equation)

Calculated Dimensionless Wave Parameters:

Wave celerity, c/c_0
Position, x/h
Position adjusted for full dye concentration at start, x/h
Adjusted position factored by Richardson number, $x/h*J$
Dye concentration count (wave area noted)
Dye concentration, % (see analysis procedure)

Analysis Procedure

Grayscale images corresponding to the measurements have been saved as Tagged Interchange File Format (TIFF) binary files of dimension 512 x 768 pixels. The intensity value for each pixel in these images ranges from 0 (black) to 255 (white). A value of 255 would correspond to unmixed fluid from the initial wave generation collapse, while lower values occur as dyed fluid is mixed with fluid from outside the collapsing region.

An ellipse of the size of the largest fully developed wave was superimposed on each dye image. The sum of the values of the pixels within this region is shown beneath each image as the count, while the number of pixels in the ellipse is noted before each group of images. Dividing the count by the number of pixels yields the average pixel intensity within the ellipse. It must be noted that the ellipse area given is the actual number of pixels counted by the computer program and due to rounding errors varies slightly from that which might be computed by a geometric formula.

Raw flushing data are shown on Figure A8.1, where the concentration of dye in the wave (expressed as a percentage of the maximum possible concentration of dye in the ellipse) is plotted against the dimensionless position, x/h. A good deal of scatter in the data is apparent, but some consistent behaviour is also seen. A typical wave displayed three distinct zones of behaviour as it travelled. During its generation phase, the concentration stayed relatively constant, whereas after wave development, when entrainment began, the concentration dropped at a rate linear with distance. As the wave emptied of dye, when the concentration dropped to approximately 10%, the residual flushing phase began. Here dye held in the vortex regions of the wave was gradually expelled at a much lower rate than in the primary flushing phase.

Figure A8.1 shows that many waves did not start out with a full concentration of dye, and many travelled some distance before starting to flush dye. Reasons for the former include the loss of dye from the wave during the initial disturbance of the

gate pull during generation. For the latter, a likely explanation is the introduction of new dye into the wave before it separated from the following current.

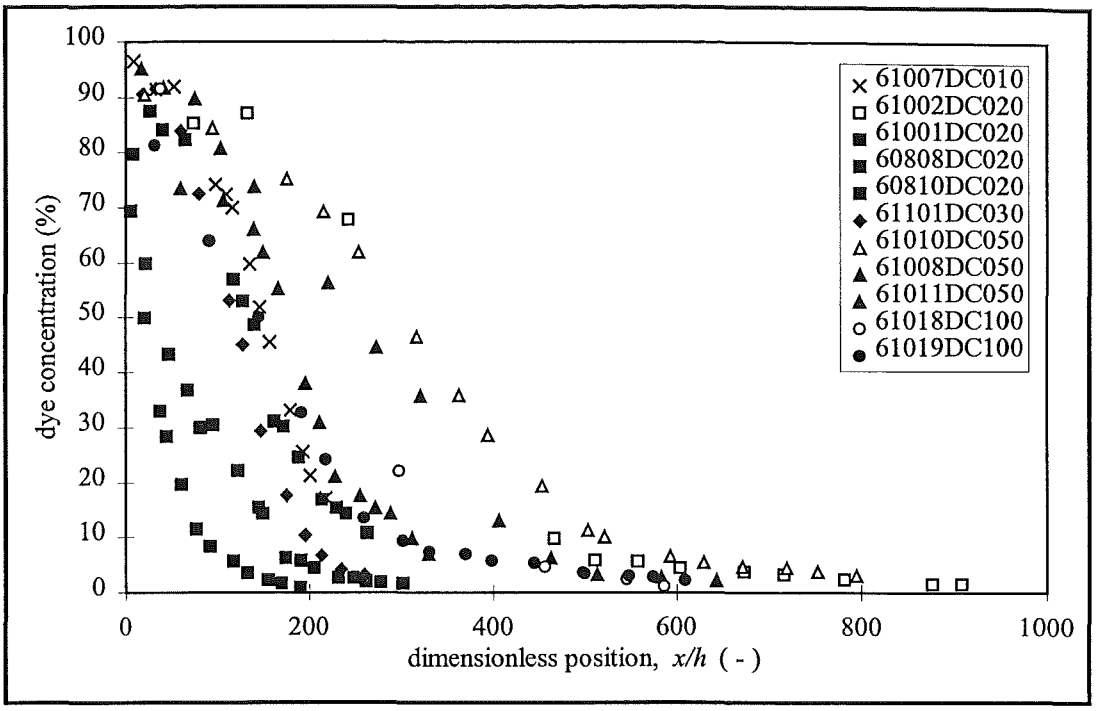

Figure A8.1 - Raw dye flushing data

To introduce some consistency into the starting point of the wave, a linear regression was fitted to the data from the primary flushing portion of each run. This was then used to compute an *x/h* value corresponding to a theoretical 100% concentration for each run. Measured values of *x/h* were then offset by this value, and data points in the wave generation phase were dropped from the analysis so that the data from each run represented only the primary and residual flushing phases. The linear regression lines and calculated offsets are shown on Figure A8.2, and the experimental data with the offsets applied are shown on Figure A8.3.

It is apparent from Figure A8.3 that the adjustment of distances to reflect equivalent generation conditions does not result in a display of similitude between different runs. It was found, though, that the runs seem to be ordered by their representative Richardson number.

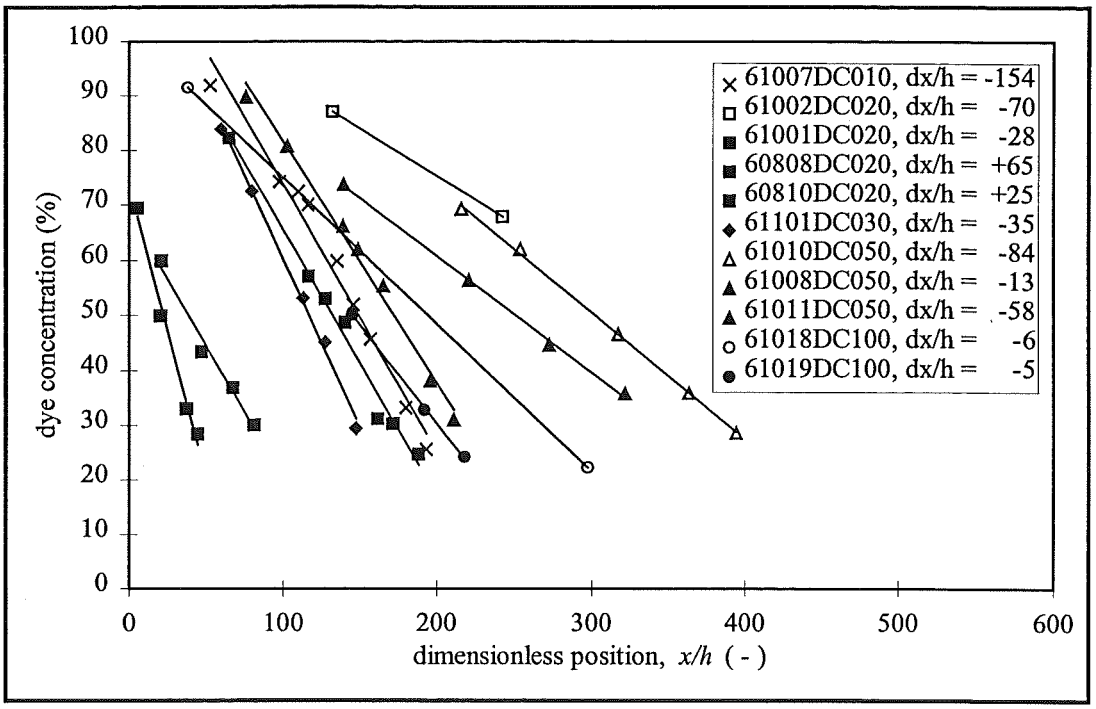

Figure A8.2 - Calculation of x/h offsets for dye flushing analysis

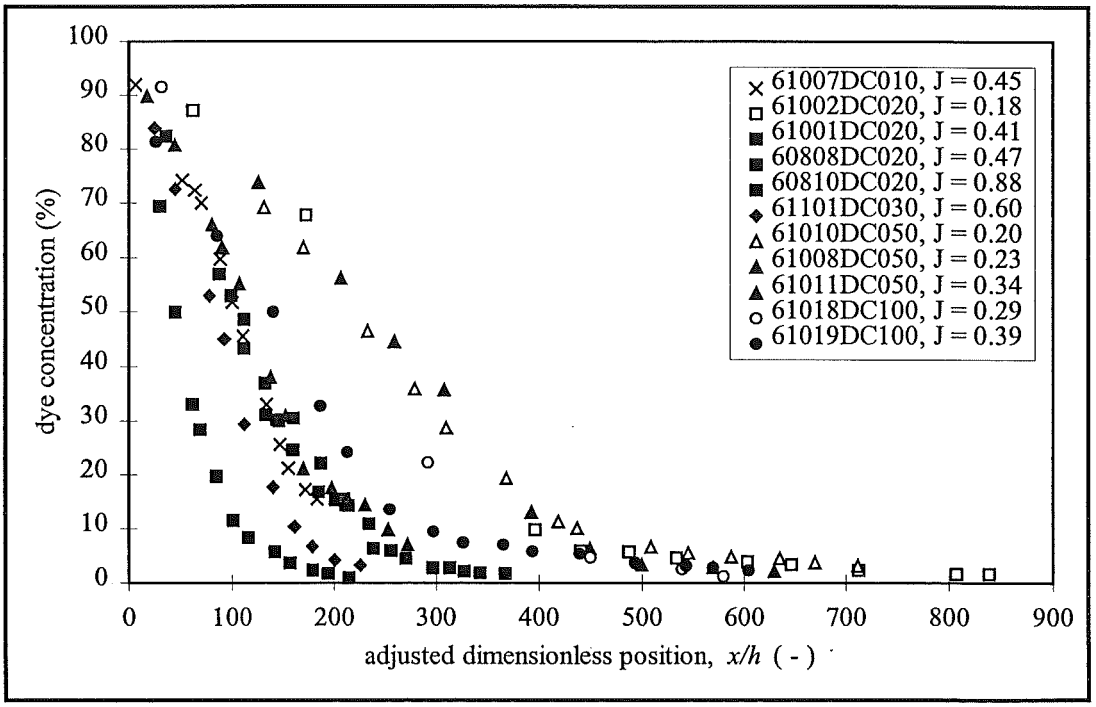

Figure A8.3 - Dye flushing data after distance adjustment

Figure A8.4 is the result of introducing the Richardson number as a factor to the dimensionless distance, and this figure displays a reasonable consistency over a set of experiments that spans almost an order of magnitude in densimetric factors. This

figure appears in the main body of the thesis as Figure 7.9. Error bars have been added to this figure according to the method described in Appendix 12.

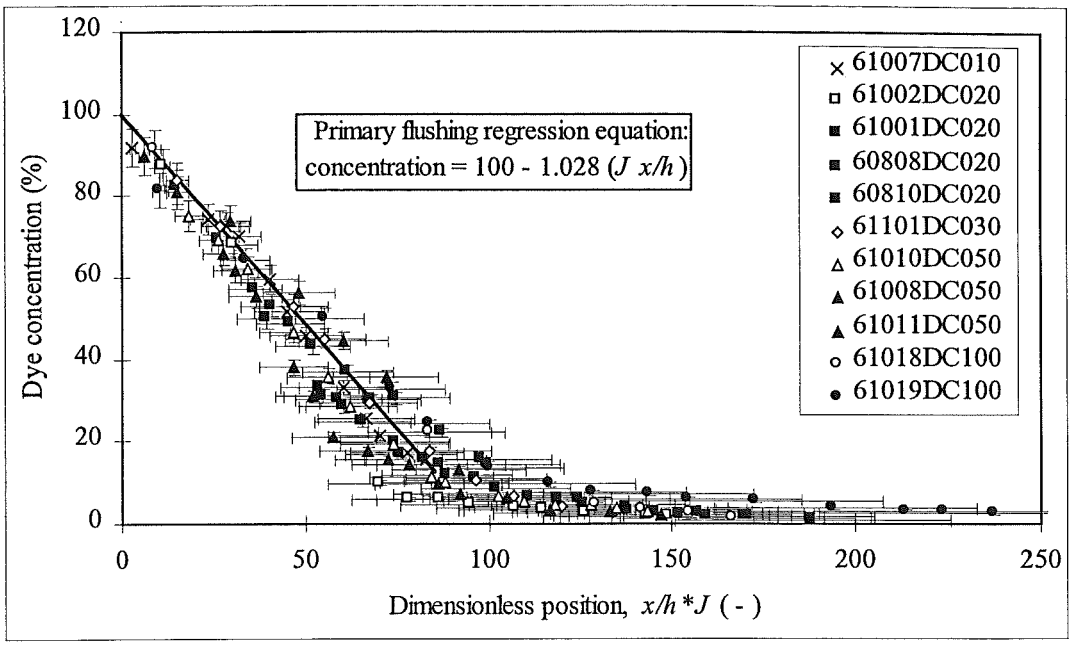

Figure A8.4 - Dimensionless dye flushing data

Table A8.1 - Experimental data from run 61007DC010

61007DC010		Infinitesimal Wave Speed Parameters					Distance Equation Coefficients		
		ω	h	H/h	δ	c_0	k_1	k_2	k_3
		0.0033	0.0187	16	0.065	0.0166	-2.39E-05	3.84E-02	-1.19E-01
(start)	time	position	celerity	celerity	position	adjusted	adjusted	(area)	dye
timeprint	t	x	c	c/c_0	x/h	x/h	$x/h*J$	count	concentration
(1:05.19)	(s)	(m)	(m/s)				($J = 0.452$)	(79461)	(%)
1:12.69	7.5	0.17	0.038	2.289	9			19548267	96.5
1:24.49	19.3	0.61	0.037	2.255	33			18532083	91.5
1:34.37	29.18	0.98	0.037	2.227	52	7	3	18638602	92.0
1:57.55	52.36	1.82	0.036	2.160	98	52	23	15043204	74.2
2:03.82	58.63	2.05	0.036	2.142	110	64	29	14667166	72.4
2:07.31	62.12	2.17	0.035	2.132	116	70	32	14194209	70.1
2:17.23	72.04	2.52	0.035	2.103	135	89	40	12109288	59.8
2:23.11	77.92	2.73	0.035	2.086	146	100	45	10498682	51.8
2:29.07	83.88	2.93	0.034	2.069	157	111	50	9226952	45.5
2:41.68	96.49	3.36	0.034	2.033	180	134	60	6696845	33.1
2:49.08	103.9	3.61	0.033	2.011	193	147	66	5179550	25.6
2:53.52	108.3	3.76	0.033	1.999	201	155	70	4299373	21.2
3:03.13	117.9	4.07	0.033	1.971	218	172	78	3482446	17.2
3:09.69	124.5	4.29	0.032	1.952	229	183	83	3130972	15.5

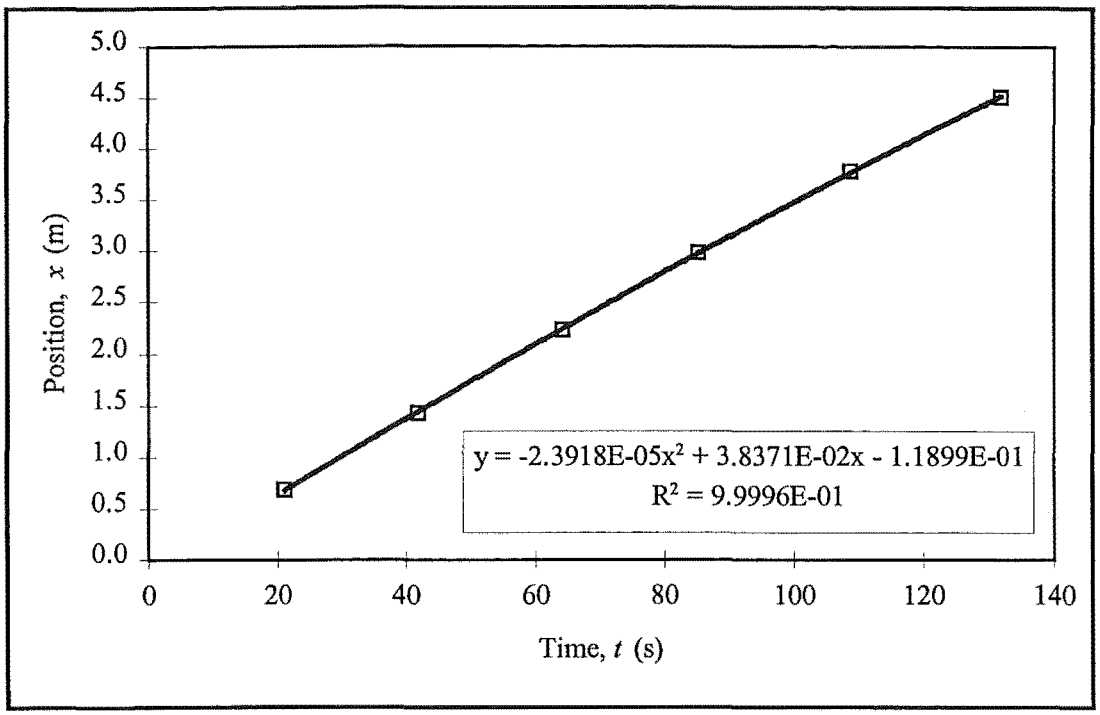

Figure A8.5a - Time-position data from run 61007DC010

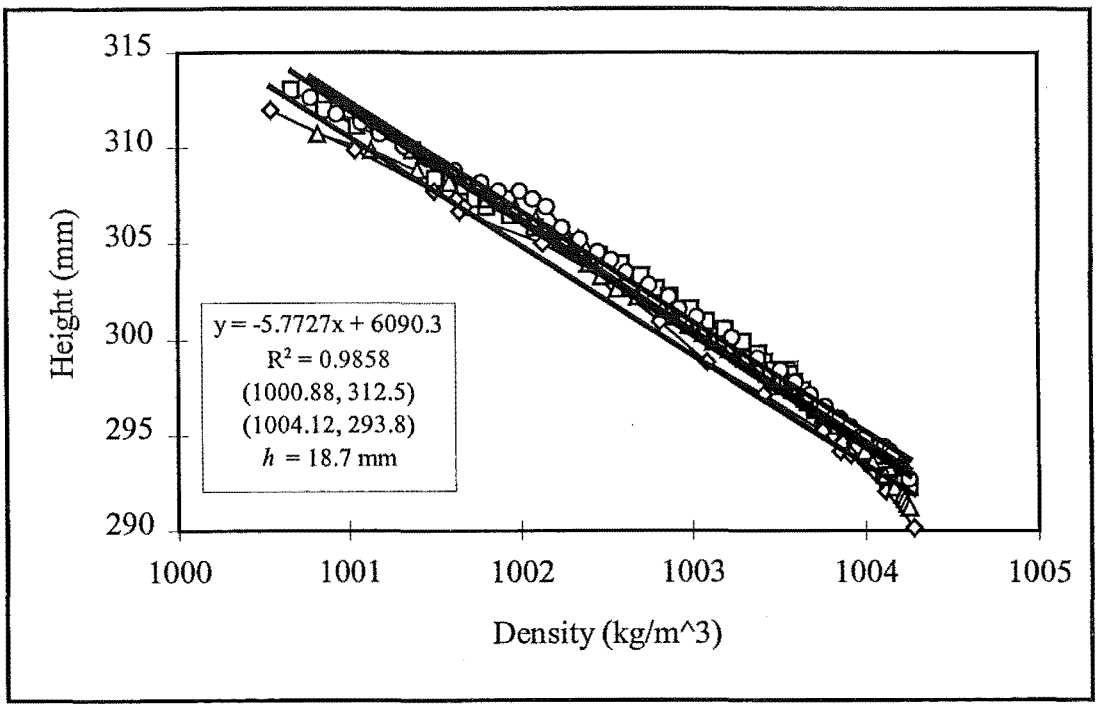

Figure A8.5b - Interfacial region density profile from run 61007DC010

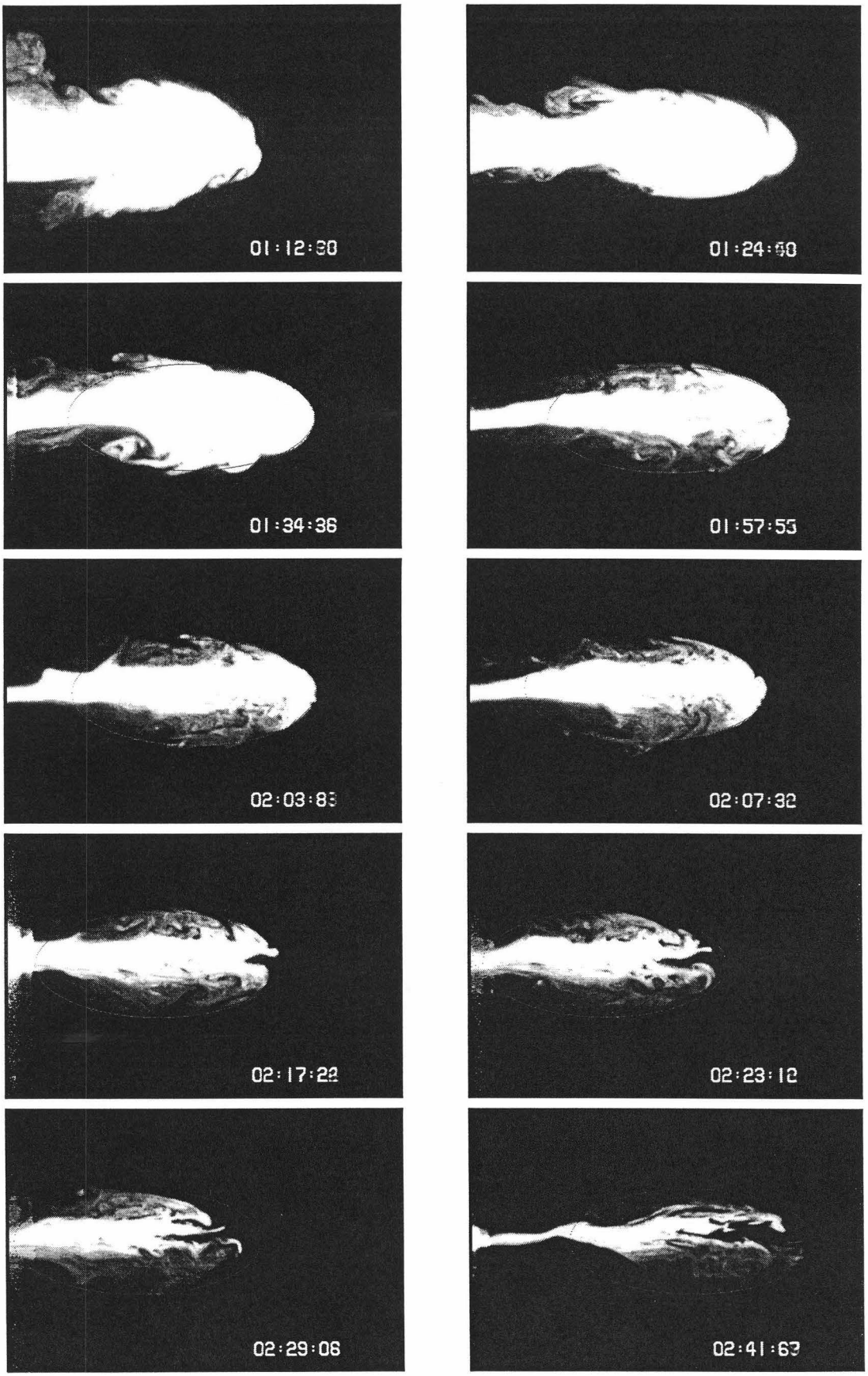
01:12:30
01:24:60
01:34:36
01:57:53
02:03:83
02:07:32
02:17:22
02:23:12
02:29:06
02:41:67

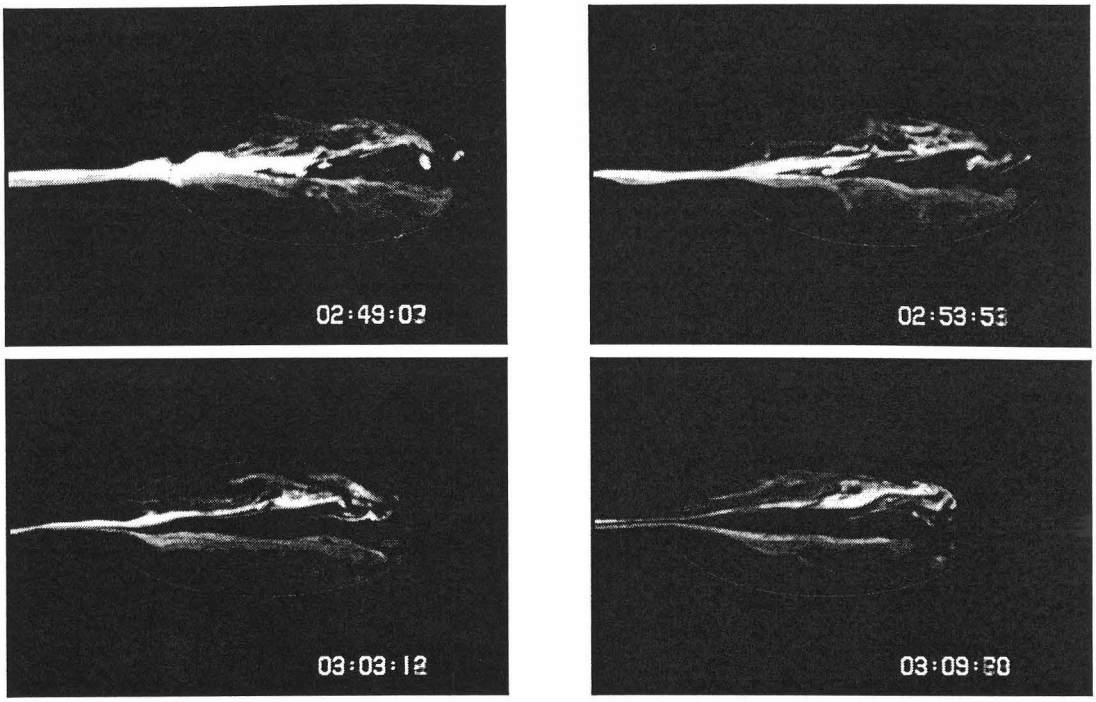

Figure A8.5c - Flow images from run 61007DC010

Table A8.2 - Experimental data from run 61002DC020

61002DC020		Infinitesimal Wave Speed Parameters					Distance Equation Coefficients		
		ω	h	H/h	δ	c_0	k_1	k_2	k_3
		0.0072	0.0037	81	0.012	0.0113	-5.49E-05	4.14E-02	-4.32E-03
(start)	time	position	celerity	celerity	position	adjusted	adjusted	(area)	dye
timeprint	t	x	c	c/c_0	x/h	x/h	$x/h*J$	count	concentration
(2:36.67)	(s)	(m)	(m/s)				(J = 0.178)	(21467)	(%)
2:43.42	6.75	0.27	0.041	3.588	74	4		4670710	85.3
2:48.78	12.11	0.49	0.040	3.536	132	62	11	4771463	87.2
2:59.11	22.44	0.90	0.039	3.435	242	172	31	3713403	67.8
3:21.06	44.39	1.72	0.036	3.223	466	396	70	536599	9.8
3:25.63	48.96	1.89	0.036	3.178	511	441	78	323062	5.9
3:30.44	53.77	2.06	0.035	3.132	557	487	87	313997	5.7
3:35.32	58.65	2.23	0.035	3.084	604	534	95	248887	4.5
3:42.78	66.11	2.49	0.034	3.012	673	603	107	210538	3.8
3:47.48	70.81	2.65	0.034	2.966	716	646	115	181639	3.3
3:54.81	78.14	2.89	0.033	2.895	782	712	127	129875	2.4
4:05.73	89.06	3.24	0.032	2.789	877	807	143	87968	1.6
4:09.41	92.74	3.36	0.031	2.754	908	838	149	87235	1.6

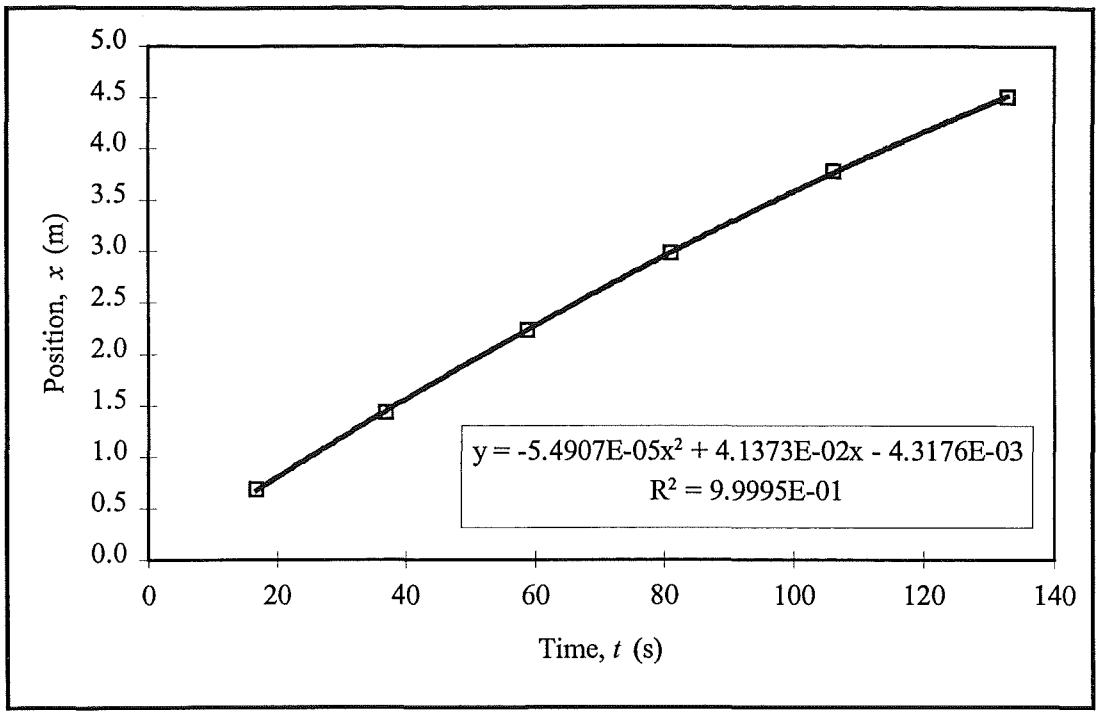

Figure A8.6a - Time-position data from run 61002DC020

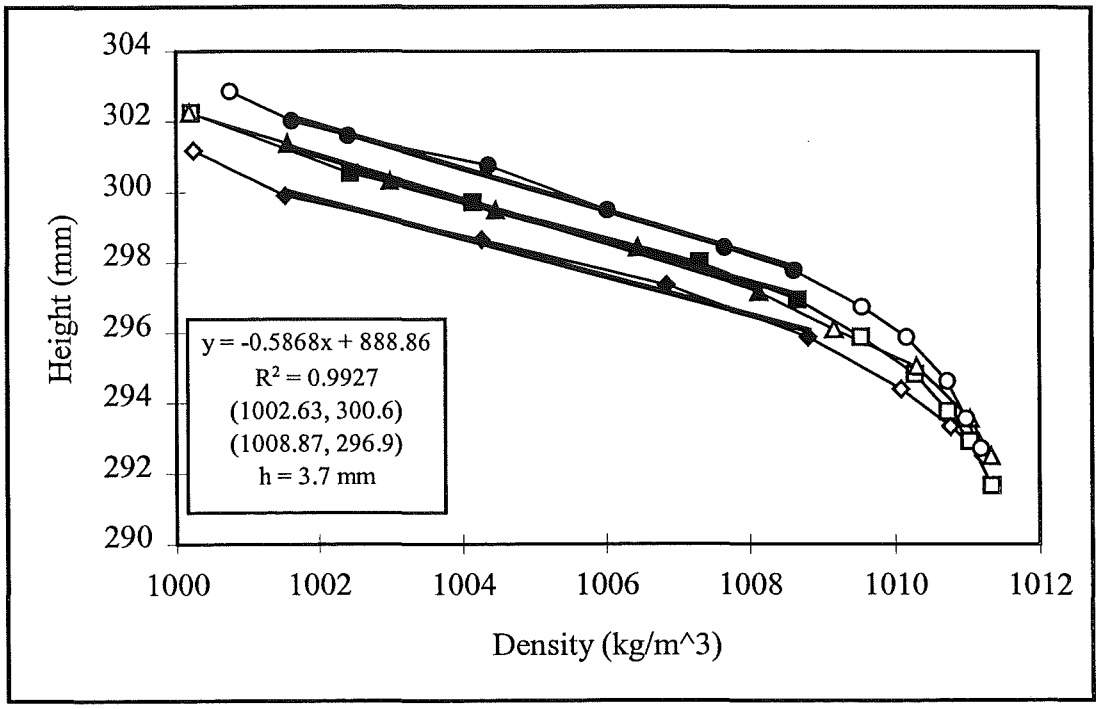

Figure A8.6b - Interfacial region density profile from run 61002DC020

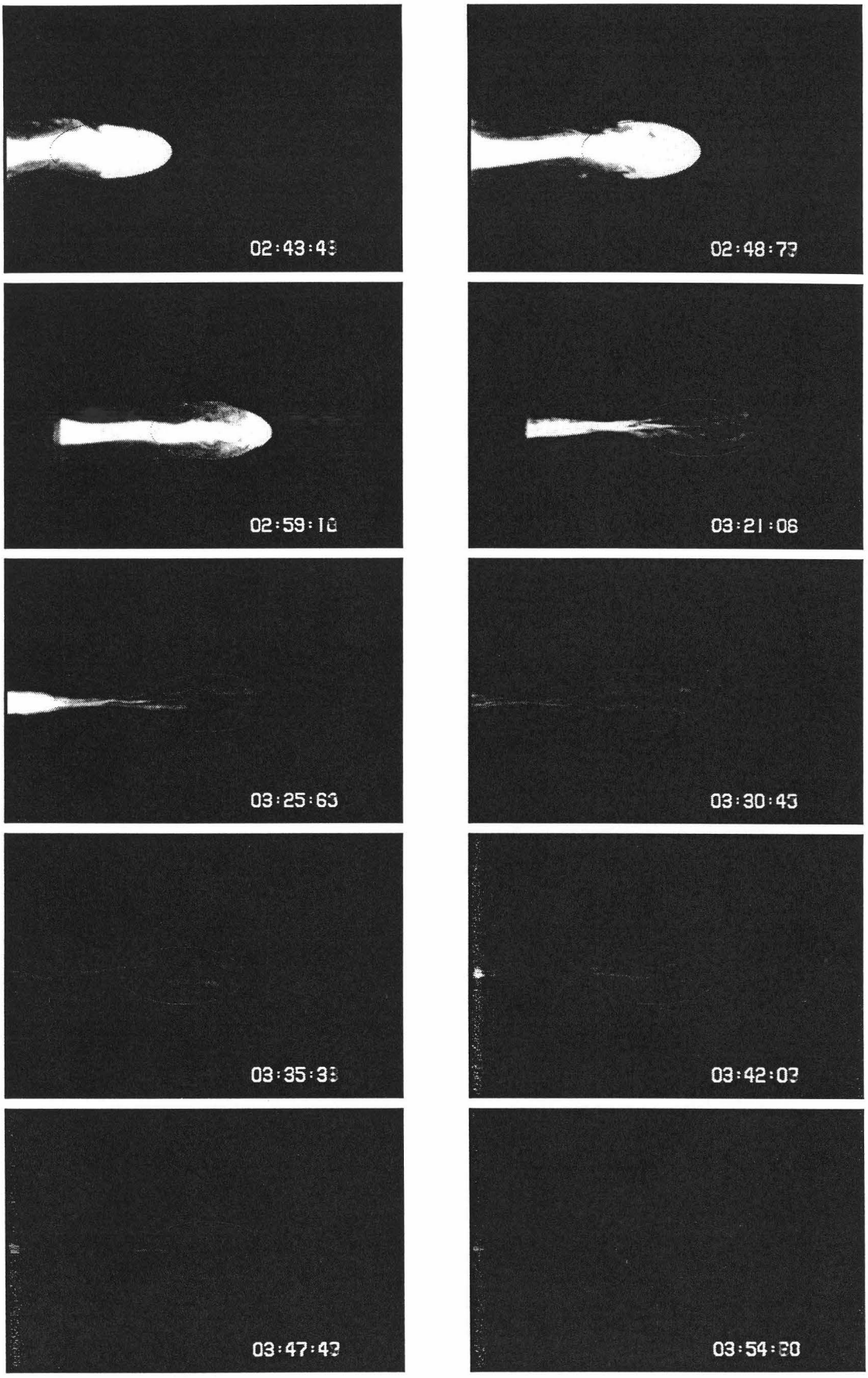
02:43:43
02:48:73
02:59:10
03:21:06
03:25:63
03:30:43
03:35:33
03:42:03
03:47:43
03:54:30

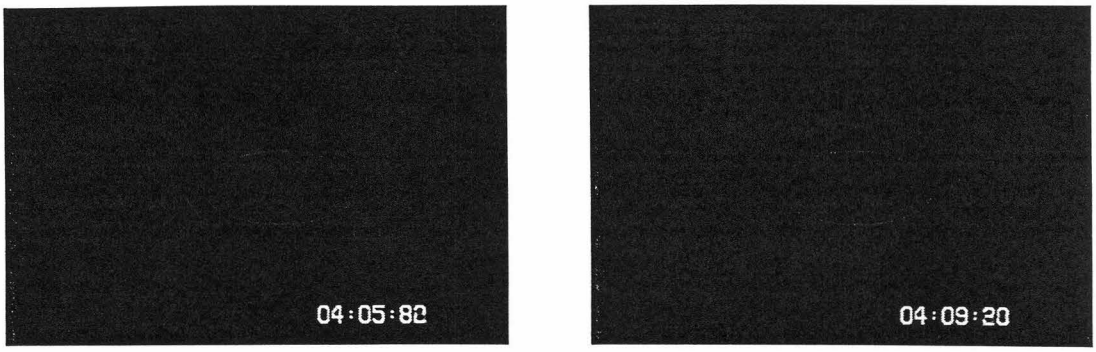

Figure A8.6c - Flow images from run 61002DC020

Table A8.3 - Experimental data from run 61001DC020

61001DC020		Infinitesimal Wave Speed Parameters					Distance Equation Coefficients		
		ω	h	H/h	δ	c_0	k_1	k_2	k_3
		0.0072	0.0156	19	0.054	0.0226	-3.51E-05	5.35E-02	-1.17E-01
(start)	time	position	celerity	celerity	position	adjusted	adjusted	(area)	dye
timeprint	t	x	c	c/c_0	x/h	x/h	$x/h*J$	count	concentration
(0:34.59)	(s)	(m)	(m/s)				(J = 0.410)	(75827)	(%)
0:39.12	4.53	0.12	0.053	2.358	8			15427802	79.8
0:44.57	9.98	0.41	0.053	2.341	27			16933593	87.6
0:48.65	14.06	0.63	0.053	2.328	40	12	5	16279178	84.2
0:55.85	21.26	1.01	0.052	2.305	64	36	15	15920973	82.3
1:11.58	36.99	1.82	0.051	2.256	116	88	36	11023273	57.0
1:14.94	40.35	1.99	0.051	2.246	127	99	41	10239631	53.0
1:18.90	44.31	2.19	0.050	2.234	140	112	46	9400714	48.6
1:25.62	51.03	2.52	0.050	2.213	162	133	55	6002889	31.0
1:28.78	54.19	2.68	0.050	2.203	172	144	59	5843817	30.2
1:33.91	59.32	2.94	0.049	2.187	188	160	66	4758868	24.6
1:41.99	67.4	3.33	0.049	2.162	214	185	76	3251426	16.8
1:47.11	72.52	3.58	0.048	2.146	230	201	83	2963301	15.3
1:50.47	75.88	3.74	0.048	2.135	240	212	87	2773201	14.3
1:58.00	83.41	4.10	0.048	2.112	263	235	96	2101060	10.9

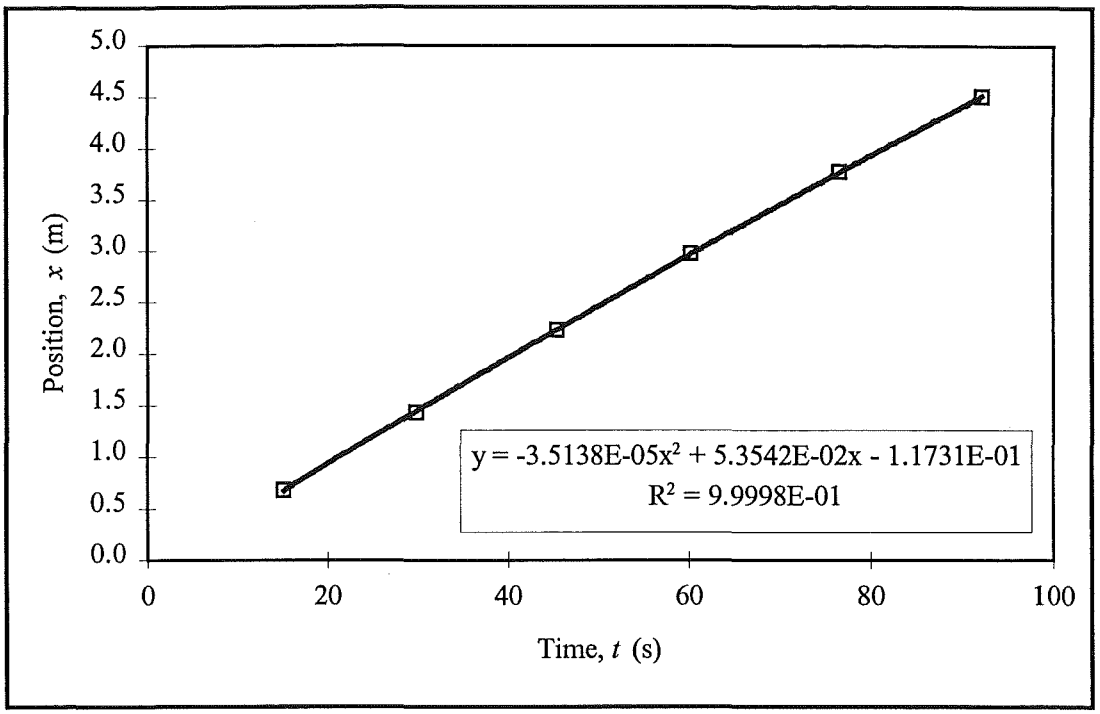

Figure A8.7a - Time-position data from run 61001DC020

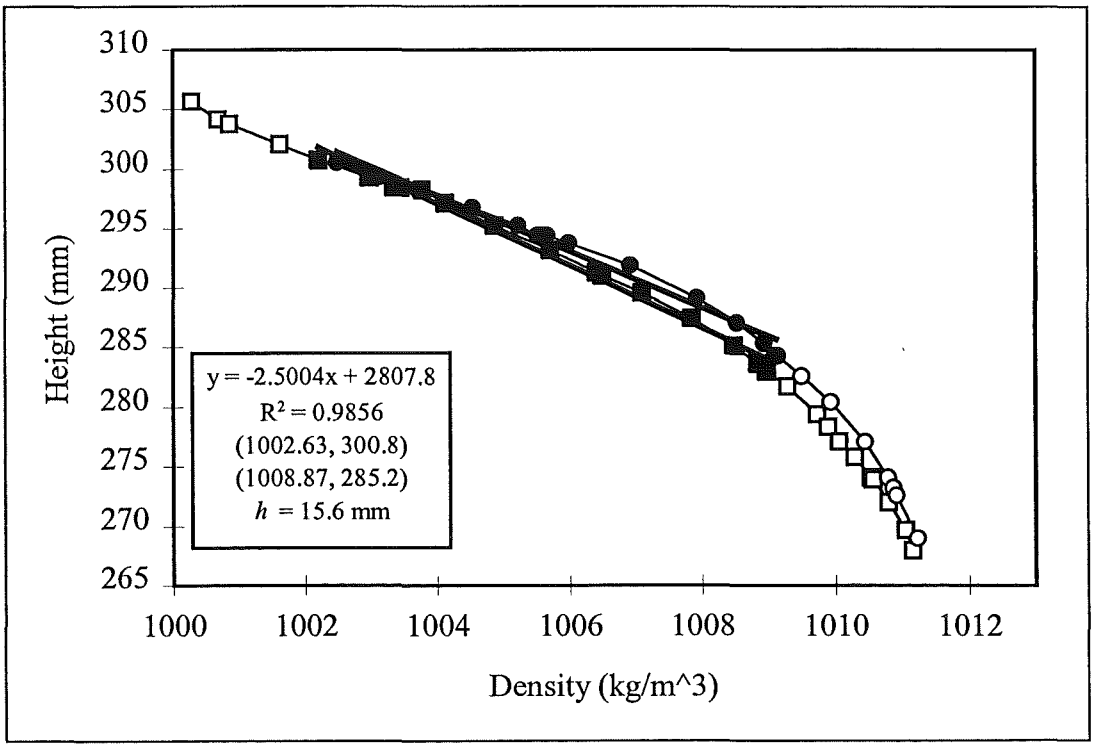

Figure A8.7b - Interfacial region density profiles from run 61001DC020

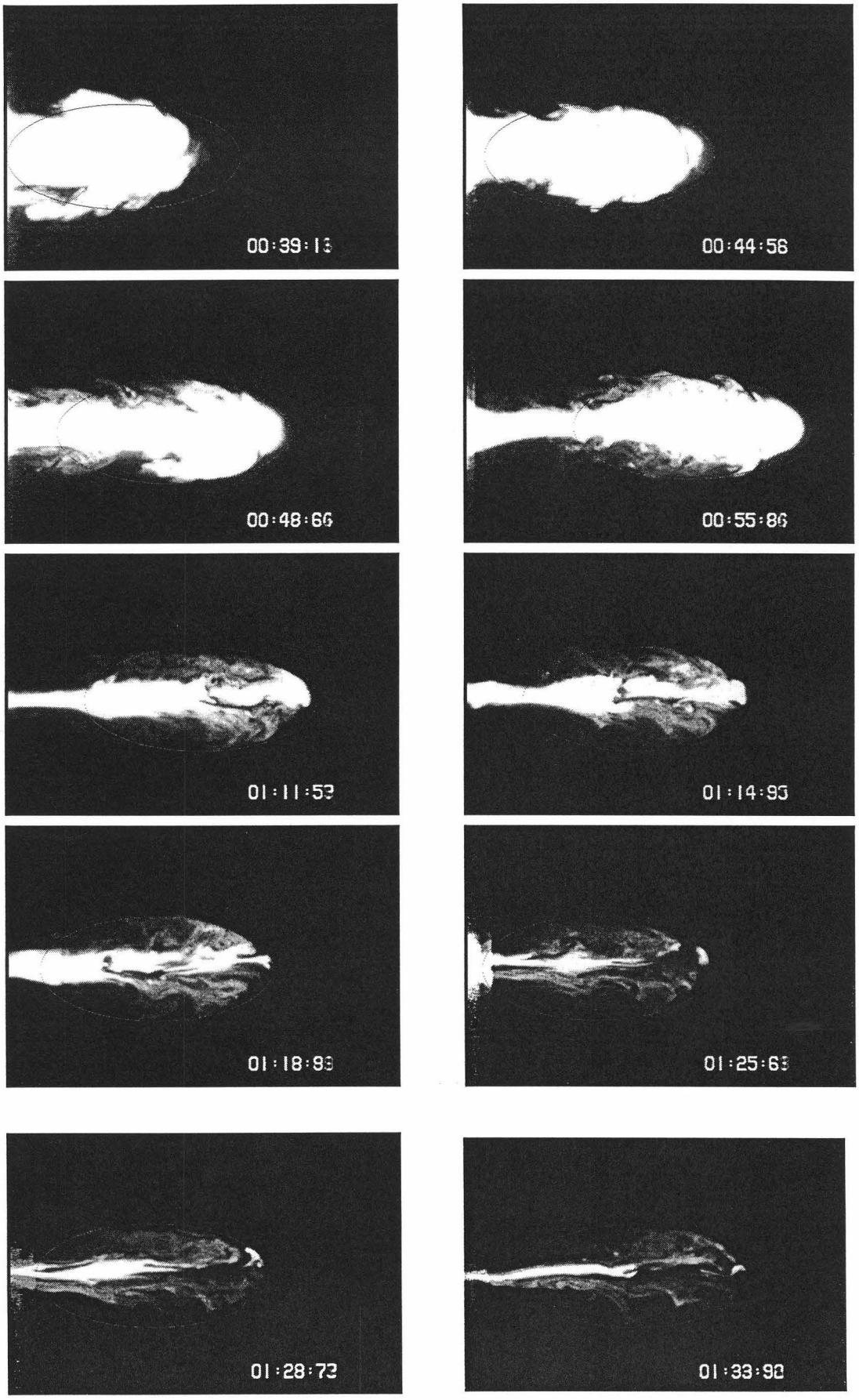
00:39:13
00:44:56
00:48:66
00:55:86
01:11:53
01:14:93
01:18:93
01:25:63
01:28:73
01:33:93

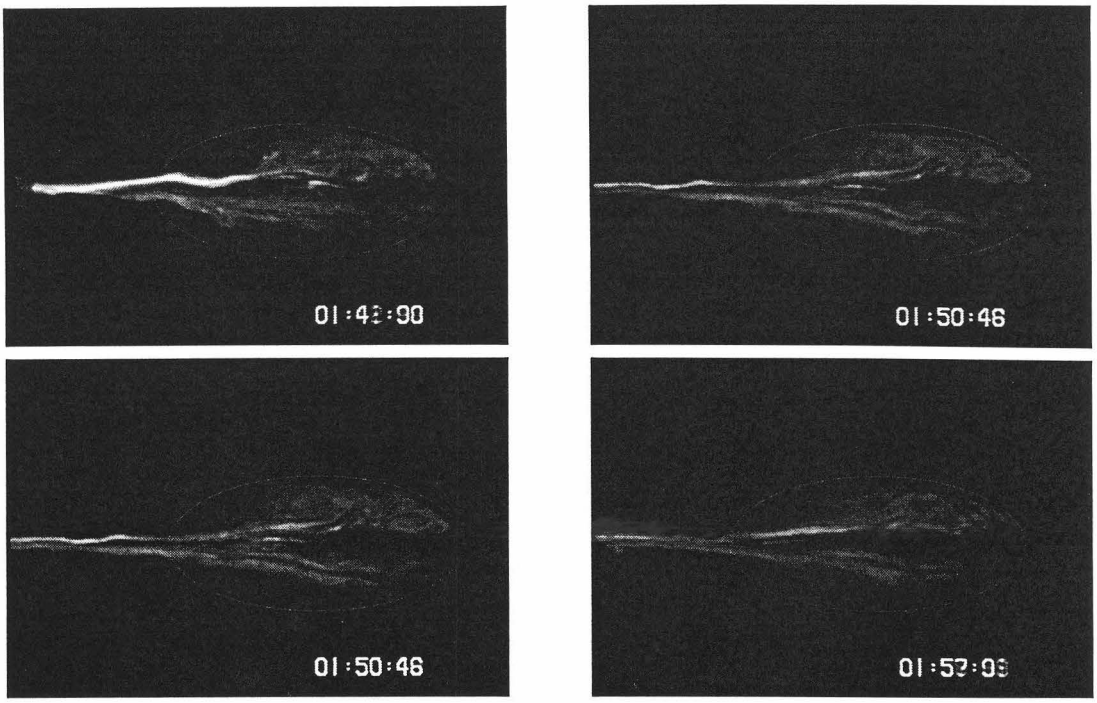

Figure A8.7c - Flow images from run 61001DC020

Table A8.4 - Experimental data from run 60808DC020

60808DC020		Infinitesimal Wave Speed Parameters					Distance Equation Coefficients		
		ω	h	H/h	δ	c_0	k_1	k_2	k_3
		0.0070	0.0143	21	0.049	0.0214	-3.04E-05	4.77E-02	-8.23E-02
(start)	time	position	celerity	celerity	position	adjusted	adjusted	(area)	dye
timeprint	t	x	c	c/c_0	x/h	x/h	$x/h*J$	count	concentration
(2:04.14)	(s)	(m)	(m/s)				($J = 0.465$)	(48039)	(%)
2:12.15	8.01	0.30	0.047	2.207	21			7330731	59.8
2:20.08	15.94	0.67	0.047	2.184	47	112	52	5309816	43.3
2:26.32	22.18	0.96	0.046	2.167	67	132	62	4514403	36.9
2:30.64	26.50	1.16	0.046	2.154	81	146	68	3676279	30.0
2:34.88	30.74	1.35	0.046	2.142	95	160	74	3734939	30.5
2:43.48	39.34	1.75	0.045	2.118	122	187	87	2710800	22.1
2:50.69	46.55	2.07	0.045	2.097	145	210	98	1896738	15.5
2:52.01	47.87	2.13	0.045	2.094	149	214	100	1751220	14.3
2:59.97	55.83	2.48	0.044	2.071	174	239	111	772939	6.3
3:05.53	61.39	2.73	0.044	2.055	191	256	119	718595	5.9
3:10.23	66.09	2.94	0.044	2.042	205	270	126	547951	4.5
3:18.94	74.80	3.31	0.043	2.017	232	297	138	337651	2.8
3:24.38	80.24	3.55	0.043	2.002	248	313	146	331764	2.7
3:29.10	84.96	3.75	0.043	1.988	262	327	152	263660	2.2
3:34.34	90.20	3.97	0.042	1.973	278	343	159	229278	1.9
3:42.71	98.57	4.32	0.042	1.950	302	367	171	214593	1.8

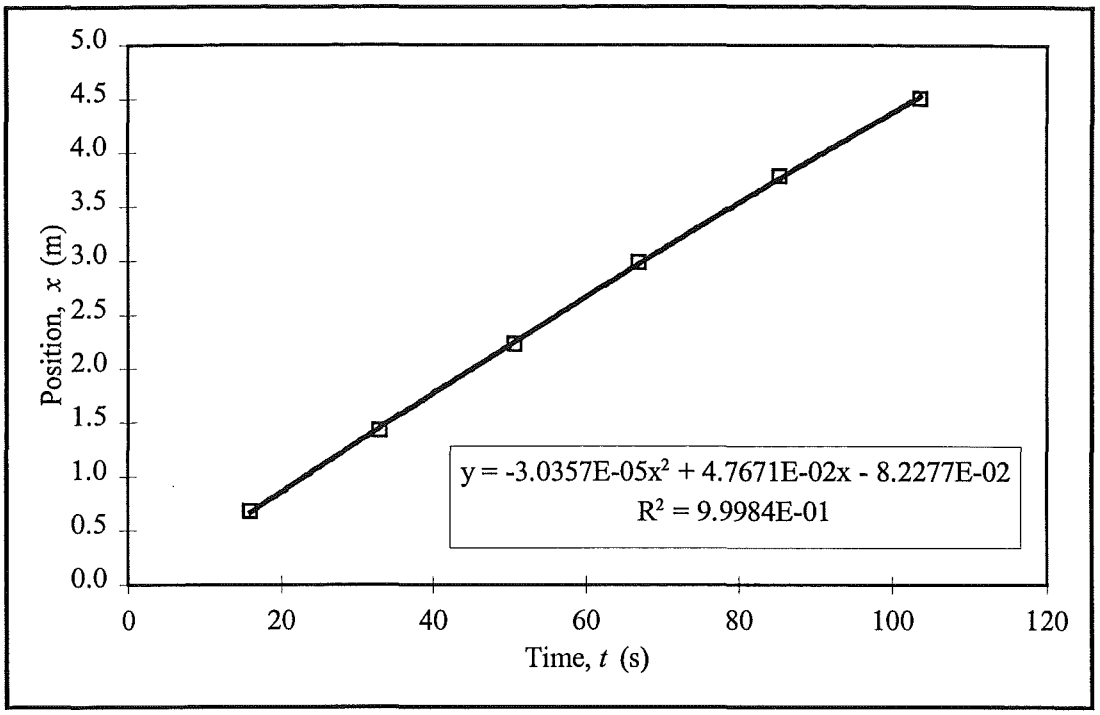

Figure 8.8a - Time-position data from run 60808DC020

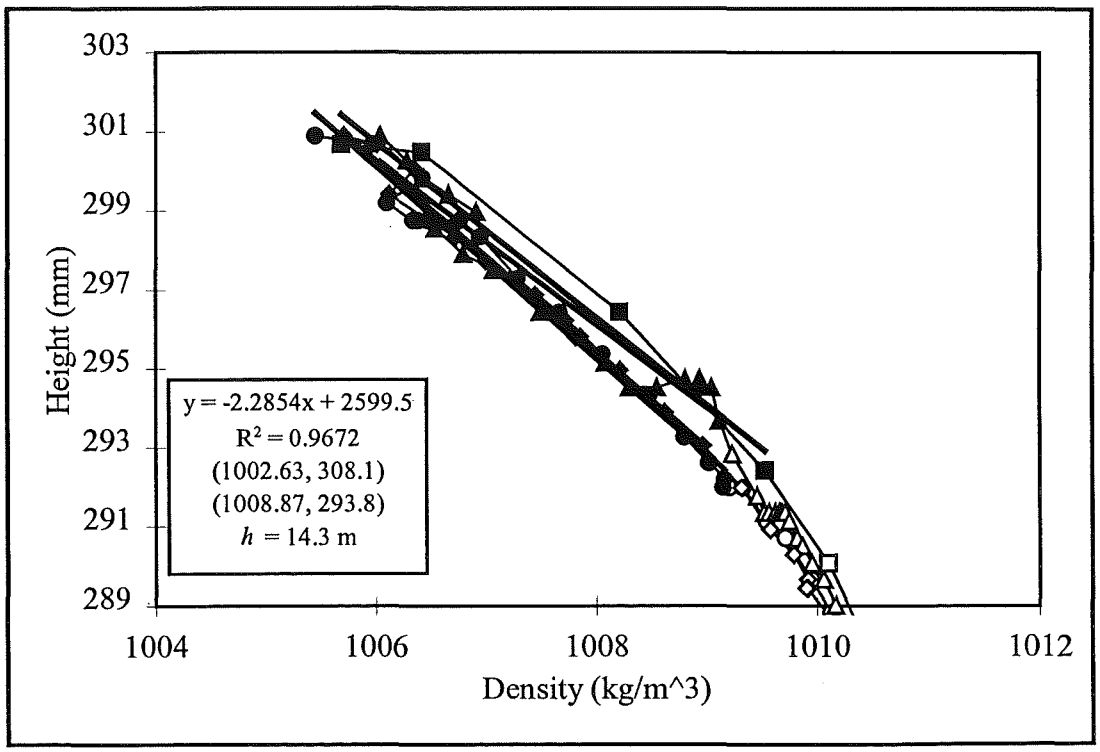

Figure 8.8b - Interfacial region density profiles from run 60808DC020

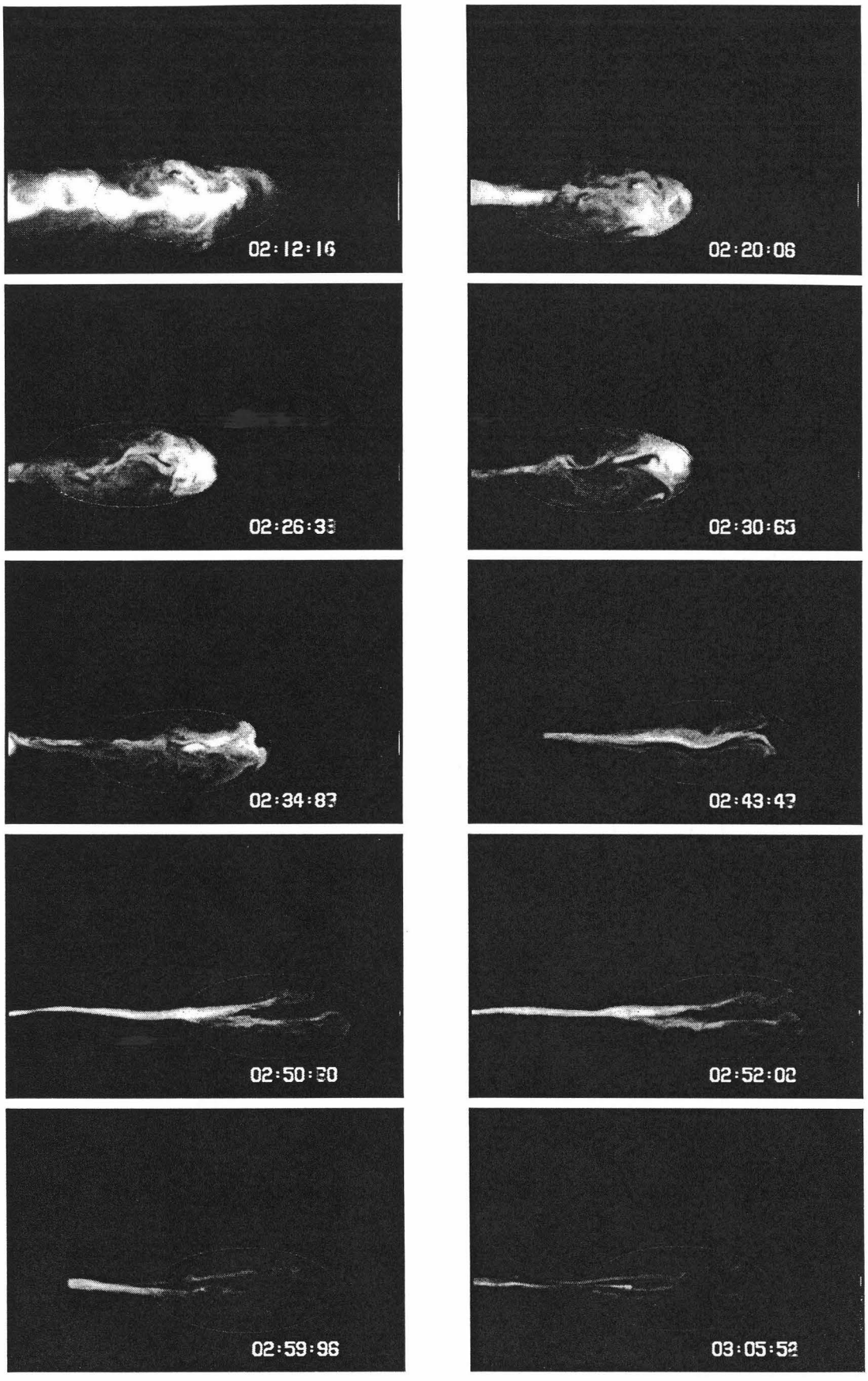
02:12:16
02:20:06
02:26:33
02:30:63
02:34:83
02:43:43
02:50:30
02:52:02
02:59:96
03:05:52

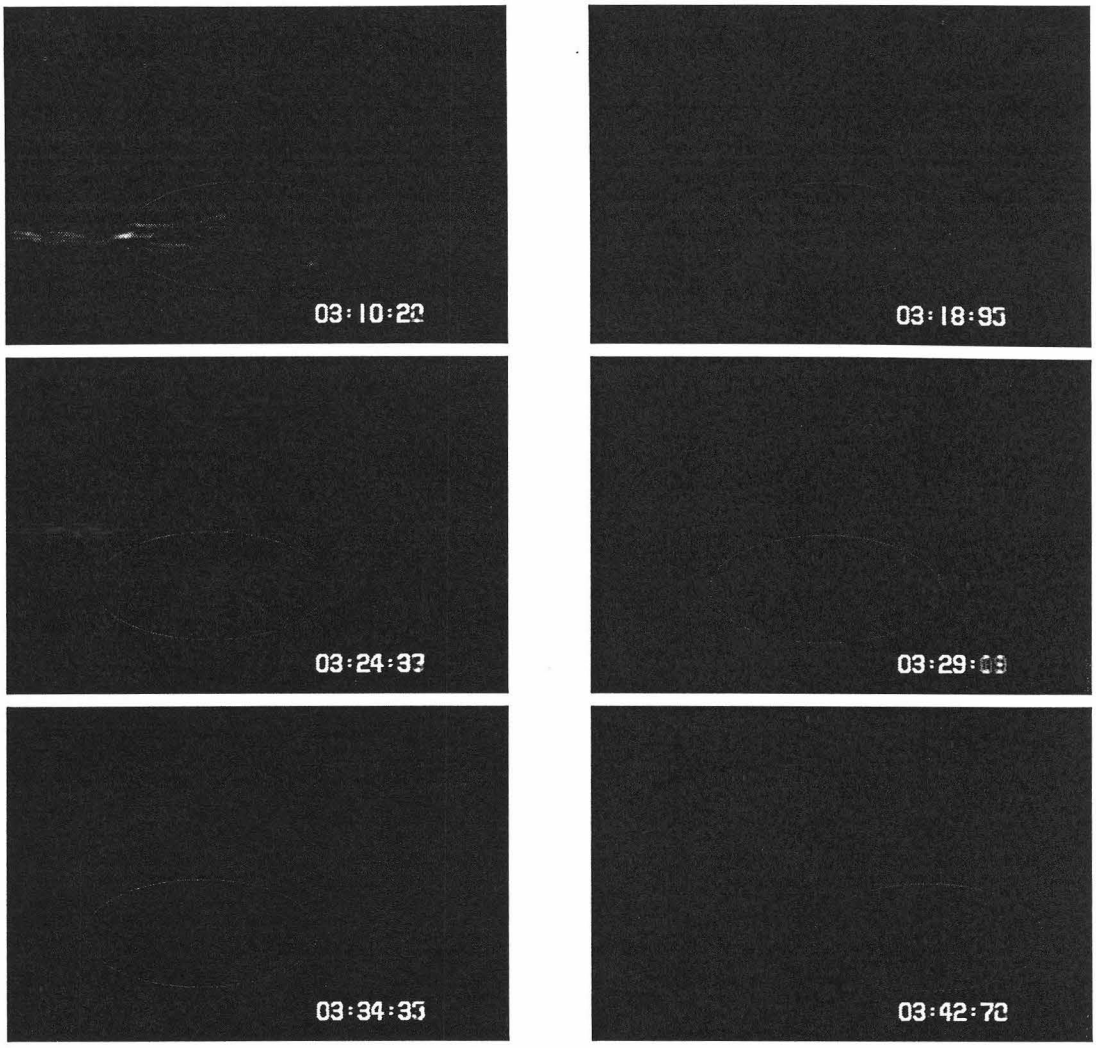

Figure 8.8c - Flow images from run 60808DC020

Table A8.5 - Experimental data from run 60810DC020

60810DC020		Infinitesimal Wave Speed Parameters					Distance Equation Coefficients		
		ω	h	H/h	δ	c_0	k_1	k_2	k_3
		0.0071	0.0143	21	0.049	0.0215	-3.72E-05	3.65E-02	-1.41E-01
(start)	time	position	celerity	celerity	position	adjusted	adjusted	(area)	dye
timeprint	t	x	c	c/c_0	x/h	x/h	$x/h*J$	count	concentration
(1:22.85)	(s)	(m)	(m/s)				($J = 0.876$)	(12545)	(%)
1:28.90	6.05	0.08	0.036	1.674	5	30	26	2220459	69.4
1:34.85	12.00	0.29	0.036	1.653	20	45	39	1597260	49.9
1:41.57	18.72	0.53	0.035	1.630	37	62	54	1055763	33.0
1:44.57	21.72	0.63	0.035	1.619	44	69	60	907523	28.4
1:51.25	28.40	0.86	0.034	1.596	60	85	75	628822	19.7
1:57.90	35.05	1.09	0.034	1.573	76	101	88	369419	11.5
2:04.38	41.53	1.31	0.033	1.551	92	116	102	268489	8.4
2:15.58	52.73	1.68	0.033	1.512	117	142	124	181804	5.7
2:22.22	59.37	1.89	0.032	1.489	132	157	138	116383	3.6
2:32.31	69.46	2.21	0.031	1.454	155	179	157	73994	2.3
2:39.03	76.18	2.42	0.031	1.431	169	194	170	54240	1.7
2:48.79	85.94	2.72	0.030	1.397	190	215	188	30467	1.0
2:56.70	93.85	2.96	0.030	1.370	207				
3:04.20	101.35	3.17	0.029	1.344	222				
3:14.92	112.07	3.48	0.028	1.307	243				
3:24.73	121.88	3.75	0.027	1.273	262				
3:31.41	128.56	3.93	0.027	1.250	275				
3:38.53	135.68	4.12	0.026	1.225	288				
3:50.78	147.93	4.44	0.025	1.183	311				

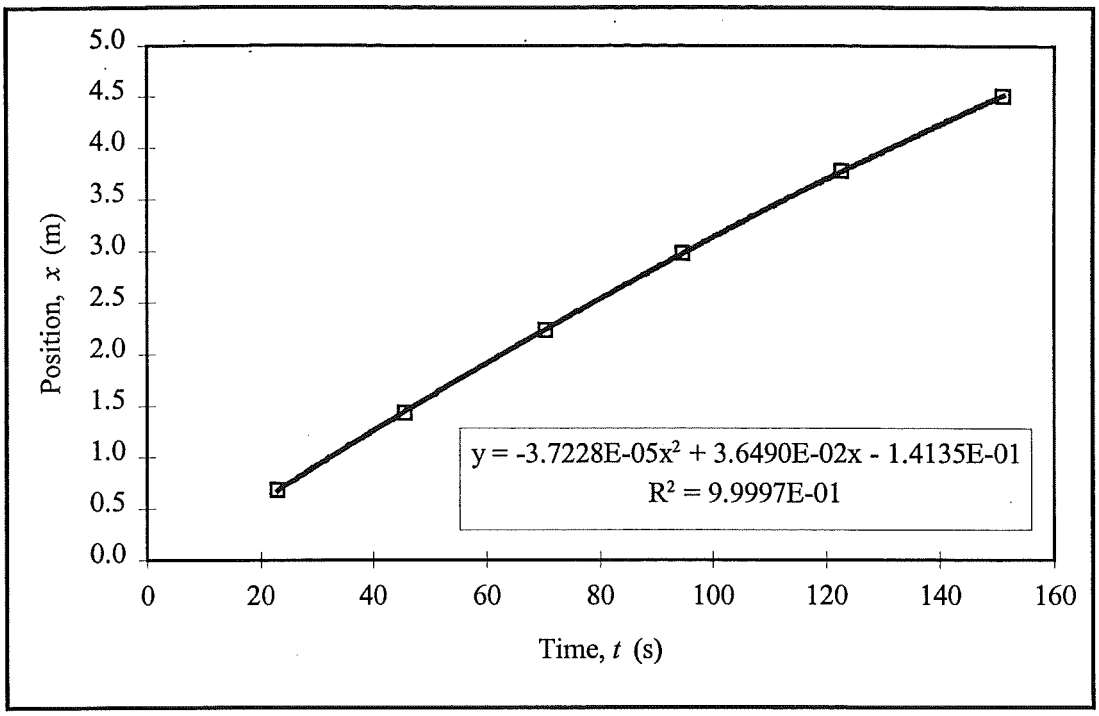

Figure 8.9a - Time-position data from run 60810DC020

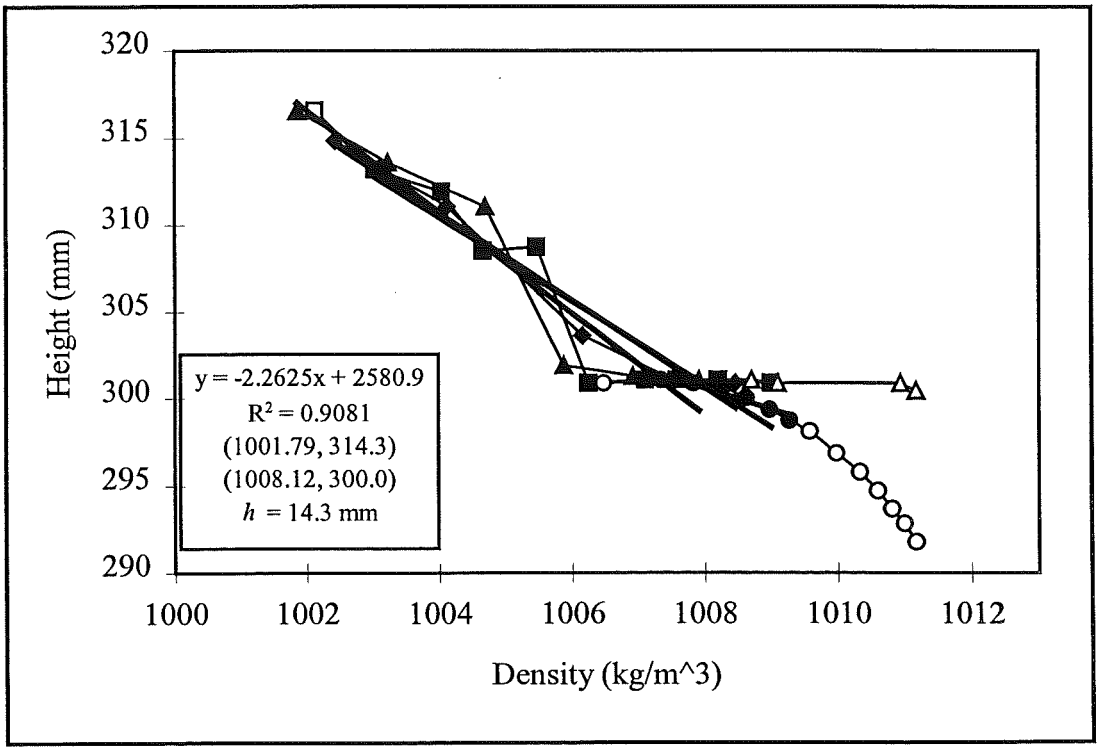

Figure 8.9b - Interfacial region density profiles from run 60810DC020

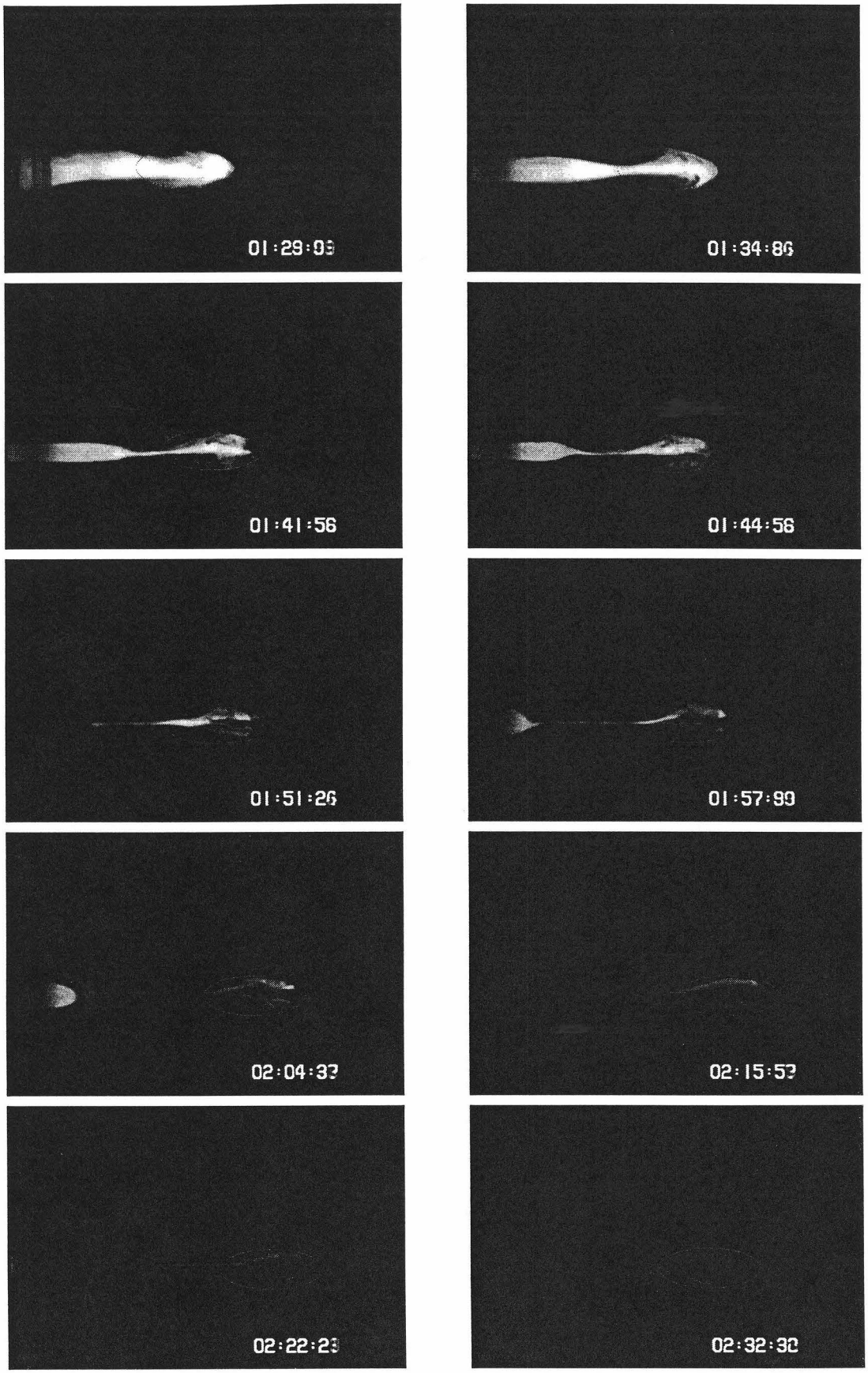
01:29:09
01:34:86
01:41:56
01:44:56
01:51:26
01:57:99
02:04:33
02:15:53
02:22:23
02:32:30

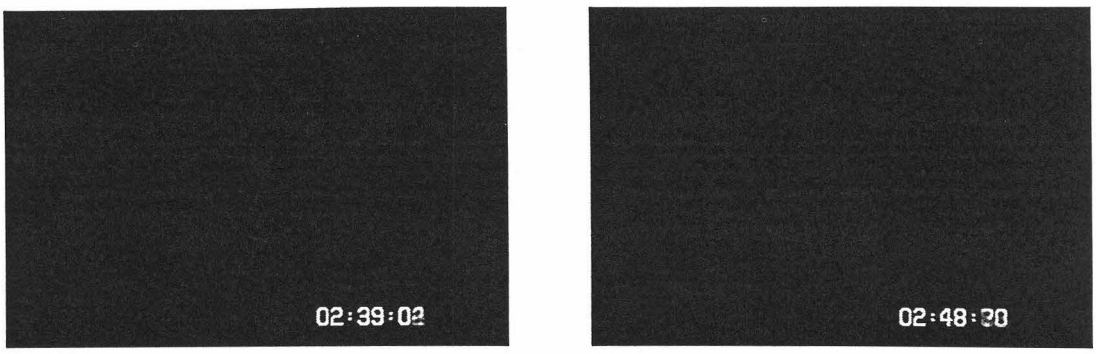

Figure 8.9c - Flow images from run 60810DC020

Table A8.6 - Experimental data from run 61101DC030

61101DC030		Infinitesimal Wave Speed Parameters					Distance Equation Coefficients		
		ω	h	H/h	δ	c_0	k_1	k_2	k_3
		0.0108	0.0169	18	0.059	0.0287	-8.77E-05	5.89E-02	-9.82E-02
(start)	time	position	celerity	celerity	position	adjusted	adjusted	(area)	dye
timeprint	t	x	c	c/c_0	x/h	x/h	$x/h*J$	count	concentration
(0:21.57)	(s)	(m)	(m/s)				(J = 0.597)	(43955)	(%)
0:28.55	6.98	0.31	0.058	2.010	18			10156918	90.6
0:32.79	11.22	0.55	0.057	1.984	33			10265045	91.6
0:40.95	19.38	1.01	0.055	1.934	60	25	15	9405922	83.9
0:47.05	25.48	1.35	0.054	1.897	80	45	27	8132395	72.6
0:57.56	35.99	1.91	0.053	1.833	113	78	47	5942695	53.0
1:02.28	40.71	2.15	0.052	1.804	127	93	55	5048224	45.0
1:08.84	47.27	2.49	0.051	1.764	147	113	67	3294024	29.4
1:18.29	56.72	2.96	0.049	1.706	175	141	84	1983992	17.7
1:25.53	63.96	3.31	0.048	1.662	196	161	96	1166836	10.4
1:31.85	70.28	3.61	0.047	1.623	213	179	107	755435	6.7
1:39.90	78.33	3.98	0.045	1.574	235	201	120	471554	4.2
1:49.50	87.93	4.40	0.043	1.515	260	226	135	363125	3.2

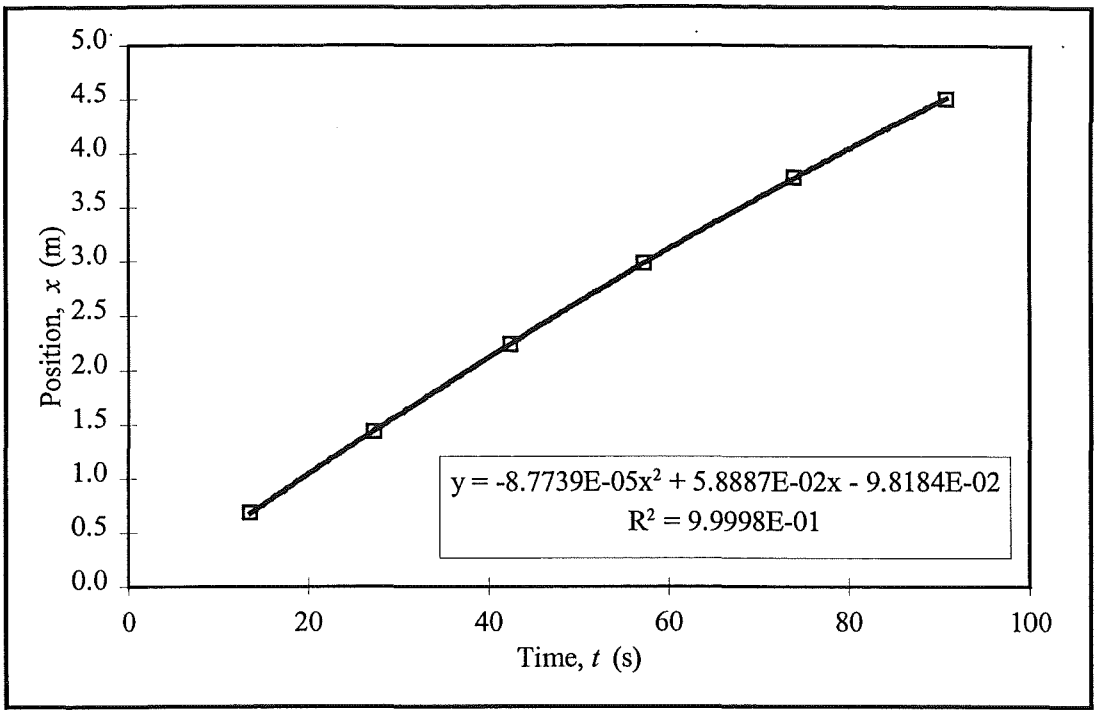

Figure 8.10a - Time-position data from run 61101DC030

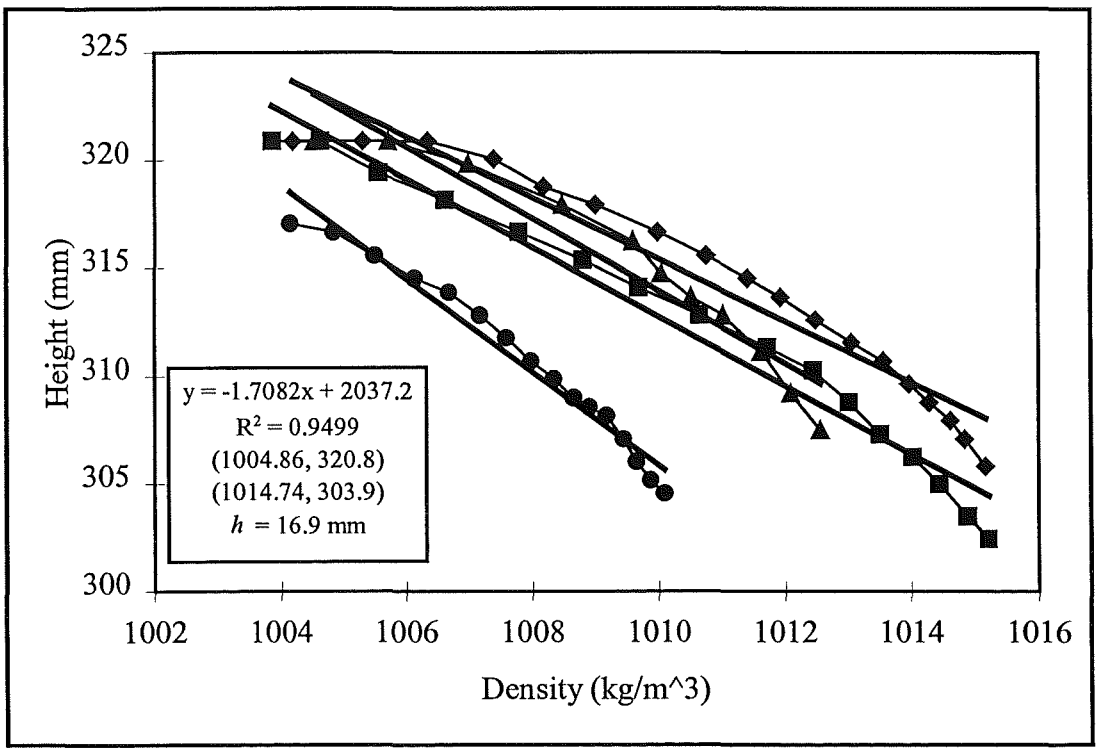

Figure 8.10b - Interfacial region density profiles from run 61101DC030

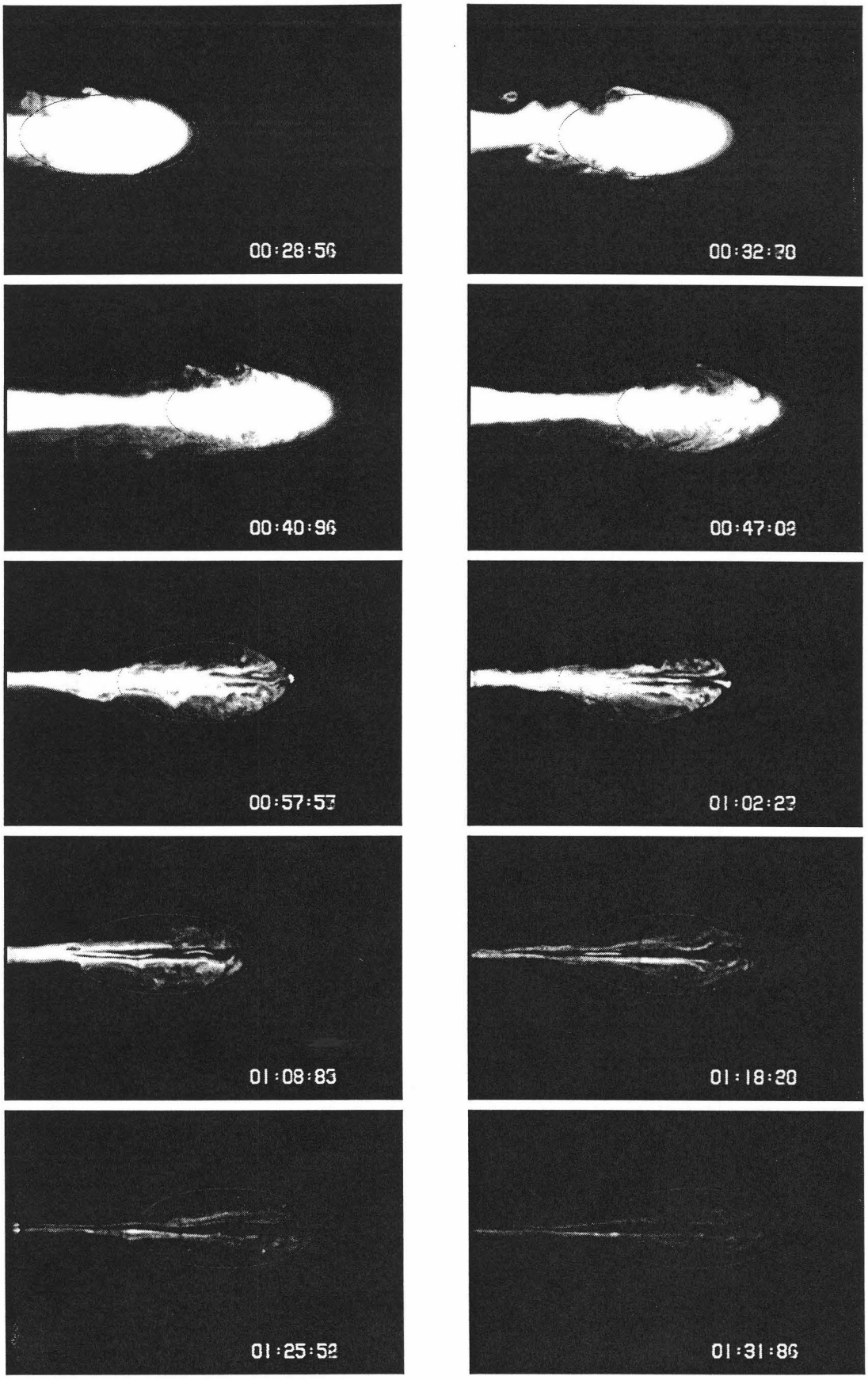
00:28:56
00:32:20
00:40:96
00:47:08
00:57:57
01:02:23
01:08:83
01:18:20
01:25:52
01:31:86

Figure 8.10c - Flow images from run 61101DC030

Table A8.7 - Experimental data from run 61010DC050

61010DC050		Infinitesimal Wave Speed Parameters					Distance Equation Coefficients		
		ω	h	H/h	δ	c_0	k_1	k_2	k_3
		0.0173	0.0056	54	0.019	0.0215	-8.14E-05	7.19E-02	-1.10E-01
(start)	time	position	celerity	celerity	position	adjusted	adjusted	(area)	dye
timeprint	t	x	c	c/c_0	x/h	x/h	$x/h*J$	count	concentration
(3:51.89)	(s)	(m)	(m/s)				(J = 0.201)	(48039)	(%)
3:55.01	3.12	0.11	0.071	3.319	20			9724664	90.4
4:00.85	8.96	0.53	0.070	3.275	94	10	2	9080892	84.4
4:07.33	15.44	0.98	0.069	3.226	175	91	18	8091625	75.2
4:10.61	18.72	1.21	0.069	3.201	215	131	26	7438758	69.2
4:13.73	21.84	1.42	0.068	3.177	254	170	34	6655253	61.9
4:18.97	27.08	1.78	0.067	3.138	317	233	47	4993237	46.4
4:22.82	30.93	2.03	0.067	3.108	363	279	56	3853809	35.8
4:25.42	33.53	2.21	0.066	3.089	394	310	62	3075274	28.6
4:30.38	38.49	2.54	0.066	3.051	453	369	74	2085907	19.4
4:34.70	42.81	2.82	0.065	3.018	503	419	84	1220795	11.4
4:36.26	44.37	2.92	0.065	3.007	521	437	88	1089860	10.1
4:42.50	50.61	3.32	0.064	2.959	592	508	102	708363	6.6
4:45.74	53.85	3.52	0.063	2.935	629	545	110	589749	5.5
4:49.51	57.62	3.76	0.062	2.906	671	587	118	510334	4.7
4:53.83	61.94	4.03	0.062	2.873	719	635	128	484950	4.5
4:56.91	65.02	4.22	0.061	2.850	753	669	135	407016	3.8
5:00.75	68.86	4.45	0.061	2.821	795	711	143	335226	3.1

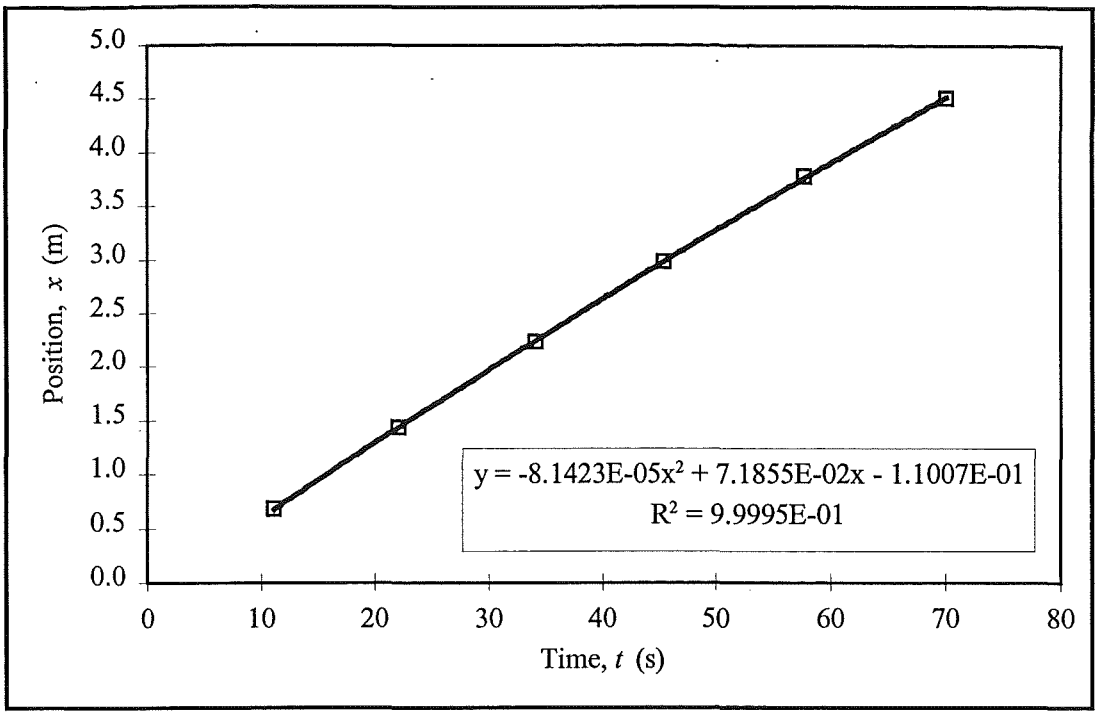

Figure A8.11a - Time-position data from run 61010DC050

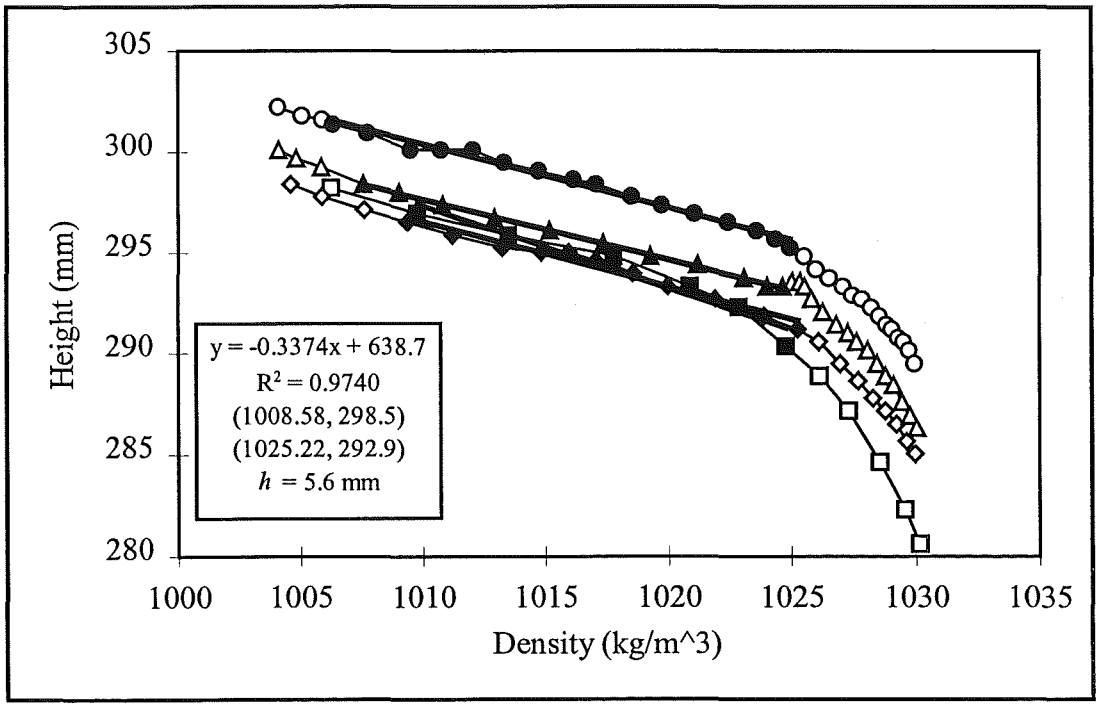

Figure A8.11b - Interfacial region density profiles from run 61010DC050

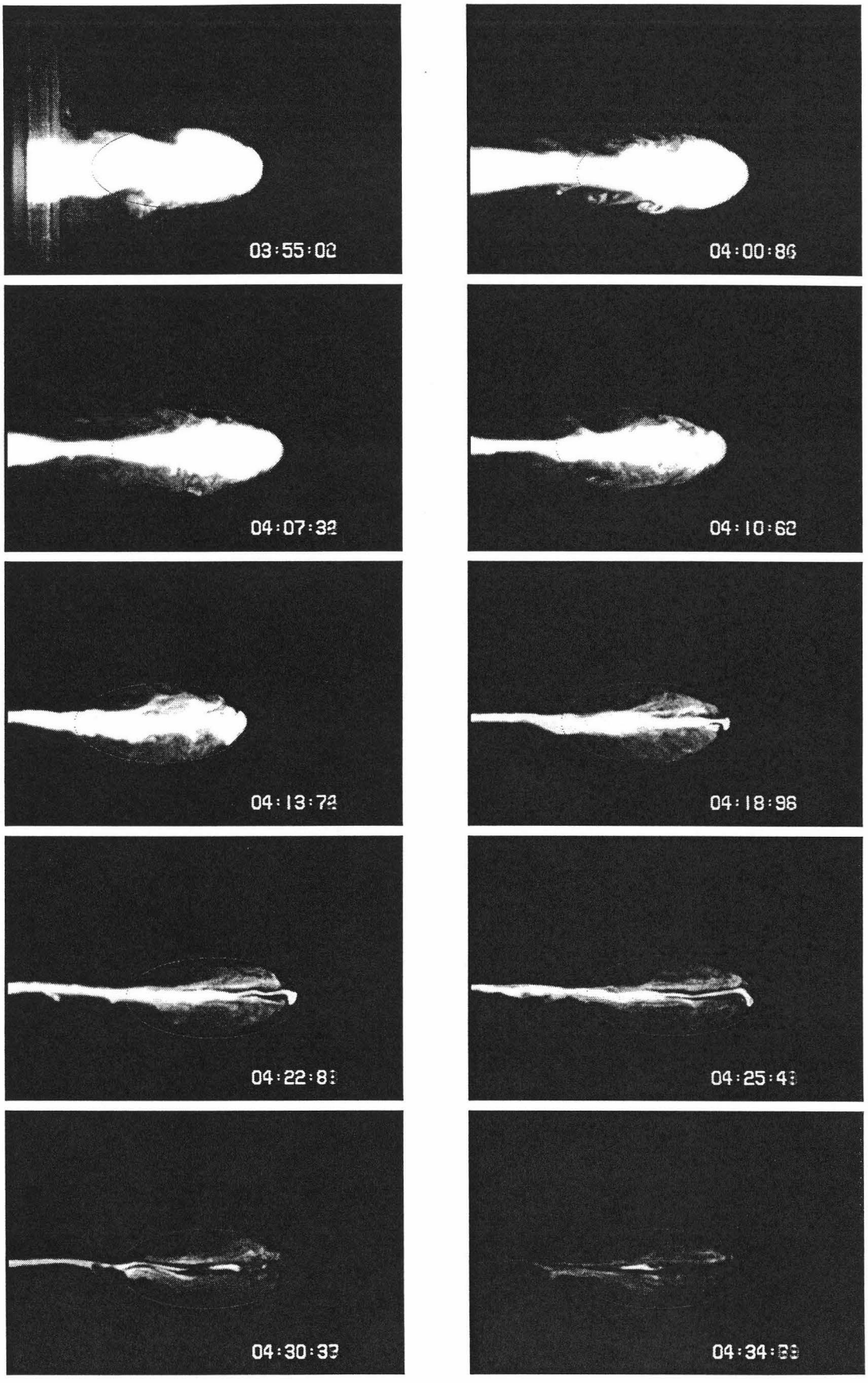
03:55:02
04:00:86
04:07:32
04:10:62
04:13:72
04:18:96
04:22:81
04:25:41
04:30:33
04:34:88

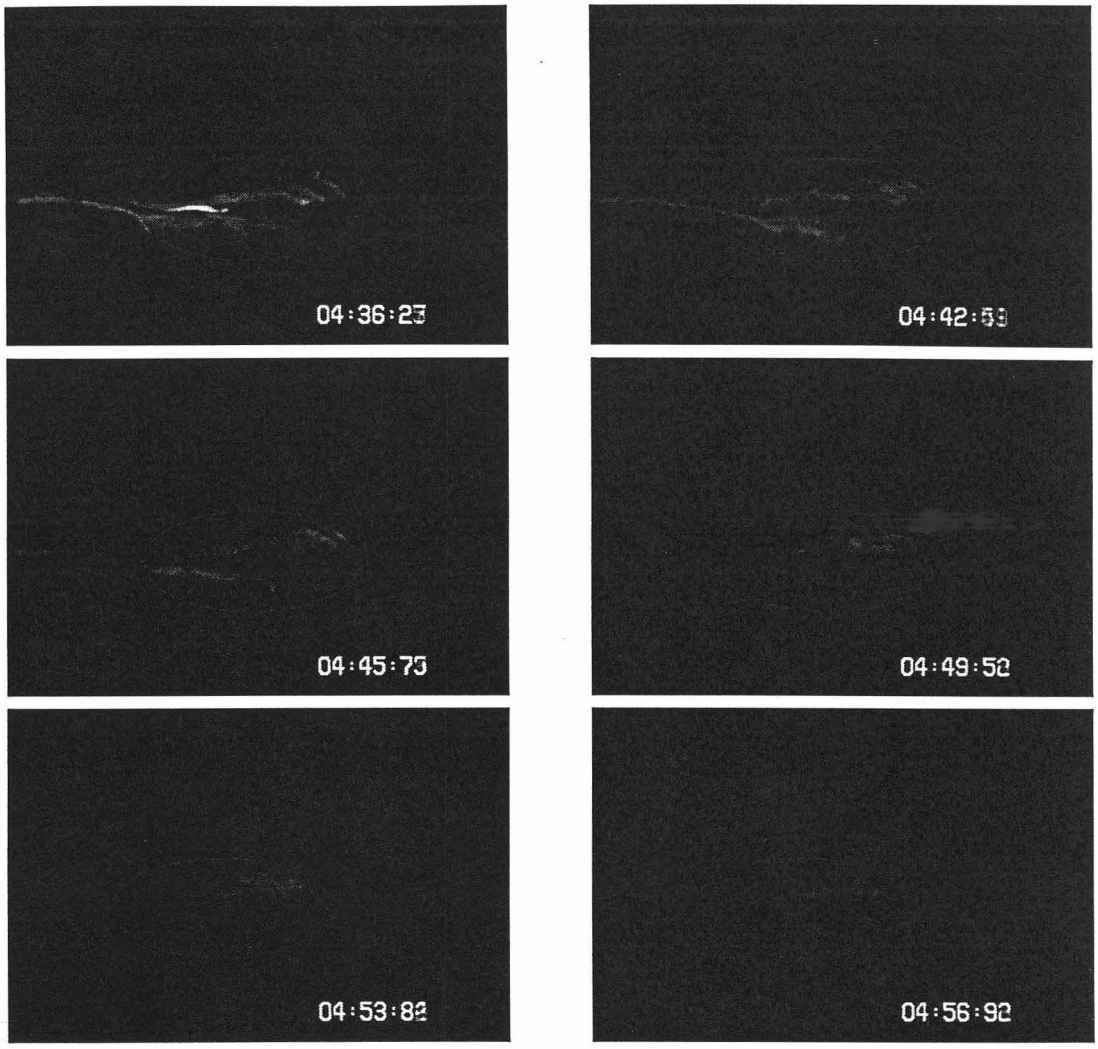

Figure A8.11c - Flow images from run 61010DC050

Table A8.8 - Experimental data from run 61008DC050

61008DC050		Infinitesimal Wave Speed Parameters					Distance Equation Coefficients		
		ω	h	H/h	δ	c_0	k_1	k_2	k_3
		0.0174	0.0043	70	0.014	0.0190	-1.02E-04	5.93E-02	-4.58E-02
(start)	time	position	celerity	celerity	position	adjusted	adjusted	(area)	dye
timeprint	t	x	c	c/c_0	x/h	x/h	$x/h*J$	count	concentration
(1:06.69)	(s)	(m)	(m/s)				(J = 0.233)	(23147)	(%)
1:11.80	5.11	0.25	0.058	3.075	59	46	11	4338786	73.5
1:15.28	8.59	0.46	0.058	3.038	106	93	22	4208937	71.3
1:17.76	11.07	0.60	0.057	3.011	139	126	29	4354880	73.8
1:23.93	17.24	0.95	0.056	2.945	220	207	48	3320773	56.3
1:28.01	21.32	1.17	0.055	2.901	273	259	61	2629695	44.6
1:31.85	25.16	1.38	0.054	2.860	321	308	72	2106738	35.7
1:38.65	31.96	1.75	0.053	2.787	406	393	92	771823	13.1
1:43.29	36.60	1.99	0.052	2.737	463	449	105	374811	6.4
1:47.50	40.81	2.21	0.051	2.692	513	500	117	197826	3.4
1:53.50	46.81	2.51	0.050	2.628	583	570	133	165871	2.8
1:58.70	52.01	2.76	0.049	2.572	643	630	147	127951	2.2
2:19.79	73.10	3.75	0.044	2.346	872				

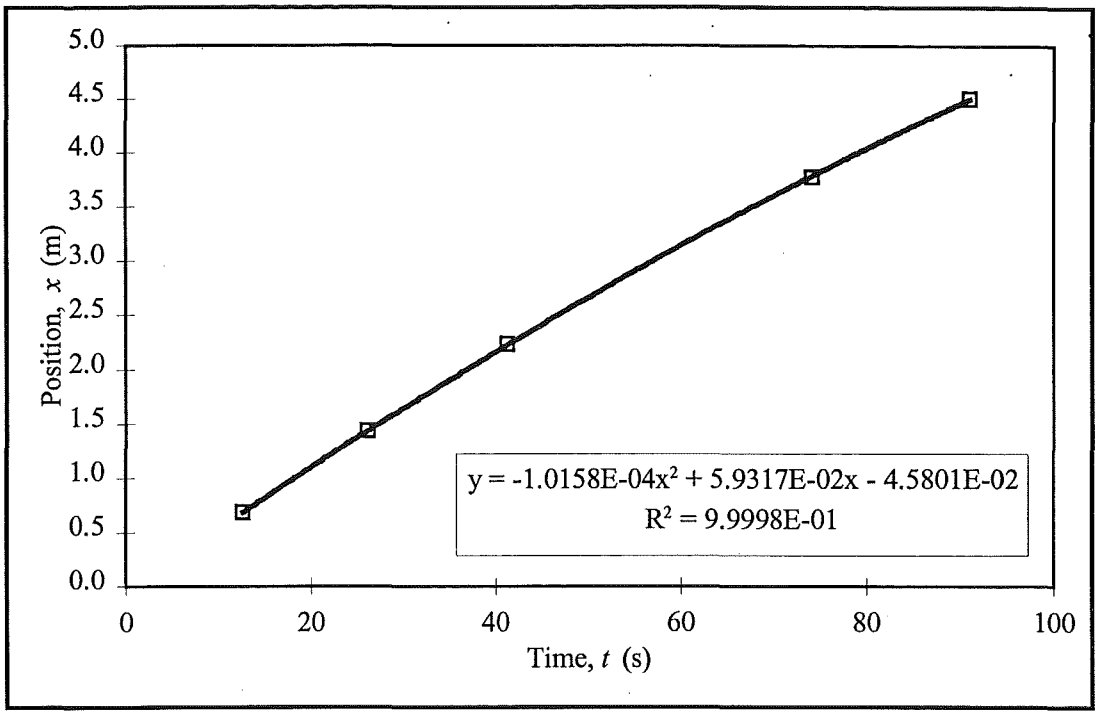

Figure A8.12a - Time-position data from run 61008DC050

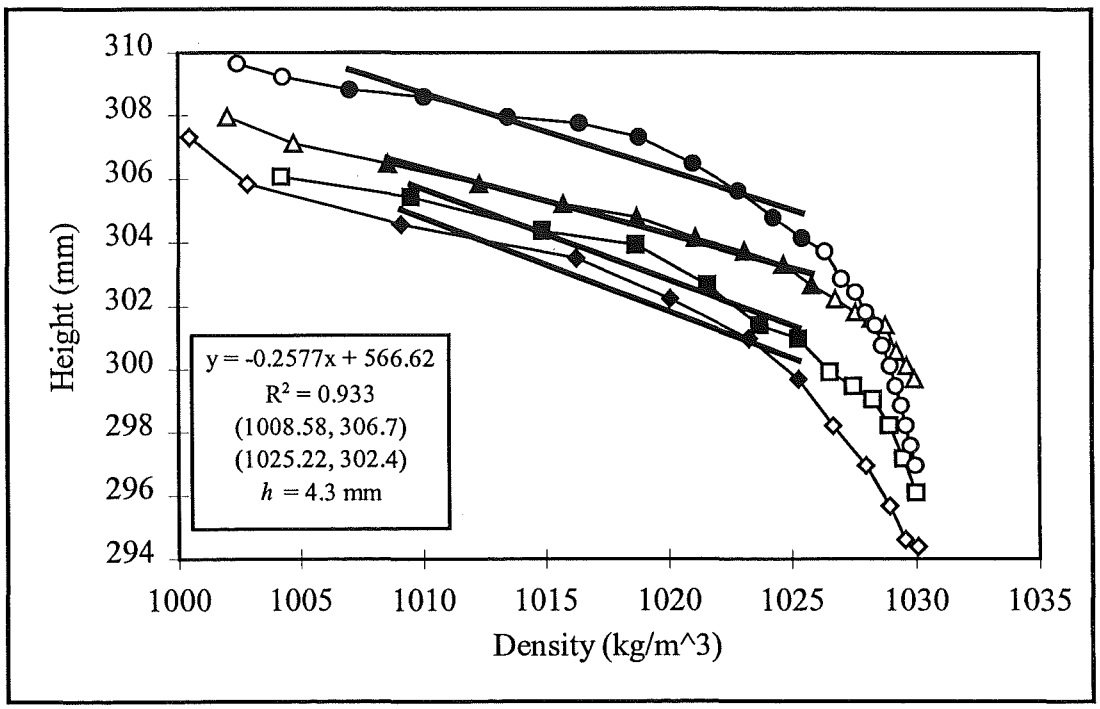

Figure A8.12b - Interfacial region density profiles from run 61008DC050

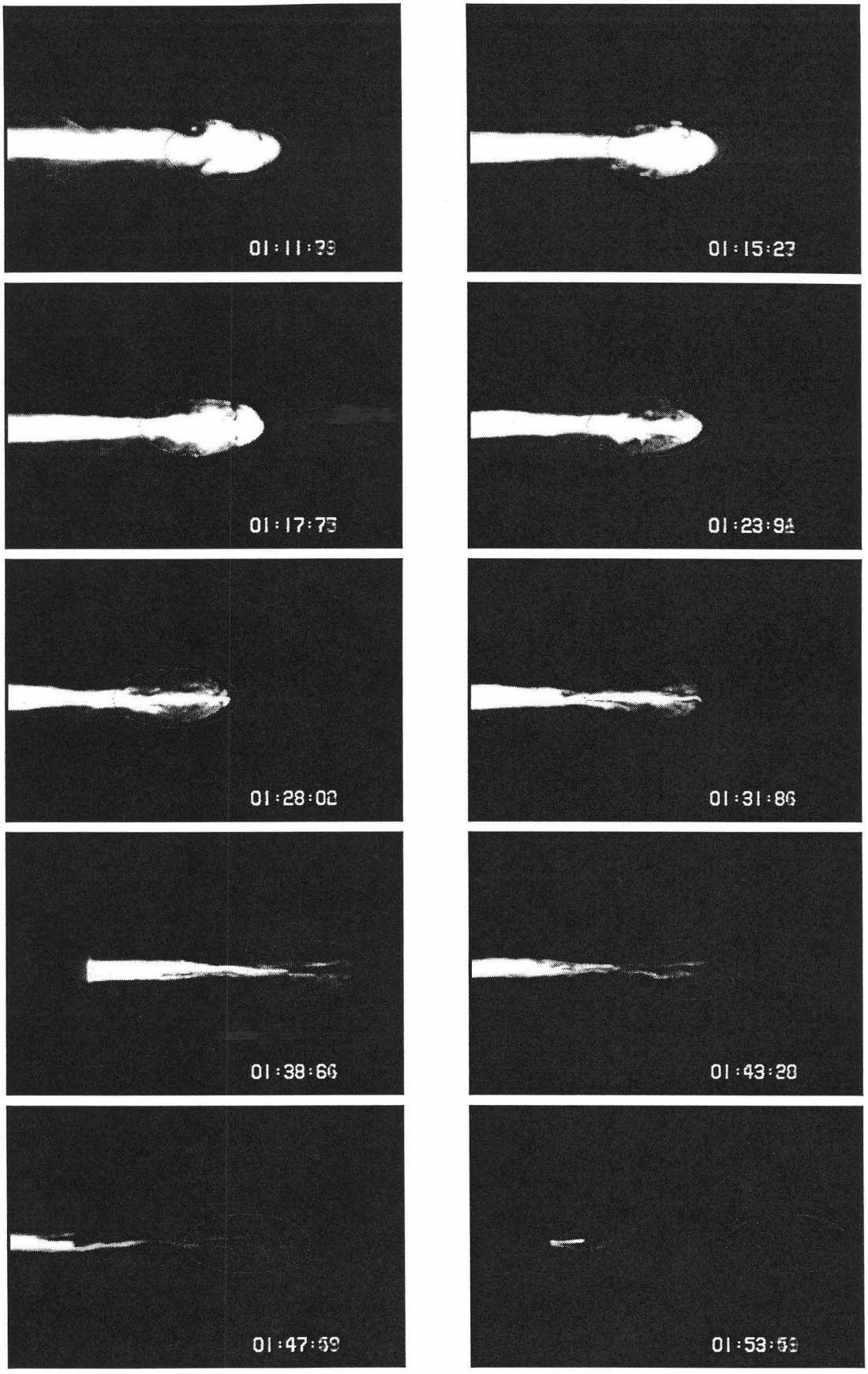
01:11:39
01:15:27
01:17:73
01:23:94
01:28:02
01:31:86
01:38:66
01:43:20
01:47:69
01:53:69

Figure A8.12c - Flow images from run 61008DC050

Table A8.9 - Experimnetal data from run 61011DC050

61011DC050		Infinitesimal Wave Speed Parameters					Distance Equation Coefficients		
		ω	h	H/h	δ	c_0	k_1	k_2	k_3
		0.0176	0.0130	23	0.045	0.0324	-1.17E-04	8.50E-02	-1.15E-01
(start)	time	position	celerity	celerity	position	adjusted	adjusted	(area)	dye
timeprint	t	x	c	c/c_0	x/h	x/h	$x/h*J$	count	concentration
(1:20.32)	(s)	(m)	(m/s)				(J = 0.340)	(75827)	(%)
1:24.29	3.97	0.22	0.084	2.593	17			18396463	95.1
1:28.10	7.78	0.54	0.083	2.565	41			17754371	91.8
1:33.46	13.14	0.98	0.082	2.527	76	17	6	17361636	89.8
1:37.78	17.46	1.33	0.081	2.496	103	44	15	15618988	80.8
1:43.66	23.34	1.81	0.080	2.453	139	80	27	12770994	66.0
1:45.26	24.94	1.93	0.079	2.442	149	90	31	11963042	61.9
1:47.98	27.66	2.15	0.079	2.422	165	107	36	10678794	55.2
1:53.07	32.75	2.54	0.077	2.386	196	137	47	7353998	38.0
1:55.63	35.31	2.74	0.077	2.367	211	152	52	5965871	30.9
1:58.51	38.19	2.96	0.076	2.347	228	169	58	4076289	21.1
2:03.27	42.95	3.32	0.075	2.312	255	197	67	3384787	17.5
2:06.07	45.75	3.53	0.074	2.292	272	213	73	2976314	15.4
2:09.03	48.71	3.75	0.074	2.271	288	230	78	2771095	14.3
2:13.15	52.83	4.05	0.073	2.241	312	253	86	1898561	9.8
2:16.44	56.12	4.29	0.072	2.218	330	271	92	1353632	7.0

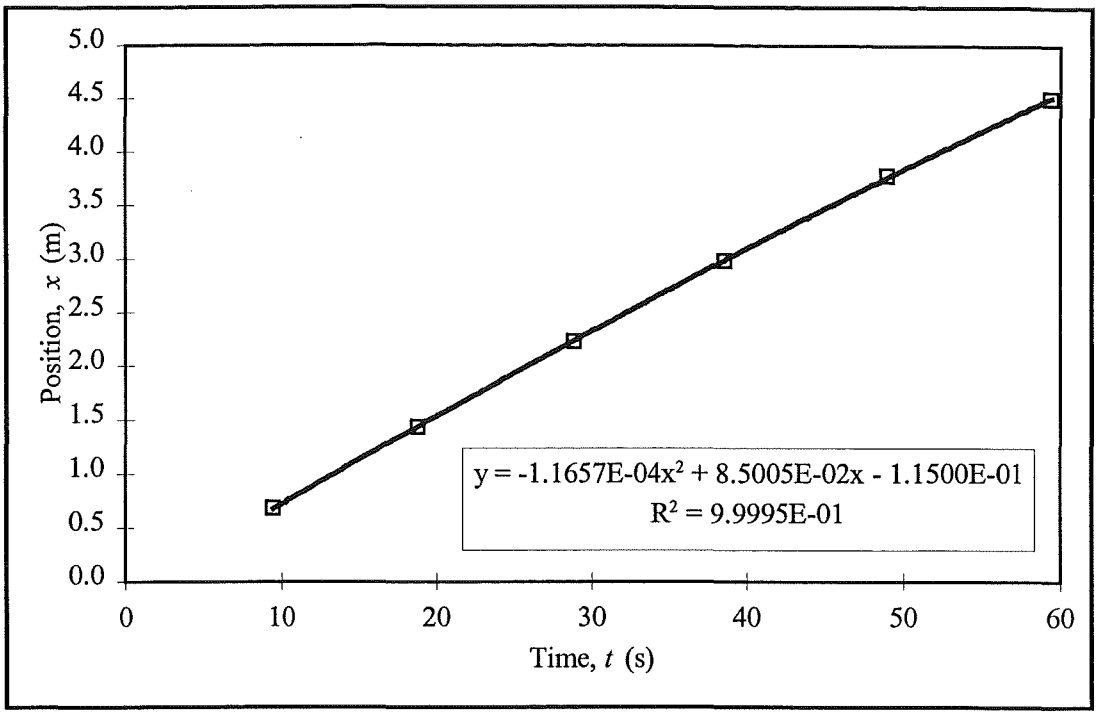

Figure A8.13a - Time-position data from run 61011DC050

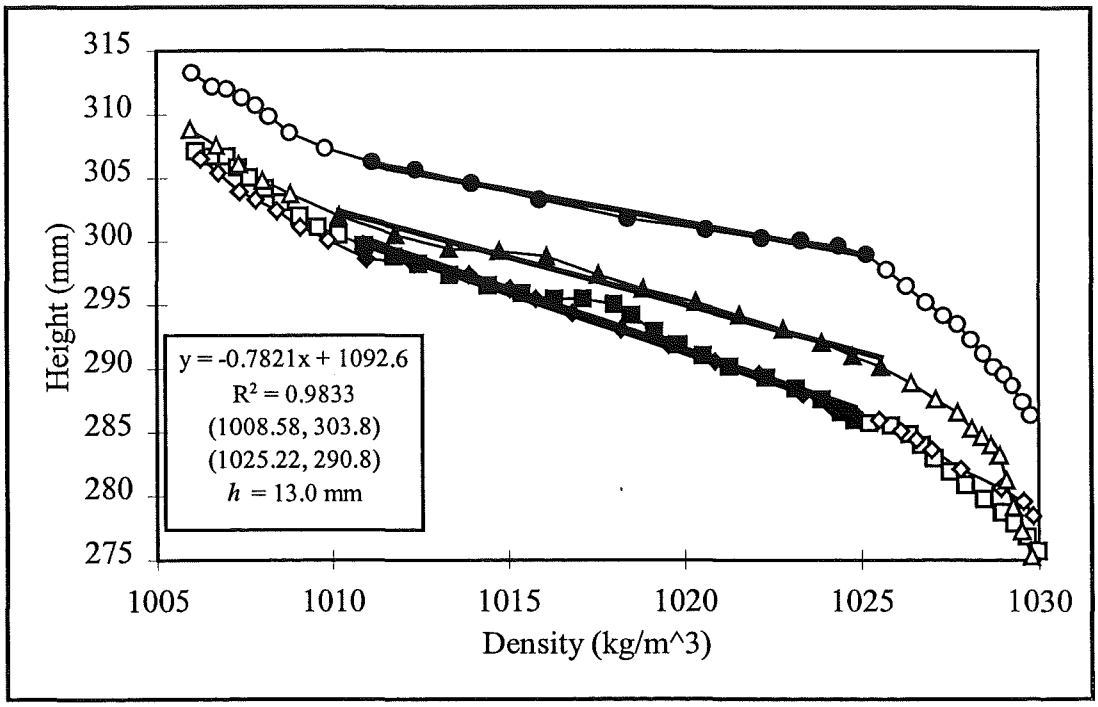

Figure A8.13b - Interfacial region density profiles from run 61011DC050

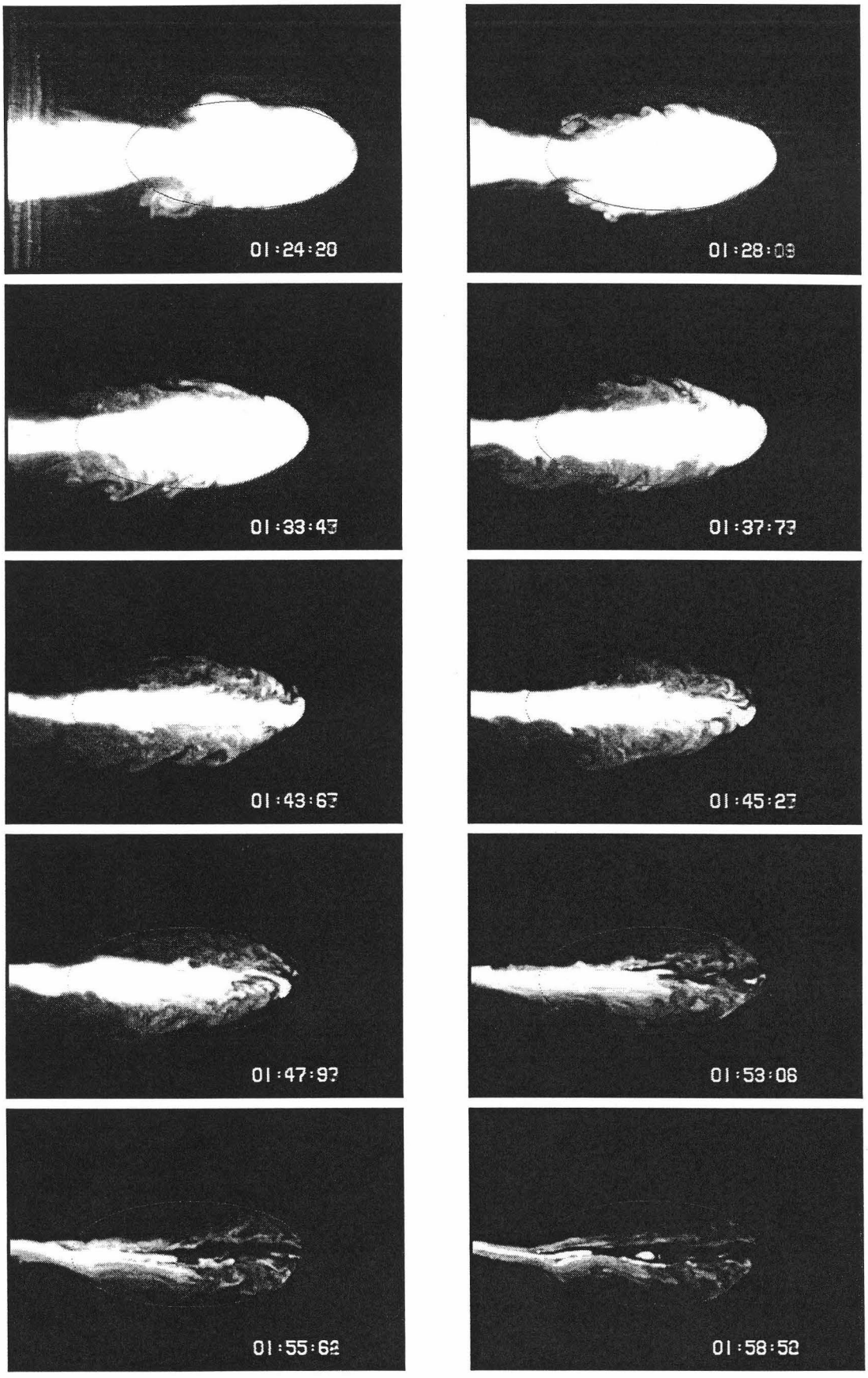
01:24:20
01:28:08
01:33:43
01:37:73
01:43:67
01:45:23
01:47:97
01:53:06
01:55:62
01:58:52

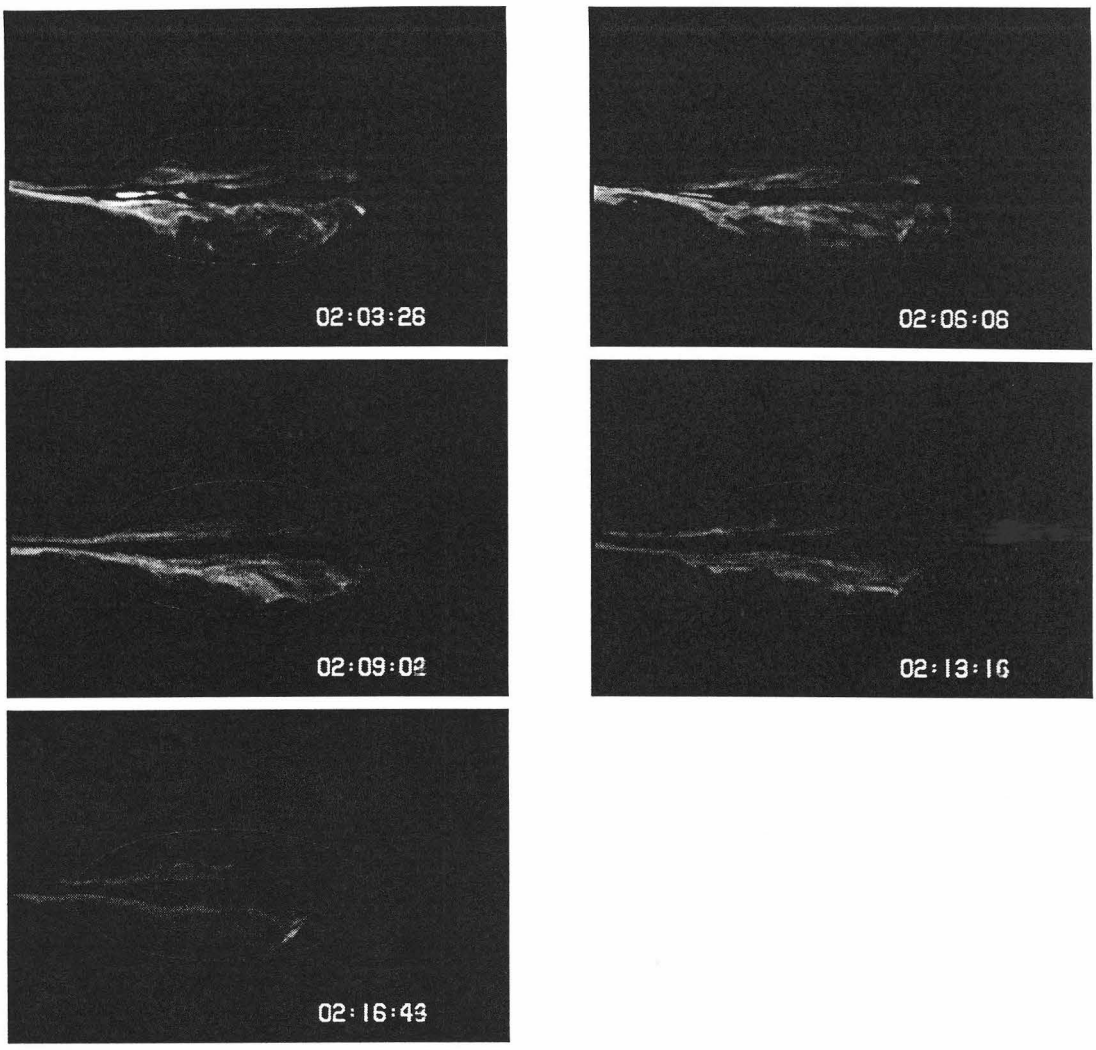

Figure A8.13c - Flow images from run 61011DC050

Table A8.10 - Experimental data from run 61018DC100

61018DC100		Infinitesimal Wave Speed Parameters					Distance Equation Coefficients		
		ω	h	H/h	δ	c_0	k_1	k_2	k_3
		0.0371	0.0074	41	0.025	0.0360	-3.50E-05	9.79E-02	-5.82E-04
(start)	time	position	celerity	celerity	position	adjusted	adjusted	(area)	dye
timeprint	t	x	c	c/c_0	x/h	x/h	$x/h*J$	count	concentration
(1:41.09)	(s)	(m)	(m/s)				(J = 0.288)	(34379)	(%)
1:43.95	2.86	0.28	0.098	2.711	38	32	9	8027774	91.6
2:03.79	22.70	2.20	0.096	2.673	298	292	84	1945280	22.2
2:16.00	34.91	3.37	0.095	2.649	456	450	129	415138	4.7
2:19.40	38.31	3.70	0.095	2.642	500	494	142	309292	3.5
2:22.96	41.87	4.04	0.095	2.636	545	539	155	220728	2.5
2:26.12	45.03	4.34	0.095	2.629	586	580	167	106767	1.2

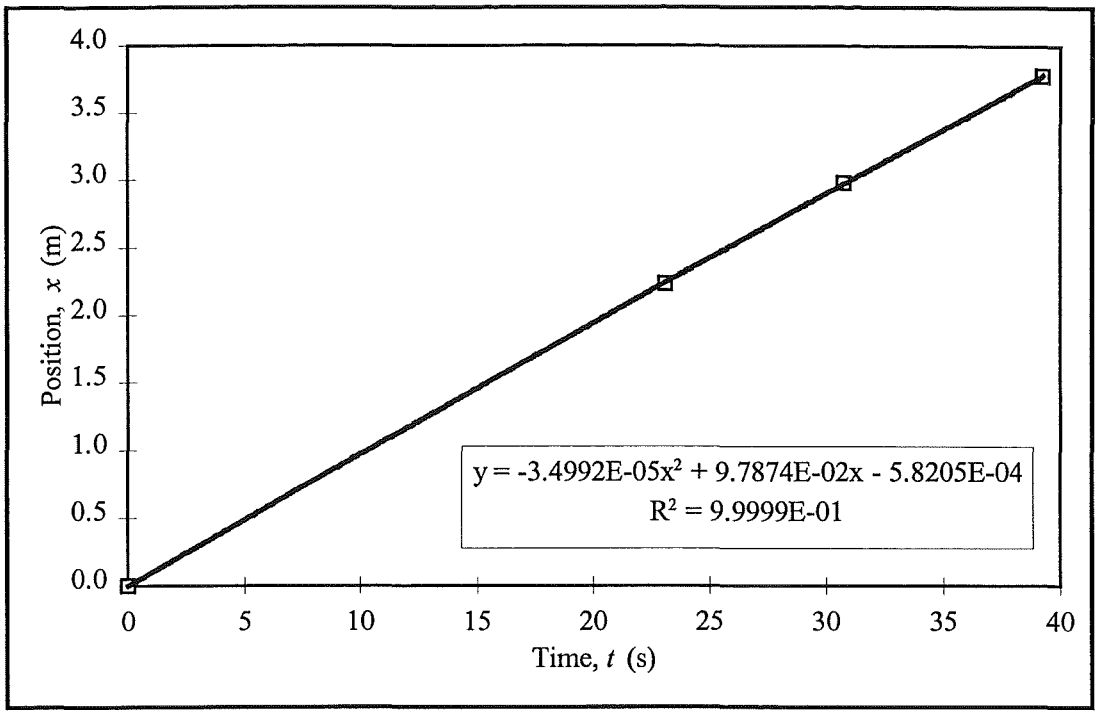

Figure A8.14a - Time-position data from run 61018DC100

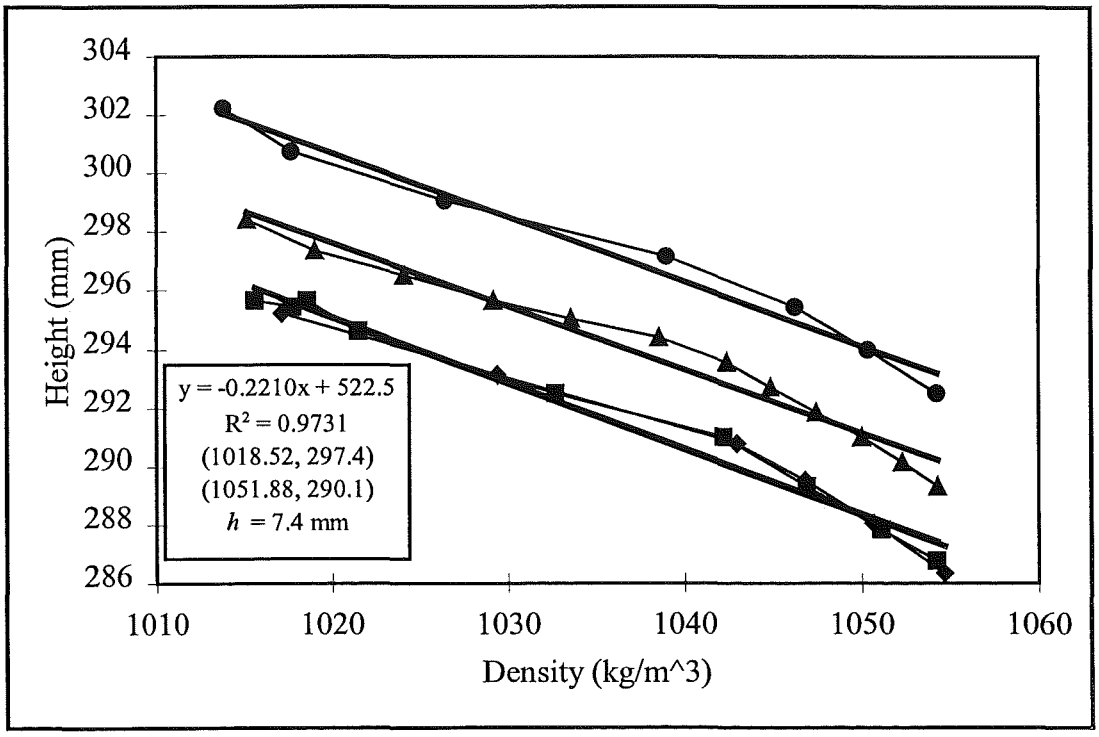

Figure A8.14b - Interfacial region density profiles from run 61018DC100

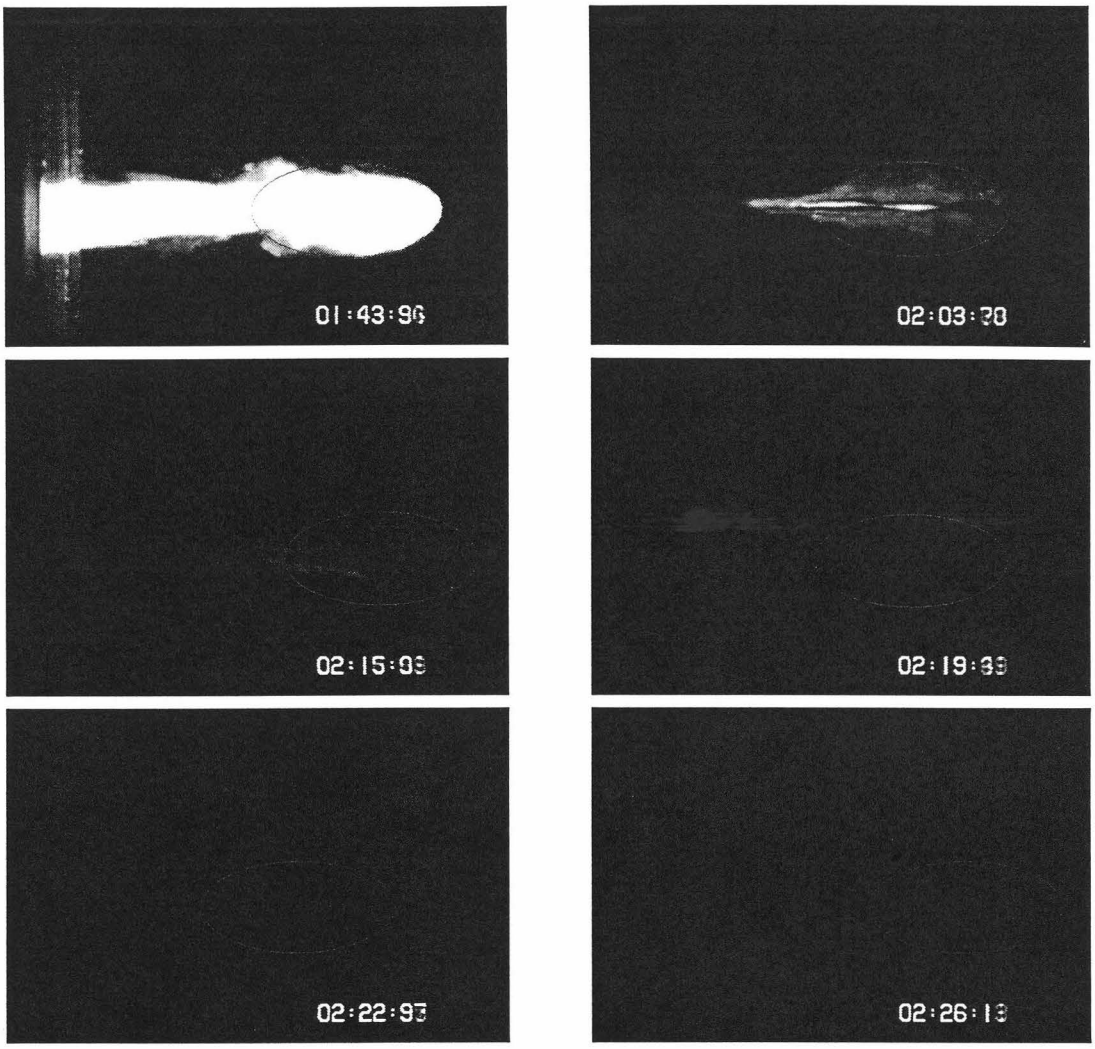

Figure A8.14c - Flow images from run 61018DC100

Table A8.11 - Experimental data from run 61019DC100

61019DC100		Infinitesimal Wave Speed Parameters					Distance Equation Coefficients		
		ω	h	H/h	δ	c_0	k_1	k_2	k_3
		0.0375	0.0066	45	0.022	0.0343	-4.05E-05	7.98E-02	-8.46E-02
(start)	time	position	celerity	celerity	position	adjusted	adjusted	(area)	dye
timeprint	t	x	c	c/c_0	x/h	x/h	$x/h*J$	count	concentration
(0:21.76)	(s)	(m)	(m/s)				(J = 0.393)	(12715)	(%)
0:25.41	3.65	0.21	0.079	2.319	31	26	10	2637313	81.3
0:30.33	8.57	0.60	0.079	2.308	90	85	34	2075612	64.0
0:34.90	13.14	0.96	0.079	2.297	145	140	55	1622418	50.0
0:38.82	17.06	1.26	0.078	2.288	192	187	73	1060580	32.7
0:41.02	19.26	1.44	0.078	2.282	218	213	84	782456	24.1
0:44.58	22.82	1.71	0.078	2.274	260	255	100	438460	13.5
0:48.14	26.38	1.99	0.078	2.266	302	297	117	306215	9.4
0:50.62	28.86	2.18	0.077	2.260	331	326	128	240478	7.4
0:53.98	32.22	2.44	0.077	2.252	370	365	144	227058	7.0
0:56.38	34.62	2.63	0.077	2.246	398	393	155	189877	5.9
1:00.35	38.59	2.93	0.077	2.237	445	440	173	175592	5.4
1:04.95	43.19	3.29	0.076	2.226	498	493	194	121239	3.7
1:09.27	47.51	3.61	0.076	2.216	548	543	213	101824	3.1
1:11.59	49.83	3.79	0.076	2.210	574	569	224	92887	2.9
1:14.63	52.87	4.02	0.076	2.203	609	604	238	75847	2.3

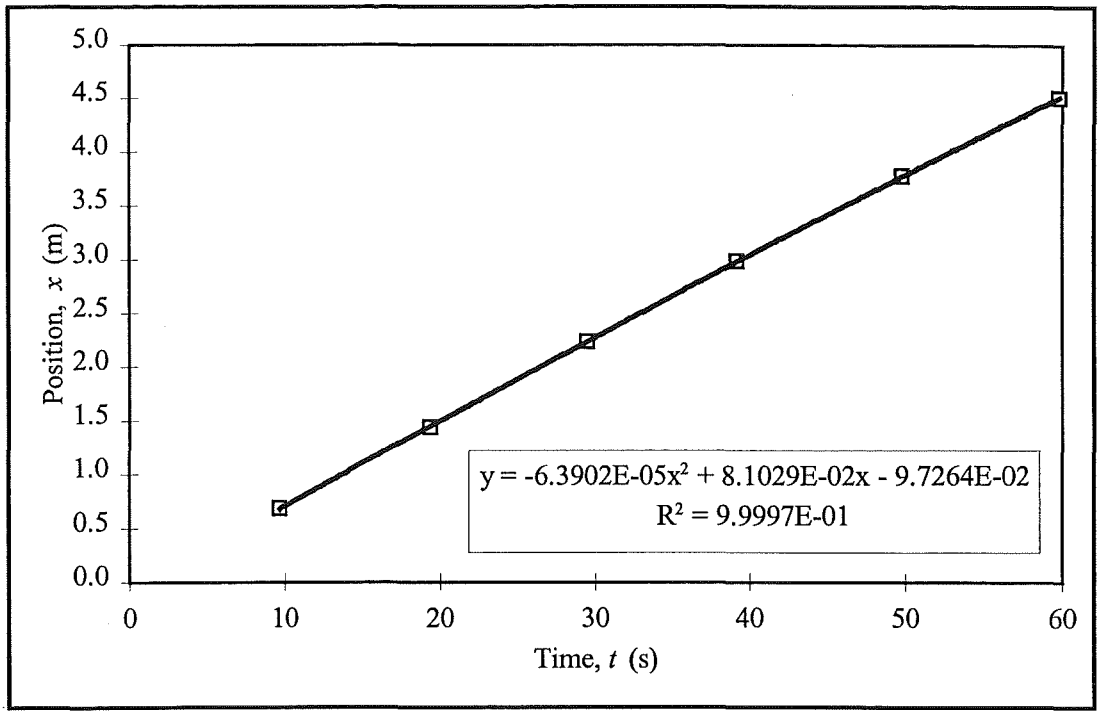

Figure A8.15a - Time-position data from run 61019DC100

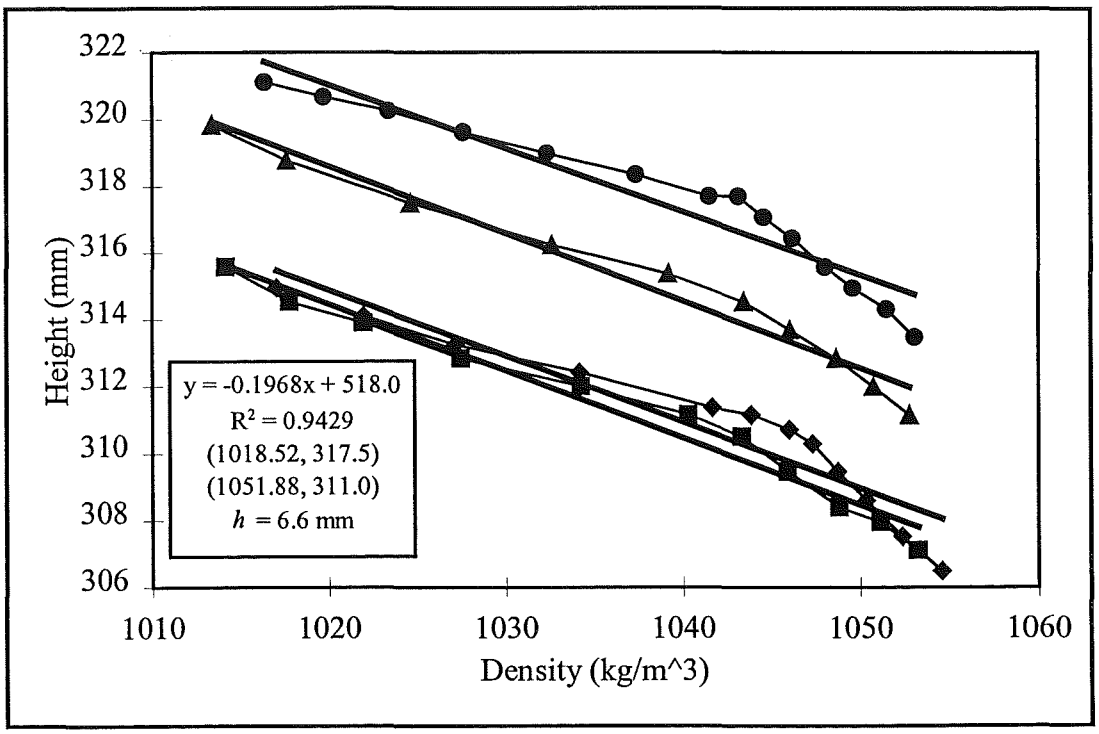

Figure A8.15b - Interfacial region density profiles from run 61019DC100

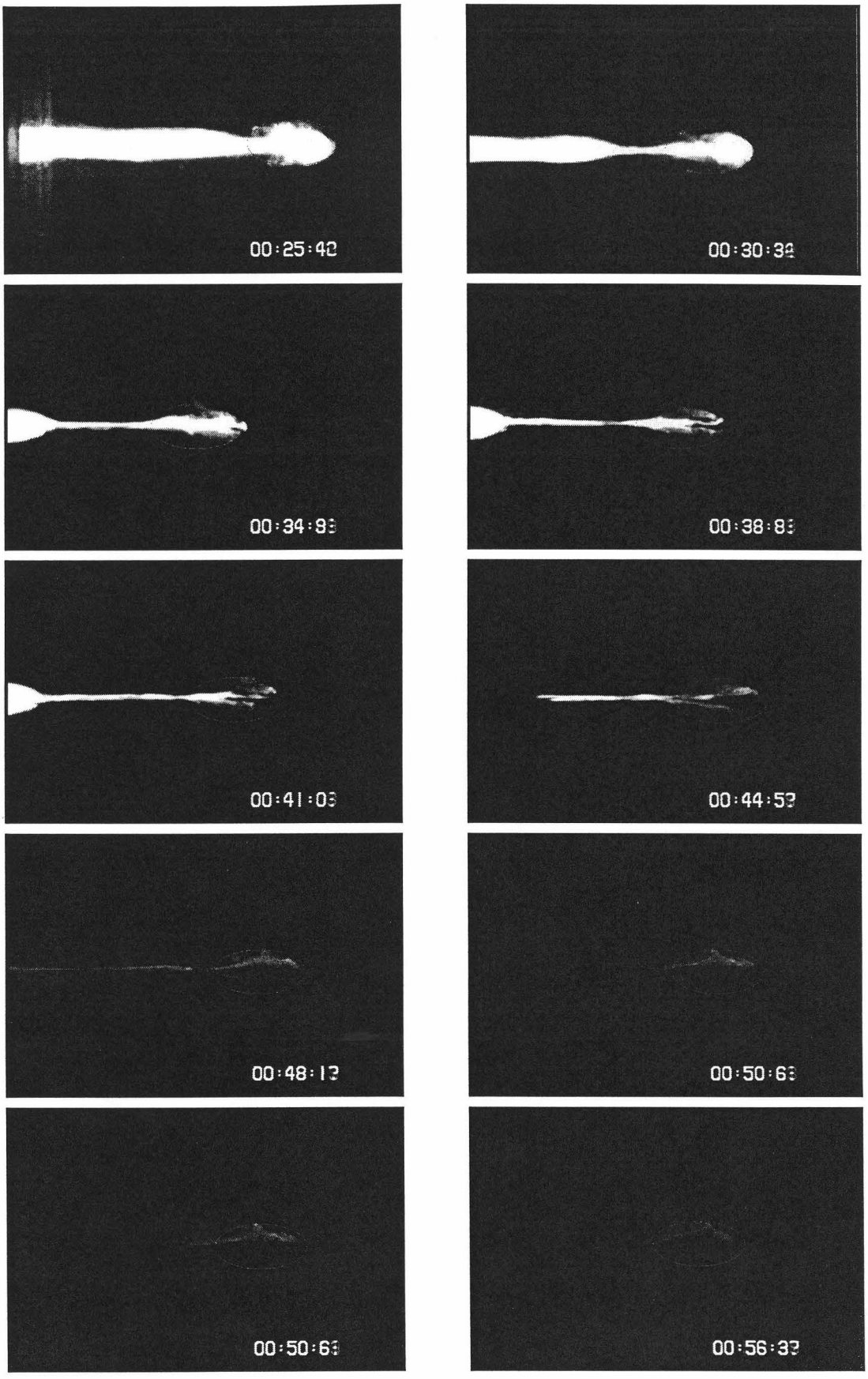
00:25:42
00:30:39
00:34:93
00:38:83
00:41:03
00:44:53
00:48:13
00:50:63
00:50:63
00:56:33

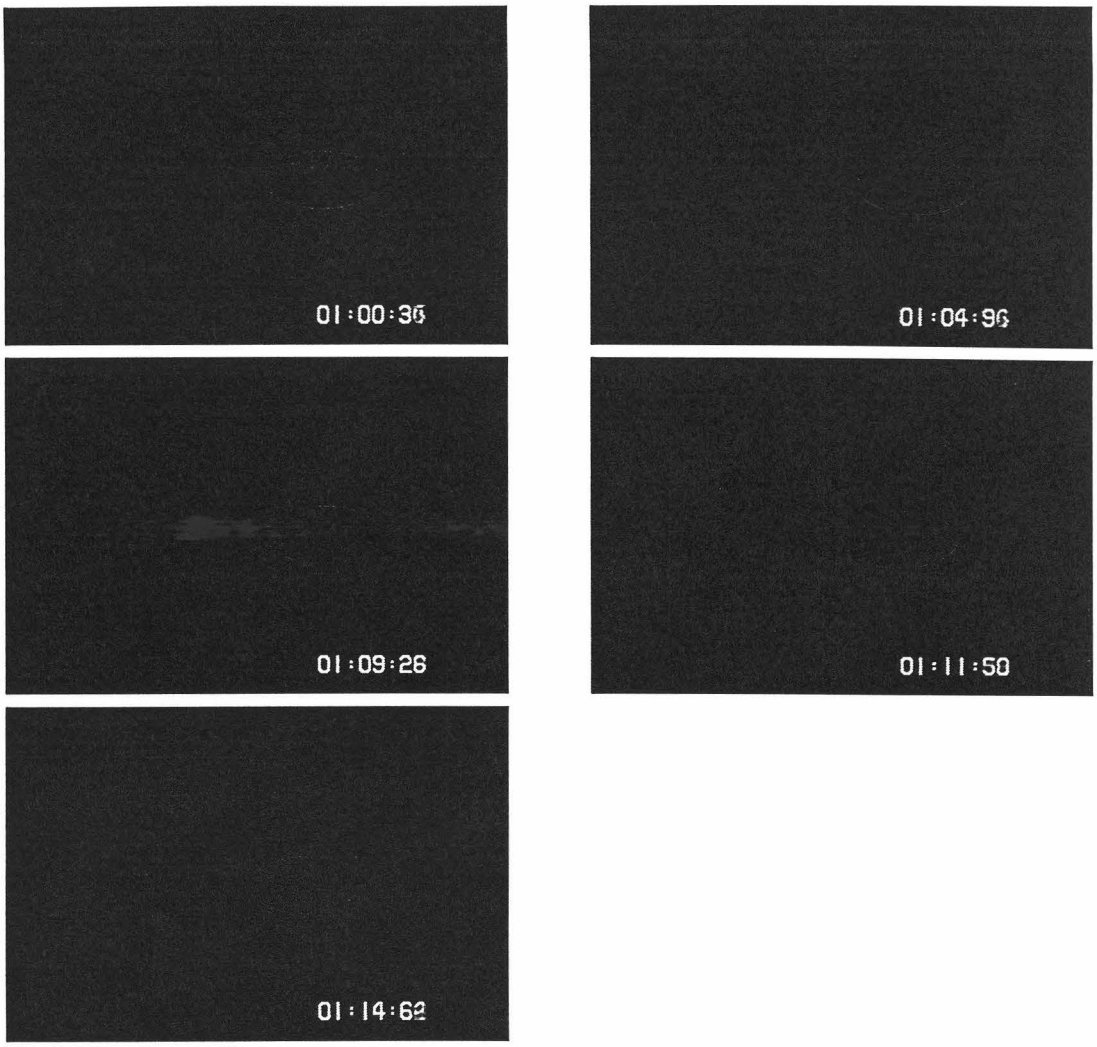

Figure A8.15c - Flow images from run 61019DC100

Table A8.12 - Experimental data from run 61025DC030

61025DC030	Infinitesimal Wave Speed Parameters					Distance Equation Coefficients		
	ω	h	H/h	δ	c_0	k_1	k_2	k_3
	0.0371	0.0074	41	0.025	0.0360	-3.50E-05	9.79E-02	-5.82E-04

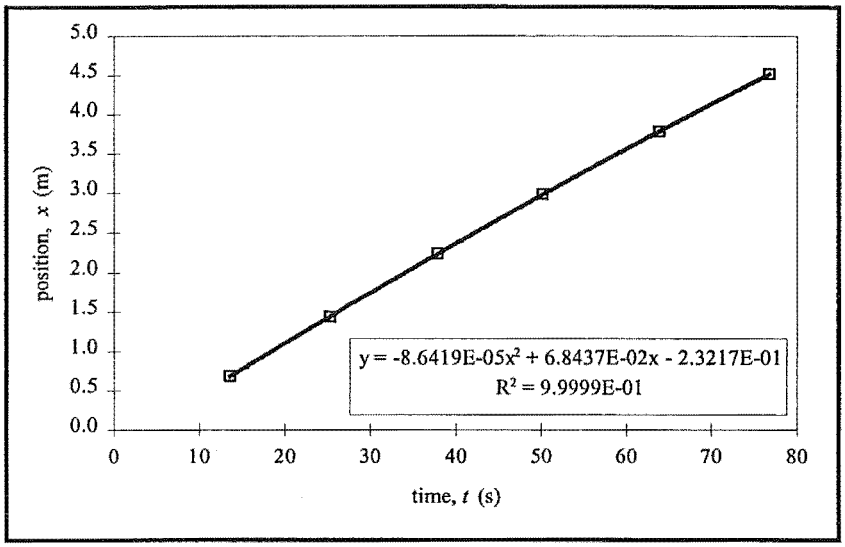

Figure A8.16a - Time-position data from run 61025DC030

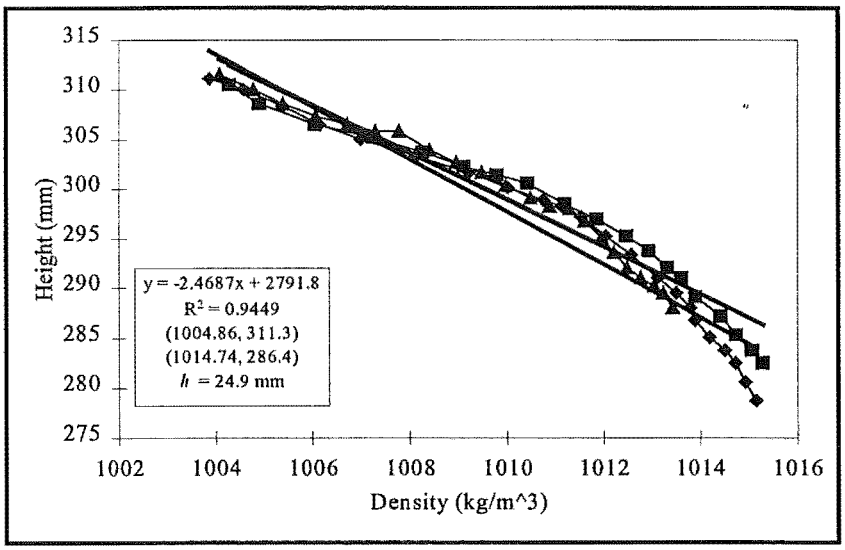

Figure A8.16b - Interfacial region density profiles from run 61025DC030

Table A8.13 - Experimental data from run 61028PC030

61028PC030		Infinitesimal Wave Speed Parameters					Distance Equation Coefficients		
		ω	h	H/h	δ	c_0	k_1	k_2	k_3
		0.0109	0.0406	7.4	0.135	0.047	-9.28E-05	6.98E-02	-1.08E-01
(start)	time	position	celerity	amplitude	celerity	position	amplitude		
timeprint	t	x	c	a	c/c_0	x/h	a/h		
(1:31.40)	(s)	(m)	(m/s)	(m)					
01:46.90	15.50	0.95	0.067	0.0550	1.435	23	1.354		
01:53.00	21.60	1.36	0.066	0.0535	1.411	33	1.317		
02:00.10	28.70	1.82	0.064	0.0520	1.383	45	1.280		
02:05.60	34.20	2.17	0.063	0.0570	1.361	53	1.403		
02:11.70	40.30	2.55	0.062	0.0525	1.337	63	1.293		
02:17.20	45.80	2.89	0.061	0.0545	1.301	71	1.342		
02:26.60	55.20	3.46	0.060	0.0520	1.277	85	1.280		
02:30.00	58.60	3.66	0.059	0.0495	1.264	90	1.219		
02:38.10	66.70	4.13	0.057	0.0490	1.231	102	1.206		
02:38.90	67.50	4.18	0.057	0.0480	1.228	103	1.182		

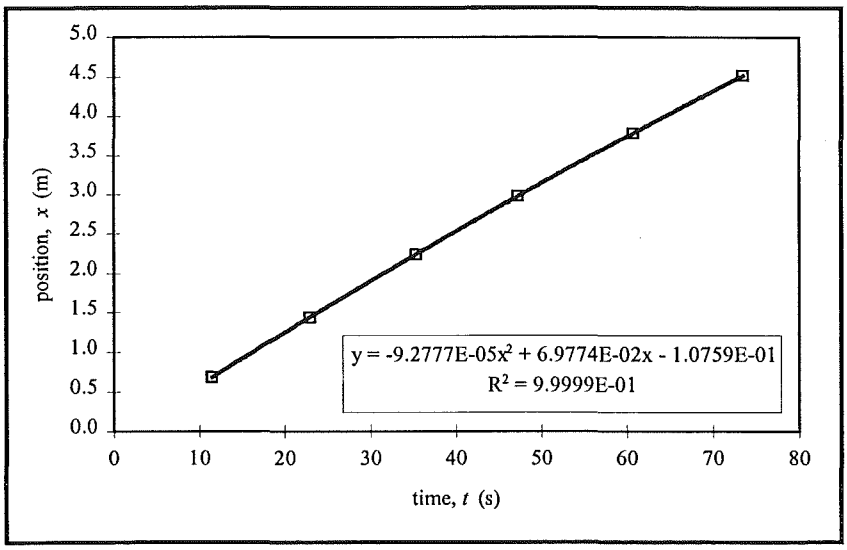

Figure A8.17a - Time-position data from run 61028PC030

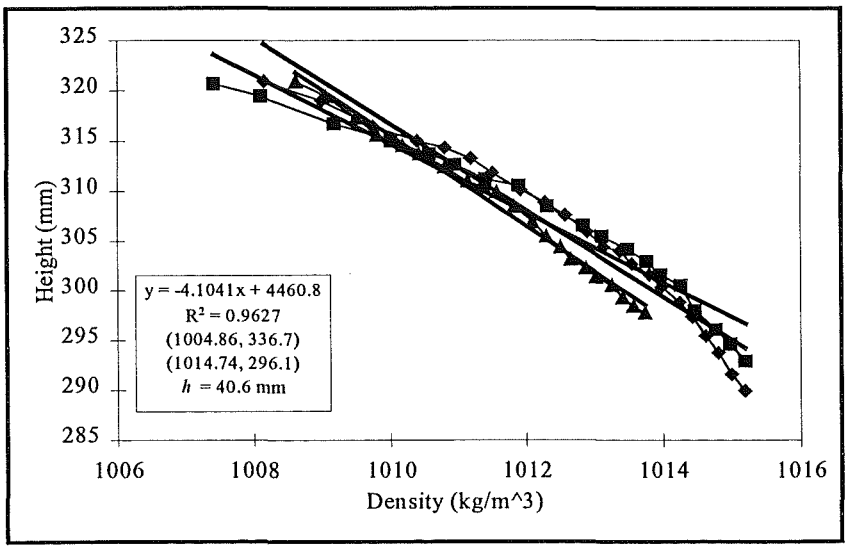

Figure A8.17b - Interfacial region density profiles from run 61028PC030

Table A8.14 - Experimental data from run 61030PC030

61030PC030		Infinitesimal Wave Speed Parameters					Distance Equation Coefficients		
		ω	h	H/h	δ	c_0	k_1	k_2	k_3
		0.0106	0.0289	10.4	0.096	0.0390	-4.16E-05	5.90E-02	-1.14E-01
(start)	time	position	celerity	amplitude	celerity	position	amplitude		
timeprint	t	x	c	a	c/c_0	x/h	a/h		
(0:48.30)	(s)	(m)	(m/s)	(m)					
01:06.20	17.90	0.93	0.058	0.0415	1.48	32	1.44		
01:13.40	25.10	1.34	0.057	0.0425	1.47	46	1.47		
01:21.10	32.80	1.78	0.056	0.0410	1.45	61	1.42		
01:28.70	40.40	2.20	0.056	0.0380	1.44	76	1.31		
01:34.70	46.40	2.53	0.055	0.0375	1.42	88	1.30		
01:41.30	53.00	2.90	0.055	0.0370	1.41	100	1.28		
01:49.30	61.00	3.33	0.054	0.0360	1.39	115	1.25		
01:54.90	66.60	3.63	0.053	0.0360	1.38	126	1.25		
02:03.80	75.50	4.10	0.053	0.0360	1.36	142	1.25		
02:09.90	81.60	4.42	0.052	0.0345	1.35	153	1.19		

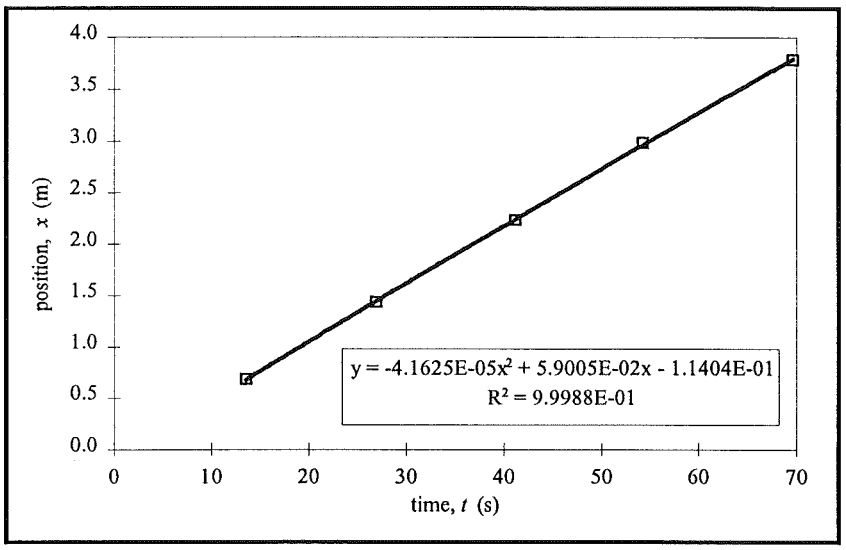

Figure A8.18a - Time-position data from run 61030PC030

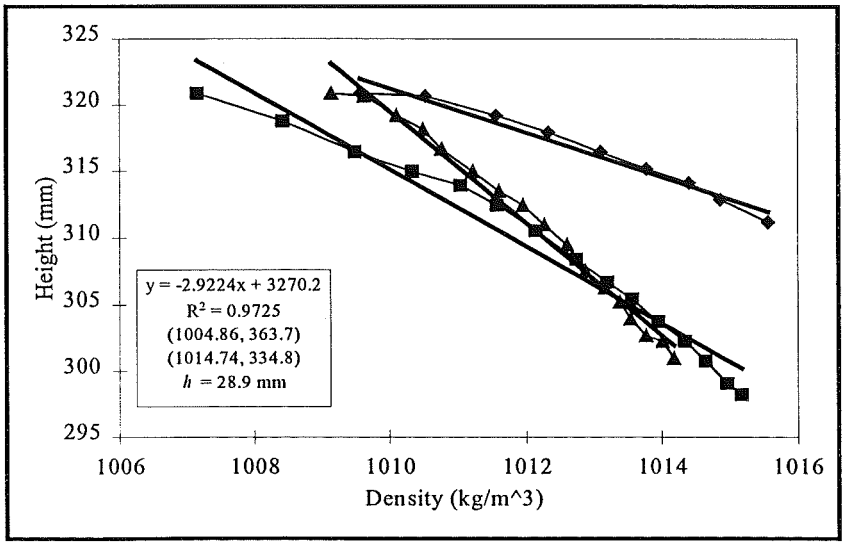

Figure A8.18b - Interfacial region density profiles from run 61030PC030

Table A8.15 - Experimental data from run 61031PC050

61031PC050		Infinitesimal Wave Speed Parameters					Distance Equation Coefficients		
		ω	h	H/h	δ	c_0	k_1	k_2	k_3
		0.0176	0.0200	15	0.066	0.0420	-9.59E-05	7.73E-02	-1.11E-01
(start)	time	position	celerity	amplitude	celerity	position	amplitude		
timeprint	t	x	c	a	c/c_0	x/h	a/h		
(0:45.97)	(s)	(m)	(m/s)	(m)					
01:10.10	24.13	1.70	0.073	0.0405	1.750	85	2.03		
01:05.90	19.93	1.39	0.074	0.0415	1.769	70	2.08		
01:11.00	25.03	1.76	0.073	0.0415	1.745	88	2.08		
01:17.60	31.63	2.24	0.071	0.0410	1.715	112	2.05		
01:21.80	35.83	2.54	0.070	0.0425	1.696	127	2.13		
01:27.40	41.43	2.93	0.069	0.0385	1.670	146	1.93		
01:34.00	48.03	3.38	0.068	0.0365	1.639	169	1.83		
01:37.90	51.93	3.65	0.067	0.0360	1.621	182	1.80		
01:43.80	57.83	4.04	0.066	0.0340	1.594	202	1.70		
01:50.50	64.53	4.48	0.065	0.0345	1.563	224	1.73		

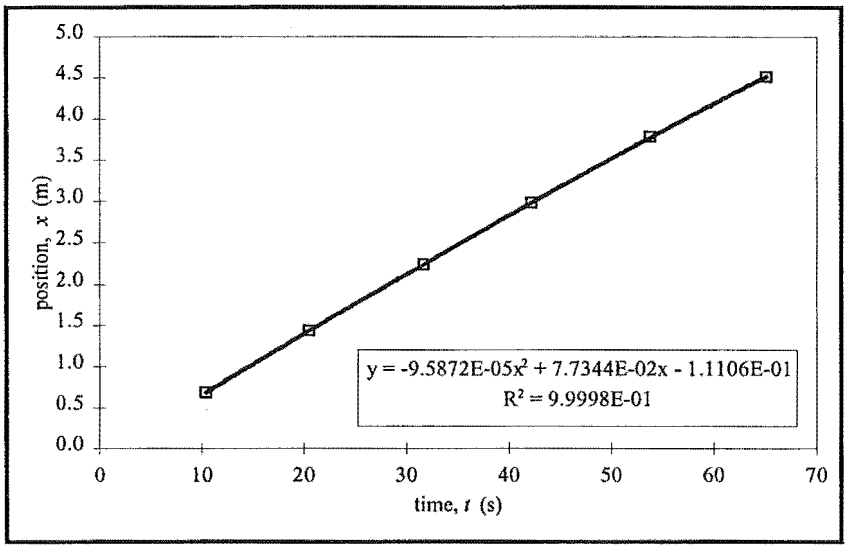

Figure A8.19a - Time-position data from run 61031PC050

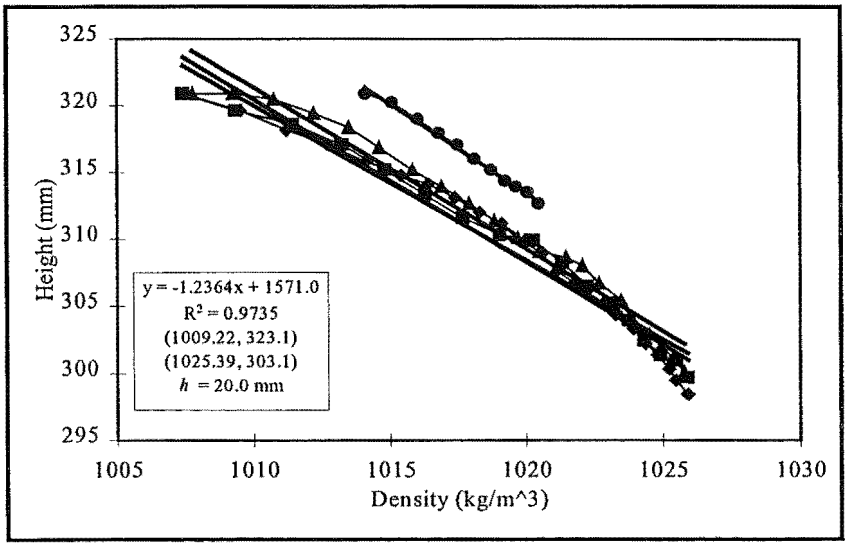

Figure A8.19b - Interfacial region density profiles from run 61031PC050

Appendix 9 - Rankine Oval Exterior Kinetic Energy Calculation

The kinetic energy of a second mode wave may be divided into two components, one internal to the wave and one external. The internal kinetic energy is easily approximated by assuming the entire volume within the "zero streamline" moves at the wave celerity, c, while an estimate of the external kinetic energy first requires that the external velocity field be known. In the present study this was done by approximating the wave with a Rankine oval, the theory of which is discussed in Section A9.1. A computer program was written to calculate the external velocity field based on the streamfunction computed using Rankine oval theory. This program provided a value for the ratio of external to internal kinetic energy associated with the wave. This value was found to be constant over a range of wave parameters. Graphical output describing the streamline configuration and velocity field were also provided. A description of the computer program is found in Section A9.2. Results from computational runs are provided in Section A9.3, while a printout of the program's Fortran code is found in Section A9.4.

A9.1 - Rankine Oval Theory

A Rankine oval (White, 1986) consists of a source and sink of equal strength, m, separated by a distance, $2a$, in a uniform velocity field, U_∞ (the notation in this appendix is that of White, 1986). The alignment of the source, sink and velcity field is shown in Figure A9.1. The shape of the oval depends on the values of m, U_∞ and a. For a 2:1 aspect ratio ($L/h = 2.000$) which approximates a second mode wave, $m/U_\infty a = 0.3200$, $h/a = 0.6408$ and $L/a = 1.2806$. This produces a maximum velocity at the shoulder of the wave of $u/U_\infty = 1.4537$. Given the values of the aforementioned parameters, the streamfunction around the wave may be calculated with the following equation:

$$\psi = U_\infty y - m\tan^{-1}\frac{2ay}{x^2 + y^2 - a^2} = U_\infty r\sin\theta + m\left(\theta_1 - \theta_2\right) \quad \text{(A9.1)}$$

Equation A9.1 was used in the computer program discussed here to compute the stream function in the vicinity of the oval.

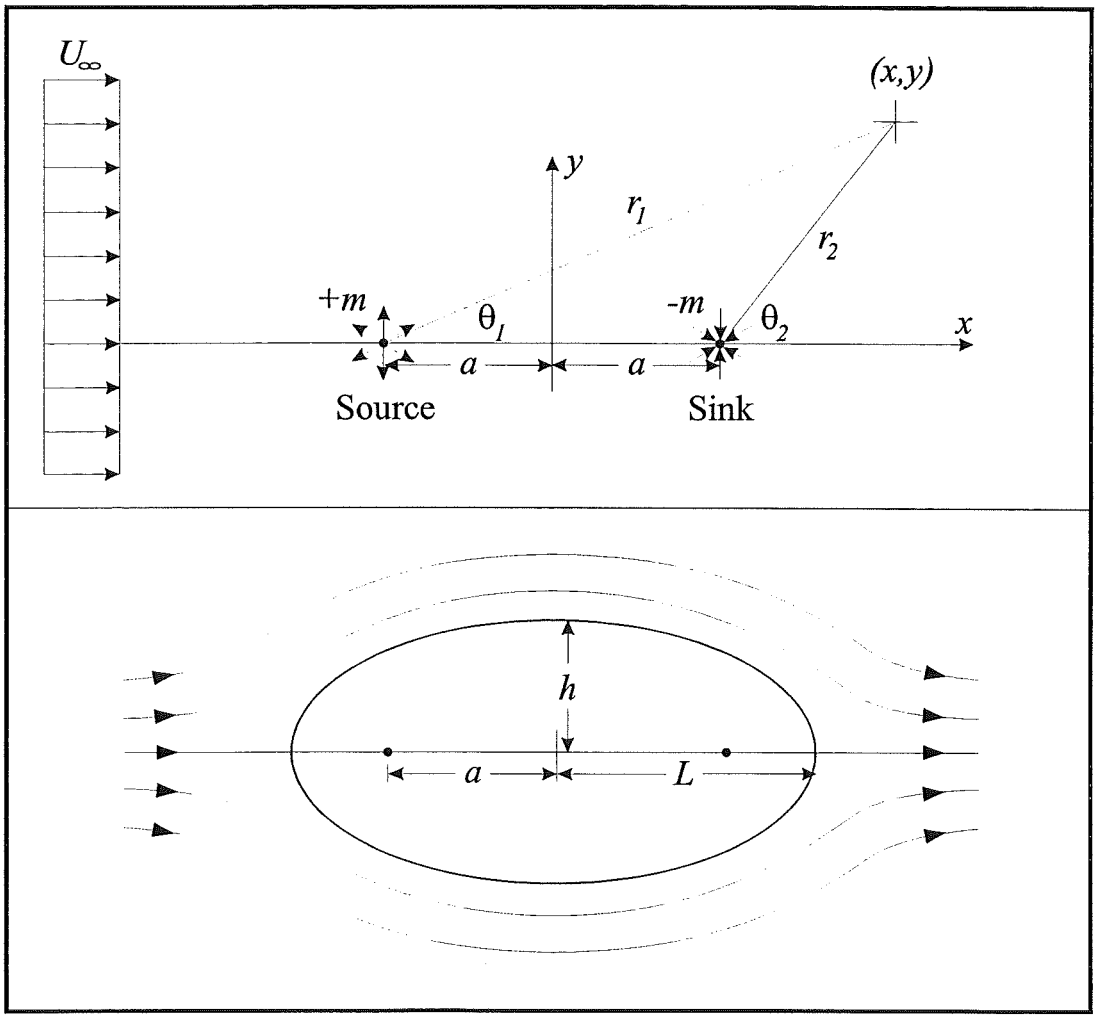

Figure A9.1 - Flow past a Rankine oval (based on White, 1986)

A9.2 - Description of Computer Program

The computer program, EXTVEL, is written in Fortran 77. The program first calls the subroutine setup, in which domain, discretisation and Rankine oval parameters are read. After returning to the main program, the subroutine stream is called. This part of the program computes the value of the stream function at every point in the domain, using a variation of Equation A9.1. The specific form of the equation depends on the position of the point relative to source, sink and centreline, as problems with the sign of the various streamfunction components arise if the position is not taken into account. The next subroutine to be called is velocity, in which the *u*- and *v*-components of fluid velocity are computed for each point based on the gradients of the streamfunction in the *x*- and *y*-directions. The subroutine intext then identifies which points in the domain are inside the oval. On returning

to the main program, the total interior and exterior kinetic energies are computed and printed on screen. The output subroutine is then entered to produce a TIFF (tagged interchange file format) graphics file which describes the streamline configuration (upper and lower sections are divided into ten streamtubes) and velocity field (background shading black = stagnation; white = highest velocity). The body of the oval is been masked in black.

A9.3 - Results

The EXTVEL program was run for a variety of wave parameters and discretisations to examine the ratio of internal to external kinetic energies. The results from the computational runs are shown in Figure A9.1.

Table A9.1 - Wave energies computed with EXTVEL program

amplitude a (mm)	celerities c (mm/s)	discretisation dx, dy (mm)	domain l x d (mm)	ratio int:ext
5	10 - 50	0.5, 0.5	450 x 250	1.904
5	50	1.0, 1.0	450 x 250	1.844
10	10 - 50	0.5, 0.5	450 x 250	1.940
10	50	1.0, 1.0	450 x 250	1.906
15	10 - 50	0.5, 0.5	450 x 250	1.946
15	50	1.0, 1.0	450 x 250	1.932

The results shown in Table A9.1 show a reasonably consistent ratio of internal to external kinetic energy of approximately 1.9, the inverse of which provides the 53% estimate used in Chapter 8. Waves of larger amplitude were not tested as they would not accurately represent deep water waves. Differences in ratio between identical runs at different discretisations are likely due to differences in the assignment of what constitutes an "internal" and "external" point. An example of the graphical output from the program is shown in Figure A9.2.

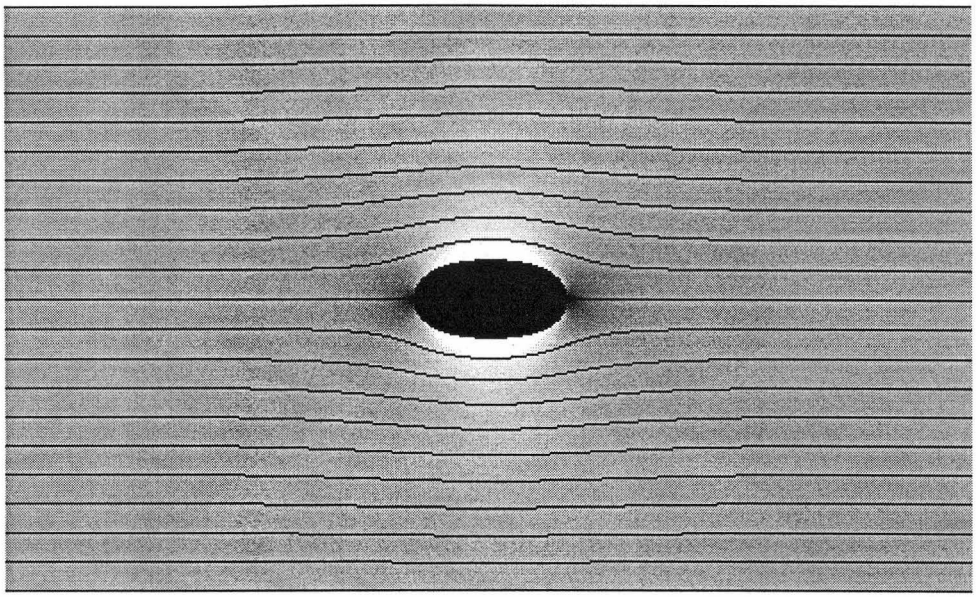

Figure A9.2 - Graphical output from external velocity field program

A9.4 - Computer Program Code

The Fortran 77 code for the EXTRAN computer program is as follows:

```
program extvel

C  This program examines the kinetic energy in the
C  flow about an oval cylinder.  Streamlines representing the potential
C  flow about the cylinder are determined based on a Rankine oval, and
C  these are used to determine the two-dimensional velocity field about
C  the cylinder.  The velocity field is then used to calculate the sum of
C  the external kinetic energy in the vicinity of the oval.  More info on the
C  Rankine oval may be seen in Frank White's text "Fluid Mechanics, 2nd ed."
C  on page 459.

C  Written by Nathan Schmidt - University of Canterbury - July 1997

      implicit none
      integer*2 m,n,i,j,mask(2001,1201)
      real*4 depth,length,dx,dy,h,l,uinf,mua,a,mm
      real*4 version,sigmaphi,t,dens,rho1,rho2
      parameter (version=1.0)
      character*24 date_string
      character*1 ans
      integer*2 outf,msize,interior(2001,1201)
      real*4 psi(2001,1201),u(2001,1201),v(2001,1201),phi(2001,1201)
      real*4 inter,exter,de,ratio

      common psi,u,v,phi,mask,interior,mu1,mu2
C
C  Output program version and date
C
      write(*,'(/," ### PROGRAM EXTVEL version ",
     +                          f5.2," ### ")') version
      call fdate (date_string)
      write(*,'(//,1x,a,/)') date_string
C
C  Check to see if old output files exist
C
      call checkfile()
C
C  Set up domain after acquiring input parameters
C
      call setup(m,n,depth,length,dx,dy,h,l,uinf,mua,a,mm)
C
C  Calculate stream function for domain
C
      call stream(m,n,depth,length,dx,dy,h,l,uinf,mua,a,mm)
C
C  Calculate velocity vectors for domain
C
      call velocity(m,n,depth,length,dx,dy,h,l,uinf,mua,a,mm)
C
C  Calculate interior and exterior grid points
C
      call intext(m,n,depth,length,dx,dy,h,l,uinf,mua,a,mm)
C
C  Calculate internal and external kinetic energies
C
      rho1 = 1000
      rho2 = 1020
      inter = 0.0
      exter = 0.0
      do i = 1,m+1
        do j = 1,n+1
          if (interior(i,j).eq.0) then     ! exterior point
            de = 0.5*(rho1+rho2)/2*dx*dy*((u(i,j)-uinf)**2+v(i,j)**2)
            exter = exter + de
          else                             ! interior point
            de = 0.5*(rho1+rho2)/2*dx*dy*uinf**2
            inter = inter + de
          end if
        end do
      end do
      ratio = inter/exter
      write(*,'(" Internal energy is ",f8.6," J/m width.")') inter
      write(*,'(" External energy is ",f8.6," J/m width.")') exter
      write(*,'(" Ratio Internal:External is ",f6.4)') ratio
C
C  Produce graphical output file
C
      call output(m,n,depth,length,dx,dy,h,l,uinf,mua,a,mm)
C
      end
C
C-----------------------------------------------------------------
C
      subroutine checkfile()

C     This subroutine checks to see if any  output
C     files exist from previous runs, and allows their removal or
C     quitting of the program (note: program will crash if they are
C     left alone).

      character*1  ans
      logical      fexist

      inquire(file='output.tif',exist=fexist)
      if (fexist) then
        write(*,'(/,"Output tiffs from previous runs still exist")')
        ans = 'y'
 10     call help_read_c(ans,ans,'Hit (y) to delete or (n) to leave',
```

```
     +    2,1,0,7,15)
          if (ans.eq.'y' .or. ans.eq.'Y') then
            status = system('rm output.tif')
          else if (ans.eq.'n' .or. ans.eq.'N') then
            stop
          else
            go to 10
          end if
        end if

        return
        end
C
C-----------------------------------------------------------------------
C
        subroutine stream(m,n,depth,length,dx,dy,h,l,uinf,mua,a,mm)

C   This subroutine calculates the stream function at every point
C   in the domain.  Modifications to original streamfunction
C   equation required due to sign problems in interpreting atan
C   function.  Works now.

        integer*2 m,n,i,j,mask(2001,1201)
        real*4 depth,length,dx,dy,h,l,uinf,mua,a,mm,x,y
        real*4 psi(2001,1201),u(2001,1201),v(2001,1201),phi(2001,1201)
        integer*2 interior(2001,1201)

        common psi,u,v,phi,mask,interior,mu1,mu2

        write(*,'(/," Beginning stream function calculation")')

        do i = 1,m+1
          x = (i-1)*dx - length/2.
          do j = 1,n+1
            y = depth/2-(j-1)*dy

            psi(i,j) = uinf*y     ! UNIFORM FLOW
                                  ! ABOVE CENTRELINE
            if (y.gt.0) then          ! SOURCE
              if ((x+a).gt.0) then      ! RIGHT OF SOURCE
                psi(i,j) = psi(i,j) + mm*atan(y/(x+a))
              else if ((x+a).lt.0) then  ! LEFT OF SOURCE
                psi(i,j) = psi(i,j) + mm*(3.1415927 - atan(y/(-(x+a))))
              else   ! x+a = 0          ! ABOVE SOURCE
                psi(i,j) = psi(i,j) + mm*(3.1415927/2)
              end if                    ! SINK
              if ((x-a).gt.0) then      ! RIGHT OF SINK
                psi(i,j) = psi(i,j) - mm*atan(y/(x-a))
              else if ((x-a).lt.0) then  ! LEFT OF SINK
                psi(i,j) = psi(i,j) - mm*(3.1415927 - atan(y/(-(x-a))))
              else   ! x-a = 0          ! ABOVE SOURCE
                psi(i,j) = psi(i,j) - mm*(3.1415927/2)
              end if                 ! BELOW CENTRELINE
            else if (y.le.0) then     ! SOURCE
              if ((x+a).lt.0) then      ! RIGHT OF SOURCE
                psi(i,j) = psi(i,j) + mm*(3.1415927+atan(-y/-((x+a))))
              else if ((x+a).gt.0) then  ! LEFT OF SOURCE
                psi(i,j) = psi(i,j) + mm*(2*3.1415927-atan(-y/(x+a)))
              else   ! x+a = 0          ! BELOW SOURCE
                psi(i,j) = psi(i,j) + mm*(1.5*3.1415927)
              end if                    ! SINK
              if ((x-a).lt.0) then      ! RIGHT OF SINK
                psi(i,j) = psi(i,j) - mm*(3.1415927+atan(-y/(-(x-a))))
              else if ((x-a).gt.0) then  ! LEFT OF SINK
                psi(i,j) = psi(i,j) - mm*(2*3.1415927-atan(-y/(x-a)))
              else   ! x-a = 0          ! BELOW SINK
                psi(i,j) = psi(i,j) - mm*(1.5*3.1415927)
              end if
            end if
C
C  Image sources and sinks for upper & lower boundary conditions
C
            ! LOWER IMAGES
              if ((x+a).gt.0) then      ! RIGHT OF SOURCE
                psi(i,j) = psi(i,j) + mm*atan((depth+y)/(x+a))
              else if ((x+a).lt.0) then  ! LEFT OF SOURCE
                psi(i,j) = psi(i,j) + mm*(3.1415927 -
     +                   atan((depth+y)/(-(x+a))))
              else   ! x+a = 0          ! ABOVE SOURCE
                psi(i,j) = psi(i,j) + mm*(3.1415927/2)
              end if
              if ((x-a).gt.0) then      ! RIGHT OF SINK
                psi(i,j) = psi(i,j) - mm*atan((depth+y)/(x-a))
              else if ((x-a).lt.0) then  ! LEFT OF SINK
                psi(i,j) = psi(i,j) - mm*(3.1415927 -
     +                   atan((depth+y)/(-(x-a))))
              else   ! x-a = 0          ! ABOVE SOURCE
                psi(i,j) = psi(i,j) - mm*(3.1415927/2)
              end if
              ! UPPER IMAGES
              if ((x+a).lt.0) then      ! LEFT OF SOURCE
                psi(i,j) = psi(i,j) + mm*(3.1415927 +
     +                   atan((depth-y)/-((x+a))))
              else if ((x+a).gt.0) then  ! RIGHT OF SOURCE
                psi(i,j) = psi(i,j) + mm*(2*3.1415927 -
     +                   atan((depth-y)/(x+a)))
              else   ! x+a = 0          ! BELOW SOURCE
                psi(i,j) = psi(i,j) + mm*(1.5*3.1415927)
              end if
              if ((x-a).lt.0) then      ! LEFT OF SINK
                psi(i,j) = psi(i,j) - mm*(3.1415927 +
     +                   atan((depth-y)/(-(x-a))))
              else if ((x-a).gt.0) then  ! RIGHT OF SINK
                psi(i,j) = psi(i,j) - mm*(2*3.1415927 -
     +                   atan((depth-y)/(x-a)))
              else   ! x-a = 0          ! BELOW SINK
                psi(i,j) = psi(i,j) - mm*(1.5*3.1415927)
              end if
            end do
          end do

          write(*,'(" Finished stream function calculation")')

          return
          end
C
C-----------------------------------------------------------------------
C
          subroutine velocity(m,n,depth,length,dx,dy,h,l,uinf,mua,a,mm)
C
C   This subroutine calculates the velocities in the x and y
C   directions at every point in the domain
C
          integer*2 m,n,i,j,mask(2001,1201)
          real*4 depth,length,dx,dy,h,l,uinf,mua,a,mm
          real*4 psi(2001,1201),u(2001,1201),v(2001,1201),phi(2001,1201)
          integer*2 interior(2001,1201)

          common psi,u,v,phi,mask,interior,mu1,mu2

          write(*,'(/," Beginning velocity calculation")')
C
C  Compute velocities from stream function derivatives
C
          do i = 2,m
            do j = 2,n
              u(i,j) = (psi(i,j-1)-psi(i,j+1))/(2*dy)
              v(i,j) = (psi(i+1,j)-psi(i-1,j))/(2*dx)
            end do
          end do

          do i = 1,m+1
            u(i,1) = u(i,2)
            u(i,n+1) = u(i,n)
            v(i,1) = v(i,2)
            v(i,n+1) = v(i,n)
          end do

          do j = 1,n+1
            u(1,j) = u(2,j)
            u(m+1,j) = u(m,j)
            v(1,j) = v(2,j)
            v(m+1,j) = v(m,j)
          end do

          write(*,'(" Finished velocity calculation")')

          return
          end
C
C-----------------------------------------------------------------------
C
          subroutine intext(m,n,depth,length,dx,dy,h,l,uinf,mua,a,mm,
     +                rho1,rho2)
C
C   This subroutine identifies which points are inside the oval and
C   flags the corresponding parameter "interior"
C
          integer*2 m,n,i,j,mask(2001,1201)
          real*4 depth,length,dx,dy,h,l,uinf,mua,a,mm
          real*4 psi(2001,1201),u(2001,1201),v(2001,1201),phi(2001,1201)
          integer*2 interior(2001,1201)

          common psi,u,v,phi,mask,interior

          write(*,'(/," Identifying interior region")')
C
C  Identify upper and lower boundaries of the Rankine oval
C
          do i = 1,m+1
            x = -length/2. + dx*(i-1)
            do j = 1,n+1
              y = depth/2. - dy*(j-1)
              interior(i,j) = 0
              if (psi(i,j).lt.0.and.y.gt.0) then
                interior(i,j) = 1
              else if (psi(i,j).gt.0.and.y.lt.0) then
                interior(i,j) = 1
              else if (y.eq.0.and.x.gt.-l.and.x.lt.l) then
                interior(i,j) = 1
              end if
            end do
          end do
```

```
      write(*,'(" Identified interior region")')

      return
      end
C
C-----------------------------------------------------------------
C
      subroutine setup(m,n,depth,length,dx,dy,h,l,uinf,mua,a,mm)

C  This subroutine inputs information about the ellipse size as well
C  as the the dimensions of the computational domain and its spatial
C  discretisation.

      implicit  none
      integer*2 m,n,j,k
      real*4    dx,dy,h,l,uinf,mua,a,mm,depth,length

      dx    = 1
      dy    = 1
C
C  Input ellipse size information
C
      call help_read_r(h,h,
     + 'Enter amplitude of wave (mm) ',2,4,1,8,15)
      call help_read_r(uinf,uinf,
     + 'Enter wave celerity (mm/s) ',2,3,1,9,15)

      h = h/1000.
      uinf = uinf/1000.
      l = h*2.
      a = l/1.2806
      mm = 0.32*uinf*a

      write(*,'(/," A 2 to 1 aspect ratio yields a Rankine oval of"
     + ,/," semi-major axis ",f5.3," m and semi-minor axis ",f5.3,
     + " m.")') l,h
      write(*,'(/," The wave celerity of ",f5.3," m/s combined ",
     + "with an m/uinfa",/," value of 0.320 yields a value for ",
     + "source/sink distance",/," of ",f5.3," m and an m",
     + " value of ",f7.5,".")') uinf,a,mm
C
C  Input physical dimensions of domain
C
      depth = 300
      length = 500

      call help_read_r(depth,depth,
     + 'Enter depth of ambient region (max 600 mm) ',2,3,1,8,15)
      call help_read_r(length,length,
     + 'Enter length of ambient region (max 1000 mm) ',2,4,1,9,15)

      depth = depth/1000.
      length = length/1000.
C
C  State physical dimensions of domain
C
      write(*,'(/," The experimental domain has a length of ",
     + f7.2," m and a depth of ",f6.2," m.")') length,depth

C
C  Input physical dimensions of cells
C
      call help_read_r(dx,dx,
     + 'Enter x discretisation (mm) ',2,4,2,10,15)
      call help_read_r(dy,dy,
     + 'Enter y discretisation (mm) ',2,4,2,11,15)

      dx = dx/1000.
      dy = dy/1000.

      m = nint(length/dx)
      n = nint(depth/dy)
C
C  State cellwise dimensions of domain
C
      write(*,'(/," The computational domain has a length of ",
     + i4," cells and a depth of ",i3," cells.")') m,n

      return
      end
C
C-----------------------------------------------------------------
C
      subroutine pauser
      implicit none

C  this subroutine was lifted from David Luketina (UNSW)

      character*1 ans

      write(*,'(/," press return key to continue ")')
      read(*,'(a)') ans

      return
      end
C
C-----------------------------------------------------------------
C
      subroutine write_word(word)

C  subroutine writes four byte word to TIFF file
C  writes in little endian byte order

      implicit none
      integer*2 fputc,status,i,j
      integer*4 ctr,word
      byte bite_o_file

      do i = 0,3
       ctr = word
       do j = 2,i,-1
        ctr = ctr-int(ctr/256**(j+1))*256**(j+1)
       end do
       bite_o_file = int(ctr/256**i)
       status = fputc(9,bite_o_file)
      end do

      return
      end
C
C-----------------------------------------------------------------
C
      subroutine convert(int_in,int_out)

C  lifted from David Luketina (UNSW)

      implicit none
      integer*1 int_in,int_out

      int_out = int_in

      return
      end
C
C-----------------------------------------------------------------
C
      subroutine output(m,n,depth,length,dx,dy,h,l,uinf,mua,a,mm)

C  This subroutine will create a TIFF file showing densities scaled
C  linearly from lowest (0 = black) to highest (255 = white), with a
C  gray (= 127) border around it.  Cells will be represented by an a*a pixel
C  block, where a is an integer (represented by variable "factor") which
C  yields the closest file width to the value of the variable "msize".
C  Superimposed on the density field graphic are vectors, proportionally
C  scaled so that they will not overlap, and markers as well.
C  Hash pointer routine lifted from David Luketina (UNSW)

      implicit    none
      byte        bite_o_file
      integer*1   int_in
      integer*2   fputc,status,ic,i,j,k,m,n
      integer*2   msize,nsize,factor,dvplot(2001,1201),outf
      real*4      depth,length,dx,dy,h,l,uinf,mua,a,mm,x,y
      real*4      minvort,maxvort,dvdx,dudy,streaminc,max
      integer*4   word,words(40)
      character*1 char_out
      character*3 string
      character*50 str
      character*256 fname
      real*4      hunk,hash_pointer,psi(2001,1201),uv(2001,1201)
      real*4      phi(2001,1201),u(2001,1201),v(2001,1201)
      integer*2   mask(2001,1201)
      real*4      mu1,mu2
      integer*2   interior(2001,1201)

      common      psi,u,v,phi,mask,interior,mu1,mu2
C
C  Fill array dvplot with information
C
      write(*,'(/," performing plot shading ")')
C
C  Velocity shading (largest = white; zero = black; no negatives)
C
C  Set interior velocities to zero
C
      do i = 1,m+1
       x = -length/2. + dx*(i-1)
       do j = 1,n+1
        y = depth/2. - dy*(j-1)
        mask(i,j) = 0
        if (psi(i,j).lt.0.and.y.gt.0) then
         u(i,j) = 0
         v(i,j) = 0
         mask(i,j) = 1
        else if (psi(i,j).gt.0.and.y.lt.0) then
         u(i,j) = 0
         v(i,j) = 0
         mask(i,j) = 1
        else if (y.eq.0.and.x.gt.-l.and.x.lt.l) then
         u(i,j) = 0
         v(i,j) = 0
         mask(i,j) = 1
        end if
       end do
```

```
      end do
      max = 0
      do i = 1,m+1
       do j = 1,n+1
        uv(i,j) = (u(i,j)**2+v(i,j)**2)**0.5
        if (uv(i,j).gt.max) max = uv(i,j)
       end do
      end do
      do i = 1,m+1
       do j = 1,n+1
        dvplot(i,j) = int(real(uv(i,j)*255./max))
       end do
      end do
C
5     write(*,'(" placing streamlines ")')
C      go to 10
      streaminc = psi(1,1)/10
      do i = 1,m+1
       k = -10
       do j = n+1,int(n/2),-1    ! lower streamlines
        if (psi(i,j).gt.streaminc*-0.5) goto 2
        if (psi(i,j).ge.streaminc*k) then
         dvplot(i,j) = 0
         k = k+1
        end if
2      end do
      end do
      do i = 1,m+1
       k = 10
       do j = 1,int(n/2)        ! upper streamlines
        if (psi(i,j).lt.streaminc*0.5) goto 3
        if (psi(i,j).le.streaminc*k) then
         dvplot(i,j) = 0
         k = k-1
        end if
3      end do
      end do
4     do i = 1,m+1
      do j = 1,n               ! zero streamline
       if (psi(i,j).eq.0) then
        dvplot(i,j) = 0
      else if (psi(i,j).gt.0.and.psi(i,j+1).lt.0) then
        if (psi(i,j).gt.-psi(i,j+1)) then
         dvplot(i,j+1) = 0
        else
         dvplot(i,j) = 0
        end if
       end if
      end do
      end do
C
C Open output file
C
10    fname = 'output.tif'
      write(*,'(" opening file ",a,$)') fname(1:12)
      open(unit=9,file=fname,status='NEW',form='UNFORMATTED')
C
C Put out TIFF format header
C
      write(*,'(" writing header ",$)')

      word = 2771273                    ! Write II42
      call write_word(word)
      word = 8                          ! Write IFD offset
      call write_word(word)
      bite_o_file = 13                  ! Write number of
      status = fputc(9,bite_o_file)                 ! IFD entries
      bite_o_file = 0
      status = fputc(9,bite_o_file)
C
C Write Image File Directory entries
C
      data words/262398,1,0,196864,1,0,196865,1,0,196866,1,8,
     +  196869,1,1,196872,1,1,262417,1,170,196885,1,1,196886,1,
     +  0,262423,1,0,327962,1,182,327963,1,182,196904,1,2,0/

      words(6) = m+1
      words(9) = n+1
      words(30) = (m+1)*(n+1)

      do j = 1,40
       word = words(j)
       call write_word(word)
      end do
C
C Write out data
C
      write(*,'(" writing pixel array ")')
      hunk = real(n+1)*real(m+1)/70.0
      hash_pointer = 0.0

      do j = 1, n+1
       do i = 1, m+1
        int_in = dvplot(i,j)
        call convert(int_in,char_out)
        status = fputc(9,char_out)
C
C Show loading progress
C
        hash_pointer = hash_pointer + 1.0
        if ( hash_pointer.gt.hunk ) then
         write(*,'("#",$)')
         hash_pointer = 0.0
        end if
              end do
      end do

      close(9)
      write(*,'(/," finished writing output file ")')

      return
      end
```

Appendix 10 - Dissipation Data from Present Study

Detailed data from the eight experimental runs which were used in Chapter 8 (Results: Dissipation) are presented in this appendix. These runs represent a subset of the twenty-seven experimental runs presented in Appendix 6, therefore some data may be found there. The relevant dissipation data are given in Tables A10.1a-12a, which provide values for quantities corresponding to run parameters and wave energy measurements, and Tables A10.1b-12b, which provide values for quantities corresponding to run parameters and dissipation force calculations. The recorded quantities include:

Run Parameters:

Run name
Intermediate density, ρ_2
Density difference, $\Delta\rho\ (= \rho_3 - \rho_1)$
Wave amplitude decay rate, da/dx
Flume width, w

Measured or Calculated Wave Energy Parameters:

Time stamp (time of gate release noted)
Dimensionless wave amplitude, a/h
Total wave energy, E (from Equation 8.19)
Wave energy decay rate, dE/dx (from curve fit)
Wave energy decay rate, dE/dx (from Equation 8.40)
Wave energy decay rate, dE/dx (from Equation 8.41)
Error bar calculations for wave amplitude decay rate

Measured or Calculated Wave Dissipation Force Parameters:

Fluid drag ($0.5C_D w\rho c^2(2a)$)
Wall drag ($3.31\rho c^2 a\lambda/Re_\lambda^{1/2}$; $Re_\lambda = c\lambda/\nu$)
Wave energy decay rate, dE/dx (from Equation 8.40)
Wall drag proportion, dE/dx / *wall drag*
Remaining drag, dE/dx - *wall drag*
Calculated amplitude Reynolds number, $Re_a = 2ac/\nu$
Densimetric drag coefficient, C_D
Calculated total drag (calculated wall drag + fluid drag)

Run names are given in the format **YMMDDVGFFF**, where the first five digits give the date of the experimental run (**Y** is the last digit of the year, **MM** the month from 1-12 and **DD** the day from 1-31). **V** stands for the flow visualisation method, and is either "D" for fluorescent dye or "P" for neutrally buoyant particles. **G** stands for the wave generation method, with "E", "I", and "C" representing the exchange flow, forced inflow and collapse methods, respectively. The last three characters, **FFF**, stand for the mass fraction of salt in the lower layer, multiplied by ten. As an example, the run name 51007PC050 would represent a run performed on 7 October 1995, using particle visualisation and a collapse generation technique, with a lower layer salt mass fraction of 5.0%.

Images of the waves with a square grid used for amplitude and wavelength measurements are shown in Figures A10.1-8. It is hoped that these images will provide the reader with a clearer idea of what was happening as the waves decayed. No images were available for the runs of Stamp & Jacka (1995) which have been included here.

Table A10.1a - Wave energy data from run 50111PE015

50111PE015		Wave Energy Parameters				error bar calculations			
		ρ2	Δρ	-da/dx	w	n=	7	s^2=	0.01483
		1003.30	10.63	0.00521	0.25	Bhat=	-0.00521	xbar=	130.36
(start)	amplitude	wave	curve fit	eqn 8.40	eqn 8.41	t(0.025)=	2.571	sum xi^2=	17162
timeprint	*a/h*	energy	dE/dx	dE/dx	dE/dx				
(0:37.00)	(-)	(J)	(J/m)	(J/m)	(J/m)	Yhat	(Y-Yhat)^2	xi^2	
0:45.20	1.846	0.000094	-0.000128	-0.000152	-0.000180	1.89857	0.00275	7820	
0:56.53	1.846	0.000090	-0.000109	-0.000152	-0.000180	1.67308	0.02996	2039	
1:04.70	1.346	0.000038	-0.000096	-0.000084	-0.000099	1.52047	0.03039	251	upper
1:12.08	1.394	0.000042	-0.000085	-0.000090	-0.000106	1.38981	0.00002	85	-0.00760
1:19.98	1.346	0.000041	-0.000074	-0.000084	-0.000099	1.25752	0.00786	1198	lower
1:22.70	1.231	0.000033	-0.000070	-0.000072	-0.000084	1.21379	0.00029	1849	-0.0028
1:29.29	1.058	0.000021	-0.000062	-0.000054	-0.000064	1.11167	0.00291	3919	

Table A10.1b - Dissipation force data from run 50111PE015

50111PE015			Infinitesimal Wave Speed Parameters					Wave Energy Parameters					
			ω	*h*	*H/h*	*δ*	*c0*	*ν*	*ρ2*	*-da/dx*	*w*		
			0.0053	0.0052	58	0.018	0.0115	1.07E-06	1003.30	0.00521	0.25		
Fluid Drag			Wall Drag				eqn 8.40	dE/dx ÷	dE/dx -	calculated			Calculated
c^2 a	wρc^2a	x C_D	3.31ρc^2aλ	Re_λ	Drag		dE/dx	Wall Drag	Wall Drag	C_D	Re_a	C_D x ω^1/3	Total Drag
(m^3/s^2)	(N)	(N)	(N)	(-)	(N)		(J/m)	(-)	(N)	(-)	(-)	(-)	(N)
0.0000041	0.001019	0.000146	0.000305	434	0.000015		0.000152	10.397	0.000137	0.128	369	0.022	0.000161
0.0000035	0.00088	0.000127	0.000253	387	0.000013		0.000152	11.826	0.000139	0.128	344	0.022	0.000140
0.0000023	0.00058	0.000083	0.000130	288	0.000008		0.000084	11.039	0.000077	0.135	237	0.024	0.000090
0.0000021	0.00054	0.000077	0.000127	286	0.000007		0.000090	12.015	0.000083	0.134	233	0.023	0.000085
0.0000018	0.00046	0.000066	0.000112	279	0.000007		0.000084	12.541	0.000078	0.134	212	0.023	0.000073
0.0000016	0.00040	0.000058	0.000094	261	0.000006		0.000072	12.277	0.000066	0.136	190	0.024	0.000064
0.0000012	0.00031	0.000045	0.000063	215	0.000004		0.000054	12.613	0.000050	0.141	155	0.025	0.000049

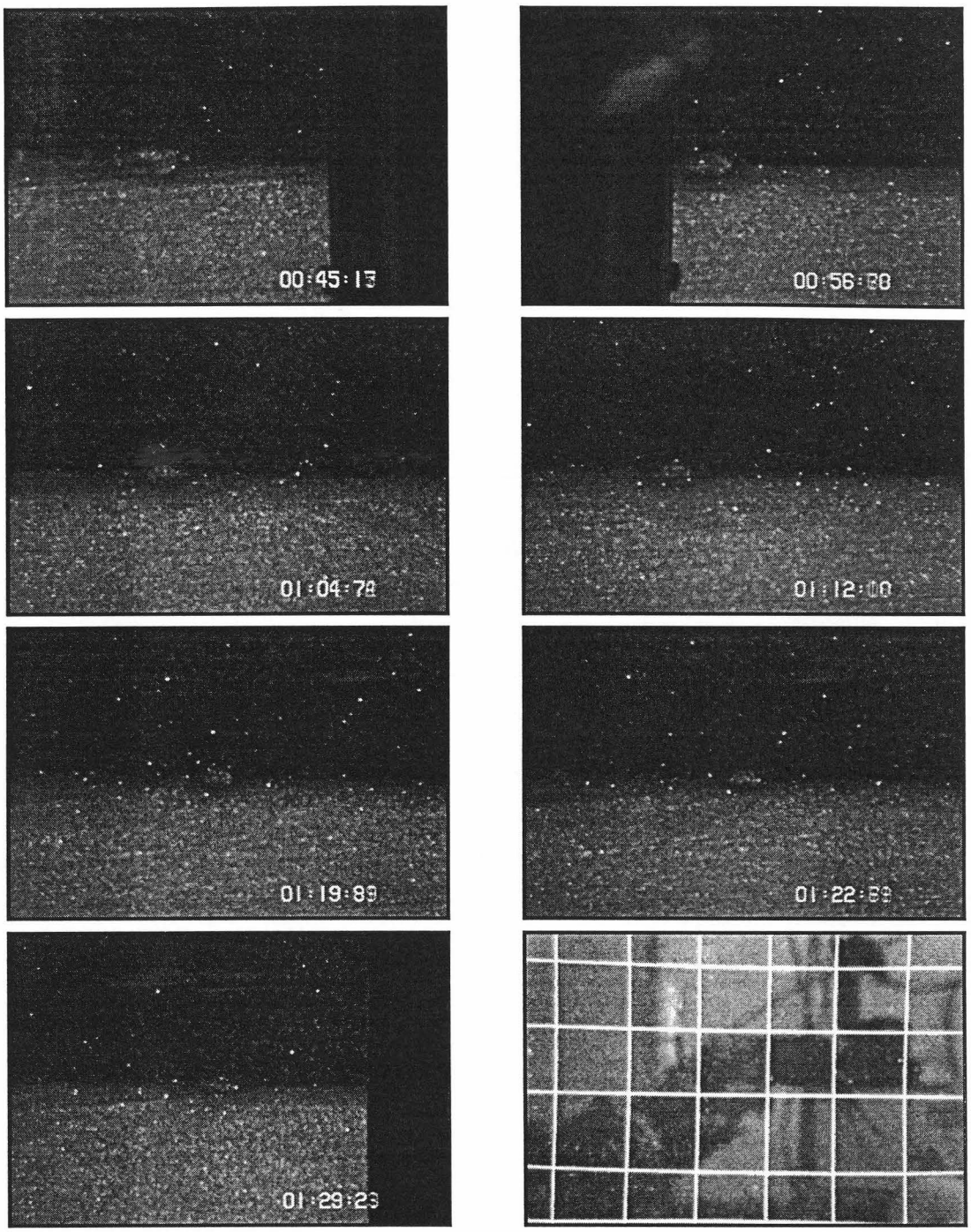

Figure A10.1 - Images from run 50111PE015 (50 mm square calibration grid)

Table A10.2a - Wave energy data from run 50110PE020

50110PE020		Wave Energy Parameters				error bar calculations			
		ρ_2	$\Delta\rho$	-da/dx	w	n=	8	s^2=	0.04010
		1005.10	14.27	0.00552	0.25	Bhat=	-0.00552	xbar=	474.34
(start)	amplitude	wave	curve fit	eqn 8.40	eqn 8.41	t(0.025)=	2.447	sum xi^2=	208454
timeprint	*a/h*	energy	dE/dx	dE/dx	dE/dx				
(1:04.30)	(-)	(J)	(J/m)	(J/m)	(J/m)	Yhat	(Y-Yhat)^2	xi^2	
1:33.70	3.756	0.000502	-0.000372	-0.000574	-0.000686	4.05287	0.08824	51512	
1:41.98	3.826	0.000513	-0.000345	-0.000595	-0.000711	3.71663	0.01187	27572	
1:50.38	3.477	0.000445	-0.000320	-0.000494	-0.000590	3.38844	0.00780	11363	
1:58.60	3.407	0.000363	-0.000296	-0.000475	-0.000567	3.07990	0.10698	2571	upper
2:07.90	2.709	0.000190	-0.000270	-0.000306	-0.000364	2.74586	0.00134	96	-0.00659
2:19.08	2.221	0.000101	-0.000240	-0.000210	-0.000249	2.36543	0.02088	6199	lower
2:39.78	1.663	0.000057	-0.000190	-0.000121	-0.000143	1.72196	0.00350	38144	-0.00445
2:53.87	1.326	0.000026	-0.000159	-0.000080	-0.000094	1.32921	0.00001	70998	

Table A10.2b - Dissipation force data from run 50110PE020

50110PE020			Infinitesimal Wave Speed Parameters					Wave Energy Parameters					
			ω	*h*	*H/h*	δ	c_0	ν	ρ_2	-da/dx		w	
			0.0071	0.0043	70	0.014	0.0121	1.09E-06	1005.10	0.00552		0.25	
Fluid Drag			Wall Drag				eqn 8.40	dE/dx ÷	dE/dx -	calculated			Calculated
c^2 a	wρc^2a	x C_D	3.31ρc^2aλ	Re_λ	Drag		dE/dx	Wall Drag	Wall Drag	C_D	Re_λ	C_D x ω^1/3	Total Drag
(m^3/s^2)	(N)	(N)	(N)	(-)	(N)		(J/m)	(-)	(N)	(-)	(-)	(-)	(N)
0.0000168	0.004215	0.000548	0.001767	936	0.000058		0.000574	9.939	0.000516	0.128	955	0.025	0.000606
0.0000158	0.003982	0.000518	0.001645	888	0.000055		0.000595	10.780	0.000540	0.127	937	0.024	0.000573
0.0000133	0.003343	0.000435	0.001451	897	0.000048		0.000494	10.208	0.000446	0.128	818	0.025	0.000483
0.0000120	0.003021	0.000393	0.001113	731	0.000041		0.000475	11.552	0.000434	0.129	770	0.025	0.000434
0.0000087	0.002184	0.000284	0.000667	578	0.000028		0.000306	11.028	0.000278	0.132	584	0.025	0.000312
0.0000063	0.001585	0.000206	0.000381	428	0.000018		0.000210	11.377	0.000191	0.136	450	0.026	0.000225
0.0000037	0.000928	0.000121	0.000227	386	0.000012		0.000121	10.499	0.000110	0.140	298	0.027	0.000132
0.0000024	0.000614	0.000080	0.000109	254	0.000007		0.000080	11.705	0.000073	0.147	217	0.028	0.000087

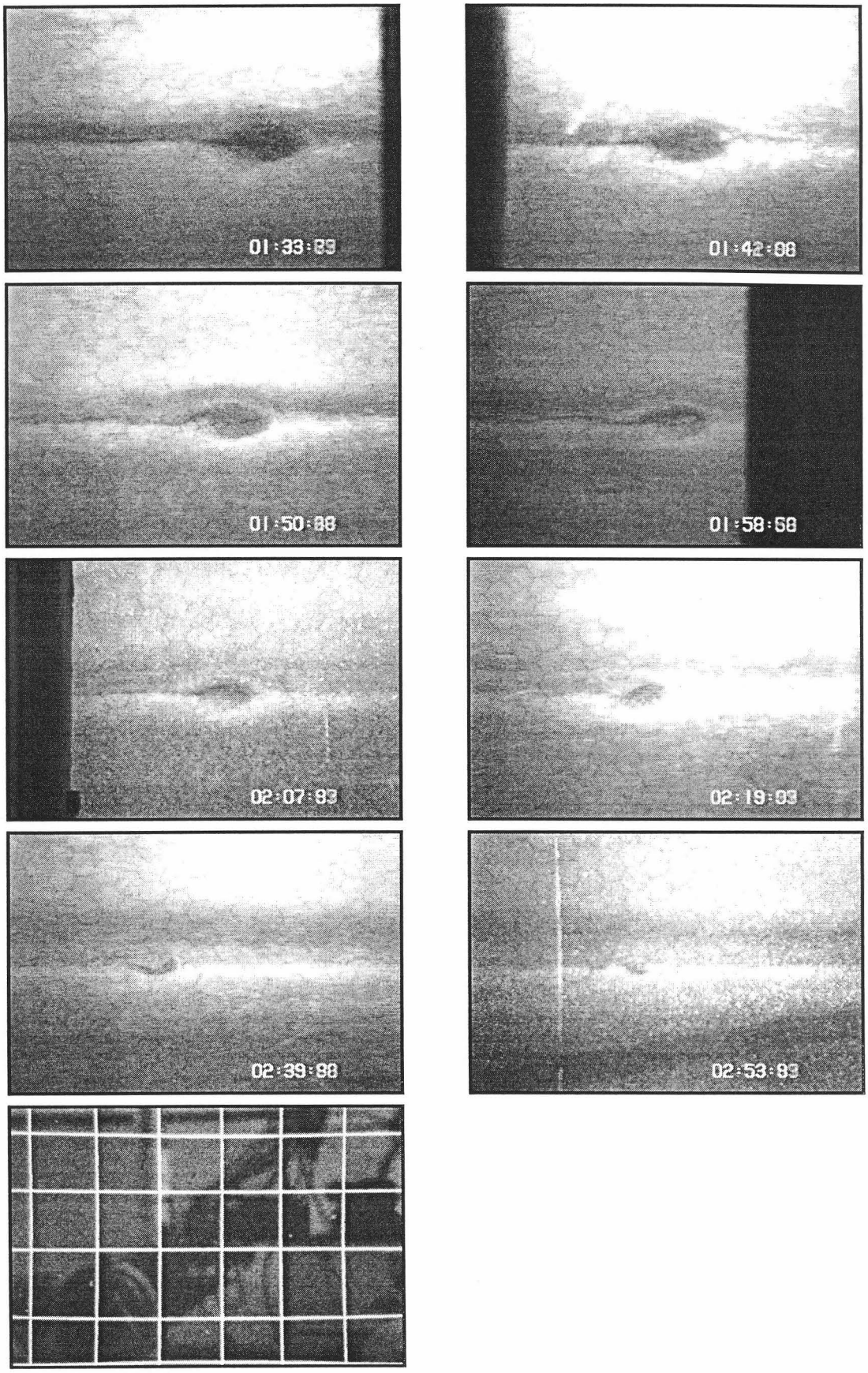

Figure A10.2 - Images from run 50110PE020 (50 mm square calibration grid)

Table A10.3a - Wave energy data from run 50123PE022

50123PE022		Wave Energy Parameters				error bar calculations			
		ρ2	Δρ	-da/dx	w	n=	11	s^2=	0.02676
		1005.80	15.69	0.00595	0.25	Bhat=	-0.00595	xbar=	718.57
(start)	amplitude	wave	curve fit	eqn 8.40	eqn 8.41	t(0.025)=	2.262	sum xi^2=	481471
timeprint	*a/h*	energy	dE/dx	dE/dx	dE/dx				
(0:58.69)	(-)	(J)	(J/m)	(J/m)	(J/m)	Yhat	(Y-Yhat)^2	xi^2	
1:41.05	5.088	0.001268	-0.001054	-0.001062	-0.001272	5.11415	0.00071	112076	
1:48.94	4.775	0.001052	-0.000930	-0.000939	-0.001123	4.73212	0.00184	73209	
1:59.34	4.263	0.000735	-0.000772	-0.000753	-0.000900	4.24735	0.00023	35758	
2:06.76	3.763	0.000518	-0.000664	-0.000591	-0.000705	3.91455	0.02312	17733	
2:17.39	3.563	0.000419	-0.000515	-0.000531	-0.000634	3.45671	0.01119	3160	
2:24.67	3.200	0.000303	-0.000417	-0.000432	-0.000515	3.15604	0.00193	32	
2:38.02	2.750	0.000206	-0.000246	-0.000323	-0.000384	2.63188	0.01395	6791	upper
2:45.24	2.438	0.000146	-0.000159	-0.000256	-0.000305	2.36307	0.00554	16279	-0.00648
2:54.59	1.875	0.000062	-0.000051	-0.000156	-0.000185	2.03026	0.02410	33681	lower
3:05.89	1.325	0.000026		-0.000082	-0.000096	1.65108	0.10633	61133	-0.00542
3:25.70	1.275	0.000022		-0.000076	-0.000089	1.04722	0.05188	121619	

Table A10.3b - Dissipation force data from run 50123PE022

50123PE022			Infinitesimal Wave Speed Parameters				Wave Energy Parameters					
			ω	*h*	*H/h*	*δ*	*c0*	*ν*	*ρ2*	*-da/dx*		*w*
			0.0078	0.0040	75	0.013	0.0122	1.06E-06	1005.80	0.00595		0.25
Fluid Drag			Wall Drag				eqn 8.40	dE/dx ÷	dE/dx -	calculated			Calculated
c^2 a	wρc^2a	x C_D	3.31ρc^2aλ	Re_λ	Drag		dE/dx	Wall Drag	Wall Drag	C_D	Re_a	C_D x ω^1/3	Total Drag
(m^3/s^2)	(N)	(N)	(N)	(-)	(N)		(J/m)	(-)	(N)	(-)	(-)	(-)	(N)
0.0000223	0.005598	0.000706	0.003399	1431	0.000090		0.001062	11.822	0.000972	0.134	1270	0.027	0.000795
0.0000196	0.004926	0.000621	0.002818	1305	0.000078		0.000939	12.034	0.000861	0.135	1154	0.027	0.000699
0.0000160	0.004026	0.000508	0.002018	1094	0.000061		0.000753	12.336	0.000692	0.136	986	0.027	0.000569
0.0000132	0.003329	0.000420	0.001511	959	0.000049		0.000591	12.108	0.000542	0.138	842	0.027	0.000468
0.0000114	0.002859	0.000360	0.001169	823	0.000041		0.000531	13.042	0.000491	0.139	760	0.028	0.000401
0.0000095	0.002396	0.000302	0.000878	713	0.000033		0.000432	13.134	0.000399	0.140	659	0.028	0.000335
0.0000072	0.001800	0.000227	0.000607	613	0.000025		0.000323	13.174	0.000298	0.142	529	0.028	0.000251
0.0000059	0.001478	0.000186	0.000451	533	0.000020		0.000256	13.145	0.000237	0.145	452	0.029	0.000206
0.0000041	0.001025	0.000129	0.000224	364	0.000012		0.000156	13.259	0.000144	0.151	330	0.030	0.000141
0.0000025	0.000634	0.000080	0.000116	285	0.000007		0.000082	11.866	0.000075	0.159	218	0.032	0.000087
0.0000019	0.000472	0.000059	0.000078	226	0.000005		0.000076	14.684	0.000071	0.160	185	0.032	0.000065

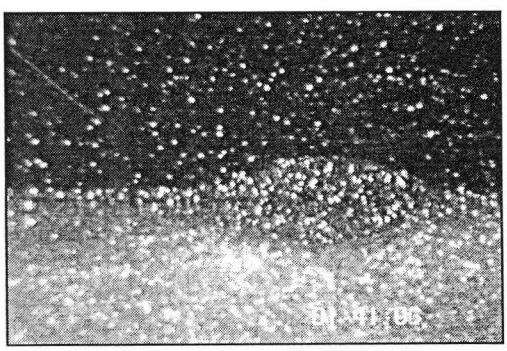

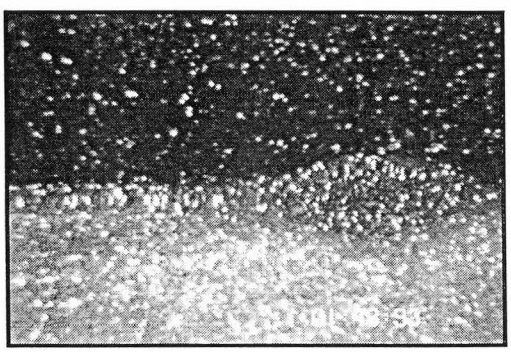

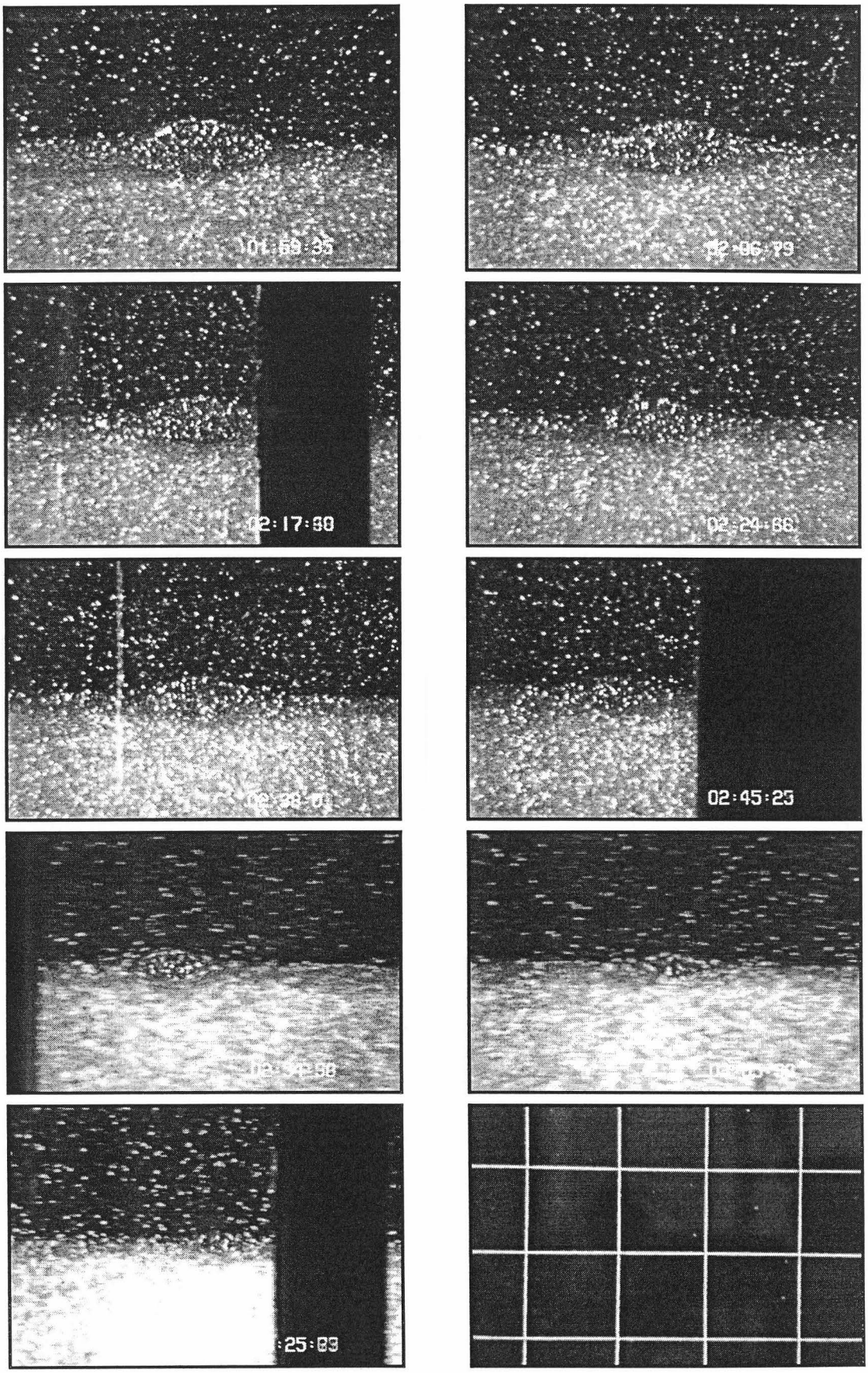

Figure A10.3 - Images from run 50123PE022 (50 mm square calibration grid)

Table A10.4a - Wave energy data from run 50827PE025

50827PE025		Wave Energy Parameters ρ2	Δρ	-da/dx	w	error bar calculations n=	9	s^2=	0.66721
		1006.70	17.52	0.00593	0.25	Bhat=	-0.00593	xbar=	750.87
(start)	amplitude	wave	curve fit	eqn 8.40	eqn 8.41	t(0.025)=	2.365	sum xi^2=	1399076
timeprint	*a/h*	energy	dE/dx	dE/dx	dE/dx				
(1:10.55)	(-)	(J)	(J/m)	(J/m)	(J/m)	Yhat	(Y-Yhat)^2	xi^2	
1:24.22	8.000	0.001940	-0.001659	-0.001615	-0.001940	7.97865	0.00046	304466	
1:32.63	8.000	0.002183	-0.001452	-0.001615	-0.001940	7.30510	0.48289	192019	
1:42.27	7.500	0.001640	-0.001225	-0.001423	-0.001708	6.56845	0.86778	98581	
1:50.60	5.167	0.000560	-0.001039	-0.000685	-0.000821	5.96239	0.63318	44848	
1:56.70	4.000	0.000280	-0.000908	-0.000416	-0.000497	5.53650	2.36083	19587	upper
2:35.00	3.667	0.000227	-0.000192	-0.000352	-0.000420	3.20866	0.20977	63806	-0.00756
2:47.90	2.667	0.000089		-0.000191	-0.000227	2.55909	0.01157	131145	lower
3:04.00	1.667	0.000024		-0.000078	-0.000092	1.84343	0.03125	233118	-0.00430
3:15.50	1.667	0.000023		-0.000078	-0.000092	1.39688	0.07279	311506	

Table A10.4b - Dissipation force data from run 50827PE025

50827PE025			Infinitesimal Wave Speed Parameters ω	h	H/h	δ	c_0	Wave Energy Parameters ν	ρ_2	-da/dx	w
			0.0087	0.0030	100	0.010	0.0112	1.22E-06	1006.70	0.00593	0.25
Fluid Drag			Wall Drag				eqn 8.40	dE/dx ÷	dE/dx -	calculated			Calculated
c^2 a	wρc^2a	x C_D	3.31ρc^2aλ	Re_λ	Drag		dE/dx	Wall Drag	Wall Drag	C_D	Re_s	C_D x ω^1/3	Total Drag
(m^3/s^2)	(N)	(N)	(N)	(-)	(N)		(J/m)	(-)	(N)	(-)	(-)	(-)	(N)
0.0000411	0.010345	0.001257	0.006190	1533	0.000158		0.001615	10.218	0.001457	0.132	1628	0.027	0.001416
0.0000377	0.009497	0.001154	0.006392	1652	0.000157		0.001615	10.272	0.001458	0.130	1560	0.027	0.001312
0.0000319	0.008034	0.000977	0.004623	1342	0.000126		0.001423	11.273	0.001296	0.131	1389	0.027	0.001103
0.0000200	0.005042	0.000613	0.002089	922	0.000069		0.000685	9.960	0.000616	0.136	913	0.028	0.000682
0.0000144	0.003635	0.000442	0.001255	741	0.000046		0.000416	9.034	0.000370	0.139	682	0.029	0.000488
0.0000079	0.001989	0.000242	0.000663	554	0.000028		0.000352	12.472	0.000323	0.138	483	0.028	0.000270
0.0000047	0.001174	0.000143	0.000289	369	0.000015		0.000191	12.638	0.000175	0.143	317	0.029	0.000158
0.0000022	0.000546	0.000066	0.000093	219	0.000006		0.000078	12.488	0.000072	0.153	171	0.031	0.000073
0.0000017	0.000429	0.000052	0.000070	188	0.000005		0.000078	15.238	0.000073	0.152	151	0.031	0.000057

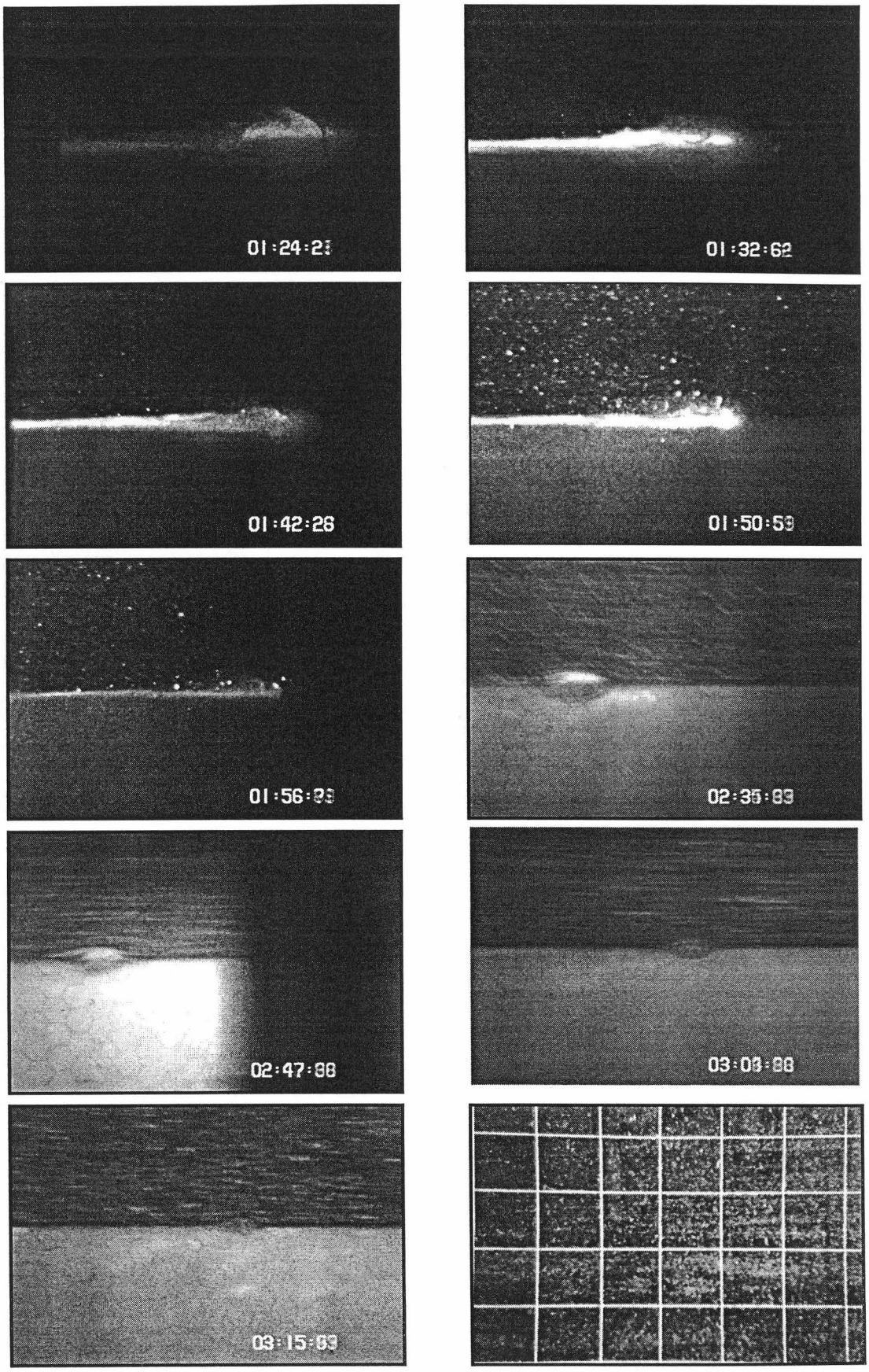

Figure A10.4 - Images from run 50827PE025 (50 mm square calibration grid)

Table A10.5a - Wave energy data from run 50109PE030

50109PE030		Wave Energy Parameters				error bar calculations			
		ρ_2	$\Delta\rho$	-da/dx	w	n=	6	s^2=	0.00820
		1008.60	21.38	0.00524	0.25	Bhat=	-0.00593	xbar=	669.95
(start)	amplitude	wave	curve fit	eqn 8.40	eqn 8.41	t(0.025)=	2.776	sum xi^2=	22048
timeprint	*a/h*	energy	dE/dx	dE/dx	dE/dx				
(1:46.77)		(J)	(J/m)	(J/m)	(J/m)	Yhat	(Y-Yhat)^2	xi^2	
3:03.00	3.047	0.001693	-0.001243	-0.001208	-0.001439	3.03516	0.00014	12579	
3:16.50	2.570	0.001058	-0.001028	-0.000872	-0.001036	2.64297	0.00528	1392	upper
3:26.00	2.367	0.000846	-0.000889	-0.000745	-0.000885	2.38869	0.00046	126	-0.00762
3:27.30	2.438	0.000860	-0.000870	-0.000788	-0.000936	2.35435	0.00691	316	lower
3:33.30	2.305	0.000647	-0.000788	-0.000708	-0.000841	2.20367	0.01020	2164	-0.00424
3:39.30	1.961	0.000481	-0.000709	-0.000522	-0.000617	2.05988	0.00979	5471	

Table A10.5b - Dissipation force data from run 50109PE030

50109PE030			Infinitesimal Wave Speed Parameters					Wave Energy Parameters					
			ω	*h*	*H/h*	δ	c_0	ν	ρ_2	-da/dx		w	
			0.0106	0.0064	47	0.022	0.0180	1.09E-06	1008.60	0.00524		0.25	
Fluid Drag			Wall Drag				eqn 8.40	dE/dx ÷	dE/dx -	calculated			Calculated
c^2 a	wρc^2a	x C_D	3.31ρc^2aλ	Re_λ	Drag		dE/dx	Wall Drag	Wall Drag	C_D	Re_*	C_D x ω^1/3	Total Drag
(m^3/s^2)	(N)	(N)	(N)		(N)		(J/m)		(N)				(N)
0.0000268	0.006754	0.000769	0.004376	1664	0.000107		0.001208	11.258	0.001101	0.120	1326	0.026	0.000876
0.0000189	0.004768	0.000543	0.002713	1337	0.000074		0.000872	11.749	0.000798	0.123	1023	0.027	0.000617
0.0000152	0.003836	0.000437	0.002058	1178	0.000060		0.000745	12.428	0.000685	0.124	881	0.027	0.000496
0.0000154	0.003872	0.000441	0.001992	1118	0.000060		0.000788	13.228	0.000728	0.124	898	0.027	0.000500
0.0000133	0.003341	0.000380	0.001447	899	0.000048		0.000708	14.681	0.000660	0.125	811	0.028	0.000428
0.0000102	0.002583	0.000294	0.001149	880	0.000039		0.000522	13.475	0.000483	0.127	658	0.028	0.000333

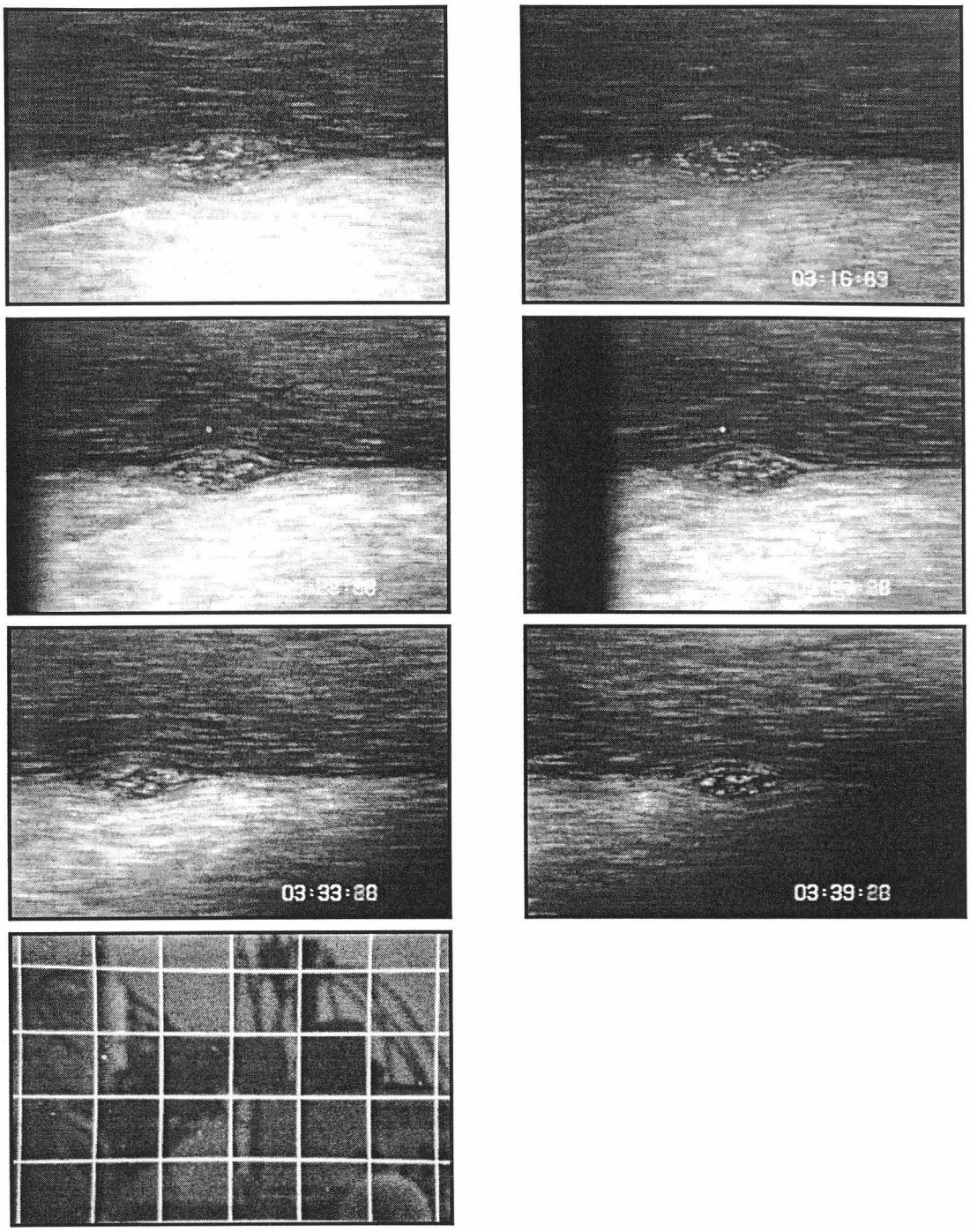

Figure A10.5 - Images from run 50109PE030 (50 mm square calibration grid)

Table A10.6a - Wave energy data from run 50903PE040

50903PE040		Wave Energy Parameters				error bar calculations			
		ρ2	Δρ	-da/dx	w	n=	7	s^2=	0.04875
		1012.10	28.54	0.00383	0.25	Bhat=	-0.00383	xbar=	822.76
(start)	amplitude	wave	curve fit	eqn 8.40	eqn 8.41	t(0.025)=	2.571	sum xi^2=	818759
timeprint	*a/h*	energy	dE/dx	dE/dx	dE/dx				
(1:33.51)		(J)	(J/m)	(J/m)	(J/m)	Yhat	(Y-Yhat)^2	xi^2	
1:52.21	7.375	0.005482	-0.001841	-0.002575	-0.003091	7.20715	0.02817	295698	
1:58.01	6.750	0.004515	-0.001734	-0.002164	-0.002596	6.91685	0.02784	219009	
2:35.00	5.375	0.002448	-0.001101	-0.001385	-0.001659	5.20666	0.02834	461	upper
2:49.20	4.250	0.001378	-0.000883	-0.000876	-0.001048	4.61502	0.13324	17693	-0.00446
2:57.40	4.375	0.001444	-0.000762	-0.000927	-0.001109	4.28975	0.00727	47499	lower
3:04.40	4.000	0.001112	-0.000663	-0.000779	-0.000931	4.02158	0.00047	82921	-0.00320
3:15.50	3.750	0.000906	-0.000513	-0.000687	-0.000821	3.61427	0.01842	155479	

Table A10.6b - Dissipation force data from run 50903PE040

50903PE040			Infinitesimal Wave Speed Parameters					Wave Energy Parameters					
			ω	*h*	*H/h*	*δ*	*c0*	*ν*	*ρ2*	*-da/dx*	*w*		
			0.0141	0.0040	75	0.013	0.0165	1.20E-06	1012.10	0.00383	0.25		
Fluid Drag			Wall Drag				eqn 8.40	dE/dx ÷	dE/dx -	calculated			Calculated
c^2 a	wρc^2a	x C_D	3.31ρc^2aλ	Re_λ	Drag		dE/dx	Wall Drag	Wall Drag	C_D	Re_*	C_D x ω^1/3	Total Drag
(m^3/s^2)	(N)	(N)	(N)		(N)		(J/m)		(N)				(N)
0.0000823	0.020820	0.002155	0.014299	2283	0.000299		0.002575	8.605	0.002276	0.081	2597	0.020	0.002454
0.0000723	0.018284	0.001892	0.012346	2199	0.000263		0.002164	8.218	0.001900	0.081	2328	0.020	0.002155
0.0000432	0.010937	0.001132	0.006315	1630	0.000156		0.001385	8.851	0.001228	0.082	1607	0.020	0.001288
0.0000303	0.007657	0.000792	0.003980	1380	0.000107		0.000876	8.178	0.000769	0.083	1195	0.020	0.000899
0.0000289	0.007321	0.000758	0.003763	1316	0.000104		0.000927	8.933	0.000823	0.083	1186	0.020	0.000861
0.0000248	0.006271	0.000649	0.002970	1173	0.000087		0.000779	8.981	0.000692	0.084	1050	0.020	0.000736
0.0000209	0.005277	0.000546	0.002317	1030	0.000072		0.000687	9.522	0.000615	0.085	932	0.020	0.000618

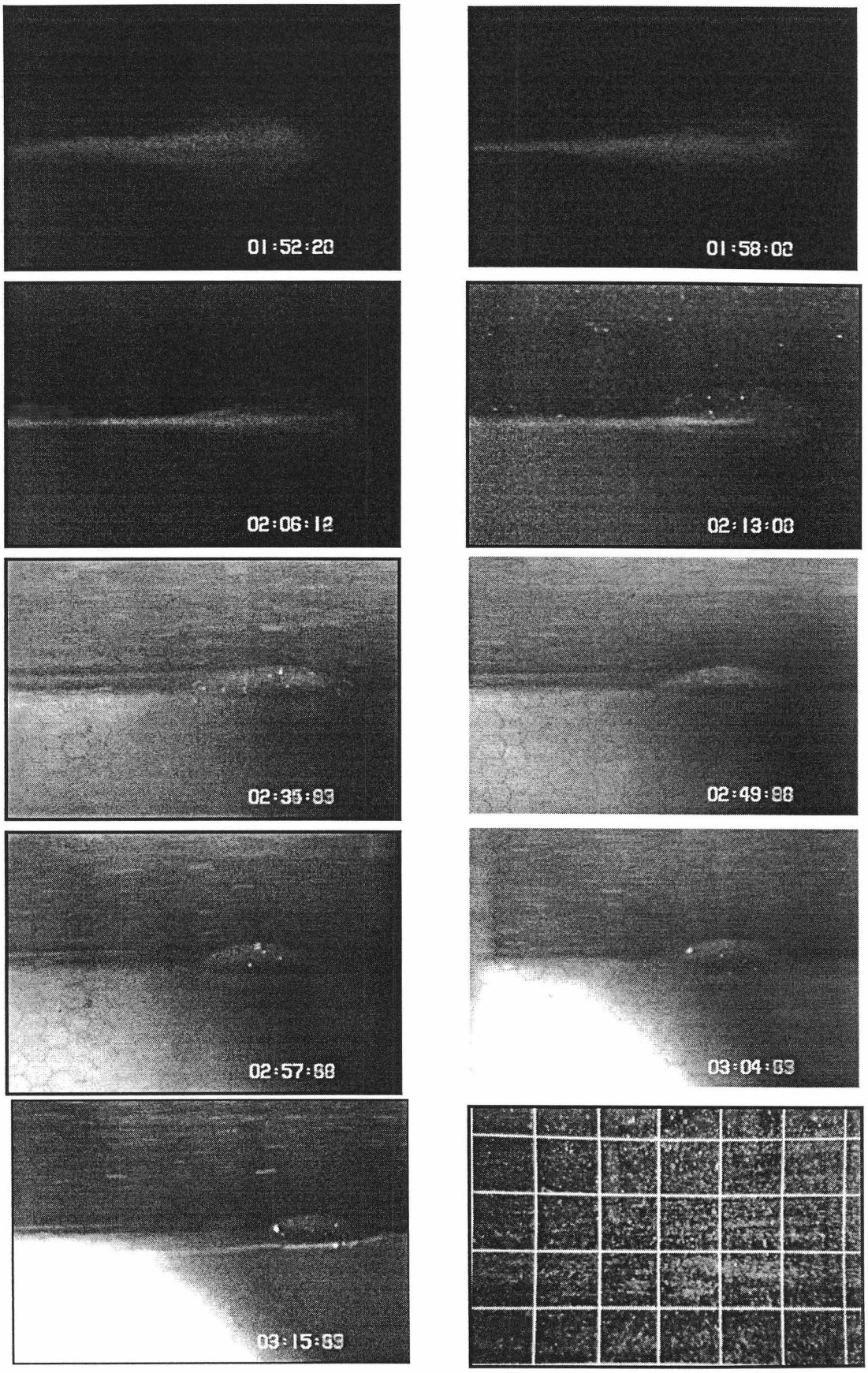

Figure A10.6 - Images from run 50903PE040 (50 mm square calibration grid)

Table A10.7a - Wave energy data from run 41224PE050

41224PE050		Wave Energy Parameters				error bar calculations			
		ρ_2	$\Delta\rho$	-da/dx	w	n=	5	s^2=	0.06162
		1015.60	35.75	0.00461	0.25	Bhat=	-0.00461	xbar=	640.32
(start)	amplitude	wave	curve fit	eqn 8.40	eqn 8.41	t(0.025)=	3.182	sum xi^2=	550683
timeprint	*a/h*	energy	dE/dx	dE/dx	dE/dx				
(0:51.81)		(J)	(J/m)	(J/m)	(J/m)	Yhat	(Y-Yhat)^2	xi^2	
1:03.52	8.276	0.019069	-0.003181	-0.007309	-0.008778	8.42230	0.02155	1741	upper
1:36.70	6.469	0.010811	-0.003898	-0.004504	-0.005402	6.45041	0.00036	1395	-0.00567
1:43.62	6.327	0.010574	-0.004031	-0.004311	-0.005170	6.08588	0.05791	15502	lower
1:51.63	5.847	0.008603	-0.004177	-0.003694	-0.004427	5.68408	0.02652	122041	-0.00355
2:14.70	4.367	0.003304	-0.004553	-0.002090	-0.002499	4.64758	0.07853	410005	

Table A10.7a - Dissipation force data from run 41224PE050

41224PE050			Infinitesimal Wave Speed Parameters				Wave Energy Parameters			
			ω	h	H/h	δ	c_0	ν	ρ_2	-da/dx	w
			0.0176	0.0049	61	0.017	0.0203	1.11E-06	1015.60	0.00461	0.25
Fluid Drag			Wall Drag			eqn 8.40	dE/dx +	dE/dx -	calculated			Calculated
c^2 a	wρc^2a	x C_D	3.31ρc^2aλ	Re_λ	Drag	dE/dx	Wall Drag	Wall Drag	C_D	Re_*	C_D x ω^1/3	Total Drag
(m^3/s^2)	(N)	(N)	(N)		(N)	(J/m)		(N)				(N)
0.0001937	0.049171	0.004726	0.049634	4747	0.000720	0.007309	10.145	0.006588	0.099	5049	0.026	0.005446
0.0001038	0.026361	0.002534	0.024685	3647	0.000409	0.004504	11.018	0.004095	0.100	3269	0.026	0.002942
0.0000929	0.023595	0.002268	0.022597	3568	0.000378	0.004311	11.395	0.003932	0.099	3058	0.026	0.002646
0.0000771	0.019582	0.001882	0.017865	3221	0.000315	0.003694	11.734	0.003379	0.099	2678	0.026	0.002197
0.0000407	0.010341	0.000994	0.006494	1864	0.000150	0.002090	13.895	0.001939	0.103	1682	0.027	0.001144

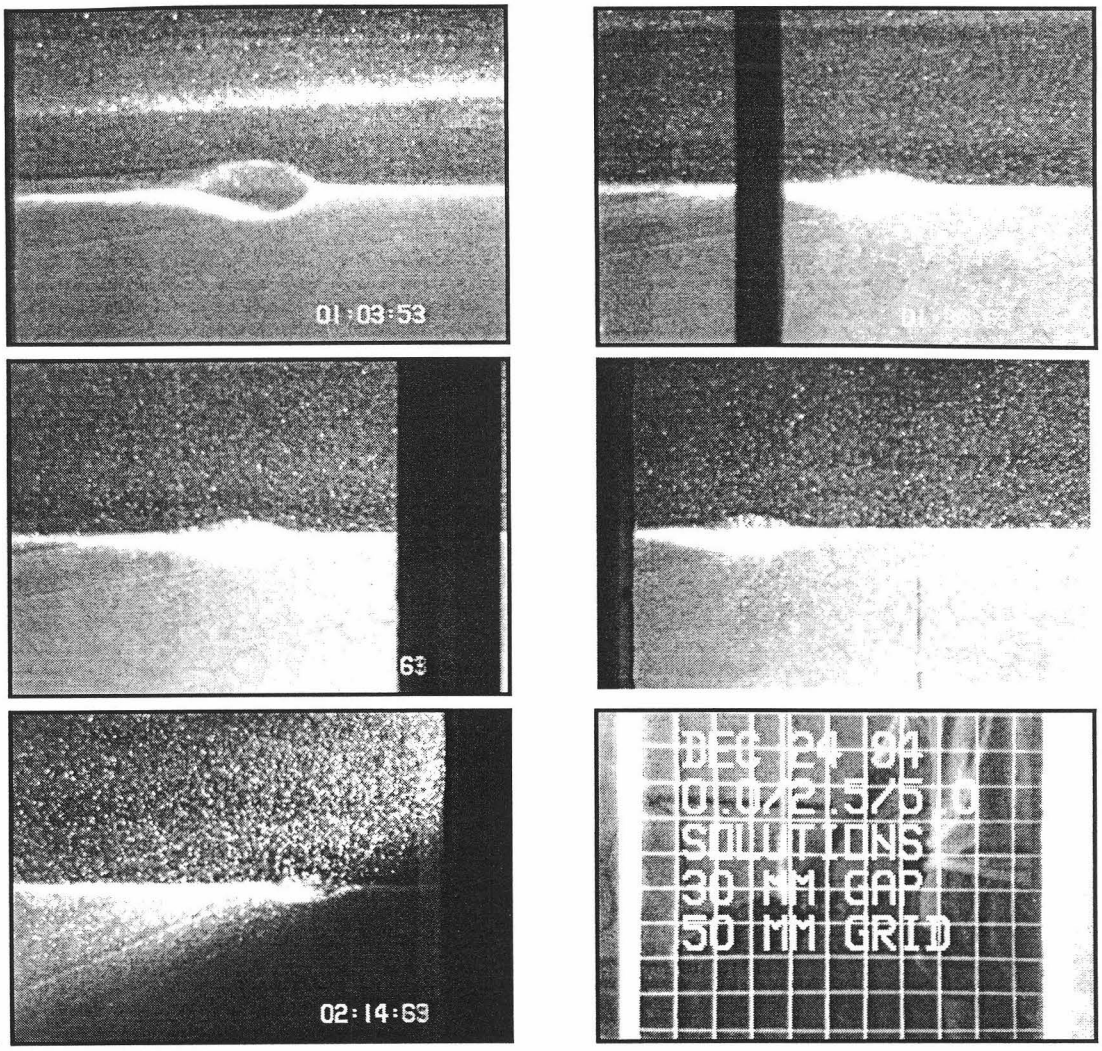

Figure A10.7 - Images from run 41224PE050 (50 mm square calibration grid)

Table A10.8a - Wave energy data from run 50121PE050

50121PE050		Wave Energy Parameters				error bar calculations			
		ρ2	Δρ	-da/dx	w	n=	7	s^2=	0.00637
		1015.60	35.75	0.00469	0.25	Bhat=	-0.00469	xbar=	1101.20
(start)	amplitude	wave	curve fit	eqn 8.40	eqn 8.41	t(0.025)=	2.571	sum xi^2=	76402
timeprint	*a/h*	energy	dE/dx	dE/dx	dE/dx				
(1:17.26)		(J)	(J/m)	(J/m)	(J/m)	Yhat	(Y-Yhat)^2	xi^2	
2:18.26	5.088	0.003320	-0.002204	-0.001908	-0.002284	5.08489	0.00001	31872	
2:25.38	4.738	0.002582	-0.002038	-0.001660	-0.001987	4.70820	0.00086	9645	
2:29.79	4.438	0.002211	-0.001940	-0.001461	-0.001748	4.48652	0.00240	2595	upper
2:37.95	4.088	0.001662	-0.001769	-0.001246	-0.001489	4.09978	0.00015	993	-0.00543
2:41.31	4.038	0.001482	-0.001703	-0.001216	-0.001454	3.94938	0.00777	4043	lower
2:45.95	3.625	0.001031	-0.001615	-0.000987	-0.001178	3.75017	0.01567	11249	-0.00395
2:48.27	3.725	0.001019	-0.001572	-0.001040	-0.001242	3.65426	0.00500	16005	

Table A10.8b - Dissipation force data from run 50121PE050

50121PE050			Infinitesimal Wave Speed Parameters					Wave Energy Parameters			
			ω	*h*	*H/h*	*δ*	c_0	*v*	ρ_2	*-da/dx*	*w*
			0.0176	0.0040	75	0.013	0.0184	1.07E-06	1015.60	0.00469	0.25
Fluid Drag			Wall Drag				eqn 8.40	dE/dx +	dE/dx -	calculated			Calculated
c^2 a	wρc^2a	x C_D	3.31ρc^2aλ	Re_λ	Drag		dE/dx	Wall Drag	Wall Drag	C_D	Re_*	C_D x ω^1/3	Total Drag
(m^3/s^2)	(N)	(N)	(N)		(N)		(J/m)		(N)				(N)
0.0000440	0.011177	0.001074	0.007798	2291	0.000163		0.001908	11.708	0.001745	0.104	1769	0.027	0.001237
0.0000362	0.009202	0.000884	0.005759	1932	0.000131		0.001660	12.670	0.001529	0.104	1549	0.027	0.001015
0.0000313	0.007955	0.000765	0.004859	1811	0.000114		0.001461	12.801	0.001347	0.105	1394	0.027	0.000879
0.0000247	0.006259	0.000602	0.003387	1483	0.000088		0.001246	14.164	0.001158	0.106	1187	0.027	0.000690
0.0000227	0.005773	0.000555	0.002854	1309	0.000079		0.001216	15.422	0.001137	0.106	1133	0.028	0.000634
0.0000185	0.004695	0.000451	0.002004	1076	0.000061		0.000987	16.157	0.000926	0.107	968	0.028	0.000512
0.0000181	0.004583	0.000440	0.001832	982	0.000058		0.001040	17.801	0.000982	0.108	969	0.028	0.000499

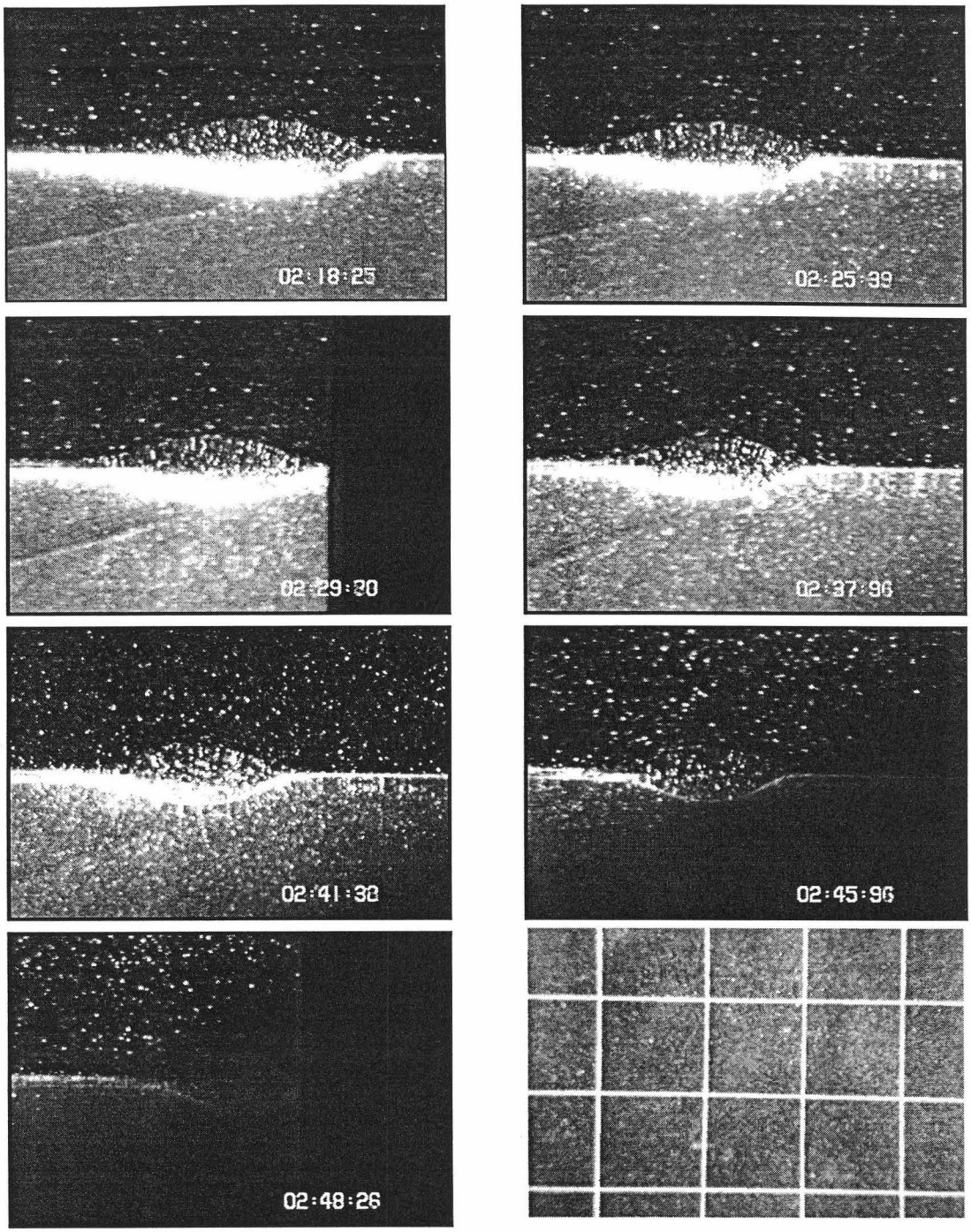

Figure A10.8 - Images from run 50121PE050 (50 mm square calibration grid)

Table A10.9a - Wave energy data from Stamp & Jacka (1995), ω = 0.0253

S&J, ω = 0.0253		Wave Energy Parameters				error bar calculations			
		ρ2	Δρ	-da/dx	w	n=	21	s^2=	0.00795
		1023.30	51.78	0.00366	0.15	Bhat=	-0.00366	xbar=	221.95
(start)	amplitude	wave	curve fit	eqn 8.40	eqn 8.41	t(0.025)=	2.093	sum xi^2=	381609
timeprint	*a/h*	energy	dE/dx	dE/dx	dE/dx				
(n/a)		(J)	(J/m)	(J/m)	(J/m)	Yhat	(Y-Yhat)^2	xi^2	
	3.067	0.000100	-0.000127	-0.000153	-0.000183	3.12283	0.00315	48379	
	2.889	0.000084	-0.000124	-0.000137	-0.000163	3.05329	0.02703	40382	
	2.978	0.000092	-0.000121	-0.000145	-0.000173	2.97643	0.00000	32383	
	2.978	0.000092	-0.000118	-0.000145	-0.000173	2.89591	0.00670	24949	
	2.889	0.000084	-0.000115	-0.000137	-0.000163	2.81539	0.00540	18483	
	2.756	0.000074	-0.000111	-0.000125	-0.000149	2.72755	0.00078	12533	
	2.533	0.000058	-0.000108	-0.000106	-0.000126	2.64703	0.01293	8091	
	2.533	0.000058	-0.000104	-0.000106	-0.000126	2.55187	0.00034	4090	
	2.444	0.000052	-0.000101	-0.000099	-0.000118	2.47501	0.00093	1845	
	2.444	0.000052	-0.000098	-0.000099	-0.000118	2.39815	0.00214	482	
	2.311	0.000044	-0.000095	-0.000089	-0.000106	2.31763	0.00004	0	
	2.444	0.000052	-0.000092	-0.000099	-0.000118	2.23711	0.04299	486	
	2.311	0.000044	-0.000089	-0.000089	-0.000106	2.15293	0.02502	2029	
	2.089	0.000033	-0.000086	-0.000074	-0.000087	2.07607	0.00016	4362	
	2.000	0.000029	-0.000082	-0.000068	-0.000080	1.98823	0.00014	8109	
	1.867	0.000024	-0.000078	-0.000060	-0.000071	1.89673	0.00090	13236	
	1.867	0.000024	-0.000076	-0.000060	-0.000071	1.82353	0.00186	18238	upper
	1.644	0.000017	-0.000072	-0.000047	-0.000055	1.74301	0.00972	24664	-0.00396
	1.644	0.000017	-0.000069	-0.000047	-0.000055	1.66249	0.00033	32058	lower
	1.556	0.000014	-0.000067	-0.000042	-0.000050	1.59661	0.00169	38828	-0.00336
	1.422	0.000011	-0.000063	-0.000036	-0.000042	1.51609	0.00881	47982	

Table A10.9b - Dissipation force data from Stamp & Jacka (1995), ω = 0.0253

Stamp & Jacka, ω = 0.0253	Infinitesimal Wave Speed Parameters					Wave Energy Parameters				
	ω	h	H/h	δ	c_0	ν	ρ_2	$-da/dx$		w
	0.0253	0.0023	67		0.0167	1.03E-06	1023.30	0.00366		0.15

Fluid Drag			Wall Drag			eqn 8.40	dE/dx +	dE/dx -	calculated			Calculated
c^2 a	wρc^2a	x C_D	3.31ρc^2aλ	Re_λ	Drag	dE/dx	Wall Drag	Wall Drag	C_D	Re_a	C_D x ω^1/3	Total Drag
(m^3/s^2)	(N)	(N)	(N)		(N)	(J/m)		(N)				(N)
0.0000121	0.001852	0.000158	0.000650	646	0.000026	0.000153	5.997	0.000128	0.081	560	0.024	0.000183
0.0000106	0.001625	0.000138	0.000541	591	0.000022	0.000137	6.147	0.000115	0.082	509	0.024	0.000161
0.0000113	0.001736	0.000148	0.000594	618	0.000024	0.000145	6.071	0.000121	0.082	535	0.024	0.000172
0.0000113	0.001736	0.000148	0.000594	618	0.000024	0.000145	6.071	0.000121	0.082	535	0.024	0.000172
0.0000106	0.001625	0.000138	0.000541	591	0.000022	0.000137	6.147	0.000115	0.082	509	0.024	0.000161
0.0000096	0.001468	0.000125	0.000468	552	0.000020	0.000125	6.262	0.000105	0.082	473	0.024	0.000145
0.0000080	0.001227	0.000105	0.000364	489	0.000016	0.000106	6.460	0.000090	0.083	415	0.024	0.000121
0.0000080	0.001227	0.000105	0.000364	489	0.000016	0.000106	6.460	0.000090	0.083	415	0.024	0.000121
0.0000074	0.001139	0.000097	0.000327	465	0.000015	0.000099	6.542	0.000084	0.084	392	0.025	0.000112
0.0000074	0.001139	0.000097	0.000327	465	0.000015	0.000099	6.542	0.000084	0.084	392	0.025	0.000112
0.0000066	0.001013	0.000086	0.000278	429	0.000013	0.000089	6.666	0.000076	0.084	360	0.025	0.000100
0.0000074	0.001139	0.000097	0.000327	465	0.000015	0.000099	6.542	0.000084	0.084	392	0.025	0.000112
0.0000066	0.001013	0.000086	0.000278	429	0.000013	0.000089	6.666	0.000076	0.084	360	0.025	0.000100
0.0000054	0.000825	0.000070	0.000207	374	0.000011	0.000074	6.876	0.000063	0.086	309	0.025	0.000081
0.0000049	0.000756	0.000064	0.000183	353	0.000010	0.000068	6.961	0.000058	0.086	289	0.025	0.000074
0.0000043	0.000660	0.000056	0.000151	322	0.000008	0.000060	7.089	0.000051	0.087	261	0.026	0.000065
0.0000043	0.000660	0.000056	0.000151	322	0.000008	0.000060	7.089	0.000051	0.087	261	0.026	0.000065
0.0000034	0.000517	0.000044	0.000107	274	0.000006	0.000047	7.299	0.000041	0.089	217	0.026	0.000050
0.0000034	0.000517	0.000044	0.000107	274	0.000006	0.000047	7.299	0.000041	0.089	217	0.026	0.000050
0.0000030	0.000466	0.000040	0.000092	255	0.000006	0.000042	7.381	0.000037	0.090	200	0.026	0.000045
0.0000026	0.000395	0.000034	0.000072	229	0.000005	0.000036	7.498	0.000031	0.091	176	0.027	0.000038

Table A10.10a - Wave energy data from Stamp & Jacka (1995), ω = 0.0485

S&J, ω = 0.0485		Wave Energy Parameters				error bar calculations			
		ρ2	Δρ	-da/dx	w	n=	30	s^2=	0.00382
		1046.50	101.51	0.00309	0.15	Bhat=	-0.00309	xbar=	264.37
(start)	amplitude	wave	curve fit	eqn 8.40	eqn 8.41	t(0.025)=	2.045	sum xi^2=	736609
timeprint	a/h	energy	dE/dx	dE/dx	dE/dx				
(n/a)		(J)	(J/m)	(J/m)	(J/m)	Yhat	(Y-Yhat)^2	xi^2	
	2.473	0.000193	-0.000201	-0.000251	-0.000298	2.59613	0.01523	68836	
	2.473	0.000193	-0.000197	-0.000251	-0.000298	2.54669	0.00547	60697	
	2.473	0.000193	-0.000192	-0.000251	-0.000298	2.48489	0.00015	51242	
	2.364	0.000169	-0.000187	-0.000230	-0.000274	2.42927	0.00431	43417	
	2.364	0.000169	-0.000183	-0.000230	-0.000274	2.37365	0.00010	36239	
	2.364	0.000169	-0.000179	-0.000230	-0.000274	2.31803	0.00208	29710	
	2.291	0.000155	-0.000175	-0.000217	-0.000258	2.26550	0.00065	24139	
	2.182	0.000135	-0.000170	-0.000198	-0.000235	2.20679	0.00062	18596	
	2.109	0.000122	-0.000165	-0.000186	-0.000220	2.14808	0.00152	13775	
	2.182	0.000135	-0.000161	-0.000198	-0.000235	2.09555	0.00744	10073	
	2.109	0.000122	-0.000157	-0.000186	-0.000220	2.03993	0.00478	6784	
	2.000	0.000105	-0.000152	-0.000168	-0.000199	1.98122	0.00035	4015	
	2.000	0.000105	-0.000148	-0.000168	-0.000199	1.92251	0.00601	1968	
	2.000	0.000105	-0.000143	-0.000168	-0.000199	1.86689	0.01772	695	
	1.818	0.000080	-0.000139	-0.000140	-0.000166	1.80818	0.00010	54	
	1.891	0.000090	-0.000134	-0.000151	-0.000179	1.74947	0.02001	135	
	1.709	0.000067	-0.000130	-0.000125	-0.000148	1.69694	0.00015	820	
	1.636	0.000060	-0.000126	-0.000115	-0.000136	1.64750	0.00012	1992	
	1.636	0.000060	-0.000122	-0.000115	-0.000136	1.58879	0.00226	4049	
	1.455	0.000043	-0.000117	-0.000093	-0.000109	1.53008	0.00571	6828	
	1.455	0.000043	-0.000112	-0.000093	-0.000109	1.47137	0.00028	10329	
	1.455	0.000043	-0.000109	-0.000093	-0.000109	1.42193	0.00106	13838	
	1.345	0.000035	-0.000104	-0.000080	-0.000094	1.36631	0.00043	18396	
	1.273	0.000030	-0.000100	-0.000072	-0.000085	1.30760	0.00122	23911	
	1.200	0.000025	-0.000095	-0.000065	-0.000076	1.24889	0.00239	30149	
	1.200	0.000025	-0.000091	-0.000065	-0.000076	1.19945	0.00000	35961	upper
	1.091	0.000019	-0.000086	-0.000055	-0.000064	1.13765	0.00218	43946	-0.00324
	1.018	0.000016	-0.000082	-0.000048	-0.000056	1.08203	0.00408	51817	lower
	1.018	0.000016	-0.000078	-0.000048	-0.000056	1.03259	0.00021	59357	-0.00294
	1.018	0.000016	-0.000075	-0.000048	-0.000056	0.99860	0.00038	64838	

Table A10.10b - Dissipation force data from Stamp & Jacka (1995), ω = 0.0485

Stamp & Jacka, ω = 0.0485			Infinitesimal Wave Speed Parameters					Wave Energy Parameters					
			ω	h	H/h	δ	c_0	ν	ρ_2		-da/dx		w
			0.0485	0.0028	55		0.0244	1.07E-06	1046.50		0.00309		0.15
Fluid Drag			Wall Drag			eqn 8.40	dE/dx +	dE/dx -	calculated			Calculated
c^2 a	wρc^2a	x C_D	3.31ρc^2aλ	Re_λ	Drag	dE/dx	Wall Drag	Wall Drag	C_D	Re_a	C_D x ω^1/3	Total Drag
(m^3/s^2)	(N)	(N)	(N)		(N)	(J/m)		(N)				(N)
0.0000218	0.003416	0.000234	0.001212	850	0.000042	0.000251	6.040	0.000210	0.070	719	0.025	0.000276
0.0000218	0.003416	0.000234	0.001212	850	0.000042	0.000251	6.040	0.000210	0.070	719	0.025	0.000276
0.0000218	0.003416	0.000234	0.001212	850	0.000042	0.000251	6.040	0.000210	0.070	719	0.025	0.000276
0.0000198	0.003109	0.000213	0.001061	798	0.000038	0.000230	6.134	0.000193	0.070	671	0.026	0.000251
0.0000198	0.003109	0.000213	0.001061	798	0.000038	0.000230	6.134	0.000193	0.070	671	0.026	0.000251
0.0000198	0.003109	0.000213	0.001061	798	0.000038	0.000230	6.134	0.000193	0.070	671	0.026	0.000251
0.0000186	0.002915	0.000200	0.000969	764	0.000035	0.000217	6.197	0.000182	0.070	639	0.026	0.000235
0.0000168	0.002638	0.000181	0.000841	714	0.000031	0.000198	6.292	0.000166	0.071	594	0.026	0.000212
0.0000157	0.002463	0.000169	0.000763	682	0.000029	0.000186	6.356	0.000156	0.071	564	0.026	0.000198
0.0000168	0.002638	0.000181	0.000841	714	0.000031	0.000198	6.292	0.000166	0.071	594	0.026	0.000212
0.0000157	0.002463	0.000169	0.000763	682	0.000029	0.000186	6.356	0.000156	0.071	564	0.026	0.000198
0.0000141	0.002214	0.000152	0.000656	635	0.000026	0.000168	6.453	0.000142	0.072	521	0.026	0.000178
0.0000141	0.002214	0.000152	0.000656	635	0.000026	0.000168	6.453	0.000142	0.072	521	0.026	0.000178
0.0000141	0.002214	0.000152	0.000656	635	0.000026	0.000168	6.453	0.000142	0.072	521	0.026	0.000178
0.0000117	0.001836	0.000126	0.000502	560	0.000021	0.000140	6.614	0.000119	0.073	452	0.027	0.000147
0.0000126	0.001982	0.000136	0.000560	590	0.000023	0.000151	6.550	0.000128	0.073	479	0.026	0.000159
0.0000104	0.001630	0.000112	0.000424	517	0.000019	0.000125	6.710	0.000106	0.074	413	0.027	0.000130
0.0000096	0.001500	0.000103	0.000376	490	0.000017	0.000115	6.773	0.000098	0.074	388	0.027	0.000120
0.0000096	0.001500	0.000103	0.000376	490	0.000017	0.000115	6.773	0.000098	0.074	388	0.027	0.000120
0.0000077	0.001205	0.000083	0.000275	424	0.000013	0.000093	6.925	0.000079	0.076	328	0.028	0.000096
0.0000077	0.001205	0.000083	0.000275	424	0.000013	0.000093	6.925	0.000079	0.076	328	0.028	0.000096
0.0000077	0.001205	0.000083	0.000275	424	0.000013	0.000093	6.925	0.000079	0.076	328	0.028	0.000096
0.0000067	0.001046	0.000072	0.000225	386	0.000011	0.000080	7.010	0.000069	0.077	294	0.028	0.000083
0.0000060	0.000948	0.000065	0.000195	362	0.000010	0.000072	7.063	0.000062	0.078	272	0.029	0.000075
0.0000054	0.000855	0.000059	0.000168	338	0.000009	0.000065	7.113	0.000056	0.079	251	0.029	0.000068
0.0000054	0.000855	0.000059	0.000168	338	0.000009	0.000065	7.113	0.000056	0.079	251	0.029	0.000068
0.0000046	0.000725	0.000050	0.000133	304	0.000008	0.000055	7.178	0.000047	0.081	220	0.030	0.000057
0.0000041	0.000646	0.000044	0.000112	283	0.000007	0.000048	7.214	0.000042	0.082	201	0.030	0.000051
0.0000041	0.000646	0.000044	0.000112	283	0.000007	0.000048	7.214	0.000042	0.082	201	0.030	0.000051
0.0000041	0.000646	0.000044	0.000112	283	0.000007	0.000048	7.214	0.000042	0.082	201	0.030	0.000051

Table A10.11a - Wave energy data from Stamp & Jacka (1995), ω = 0.0707

S&J, ω = 0.0707		Wave Energy Parameters				error bar calculations			
		ρ2	Δρ	-da/dx	w	n=	30	s^2=	0.00725
		1068.70	151.11	0.00280	0.15	Bhat=	-0.00280	xbar=	290.67
(start)	amplitude	wave	curve fit	eqn 8.40	eqn 8.41	t(0.025)=	2.045	sum xi^2=	903493
timeprint	*a/h*	energy	dE/dx	dE/dx	dE/dx				
(n/a)		(J)	(J/m)	(J/m)	(J/m)	Yhat	(Y-Yhat)^2	xi^2	
	3.120	0.000421	-0.000404	-0.000437	-0.000521	2.97670	0.02054	84487	
	2.920	0.000348	-0.000392	-0.000385	-0.000458	2.92350	0.00001	73803	
	2.800	0.000308	-0.000380	-0.000355	-0.000423	2.86750	0.00456	63336	
	2.800	0.000308	-0.000367	-0.000355	-0.000423	2.81150	0.00013	53669	
	2.800	0.000308	-0.000354	-0.000355	-0.000423	2.75270	0.00224	44380	
	2.720	0.000283	-0.000341	-0.000336	-0.000400	2.69110	0.00084	35595	
	2.640	0.000260	-0.000330	-0.000317	-0.000377	2.64070	0.00000	29127	
	2.640	0.000260	-0.000317	-0.000317	-0.000377	2.58470	0.00306	22700	
	2.400	0.000198	-0.000305	-0.000264	-0.000314	2.52870	0.01656	17074	
	2.400	0.000198	-0.000292	-0.000264	-0.000314	2.47270	0.00529	12247	
	2.320	0.000180	-0.000280	-0.000248	-0.000294	2.41670	0.00935	8220	
	2.200	0.000154	-0.000268	-0.000224	-0.000266	2.36070	0.02582	4994	
	2.320	0.000180	-0.000255	-0.000248	-0.000294	2.30470	0.00023	2567	
	2.200	0.000154	-0.000243	-0.000224	-0.000266	2.24870	0.00237	940	
	2.120	0.000139	-0.000231	-0.000209	-0.000248	2.19270	0.00529	114	
	2.320	0.000180	-0.000217	-0.000248	-0.000294	2.13110	0.03568	128	
	2.120	0.000139	-0.000205	-0.000209	-0.000248	2.07510	0.00202	982	
	2.000	0.000118	-0.000192	-0.000187	-0.000222	2.01910	0.00036	2635	
	2.000	0.000118	-0.000180	-0.000187	-0.000222	1.96310	0.00136	5088	
	2.000	0.000118	-0.000167	-0.000187	-0.000222	1.90710	0.00863	8342	
	2.000	0.000118	-0.000155	-0.000187	-0.000222	1.85110	0.02217	12395	
	1.800	0.000087	-0.000142	-0.000154	-0.000181	1.79230	0.00006	17512	
	1.720	0.000077	-0.000130	-0.000141	-0.000166	1.73630	0.00027	23205	
	1.800	0.000087	-0.000117	-0.000154	-0.000181	1.68030	0.01433	29699	
	1.600	0.000063	-0.000107	-0.000123	-0.000145	1.63270	0.00107	35847	
	1.520	0.000054	-0.000094	-0.000112	-0.000132	1.57670	0.00321	43820	upper
	1.400	0.000043	-0.000081	-0.000096	-0.000113	1.51510	0.01325	53515	-0.00298
	1.400	0.000043	-0.000068	-0.000096	-0.000113	1.45910	0.00349	63168	lower
	1.400	0.000043	-0.000056	-0.000096	-0.000113	1.40310	0.00001	73622	-0.00262
	1.400	0.000043	-0.000049	-0.000096	-0.000113	1.36950	0.00093	80278	

Table A10.11b - Dissipation force data from Stamp & Jacka (1995), ω = 0.0707

Stamp & Jacka, ω = 0.0707	Infinitesimal Wave Speed Parameters					Wave Energy Parameters				
	ω	*h*	*H/h*	*δ*	*c0*	*v*	*ρ2*	*-da/dx*		*w*
	0.0707	0.0025	60		0.0294	1.11E-06	1068.70	0.00280		0.15

Fluid Drag			Wall Drag			eqn 8.40	dE/dx +	dE/dx -	calculated			Calculated
c^2 a	wρc^2a	x C_D	3.31ρc^2aλ	Re_λ	Drag	dE/dx	Wall Drag	Wall Drag	C_D	Re_*	C_D x ω^1/3	Total Drag
(m^3/s^2)	(N)	(N)	(N)		(N)	(J/m)		(N)				(N)
0.0000432	0.006932	0.000419	0.002744	1203	0.000079	0.000437	5.525	0.000358	0.061	1046	0.025	0.000498
0.0000374	0.005995	0.000362	0.002238	1091	0.000068	0.000385	5.680	0.000317	0.062	941	0.026	0.000430
0.0000341	0.005474	0.000331	0.001969	1026	0.000061	0.000355	5.775	0.000294	0.062	881	0.026	0.000392
0.0000341	0.005474	0.000331	0.001969	1026	0.000061	0.000355	5.775	0.000294	0.062	881	0.026	0.000392
0.0000341	0.005474	0.000331	0.001969	1026	0.000061	0.000355	5.775	0.000294	0.062	881	0.026	0.000392
0.0000321	0.005143	0.000311	0.001803	983	0.000058	0.000336	5.840	0.000278	0.062	842	0.026	0.000368
0.0000301	0.004825	0.000292	0.001648	942	0.000054	0.000317	5.906	0.000264	0.063	803	0.026	0.000345
0.0000301	0.004825	0.000292	0.001648	942	0.000054	0.000317	5.906	0.000264	0.063	803	0.026	0.000345
0.0000246	0.003948	0.000239	0.001242	823	0.000043	0.000264	6.109	0.000221	0.063	693	0.026	0.000282
0.0000246	0.003948	0.000239	0.001242	823	0.000043	0.000264	6.109	0.000221	0.063	693	0.026	0.000282
0.0000230	0.003680	0.000223	0.001124	784	0.000040	0.000248	6.178	0.000208	0.064	658	0.026	0.000263
0.0000206	0.003301	0.000200	0.000963	729	0.000036	0.000224	6.283	0.000188	0.064	606	0.027	0.000235
0.0000230	0.003680	0.000223	0.001124	784	0.000040	0.000248	6.178	0.000208	0.064	658	0.026	0.000263
0.0000206	0.003301	0.000200	0.000963	729	0.000036	0.000224	6.283	0.000188	0.064	606	0.027	0.000235
0.0000191	0.003062	0.000185	0.000866	693	0.000033	0.000209	6.354	0.000176	0.065	573	0.027	0.000218
0.0000230	0.003680	0.000223	0.001124	784	0.000040	0.000248	6.178	0.000208	0.064	658	0.026	0.000263
0.0000191	0.003062	0.000185	0.000866	693	0.000033	0.000209	6.354	0.000176	0.065	573	0.027	0.000218
0.0000170	0.002724	0.000165	0.000733	641	0.000029	0.000187	6.460	0.000158	0.065	525	0.027	0.000194
0.0000170	0.002724	0.000165	0.000733	641	0.000029	0.000187	6.460	0.000158	0.065	525	0.027	0.000194
0.0000170	0.002724	0.000165	0.000733	641	0.000029	0.000187	6.460	0.000158	0.065	525	0.027	0.000194
0.0000170	0.002724	0.000165	0.000733	641	0.000029	0.000187	6.460	0.000158	0.065	525	0.027	0.000194
0.0000138	0.002215	0.000134	0.000546	558	0.000023	0.000154	6.638	0.000130	0.066	449	0.027	0.000157
0.0000127	0.002029	0.000123	0.000482	526	0.000021	0.000141	6.708	0.000120	0.067	420	0.028	0.000144
0.0000138	0.002215	0.000134	0.000546	558	0.000023	0.000154	6.638	0.000130	0.066	449	0.027	0.000157
0.0000110	0.001769	0.000107	0.000396	480	0.000018	0.000123	6.812	0.000105	0.068	379	0.028	0.000125
0.0000100	0.001608	0.000097	0.000346	451	0.000016	0.000112	6.879	0.000096	0.068	352	0.028	0.000113
0.0000086	0.001383	0.000084	0.000278	408	0.000014	0.000096	6.976	0.000082	0.069	313	0.029	0.000097
0.0000086	0.001383	0.000084	0.000278	408	0.000014	0.000096	6.976	0.000082	0.069	313	0.029	0.000097
0.0000086	0.001383	0.000084	0.000278	408	0.000014	0.000096	6.976	0.000082	0.069	313	0.029	0.000097
0.0000086	0.001383	0.000084	0.000278	408	0.000014	0.000096	6.976	0.000082	0.069	313	0.029	0.000097

Table A10.12a - Wave energy data from Stamp & Jacka (1995), $\omega = 0.0917$

S&J, $\omega = 0.917$		Wave Energy Parameters				error bar calculations			
		ρ_2	$\Delta\rho$	-da/dx	w	n=	29	s^2=	0.01169
		1089.70	199.85	0.00248	0.15	Bhat=	-0.00248	xbar=	279.66
(start)	amplitude	wave	curve fit	eqn 8.40	eqn 8.41	t(0.025)=	2.048	sum xi^2=	806497
timeprint	*a/h*	energy	dE/dx	dE/dx	dE/dx				
(n/a)		(J)	(J/m)	(J/m)	(J/m)	Yhat	(Y-Yhat)^2	xi^2	
	2.920	0.000460	-0.000310	-0.000451	-0.000537	2.91372	0.00004	78207	
	2.920	0.000460	-0.000307	-0.000451	-0.000537	2.86412	0.00312	67421	
	2.720	0.000375	-0.000303	-0.000393	-0.000468	2.81452	0.00893	57435	
	2.600	0.000329	-0.000300	-0.000361	-0.000429	2.76492	0.02720	48248	
	2.600	0.000329	-0.000297	-0.000361	-0.000429	2.71532	0.01330	39862	
	2.600	0.000329	-0.000294	-0.000361	-0.000429	2.66572	0.00432	32276	
	2.600	0.000329	-0.000290	-0.000361	-0.000429	2.61612	0.00026	25490	
	2.520	0.000301	-0.000287	-0.000340	-0.000404	2.56652	0.00216	19504	
	2.520	0.000301	-0.000284	-0.000340	-0.000404	2.51692	0.00001	14317	
	2.520	0.000301	-0.000280	-0.000340	-0.000404	2.46732	0.00278	9931	
	2.600	0.000329	-0.000277	-0.000361	-0.000429	2.41772	0.03323	6345	
	2.400	0.000262	-0.000274	-0.000310	-0.000368	2.36812	0.00102	3559	
	2.400	0.000262	-0.000270	-0.000310	-0.000368	2.31852	0.00664	1573	
	2.200	0.000204	-0.000267	-0.000263	-0.000311	2.26892	0.00475	386	
	2.520	0.000301	-0.000264	-0.000340	-0.000404	2.21932	0.09041	0	
	2.000	0.000156	-0.000261	-0.000219	-0.000260	2.16972	0.02880	414	
	2.200	0.000204	-0.000257	-0.000263	-0.000311	2.12012	0.00638	1628	
	2.120	0.000184	-0.000254	-0.000245	-0.000290	2.07052	0.00245	3641	
	2.200	0.000204	-0.000251	-0.000263	-0.000311	2.02092	0.03207	6455	
	2.000	0.000156	-0.000247	-0.000219	-0.000260	1.97132	0.00082	10069	
	2.000	0.000156	-0.000244	-0.000219	-0.000260	1.92172	0.00613	14483	
	1.920	0.000139	-0.000241	-0.000203	-0.000240	1.87212	0.00229	19697	
	1.800	0.000115	-0.000237	-0.000180	-0.000213	1.82252	0.00051	25710	
	1.720	0.000102	-0.000234	-0.000165	-0.000195	1.77292	0.00280	32524	
	1.600	0.000083	-0.000231	-0.000144	-0.000170	1.72332	0.01521	40138	upper
	1.600	0.000083	-0.000228	-0.000144	-0.000170	1.67372	0.00543	48552	-0.00273
	1.520	0.000072	-0.000224	-0.000131	-0.000154	1.62412	0.01084	57766	lower
	1.520	0.000072	-0.000221	-0.000131	-0.000154	1.57452	0.00297	67779	-0.00223
	1.520	0.000072	-0.000219	-0.000131	-0.000154	1.54972	0.00088	73086	

Table A10.12b - Dissipation force data from Stamp & Jacka (1995), ω = 0.0917

Stamp & Jacka, ω = 0.917			Infinitesimal Wave Speed Parameters					Wave Energy Parameters					
			ω	h	H/h	δ	c_0	ν	ρ_2	-da/dx			w
			0.0917	0.0025	60		0.0335	1.17E-06	1089.70	0.00248			0.15
Fluid Drag			Wall Drag			eqn 8.40	dE/dx +	dE/dx -	calculated			Calculated
c^2 a	wρc^2a	x C_D	3.31ρc^2aλ	Re_λ	Drag	dE/dx	Wall Drag	Wall Drag	C_D	Re_a	C_D x ω^1/3	Total Drag
(m^3/s^2)	(N)	(N)	(N)		(N)	(J/m)		(N)				(N)
0.0000485	0.007928	0.000440	0.002959	1178	0.000086	0.000451	5.229	0.000365	0.054	1017	0.024	0.000526
0.0000485	0.007928	0.000440	0.002959	1178	0.000086	0.000451	5.229	0.000365	0.054	1017	0.024	0.000526
0.0000416	0.006802	0.000377	0.002385	1062	0.000073	0.000393	5.377	0.000320	0.054	909	0.025	0.000450
0.0000378	0.006178	0.000342	0.002082	996	0.000066	0.000361	5.468	0.000295	0.055	847	0.025	0.000408
0.0000378	0.006178	0.000342	0.002082	996	0.000066	0.000361	5.468	0.000295	0.055	847	0.025	0.000408
0.0000378	0.006178	0.000342	0.002082	996	0.000066	0.000361	5.468	0.000295	0.055	847	0.025	0.000408
0.0000378	0.006178	0.000342	0.002082	996	0.000066	0.000361	5.468	0.000295	0.055	847	0.025	0.000408
0.0000354	0.005783	0.000321	0.001897	952	0.000061	0.000340	5.530	0.000279	0.055	807	0.025	0.000382
0.0000354	0.005783	0.000321	0.001897	952	0.000061	0.000340	5.530	0.000279	0.055	807	0.025	0.000382
0.0000354	0.005783	0.000321	0.001897	952	0.000061	0.000340	5.530	0.000279	0.055	807	0.025	0.000382
0.0000378	0.006178	0.000342	0.002082	996	0.000066	0.000361	5.468	0.000295	0.055	847	0.025	0.000408
0.0000319	0.005222	0.000289	0.001642	889	0.000055	0.000310	5.625	0.000255	0.055	748	0.025	0.000345
0.0000319	0.005222	0.000289	0.001642	889	0.000055	0.000310	5.625	0.000255	0.055	748	0.025	0.000345
0.0000267	0.004365	0.000242	0.001274	788	0.000045	0.000263	5.785	0.000217	0.056	655	0.025	0.000287
0.0000354	0.005783	0.000321	0.001897	952	0.000061	0.000340	5.530	0.000279	0.055	807	0.025	0.000382
0.0000220	0.003603	0.000200	0.000970	692	0.000037	0.000219	5.948	0.000182	0.057	567	0.026	0.000237
0.0000267	0.004365	0.000242	0.001274	788	0.000045	0.000263	5.785	0.000217	0.056	655	0.025	0.000287
0.0000248	0.004049	0.000224	0.001145	749	0.000042	0.000245	5.850	0.000203	0.056	619	0.025	0.000266
0.0000267	0.004365	0.000242	0.001274	788	0.000045	0.000263	5.785	0.000217	0.056	655	0.025	0.000287
0.0000220	0.003603	0.000200	0.000970	692	0.000037	0.000219	5.948	0.000182	0.057	567	0.026	0.000237
0.0000220	0.003603	0.000200	0.000970	692	0.000037	0.000219	5.948	0.000182	0.057	567	0.026	0.000237
0.0000203	0.003323	0.000184	0.000865	656	0.000034	0.000203	6.013	0.000169	0.057	534	0.026	0.000218
0.0000179	0.002930	0.000162	0.000722	603	0.000029	0.000180	6.111	0.000150	0.058	485	0.026	0.000192
0.0000164	0.002684	0.000149	0.000638	569	0.000027	0.000165	6.176	0.000138	0.058	454	0.026	0.000176
0.0000143	0.002340	0.000130	0.000524	519	0.000023	0.000144	6.271	0.000121	0.059	409	0.027	0.000153
0.0000143	0.002340	0.000130	0.000524	519	0.000023	0.000144	6.271	0.000121	0.059	409	0.027	0.000153
0.0000130	0.002126	0.000118	0.000457	487	0.000021	0.000131	6.333	0.000110	0.060	380	0.027	0.000139
0.0000130	0.002126	0.000118	0.000457	487	0.000021	0.000131	6.333	0.000110	0.060	380	0.027	0.000139
0.0000130	0.002126	0.000118	0.000457	487	0.000021	0.000131	6.333	0.000110	0.060	380	0.027	0.000139

Appendix 11 - Numerical Modelling Procedure

In an attempt to improve on the numerical models of Davis & Acrivos (1967) and Tung, Chan & Kubota (1982), a model based on the two-dimensional Navier-Stokes equations was created. This avoided the inviscid assumptions of preceding studies and considered unsteady flows to allow the modelling of wave generation as well as propagation and decay.

A11.1 - Overview

The model used a staggered grid method, as described by Fletcher (1988), in which u and v velocities as well as pressures were all evaluated at different points on the grid into which the experimental domain was discretised. The two Navier-Stokes equations were discretised according to a third order scheme as used by Davis & Moore (1982), upon which expressions for fluid velocities at adjacent time steps were substituted into the continuity equation to produce an equation which could be solved to describe the pressure field.

This method allowed the explicit solution of the set of governing equations, as the pressure field solution at time step $n+1$ was based on fluid velocities at time step n, with the two dimensional velocity field at time step $n+1$ then being based on the velocity field at time step n and the pressure field at time step $n+1$. An iterative Poisson solver was used to solve for the pressure field, and a marker-and-cell (MAC) method, as first used by Harlow & Welch (1965), was used to keep track of the density of fluid at specific points as it convected through the grid.

Problems with computational instability meant that only very limited success was achieved with this model. A large computational domain combined with small time steps yielded a very slow running program that became unstable in the early stages of wave generation, precluding any examination of fully fledged waves. The computational scheme, program and results are included here to assist in future research.

A11.2 - Algorithm Details

The governing equations for this model were based on Fletcher (1988) and Davis & Moore (1982). The latter's third-order approximation of the two-dimensional Navier-Stokes equations was used and these two equations were used in conjunction with the continuity equation. A description of the derivation and discretisation of the governing equations follows.

A11.2.1 - Explicit algorithm for *u*-velocity

Begin with the Navier-Stokes equation in the *x*-direction:

$$\rho g_x - \frac{\partial p}{\partial x} + \frac{\partial \tau_{xx}}{\partial x} + \frac{\partial \tau_{yx}}{\partial y} + \frac{\partial \tau_{zx}}{\partial z} = \rho\left(\frac{\partial u}{\partial t} + u\frac{\partial u}{\partial x} + v\frac{\partial u}{\partial y} + w\frac{\partial u}{\partial z}\right) \quad \text{(A11.1)}$$

Dropping terms which go to zero (body force as $g_x = 0$, all derivatives with respect to *z* due to 2-dimensional flow) and substituting in for shear stress terms yields:

$$\frac{\partial u}{\partial t} + u\frac{\partial u}{\partial x} + v\frac{\partial u}{\partial y} = -\frac{1}{\rho}\frac{\partial p}{\partial x} + \nu\frac{\partial^2 u}{\partial x^2} + \nu\frac{\partial^2 u}{\partial y^2} \quad \text{(A11.2)}$$

To construct a higher-order discretisation for this equation, the technique described in Davis & Moore (1982) is followed. Expanding *u* about time level *n* yields:

$$u^{n+1} = u^n + \Delta t\left.\frac{\partial u}{\partial t}\right|^n + \frac{1}{2}\Delta t^2\left.\frac{\partial^2 u}{\partial t^2}\right|^n + \frac{1}{6}\Delta t^3\left.\frac{\partial^3 u}{\partial t^3}\right|^n + O\left(\Delta t^4\right) \quad \text{(A11.3)}$$

Equation A11.2 is then rearranged and differentiated (recognising that $dx = udt$) to provide expressions for the derivative terms in Equation A11.3:

$$\frac{\partial u}{\partial t} = -\frac{1}{\rho}\frac{\partial p}{\partial x} - u\frac{\partial u}{\partial x} - v\frac{\partial u}{\partial y} + \nu\frac{\partial^2 u}{\partial x^2} + \nu\frac{\partial^2 u}{\partial y^2} \quad \text{(A11.4)}$$

$$\frac{\partial^2 u}{\partial t^2} = \frac{u}{\rho}\frac{\partial^2 p}{\partial x^2} + u^2\frac{\partial^2 u}{\partial x^2} + v^2\frac{\partial^2 u}{\partial y^2} - 2vu\frac{\partial^3 u}{\partial x^3} - 2v\nu\frac{\partial^3 u}{\partial y^3} \quad \text{(A11.5)}$$

$$\frac{\partial^3 u}{\partial t^3} = -\frac{u^2}{\rho}\frac{\partial^3 p}{\partial x^3} - u^3\frac{\partial^3 u}{\partial x^3} - v^3\frac{\partial^3 u}{\partial y^3} \tag{A11.6}$$

Note that in Equation A11.6, fourth-order spatial derivatives have been neglected. Equations A11.4-6 are then substituted into Equation A11.3 to produce:

$$\begin{aligned} u^{n+1} = u^n + \Delta t\left(-\frac{1}{\rho}\frac{\partial p}{\partial x} - u\frac{\partial u}{\partial x} - v\frac{\partial u}{\partial y} + \nu\frac{\partial^2 u}{\partial x^2} + \nu\frac{\partial^2 u}{\partial y^2}\right)^n \\ + \frac{1}{2}\Delta t^2\left(\frac{u}{\rho}\frac{\partial^2 p}{\partial x^2} + u^2\frac{\partial^2 u}{\partial x^2} + v^2\frac{\partial^2 u}{\partial y^2} - 2vu\frac{\partial^3 u}{\partial x^3} - 2vv\frac{\partial^3 u}{\partial y^3}\right)^n \\ + \frac{1}{6}\Delta t^3\left(-\frac{u^2}{\rho}\frac{\partial^3 p}{\partial x^3} - u^3\frac{\partial^3 u}{\partial x^3} - v^3\frac{\partial^3 u}{\partial y^3}\right)^n \end{aligned} \tag{A11.7}$$

Equation A11.7 is then rearranged as:

$$\begin{aligned} u^{n+1} = u^n - \Delta t\frac{1}{\rho}\frac{\partial p}{\partial x} - \Delta tu\frac{\partial u}{\partial x} - \Delta tv\frac{\partial u}{\partial y} + \Delta t\nu\frac{\partial^2 u}{\partial x^2} + \Delta t\nu\frac{\partial^2 u}{\partial y^2} \\ + \frac{1}{2}\Delta t^2\frac{u}{\rho}\frac{\partial^2 p}{\partial x^2} + \frac{1}{2}\Delta t^2u^2\frac{\partial^2 u}{\partial x^2} + \frac{1}{2}\Delta t^2v^2\frac{\partial^2 u}{\partial y^2} - \Delta t^2\nu u\frac{\partial^3 u}{\partial x^3} - \Delta t^2\nu v\frac{\partial^3 u}{\partial y^3} \\ - \frac{1}{6}\Delta t^3\frac{u^2}{\rho}\frac{\partial^3 p}{\partial x^3} - \frac{1}{6}\Delta t^3u^3\frac{\partial^3 u}{\partial x^3} - \frac{1}{6}\Delta t^3v^3\frac{\partial^3 u}{\partial y^3} \end{aligned} \tag{A11.8}$$

This equation is then discretised according to the scheme defined in Figure A11.1, and simplified by defining two Courant numbers, $C_x = u_{j+1/2,k}\Delta t/\Delta x$ and $C_y = v_{j+1/2,k}\Delta t/\Delta y$ and two inverse Reynolds numbers as $\gamma_x = \nu\Delta t/\Delta x^2$ and $\gamma_y = \nu\Delta t/\Delta y^2$. This results in Equations A11.10-11, which may be solved explicitly for the *u*-velocity at time step $n+1$, if the pressure field at that time step is known.

$$\begin{aligned} u_{j+1/2,k}^{n+1} = F_{j+1/2,k}^n - \frac{\Delta t}{\Delta x}\frac{1}{\rho}\left(p_{j+1,k}^{n+1} - p_{j,k}^{n+1}\right) \\ + \frac{1}{4}\frac{\Delta t}{\Delta x}\frac{C_x}{\rho}\left(p_{j+2,k}^{n+1} - p_{j+1,k}^{n+1} - p_{j,k}^{n+1} + p_{j-1,k}^{n+1}\right) \\ - \frac{1}{6}\frac{\Delta t}{\Delta x}\frac{C_x^2}{\rho}\left(p_{j+2,k}^{n+1} - 3p_{j+1,k}^{n+1} - 3p_{j,k}^{n+1} + p_{j-1,k}^{n+1}\right) \end{aligned} \tag{A11.10}$$

Where:

$$
\begin{aligned}
F^n_{j+1/2,k} = u^n_{j+1/2,k} &- \frac{1}{2}C_x\left(u^n_{j+3/2,k} - u^n_{j-1/2,k}\right) - \frac{1}{2}C_y\left(u^n_{j+1/2,k-1} - u^n_{j+1/2,k+1}\right) \\
&+ \left(\gamma_x + \frac{1}{2}C_x^2\right)\left(u^n_{j+3/2,k} - 2u^n_{j+1/2,k} + u^n_{j-1/2,k}\right) \\
&+ \left(\gamma_y + \frac{1}{2}C_y^2\right)\left(u^n_{j+1/2,k-1} - 2u^n_{j+1/2,k} + u^n_{j+1/2,k+1}\right) \\
&- \left(\frac{1}{6}C_x^3 + C_x\gamma_x\right)\left(u^n_{j+3/2,k} - 3u^n_{j+1/2,k} - 3u^n_{j-1/2,k} + u^n_{j-3/2,k}\right) \\
&- \left(\frac{1}{6}C_y^3 + C_y\gamma_y\right)\left(u^n_{j+1/2,k-1} - 3u^n_{j+1/2,k} - 3u^n_{j+1/2,k+1} + u^n_{j+1/2,k+2}\right)
\end{aligned}
\qquad \text{(A11.11)}
$$

The Courant, C, and inverse Reynolds, γ, numbers are further defined as:

$$
\begin{aligned}
C_x &= u_{j+1/2,k}\frac{\Delta t}{\Delta x} \qquad C_y = \frac{v_{j+1,k+1/2} + v_{j+1,k-1/2} + v_{j,k+1/2} + v_{j,k-1/2}}{4}\frac{\Delta t}{\Delta y} \\
\gamma_x &= \nu\frac{\Delta t}{\Delta x^2} \qquad \gamma_y = \nu\frac{\Delta t}{\Delta y^2}
\end{aligned}
\qquad \text{(A11.12)}
$$

Equations A11.10-12 are then used in the computer program as described in Sections A11.4-5.

A11.2.2 - Explicit algorithm for new v-velocity

Begin with the Navier-Stokes equation in the y-direction:

$$
\rho g_y - \frac{\partial p}{\partial y} + \frac{\partial \tau_{xy}}{\partial x} + \frac{\partial \tau_{yy}}{\partial y} + \frac{\partial \tau_{zy}}{\partial z} = \rho\left(\frac{\partial v}{\partial t} + u\frac{\partial v}{\partial x} + v\frac{\partial v}{\partial y} + w\frac{\partial v}{\partial z}\right) \qquad \text{(A11.13)}
$$

Dropping terms which go to zero (all derivatives with respect to z due to 2-dimensional flow) and substituting in for shear stress terms yields:

$$
\frac{\partial v}{\partial t} + u\frac{\partial v}{\partial x} + v\frac{\partial v}{\partial y} = -\frac{1}{\rho}\frac{\partial p}{\partial y} + g_y + \nu\frac{\partial^2 v}{\partial x^2} + \nu\frac{\partial^2 v}{\partial y^2} \qquad \text{(A11.14)}
$$

To construct a higher-order discretisation for this equation, the technique described in Davis & Moore (1982) is followed. Expanding v about time level n yields:

$$v^{n+1} = v^n + \Delta t \frac{\partial v}{\partial t}\bigg|^n + \frac{1}{2}\Delta t^2 \frac{\partial^2 v}{\partial t^2}\bigg|^n + \frac{1}{6}\Delta t^3 \frac{\partial^3 v}{\partial t^3}\bigg|^n + O\left(\Delta t^4\right) \quad \text{(A11.15)}$$

Equation A11.14 is then rearranged and differentiated (recognising that $dy = vdt$) to provide expressions for the derivative terms in Equation A11.15:

$$\frac{\partial v}{\partial t} = -\frac{1}{\rho}\frac{\partial p}{\partial y} + g_y - u\frac{\partial v}{\partial x} - v\frac{\partial v}{\partial y} + \nu\frac{\partial^2 v}{\partial x^2} + \nu\frac{\partial^2 v}{\partial y^2} \quad \text{(A11.16)}$$

$$\frac{\partial^2 v}{\partial t^2} = \frac{\nu}{\rho}\frac{\partial^2 p}{\partial y^2} + u^2\frac{\partial^2 v}{\partial x^2} + v^2\frac{\partial^2 v}{\partial y^2} - 2vu\frac{\partial^3 v}{\partial x^3} - 2v\nu\frac{\partial^3 v}{\partial y^3} \quad \text{(A11.17)}$$

$$\frac{\partial^3 v}{\partial t^3} = -\frac{v^2}{\rho}\frac{\partial^3 p}{\partial y^3} - u^3\frac{\partial^3 v}{\partial x^3} - v^3\frac{\partial^3 v}{\partial y^3} \quad \text{(A11.18)}$$

Note that in Equation A11.18, fourth-order spatial derivatives have been neglected. Equations A11.16-18 are then substituted into Equation A11.15 to produce:

$$\begin{aligned} v^{n+1} = v^n &+ \Delta t\left(-\frac{1}{\rho}\frac{\partial p}{\partial y} + g_y - u\frac{\partial v}{\partial x} - v\frac{\partial v}{\partial y} + \nu\frac{\partial^2 v}{\partial x^2} + \nu\frac{\partial^2 v}{\partial y^2}\right)^n \\ &+ \frac{1}{2}\Delta t^2\left(\frac{\nu}{\rho}\frac{\partial^2 p}{\partial y^2} + u^2\frac{\partial^2 v}{\partial x^2} + v^2\frac{\partial^2 v}{\partial y^2} - 2vu\frac{\partial^3 v}{\partial x^3} - 2v\nu\frac{\partial^3 v}{\partial y^3}\right)^n \\ &+ \frac{1}{6}\Delta t^3\left(-\frac{v^2}{\rho}\frac{\partial^3 p}{\partial y^3} - u^3\frac{\partial^3 v}{\partial x^3} - v^3\frac{\partial^3 v}{\partial y^3}\right)^n \end{aligned} \quad \text{(A11.19)}$$

Equation A11.19 is then expanded as:

$$\begin{aligned} v^{n+1} = v^n &- \Delta t\frac{1}{\rho}\frac{\partial p}{\partial y} - g_y - \Delta tu\frac{\partial v}{\partial x} - \Delta tv\frac{\partial v}{\partial y} + \Delta t\nu\frac{\partial^2 v}{\partial x^2} + \Delta t\nu\frac{\partial^2 v}{\partial y^2} \\ &+ \frac{1}{2}\Delta t^2\frac{\nu}{\rho}\frac{\partial^2 p}{\partial y^2} + \frac{1}{2}\Delta t^2u^2\frac{\partial^2 v}{\partial x^2} + \frac{1}{2}\Delta t^2v^2\frac{\partial^2 v}{\partial y^2} - \Delta t^2vu\frac{\partial^3 v}{\partial x^3} - \Delta t^2v\nu\frac{\partial^3 v}{\partial y^3} \\ &- \frac{1}{6}\Delta t^3\frac{v^2}{\rho}\frac{\partial^3 p}{\partial y^3} - \frac{1}{6}\Delta t^3u^3\frac{\partial^3 v}{\partial x^3} - \frac{1}{6}\Delta t^3v^3\frac{\partial^3 v}{\partial y^3} \end{aligned} \quad \text{(A11.20)}$$

This equation is then discretised according to the scheme defined in Figure A11.1, and simplified by defining two Courant numbers, $C_x = u_{j+1/2,k}\Delta t/\Delta x$ and $C_y = v_{j+1/2,k}\Delta t/\Delta y$ and two inverse Reynolds numbers as $\gamma_x = \nu\Delta t/\Delta x^2$ and $\gamma_y = \nu\Delta t/\Delta y^2$.

This results in Equations A11.21-23, which may be solved explicitly for the *v*-velocity at time step *n+1*, if the pressure field at that time step is known.

$$\begin{aligned} v_{j,k+1/2}^{n+1} &= G_{j,k+1/2}^{n} - \frac{\Delta t}{\Delta y}\frac{1}{\rho}\left(p_{j,k}^{n+1} - p_{j,k+1}^{n+1}\right) \\ &+ \frac{1}{4}\frac{\Delta t}{\Delta y}\frac{C_y}{\rho}\left(p_{j,k-1}^{n+1} - p_{j,k}^{n+1} - p_{j,k+1}^{n+1} + p_{j,k+2}^{n+1}\right) \\ &- \frac{1}{6}\frac{\Delta t}{\Delta y}\frac{C_y^2}{\rho}\left(p_{j,k-1}^{n+1} - 3p_{j,k}^{n+1} - 3p_{j,k+1}^{n+1} + p_{j,k+2}^{n+1}\right) \end{aligned} \qquad \text{(A11.21)}$$

Where:

$$\begin{aligned} G_{j,k+1/2}^{n} &= v_{j,k+1/2}^{n} - \Delta t g_y \\ &- \frac{1}{2}C_x\left(v_{j+1,k+1/2}^{n} - v_{j-1,k+1/2}^{n}\right) - \frac{1}{2}C_y\left(v_{j,k-1/2}^{n} - v_{j,k+3/2}^{n}\right) \\ &+ \left(\gamma_x + \frac{1}{2}C_x^{\,2}\right)\left(v_{j+1,k+1/2}^{n} - 2v_{j,k+1/2}^{n} + v_{j-1,k+1/2}^{n}\right) \\ &+ \left(\gamma_y + \frac{1}{2}C_y^2\right)\left(v_{j,k-1/2}^{n} - 2v_{j,k+1/2}^{n} + v_{j,k+3/2}^{n}\right) \\ &- \left(C_x\gamma_x + \frac{1}{6}C_x^3\right)\left(v_{j+2,k+1/2}^{n} - 3v_{j+1,k+1/2}^{n} - 3v_{j,k+1/2}^{n} + v_{j-1,k+1/2}^{n}\right) \\ &- \left(C_y\gamma_y + \frac{1}{6}C_y^3\right)\left(v_{j,k-3/2}^{n} - 3v_{j,k-1/2}^{n} - 3v_{j,k+1/2}^{n} + v_{j,k+3/2}^{n}\right) \end{aligned} \qquad \text{(A11.22)}$$

The Courant (*different* from those in Equation A11.12) and inverse Reynolds numbers are further defined as:

$$C_x = \frac{u_{j+1/2,k} + u_{j+1/2,k+1} + u_{j-1/2,k+1} + u_{j-1/2,k}}{4}\frac{\Delta t}{\Delta x} \qquad C_y = v_{j,k+1/2}\frac{\Delta t}{\Delta y}$$
$$\gamma_x = \nu\frac{\Delta t}{\Delta x^2} \qquad \gamma_y = \nu\frac{\Delta t}{\Delta y^2} \qquad \text{(A11.23)}$$

Equations A11.21-23 are then used in the computer program as described in Sections A11.4-5.

A11.2.3 - Iterative solution for new pressure field

The pressure field at the next time step is solved for using the continuity equation:

$$\frac{\partial u}{\partial x} + \frac{\partial v}{\partial y} = 0 \tag{A11.24}$$

which is discretised as:

$$D_{j,k}^{n+1} = \frac{\left(u_{j+1/2,k}^{n+1} - u_{j-1/2,k}^{n+1}\right)}{\Delta x} + \frac{\left(v_{j,k-1/2}^{n+1} - v_{j,k+1/2}^{n+1}\right)}{\Delta y} = 0 \tag{A11.25}$$

where $D_{j,k}$ is the dilatation for the cell. Equations (A11.10) and (A11.21) are then substituted into this equation to produce the following:

$$\begin{aligned}
0 = & \frac{F_{j+1/2,k}^{n} - \frac{\Delta t}{\Delta x}\frac{1}{\rho}\left(p_{j+1,k}^{n+1} - p_{j,k}^{n+1}\right) + \frac{1}{4}\frac{\Delta t}{\Delta x}\frac{C_{x;j+1/2,k}}{\rho}\left(p_{j+2,k}^{n+1} - p_{j+1,k}^{n+1} - p_{j,k}^{n+1} + p_{j-1,k}^{n+1}\right)}{\Delta x} \\
& - \frac{\frac{1}{6}\frac{\Delta t}{\Delta x}\frac{C_{x;j+1/2,k}^{2}}{\rho}\left(p_{j+2,k}^{n+1} - 3p_{j+1,k}^{n+1} - 3p_{j,k}^{n+1} + p_{j-1,k}^{n+1}\right)}{\Delta x} \\
& - \frac{F_{j-1/2,k}^{n} - \frac{\Delta t}{\Delta x}\frac{1}{\rho}\left(p_{j,k}^{n+1} - p_{j-1,k}^{n+1}\right) + \frac{1}{4}\frac{\Delta t}{\Delta x}\frac{C_{x;j-1/2,k}}{\rho}\left(p_{j+1,k}^{n+1} - p_{j,k}^{n+1} - p_{j-1,k}^{n+1} + p_{j-2,k}^{n+1}\right)}{\Delta x} \\
& + \frac{\frac{1}{6}\frac{\Delta t}{\Delta x}\frac{C_{x;j-1/2,k}^{2}}{\rho}\left(p_{j+1,k}^{n+1} - 3p_{j,k}^{n+1} - 3p_{j-1,k}^{n+1} + p_{j-2,k}^{n+1}\right)}{\Delta x} \\
& + \frac{G_{j,k-1/2}^{n} - \frac{\Delta t}{\Delta y}\frac{1}{\rho}\left(p_{j,k-1}^{n+1} - p_{j,k}^{n+1}\right) + \frac{1}{4}\frac{\Delta t}{\Delta y}\frac{C_{y;j,k-1/2}}{\rho}\left(p_{j,k-2}^{n+1} - p_{j,k-1}^{n+1} - p_{j,k}^{n+1} + p_{j,k+1}^{n+1}\right)}{\Delta y} \\
& - \frac{\frac{1}{6}\frac{\Delta t}{\Delta y}\frac{C_{y;j,k-1/2}^{2}}{\rho}\left(p_{j,k-2}^{n+1} - 3p_{j,k-1}^{n+1} - 3p_{j,k}^{n+1} + p_{j,k+1}^{n+1}\right)}{\Delta y} \\
& - \frac{G_{j,k+1/2}^{n} - \frac{\Delta t}{\Delta y}\frac{1}{\rho}\left(p_{j,k}^{n+1} - p_{j,k+1}^{n+1}\right) + \frac{1}{4}\frac{\Delta t}{\Delta y}\frac{C_{y;j,k+1/2}}{\rho}\left(p_{j,k-1}^{n+1} - p_{j,k}^{n+1} - p_{j,k+1}^{n+1} + p_{j,k+2}^{n+1}\right)}{\Delta y} \\
& + \frac{\frac{1}{6}\frac{\Delta t}{\Delta y}\frac{C_{y;j,k+1/2}^{2}}{\rho}\left(p_{j,k-1}^{n+1} - 3p_{j,k}^{n+1} - 3p_{j,k+1}^{n+1} + p_{j,k+2}^{n+1}\right)}{\Delta y}
\end{aligned} \tag{A11.26}$$

Which may be rearranged to yield:

$$
\begin{aligned}
&\frac{F_{j+1/2,k} - F_{j-1/2,k}}{\Delta x} + \frac{G_{j,k-1/2} - G_{j,k+1/2}}{\Delta x} \\
&= \frac{\Delta t}{\Delta x^2}\left[\frac{\left(p^{n+1}_{j+1,k} - p^{n+1}_{j,k}\right) - \frac{C_{x:j+1/2,k}}{4}\left(p^{n+1}_{j+2,k} - p^{n+1}_{j+1,k} - p^{n+1}_{j,k} + p^{n+1}_{j-1,k}\right)}{\left(\rho_{j+1,k} + \rho_{j,k}\right)/2}\right. \\
&\quad + \frac{\frac{C^2_{x:j+1/2,k}}{6}\left(p^{n+1}_{j+2,k} - 3p^{n+1}_{j+1,k} - 3p^{n+1}_{j,k} + p^{n+1}_{j-1,k}\right)}{\left(\rho_{j+1,k} + \rho_{j,k}\right)/2} \\
&\quad + \frac{-\left(p^{n+1}_{j,k} - p^{n+1}_{j-1,k}\right) + \frac{C_{x:j-1/2,k}}{4}\left(p^{n+1}_{j+1,k} - p^{n+1}_{j,k} - p^{n+1}_{j-1,k} + p^{n+1}_{j-2,k}\right)}{\left(\rho_{j,k} + \rho_{j-1,k}\right)/2} \\
&\quad \left. - \frac{\frac{C^2_{x:j-1/2,k}}{6}\left(p^{n+1}_{j+1,k} - 3p^{n+1}_{j,k} - 3p^{n+1}_{j-1,k} + p^{n+1}_{j-2,k}\right)}{\left(\rho_{j,k} + \rho_{j-1,k}\right)/2}\right] \\
&+ \frac{\Delta t}{\Delta y^2}\left[\frac{\left(p^{n+1}_{j,k-1} - p^{n+1}_{j,k}\right) - \frac{C_{y:j,k-1/2}}{4}\left(p^{n+1}_{j,k-2} - p^{n+1}_{j,k-1} - p^{n+1}_{j,k} + p^{n+1}_{j,k+1}\right)}{\left(\rho_{j,k-1} + \rho_{j,k}\right)/2}\right. \\
&\quad + \frac{\frac{C^2_{y:j,k-1/2}}{6}\left(p^{n+1}_{j,k-2} - 3p^{n+1}_{j,k-1} - 3p^{n+1}_{j,k} + p^{n+1}_{j,k+1}\right)}{\left(\rho_{j,k-1} + \rho_{j,k}\right)/2} \\
&\quad + \frac{-\left(p^{n+1}_{j,k} - p^{n+1}_{j,k+1}\right) + \frac{C_{y:j,k+1/2}}{4}\left(p^{n+1}_{j,k-1} - p^{n+1}_{j,k} - p^{n+1}_{j,k+1} + p^{n+1}_{j,k+2}\right)}{\left(\rho_{j,k} + \rho_{j,k+1}\right)/2} \\
&\quad \left. - \frac{\frac{C^2_{y:j,k+1/2}}{6}\left(p^{n+1}_{j,k-1} - 3p^{n+1}_{j,k} - 3p^{n+1}_{j,k+1} + p^{n+1}_{j,k+2}\right)}{\left(\rho_{j,k} + \rho_{j,k+1}\right)/2}\right]
\end{aligned}
\qquad \text{(A11.27)}
$$

As a simplification in subsequent equations, the sum of densities in adjacent cells are calculated in advance, as shown in Equation A11.28:

$$
\begin{aligned}
rhoup &= \left(rho_{j,k} + rho_{j,k-1}\right) \\
rholt = \left(rho_{j,k} + rho_{j-1,k}\right) &\qquad rhort = \left(rho_{j+1,k} + rho_{j,k}\right) \\
rhodn &= \left(rho_{j,k+1} + rho_{j,k}\right)
\end{aligned}
\qquad \text{(A11.28)}
$$

The expansion and rearrangement of Equation A11.27 then yields an expression for the pressure in any cell as a function of the pressures in surrounding cells as well as values of F and G:

$$
\begin{aligned}
p_{j,k}^{(nn+1)} = {} & \left[\frac{rhoup*rhodn*\left(rholt\left(\frac{C_{x;j+1/2,k}^2}{2} - \frac{C_{x;j+1/2,k}}{4} + 1 \right) + rhort\left(-\frac{C_{x;j-1/2,k}^2}{2} + \frac{C_{x;j-1/2,k}}{4} + 1 \right) \right)}{\Delta x^2} \right. \\
& \left. + \frac{rhort*rholt*\left(rhodn\left(\frac{C_{y;j,k-1/2}^2}{2} - \frac{C_{y;j,k-1/2}}{4} + 1 \right) + rhoup\left(-\frac{C_{y;j,k+1/2}^2}{2} + \frac{C_{y;j,k+1/2}}{4} + 1 \right) \right) p_{j,k}^{n+1}}{\Delta y^2} \right] \\
= {} & rhoup*rhodn* \left[\frac{rholt\left(\frac{C_{x;j+1/2,k}^2}{6} - \frac{C_{x;j+1/2,k}}{4} \right) p_{j+2,k}^{(nn)} + \left(rholt\left(-\frac{C_{x;j+1/2,k}^2}{2} + \frac{C_{x;j+1/2,k}}{4} + 1 \right) + rhort\left(-\frac{C_{x;j-1/2,k}^2}{6} + \frac{C_{x;j-1/2,k}}{4} \right) \right) p_{j+1,k}^{(nn)}}{\Delta x^2} \right. \\
& \left. + \frac{\left(rholt\left(\frac{C_{x;j+1/2,k}^2}{6} - \frac{C_{x;j+1/2,k}}{4} \right) + rhort\left(\frac{C_{x;j-1/2,k}^2}{2} - \frac{C_{x;j-1/2,k}}{4} + 1 \right) \right) p_{j-1,k}^{(nn)} + rhort\left(-\frac{C_{x;j-1/2,k}^2}{6} + \frac{C_{x;j-1/2,k}}{4} \right) p_{j-2,k}^{(nn)}}{\Delta x^2} \right] \\
& + rhort*rholt* \left[\frac{rhodn\left(\frac{C_{y;j,k-1/2}^2}{6} - \frac{C_{y;j,k-1/2}}{4} \right) p_{j,k-2}^{(nn)} + \left(rhodn\left(-\frac{C_{y;j,k-1/2}^2}{2} + \frac{C_{y;j,k-1/2}}{4} + 1 \right) + rhoup\left(-\frac{C_{y;j,k+1/2}^2}{6} + \frac{C_{y;j,k+1/2}}{4} \right) \right) p_{j,k-1}^{(nn)}}{\Delta y^2} \right. \\
& \left. + \frac{\left(rhodn\left(\frac{C_{y;j,k-1/2}^2}{6} - \frac{C_{y;j,k-1/2}}{4} \right) + rhoup\left(\frac{C_{y;j,k+1/2}^2}{2} - \frac{C_{y;j,k+1/2}}{4} + \right) \right) p_{j,k+1}^{(nn)} + rhoup\left(-\frac{C_{y;j,k+1/2}^2}{6} + \frac{C_{y;j,k+1/2}}{4} \right) p_{j,k+2}^{(nn)}}{\Delta y^2} \right] \\
& - \frac{rhort*rholt*rhoup*rhodn}{2\Delta t} \left[\frac{F_{j+1/2,k} - F_{j-1/2,k}}{\Delta x} + \frac{G_{j,k-1/2} - G_{j,k+1/2}}{\Delta y} \right]
\end{aligned}
\tag{A11.29}
$$

The last term of Equation A11.29 is available for explicit calculation using the arrays F and G, and shall be denoted in following equations as $\mathrm{RHS}^{(n)}$.

A11.3 - Boundary Conditions

For the calculation of pressures and velocities at every point within the computational domain, some quantities outside of this domain must be used as boundary conditions. This makes it necessary to consider a virtual domain, discussed in Section A11.4, of a size slightly larger than the computational domain. Here, a method following that of Fletcher (1988) is used to calculate of boundary conditions at the top and bottom, end wall and corners of the computational domain.

A11.3.1 - Top & Bottom

Calculation of the pressure adjacent to the top and bottom of the experimental domain requires a value of pressure, as well as two u-velocities and a v-velocity, outside the experimental domain. Values of v-velocities at the domain boundary are necessarily zero.

If Equation A11.14 is evaluated when centred at the boundary, the fact that the v-velocities and gradients of v in the x-direction go to zero at the wall results in the following discretisation:

$$\frac{p_{j,k+1} - p_{j,k}}{\left(rho_{j,k+1} + rho_{j,k}\right)/2} = \nu\frac{v_{j,k+3/2} - 2v_{j,k+1/2} + v_{j,k-1/2}}{\Delta y} \qquad \text{(A11.30)}$$

Now, to satisfy continuity (Equation A11.24) at the wall, $\partial v/\partial y$ must be zero, so $v_{j,k-1/2} = v_{j,k+3/2}$, and we also know that $v_{j,k+1/2}$ equals zero, so at the bottom this equation becomes:

$$p_{j,k+1} = p_{j,k} - 0.5*\left(rho_{j,k+1} + rho_{j,k}\right)*\left[\nu\frac{2v_{j,k+3/2}}{\Delta y} + g_y\Delta y\right] \qquad \text{(A11.31)}$$

And at the top it becomes:

$$p_{j,k-1} = p_{j,k} + 0.5*\left(rho_{j,k} + rho_{j,k-1}\right)*\left[\nu\frac{2v_{j,k+1/2}}{\Delta y} + g_y\Delta y\right] \qquad \text{(A11.32)}$$

As noted previously, the boundary conditions for v-velocities at the top and bottom are:

$$v_{j,k-1/2} = v_{j,k+3/2} \quad and \quad v_{j,k-3/2} = v_{j,k+5/2} \quad for\ wall\ at\ \ v_{j,k+1/2} \qquad \text{(A11.33)}$$

The boundary conditions for u-velocities at the top and bottom are determined by considering that to satisfy the no-slip condition at the boundary, the average of the velocities above and below the boundary must equal zero, so:

$$u_{j,k-1/2} = -\,u_{j,k+1/2} \quad and \quad u_{j,k-3/2} = -\,u_{j,k+3/2} \quad for\ wall\ at\ \ u_{j,k} \qquad \text{(A11.34)}$$

A11.3.2 - End Walls

Calculation of the pressure adjacent to the ends of the experimental domain requires a value of pressure, as well as a u-velocity and two v-velocities, outside the experimental domain. Values of u-velocities at the domain boundary are necessarily zero.

If Equation A11.2 is evaluated when centred at the boundary, the fact that the u-velocities and gradients of u in the y-direction go to zero results in the following discretisation:

$$\frac{p_{j+1,k} - p_{j,k}}{\left(rho_{j+1,k} + rho_{j,k}\right)*0.5} = \nu\frac{u_{j+3/2,k} - 2u_{j+1/2,k} + u_{j-1/2,k}}{\Delta x} \qquad \text{(A11.35)}$$

Now, to satisfy continuity (Equation A11.24) at the wall, $\partial u/\partial x$ must be zero, so $u_{j-1/2,k} = u_{j+3/2,k}$, and we also know that $u_{j+1/2,k}$ equals zero, so at the far end this equation becomes:

$$p_{j+1,k} = p_{j,k} + 0.5*\left(rho_{j+1,k} + rho_{j,k}\right)*\left[\nu\frac{2u_{j-1/2,k}}{\Delta x}\right] \qquad \text{(A11.36)}$$

And at the near end it becomes:

$$p_{j-1,k} = p_{j,k} - 0.5*\left(rho_{j,k} + rho_{j-1,k}\right)*\left[\nu\frac{2u_{j+1/2,k}}{\Delta x}\right] \qquad \text{(A11.37)}$$

As noted previously, the boundary conditions for u-velocities at the top and bottom are:

$$u_{j-1/2,k} = u_{j+3/2,k} \quad and \quad u_{j-3/2,k} = u_{j+5/2,k} \quad for\ wall\ at\ u_{j+1/2,k} \qquad \text{(A11.38)}$$

The boundary conditions for v-velocities at the top and bottom are determined by considering that to satisfy the no-slip condition at the boundary, the average of the velocities above and below the boundary must equal zero, so:

$$v_{j-1/2,k} = -v_{j+1/2,k} \quad and \quad v_{j-3/2,k} = -v_{j+3/2,k} \quad for\ wall\ at\ v_{j,k} \qquad (A11.39)$$

A11.3.3 - Corners

The pressures and velocities at the corners of the virtual domain are not considered, since they are not used in the calculation of any other quantities and do not exist in the computational domain.

A11.4 - Application to Computational Domain

The derived Equations A11.10-12 and A11.21-23 sit at the heart of the computational model described here. In writing the computer code, it was necessary to apply great care to the relation between the parameter indices used in these equations and the array ordinates used in the code.

For the calculation of velocities and pressures within the computational domain, it was necessary to calculate the value of some quantities outside of this domain to apply to the boundary condition equations. Because of this, if the computational domain consists of m x n cells, the size of quantity arrays are as follows: u, F - $m+3$ x $n+2$; v, G - $m+2$ x $n+3$; p, ρ, rhs - $m+2$ x $n+2$. A diagram of the computational and virtual domains, as well as a definition of the sign convention used in the program, is shown on Figure A11.1.

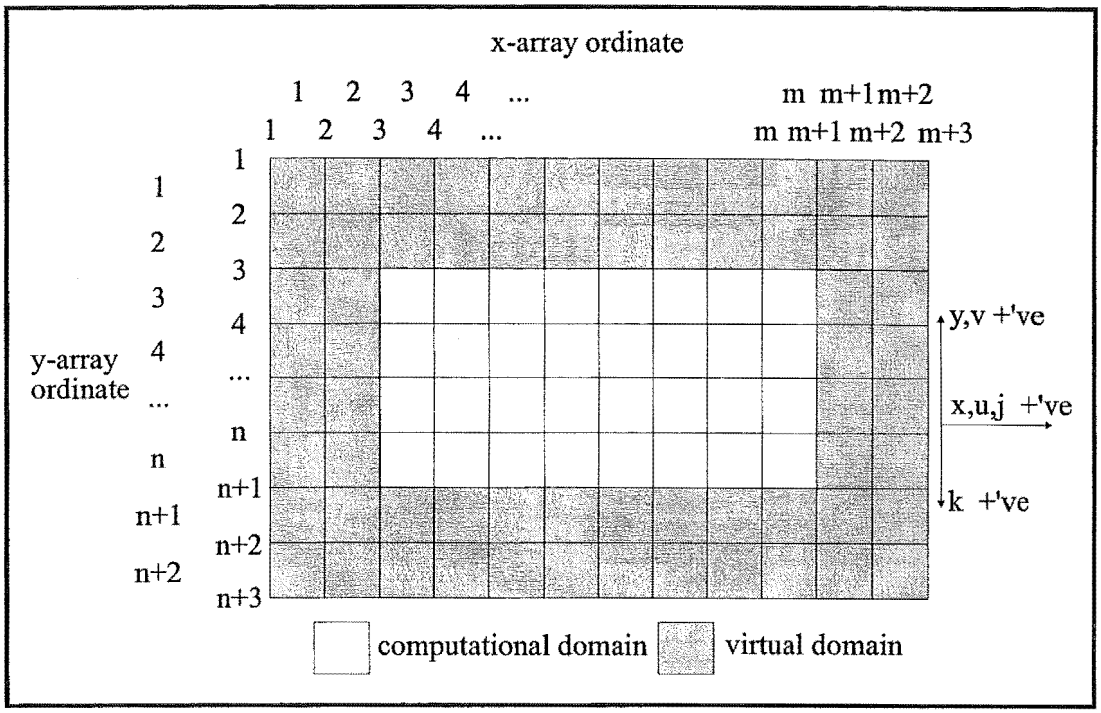

Figure A11.1 - Computational & virtual domains and sign conventions

The computational algorithms for the new *u*-velocity (Equations A11.10-12) then become:

$$\begin{aligned} cx &= u(j,k)*dt/dx \\ cy &= \left(v(j,k)+v(j,k+1)+v(j-1,k+1)+v(j-1,k)\right)*dt/(4*dy) \\ gx &= nu*dt/dx**2 \\ gy &= nu*dt/dy**2 \end{aligned} \qquad \text{(A11.40)}$$

$$\begin{aligned} F(j,k) \;=\; & u(j,k) \\ & - cx*\left(u(j+1,k)-u(j-1,k)\right)/2 \\ & - cy*\left(u(j,k-1)-u(j,k+1)\right)/2 \\ & + \left(gx + cx**2/2\right)*\left(u(j+1,k)-2u(j,k)+u(j-1,k)\right) \\ & + \left(gy + cy**2/2\right)*\left(u(j,k-1)-2u(j,k)+u(j,k+1)\right) \\ & - \left(cx**3/6 + cx*gx\right) \\ & \quad *\left(u(j+1,k) - 3u(j,k) - 3u(j-1,k) + u(j-2,k)\right) \\ & - \left(cy**3/6 + cy*gy\right) \\ & \quad *\left(u(j,k-1) - 3u(j,k) - 3u(j,k+1) + u(j,k+2)\right) \end{aligned} \qquad \text{(A11.41)}$$

$$
\begin{aligned}
u(j,k) \;=\; & F(j,k) \;-\; \big(p(j,k)-p(j-1,k)\big) \\
& \quad *\Big[2*dt\,/\,\big(dx*\big(rho(j+1,k)+rho(j,k)\big)\big)\Big] \\
& +\; \big(p(j+1,k) \;-\; p(j,k) \;-\; p(j-1,k) \;+\; p(j-2,k)\big) \\
& \quad *\Big[dt*cx\,/\,\big(2*dx*\big(rho(j+1,k)+rho(j,k)\big)\big)\Big] \\
& -\; \big(p(j+1,k) \;-\; 3p(j,k) \;-\; 3p(j-1,k) \;+\; p(j-2,k)\big) \\
& \quad *\Big[dt*cx**2\,/\,\big(3*dx*\big(rho(j+1,k)+rho(j,k)\big)\big)\Big]
\end{aligned}
\tag{A11.42}
$$

The computational algorithms for the new v-velocity (Equations A11.21-23) then become:

$$
\begin{aligned}
cx \;&=\; \big(u(j+1,k-1)+u(j+1,k)+u(j,k)+u(j,k-1)\big)*dt\,/\,(4*dx) \\
cy \;&=\; v(j,k)*dt\,/\,dy \\
gx \;&=\; nu*dt\,/\,dx**2 \\
gy \;&=\; nu*dt\,/\,dy**2
\end{aligned}
\tag{A11.43}
$$

$$
\begin{aligned}
G(j,k) \;=\; & v(j,k) \;-\; dt*g \\
& -\; cx*\big(v(j+1,k)-\;v(j-1,k)\big)\,/\,2 \\
& -\; cy*\big(v(j,k-1)-\;v(j,k+1)\big)\,/\,2 \\
& +\; (gx \;+\; cx**2\,/\,2)*\big(v(j+1,k)-\;2v(j,k)+\;v(j-1,k)\big) \\
& +\; (gy \;+\; cy**2\,/\,2)*\big(v(j,k-1)-\;2v(j,k)+\;v(j,k+1)\big) \\
& -\; (cx*gx+\;cx**3\,/\,6) \\
& \quad *\big(v(j+2,k)-\;3v(j+1,k)-\;3(j,k)+\;v(j-1,k)\big) \\
& -\; (cy*gy+\;cy**3\,/\,6) \\
& \quad *\big(v(j,k-2)-\;3v(j,k-1)-\;3v(j,k)+\;v(j,k+1)\big)
\end{aligned}
\tag{A11.44}
$$

$$
\begin{aligned}
v(j,k) \;=\; & G(j,k) \;-\; \big(p(j,k-1)-p(j,k)\big) \\
& \quad *\Big[2*dt\,/\,\big(dy*\big(rho(j,k-1)+rho(j,k)\big)\big)\Big] \\
& +\; \big(p(j,k-2) \;-\; p(j,k-1) \;-\; p(j,k) \;+\; p(j,k+1)\big) \\
& \quad *\Big[dt*cy\,/\,\big(2*dy*\big(rho(j,k-1)+rho(j,k)\big)\big)\Big] \\
& -\; \big(p(j,k-2) \;-\; 3p(j,k-1) \;-\; 3p(j,k) \;+\; p(j,k+1)\big) \\
& \quad *\Big[dt*cy**2\,/\,\big(3*dy*\big(rho(j,k-1)+rho(j,k)\big)\big)\Big]
\end{aligned}
\tag{A11.45}
$$

The computational algorithms for the new pressure (Equations A11.28-9) then become:

$$p(j,k)^{(nn+1)} = \frac{P2 + P3 - RHS}{P1} \tag{A11.46}$$

$$\begin{aligned} rhoup &= (rho(j,k) + rho(j,k-1)) \\ rholt = (rho(j,k) + rho(j-1,k)) \qquad & rhort = (rho(j+1,k) + rho(j,k)) \\ rhodn &= (rho(j,k+1) + rho(j,k)) \end{aligned} \tag{A11.47}$$

$$RHS(j,k)^{(nn)} = \frac{rhoup*rhodn*rholt*rhort}{2\Delta t}\left[\frac{F(j+1,k)-F(j,k)}{\Delta x} + \frac{G(j,k)-G(j,k+1)}{\Delta y}\right] \tag{A11.48}$$

$$P1 = \frac{rhoup*rhodn*\left(rholt\left(1-\frac{cx(j+1,k)}{4}+\frac{cx(j+1,k)**2}{2}\right)+rhort\left(1+\frac{cx(j,k)}{4}-\frac{cx(j,k)**2}{2}\right)\right)}{\Delta x^2} + \frac{rholt*rhort*\left(rhodn\left(1-\frac{cy(j,k)}{4}+\frac{cy(j,k)**2}{2}\right)+rhoup\left(1+\frac{cy(j,k+1)}{4}-\frac{cy(j,k+1)**2}{2}\right)\right)}{\Delta y^2} \tag{A11.49}$$

$$P2 = rhoup*rhodn*\left[\frac{rholt\left(\frac{cx(j+1,k)**2}{6}-\frac{cx(j+1,k)}{4}\right)p^{(nn)}_{j+2,k}+\left(rholt\left(-\frac{cx(j+1,k)**2}{2}+\frac{cx(j+1,k)}{4}+1\right)+rhort\left(-\frac{cx(j,k)**2}{6}+\frac{cx(j,k)}{4}\right)\right)p^{(nn)}_{j+1,k}}{\Delta x^2} + \frac{\left(rholt\left(\frac{cx(j+1,k)**2}{6}-\frac{cx(j+1,k)}{4}\right)+rhort\left(\frac{cx(j,k)**2}{2}-\frac{cx(j,k)}{4}+1\right)\right)p^{(nn+1)}_{j-1,k}+rhort\left(-\frac{cx(j,k)**2}{6}+\frac{cx(j,k)}{4}\right)p^{(nn+1)}_{j-2,k}}{\Delta x^2}\right] \tag{A11.50}$$

$$P3 = rhort*rholt*\left[\frac{rhodn\left(\frac{cy(j,k)**2}{6}-\frac{cy(j,k)}{4}\right)p^{(nn+1)}_{j,k+2}+\left(rhodn\left(-\frac{cy(j,k)**2}{2}+\frac{cy(j,k)}{4}+1\right)+rhoup\left(-\frac{cy(j,k+1)**2}{6}+\frac{cy(j,k+1)}{4}\right)\right)p^{(nn+1)}_{j,k+1}}{\Delta y^2} + \frac{\left(rhodn\left(\frac{cy(j,k)**2}{6}-\frac{cy(j,k)}{4}\right)+rhoup\left(\frac{cy(j,k+1)**2}{2}-\frac{cy(j,k+1)}{4}+1\right)\right)p^{(nn)}_{j,k-1}+rhoup\left(-\frac{cy(j,k+1)**2}{6}+\frac{cy(j,k+1)}{4}\right)p^{(nn)}_{j,k-2}}{\Delta y^2}\right] \tag{A11.51}$$

Note that the new pressure calculation is set up in a Gauss-Seidel scheme, as the computational technique lends itself to this method due to the fact that it is not necessary to keep two complete arrays of pressure values in memory. A diagram illustrating the relationship between algorithm indices and program array ordinates is shown in Figure A11.2.

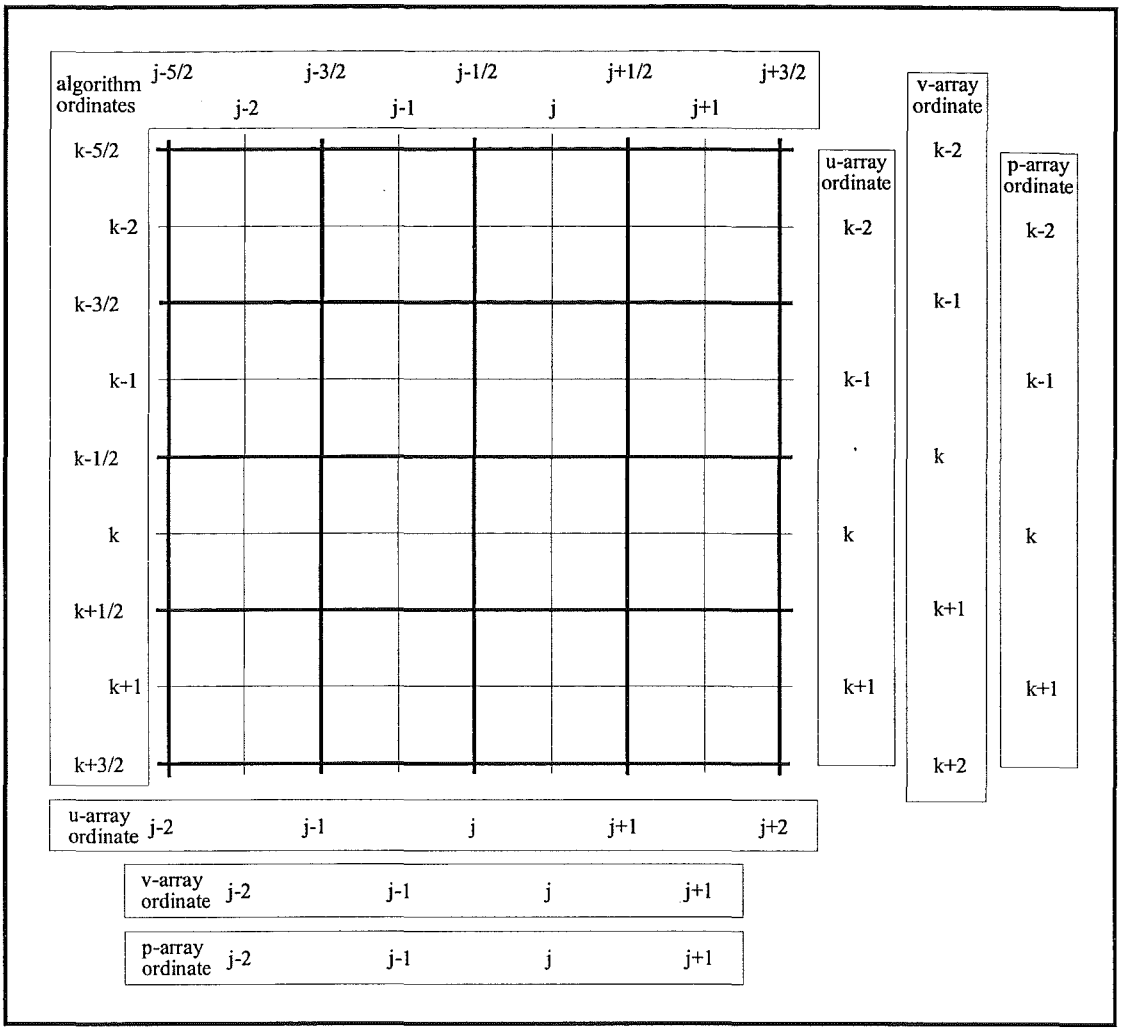

Figure A11.2 - Relation between algorithm indices and program array ordinates

A11.5 - Computer Program

The algorithms derived here have been implemented in a fortran program called *collapse*. After some preliminary steps, the program enters the *setup* subroutine. Several subroutines are called from here. The *domain* subroutine sets up the dimensions of the computational and virtual domains, while the *initialise_p*, *initialise_u* and *initialise_m* subroutines setup up the initial pressure, velocity and marker conditions, respectively.

The program then enters the *simulate* subroutine, which calls various subroutines which model the fluid motion. The *new_velocity* subroutine calculates values of the F and G arrays from Equations A11.11 and A11.22 before calling the *new_pressure* subroutine. This performs an iterative solution for the new pressure field based on

the newly calculated F and G arrays before returning to the *new_velocity* subroutine where both the new pressure and F and G arrays are used to calculate the new velocity field.

The new velocity field is then used to calculate displacements for the markers in the subroutine *marker_move*, and the new density field is calculated, based on the densities of the displaced markers, in the subroutine *new_rho*. Periodically, the state of the velocity and density fields is output in the form of a TIFF graphics file. In this image, velocity vectors and marker positions are superimposed on a representation of the density field in which low-density regions are black, high-density regions are white, and intermediate densities are assigned gray scale colours proportional to their values.

When these steps have been completed, the program advances one time step and reenters the *new_velocity* subroutine.

A printout of the fortran code associated with the program *collapse* follows.

```
program collapse

C  This program is a marker-and-cell simulation of the generation of
C  a region which collapses due to hydrostatic pressure differences.
C  It is set up initially for the case of an intermediate density fluid in a
C  three-layer system collapsing into the interfacial region of a two-
C  layer system, an action which may result in the generation of a
C  second-mode internal solitary wave.

C  Written by Nathan Schmidt - University of Canterbury - June 1996

      implicit none
      real*4 version
      parameter (version=1.0)
      character*24 date_string
      character*1 ans
      integer*2 outf,msize,simcode
      real*4 p(4002,602),rho(4002,602),u(4003,602),v(4002,603)
      real*4 mmx(8000,1200),mmy(8000,1200),mmrho(8000,1200)
      real*4 ff(4003,602),gg(4002,603)

      common p,rho,u,v,mmx,mmy,mmrho,ff,gg
C
C  Output program version and date
C
      write(*,'(/," ### PROGRAM COLLAPSE version ",
     +                        f5.2," ### "/) version
      call fdate (date_string)
      write(*,'(//,1x,a,/)') date_string
C
C  Check to see if old output files exist
C
      call checkfile()
C
C  Input output particulars (format and size)
C
      msize = 1000
      outf  = 4
      call help_read_i(outf,outf,'Output format (1d,2dv,3dm,4dvm)',
     + 2,1,0,1,15)
      call help_read_i(msize,msize,'Width of output file (pixels)',
     + 2,4,0,2,15)

      ans = 's'
10    call help_read_c(ans,ans,'Hit (s) for soliton or (l) for lock exch
     +ange simulation',2,1,0,6,15)
      if (ans.eq.'s' .or. ans.eq.'S') then
        simcode = 1
      else if (ans.eq.'l' .or. ans.eq.'L') then
        simcode = 2
      else
        go to 10
      end if
C
C  Set up and simulate a solitary wave generation or lock exchange
C

20    call setup(outf,msize,simcode)

      end
C
C-----------------------------------------------------------------------
C
      subroutine checkfile()

C     This subroutine checks to see if any density or combined output
C     files exist from previous runs, and allows their removal or
C     quitting of the program (note: program will crash if they are
C     left alone).

      character*1  ans
      logical      fexist

      inquire(file='out000.tif',exist=fexist)
      if (fexist) then
        write(*,'(/,"Output tiffs from previous runs still exist")')
        ans = 'y'
10      call help_read_c(ans,ans,'Hit (y) to delete or (n) to leave',
     +   2,1,0,7,15)
        if (ans.eq.'y' .or. ans.eq.'Y') then
          status = system('rm *.tif')
        else if (ans.eq.'n' .or. ans.eq.'N') then
          stop
        else
          go to 10
        end if
      end if

      return
      end
```

```
C
C-----------------------------------------------------------------
C
                subroutine setup(outf,msize,simcode)

C  This program is a marker-and-cell simulation of the generation of
C  an internal second-mode solitary wave by the collapse of a region
C  of intermediate density fluid into the interface of a sharply
C  stratified fluid.

      implicit none
      integer*2 m,n,outt,outf,msize,simcode
      real*4 rho1,rho2,rho3,thk1,thk2,thk3,inthk,g
      real*4 dx,dy,dt,xdc,temp,nu,t,crit1,crit2,maxuv
      character*1 ans
      real*4 p(4002,602),rho(4002,602),u(4003,602),v(4002,603)
      real*4 mmx(8000,1200),mmy(8000,1200),mmrho(8000,1200)
      real*4 ff(4003,602),gg(4002,603)

      common p,rho,u,v,mmx,mmy,mmrho,ff,gg
C
C  Input experimental domain dimensions and densities
C
10    call domain(m,n,dx,dy,rho1,rho2,rho3,thk1,thk2,thk3,
     +          inthk,xdc,simcode)
C
C  Generate initial densities, pressures, velocities and markers
C
      dx = dx/1000
      dy = dy/1000

      call initialise_p(m,n,dx,dy,rho1,rho2,rho3,thk1,thk2,
     +              thk3,inthk,xdc,simcode)
      call initialise_u(m,n)
      call initialise_m(m,n,dx,dy)
C
C  Input time step, duration and output interval
C
      temp = 20.0
      call help_read_r(temp,temp,'Enter water temperature (deg C)',
     +  2,3,0,4,15)
      if (temp.ge.0.0 .and. temp.le.40.0) then
        nu = 0.00000000055786*temp**2-
     +       0.000000049884*temp+0.0000017758
        write(*,'(/," The kinematic viscosity is calculated as ",
     +  e7.2," m^2/s")')nu
      else
        write(*,'(/,"Temperature is outside normal range")')
        call help_read_r(nu,nu,'Enter kinematic viscosity x10e6 m^2/s',
     +  2,4,2,5,15)
      endif

      g = 9.81
      crit1 = dx**2/(4*nu)
      crit2 = dx/sqrt(g*n*dy)
      if (crit2.lt.crit1) then
        crit1 = crit2
      end if

      write(*,'(/," Recommended maximum time step is ",f6.4," s")'),
     + crit1

      dt  = real(int(crit1*10000))/10000
      t   = 10.0
      outt = 1

      call help_read_r(dt,dt,'Enter time step (s)',2,1,4,1,15)
      call help_read_r(t,t,'Enter running time (s)',2,4,0,2,15)
      temp = t/dt
      write(*,'(/," Program will run for ",f6.0," time steps")'),
     + temp
      call help_read_i(outt,outt,'Output interval (time steps)',2,
     + 2,0,3,15)
      temp = real(outt)*dt
      write(*,'(/," Results will be output every ",f6.4,
     +    " seconds")')temp

      crit1 = 4*nu*dt/dx**2
      if (crit1.ge.1) then
        write(*,'(" *** WARNING *** 4*nu*dt/dx^2 must be less than 1",
     +      " for stability.")')
      else
        write(*,'(" Value of dt meets first stability criterion ",
     +         "(dt <= dx^2/4nu).")')
      end if
C     maxuv = 0.1
C     crit2 = 4*nu/maxuv**2
C     write(*,'(" Dummy value for (|u|+|v|) of ",f4.2,
C     +      " used.")')maxuv
C     if (dt.gt.crit2) then
C       write(*,'(" *** WARNING *** dt must be less than "
C     +  ,f7.5," for stability.")')crit2
C     else
C       write(*,'(" Value of dt meets third stability criterion ",
C     +         "(dt <= 4nu/(|u|+|v|)^2).")')
C     end if
      crit2 = g*n*dy*dt**2/dy**2
      if (crit2.ge.1) then
        write(*,'(" *** WARNING *** g*d*dt^2/dy^2 must be less than 1",
     +      " for stability.")')
      else
        write(*,'(" Value of dt meets second stability criterion ",
     +         "(dt <= dx/sqrt(gd)).")')
      end if

      ans = 'c'
20    call help_read_c(ans,ans,'Hit (c) to continue or (r) to re-enter v
     +alues',2,1,0,6,15)
      if (ans.eq.'c' .or. ans.eq.'C') then
        go to 30
      else if (ans.eq.'r' .or. ans.eq.'R') then
        go to 10
      else
        go to 20
      end if

30    call simulate(m,n,rho1,rho3,dx,dy,dt,nu,outt,outf,msize,t)

      return
      end
C
C-----------------------------------------------------------------
C
      subroutine domain(m,n,dx,dy,rho1,rho2,rho3,thk1,thk2,thk3,
     +              inthk,xdc,simcode)

C  This subroutine inputs the dimensions of the various regions in
C  the experimental domain as well as information about the spatial
C  discretisation of the domain.

      implicit  none
      integer*2 m,n,j,k,simcode
      real*4    dx,dy,rho1,rho2,rho3,thk1,thk2,thk3,inthk
      real*4    xda,xdc,xd,yd,rhobar,delrho,rhoz,h

      dx   = 20
      dy   = 20
      rho1  = 1000
      rho3  = 1020
      rho2  = 1010
      xda   = 500
      xdc   = 500
      thk1  = 300
      thk3  = 300
      thk2  = 100
      inthk = 10

      if (simcode.eq.1) then
C
C  Input ambient region information for SOLITON GENERATION
C
      call help_read_r(rho1,rho1,
     + 'Enter upper layer density (kg/m^3) ',2,4,2,1,15)
      call help_read_r(rho3,rho3,
     + 'Enter lower layer density (kg/m^3) ',2,4,2,2,15)
      call help_read_r(thk1,thk1,
     + 'Enter upper layer thickness (mm) ',2,3,1,3,15)
      call help_read_r(thk3,thk3,
     + 'Enter lower layer thickness (mm) ',2,3,1,4,15)
      call help_read_r(inthk,inthk,
     + 'Enter interfacial half-thickness (mm) ',2,2,1,5,15)
C
C  Input collapsing region information
C
      call help_read_r(rho2,rho2,
     + 'Enter collapsing region density (kg/m^3) ',2,4,2,6,15)
      call help_read_r(thk2,thk2,
     + 'Enter collapsing region thickness (mm) ',2,3,1,7,15)
C
C  Input physical dimensions of domain
C
      call help_read_r(xda,xda,
     + 'Enter length of ambient region (mm) ',2,4,1,8,15)
      call help_read_r(xdc,xdc,
     + 'Enter length of collapse region (mm) ',2,3,1,9,15)
      yd = thk1 + thk3
      xd = xda + xdc
C
C  State physical dimensions of domain
C
      write(*,'(/," The experimental domain has a length of ",
     + f6.1," mm and a depth of ",f5.1," mm.")') xd,yd

      elseif (simcode.eq.2) then
C
C  Input ambient region information for LOCK EXCHANGE
C  SIMULATION
C
      call help_read_r(rho1,rho1,
     + 'Enter left side density (kg/m^3) ',2,4,2,1,15)
      call help_read_r(rho2,rho2,
     + 'Enter right side density (kg/m^3) ',2,4,2,2,15)
      call help_read_r(thk1,thk1,
```

```
     + 'Enter total thickness (mm) ',2,3,1,3,15)
      call help_read_r(xdc,xdc,
     + 'Enter left side length (mm) ',2,3,1,4,15)
      call help_read_r(xda,xda,
     + 'Enter right side length (mm) ',2,3,1,4,15)

      rho3 = rho2      ! necessary to set this for output routine
      xd   = xdc+xda
      yd   = thk1
C
C  State physical dimensions of domain
C
      write(*,'(/," The experimental domain has a length of ",
     + f6.1," mm and a depth of ",f5.1," mm.")') xd,thk1

      end if
C
C  Input physical dimensions of cells
C
      call help_read_r(dx,dx,
     + 'Enter cell width (mm) ',2,4,2,10,15)
      call help_read_r(dy,dy,
     + 'Enter cell height (mm) ',2,4,2,11,15)

      m = int(xd/dx)
      n = int(yd/dy)

C
C  State cellwise dimensions of domain
C
      write(*,'(/," The experimental domain has a length of ",
     + i4," cells and a depth of ",i3," cells.")') m,n

      return
      end
C
C-----------------------------------------------------------------------
C
      subroutine initialise_p(m,n,dx,dy,rho1,rho2,rho3,thk1,thk2,
     +                        thk3,inthk,xdc,simcode)

C  This subroutine will generate an initial density stratification based
C  on two layer depths and densities as well as an interfacial
C  thickness to which it applies an hyperbolic tangent density profile
C  it also calculates the position of the collapsing region from
C  hydrostatics.

      implicit  none
      integer*2 m,n,j,k,simcode
      real*4    dx,dy,rho1,rho2,rho3
      real*4    thk1,thk2,thk3,inthk,thk3c,colcent
      real*4    xda,xdc,xd,yd,rhobar,delrho,rhoz,h
      real*4    p(4002,602),rho(4002,602),u(4003,602),v(4002,603)
      real*4    mmx(8000,1200),mmy(8000,1200),mmrho(8000,1200)
      real*4    ff(4003,602),gg(4002,603)

      common    p,rho,u,v,mmx,mmy,mmrho,ff,gg

      if  (simcode.eq.1)  then  !  INITIALISE  SOLITON  GEN
CONDITIONS
C
C  Calculate position of collapsing region
C
      thk3c = thk3 - thk2*(rho2-rho1)/(rho3-rho1)
      colcent = thk1 + thk3 - thk3c - thk2/2
C
C  State initial ambient and collapse region conditions
C
      write(*,'(/," Ambient fluid consists of a ",f5.1,
     + " mm thick layer of ",f7.2," kg/m^3 fluid on",/," top "
     + "of a ",f5.1," mm thick layer of ",f7.2," kg/m^3 fluid."
     + )') thk1,rho1,thk3,rho3
      write(*,'(/," The interfacial half-thickness at the transition "
     + "between the two layers is ",f4.1," mm.")') inthk
      write(*,'(/," The collapse region has a ",f5.1," mm "
     + " thickness of ",f7.2," kg/m^3 fluid centered",/," at ",
     + f5.1," mm below the surface.")') thk2,rho2,colcent
C
C  Initialise densities for collapsing region
C
      write(*,'(/," Initialising collapsing region densities ")')

      xdc = xdc/1000
      thk1 = thk1/1000
      thk2 = thk2/1000
      thk3 = thk3/1000
      inthk = inthk/1000
      thk3c = thk3c/1000
      colcent = colcent/1000

      do j = 1,int(xdc/dx)+1
        do k = 1,nint((thk1+thk3-thk3c-thk2)/dy)
          rho(j,k) = rho1
        end do
        do k = nint((thk1+thk3-thk3c-thk2)/dy+1),
     +         nint((thk1+thk3-thk3c)/dy+1)
          rho(j,k) = rho2
        end do
        do k = nint((thk1+thk3-thk3c)/dy+2),n+2
          rho(j,k) = rho3
        end do
      end do
C
C  Initialise densities for ambient region
C
      write(*,'(" Initialising ambient region densities ")')

      rhobar = (rho1 + rho3)/2
      delrho = (rho3 - rho1)
      h = inthk/dy
      do k = 1,n+2
        rhoz = rhobar*(1-(delrho/(2*rhobar))*tanh(-(k-1-thk1/dy)/h))
        if ((rhoz-rho1).lt.0.001) then
          rhoz = rho1
        else if ((rho3-rhoz).lt.0.001) then
          rhoz = rho3
        end if
        do j = int(xdc/dx+2),m+2
          rho(j,k) = rhoz
        end do
      end do

      elseif (simcode.eq.2) then ! INIT LOCK EXCH CONDITIONS
C
C  State initial left and right side region conditions
C
      write(*,'(/," Right side consists of a ",f5.1,
     + " mm thick layer of ",f7.2," kg/m^3 fluid."
     + )') thk1,rho1
      write(*,'(/," Left side consists of a ",f5.1," mm "
     + " mm thick layer of ",f7.2," kg/m^3 fluid."
     + )') thk1,rho2
C
C  Initialise densities for collapsing region
C
      write(*,'(/," Initialising left side densities ")')

      xdc  = xdc/1000
      thk1 = thk1/1000

      do j = 1,int(xdc/dx)+1
        do k = 1,n+2
          rho(j,k) = rho1
        end do
      end do
C
C  Initialise densities for ambient region
C
      write(*,'(" Initialising right side densities ")')

      do j = int(xdc/dx+2),m+2
        do k = 1,n+2
          rho(j,k) = rho2
        end do
      end do

      end if

      do k = 1,n+2
        do j = 1,m+2
          if (k.eq.1) then
            p(j,k) = - 0.5*rho(j,k)*9.81*dy
          else
            p(j,k) = p(j,k-1) + 0.5*(rho(j,k)+rho(j,k-1))*9.81*dy
          end if
        end do
      end do

      return
      end
C
C-----------------------------------------------------------------------
C
      subroutine initialise_u(m,n)

C  This subroutine will initialise the arrays for u and v and should
C  be called only once from the generate subroutine.

      implicit  none
      integer*2 m,n,j,k
      real*4    p(4002,602),rho(4002,602),u(4003,602),v(4002,603)
      real*4    mmx(8000,1200),mmy(8000,1200),mmrho(8000,1200)
      real*4    ff(4003,602),gg(4002,603)

      common    p,rho,u,v,mmx,mmy,mmrho,ff,gg

      write(*,'(" Initialising velocity arrays ")')

      do k = 1,n+2
        do j = 1,m+3
          u(j,k) = 0.0
        end do
      end do
      do k = 1,n+3
```

```
      do j = 1,m+2
        v(j,k) = 0.0
      end do
    end do

    return
    end
C
C-----------------------------------------------------------------
C
    subroutine initialise_m(m,n,dx,dy)

C  this subroutine will initialise the arrays for marker coordinates and
C  densities and should be called only once from the generate
C  subroutine

    implicit  none
    integer*2 m,n,j,k
    real*4    dx,dy
    real*4    p(4002,602),rho(4002,602),u(4003,602),v(4002,603)
    real*4    mmx(8000,1200),mmy(8000,1200),mmrho(8000,1200)
    real*4    ff(4003,602),gg(4002,603)

    common    p,rho,u,v,mmx,mmy,mmrho,ff,gg

    write(*,'(" Initialising marker arrays ")')

    do j = 1,2*m
      do k = 1,2*n
        mmrho(j,k) = rho(int((j-1)/2)+2,int((k-1)/2)+2)
        mmx(j,k)   = (j*dx-dx/2)/2
        mmy(j,k)   = (k*dy-dy/2)/2
      end do
    end do

    return
    end
C
C-----------------------------------------------------------------
C
    subroutine pauser
    implicit none

C  this subroutine was lifted from David Luketina (UNSW)

    character*1 ans

    write(*,'(/," press return key to continue ")')
    read(*,'(a)') ans

    return
    end
C
C-----------------------------------------------------------------
C
    subroutine write_word(word)

C  subroutine writes four byte word to TIFF file
C  writes in little endian byte order

    implicit none
    integer*2 fputc,status,i,j
    integer*4 ctr,word
    byte bite_o_file

    do i = 0,3
      ctr = word
      do j = 2,i,-1
        ctr = ctr-int(ctr/256**(j+1))*256**(j+1)
      end do
      bite_o_file = int(ctr/256**i)
      status = fputc(9,bite_o_file)
    end do

    return
    end
C
C-----------------------------------------------------------------
C
    subroutine convert(int_in,int_out)

C  lifted from David Luketina (UNSW)

    implicit none
    integer*1 int_in,int_out

    int_out = int_in

    return
    end
C
C-----------------------------------------------------------------
C
    subroutine simulate(m,n,rho1,rho3,dx,dy,dt,nu,outt,outf,msize,t)

C  This subroutine handles the time stepping and alternately calls
C  the subroutines new_velocity (to compute new u and v velocities),
C  marker_move (to move marker particles) and new_rho (to
C  compute new densities based on marker movement).  Note that
C  subroutine new_pressure (to compute new cell pressures based
C  on new densities and velocities) is called from *within* the
C  new_velocity subroutine.  The simulate subroutine also calls
C  subroutine output which writes graphical output files showing the
C  density field, velocity field and/or combined density,velocity, and
C  marker fields at specified time intervals.

    implicit  none
    integer*2 m,n,i,j,k,outt,time,outf,msize,jj,kk
    real*4    rho1,rho3,dx,dy,dt,nu,t,g
    real*4    p(4002,602),rho(4002,602),u(4003,602),v(4002,603)
    real*4    mmx(8000,1200),mmy(8000,1200),mmrho(8000,1200)
    real*4    ff(4003,602),gg(4002,603)

    common    p,rho,u,v,mmx,mmy,mmrho,ff,gg

    write(*,'(/," *****  BEGIN SIMULATION  ***** "./)')
    i = 0
    j = 0
    time = 0
    call output(m,n,dx,dy,rho1,rho3,time,outf,msize,i,dt)

    do i = 1,int(t/dt)

      call new_velocity(m,n,dx,dy,dt,nu,time,rho1,i)
      call marker_move(m,n,dx,dy,dt)
      call new_rho(m,n,dx,dy)
      j = j + 1
      if (j.eq.outt) then
        write(*,'(/,"Outputting results at time step",I5)')i
        time = i/outt
        call output(m,n,dx,dy,rho1,rho3,time,outf,msize,i,dt)
        j = 0
      end if
    end do
    if (j.gt.0) then
      write(*,'(/,"Outputting results at last time step")')
      time = i/outt
      call output(m,n,dx,dy,rho1,rho3,time,outf,msize,i,dt)
    end if

    return
    end
C
C-----------------------------------------------------------------
C
    subroutine new_velocity(m,n,dx,dy,dt,nu,time,rho1,i)

C  This subroutine explicitly computes the velocities at the new time
C  step, based on the new pressure and the velocities from the last
C  time step.

    implicit  none
    integer*2 m,n,i,j,k,time
    real*4    nu,dy,dx,dt,t1(4003,603),t2,t3,t4,t5,t6,g,sumv,sumwt
    real*4    p(4002,602),rho(4002,602),u(4003,602),v(4002,603)
    real*4    mmx(8000,1200),mmy(8000,1200),mmrho(8000,1200)
    real*4    ff(4003,602),gg(4002,603),di,dil(4002,602),rho1

    common    p,rho,u,v,mmx,mmy,mmrho,ff,gg

C
C  Computation of new ff array
C
    do j = 2,m+2
      do k = 2,n+1
        t2 = nu*(u(j+1,k)-2*u(j,k)+u(j-1,k))/(dx**2)
        t3 = nu*(u(j,k-1)-2*u(j,k)+u(j,k+1))/(dy**2)
        t4 = u(j,k)*(u(j+1,k)-u(j-1,k))/(2*dx)
        t5 = (((u(j,k-1)+u(j,k))*0.5)*((v(j,k)+v(j-1,k))*0.5))/dy
        t6 = (((u(j,k)+u(j,k+1))*0.5)*((v(j,k+1)+v(j-1,k+1))*0.5))/dy
        ff(j,k)  = u(j,k) + dt*(t2+t3-t4-t5+t6)
      end do
      ff(j,1)   = -ff(j,2)     ! bdy condition at top
      ff(j,n+2) = -ff(j,n+1)   ! bdy condition at bottom
    end do
C
C  Boundary conditions at near & far ends
C
    do k = 1,n+2
      ff(1,k)   = ff(3,k)
      ff(m+3,k) = ff(m+1,k)
    end do
C
C  Computation of new gg array
C
    g = 9.81
    do j = 2,m+1
      do k = 2,n+2
        t2 = nu*(v(j+1,k)-2*v(j,k)+v(j-1,k))/(dx**2)
        t3 = nu*(v(j,k-1)-2*v(j,k)+v(j,k+1))/(dy**2)
        t4 = v(j,k)*(v(j,k-1)-v(j,k+1))/(2*dy)
        t5 = (((u(j+1,k)+u(j+1,k-1))*0.5)*((v(j+1,k)+v(j,k))*0.5))/dx
        t6 = (((u(j,k)+u(j,k-1))*0.5)*((v(j,k)+v(j-1,k))*0.5))/dx
        gg(j,k)  = v(j,k) + dt*(t2+t3-t4-t5+t6)
```

```
      end do
      gg(j,1)   = gg(j,3)     ! bdy condition at top
      gg(j,n+3) = gg(j,n+1)   ! bdy condition at bottom
     end do
C
C  Boundary conditions at near & far walls
C
     do k = 1,n+3
      gg(1,k)   = -gg(2,k)
      gg(m+2,k) = -gg(m+1,k)
     end do
C
C  New ff's and gg's have been computed, now call new_pressure
C
     call new_pressure(m,n,dx,dy,dt,nu,rho1,i)

     write(*,'(/," computing new velocities ",$)')
C
C  Computation of new u velocities
C
     do j = 2,m+2
      do k = 2,n+1
       if (j.eq.2 .or. j.eq.m+2) then
        u(j,k) = 0.0  ! no flow through wall
       else
       t1(j,k) = dt/dx*(p(j,k)-p(j-1,k))/((rho(j,k)+rho(j-1,k))/2)
       u(j,k) = ff(j,k) - t1(j,k)
       end if
      end do
C
C  Boundary conditions at top & bottom
C
      u(j,1)   = -u(j,2)
      u(j,n+2) = -u(j,n+1)
     end do
C
C  Computation of new v velocities
C

     do j = 2,m+1
      do k = 2,n+2
      t1(j,k) = (p(j,k-1)-p(j,k))/((rho(j,k)+rho(j,k-1))/2)*dt/dy
       if (k.eq.2 .or. k.eq.n+2) then
        v(j,k) = 0.0  ! no flow through top/bottom
       else
        v(j,k) = gg(j,k) - t1(j,k) - g*dt
       end if
      end do

C
C  Boundary conditions at top & bottom
C
      v(j,1)   = v(j,3)
      v(j,n+3) = v(j,n+1)
     end do

     return
     end
C
C-----------------------------------------------------------------------
C
     subroutine new_pressure(m,n,dx,dy,dt,nu,rho1,i)

C  This subroutine computes the pressure field in the domain based
C  on the solution of a Poisson equation for pressure.  The equation
C  is solved by a Gauss-Seidel iterative method.  First the RHS array
C  of the Poisson equation is computed.  The formulation used in
C  Fletcher is not used here, as it is less simple to adapt for a
C  density-stratified situation.  Instead, the "ff" and "gg" arrays are
C  computed in the new_velocity subroutine and passed down for
C  use here.

     implicit  none
     integer*2 m,n,i,j,k,jj,kk
     integer*4 maxit,it
     real*4    dx,dy,dt,nu,tol,pold,dtol,sum,sum1,sum2,r1,r2
     real*4    p1,p2,p3,p4,p5,p6,u1,u2,v1,v2,rho1,lhs,rhs1,dil3,dil4
     real*4    g,rholt,rhort,rhoup,rhodn,rhojk,rhs(4002,602),celdil
     real*4    p(4002,602),rho(4002,602),u(4003,602),v(4002,603)
     real*4    mmx(8000,1200),mmy(8000,1200),mmrho(8000,1200)
     real*4    ff(4003,602),gg(4002,603),di(4002,602),dil,adil

     common    p,rho,u,v,mmx,mmy,mmrho,ff,gg

     write(*,'(" computing rhs for poisson calculation ",$)')

     do k = 2,n+1
      do j = 2,m+1
       rhoup = rho(j,k) + rho(j,k-1)
       rhodn = rho(j,k) + rho(j,k+1)
       rholt = rho(j,k) + rho(j-1,k)
       rhort = rho(j,k) + rho(j+1,k)
       rhs(j,k) = (rhoup*rhodn*rholt*rhort)/(2*dt)*((ff(j+1,k)-
+                ff(j,k))/dx + (gg(j,k)-gg(j,k+1))/dy)
      end do
     end do

C  At this point an array of RHS values has been calculated, and the
C  iterative solution of new pressure values should be calculated.

     write(*,'(" beginning iterative poisson calculation ",$)')

     g = 9.81
     maxit = 100000
     it = 0
     tol = 0.000001
10   dtol = 0.0
     do j = 1,m+2
      do k = 1,n+2
       pold = p(j,k)
       if (j.eq.1) then                ! near end
        p(j,k) = p(j+1,k) - 0.5*(rho(j,k)+rho(j+1,k))*
+               2*nu*u(j+2,k)/dx
       else if (j.eq.m+2) then         ! far end
        p(j,k) = p(j-1,k) + 0.5*(rho(j,k)+rho(j-1,k))*
+               2*nu*u(j-1,k)/dx
       else if (k.eq.1) then           ! top boundary
        p(j,k) = p(j,k+1) - 0.5*(rho(j,k)+rho(j,k+1))*
+              (2*nu*(-v(j,k+2))/dy+g*dy)
       else if (k.eq.n+2) then         ! bottom boundary
        p(j,k) = p(j,k-1) + 0.5*(rho(j,k)+rho(j,k-1))*
+              (2*nu*(-v(j,k-1))/dy+g*dy)
       else                            ! interior point
        rhoup = rho(j,k) + rho(j,k-1)
        rhodn = rho(j,k) + rho(j,k+1)
        rholt = rho(j,k) + rho(j-1,k)
        rhort = rho(j,k) + rho(j+1,k)
        p1 = rhodn*rhoup*(rholt*p(j+1,k)+rhort*p(j-1,k))
        p2 = rhort*rholt*(rhoup*p(j,k+1)+rhodn*p(j,k-1))
        p3 = (rhodn*rhoup*(rholt+rhort))
        p4 = (rholt*rhort*(rhodn+rhoup))
        p(j,k) = (p1/dx**2 + p2/dy**2 - rhs(j,k))/
+              (p3/dx**2 + p4/dy**2)
       end if
       dtol = dtol + abs(pold-p(j,k))
      end do
     end do

     it = it + 1

     if (it.ge.maxit) then
     write(*,'(" maximum iterations of ",i5," exceeded ",$)')maxit
     write(*,'("- rms difference on pressure array = ",f14.3)') dtol
      goto 20
     end if

     if (dtol.gt.tol) then
      goto 10
     end if

     write(*,'(" convergence to total rms ",f6.3," Pa",$)')dtol
     write(*,'(" achieved in ",i4," iterations")') it

C
C   Check boundary condition (Fletcher 17.16)
C
     sum = 0.0
     do j = 2,m+1
      do k = 2,n+1
       sum = sum +
+   ((ff(j+1,k)-ff(j,k))/dx+(gg(j,k)-gg(j,k+1))/dy)/dt*dy*dx
      end do
     end do
     lhs = sum

     write(*,'(" sum lhs 17.16 = ",f10.7,$)') sum
     sum = 0.0
     do j = 1,m+2
       sum1 = (p(j,1)-p(j,2))/(dy*(rho(j,1)+rho(j,2)))*2*dx ! top bdy
       sum = sum + sum1
     end do

     do j = 1,m+2
      sum2 = (p(j,n+2)-p(j,n+1))/(dy*(rho(j,n+2)+rho(j,n+1)))*2*dx ! btm
       sum = sum + sum2
     end do

     do k = 1,n+2
      sum1 = (p(1,k)-p(2,k))/(dx*(rho(1,k)+rho(2,k)))*2*dy    ! left side
      sum2 = (p(m+2,k)-p(m+1,k))/(dx*(rho(m+2,k)+rho(m+1,k)))*2*dy
               !right side
      sum = sum + (sum1 + sum2)
     end do
     rhs1 = sum
     write(*,'(" sum rhs 17.16 = "f10.7)') sum
C
C  Check old dilatations in experimental domain based on velocities
C  only
C
     dil = 0.0
     adil = 0.0
     do j = 2,m+1
      do k = 2,n+1
       celdil = (u(j+1,k)-u(j,k))/dx+(v(j,k)-v(j,k+1))/dy
```

```
      dil = dil + celdil
      adil = adil + abs(celdil)
C       write(*,'(" celdil j k = ",f10.6,2i5)')celdil,j,k
     end do
    end do
    write(*,'(" old sum dil = "f10.6,$)') dil
    write(*,'(" old abs sum dil = "f10.6)') adil
C
C Check new dilatations in experimental domain based on ff,gg's
C and pressures
C
    dil3 = 0.0
    dil4 = 0.0
    do j = 2,m+1
     do k = 2,n+1
      u2 = ff(j+1,k)-2*dt/dx*(p(j+1,k)-p(j,k))/(rho(j+1,k)+rho(j,k))
      u1 = ff(j,k)-2*dt/dx*(p(j,k)-p(j-1,k))/(rho(j,k)+rho(j-1,k))
      v2 = gg(j,k)-2*dt/dy*(p(j,k-1)-p(j,k))/(rho(j,k-1)+rho(j,k))
      v1 = gg(j,k+1)-2*dt/dy*(p(j,k)-p(j,k+1))/(rho(j,k)+rho(j,k+1))
      if (j.eq.2) then
       u1 = 0.0
      else if (j.eq.m+1) then
       u2 = 0.0
      end if
      if (k.eq.2) then
       v1 = gg(j,k+1) - g*dt
     +     - 2*dt/dy*(p(j,k)-p(j,k+1))/(rho(j,k)+rho(j,k+1))
       v2 = 0.0
      else if (k.eq.n+1) then
       v1 = 0.0
       v2 = gg(j,k) - g*dt
     +     - 2*dt/dy*(p(j,k-1)-p(j,k))/(rho(j,k-1)+rho(j,k))
      end if
      celdil = (u2-u1)/dx+(v2-v1)/dy
      dil3 = dil3 + abs(celdil)
      dil4 = dil4 + celdil
     end do
    end do
    write(*,'(" new sum dil = "f10.6,$)') dil4
    write(*,'(" new abs sum dil = "f10.6,$)') dil3

    call vital_output(i,it,lhs,rhs1,dil,adil)

20   return
    end
C
C-----------------------------------------------------------------
C
    subroutine new_rho(m,n,dx,dy)

C This subroutine determines the new densities by averaging the
C densities of any markers within the cell.  It uses a weighted
C average which depends on the distance of the marker from the
C center of the cell.  The subroutine first sweeps through the marker
C array, determining which cell each marker is present in.  If the cell
C has not been assigned a density yet this call, it clears the cell
C density.  Whether this is the first time or not, it then adds the
C value of marker density divided by distance from the center of the
C cell to the cell density, and adds the inverse of the distance from
C the centre of the cell to an array variable called dwt (distance
C weight).  After all markers have been addressed, any cell which
C has had its density changed will have the value divided its
C respective dwt to produce the weighted average.  The array dwt is
C then cleared to act as a pointer to say whether we're in the first
C pass or not.

    implicit  none
    integer*2 m,n,j,k,jj,kk
    real*4   dx,dy,tol,oldrho,dwti,dwt(4003,603)
    real*4   p(4002,602),rho(4002,602),u(4003,602),v(4002,603)
    real*4   mmx(8000,1200),mmy(8000,1200),mmrho(8000,1200)
    real*4   ff(4003,602),gg(4002,603)

    common   p,rho,u,v,mmx,mmy,mmrho,ff,gg

C
C Clear density and weighted distance arrays
C
    write(*,'(" computing new densities ")')

    do j = 2,m+1
     do k = 2,n+1
      rho(j,k) = 0.0
      dwt(j,k) = 0.0
     end do
    end do
    do jj = 1,2*m
     do kk = 1,2*n
C
C See which cell marker is attached to
C
      j = int(mmx(jj,kk)/dx)+2   ! yields j value of pressure cell
      k = int(mmy(jj,kk)/dy)+2   ! yields k value of pressure cell
C
C Add weighted cell density and weighted distance
C
      dwti = ((j*dx-dx*1.5)-mmx(jj,kk))**2
     +     + ((k*dy-dy*1.5)-mmy(jj,kk))**2
      if (dwti.eq.0.0) then  ! Marker is coincident with cell centre
       rho(j,k) = mmrho(jj,kk)
       dwt(j,k) = -1.0
      else
       rho(j,k) = rho(j,k) + mmrho(jj,kk)/dwti
       dwt(j,k) = dwt(j,k) + 1/dwti
      end if
     end do
    end do
C
C Divide cell density sums by weighting sums
C
    do j = 2,m+1
     do k = 2,n+1
      if (dwt(j,k).gt.0.0) then
       rho(j,k) = rho(j,k)/dwt(j,k)
      end if
     end do
    end do
C
C Assign densities for cells that have no markers in them
C
20   tol = 0.0
    do j = 2,m+1
     do k = 2,n+1
      if (dwt(j,k).eq.0.0) then
       oldrho = rho(j,k)
       rho(j,k) = (rho(j-1,k)+rho(j+1,k)+rho(j,k-1)+rho(j,k+1))/4
       tol = tol + rho(j,k) - oldrho
      end if
     end do
    end do

    if (tol.gt.0.01) then
     goto 20
    endif

    return
    end
C
C-----------------------------------------------------------------
C
    subroutine marker_move(m,n,dx,dy,dt)

C This subroutine will update the arrays for marker coordinates and
C will be called once each time step from the simulate subroutine.

    implicit  none
    integer*2 m,n,j,k,upx,upy,vpx,vpy
    real*4   dx,dy,dt,uu,vv
    real*4   uwt1,uwt2,uwt3,uwt4,vwt1,vwt2,vwt3,vwt4
    real*4   dummy0(4003,603),dummy1(4003,603)
    real*4   p(4002,602),rho(4002,602),u(4003,602),v(4002,603)
    real*4   mmx(8000,1200),mmy(8000,1200),mmrho(8000,1200)
    real*4   ff(4003,602),gg(4002,603) ,dummy2(4003,603)

    common   p,rho,u,v,mmx,mmy,mmrho,ff,gg

    write(*,'(" moving markers ",$)')
    do j = 1,m*2
     do k = 1,n*2
C
C Calculate u and v velocities based on weighted average
C
      upx = nint(mmx(j,k)/dx+1)
      upy = nint(mmy(j,k)/dy+1)
      vpx = nint(mmx(j,k)/dx+1.5)
      vpy = nint(mmy(j,k)/dy+1.5)

      uwt1 = (mmx(j,k)-(upx-2)*dx)**2 + (mmy(j,k)-(upy-1.5)*dy)**2
      uwt2 = (mmx(j,k)-(upx-1)*dx)**2 + (mmy(j,k)-(upy-1.5)*dy)**2
      uwt3 = (mmx(j,k)-(upx-2)*dx)**2 + (mmy(j,k)-(upy-0.5)*dy)**2
      uwt4 = (mmx(j,k)-(upx-1)*dx)**2 + (mmy(j,k)-(upy-0.5)*dy)**2

      vwt1 = (mmx(j,k)-(vpx-1.5)*dx)**2 + (mmy(j,k)-(vpy-2)*dy)**2
      vwt2 = (mmx(j,k)-(vpx-0.5)*dx)**2 + (mmy(j,k)-(vpy-2)*dy)**2
      vwt3 = (mmx(j,k)-(vpx-1.5)*dx)**2 + (mmy(j,k)-(vpy-1)*dy)**2
      vwt4 = (mmx(j,k)-(vpx-0.5)*dx)**2 + (mmy(j,k)-(vpy-1)*dy)**2

      uu                                                          =
(u(upx,upy)/uwt1+u(upx+1,upy)/uwt2+u(upx,upy+1)/uwt3+
     +     u(upx+1,upy+1)/uwt4)/(1/uwt1+1/uwt2+1/uwt3+1/uwt4)
      vv = (v(vpx,vpy)/vwt1+v(vpx+1,vpy)/vwt2+v(vpx,vpy+1)/vwt3+
     +     v(vpx+1,vpy+1)/vwt4)/(1/vwt1+1/vwt2+1/vwt3+1/vwt4)

      mmx(j,k) = mmx(j,k) + uu*dt
      mmy(j,k) = mmy(j,k) - vv*dt
     end do
    end do

    return
    end
C
C-----------------------------------------------------------------
C
    subroutine output(m,n,dx,dy,rho1,rho3,time,outf,msize,l,dt)
```

```
C  This subroutine will create a TIFF file showing densities scaled
C  linearly from lowest (0 = black) to highest (255 = white), with a
C  gray (= 127) border around it.  Cells will be represented by an a*a
C    pixel block, where a is an integer (represented by variable
"factor")
C  which yields the closest file width to the value of the variable
C  "msize". Superimposed on the density field graphic are vectors,
C  proportionally scaled so that they will not overlap, and markers as
C  well.  Hash pointer routine lifted from David Luketina (UNSW)

      implicit    none
      byte        bite_o_file
      integer*1   int_in
      integer*2   fputc,status,ic,i,j,k,m,n,time,t1,t2,t3,t4,t5
      integer*2   s,jj,kk,iu,iv,ii,oldiv,oldiu,xpos,ypos,skip
      integer*2   msize,nsize,factor,dvplot(5003,603),outf
      integer*2   markerpix,vectorpix,px,py,t6,t7,t7a,t8,t9,t10
      integer*2   t11,t12,t13,t14,t15,t16,t17
      integer*4   word,words(40)
      character*1  char_out
      character*3  string
      character*50  str
      character*256 fname
      real*4      hunk,hash_pointer,rho1,rho3,dx,dy,dt,tt
      real*4      uval,vval,mag,mmag,lnu,lnv,dummy,delta
      real*4      p(4002,602),rho(4002,602),u(4003,602),v(4002,603)
      real*4      mmx(8000,1200),mmy(8000,1200)
      real*4      ff(4003,602),gg(4002,603) ,mmrho(8000,1200)

      common      p,rho,u,v,mmx,mmy,mmrho,ff,gg

      vectorpix = 20
      markerpix = 20
C
C  Establish size of output plot
C

if (msize.gt.5000) then
      msize = 5000
     end if
     factor = nint(real(msize)/real(m)) ! factor = pixels per cell
     if (factor.lt.1) then
      factor = 1
     end if
     msize  = m*factor
     dummy  = msize*real(n)/real(m)
     nsize  = nint(dummy)            ! height of output graphic
C
C  Fill array dvplot with density information
C
     do kk = 1, factor*n+2
      do jj = 1, factor*m+2
       if (kk.eq.1 .or. kk.eq.factor*n+2) then
        dvplot(jj,kk) = 127
       else if (jj.eq.1 .or. jj.eq.factor*m+2) then
        dvplot(jj,kk) = 127
       else
        j = int((jj-1)/factor)+2
        k = int((kk-1)/factor)+2
        dvplot(jj,kk) = int((rho(j,k)-rho1)/(rho3-rho1)*255)
       end if
      end do
     end do
C
C  Superimpose velocity vectors on array dvplot
C
     if (outf.eq.2 .or. outf.eq.4) then
C
C  Determine vector frequency (plot every sth corner)
C
      s = int(vectorpix/factor)! plot velocity at every s'th corner cell
      if (s.lt.1) then
       s = 1
      end if
C
C  Determine magnitude of maximum velocity vector - j and k are u,v
C  indices, while jj and kk are velocity array indices
C
      mmag = 0.0
      do j = s,m-s,s
       do k = s,n-s,s
        uval = (u(j+2,k+1)+u(j+2,k+2))/2
        vval = (v(j+1,k+2)+v(j+2,k+2))/2
        mag  = (uval**2+vval**2)**0.5     ! magnitude of velocity
        if (mag.gt.mmag) then
         mmag = mag                 ! determine maximum magnitude
        endif
       end do
      end do
      write(*,'(" maximum vector magnitude ",f5.3," m/s",$)')mmag
      if (mmag.eq.0.0) then
       mmag = 100
      end if
C
C  Construct velocity vector arrows at every "s" corner of cell - j and k
C  are u,v indices, while jj and kk are velocity array indices
C
      do j = s,m-s,s
       do k = s,n-s,s
        uval = (u(j+2,k+1)+u(j+2,k+2))/2
        vval = (v(j+1,k+2)+v(j+2,k+2))/2
        mag  = (uval**2+vval**2)**0.5     ! magnitude of velocity
        lnu  = uval/mmag                  ! u-length of vector (pixels)
        lnv  = vval/mmag                  ! v-length of vector (pixels)
C
C  Define vplot array indices
C
        jj = factor*j
        kk = factor*k
C
C  Construct vector in contrast to density color
C
        ii = factor*s
        oldiv = 100
        oldiu = 100
        do ic = 0,ii
         iu = nint(ic*lnu)
         iv = nint(ic*lnv)
         if (iu.ne.oldiu .or. iv.ne.oldiv) then
          if (dvplot(jj+iu,kk-iv).gt.127) then
           dvplot(jj+iu,kk-iv) = 0
          else
           dvplot(jj+iu,kk-iv) = 255
          end if
          oldiu = iu
          oldiv = iv
         end if
        end do
       end do
      end do
      write(*,'(" velocity vectors done ",$)')
     end if

     if (outf.eq.3 .or. outf.eq.4) then
C
C  Superimpose tracer particle positions on array dvplot - j and k are
C  u,v indices, while jj and kk are velocity array indices
C
C  Determine marker frequency (plot every sth marker)
C
      s = int(markerpix/factor)
      if (s.eq.0) then
       s = 1
      end if

      do j = 2,m*2,s
       do k = 2,n*2,s
C
C  Determine dvplot array position of tracer particle and plot as "+"
C
        xpos = int(mmx(j,k)/dx*markerpix/s)+1
        ypos = int(mmy(j,k)/dy*markerpix/s)+1
        do ic = -1,1,1
         if (dvplot(xpos+ic,ypos).gt.127) then
          dvplot(xpos+ic,ypos) = 0
         else
          dvplot(xpos+ic,ypos) = 255
         end if
        end do
        do ic = -1,1,2
         if (dvplot(xpos,ypos+ic).gt.127) then
          dvplot(xpos,ypos+ic) = 0
         else
          dvplot(xpos,ypos+ic) = 255
         end if
        end do
       end do
      end do
      write(*,'(" markers done ")')
     end if


C
C  Output will handle from 0 to 999 output files
C
     t1 = int(time/100)
     t2 = int((time-int(time/100)*100)/10)
     t3 = int(time-int(time/10)*10)
     string = char(t1+48)//char(t2+48)//char(t3+48)
     fname = 'out'//string//'.tif'
     write(*,'(" opening file ",a,$)') fname(1:12)
     open(unit=9,file=fname,status='NEW',form='UNFORMATTED')
C
C  Put out TIFF format header
C
     write(*,'(" writing header ",$)')

     word = 2771273                    ! Write II42
     call write_word(word)
     word = 8                          ! Write IFD offset
     call write_word(word)
     bite_o_file = 13                  ! Write number of
     status = fputc(9,bite_o_file)             ! IFD entries
     bite_o_file = 0
```

```
      status = fputc(9,bite_o_file)
C
C  Write Image File Directory entries
C
      data words/262398,1,0,196864,1,0,196865,1,0,196866,1,8,
     + 196869,1,1,196872,1,1,262417,1,170,196885,1,1,196886,1,
     + 0,262423,1,0,327962,1,182,327963,1,182,196904,1,2,0/

      words(6) = factor*m+2
      words(9) = factor*n+2
      words(30) = (factor*m+2)*(factor*n+2)

      do j = 1,40
        word = words(j)
        call write_word(word)
      end do
C
C  Write out data
C
      write(*,'(" writing pixel array ")')
      write(*,'(" scale factor ",i3," pixels per cell,",$)')factor
      write(*,'(" plotting velocities every ",i2," cell(s)")')s
      hunk = real(factor*n+2)*real(factor*m+2)/70.0
      hash_pointer = 0.0

      do k = 1, factor*n+2
        do j = 1, factor*m+2
          int_in = dvplot(j,k)
          call convert(int_in,char_out)
          status = fputc(9,char_out)
C
C  Show loading progress
C
          hash_pointer = hash_pointer + 1.0
          if ( hash_pointer.gt.hunk ) then
            write(*,'("#",$)')
            hash_pointer = 0.0
          end if
                end do
      end do

      close(9)
      write(*,'(/," finished writing output file ")')

      return
      end
```

A11.6 - Results

The preceding program was compiled in fortran 77 and run on a DEC Alpha machine. Previously noted problems with numerical instability meant that no meaningful results were obtained, though the technique does show potential for accurate modelling of second mode waves generated by collapsing regions.

Results from a typical run are shown on Figures A11.3-4. This particular run involved a density factor of $\omega = 0.0099$, a total depth of 600 mm and a domain length of 1000 mm. The collapsing region was 50 mm thick and 300 mm long. This simulation ran for just over 2000 time steps (1.00 seconds in real time) before becoming unstable.

The state of the fluid at 1.00 seconds is shown on Figure A11.4, where it can be seen that the intermediate density region has begun to collapse into the interfacial region. Larger, cross-shaped marks on the images represent markers, though not all are shown to prevent cluttering of the diagram. Smaller dots represent vectors, which tend towards zero outside of the vicinity on the nose of the intrusion. A slight "notching" into the intrusion halfway up from the centreline is evident in the second image. Regrettably, the program ran quite slowly (the example shown took in excess of 24 hours to run) and never reached the stage where the head of the intrusion might separate from the body and form a second mode wave.

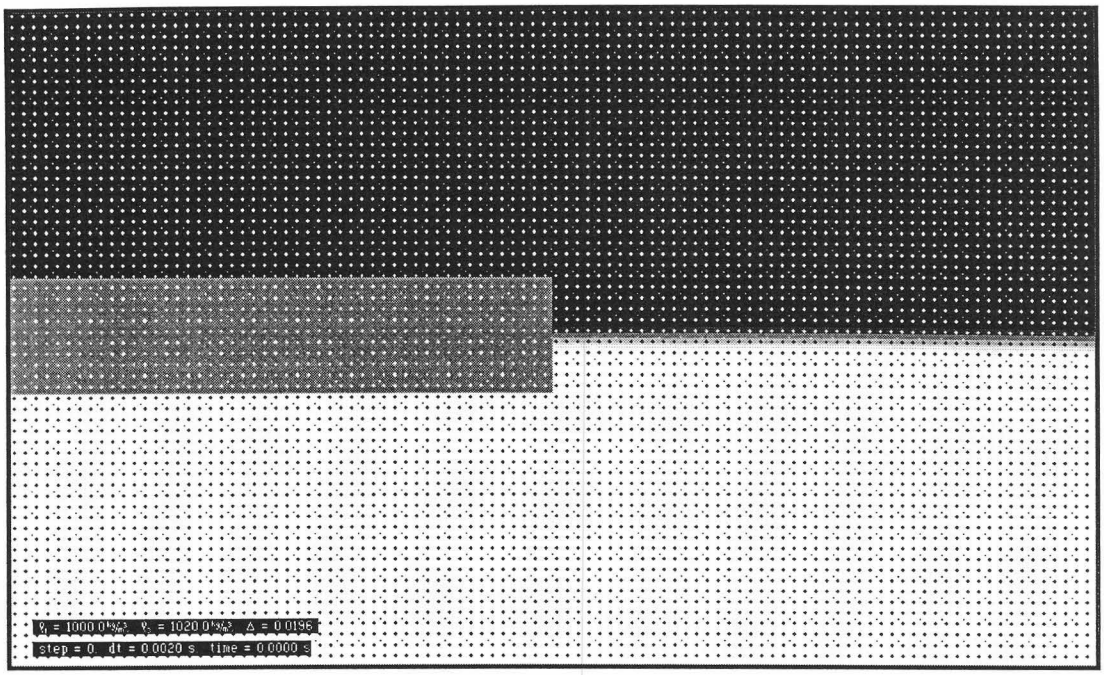

Figure A11.3 - Initial conditions (ω = 0.0099, 600 x 1000 mm domain)

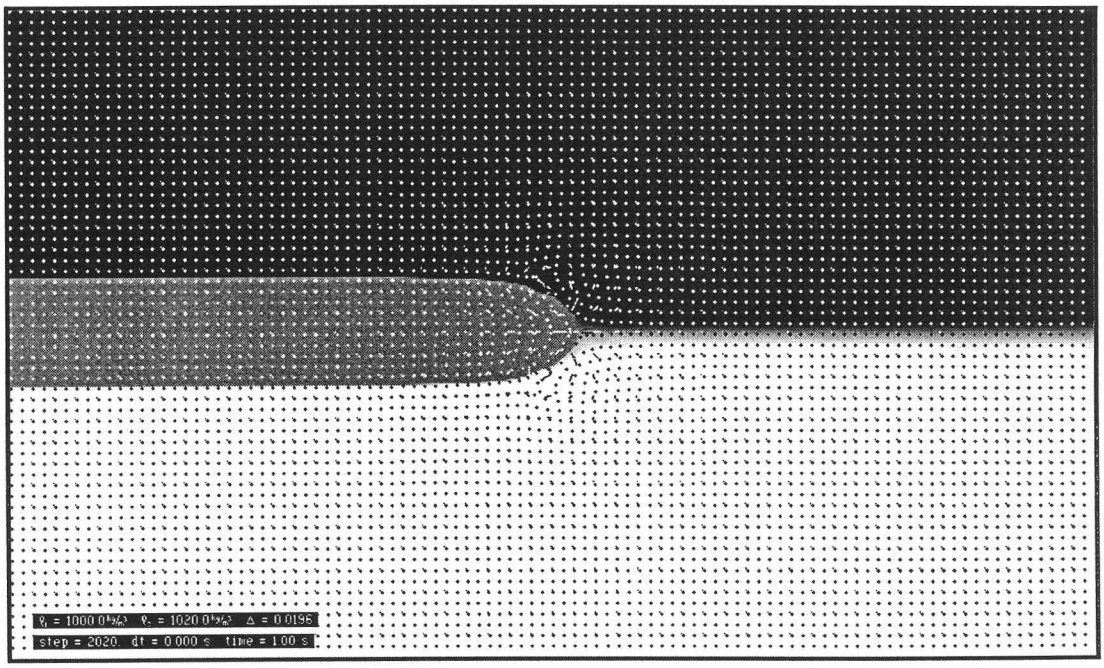

Figure A11.4 - Final conditions (ω = 0.0099, 600 x 1000 mm domain)

The development of the computational algorithm and computer code (including input and output interfaces), as well as provisional results, have been included here in the hope that they may assist future researchers in constructing an accurate model of this phenomenon.

Appendix 12 - Experimental Error

The error in measurement of quantities used in the experimental analysis is an important topic for consideration, as the analysis of this error allows an assessment of the accuracy of the data. In this section the potential errors in measured and derived experimental quantities are discussed.

A12.1 Measured Quantities

For the purposes of this exercise, measured quantities are defined as those measured directly by experimental methods. These include wave and particle displacements, wave dimensions, elapsed time, temperature and interfacial half-thickness. Limit errors (the maximum uncertainty in the observed value) were estimated for these quantities.

A12.1.1 Wave Displacement

The displacement of the wave was measured using a procedure which was discussed in Section 6.1.1. This method involved examining the video record of the experiment and recording the arrival of the stagnation point at the nose of the wave at a fixed point in the tank. It is estimated that this method provided measurements accurate to ±2 mm.

A12.1.2 Wave Dimensions and Particle Displacements

Wavelengths and amplitudes were measured using a procedure described in Section 6.1.2. This method involves superimposing a grid calibration image on a wave streakline image. Particle displacements were measured by a similar method involving photographic grid and streakline images. It is estimated that these methods provided measurements accurate to ±2 mm.

A12.1.3 Elapsed Time

Time was measured by two methods during these experiments. The video record of the experiments was marked with a digital time stamp accurate to 1/50 second. When streakline photographs were taken, the exposure time was accurate to better than 1/100 second.

A12.1.4 Temperature

Temperature was measured by two methods during these experiments. The in situ fluid layer temperatures were measured using a mercury thermometer. The temperature of fluid samples during analysis in the Anton-Paar density meter was measured using a digital thermometer. Both of these provided a measurement accuracy of 0.1 °C.

A12.1.5 Interfacial Half-Thickness

The shape of the experimental density profile was measured using a conductivity probe as described in Section 3.3.2. These probes are suited to density profiling due to their quick response and small sampling volume, though they are prone to inaccuracy due to probe damage and drift. It is also possible that the development of a boundary layer on the surface of the probe electrodes prevents complete "washing" by the fluid being measured. For these reasons, this method was not used to determine layer densities, but only the shape of the density profile.

Initial experiments involved only one measurement of density profile in the stratified region. During later experiments (refer to Appendix 8), four measurements were made along the length of the stratified region. These revealed good consistency between measurements for most experiments. Based on these observations, an experimental error of 10% is estimated for measurements of interfacial half-thickness.

A12.2 Derived Quantities

For the purposes of this exercise, derived quantities are defined as those dependent on measured quantities. This include wave and particle celerities, fluid density, densimetric factor and infinitesimal first-mode wave celerity. Limit errors for these quantities were calculated based on the limit errors of their component measured quantities.

A12.2.1 Particle Celerity

Particle celerities were determined based on measured particle displacements recorded by time-lapse photography, as discussed in Section A12.1.2. The particle celerity was calculated with the following equation:

$$v = \Delta x/\Delta t \tag{A12.1}$$

The limit error is then calculated as:

$$\delta v = v\left\{\frac{\delta\Delta x}{|\Delta x|} + \frac{\delta\Delta t}{|\Delta t|}\right\} \tag{A12.2}$$

The values of $\delta\Delta x$ and $\delta\Delta t$ have previously been established as 2 mm and 0.01 s, respectively, thus for a typical measurement with a displacement of Δx = 30 mm and elapsed time of Δt = 0.5 s, the celerity and error are calculated as v = 60 mm/s and δv = 5 mm/s, respectively.

A12.2.2 Wave Celerity

Wave celerity was measured by the method described in Section 6.1.1. This involved fitting a quadratic curve to time-displacement data and taking the first derivative of this best-fit equation to provide an expression for wave celerity.

To formulate an estimate for the magnitude of error, δc, in wave celerity, c, it is necessary to recall that the wave celerity was calculated as the time derivative of displacement, $x(t)$, where the latter was the quadratic curve fitted to observed values

of wave displacement, x, vs. elapsed time, t. There is thus no direct measure for δc, and a reasonable approach would be to use the standard errors of the coefficients for the regression of x on t (k_1, k_2 and k_3 in Appendix 6), as it is these coefficients that give the value of the derivative dx/dt. Since the regression is a second-order model (i.e. not linear but quadratic), no simple expressions are available for the standard errors on k_1, k_2 and k_3. However, based on expressions for standard errors for linear models, the standard error for dx/dt should be of the order:

$$\delta c = \text{Standard error in } \frac{dx}{dt} = O\left(\frac{s_x}{\sqrt{(t_i - \bar{t})^2}}\right) = O\left(\frac{\sqrt{\frac{\Sigma(y_i - \hat{y}_i)^2}{n-1}}}{\sqrt{(t_i - \bar{t})^2}}\right) \quad \text{(A12.3)}$$

The application of Equation A12.3 to the experimental data typically returns values for δc on the order of 10^{-4}. Comparing this to wave celerity values on the order of 10^{-2} yields an estimated value of $\delta c/c = 1\%$.

A12.2.3 Fluid Density

Fluid density was measured by extracting samples of fluid from the centre of the upper and lower fluid layers in the stratified region, and later determining the sample density using an Anton-Paar density meter, as discussed in Section 3.3.1. The layer temperature was measured immediately after the experiment and the sample was maintained at this temperature during density measurements. Therefore, the experimental error was dependent on the accuracy of both the density meter and the temperature measurement.

The Anton-Paar manual notes that the accuracy of the instrument is $\pm 5 \times 10^{-4}$ kg/m^3, with 60% of the error attributable to oscillator deviations and 40% due to changes in sample density during measurement. A maximum error of 1.9×10^{-2} kg/m^3 is also possible due to the sample temperature measurement error. This indicates a maximum error of 2.0×10^{-2} kg/m^3 in fluid sample density measurements.

A12.2.4 Densimetric Factor

The magnitude of the densimetric factor, ω, is based on measurements of the upper and lower fluid densities. The equation for this calculation is:

$$\omega = \frac{\rho_3 - \rho_1}{\rho_3 + \rho_1} \tag{A12.4}$$

Thus the error in both the numerator and denominator may be expressed as $2\delta\rho$, and the error in ω may be calculated by:

$$\delta\omega = \omega\left\{\frac{2\delta\rho}{\rho_3 - \rho_1} + \frac{2\delta\rho}{\rho_3 + \rho_1}\right\} \tag{A12.5}$$

Given that the magnitude of the first term in parentheses is much greater than the second term, this may be approximated by:

$$\delta\omega = \omega\frac{2\delta\rho}{\rho_3 - \rho_1} = \frac{2\delta\rho}{\rho_3 + \rho_1} \cong \frac{2\left(2\,x\,10^{-2}\right)}{2000} = 2\,x\,10^{-5} \tag{A12.6}$$

Thus the estimated error in measurement of the densimetric factor is not significant in terms of the presentation of its value (stated only to four decimal places), but this value may be used in the subsequent calculation of error in other quantities.

A12.2.5 Infinitesimal First-Mode Wave Celerity

The quantity c_0 is calculated based on measured values of densimetric factor, ω, and interfacial half-thickness, h, using the following equation:

$$c_0 = f(\omega,h) = \sqrt{\frac{g\,\omega\,h}{2}} \tag{A12.7}$$

The experimental measurement error may be calculated with the following equation:

$$\delta c_0 = \left|\frac{\partial f}{\partial \omega}\right| \delta\omega + \left|\frac{\partial f}{\partial h}\right| \delta h \tag{A12.8}$$

$$\delta c_0 = \sqrt{\frac{g\,h}{8\,\omega}}\,\delta\omega + \sqrt{\frac{g\omega}{8\,h}}\,\delta h = \sqrt{\frac{g}{8}}\left(\sqrt{\frac{h}{\omega}}\,\delta\omega + \sqrt{\frac{\omega}{h}}\,\delta h\right) \qquad \text{(A12.9)}$$

This expression can be rearranged to show that:

$$\frac{\delta c_0}{c_0} = \frac{1}{2}\left(\frac{\delta\omega}{\omega} + \frac{\delta h}{h}\right) \qquad \text{(A12.10)}$$

Given that the second term in parentheses dominates ($\delta h/h = 0.1$ compares to $\delta\omega/\omega$ values which range from 0.0005 to 0.0070), this expression shows that the limit error for the infinitesimal first-mode wave celerity is approximately 5%.

12.2.6 Wave Energy

The quantity E is calculated based on measured values of density, $\Delta\rho$, wavelength, λ, and wave amplitude, a, using the following equation:

$$E = 1.735\, w\, g\, \Delta\rho\, \lambda\, a^2 \qquad \text{(A12.11)}$$

The experimental measurement error may be calculated with the following equation:

$$\delta c_0 = \left|\frac{\partial E}{\partial \Delta\rho}\right| \delta\Delta\rho + \left|\frac{\partial E}{\partial \lambda}\right| \delta\lambda + \left|\frac{\partial E}{\partial a}\right| \delta a \qquad \text{(A12.12)}$$

This expression can be rearranged to show that:

$$\frac{\delta E}{E} = \left(\frac{\delta\Delta\rho}{\Delta\rho} + \frac{\delta\lambda}{\lambda} + 2\,\frac{\delta a}{a}\right) \qquad \text{(A12.13)}$$

Given that the first term on the right hand side of the equation is much smaller than either of the others, this expression can be approximated by:

$$\frac{\delta E}{E} \cong \left(\frac{\delta\lambda}{\lambda} + 2\,\frac{\delta a}{a}\right) \qquad \text{(A12.14)}$$

A12.2.7 Kinematic Viscosity

The magnitude of the kinematic viscosity, ν, is based in part on water temperature, the measurement error of which has been discussed in Section A12.1.4. The viscosity measurement error may be determined by examining the gradient of a curve fitted to data relating temperature and viscosity. Over the range of 10 - 20°C, a temperature measurement error of 0.1°C represents a potential viscosity measurement error, $\delta\nu$, of 3×10^{-9} m^2/s.

A12.3 Dimensionless Quantities

Dimensionless quantities were calculated based on combinations of measured or derived quantities for use in presenting the data. These include dimensionless amplitude and wavelength, wave celerity, energy and amplitude decay rates, Richardson and Reynolds numbers. Limit errors for these quantities were calculated based on the limit errors of their component measured and derived quantities.

A12.3.1 Dimensionless Wavelength, Amplitude and Displacement

The limit errors for the dimensionless wavelength, amplitude and displacement are calculated based on the magnitude and the limit error of the interfacial half-thickness as well as the wavelength and amplitude, respectively:

$$\delta\left(\frac{\lambda}{h}\right) = \frac{\lambda}{h}\left\{\frac{\delta\lambda}{|\lambda|} + \frac{\delta h}{|h|}\right\} \qquad \text{(A12.15)}$$

$$\delta\left(\frac{a}{h}\right) = \frac{a}{h}\left\{\frac{\delta a}{|a|} + \frac{\delta h}{|h|}\right\} \qquad \text{(A12.16)}$$

$$\delta\left(\frac{x}{h}\right) = \frac{x}{h}\left\{\frac{\delta x}{|x|} + \frac{\delta h}{|h|}\right\} \qquad \text{(A12.17)}$$

Given that the limit errors for amplitude and wavelength have been estimated to be 2 mm and that for interfacial half-thickness has been estimated to be 10%, these error expressions may be restated as:

$$\delta\left(\frac{\lambda}{h}\right) = \frac{\lambda}{h}\left\{\frac{2\text{ mm}}{|\lambda|} + 0.1\right\} \tag{A12.18}$$

$$\delta\left(\frac{a}{h}\right) = \frac{a}{h}\left\{\frac{2\text{ mm}}{|a|} + 0.1\right\} \tag{A12.19}$$

$$\delta\left(\frac{x}{h}\right) = \frac{x}{h}\left\{\frac{2\text{ mm}}{|x|} + 0.1\right\} \tag{A12.20}$$

A12.3.2 Dimensionless Wave Celerity

The limit error for the dimensionless wave celerity is calculated based on the magnitude and the limit error of the wave celerity and infinitesimal first-mode wave celerity:

$$\delta\left(\frac{c}{c_0}\right) = \frac{c}{c_0}\left\{\frac{\delta c}{|c|} + \frac{\delta c_0}{|c_0|}\right\} \tag{A12.21}$$

Given that previously established worst-case limit errors for wave celerity and infinitesimal first-mode wave celerity are 1% and 5%, respectively, it is evident that the limit error for dimensionless wave celerity is approximately 6%.

A12.3.4 Richardson Number

It was shown in Equation 7.2 that the bulk Richardson number can be expressed as a function of the wave celerity and the infinitesimal first-mode wave celerity:

$$J = \frac{g\dfrac{d\rho}{dy}}{\rho\left(\dfrac{du}{dy}\right)^2} = \frac{g\dfrac{(\rho_2-\rho_1)}{h}}{\rho\left(\dfrac{c}{h}\right)^2} = \frac{g\,\omega\,h}{c^2} = \frac{2\,c_0^2}{c^2} = f(c,c_0) \tag{A12.22}$$

The experimental measurement error may be calculated with the following equation:

$$\delta J = \left|\frac{\partial J}{\partial c}\right| \delta c + \left|\frac{\partial J}{\partial c_0}\right| \delta c_0 \qquad \text{(A12.23)}$$

This expression can be rearranged to show that:

$$\frac{\delta J}{J} = 2\left(\frac{\delta c}{c} + \frac{\delta c_0}{c_0}\right) \qquad \text{(A12.24)}$$

It has been previously established that the first term in parentheses is much smaller than the second term, so this expression may be approximated by:

$$\frac{\delta J}{J} \cong 2\,\frac{\delta c_0}{c_0} = 10\% \qquad \text{(A12.25)}$$

A12.3.5 Displacement Richardson Number

The experimental measurement error for the displacement Richardson number may be calculated with the following equation:

$$\delta(Jx/h) = \left|\frac{\partial Jx/h}{\partial x}\right| \delta x + \left|\frac{\partial Jx/h}{\partial J}\right| \delta J + \left|\frac{\partial Jx/h}{\partial h}\right| \delta h \qquad \text{(A12.26)}$$

This expression can be rearranged to show that:

$$\frac{\delta(Jx/h)}{(Jx/h)} = \frac{\delta x}{x} + \frac{\delta J}{J} + \frac{\delta h}{h} \qquad \text{(A12.27)}$$

The first term in parentheses is much smaller than the second and third terms, so this expression may be approximated by:

$$\frac{\delta(Jx/h)}{(Jx/h)} \cong \frac{\delta J}{J} + \frac{\delta h}{h} = 20\% \qquad \text{(A12.28)}$$

A12.3.6 Amplitude Decay Rate

The standard (not limit) errors in amplitude decay rates, *da/dx*, were calculated for individual experimental runs in Appendix 10.

A12.3.7 Wall Reynolds Number

The wall Reynolds number is calculated as a function of densimetric factor, ω, interfacial half-thickness, h, flume width, w, and kinematic viscosity, ν:

$$\mathrm{Re}_w = \frac{c_0 w}{\nu} = \sqrt{\frac{g\omega h}{2}}\frac{w}{\nu} \qquad \text{(A12.29)}$$

Assuming a negligible measurement error for the flume width results in the following expression for experimental error:

$$\delta \mathrm{Re}_w = \left|\frac{\partial \mathrm{Re}_w}{\partial \omega}\right| \delta\omega + \left|\frac{\partial \mathrm{Re}_w}{\partial h}\right| \delta h + \left|\frac{\partial \mathrm{Re}_w}{\partial \nu}\right| \delta\nu \qquad \text{(A12.30)}$$

The resulting error can be expressed as:

$$\frac{\delta \mathrm{Re}_w}{\mathrm{Re}_w} = \frac{1}{2}\frac{\delta\omega}{\omega} + \frac{1}{2}\frac{\delta h}{\mathrm{h}} + \frac{\delta\nu}{\nu} \qquad \text{(A12.31)}$$

A12.3.8 Interfacial Reynolds Number

The interfacial Reynolds number is calculated as a function of densimetric factor, ω, interfacial half-thickness, h, and kinematic viscosity, ν:

$$\mathrm{Re}_h = \frac{c_0 h}{\nu} = \sqrt{\frac{g\omega h}{2}}\frac{h}{\nu} \qquad \text{(A12.32)}$$

The experimental error for interfacial Reynolds number may then be calculated with the following expression:

$$\delta \mathrm{Re}_h = \left|\frac{\partial \mathrm{Re}_h}{\partial \omega}\right| \delta\omega + \left|\frac{\partial \mathrm{Re}_h}{\partial h}\right| \delta h + \left|\frac{\partial \mathrm{Re}_h}{\partial \nu}\right| \delta\nu \qquad \text{(A12.33)}$$

The resulting error can be expressed as:

$$\frac{\delta \mathrm{Re}_h}{\mathrm{Re}_h} = \frac{1}{2}\frac{\delta\omega}{\omega} + \frac{3}{2}\frac{\delta h}{\mathrm{h}} + \frac{\delta\nu}{\nu} \qquad \text{(A12.34)}$$

A12.3.9 Wavelength Reynolds Number

The wavelength Reynolds number is calculated as a function of wave celerity, c, wavelength, λ, and kinematic viscosity, ν:

$$\mathrm{Re}_\lambda = \frac{c\lambda}{\nu} \qquad \text{(A12.35)}$$

The experimental error for wavelength Reynolds number may then be calculated with the following expression:

$$\delta \mathrm{Re}_\lambda = \left|\frac{\partial \mathrm{Re}_\lambda}{\partial c}\right| \delta c + \left|\frac{\partial \mathrm{Re}_\lambda}{\partial \lambda}\right| \delta\lambda + \left|\frac{\partial \mathrm{Re}_\lambda}{\partial \nu}\right| \delta\nu \qquad \text{(A12.36)}$$

The resulting error can be expressed as:

$$\frac{\delta \mathrm{Re}_\lambda}{\mathrm{Re}_\lambda} = \frac{\delta c}{c} + \frac{\delta\lambda}{\lambda} + \frac{\delta\nu}{\nu} \qquad \text{(A12.37)}$$

A12.3.9 Energy Decay Rate

The spatial rate of energy decay is calculated with Equation 8.40:

$$\frac{dE}{dx} = w\, g\, \Delta\rho\, h^2 \left(2.71\left(\frac{a}{h}\right) + 10.67\left(\frac{a}{h}\right)^2\right) \frac{da}{dx} \qquad \text{(8.40)}$$

For large amplitude waves (a/h > 1), it is obvious that the second term within parentheses dominates Equation 8.40, which may then be approximated as:

$$\frac{dE}{dx} \cong 10.67\, w\, g\, \Delta\rho\, a^2 \frac{da}{dx} = f\left(\Delta\rho, a, \frac{da}{dx}\right) \qquad \text{(A12.38)}$$

The experimental error for energy decay rate may then be calculated with the following expression:

$$\delta\left(\frac{dE}{dx}\right) \cong \left|\frac{\partial\left(\frac{dE}{dx}\right)}{\partial\Delta\rho}\right| \delta\Delta\rho + \left|\frac{\partial\left(\frac{dE}{dx}\right)}{\partial a}\right| \delta a + \left|\frac{\partial\left(\frac{dE}{dx}\right)}{\partial\left(\frac{da}{dx}\right)}\right| \delta\left(\frac{da}{dx}\right) \qquad \text{(A12.39)}$$

The resulting error can be expressed as:

$$\frac{\delta\left(\frac{dE}{dx}\right)}{\left(\frac{dE}{dx}\right)} \cong \frac{\delta\Delta\rho}{\Delta\rho} + 2\frac{\delta a}{a} + \frac{\delta\left(\frac{da}{dx}\right)}{\left(\frac{da}{dx}\right)} \qquad \text{(A12.40)}$$

Recognising that the first term on the right hand side of Equation A12.40 is small compared to the other two allows this to be further approximated as:

$$\frac{\delta\left(\frac{dE}{dx}\right)}{\left(\frac{dE}{dx}\right)} \cong 2\frac{\delta a}{a} + \frac{\delta\left(\frac{da}{dx}\right)}{\left(\frac{da}{dx}\right)} \qquad \text{(A12.41)}$$

A12.3.10 Drag Coefficient

The spatial rate of energy decay is calculated with Equation 8.55:

$$C_D = \frac{9}{4}\left(\frac{h}{a}\right)^2 \left(2.71\frac{a}{h} + 10.67\left(\frac{a}{h}\right)^2\right)\frac{da}{dx} - \frac{3.31\lambda}{w\,Re_\lambda^{1/2}} \qquad \text{(8.55)}$$

For large amplitude waves (a/h > 1), it is obvious that the second term within parentheses dominates Equation 8.55, which may then be approximated as:

$$C_D = 24\frac{da}{dx} - \frac{3.31\lambda}{w\,\mathrm{Re}_\lambda^{1/2}} \qquad \text{(A12.42)}$$

The experimental error for energy decay rate may then be calculated with the following expression:

$$\delta C_D = 24\delta\left(\frac{da}{dx}\right) + \frac{3.31}{w\,\mathrm{Re}_\lambda^{1/2}}\delta\lambda + \frac{1}{2}\frac{3.31\lambda}{w\,\mathrm{Re}_\lambda^{3/2}}\delta\,\mathrm{Re}_\lambda \qquad \text{(A12.43)}$$

A12.4 Summary

A summary of limit errors for measured, derived and dimensionless quantities follows:

Quantity	Method	Limit Error
Wave displacement, x	Measured from video	2 mm
Wave amplitude, a	Measured from video	2 mm
Wavelength, λ	Measured from video	2 mm
Elapsed time, t	Measured from video	0.02 s
Elapsed time, t	Measured from still camera	0.02 s
Temperature, θ	Measured with thermometer	0.1 °C
Interfacial Half-thickness, h	Measured from density profile	$\frac{\delta h}{h} = 10\%$
Particle Celerity, v	$v = f(\Delta x, \Delta t)$	$\delta v = v\left\{\frac{2\text{ mm}}{\lvert\Delta x\rvert} + \frac{0.01\text{ s}}{\lvert\Delta t\rvert}\right\}$
Wave Celerity, c	$c = f(\Delta x, \Delta t)$	$\frac{\delta c}{c} = 1\%$
Fluid Density, ρ	$\rho = f(\theta)$	$\delta\theta = 2 \times 10^{-2}\text{ kg/m}^3$
Densimetric Factor, ω	$\omega = f(\rho_1, \rho_3)$	$\delta\omega = 2 \times 10^{-5}$
Infinitesimal First-Mode Wave Celerity, c_0	$c_0 = f(\omega, h)$	$\frac{\delta c_0}{c_0} = 5\%$
Wave Energy, E	$E = f(\Delta\rho, \lambda, a)$	$\frac{\delta E}{E} = \left\{\frac{\delta\lambda}{\lambda} + 2\frac{\delta a}{a}\right\}$
Kinematic Viscosity, ν	$\nu = f(\theta)$	$\delta\nu = 3 \times 10^{-9}\text{ m}^2/\text{s}$
Dimensionless Wave Amplitude, a/h		$\frac{\delta(a/h)}{(a/h)} = \left\{\frac{\delta a}{a} + \frac{\delta h}{h}\right\}$
Dimensionless Wavelength, λ/h		$\frac{\delta(\lambda/h)}{(\lambda/h)} = \left\{\frac{\delta\lambda}{\lambda} + \frac{\delta h}{h}\right\}$
Dimensionless Displacement, x/h		$\frac{\delta(x/h)}{(x/h)} = \left\{\frac{\delta x}{x} + \frac{\delta h}{h}\right\}$

Dimensionless Wave Celerity, c/c_0		$\frac{\delta(c/c_0)}{(c/c_0)} = 6\%$
Richardson Number, J		$\frac{\delta J}{J} = 10\%$
Displacement Richardson Number, Jx/h		$\frac{\delta(Jx/h)}{(Jx/h)} = 20\%$
Amplitude Decay Rate, da/dx		Standard error calculated in Appendix 10
Wall Reynolds Number, Re_W	$\mathrm{Re_w} = \mathrm{f}(\omega, h, \nu)$	$\frac{\delta \mathrm{Re}_w}{\mathrm{Re}_w} = \left\{\frac{1}{2}\frac{\delta\omega}{\omega} + \frac{1}{2}\frac{\delta h}{h} + \frac{\delta\nu}{\nu}\right\}$
Interfacial Reynolds Number, Re_h	$\mathrm{Re_h} = \mathrm{f}(\omega, h, \nu)$	$\frac{\delta \mathrm{Re}_h}{\mathrm{Re}_h} = \left\{\frac{1}{2}\frac{\delta\omega}{\omega} + \frac{3}{2}\frac{\delta h}{h} + \frac{\delta\nu}{\nu}\right\}$
Wavelength Reynolds Number, Re_λ	$\mathrm{Re_h} = \mathrm{f}(c, \lambda, \nu)$	$\frac{\delta \mathrm{Re}_\lambda}{\mathrm{Re}_\lambda} = \left\{\frac{\delta c}{c} + \frac{\delta\lambda}{\lambda} + \frac{\delta\nu}{\nu}\right\}$
Energy Decay Rate, dE/dx	$dE/dx = f(\Delta\rho, a, da/dx)$	$\frac{\delta(dE/dx)}{(dE/dx)} = \left\{2\frac{\delta a}{a} + \frac{\delta(da/dx)}{(da/dx)}\right\}$
Drag Coefficient, C_D	$C_D = f(\lambda, \mathrm{Re}_\lambda, da/dx)$	$\delta C_D = 24\delta\left(\frac{da}{dx}\right) + \frac{3.31}{w\mathrm{Re}_\lambda^{1/2}}\delta\lambda + \frac{1}{2}\frac{3.31\nu}{w\mathrm{Re}_\lambda^{3/2}}\delta\mathrm{Re}_\lambda$